Climate Monitoring and Diagnostics Laboratory

Summary Report No. 25

1998-1999

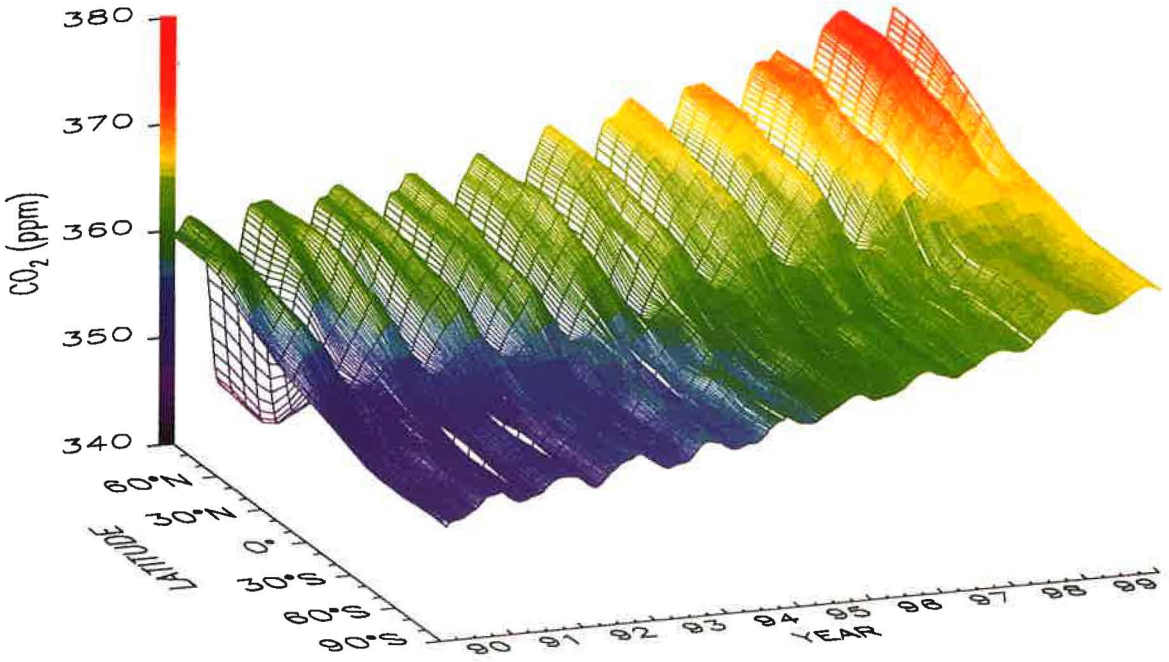

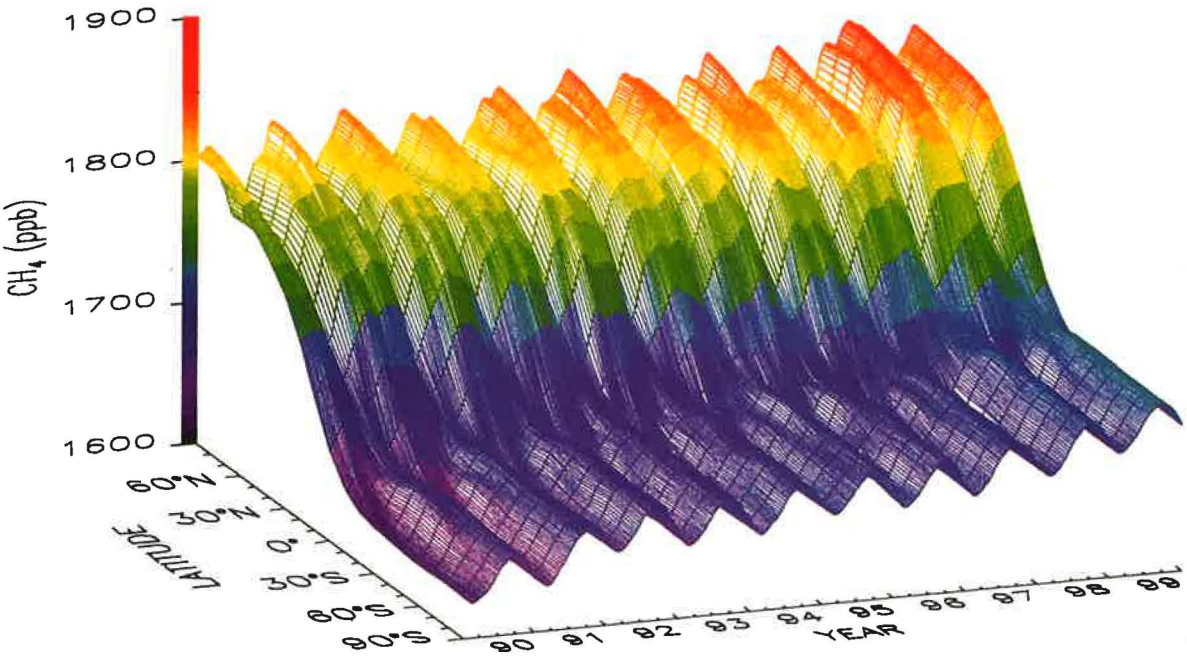

U.S. Department of Commerce
National Oceanic and Atmospheric Administration
Oceanic and Atmospheric Research

Climate Monitoring and Diagnostics Laboratory Summary Report No. 25

1998-1999

Russell C. Schnell, Editor
Daniel B. King, Editor
Rita M. Rosson, Assistant Editor

Boulder, Colorado

January 2001

U.S. DEPARTMENT OF COMMERCE
Donald L. Evans, Secretary

National Oceanic and Atmospheric Administration
Scott B. Gudes, Acting Administrator

Preface

The Climate Monitoring and Diagnostics Laboratory (CMDL) is located in Boulder, Colorado, with observatories in Barrow, Alaska; Mauna Loa, Hawaii; Cape Matatula, American Samoa; and South Pole, Antarctica. It is one of twelve components within the Office of Oceanic and Atmospheric Research (OAR) of the National Oceanic and Atmospheric Administration (NOAA). CMDL conducts research related to atmospheric constituents that are capable of forcing change in the climate of the earth through modification of the atmospheric radiative environment, for example greenhouse gases and aerosols, and those such as fluorocarbons that may cause depletion of the global ozone layer.

This report is a summary of activities of CMDL for calendar years 1998 and 1999. It is the 25th consecutive report issued by this organization and its Air Resources Laboratory/Geophysical Monitoring for Climatic Change predecessor since formation in 1972. From 1972 through 1993 (numbers 1 through 22), reports were issued annually. For 1994-1995 we began a 2-year reporting cycle, which stems from a need to most efficiently use the time and financial resources of our staff and laboratory and from a general trend towards electronic media. In this respect, CMDL has developed a comprehensive internet home page during the past several years. There you will find information about our major groups and observatories, latest events and press releases, publications, data availability, and personnel. Numerous data graphs and ftp data files are available. The URL address is http://www.cmdl.noaa.gov. Information (program descriptions, accomplishments, publications, plans, data access, etc.) on CMDL parent organizations can best be obtained via the internet. Their URL addresses are OAR: http://www.oar.noaa.gov; NOAA: http://www.noaa.gov.

This report is organized into the following major sections:

1. Observatory, Meteorology, and Data Management Operations
2. Carbon Cycle
3. Aerosols and Radiation
4. Ozone and Water Vapor
5. Halocarbons and Other Atmospheric Traces Species
6. Cooperative Programs

These are followed by a list of CMDL staff publications for 1998-1999.

Inquiries and/or comments are welcomed and should be addressed to:

Director, R/CMDL
NOAA/Climate Monitoring and Diagnostics Laboratory
325 Broadway
Boulder, CO 80305-3328
(303) 497-6074
e-mail: dhofmann@cmdl.noaa.gov

Jim Peterson joined the Geophysical Monitoring for Climatic Change (GMCC) Division of the NOAA Air Resources Laboratory in 1977. He became Director of GMCC in 1981 and served in that position until the Division was re-organized into CMDL in 1990. He was the Deputy Director of CMDL until he retired from federal service in January 1999. For the following 2 years he had a Research Scientist Emeritus position with the Cooperative Institute for Research in Environmental Sciences (CIRES).

Contents

CMDL Organization, 1999

The CMDL organization structure features five research areas organized according to scientific discipline as follows: (1) Carbon Cycle; (2) Halocarbons and Other Atmospheric Trace Species; (3) Ozone and Water Vapor; (4) Aerosols and Radiation; and (5) Observatory Operations. At the end of 1999, the laboratory staff consisted of 51 civil service personnel (excluding part-time student assistants), 33 CIRES/University of Colorado personnel, and 1 NOAA Corps officer as well as several visitors and people on special appointments.

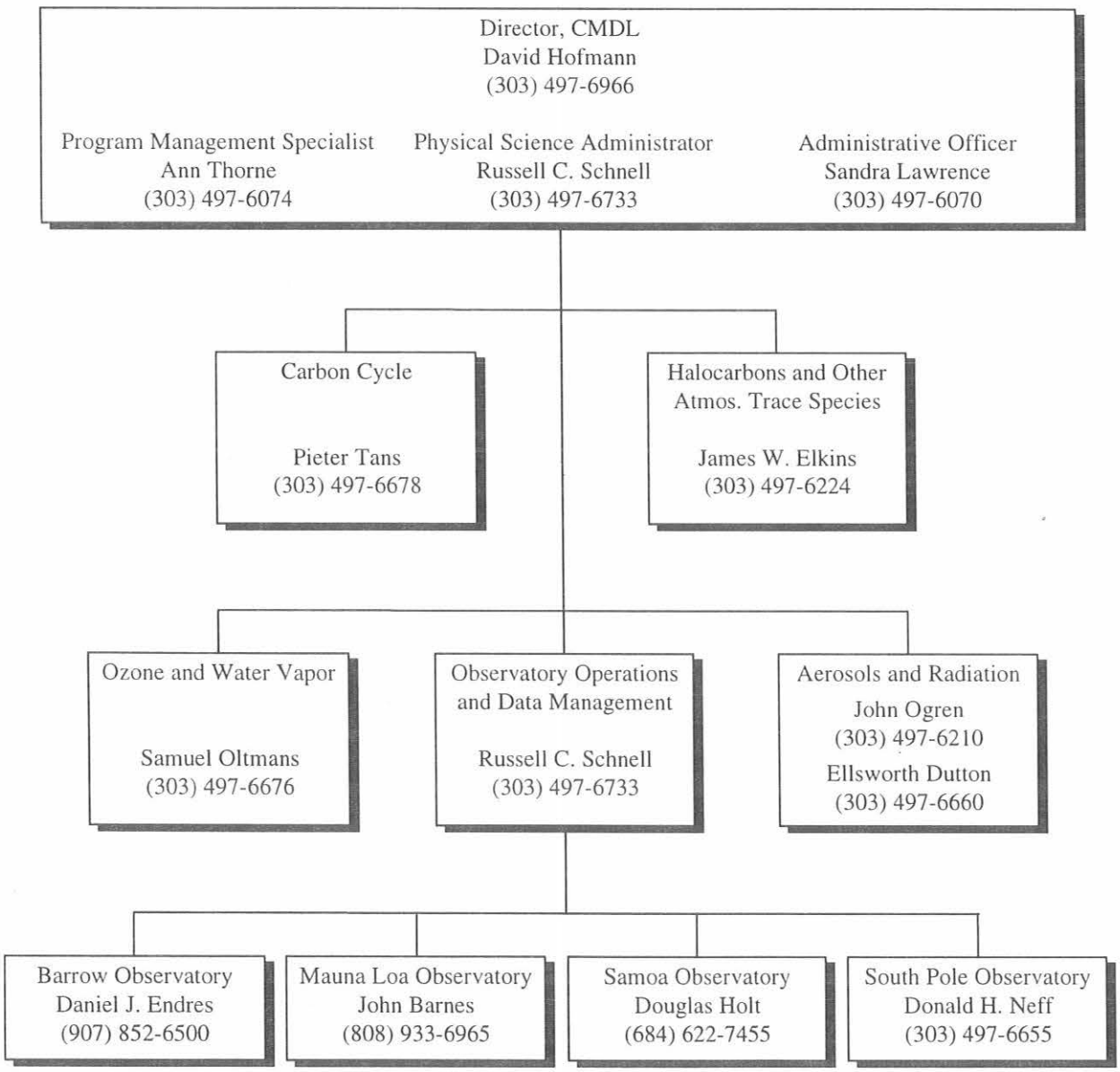

CMDL Staff, 1998/1999

Director's Office

David Hofmann, Director
Sandra Lawrence, Administrative Officer
Rita Rosson, Editorial Assistant
Russell C. Schnell, Physical Sci. Admin.
Brenda Seader, Administrative Assistant
Ann Thorne, Pgm. Management Specialist

Special Projects

Lori Bruhwiler, Physical Scientist
Eric Hackathorn, Computer Specialist

Aerosols and Radiation

Ellsworth Dutton, Meteorologist
John Ogren, Physical Scientist
Beverly O'Donnell, Secretary
Elizabeth Andrews, CIRES
Gail Anderson, USAF
Barry Bodhaine, Meteorologist
David Delene, CIRES
David Jackson, Electronic Technician
Anne Jefferson, CIRES
David Longenecker, CIRES
Donald Nelson, Meteorologist
Katie O'Gara, CIRES Student
Patrick Sheridan, Physical Scientist
Robert Stone, CIRES
Renee Tatusko, Physical Scientist
James Wendell, Electronic Technician
Norman Wood, CIRES

Ozone and Water Vapor

Samuel Oltmans, Physicist
Beverly O'Donnell, Secretary
Gloria Carbaugh, Physical Scientist
Mark Clark, CIRES
Robert Evans, Research Scientist
Joyce Harris, Res. Physical Scientist
Bryan Johnson, Res. Chemist
Michael O'Neill, CIRES
Dorothy Quincy, CIRES
Eric Rice, CIRES Student
David Sherman, CIRES
Brian Vasel, CIRES Student
Holger Vömel, CIRES

Carbon Cycle

Pieter Tans, Chief
Linda Sachetti, Secretary
Peter Bakwin, Physicist
Andrew Burr, Phys. Science Aid
J. Cervelli, CIRES Student
Thomas Conway, Research Chemist
Angela Crowley, CIRES Student
Ed Dlugokencky, Research Chemist
Laura Dukach, CIRES Student
Sara Fletcher, CIRES Gr. Res. Asst.
Brad Gore, CIRES
Douglas Guenther, CIRES
Michael Hahn, CIRES
M. Johnson, CIRES Student
Duane Kitzis, CIRES
Patricia Lang, Physical Scientist
Kenneth Masarie, Res. Physicist
John Miller, CIRES Gr. Res. Asst.
Paul Novelli, Res. Chemist
Natalie Paynter, CIRES
James T. Peterson, CIRES
Britt Stephens, CIRES
Kirk Thoning, Physicist
Michael Trudeau, CIRES
Conglong Zhao, CIRES

Halocarbons & Other Atmos. Trace Species

James Elkins, Chief
Debra Hansen, Secretary
James Butler, Research Chemist
Lori Del Negro, NRC Post Doc.
Geoffrey Dutton, CIRES
Brad Hall, Physical Scientist
Dale Hurst, CIRES
Daniel King, CIRES
Eric Kline, CIRES
Loreen Lock, CIRES
Douglas MacTaggart, CIRES
Debbie Mondeel, CIRES
Steve Montzka, Res. Chemist
Fred Moore, CIRES
David Nance, CIRES
Eric Ray, CIRES
Pavel Romashkin, CIRES
Thayne Thompson, Physicist

Observatory Operations

Russell C. Schnell, Phy. Sci. Administrator
Linda Sachetti, Secretary
Bradley Halter, CIRES
Thomas Mefford, CIRES

Daniel Endres, Station Chief, **Barrow**
Malcom Gaylord, Electronic Engineer

John Barns, Director, **Mauna Loa**
Judith Pereira, Program Support Technician
John Chin, Physicist
Darryl Kuniyuki, Electronic Engineer
Leslie Pajo, Office Automation Clerk
Steven Ryan, Physical Scientist
Robert Uchida, Electronic Technician
Alan Yoshinaga, Chemist

Douglas Holt, Station Chief, **Samoa**
Eric Sandberg, Elect. Engineer

Donald Neff, **South Pole**
Andrew Clark, Chemist
Joel Michalski, NOAA Corps

CMDL Station Information

Name:	**Barrow (BRW)**	**Mauna Loa (MLO)**
Latitude:	71.323°N	19.539°N
Longitude:	156.609°W	155.578°W
Elevation:	8 m	3397 m
Time Zone:	GMT -9	GMT -10
Office Hours:	8:00 am-5:00 pm	8:00 am-5:00 pm
Telephone		
Office hours:	(907) 852-6500	(808) 933-6965
Fax:	(907) 852-4622	(808) 933-6967
Postal Address:	Officer in Charge NOAA/ERL/CMDL Pouch 888 Barrow, AK 99723	U.S. Dept. of Commerce NOAA - Mauna Loa Observatory, Rm. 202 P.O. Box 275 Hilo, HI 96721
Freight Address:	Officer in Charge NOAA/ERL/CMDL 617 Cunningham Barrow, AK 99723	U.S. Dept. of Commerce NOAA - Mauna Loa Observatory 154 Waianuenue Ave. Hilo, HI 96720-2452

Name:	**Samoa (SMO)**	**South Pole (SPO)**
Latitude:	14.232°S	89.997°S
Longitude:	170.563°W	102.0°E
Elevation:	77 m	2837 m
Time Zone:	GMT -11	GMT +12
Office Hours:	8:00 am-5:00 pm	8:00 am - 5:00 pm
Telephone:		
Office hours:	011 (684) 622-7455	Relayed through CMDL Boulder
After hours:	011 (684) 699-9953	
Fax:	011 (684) 699-4440	
Postal Address:	Officer in Charge U.S. Dept. of Commerce NOAA - CMDL Samoa Observatory Pago Pago, American Samoa 96799	Officer in Charge NOAA/CMDL Clean Air Facility S-257 South Pole, Antarctica PSC 468 Box 402 FPO AP 96598-5402
Freight Address:	Same as above	Same as above

1. Observatory, Meteorology, and Data Management Operations

1.1. Mauna Loa Observatory

J. Barnes, J. Chin, D. Kuniyuki, L. Pajo, J. Pereira, S. Ryan, B. Uchida, and A. Yoshinaga

1.1.1. Operations

The most noticeable changes to the observatory over the past 2 years involved moving instruments into the new Network for Detection of Stratospheric Change (NDSC) building that was, for the most part, completed in late 1997. The first to move, mainly from the Keeling building, were several solar radiation instruments from CMDL and the cooperative programs. The largest instrument, the new National Institute for Water and Atmospheric Research (NIWA) ultraviolet/visible (UV/VIS) spectrophotometer, was mounted at the top of a chimney above the solar radiation room. The older spectrophotometer that had been in service for 5 years at MLO was moved to Boulder. The CMDL lidars were the next instruments to be moved. The separate frames for the ruby and Nd:YAG lidar systems were redesigned and combined to form a single structure situated in two rooms of the NDSC building. A third room functions as a control room. The CMDL Carbon Cycle Greenhouse Gases (CCGG) group instruments (carbon dioxide, methane, and carbon monoxide) are now in their own room that includes a new flask sampling system. The CMDL Halocarbons and other Atmospheric Trace Species (HATS) group instruments were likewise moved into their own room that was modified with extra thermostat-controlled ventilation to main a constant temperature. Sample lines into the NDSC building from the 40-m tower were routed into both the CCGG and HATS rooms. The computer network hardware and an electrical shop area take up two additional rooms. Significant modifications were made to the electrical system by adding ceiling outlets in several of the rooms. A portion of the building is reserved for the Jet Propulsion Laboratory/National Aeronautics and Space Administration (JPL/NASA) ozone lidar currently housed in two trailers. Some work was done on the JPL rooms, and the lidar will be moved in the summer of 2000.

The U.S. Army installed an antenna for a new radio repeater system. The system introduced an intermittent noise in the NIWA UV/VIS spectrometer that was difficult to trace. The antenna will be moved down and away from the observatory and will use a directional antenna to eliminate the interference. University groups initiated two new weekly sampling programs; the Division of Geological and Planetary Sciences at Caltech installed an interplanetary dust collector, and the State University of New York installed a CO isotope sampler. The weekly samples are collected in 1000-psi cylinders that must be shipped as hazardous material. The Department of Energy (DOE) radon program was terminated and the instrument removed from the tower base and shipped back to New York. Two new NIWA spectrometers for NO_2 and BrO were installed in a chimney in the solar radiation room in the NDSC building.

Calibrations of 2-4 weeks duration by visiting instruments to the observatory continued to increase. There were many repeat visits, as well as several new groups. For the most part, the instruments are various solar radiation measurements of varying complexity. Computer network connections were added to the visitor building to accommodate these programs. Three Japanese astronomers visited the MLO site to see if it would be a suitable location for radio astronomy experiments. The U.S. Air Force conducted radio frequency (RF) and sun viewing tests at MLO to assess the suitability of the site for a solar observatory. MLO is attractive to new astronomy groups since the Mauna Kea facilities are full under the current usage plan. NOAA Environmental Technology Laboratory (ETL) and CMDL took advantage of the low water vapor above MLO during the El Niño to conduct unique infrared (IR) measurements by installing an ETL Fourier transform infrared (FTIR) spectrometer in the Microwave building that was operated during March and April 1998.

Movie and magazine groups used the observatory road to film a shoe commercial and four car commercials. Since the film crew vehicles can cause damage to the fragile road, sizable fees were charged for road access that directly funded road repair. There was a long drought on the Big Island in 1998 due to El Niño reducing the northeastern trade winds dramatically, thus reducing orographic rain on the Big Island. There were brush fires in 1998 and 1999 that impacted the observatory observations, and for the first time in many years, snow prevented access to the observatory in December 1999. A meteorologist was hired by the University of Hawaii to forecast the summit and upper air weather for Mauna Kea. These forecasts have been useful for lidar observing conditions and visiting solar radiation groups.

The only change in staffing at MLO was the retirement of Judy Pereira. She was with the observatory for over 30 years and will be greatly missed.

Outreach

There was an increase in visitors to the observatory in the past 2 years, many of whom used the Internet to make arrangements and get information. A group from the U.S. Department of Energy and the Japan Ministry of International Trade and Industry visited twice; these visitors were attending meetings on a carbon dioxide sequestration experiment that will be conducted on the western side of the Big Island. Tours were also given to the Department of Commerce (DOC) Deputy Secretary, the NOAA Administration Deputy Assistant Secretary, and the NOAA Ocean and Atmospheres Deputy Under Secretary. Several classes from the University of Hawaii at Hilo toured MLO.

The MLO station chief lectured on climate change and pollution to a group of 50 senior citizens at the Kilauea Volcano Visitors Center and to a group at the Volcano National Park. He also judged the Hawaii County Science Fair. Two high school summer students were mentored each summer on short data analysis projects. A local high school teacher and a high school science student also worked summers on the lidar program.

The VOGNET program continued in 1998-1999. For this program, students make regular observations of volcanic aerosols from a network of schools spaced around the island in order to study the distribution and relative levels of volcanic haze or "vog" in Hawaii. Each school uses a Gardner condensation nuclei (CN) counter and a 2-wavelength sunphotometer to make several measurements per day. By the end of 1999 the students had made over 6000 observations in 3.5 years. In the summer of 1998 an inexpensive automated CN counter was developed at MLO that uses common plumbing hardware, solenoid valves, a laser pointer, and a PC. This machine has been deployed at sites around the island to

characterize the 24-hr cycle of vog concentration. An improved version was built by students at Hawaii Preparatory Academy as a science fair project that advanced through district and state fairs to eventually win third prize in the environmental division of the International Science Fair in Philadelphia in the spring of 1999.

Computers/Network

There were many changes to the MLO computer network during 1998-1999. In September 1998 the VAX was shut down and sent to Boulder and replaced by two NT servers. One is dedicated to function as an e-mail server, and the other is a main file, print, and primary administrative server for the Hilo office. The old NT server is now a dedicated web server. In January of 1998 we received about 60,000 MLO Web page hits per month, and by the end of December 1999 we were receiving about 190,000 per month.

In February 1998 the Hilo office switched to a 128-k frame relay circuit. In March of the same year the mountain site switched over to a 56-k frame relay circuit. Because of limitations of the telephone company's circuitry, 128 k at the mountain site is not available.

The network hubs and routers were moved from the Keeling building to the computer room in the NDSC building. The site's fiber optic cables were reconfigured with new topology. The NDSC building was also wired with fiber optic cabling to each room, and 10 base–T hubs are now being used with the existing coax-fiber network in various locations at the site.

At the end of 1999 MLO installed a five-camera security and sky-observation network operation at the observatory. The original camera is still located at the High Altitude Observatory facing the northern sky. The second camera is mounted about halfway up the high tower facing the eastern sky. The third camera, sponsored by JPL/NASA, is facing the southwestern sky. The fourth camera, sponsored by the Atmospheric Environment Service (AES) (Canada), is an all-sky camera vertical with the radiation deck. The fifth camera, located on the NDSC sundeck, is used to monitor the Brewer's tracking of the sun. All of the camera images can be seen on MLO's web site. About 80% of the hits to the MLO web site are looking at these live images (www.cmdl.noaa.gov/obop/mlo).

Remote control of much of the observatory's equipment was a major focus in 1999. A system to remotely turn "on" or "off" the lidar cooler was implemented as well as remote control of power to computers and other devices. Software control or monitoring through the network is available to the following systems: SO_2, new Scripps CO_2 computer, solar dome controller, AES Brewers, surface ozone, the camera computers, the power controller computer, the mountain server, and the main observer's computer. Links to monitor the CCGG and Chromatographs for Atmospheric Trace Species (CATS) gas chromatographs (GC) are available from MLO's website.

Network usage of administrative programs has increased. Payroll time and attendance is now done through the Hilo network instead of the phone line. Travel, training, and purchase orders are also completed through the network connection with the Boulder support group. In 1999 the Smithsonian Institution left MLO's Hilo network after receiving their own internet line. The U.S. Fish and Wildlife Service (FWS) has since been connected to the network and has taken the IP addresses of the Smithsonian Institution. A wireless bridge connects the FWS office to MLO's network across the street.

1.1.2. PROGRAMS

Table 1.1 summarizes the programs in operation or terminated at MLO during 1998-1999. Relevant details on some of the respective programs are as follows:

Gases

Carbon dioxide. The CMDL Siemens Ultramat-3 IR CO_2 analyzer, along with the associated equipment and the other CCGG measurement instruments (CH_4 and CO), were moved on November 13, 1998, from the original concrete block building built in 1957 to the newly constructed NDSC facility. The new location is well lighted, temperature regulated, and is approximately 15 m southeast of the old concrete block building. On November 13, 1998, a new target reference gas was added into the CO_2 system for its once daily calibration between W1, the low span reference gas, and W2, the high span reference gas. The target reference gas has a CO_2 concentration value in between W1 and W2 reference gases. The Scripps Institution of Oceanography (SIO) Applied Physics IR CO_2 analyzer (see listing under Cooperative Programs, Table 1.1) and its associated equipment remained in the same location. Both the CMDL and SIO CO_2 programs were operated without major problems throughout 1998-1999. Routine maintenance and calibrations were undertaken on both instruments as scheduled. SIO was required to purchase a freezing unit for its CO_2 program because of the CCGG equipment relocation.

The weekly CO_2, CH_4, and other gas sampling programs, using flasks at MLO and at Cape Kumukahi, were carried out according to schedule throughout the year without major problems. The Martin and Kitzis Sampler (MAKS) sampling unit for Cape Kumukahi was discontinued in early 1998 and was replaced with a new Air Kitzis sampler (AIRKIT) sampling unit. Since November 20, 1998, the 0.5-L flasks were replaced with the 2.5-L flasks for the weekly samplings through the CO_2 analyzer at MLO.

CO_2 emissions from the Mauna Loa volcano measured at MLO resumed their steady decline in 1998-1999 after a brief factor-of-2 rise in 1994-1995 that was probably due to new emissions from the upper southwest rift. Because emissions from the volcanic vents at the Mauna Loa caldera and along the northeast rift zone at Mauna Loa have fallen by over 2 orders of magnitude since 1984, the tables for MLO outgassing that appeared in prior reports have been discontinued. They will be reinstated should MLO outgassing become active again, as is the case following major eruptions.

Carbon monoxide. The Trace Analytical RBA3 reduction gas analyzer for the continuous measurement of CO mixing ratios returned from CMDL (Boulder) on November 12, 1998, and was back in operation at MLO on November 13, 1998. The stream selection valve malfunctioned in early 1999 and caused a brief downtime; otherwise, the system has been operating continuously.

Methane. The HP6890 methane GC system operated without problems during 1998-1999. Occasionally the flame died out during the normal runs and relighting was difficult. An increase in the hydrogen gas flow in the GC from 45 mL min^{-1} to 47 mL min^{-1} corrected the problem. Since April 1996, CMDL has purchased the nitrogen carrier gas (99.999% pure, size 200 cylinder, 6.5 m^3 volume) and the oxidizer from Gaspro in Hilo for the CH_4 program at discounted prices. The oxidizer is 40% oxygen in balanced nitrogen with an analytical accuracy of ±2% and an analysis precision of ±1%, (size 200 cylinder 5.7 m^3 volume). The usages of these gases are one cylinder of nitrogen per 5 weeks and one cylinder of oxidizer per 2.5 weeks.

TABLE 1.1. Summary of Measurement Programs at MLO in 1998-1999

Program	Instrument	Sampling Frequency
Gases		
CO_2	Siemens Ultramat-3 IR analyzer†	Continuous
	2.5-L glass flasks, through analyzer	1 pair wk^{-1}
CO	Trace Analytical RGA3 reduction gas analyzer no. R5†	Continuous
CO_2, CH_4, CO, and ^{13}C, ^{18}O of CO_2	2.5-L glass flasks, MAKS pump unit	1 pair wk^{-1}
	AIRKIT pump unit, 2.5-L glass flasks‡	1 pair wk^{-1}
CH_4	3-L evacuated glass flasks‡	1 pair wk^{-1}
	HP6890GC†	Continuous
SO_2	TECO model 43S pulsed-fluorescence analyzer; 4, 10, 23, 40 m†	Continuous
Surface O_3	Dasibi 1003-AH UV absorption ozone monitor†	Continuous
Total O_3	Dobson spectrophotometer no. 76†	3 day^{-1}, weekdays
O_3 profiles	Dobson spectrophotometer no. 76† (automated Umkehr method)	2 day^{-1}
	Balloonborne ECC sonde	1 wk^{-1}
N_2O, CFC-11, CFC-12, CFC-113, CH_3CCl_3, CCl_4, SF_6, HCFC-22, HCFC-141b, HCFC-142b, CH_3Br, CH_3Cl, CH_2Cl_2, $CHCl_3$, C_2HCl_3, C_2Cl_4, H-1301, H-1211, H-2402, HFC-134a	850-mL, 2.5-L, and 3-L stainless steel flasks	1 sample wk^{-1}
CFC-11, CFC-12, CFC-113, N_2O, CCl_4, CH_3CCl_3	HP5890 automated GC†	1 sample h^{-1}
N_2O	Shimadzu automated GC†	1 sample h^{-1}
CFC-11, CFC-12, CFC-113, N_2O, CH_3CCl_3, CCl_4, CH_3Br, CH_3Cl, H-1211, SF_6, HCFC-22	Automated CATS GC	1 sample h^{-1}
Aerosols		
Condensation nuclei	Pollak CNC	1 day^{-1}
	TSI CNC†	Continuous
Optical properties	Three-wavelength nephelometer: 450, 550, 700 nm	Continuous
Aerosol light absorption (black carbon)	Aethalometer†	Continuous
Stratospheric and upper tropospheric aerosols	Nd:YAG lidar: 532-, 1064-nm wavelengths	1 profile wk^{-1}
Solar Radiation		
Global irradiance	Eppley pyranometers with Q, OG1, and RG8 filters†	Continuous
Direct irradiance	Eppley pyrheliometer with Q filter†	Continuous
	Eppley pyrheliometer with Q, OG1, RG2, and RG8 filters†	3 day^{-1}
	Eppley/Kendall active cavity radiometer†	1 mo^{-1}
Diffuse irradiance	Eppley pyrgeometer with shading disk and Q filter†	Continuous
UV solar radiation	Yankee Environmental UVB pyranometer (280-320 nm)†	Continuous
Turbidity	J-202 and J-314 sunphotometers with 380-, 500-, 778-, 862-nm narrowband filters	3 day^{-1}, weekdays
	PMOD three-wavelength sunphotometer†: 380, 500, 778 nm; narrowband	Continuous
Column water vapor	Two-wavelength tracking sunphotometer: 860, 940 nm† (2 instruments)	Continuous
Meteorology		
Air temperature	Aspirated thermistor, 2-, 9-, 37-m heights†	Continuous
	max.-min. thermometers, 2.5-m height	1 day^{-1}, weekdays
Air temperature (30-70 km)	Lidar	1 profile wk^{-1}
Temperature gradient	Aspirated thermistors, 2-, 9-, 37-m heights†	Continuous
Dewpoint temperature	Dewpoint hygrometer, 2-m height†	Continuous
Relative humidity	TSL 2-m height†	Continuous
Pressure	Capacitance transducer†	Continuous
Wind (speed and direction)	8.5-, 10-, and 38-m heights†	Continuous
Precipitation	Rain gauge, 20 cm	5 wk^{-1}
	Rain gauge, 20 cm§	1 wk^{-1}
	Rain gauge, tipping bucket†	Continuous
Total precipitable water	Foskett IR hygrometer†	Continuous

TABLE 1.1. Summary of Measurement Programs at MLO in 1998-1999—continued

Program	Instrument	Sampling Frequency
Precipitation Chemistry		
pH	pH meter	1 wk^{-1}
Conductivity	Conductivity bridge	1 wk^{-1}
Cooperative Programs		
CO_2 (SIO)	Applied Physics IR analyzer†	Continuous
CO_2, ^{13}C, N_2O (SIO)	5-L evacuated glass flasks*	1 pair wk^{-1}
CO_2, CO, CH_4, $^{13}C/^{12}C$ (CSIRO)	Pressurized glass flask sample	3 pair mo^{-1}
CH_4, CH_3CCl_3, CH_3Cl, HCFC-22, CFC-12, CFC-11, CFC-113, CO, CO_2, N_2O, $CHCl_3$, CCl_4 (OGIST)	Pressurized stainless steel flasks* (Ended 6/99)	3 wk^{-1}
O_2 analyses (SIO)	5-L glass flasks through tower line and pump unit*	3 $(2\ mo)^{-1}$
O_2 analyses (URI)	3-L glass flasks through tower line and pump unit ‡ (Ended 12/98)	2 $(2\ mo)^{-1}$
CH_4 ($^{13}C/^{12}C$) (Univ. of Washington)	35-L evacuated flask (Ended 12/98)	2 mo^{-1}
Total suspended particulates (DOE)	High-volume sampler	Continuous (1 filter wk^{-1})
Ultraviolet radiation (CSU-USDA)	Multi-wavelength radiometer (direct, diffuse, shadow band)	Continuous
Radionuclide deposition (DOE)	Ion-exchange column (Started 1/98)	Quarterly sample
Aerosol chemistry (Univ. of Calif.-Davis)	Programmed filter sampler	Integrated 3-day sample, 1 continuous and 1 downslope sample $(4\ days)^{-1}$
Sulfate, nitrate, aerosols (Univ. of Hawaii)	Filter system	Daily, 2000-0600 LST
Radon (ANSTO)	Aerosol scavenging of Rn daughters†; 2-filter system	Continuous; integrated 30-min samples
AERONET sunphotometers (NASA Goddard)	Automated solar-powered sunphotometers	Continuous
Global Positioning System (GPS) Test Bed (FAA and Stanford University)	GPS-derived column water vapor profiles	Continuous
Earthquakes HVO/USGS Menlo Park	Seismometer	Continuous
Earthquakes Northwestern University	Seismometer	Continuous
CO isotopes (SUNY)	1000 psi cylinder	1 wk^{-1}
Cosmic dust (CALTECH)	Magnetic collector	1 wk^{-1}
Network for Detection of Stratospheric Change (NDSC)		
Ultraviolet radiation (NOAA and NIWA)	UV spectrometer (280-450 nm), 1-nm resolution†	Continuous
Stratospheric O_3 profile, 20-64 km (Univ. of Mass., Amherst)	Millitech Corp., 110.8-GHz microwave ozone spectroscopy	3 profiles h^{-1}
Stratospheric O_3 profiles (15-55 km), temperature (20-75 km), aerosol profiles (15-40 km) (JPL)	UV lidar†	3-4 profiles wk^{-1}
Stratospheric water vapor profiles, 40-80 km, 10-15 km resolution (NRL)	Millimeterwave spectrometer	Continuous
UV/visible radiation (NIWA and NOAA)	Slant column NO_2 spectrometer	Continuous, day
UV/visible radiation (NIWA and NOAA)	Column BrO spectrometer (Began 10/99)	Continuous, day
Column O_3, UV (AES, Canada)	Brewer spectrophotometers (Two instruments)	Daily
Solar spectra (Univ. of Denver)	FTIR spectrometer, automated†	5 days wk^{-1}

All instruments are at MLO unless indicated.
* MLO and Kumukahi
†Data from this instrument recorded and processed by microcomputers
‡Kumukahi only
§Kulani Mauka

The CH_4 data continued to show clearly defined cycles of varying frequencies. The typical diurnal cycle was well correlated with up- and downslope winds, with the marine boundary layer air having higher CH_4 concentrations. Multi-day or synoptic-scale CH_4 cycles were also observed, which apparently relate to different air mass source regions.

Sulfur dioxide. A new system, using a TECO 43S pulsed-fluorescence analyzer, was developed in Hilo in early 1998 and installed at MLO in April. By the end of June the system was fully operational. Every hour SO_2 is measured sequentially from inlets at 4,10, 23, and 40 meters on the tower, followed by a zero measurement. A single-point calibration is made once per day by injecting calibration gas into the airstream at the 40-m intake. All of the inlet lines are thermostatically maintained at 20°C. In August 1999 a break in the 40-m intake occurred, and sampling was restricted to the lower three levels for the remainder of the year while the damaged line section was removed and repaired.

This is the first time multi-point continuous vertical profiles of an atmospheric constituent have been measured at MLO. The SO_2 profiles show several features that change along with the

diurnal cycle of upslope/downslope winds. During the daytime, pollution from the Kilauea volcano is commonly brought to MLO in the upslope wind by late morning. Turbulent mixing causes the concentrations at all four tower levels to be similar. After sunset the surface temperature inversion develops, and the downslope wind commences. Residual pollution from Kilauea at that time has a SO_2 profile with concentrations increasing with height. After midnight, pollution episodes from Mauna Loa volcano are seen 10% of the time, as indicated by increases in CO_2 by up to several ppm. These are accompanied by increases in SO_2 of up to several hundred ppt above a baseline of tens of ppt with concentrations decreasing with height, indicating the gas is trapped beneath the surface temperature inversion. Throughout 1998-1999, the molecular ratio of SO_2 to CO_2 in the Mauna Loa volcanic plume remained at about 5×10^{-5}. This ratio is being monitored closely as an eruption precursor. An increase in the ratio is expected if magma migrates closer to the surface.

Ozone monitoring. The 1998-1999 MLO ozone monitoring program consisted of three measurement foci: continuous MLO surface ozone monitoring using a Dasibi model 1003-AH UV absorption ozone monitor; daily total and Umkehr ozone profile measurements using a computer-based automated Dobson instrument (Dobson no. 76); and ozone profile measurements based on weekly ascents of balloonborne electrochemical concentration cell (ECC) ozonesondes released from the NWS station at the Hilo airport.

Dobson no. 76 was operated daily during weekdays throughout the period with daily morning and afternoon Umkehr checks. Summer intercomparisons with standard Dobson no. 83 occurred in 1998 and 1999. The instrument was maintained as needed with repairs to the pedestal unit, stainless steel wedge band replacement, dome (hatch and shutter) work, and miscellaneous motor, belt, and tension spring adjustments.

The Dasibi program operated normally throughout the period, and the data transmission software and hardware were upgraded in June 1999. The Dasibi was calibrated, and yearly maintenance was carried out by MLO-based staff in 1998 and 1999. Absorption tubes were cleaned by other MLO-based staff in August 1999 at which time A/D checks were also completed. The Dasibi unit also was connected to its own uninterruptible power supply (UPS) at this time.

Ozonesondes were launched weekly whenever supplies were available from Boulder. In 1998 there were 44 ozonesonde flights, and in 1999 there were 47. The new "2Z" sondes were used beginning April 1998. These sondes send telemetry in a 1-s packet versus 6 seconds for the old "6A" type that results in much less susceptibility to radio interference. As a result, data acquisition is consistently over 90% instead of the <20% that occurred on some flights of the old sondes.

Halocarbons and other atmospheric trace species. In 1998 the Radiatively Important Trace Species (RITS) unit had airline pump board changes, a Keithley replacement, UPS battery replacements, and computer hardware repairs. In September 1998, the RITS GC and a new four-channel CATS GC were installed in the new NDSC building. The new CATS GC went through hardware changes throughout the year until June 1999 when it stabilized. CAL2 was shut down in July.

Radon. Radon has been measured continuously since 1989 by the Australian Nuclear Science and Technology Organization (ANSTO). Since March 1998, monthly manual calibrations have been made with a commercial radon source.

Aerosols

Condensation nuclei. The Thermo Systems Incorporated (TSI) unit is a continuous expansion CN counter (CNC) in which condensation occurs in butyl alcohol vapor in a chamber, and single-particle counting statistics are used as a basis for calculating CN concentrations. The TSI was in Boulder from November 1998 to October 1999 for repairs and maintenance. The Pollock CNC continues to be used as a primary daily calibration.

Aerosol light scattering. The four-wavelength nephelometer in operation at MLO for decades was retired in July 1998 and was replaced by a fast-response three-wave nephelometer measuring at 450, 550, and 700 nm. The old and new nephelometers operated together for more than 1 year.

Aerosol absorption. The aethalometer performed satisfactorily during most of 1998-1999. Since August 1998, transfer of the aethalometer data to Boulder has been done every week. The internal hoses that were cracked because of ozone attacking the rubber were replaced in July 1999.

Stratospheric and upper tropospheric aerosols. Weekly observations continued with the Nd:YAG lidar throughout 1998 and 1999. The optical framework was redesigned for the move into the NDSC building in February 1998. The lidar for the telescopes, lasers, and controls each have their own room in the new building. Only 2 weeks were needed to move and get the Nd:YAG system operating in the new building. On the other hand, the ruby system (694-nm wavelength) showed a severe loss of signal after the move. Since the Nd:YAG system measures aerosol profiles at 532 and 1064 nm, which give an interpolated 694 nm value, it was decided to discontinue the ruby observations as there was already over a year of overlap between the two systems, and the interpolated 694 nm profile is more accurate than the measured 694 nm signal.

The Nd:YAG laser power supply failed in February 1998. Fixing the problem required a service call from Spectra-Physics in California. In February 1999 a potentiometer failed on the laser and was repaired by MLO staff. Other maintenance consisted of flashlamp and cooling water changes.

Solar Radiation

The solar radiation program continued with the same instrumentation described in the previous summary report [*Hofmann et al.*, 1998]. Normal Incident Pyroheliometer data (which goes back to 1958) is calibrated periodically against an active cavity radiometer. Eight of these comparisons were done in 1998 and six in 1999. Mauna Loa Observatory is also used to calibrate handheld sunphotometers using the Langley technique; 23 instruments were calibrated in 1998, and 28 were calibrated in 1999. The observatory is also used to calibrate CMDL's Yankee UVB instruments; four were calibrated in 1998, and three were calibrated in 1999.

Meteorology

A computer-based "New Met System" measures station pressure, temperatures at the 2-, 9-, and 37-m levels, dewpoint temperature at the 2-m level, and wind speeds and directions at the 8.5-, 10-, and 38-m levels of the MLO Observation Tower. Precipitation is measured with a tipping bucket rain gauge. This new system has remained in operation unaltered and operating with high reliability to date.

Precipitation Chemistry

The MLO modified program of precipitation chemistry collection and analyses continued throughout 1998-1999 within the basic MLO operational routine. This program consists of collections of a weekly integrated precipitation sample from the Hilo National Weather Service (NWS) station and the collection of precipitation event samples at MLO. Analyses of these samples are undertaken in the Hilo laboratory for pH and conductivity.

Cooperative Programs

MLO cooperative programs are listed in Table 1.1. New programs and changes not discussed in the NDSC section are presented here.

In March 1996 MLO began calibrating automated sunphotometers for the NASA Aerosol Robotics Network (AERONET). Thirteen instruments were calibrated in 1998, and fifteen were calibrated in 1999. In September 1997 the Federal Aviation Administration (FAA) installed high quality Global Positioning Satellite (GPS) and meteorology sensors on the MLO Observation Tower in a study of atmospheric effects on GPS positioning. From this program MLO will receive nearly continuous column water vapor measurements. In November 1997 the Colorado State University (CSU) and U.S. Department of Agriculture (USDA) UV-B monitoring instruments were installed and continue to operate.

Network for the Detection of Stratospheric Change (NDSC)

All NDSC instruments operated in previous years continued observations. Two additional spectrometers operated by the National Institute for Water and Atmospheric Research (NIWA) (New Zealand) were added in December 1999 for column measurements of NO_2 and BrO. The NOAA lidar, ozonesonde, and Dobson operations, which are also part of the MLO NDSC facility, are described in other sections of this report.

UV/VIS spectroradiometer. This new instrument was put into operation in the NDSC building in November 1997. Weekly quality control calibrations were performed with a mercury lamp and a 45-W quartz lamp. An absolute-standard 1000-W FEL lamp calibration was performed twice each year. In fall 1999 an intermittent noise source in the background level was traced to the new U.S. Army radio repeater. Tracing the problem required a visit from a NIWA engineer. The problem was fixed temporarily by reducing the radio transmitter power and using a directional antenna. The permanent solution is to move the antenna down and away from the observatory; this will be completed in summer 2000.

Microwave ozone spectroscopy system. The University of Massachusetts microwave instrument measures the vertical profile of ozone from 20 to 70 km with a vertical resolution of 10 km or less up to 40 km, degrading to 15 km at 64 km. The ozone altitude distribution is retrieved from the details of the pressure-broadened line shape.

UV lidar. During the last 2 years the JPL UV lidar conducted several extensive studies of the dynamics of the middle atmosphere above MLO. Using the lidar, one can observe gravity waves, planetary waves, atmospheric tides, and mesospheric inversions. Temperature climatologies were developed using these results. Work was also done on the new space in the NDSC building. It is assumed that the more stable concrete floor in the NDSC building will allow JPL to slightly improve data quality. JPL will also use the opportunity offered by the move and the rebuilding of the lidar to extend the range of its measurements to lower altitudes. The additional space will certainly make the lidar easier to operate and maintain.

NO_2, BrO spectrometers. Since July 9, 1996, stratospheric nitrogen dioxide (NO_2) has been measured at MLO using the twilight zenith technique with a NIWA UV/VIS spectrometer. Data have been analyzed, quality confirmed, and then submitted to the NDSC archive. The new NO_2 and BrO spectrometers began operation in December 1999.

Brewer spectrophotometer. A single monochromator Brewer instrument was installed by the Canadian AES at MLO and began routine measurements of O_3 and UV-B radiation on March 24, 1997. A second instrument was added in November 1997. The measurements are supplemented by all-sky images that are recorded every 10 minutes in order to assist in the analysis of the UV-B data. Overviews of the automatic operation of the instrument and data retrievals have since been carried out remotely from AES in Downsview, Ontario, over the Internet.

The data are archived at the World Ozone and Ultraviolet Data Centre (WOUDC) in Toronto. Up-to-date preliminary data are available over the Internet from AES. Publication of some new results is planned after thorough analysis of a longer data record is completed.

Solar FTIR spectrometer. The University of Denver FTIR spectrometer routinely monitors HCl, HNO_3, O_3, N_2O, HCFC-22, HF, CH_4, NO, HCN, CO, C_2H_2, and C_2H_6. Because of the automatic nature of the instrument, the program is able to look at diurnal variations in the species. Data are not collected on Sundays or Monday mornings unless special operators are on site to add liquid nitrogen to the instrument.

1.2. BARROW OBSERVATORY

D. ENDRES AND M. GAYLORD

1.2.1. OPERATIONS

During the summer of 1881 Lt. P.H. Ray (U.S. Navy) was sent to Barrow, Alaska, with a small party to collect data on meteorology, natural history, magnetism, and other phenomena. This program lasted 3 years. A permanent weather observing program was started in 1946 and continues today under the National Weather Service. The United States Geological Survey (USGS) began a permanent magnetic observatory program in 1949 that continues today as one of 14 magnetic observatories in the United States. In January of 1973 the National Oceanic and Atmospheric Administration (NOAA) began a program of observations to detect changes in levels of background constituents that may force climate change. A network of four stations was planned with Barrow as the northernmost site.

The Barrow Observatory, Barrow, Alaska (BRW) celebrated 25 years of operation in January 1998. From a small program started in 1973 the station has grown to the point where almost every major global change study that passes through the Arctic has some connection with BRW because of the number (over 40) and longevity (some over 20 years) of programs and the quality of data produced there. Station personnel are often called upon to help with a wide range of scientific studies from a variety of sources. BRW has enjoyed the longest period of personnel stability to date with the station chief passing 15 years and the electronic engineer passing 5 years of service.

Outreach

In March 1998 the station was visited by a delegation from the U.S. Postal Service, including the Postmaster General, when they were in town to celebrate the first-day issue of Arctic animal

series stamps and to announce the approval of funds for the construction of a new post office in Barrow. Also in the group were several members of the U.S. Senate staff from the appropriations committee.

Three television documentaries were filmed at BRW over the past 2 years. A film crew from Japan was in town for 2 days and filmed station activities. A crew from Italy filmed for a day for a popular science program in Italy geared towards 8-12 year olds. The British Broadcasting Corporation (BBC) filmed at the station for 2 days for a documentary dealing with the possible consequences of climate change. An American Broadcasting Corporation (ABC) affiliate was in town to film several 5 minute segments for broadcast in San Diego during the weather segment of the news.

BRW station personnel were called on by the local high school to help judge the science fair. In 1997 a Barrow project was sent to state where it placed near the top, and in 1998 a project won first place at the state level. The local community college, Illisagvik, tapped the expertise of the station technician to help with curriculum development for technical trades.

The station chief continues to be involved with the Barrow Arctic Science Consortium and is a member of the Barrow Environmental Observatory Management Committee, and attended a meeting sponsored by the National Science Foundation held in December 1998 to have as many Arctic research programs as possible discuss the needs and future of support needed. Based on material developed at the workshop, a report was issued [*Arctic Research Consortium of the U.S. (ARCUS)*, 1999].

Station Concerns

A new 1998 Ford pick-up replaced the 1992 Ford pick-up. The old truck was sold in place and saved CMDL the cost of backhaul for the old truck. Two new snow machines were secured as replacements for the two older machines purchased in 1984.

Roadwork continued with all but the last 91 m being completed by the fall of 1999. Plans call for completion by summer of 2000. Road construction costs in Barrow are astronomically high, so an agreement was worked out with Illisagvik, the local community college, to have students in the heavy equipment operators class build the road and a consortium of government agencies provide the materials. Costs were shared by CMDL, the Department of Energy Atmospheric Radiation Measurement (ARM) Program, the USGS, and the National Science Foundation (NSF). The road is approximately 915 m (3000 ft) long and one lane wide. The road had sunk into the tundra to the point where several places were lower than the surrounding tundra, causing blockage by drifting snow every winter. The road was closed to vehicular traffic from about October until about June each year and snow machines were used to get to the station from the Distant Early Warning (DEW) line site. The new road will eliminate a less than ideal travel situation.

Funds were secured for Phase 2 of the master plan for upgrades at BRW. Phase 2 calls for a new garage to be built in place that will house compressed gas cylinders as well as cargo and vehicles. Warm storage is in high demand as building costs are prohibitively high. The ability to park the vehicles in a warm place during the day saves on wear and tear to a very large degree.

The computer network at BRW was greatly enhanced by the connection to a T-1 line provided by the ARM program. The T-1 line was part of a reciprocal agreement with the ARM program that allowed them access to land withdrawn by NOAA and personnel support whenever possible. Equipment needed to record data for weathersondes launched by the ARM program is housed at BRW, and BRW personnel helped write programs to transfer data to the ARM program computer located at the Ukpeagvik Inupiat Corporation (UIC) Naval Arctic Research Laboratory (NARL) facility. Balloons are launched once per day by ARM program personnel, and the data are formatted and transferred once per day by BRW personnel.

1.2.2. PROGRAMS

Table 1.2 lists programs for 1998-1999 at BRW. Operational highlights follow.

Aerosols

The upgraded aerosol equipment was described in the CMDL Summary Report No. 24, 1996-1997 [*Hofmann et al.*, 1998]. It worked well during the entire 2-yr period with the exception of the Thermal Systems Inc, (TSI) CN counter. It was discovered that the TSI data was being affected by the cooling fans in the aerosol rack. The instrument was being cooled to the point that the alcohol was not evaporating and data counts were too low. Station personnel built an acrylic enclosure to minimize cooling by the rack fans. Data collected at BRW continue to show a springtime high in CN concentrations along with the buildup of the Arctic haze.

Solar Radiation

Barrow snowmelt date continues to be one of the most talked about programs at the station. An annual graph is provided by the CMDL Solar Radiation group in Boulder and is the most sought after graph on site. The graph shows the melt trends from the NWS office in the town of Barrow, the melt date as measured by BRW radiation instruments, and the date of the first egg from a study of Guillemot birds on a nearby island. The Guillemot will not lay eggs on Cooper Island, the nesting grounds for the birds, until the snow cover is minimal. All three graphs show a trend towards an earlier melt date.

An Epply pyranometer was installed at about the 15-m level on the tower in 1998. It measures upwelling radiation and will be helpful for albedo measurements. A shade was installed to block the tower and station from the field of view of the instrument, minimizing any error due to obstructions from the direction of the station.

Carbon Cycle

Carbon dioxide. CO_2 mixing ratios as high as 375 ppm were seen during 1998-1999. Values as low as 355 ppm were also noted. The high values were among the highest average values ever.

The Siemens Ultramat 5-E continues to serve as the main CO_2 station instrument and worked well the entire period without any major problem. Calibrations were performed at regular intervals.

Methane. The HP6890 gas chromatograph continued to run well with minimal intervention. Data show a clearly defined frequency with high values occurring in the winter months and low values in the summer.

Carbon monoxide. A Trace Analytical gas chromatograph has been the station instrument since 1991 and continued to run with minimal routine maintenance that included changing a scrubber for Hg and replacing the UV lamp in the detector section.

Flask samples. Flask samples were collected as available and as scheduled. There were no major problems with the flask program. Isotopic composition measurements of CO_2 continues, and data from this program can be found in other sections of this summary report.

TABLE 1.2. Summary of Measurement Programs at BRW in 1998-1999

Program	Instrument	Sampling Frequency
Gases		
CO_2	Siemens Ultramat 5E analyzer	Continuous
	3-L glass flasks	1 pair wk^{-1}
	0.5-L glass flasks, through analyzer	1 pair wk^{-1}
CO_2, CH_4, CO, and $^{13}C/^{12}C$ and $^{18}O/^{16}O$ of CO_2	0.5-L glass flasks, P^3 pump unit	1 pair wk^{-1}
CH_4	Carle automated GC	1 sample $(12\ min)^{-1}$
Surface O_3	Dasibi ozone meter	Continuous
Total O_3	Dobson spectrophotometer no. 91	3 day^{-1}
N_2O, CFC-11, CFC-12, CFC-113, CH_3CCl_3, CCl_4	850-mL, 2.5-L, and 3-L stainless steel flasks	1 sample mo^{-1}
N_2O, CFC-11, CFC-12, CFC-113, CH_3CCl_3, CCl_4, SF_6, HCFC-22, HCFC-141b, HCFC-142b, CH_3Br, CH_3Cl, CH_2Cl_2, $CHCl_3$, C_2HCl_3, C_2Cl_4, H-1301, H-1211, H-2402, HFC-134a	850-mL, 2.5-L, and 3-L stainless steel flasks	1 sample mo^{-1}
CFC-11, CFC-12, CFC-113, N_2O CCl_4, CH_3CCl_3	HP5890 automated GC	1 sample h^{-1}
N_2O	Shimadzu automated GC	1 sample h^{-1}
CO	Trace Analytical GC	1 sample $(6\ min)^{-1}$
CFC-11, CFC-12, CFC-113, N_2O, CH_3CCl_3, CCl_4, CH_3Br, CH_3Cl, H-1211, SF_6, HCFC-22	Automated CATS GC	1 sample h^{-1}
Aerosols		
Condensation nuclei	Pollak CNC	1 day^{-1}
	TSI CNC	Continuous
Optical properties	Four-wavelength nephelometer	Continuous
Black carbon	Aethalometer	Continuous
Solar Radiation		
Global irradiance	Eppley pyranometers with Q and RG8 filters	Continuous
Direct irradiance	Tracking NIP	Continuous
	Eppley pyrheliometer with Q, OG1, RG2, and RG8 filters	Discrete
Albedo	Eppley pyranometer	Continuous
Terrestrial (IR) Radiation		
Upwelling and downwelling	Eppley pyrgeometers	Continuous
Meteorology		
Air temperature	Thermistor, 2 levels	Continuous
	Max.-min. thermometers	1 day^{-1}
Dewpoint temperature	Dewpoint hygrometer	Continuous
Pressure	Capacitance transducer	Continuous
	Mercurial barometer	Discrete
Wind (speed and direction)	R.M. Young Aerovane	Continuous
Precipitation	Rain gauge, tipping bucket	Continuous
Cooperative Programs		
Total surface particulates (DOE)	High-volume sampler (1 filter wk^{-1})	Continuous
Precipitation gauge (USDA)	Nipher shield, Alter shield, 2 buckets	1 mo^{-1}
Magnetic fields (USGS)	3-Component fluxgate magnetometer and total field proton magnetometer	Continuous
	Declination/inclination magnetometer sample	6 sets mo^{-1}
Hg (ATDD)	Tekran 2537A Hg vapor analyzer	Continuous
CO_2, ^{13}C, N_2O (SIO)	5-L evacuated glass flasks	1 set wk^{-1} (3 flasks set^{-1})
CH_4 (Univ. of Calif., Irvine)	Stainless steel flasks	1 pair wk^{-1}
O_2 in air (Princeton Univ.)	3-L glass flasks	1 set $(3\ mo)^{-1}$
CO_2 flux (San Diego State Univ.)	CO_2 and H_2O infrared gas analyzer and sonic anemometer	Continuous, check site 1 wk^{-1}
Magnetic fields (NAVSWC)	^3He sensors	1 $(2\ wk)^{-1}$
Magnetic micropulsations (Univ. of Tokyo)	Magnetometer and cassette recorder	1 $(3\ wk)^{-1}$
UV monitor (NSF)	UV spectrometer	1 scan per 0.5 hour
Study thaw depth in permafrost (SUNY)	Temperature probe	Continuous
Total VOC and heavy metals (Hokkaido Univ.)	Filter samples	1 $(2\ wk)^{-1}$

Meteorology

A maximum wind speed of 21 m s^{-1} was recorded during 1998-1999. The high temperature was 20°C and the low was –41°C. Equipment ran well, with only routine calibration and maintenance required. All sensor probes were calibrated and adjusted as scheduled or needed.

Ozone

Total column. The Dobson ran well the entire period with only one problem. A clutch in the Q1 lever wore out causing the lever to fall to the lowest position. The clutch was rebuilt by station personnel and seemed to work well. Dobson no. 91 continues to be the station instrument. Values as high as 440 Dobson Units (DU) and as low as 290 DU were recorded. Data collection is not possible during the winter months when the sun is below the horizon, but regular calibrations are performed to ensure proper operation of the instrument.

Surface ozone. The Dasibi ran well with only routine calibrations. Surface ozone is one of the longest running programs at BRW and continues to be of value for trend analyses. With the addition of a new cooperative program to measure Hg vapor, surface ozone has taken on a new value. There appears to be a strong correlation between surface ozone values and Hg values measured at BRW in the spring.

HATS

A new system for in situ measurements was installed during 1998 known as the Chromatograph for Atmospheric Trace Species (CATS). There were a few startup problems to be worked out, most notably the chiller for the cryo-cooled samples was replaced once, and leaks in the tubing were fixed. The compliment of gases now measured in situ for the HATS group numbers 11, nearly doubling the number of species over the old system. One of the new gases measured is sulfur hexafloride, SF_6. SF_6 is used mostly as a replacement for polychlorinated biphenyls (PCB) in transformers and has a lifetime in the atmosphere of 3200 years. It is one of the most potent greenhouse gases known.

Cooperative Projects

BRW cooperative programs are listed in Table 1.2. Only projects with major changes are discussed in this section.

A new project was started with the NOAA Atmospheric Turbulence and Diffusion Division (ATDD). The project measures precipitable Hg and complements the system in place at Alert, Canada. Springtime values seem to have a strong correlation with surface ozone and sunrise. Funding for this project is through the Environmental Protection Agency (EPA).

Filters that are analyzed for heavy metals were collected for Hokkaido University every 2 weeks. A second set of packed tubes is collected monthly and is analyzed for volatile organic compounds.

The ARM program is in the final stages of setup, and data are now being collected. The ARM program will complement the CMDL program by measuring global change parameters that CMDL cannot. Between the two programs, BRW will most likely be one of the most comprehensive climate change research sites in the world.

A hi-vol filter collector for the University of Alaska, Fairbanks (UAF) was stopped when the pump died. The project is on hold until funding can be secured for a new pump.

All other cooperative research programs continued as before with no major problems and no major changes.

1.3. Samoa Observatory

D. Holt, J. Michalski, and E. Sandberg

1.3.1. Operations

Operations at the American Samoa Observatory (SMO) were relatively uneventful during 1998-1999, with the station chief completing his term and changes in station engineer at the end of 1998.

The most significant change to the station came with a cooperative agreement between NOAA and the new cellular phone company, Blue Sky Communications. Blue Sky saw Matatula Point as an ideal location for one of its many cellular phone towers. Since NOAA's own meteorological tower was nearing the end of its useful life, it became an excellent opportunity to allow Blue Sky use of the property while allowing NOAA to use Blue Sky's new tower. The tower was completed in May 1999, and throughout the year the experiments that depended on the old tower were gradually moved to the new one. This process continued into 2000.

Effective Internet access to the observatory was still not available. Despite meetings with the local phone company and Peace Sat, a Pacific Islands initiative to connect schools and government agencies to the Internet, no effective connection scheme was found, although there is optimism that a connection will be possible sometime in 2000.

The backup diesel generator remains operational but is in urgent need of maintenance and part replacements. Although the diesel unit is in decent condition, the radiator, water pump and electronic controls all require immediate attention.

The station facilities are also in need of renovation. Because the roof has some minor leaks, a complete repainting is necessary. The interior of the main laboratory is in need of repainting and other upgrades, including new electrical wiring and lighting. Finally, the old Plexiglass windows have turned translucent from UV exposure and will to be replaced in 2000.

1.3.2. Programs

Table 1.3 summarizes the programs at SMO for 1998-1999. Operational highlights are as follows:

Carbon Dioxide

In situ monitoring and Airkit samples continued without interruption during this reporting period.

Surface Ozone

The Dasibi ozone monitor failed completely in March 1999. Because the newer Thermo Electron Instrument (TEI) UV photometric ozone analyzer was operational, the loss of the Dasibi was not critical. Plans for a new or repaired Dasibi are on order for 2000.

Total Ozone

The Dobson spectrophotometer continued to operate reliably during this reporting period. In December 1998 a new dome was installed to replace the old dome that had rusted so badly that it could no longer turn to face the sun.

Ozonesonde Balloons

Weekly ozonesonde flights continued during this reporting period using the National Weather Service (NWS) balloon inflation facility at the Tafuna airport.

TABLE 1.3. Summary of Measurement Programs at SMO in 1998-1999

Program	Instrument	Sampling Frequency
Gases		
CO_2	Siemens Ultramat-5E analyzer	Continuous
CO_2, CH_4	0.5-L glass flasks, through analyzer	1 pair wk^{-1}
	2.5-L glass flasks, MAKS pump unit	1 pair wk^{-1}
CO_2, CH_4, CO, and ^{13}C, ^{18}O of CO_2	2.5-L glass flasks, AirKit	1 pair wk^{-1}
Surface O_3	Dasibi ozone meter	Continuous
	TEI UV photometric ozone analyzer	Continuous
Total O_3	Dobson spectrophotometer no. 42	4 day^{-1}
N_2O, CFC-11, CFC-12, CFC-113, CH_3CCl_3, CCl_4	850-mL, 2.5-L, and 3-L stainless steel flasks	1 sample wk^{-1}
N_2O, CFC-11, CFC-12, CFC-113, CH_3CCl_3, CCl_4, SF_6, HCFC-22, HCFC-141b, HCFC-142b, CH_3Br, CH_3Cl, CH_2Cl_2, $CHCl_3$, C_2HCl_3, C_2Cl_4, H-1301, H-1211, H-2402, HFC-134a	850-mL, 2.5-L, and 3-L stainless steel flasks	1 sample wk^{-1}
CFC-11, CFC-12, CFC-113, N_2O, CCl_4, CH_3CCl_3	HP5890 automated GC	2 sample h^{-1}
N_2O	Shimadzu automated GC	2 sample h^{-1}
CFC-11, CFC-12, CFC-113, N_2O, CH_3CCl_3, CCl_4, CH_3Br, CH_3Cl, H-1211, SF_6, HCFC-22	Automated CATS GC	1 sample h^{-1}
Aerosols		
Condensation nuclei	Pollak CNC	1 day^{-1}
Solar Radiation		
Global irradiance	Eppley pyranometers with Q and RG8 filters	Continuous
Direct irradiance	Eppley pyrheliometer with Q filter	Continuous
	Eppley pyrheliometer with Q, OG1, RG2, and RG8 filters	Discrete
Diffuse irradiance	Eppley pyrgeometer with shading disk and Q filter	Continuous
Meteorology		
Air temperature	Thermistors (2)	Continuous
Dewpoint temperature	Polished mirror	Continuous
Pressure	Capacitance transducer	Continuous
	Mercurial barometer	1 wk^{-1}
Wind (speed and direction)	R.M. Young Windbird	Continuous
Precipitation	Rain gauge, tipping bucket	Continuous
	Rain gauge, plastic bulk	1 day^{-1}
Cooperative Programs		
CO_2, ^{13}C, N_2O (SIO)	5-L evacuated glass flasks	1 set wk^{-1} (3 flasks set^{-1})
GAGE/AGAGE project: CFC-11, CFC-12, CFC-113, N_2O, CCl_4, CH_3CCl_3, CH_4 (SIO)	HP5880/HP5890 Series II gas chromatograph	3 h^{-1}
Various trace gases (OGIST)	Stainless steel flasks	1 set wk^{-1} (3 flasks set^{-1})
Bulk deposition (DOE)	Ion exchange column	Continuous (1 filter mo^{-1})
Total suspended particulates (DOE)	High-volume sampler	Continuous (1 filter wk^{-1})
Total suspended particulates (SEASPAN)	High-volume sampler	Continuous (1 filter wk^{-1})
CH_4 ($^{13}C/^{12}C$ ratio) (Univ. of Wash.)	30-L pressurized cylinder	Biweekly
Light hydrocarbons (UCI)	1-L evacuated stainless steel flasks	3-4 flasks qtr^{-1}
O_2 (Princeton Univ.)	2.5-L glass flasks	2 pair mo^{-1}
O_2 (SIO)	3-L glass flasks	2 sets mo^{-1} (3 flasks set^{-1})

SIO - Scripps Institution of Oceanography
OGIST - Oregon Graduate Institute of Science and Technology
DOE - Department of Energy
SEASPAN - Sea-Air Exchange Experiment
UCI - University of California, Irvine
URI - University of Rhode Island

Halocarbons and Other Atmospheric Trace Species

The new Chromatograph for Atmospheric Trace Species (CATS) gas chromatograph was installed in December 1998 and ran alongside the older Radiatively Important Trace Species (RITS) system. Intercomparison continued through this reporting period, and plans for the removal of the RITS system will be carried out in 2000.

Aerosols

The only aerosol measuring instrument at Samoa is a Pollak counter. Daily Pollak observations were conducted throughout the year.

Solar Radiation and Meteorology

The solar radiation and meteorological instruments continued to operate with no significant problems. A member of the CMDL Ozone and Water Vapor (OZWV) group visited during October 1999 to add an IR pyranometer and to take a current theodolite observation of obstructions to the horizon.

Cooperative Programs

A complete list of SMO cooperative projects is found in Table 1.3. All operated essentially without problems during this reporting period.

1.4. South Pole Observatory

N. Hill and J. Michalski, NOAA Corps

1.4.1. Operations

The CMDL South Pole Observatory (SPO) is located at the geographic south pole of Antarctica at an elevation of 2838 m above sea level. The Amundsen-Scott South Pole Station is an integral part of the U.S. Antarctic Program run by the National Science Foundation (NSF) and was administered by Antarctic Support Associates (ASA), who provided logistical and operational support.

The vast majority of CMDL's projects at SPO are housed within the Clean Air Facility (CAF) that takes up the majority of the Atmospheric Research Observatory (ARO) building located 400 m grid northeast of the main station. The clean air sector is defined as an area grid northeast of ARO between grid 340° and 110°. Because the wind blows from this direction more than 90% of the time at the South Pole, the CAF is ideally situated to sample air uncontaminated by the rest of the station. Activity within the clean air sector is strictly prohibited.

CMDL's meteorological tower sits on the edge of the clean air sector at grid 340° from ARO. Meteorological sensors, sampling lines and thermal radiation instruments are located there.

CMDL's stratospheric ozonesonde program is conducted from the Balloon Inflation Facility (BIF) located grid south of the main station. This facility is shared with ASA's meteorological department.

The Amundsen-Scott station receives support from regular aircraft flights for only 3 months out of the year from November through January. The station, including CMDL's observatory, is completely isolated from the rest of the world from February through October. During this period, temperatures are too low for aircraft to operate safely. As a result, air samples taken during the austral winter cannot be returned for analysis until the station reopens each November. Data collected in situ are transferred to the home institution regularly via a satellite link to the Internet.

Station power is generally quite reliable but outages do occasionally occur. The CAF is equipped with stable power supplies for some of the more sensitive equipment.

1.4.2. Programs

Table 1.4 summarizes the programs at SPO for 1998-1999. Operational highlights are as follows:

Carbon Cycle

The Siemens continuous carbon dioxide analyzer ran without significant problems or changes. Sample flasks were filled through the analyzer twice per month and once per week with the Martin and Kitzis Sampler (MAKS) portable pump unit.

Aerosols

The four-wavelength nephelometer ran continuously without any problems. Discreet measurements were made daily with the Pollak condensation nucleus counter (CNC). The Thermo Systems Inc. (TSI) CNC went off-line on March 23, 1998, after the condenser temperature became unstable. Repairs to this unit were not possible with the spare parts available. The TSI remained off-line for the remainder of the winter until a new instrument could be flown to the observatory in November.

Solar and Terrestrial Radiation

During the austral summer, all of the solar and terrestrial radiation measuring equipment ran without any significant problems. In January of 1998 the data acquisition software was altered to record 1-min averages instead of 3-min averages, as had been the case before. After sunset each year the short-wave (solar) instruments were taken off-line for the winter.

Ozone and Water Vapor

The Dasibi surface ozone monitor ran continuously without any significant problems. Discrete measurements of total column ozone were taken three times daily during the summer months using a Dobson ozone spectrophotometer. Whenever possible, total ozone values were obtained in the winter with the Dobson using the full moon as a light source.

The balloonborne stratospheric ozonesonde program continued to run well. Profiles of ozone up to approximately 30 km were obtained once per week except during the months of severe stratospheric ozone depletion (August-November) when flights were gradually increased to one every other day.

Halocarbons and Other Atmospheric Trace Species

The two Shimadzu mini-gas chromatographs (GC) continued to run without significant interruption. A new automated four-channel custom-built Chromatograph for Atmospheric Trace Species (CATS) was installed in January 1998 to run concurrently with the Shimadzus. This new GC is intended to replace the older, more limited mini GCs. In addition to the automated sampling, sample flasks were filled twice per month to be analyzed in Boulder.

Meteorology

The meteorology program ran well with no significant problems. Weather observations by station personnel took place daily or during changing conditions.

Cooperative Programs

SIO. The Scripps Institution of Oceanography (SIO) conducts long-term monitoring of CO_2, $^{13}C/^{12}C$ ratio, and N_2O. Twice per

TABLE 1.4. Summary of Measurement Programs at SPO in 1998-1999

Program	Instrument	Sampling Frequency
Gases		
CO_2	URAS-2T and Siemans IR analyzer	Continuous
CO_2, CH_4	2.5-L glass flasks, through analyzer	1 pair $week^{-1}$
	2.5-L glass flasks, MAKS pump unit	1 pair twice mo^{-1}
Surface O_3	Dasibi ozone meter	Continuous
	Electrochemical cell (ECC)	Continuous
Total O_3	Dobson ozone spectrophotometer nos. 80 and 82	3 day^{-1}
Ozone profiles	Balloonborne ECC sonde	1 wk^{-1}, summer, autumn, winter; 3 wk^{-1}, spring
N_2O, CFC-11, CFC-12, CFC-113, CH_3CCl_3, CCl_4, SF_6, HCFC-22, HCFC-141b, HCFC-142b, CH_3Br, CH_3Cl, CH_2Cl_2, $CHCl_3$, C_2HCl_3, C_2Cl_4, H-1301, H-1211, H-2402, HFC-134a	850-mL, 2.5-L, 3-L stainless steel flasks	1 pair mo^{-1}
CFC-11, CFC-12, CFC-113, N_2O, CH_3CCl_3, CCl_4	Shimadzu automated GC	2 sample wk^{-1}
CFC-11, CFC-12, CFC-113, N_2O, CH_3CCl_3, CCl_4, CH_3Br, CH_3Cl, H-1211, SF_6, HCFC-22	Automated CATS GC	1 sample h^{-1}
Aerosols		
Condensation nuclei	Pollack CNC	2 day^{-1}
	TSI CNC	Continuous
Optical properties	Four-wavelength nephelometer	Continuous
Solar Radiation		
Global irradiance	Eppley pyranometers with Q and RG8 filters	Continuous, summer
	Eppley pyranometer with Q filter	Continuous, summer
	Net radiometer	Continuous, summer
Direct irradiance	Eppley pyrheliometer with Q, OG1, RG2, and RG8 filters	3 day^{-1}
	Eppley pyrheliometer with Q and RG8 filters	Continuous, summer
Albedo	Eppley pyranometer with Q and RG8 filters, downward facing	Continuous
Diffuse irradiance	Eppley pyranometer with shading disk and Q filter	Continuous
Terrestrial (IR) Radiation		
Upwelling and downwelling	Eppley pyrgeometers	Continuous
Meteorology		
Air temperature	Platinum resistor, 2- and 20 m heights	Continuous
Pressure	Capacitance transducer	Continuous
	Mercurial barometer	1 wk^{-1}
		2 day^{-1}
Wind (speed and direction)	Bendix Aerovane	Continuous
Frost-point temperature	Hygrometer	Continuous
Cooperative Programs		
CO_2, ^{13}C, N_2O (SIO)	5-L evacuated glass flasks	2 mo^{-1} (3 flasks $sample^{-1}$)
O_2, N_2 (SIO)	Air sampling pump and flasks	2 mo^{-1} (3 flasks set^{-1})
Total surface particulate (DOE)	High-volume pump and filters	Continuous (4 filters mo^{-1})
Interhemispheric $^{13}C/^{12}C$ (CSIRO)	Pump unit, 0.5-L and 5-L flasks	2 mo^{-1} (2 flasks set^{-1})
H_2O_2 (Univ. of Arizona)	Snow sample collection	1 wk^{-1}, 2 wk^{-1}- spring
Isotope production (SUNY)	Pressurized cylinders	N/A, checked once mo^{-1}
Trace species in the shallow snow firn (SIO)	Sampling lines, pump, 2-L glass flasks	2 yr^{-1}

month, three evacuated glass flasks were exposed to ambient air. Three glass flasks were pressurized with ambient air on the first and fifteenth of each month for the long-term monitoring of O_2 and N_2. Air samples were taken at depth intervals from within a 15-m hole drilled in the snow firn. The sampling hole was located within the clean air sector approximately 30 m grid east of the Atmospheric Research Observatory. Air samples were returned to SIO and analyzed for atmospheric trace species. Samples were taken once in the summer and once in the winter.

DOE. The U.S. Department of Energy (DOE) conducts long-term monitoring of the spatial and temporal distribution of specific and anthropogenic radionuclides in the surface air. The DOE pump ran continuously without significant problems; filters were changed once per week. Also, a monthly sample blank was collected once per month.

CSIRO. The Commonwealth Scientific and Industrial Research Organization (CSIRO) monitors the ratio $^{13}C/^{12}C$ in atmospheric CO_2 for use in a two-dimensional global carbon

cycle model. One glass flask was pressurized with ambient air every 2 weeks.

SUNY. State University of New York (SUNY). Five air-filled cylinders remained on platforms approximately 800 m downwind of the main station for the quantification of the production rate of radiocarbon by galactic cosmic rays by SUNY. The cylinders were inspected and cleared of snow once per month. Occasionally, the platforms required raising to keep clear of drifting snow.

University of Arizona. Snow samples were taken weekly for the Univiversity of Arizona to study the snow/atmosphere exchange of H_2O_2. Additionally, snow heights were measured from a "sampling grid" inside the clean air sector.

1.5. Meteorological Measurements

T. Mefford

1.5.1. Meteorology Operations

Introduction

The climatology of surface meteorological observations at the four CMDL observatories is based on hourly averaged measurements of the vector wind direction and speed, barometric pressure, ambient and dewpoint temperatures, and precipitation amount. The meteorological sensors used were selected for their high accuracy, as well as their ability to withstand the extreme conditions of the polar regions. Data are recorded as 1-min averages, so the variability within the hourly averages can be determined. To the extent that is possible, World Meteorological Organization (WMO) siting standards [*WMO*, 1969] are followed. Thermometers are also positioned at the top of the sampling towers at BRW, MLO, and SPO to measure the temperature gradient and to determine the stability of the surface boundary layer.

A detailed description of the PC-based data acquisition system may be found in *Peterson and Rosson* [1994]. Table 1.5 describes the instrument deployment as of December 31, 1999.

At BRW the complement of sensors measuring meteorological variables remained unchanged. In early 1998 and again in early 1999, the aspirator fan on the dewpoint hygrothermometer was replaced. In mid-June 1999 the dewpoint hygrothermometer sensor head was replaced since the old one failed at the beginning of June. In December 1999 a filter capacitor on the main power supply of the dewpoint hygrothermometer was replaced.

At MLO the RS-485 card, which is used by the meteorological data acquisition computer to communicate with the sensor interface modules, was replaced in March 1998. In March 1999 the sensor interface modules in the dewpoint hygrothermometer and the anemometer that measures the 10-m winds were replaced. In August 1999 the wind speed transmitter on the Bendix aerovane was replaced.

At SMO the biggest change was the move of the anemometer, the dewpoint hygrothermometer, and the platinum resistance probe from the meteorological sampling tower to the newly constructed cellular phone tower near the main building. This move took place between July 8 and 24, 1999. Table 1.6 describes the heights of the sensors before and after the move to the new tower. The pressure transducer and the rain gauge remained in the same locations.

At SPO the RS-485 card was replaced in early January 1998. The aspirator fan in the dewpoint hygrothermometer was replaced in early April 1998 and then again later in the month.

Data Management

The meteorological data acquisition system gathers data from sensors that operate continuously at each of the four CMDL observatories. Data are transferred to Boulder on a daily basis via the Internet, except for SMO. The SMO data are transferred to Boulder on a weekly basis. Preliminary hourly averages of vector wind direction and speed, barometric pressure, ambient and dewpoint temperatures, and precipitation amounts are sent to the stations on a daily basis except for SMO, where it is sent on a weekly basis.

A comparison of the number of data points recorded against that expected for the year was used to monitor the system's performance. Table 1.7 shows the performance of each system in 1998 and 1999. On average the meteorological data acquisition system for the four observatories operated 95.62% and 92.03% of

TABLE 1.5. CMDL Meteorological Sensor Deployment December 31, 1999

	BRW		MLO		SMO		SPO	
Sensor	Serial No.	Elevation, m	Serial No.	Elevation, m	Serial No.	Elevation, m	Serial No.	Elevation, m
Primary anemometer†	14584	10.5	23186	10.2	15945	22.9	14583	10.0
Secondary anemometer†			15946	38.2				
Pressure transducer‡	374199	9.5	374198	3398.4	374200	78.5	358960	2841.0
Mercurial barometer	641	9.5	278	3398.4	961	78.5	1215A	2841.0
Air temperature A§		2.4		2.0		18.9		1.6
Air temperature B§¶		15.7		37.4		18.9		22.0
Air temperature C**		2.9		2.0		18.9		2.0
Dewpoint temperature	G0001	2.9	G0004	2.0	G0008	18.9	G0007	2.0
Rain gauge		~4		0.8		~4		

Heights are in meters above surface, except for the pressure transducer and mercurial barometer, which is with respect to mean sea level.
†Propeller Anemometer, model no. 05103, R. M. Young Company, Traverse City, Michigan.
‡Pressure Transducer, model no. 270, Setra Systems, Acton, Massachusetts.
§Platinum Resistance Probe, Logan 4150 Series, Logan Enterprises, Liberty, Ohio.
¶Thermometer, positioned at the top of the local sampling tower to facilitate an estimation of boundary layer stability, except at SMO where both sensors were at the same height.
**Hygrothermometer, Technical Services Laboratory model no. 1088-400, Fort Walton Beach, Florida.

TABLE 1.6. SMO Sensor Instrument Heights on the Old Sampling Tower and the New Cellular Phone Tower

Instrument	Old Sampling Tower Sensor Heights (m)	New Cellular Phone Tower Sensor Heights (m)
Primary anemometer	13.7	22.9
Air temperature A	14.0	18.9
Air temperature B		18.9*
Air temperature C	12.8	18.9
Dewpoint temperature	12.8	18.9

*Second Platinum Resistance Probe was installed on October 22, 1999.

TABLE 1.7. CMDL Meteorological Operations Summary

Station	Expected Number of Data Points	Percent Data Capture	Number of Missing Data Points
		1998	
BRW	4,204,800	99.51%	20,716
MLO	6,832,800	91.06%	611,062
SMO	3,679,200	95.02%	183,258
SPO	4,204,800	96.89%	130,940
Average		95.62%	
		1999	
BRW	4,204,800	98.70%	54,832
MLO	6,832,800	89.82%	695,350
SMO	3,778,560	83.60%	619,545
SPO	4,204,800	96.01%	167,660
Average		92.03%	

the time for 1998 and 1999, respectively. Because of the remoteness of the observatories, power outages are common and are the main reason for data loss. Hardware failure, system restarts, and system maintenance are the other reasons for data loss. At BRW, during the winter time periods, rime, snow, and ice occasionally would build up on the sensors and have to be removed by the station personnel.

1.5.2. STATION CLIMATOLOGIES

The 23-yr station climatologies are an important record for the interpretation of measured values of aerosols, trace gases, atmospheric turbidity, solar radiation, and the long-term changes in the records themselves. The records also serve to outline periods of local contamination.

Barrow

In Figure 1.1 histograms of hourly average vector wind direction and speed at BRW are presented in 16 direction classes and 3 speed classes. Winds from the "clean air" sector, north-northeast to southeast occurred 68.5% of the time in 1998 and 64% in 1999 as compared with 61.3% for the 21-yr period from 1977 through 1997 (Figure 1.2). Wind speeds in excess of 10 ms^{-1} in 1998 (8.7%) and 1999 (5.9%) were less frequent than in the 21-yr climatology (11.3%). The average wind speed of 5.5 ms^{-1} in 1998 was the fifth lowest average, while the 4.8 ms^{-1} in 1999 was the lowest average in the 23 years at the station (Table 1.8).

The average air temperature of –8.7°C in 1998 (Table 1.8), was considerably warmer than the 21-yr average of –12.4°C, while 1999 (-12.3°C) was very close to average. A new record high temperature was recorded in May 1998, and the record high temperature was tied in March 1998. The barometric pressure in 1998 was 1.8 hPa below the 21-yr average, while the average for 1999 was close to normal. September 1999 set a new record high pressure for the month, while new record lows were set in August 1998, January 1999, and May 1999. The summertime precipitation amounts for 1998 (54 mm) and 1999 (40 mm) were both below the long-term average of 61 mm.

Mauna Loa

The climatology of MLO is best understood when it is considered in two distinctive wind regimes, the night (downslope) period (1800–0559 Hawaiian Standard Time (HST)) and the day (upslope) period (0600–1759 HST). The 21-yr night and day wind histogram illustrate the two distinct wind regimes (Figure 1.3).

For the night regime, the 21-yr wind histogram (Figure 1.3) shows that 91.5% of all winds observed had a southerly component. The percentage of occurrence of southerly winds in 1998 was 90.4% (Figure 1.4) and 92.5% in 1999 (Figure 1.5).

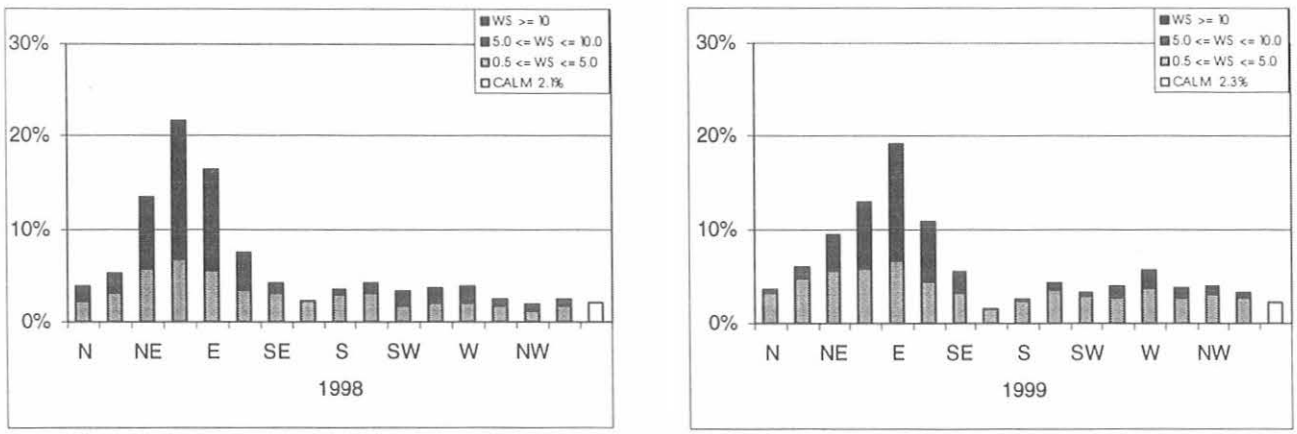

Fig. 1.1. Histogram of surface winds for BRW for 1998 (left) and 1999 (right). Percent frequency of winds is shown for each of 16 direction classes and 3 wind speed (WS) classes. Percent frequency of calm winds (WS <0.5 ms^{-1}) is indicated in the legends and is shown as an open bar on each histogram.

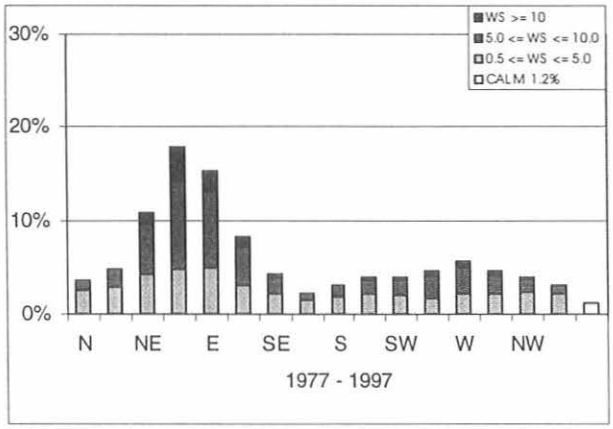

Fig. 1.2. Histogram of surface winds for BRW 1977 through 1997. Percent frequency of winds is shown for each of 16 direction classes and 3 wind speed (WS) classes. Percent frequency of calm winds (WS <0.5 ms^{-1}) is indicated in the legend and is shown as an open bar on the histogram.

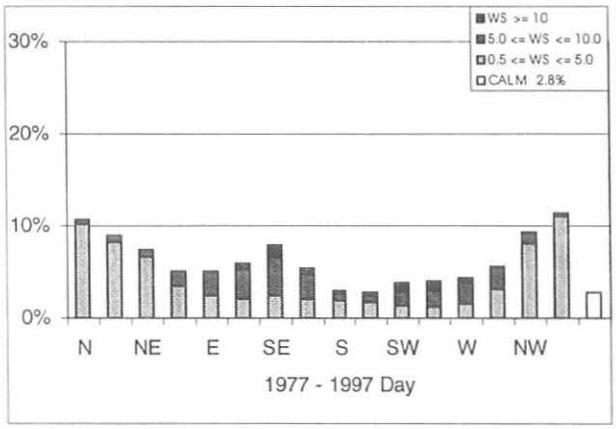

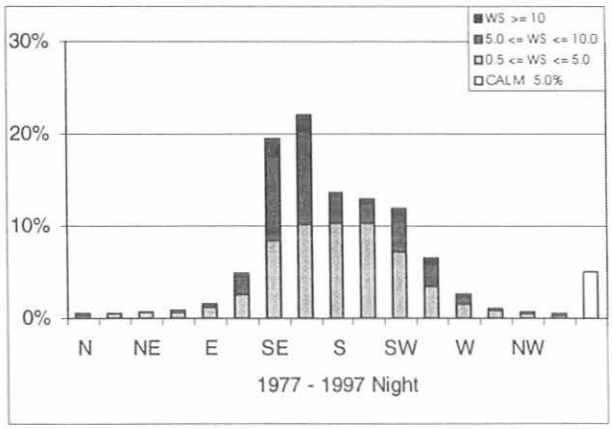

Fig. 1.3. Histograms of surface winds for MLO for 1977 through 1997 day (left) and night (right). Percent frequency of winds is shown for each of 16 direction classes and 3 wind speed (WS) classes. Percent frequency of calm winds (WS <0.5 ms^{-1}) is indicated in the legends and is shown as an open bar on each histogram.

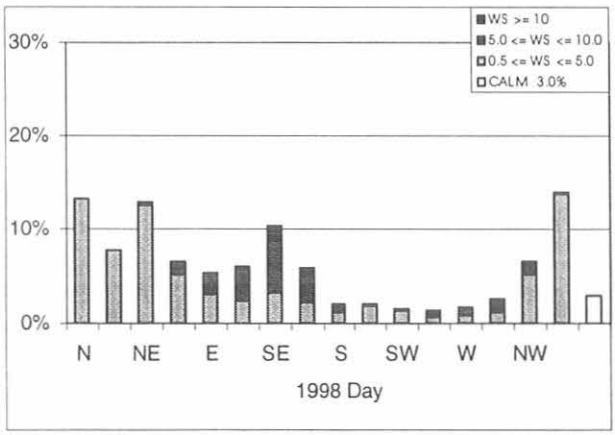

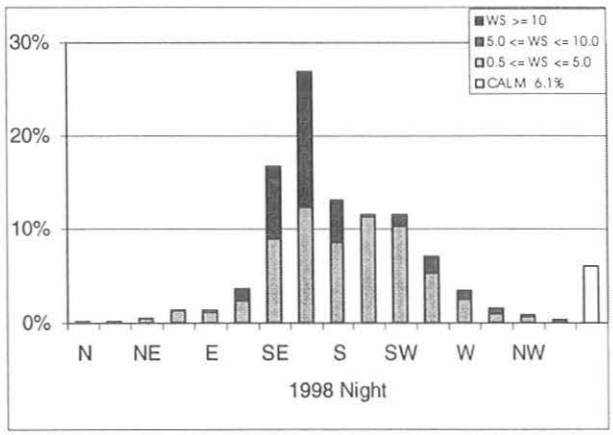

Fig. 1.4. Histograms of surface winds for MLO for 1998 day (left) and night (right). Percent frequency of winds is shown for each of 16 direction classes and 3 wind speed (WS) classes. Percent frequency of calm winds (WS <0.5 ms^{-1}) is indicated in the legends and is shown as an open bar on each histogram.

TABLE 1.8. BRW 1998 and 1999 Monthly Climate Summary

	Jan.	Feb.	March	April	May	June	July	Aug.	Sept.	Oct.	Nov.	Dec.	Year
							1998						
Prevailing wind direction	ENE	NE	E	ENE	ENE	E	E	E	ESE	ENE	ENE	SSW	ENE
Average wind speed (m s^{-1})	6.4	5.2	5.0	4.8	6.1	4.4	6.4	5.4	5.0	6.5	6.7	3.3	5.5
Maximum wind speed* (m s^{-1})	13	14	13	14	14	9	12	16	14	21	15	12	21
Direction of max. wind* (deg)	76	56	108	80	62	88	92	219	103	55	64	79	55
Average station pressure (hPa)	1022.9	1014.4	1011.6	1008.2	1012.0	1015.4	1013.1	1003.9	1007.2	1010.1	1011.0	1019.1	1012.4
Maximum pressure* (hPa)	1037	1032	1038	1029	1023	1024	1023	1018	1021	1024	1028	1044	1044
Minimum pressure* (hPa)	998	994	994	993	997	1006	1000	983	987	983	998	991	983
Average air temperature (°C)	-26.2	-26.0	-19.0	-11.4	-4.8	1.5	5.3	5.3	2.8	-4.0	-10.4	-19.9	-8.7
Maximum temperature* (°C)	-19	-11	-1	-2	8	18	15	14	9	3	0	-1	18
Minimum temperature* (°C)	-39	-36	-31	-23	-18	-3	-1	-1	-4	-19	-22	-37	-39
Average dewpoint temperature (°C)	-29.0	-29.0	-21.3	-12.9	-6.2	0.6	4.3	4.0	1.3	-6.1	-12.5	-22.0	-11.0
Maximum dewpoint temperature (°C)	-22	-13	-3	-3	4	10	11	13	7	2	0	-1	13
Minimum dewpoint temperature (°C)	-42	-40	-34	-26	-21	-4	-2	-3	-8	-22	-25	-41	-42
Precipitation (mm)	0	0	0	0	1	1	15	21	14	1	0	0	54
							1999						
Prevailing wind direction	SW	NE	NE	E	E	E	E	E	E	E	ESE	SE	E
Average wind speed (m s^{-1})	3.8	4.6	3.7	5.2	4.8	4.3	5.2	6.1	4.5	6.2	4.1	5.0	4.8
Maximum wind speed* (m s^{-1})	14	10	13	13	11	9	11	16	13	15	17	12	17
Direction of max. wind* (deg)	84	89	67	102	104	61	75	92	354	104	113	127	113
Average station pressure (hPa)	1015.4	1008.5	1019.3	1018.1	1016.6	1014.0	1014.6	1010.2	1008.9	1015.1	1010.6	1018.1	1014.2
Maximum pressure* (hPa)	1048	1026	1041	1037	1035	1020	1027	1021	1035	1031	1035	1041	1048
Minimum pressure* (hPa)	974	997	997	991	992	1001	997	1001	985	1000	993	997	974
Average air temperature (°C)	-29.0	-26.9	-27.0	-19.8	-5.8	0.1	3.9	4.5	0.4	-8.0	-18.4	-27.9	-12.3
Maximum temperature* (°C)	-9	-18	-17	-4	1	6	17	20	8	-1	-9	-17	20
Minimum temperature* (°C)	-42	-41	-41	-30	-17	-8	-2	-1	-8	-19	-29	-37	-42
Average dewpoint temperature (°C)	-31.7	-29.5	-29.7	-21.8	-6.9	-0.4	2.2	3.0	-1.4	-10.7	-20.9	-30.7	-14.8
Maximum dewpoint temperature (°C)	-9	-20	-19	-5	0	2	12	12	6	-3	-11	-20	12
Minimum dewpoint temperature (°C)	-46	-45	-46	-33	-19	-4	-2	-4	-10	-21	-32	-40	-46
Precipitation (mm)	0	0	0	0	1	6	9	19	4	0	0	0	40

Instrument heights: wind, 10.5 m; pressure, 9.5 m (MSL); air temperature, 2.9 m; dewpoint temperature, 2.9 m. Wind and temperature instruments are on a tower 25 m northeast of the main building.

*Maximum and minimum values are hourly averages.

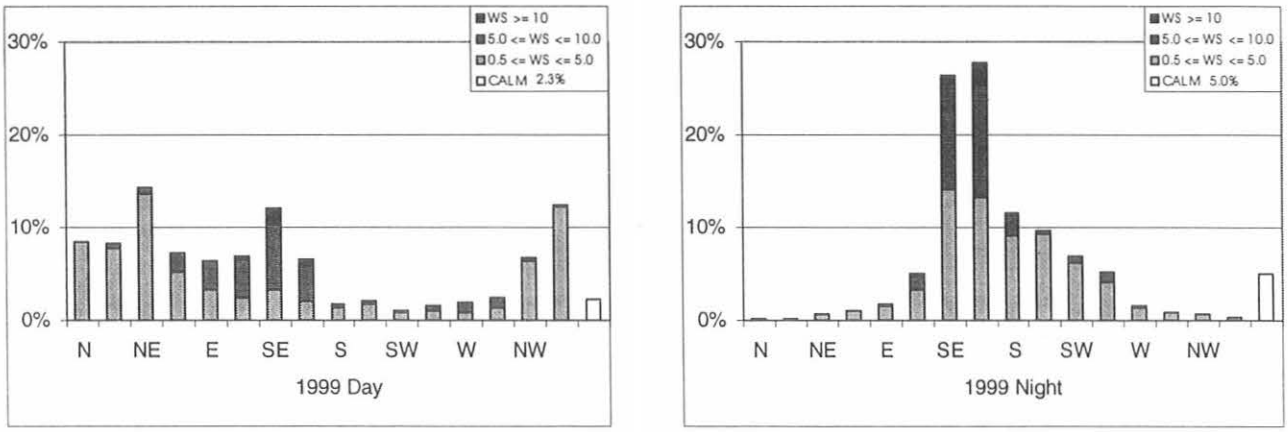

Fig. 1.5. Histograms of surface winds for MLO for 1999 day (left) and night (right). Percent frequency of winds is shown for each of 16 direction classes and 3 wind speed (WS) classes. Percent frequency of calm winds (WS <0.5 ms^{-1}) is indicated in the legends and is shown as an open bar on each histogram.

Pressure gradient controlled winds (WS ≥ 10 ms^{-1}) from predominately westerly and southeasterly directions, occurred 4.6% of the time in 1998 and 3.8% in 1999, both of which were below the 21-yr average of 7.3%. The annual average wind speeds for both 1998 and 1999 were below the long-term average (Tables 1.9 and 1.10). The upslope, or northerly component, winds (north-northwest through east-northeast) that occurred 2.5% of the time in 1998 and 1999, are the result of the daytime upslope flow extending into the early evening hours.

For the day regime the 1998 and 1999 wind histograms (Figures 1.4 and 1.5) indicate that winds from the west-northwest through east-southeast occurred 63.6% of the time in 1998 and 59.9% of the time in 1999 compared with 58.4% for the 21-yr climatology (Figure 1.3). Pressure gradient controlled winds (WS ≥ 10 ms^{-1}) occurred 3.6% of the time in 1998 and 2.9% of the time in 1999, both of which were lower than the 21-yr average of 6%. In 1998 and 1999 the pressure gradient winds, which are usually associated with storms, followed the expected pattern of fewer occurrences during the day regime. The day wind histogram is more uniformly distributed in the light wind classes than the night wind histogram. This is due to the variable wind directions during the transition periods at dawn and dusk, most of which are included in this regime.

The average ambient temperatures for 1998 and 1999 (Tables 1.9 and 1.10), combining both day and night regimes, were 8.2°C and 7.2°C, respectively, both of which were above the long-term average of 7.1°C. April 1999 and October 1999 both tied the minimum record temperature for the month. The average barometric pressure for 1998 (681.1 hPa) was above the long-term average of 680.4 hPa, while 1999 (680.0 hPa) was below the long-term average. The months of February, April, and July in 1998 each tied their maximum values for the month. The precipitation amounts in 1998 (66 mm) and 1999 (106 mm) were both much lower than the long-term average of 480 mm.

Samoa

A comparison of SMO's 1998 and 1999 wind histograms (Figure 1.6) to that of the 21-yr period (Figure 1.7) shows a considerably lower percentage (46%) of clean air sector winds (north-northwest through southeast) in 1998 while 1999 (72.4%) was considerably higher than the long-term average of 60.3%. The occurrence of winds in the 10 ms^{-1} or greater class was 5.4% in 1998 and 4.7% in 1999, while the expected occurrence based on the 21-yr average is 4.8%. The annual average wind speed for 1998 (5.9 ms^{-1}) was above normal, while 1999 (4.5 ms^{-1}) (Table 1.11) was slightly below the long-term-average of 4.9 ms^{-1}.

The average ambient temperatures for 1998 (26.2°C) and 1999 (26.7°C) were cooler than the 21-yr average of 27.1°C. Record minimum temperatures were tied in July 1998 and October 1999. The average barometric pressures for 1998 (1002.1 hPa) and 1999 (1001.8 hPa) were higher than the 21-yr average of 1000.3 hPa. High-pressure records were tied in the months of May, August, September, and October of 1998. A new high-pressure record was set in July 1998 that also ties the all time record high in 23 years of observations at SMO. The precipitation amounts in 1998 (1172 mm) and 1999 (1858 mm) were drier than the normal amount of 2108 mm.

South Pole

The distribution of the surface wind direction in 1998 and 1999 (Figure 1.8) shows a percentage of "clean air" sector (grid north-northwest through east-southeast) winds of 93.2% in 1998 and 92.7% in 1999 similar to the 21-yr average of 93.9% (Figure 1.9). The percentage of winds in the 10 ms^{-1} or greater class was 2.6% for both 1998 and 1999 compared to 3.9% for the long-term average. The annual average wind speeds for 1998 (5.2 ms^{-1}) and 1999 (5.0 ms^{-1}) were slightly less than the long-term average wind speed of 5.4 ms^{-1}.

The average temperatures for 1998 (-50.0°C) (Table 1.12) and 1999 (-49.9°C) were cooler than the long-term average of -49.0°C. January 1998 and December 1999 both tied their record minimum temperatures for the month. The minimum temperature in 1998 of -75°C occurred in May and September. The minimum temperature in 1999 of -74°C occurred in July. The annual average barometric pressure for 1998 (677.4 hPa) was 1.9 hPa lower than the 21-yr average of 679.3 hPa, while the average barometric pressure for 1999 was equal to the long-term average. May 1998 tied its record low-pressure record, and June 1999 set a new high pressure reading for the month, surpassing the old June record by 4 hPa.

TABLE 1.9. MLO 1998 Monthly Climate Summary

	Jan.	Feb.	March	April	May	June	July	Aug.	Sept.	Oct.	Nov.	Dec.	Year
							Night						
Prevailing wind direction	WSW	SW	SSE	SE	SSE	SSE	SSE	SSE	SSE	SSE	SSE	SSE	SSE
Average wind speed ($m\ s^{-1}$)	5.2	3.2	4.9	4.5	2.7	3.6	4.3	2.9	3.0	4.6	5.2	4.8	4.0
Maximum wind speed* ($m\ s^{-1}$)	16	9	13	13	9	11	14	8	10	12	14	15	16
Direction of max. wind* (deg)	249	306	149	157	159	169	169	176	159	159	159	164	249
Average station pressure (hPa)	679.6	682.0	680.9	680.8	680.9	681.5	682.0	681.5	680.5	681.4	680.8	680.4	681.1
Maximum pressure* (hPa)	683	686	684	684	683	684	686	684	682	685	684	684	686
Minimum pressure* (hPa)	671	678	677	678	678	679	679	678	678	678	677	676	671
Average air temperature (°C)	5.4	6.1	5.2	5.2	6.5	8.1	6.9	6.8	6.6	6.4	5.4	4.8	6.2
Maximum temperature* (°C)	12	13	10	12	13	17	15	14	12	12	10	10	17
Minimum temperature* (°C)	-3	-2	1	-1	0	2	1	1	2	1	1	0	-3
Average dewpoint temperature (°C)	-24.3	-20.6	-19.1	-22.0	-17.4	-15.1	-13.3	-12.0	-12.9	-13.0	-10.7	-15.5	-16.0
Maximum dewpoint temperature (°C)	1	7	2	3	5	5	6	8	7	6	6	4	8
Minimum dewpoint temperature (°C)	-33	-33	-35	-38	-31	-30	-34	-29	-27	-31	-33	-31	-38
Precipitation (mm)	7	0	0	0	0	0	1	0	0	1	7	0	16
							Day						
Prevailing wind direction	NW	NNW	SE	N	NNW	NE	NE	NNW	NE	NE	SE	SE	NNW
Average wind speed ($m\ s^{-1}$)	4.6	3.1	4.3	4.2	2.9	3.3	4.3	3.0	2.7	3.8	4.4	3.9	3.7
Maximum wind speed* ($m\ s^{-1}$)	15	12	13	13	9	10	12	10	8	11	13	14	15
Direction of max. wind* (deg)	256	310	132	159	137	155	169	141	157	164	149	162	256
Average station pressure (hPa)	679.7	681.9	681.1	681.1	681.1	681.7	682.2	681.7	680.6	681.4	680.8	680.3	681.2
Maximum pressure* (hPa)	683	686	685	685	684	684	685	684	683	685	683	684	686
Minimum pressure* (hPa)	672	678	677	678	678	679	679	678	678	678	677	676	672
Average air temperature (°C)	9.7	10.2	9.6	9.7	10.5	12.3	11.6	10.7	10.5	10.3	8.7	8.0	10.2
Maximum temperature* (°C)	17	17	15	15	17	20	18	17	18	17	15	15	20
Minimum temperature* (°C)	-2	0	0	0	2	5	3	3	2	1	1	1	-2
Average dewpoint temperature (°C)	-17.0	-12.7	-11.2	-11.6	-7.7	-7.1	-7.4	-3.4	-2.8	-6.3	-7.3	-9.3	-8.3
Maximum dewpoint temperature (°C)	4	7	7	6	7	6	8	9	8	8	8	5	9
Minimum dewpoint temperature (°C)	-32	-31	-32	-34	-30	-30	-32	-28	-27	-29	-33	-31	-34
Precipitation (mm)	1	0	0	1	3	0	4	17	3	13	7	0	50

Instrument heights: wind, 10.2 m; pressure, 3398.4 m (MSL); air temperature, 2.0 m; dewpoint temperature, 2.0 m. Wind and temperature instruments are on a tower 15 m southwest of the main building.
*Maximum and minimum values are hourly averages.

TABLE 1.10. MLO 1999 Monthly Climate Summary

	Jan.	Feb.	March	April	May	June	July	Aug.	Sept.	Oct.	Nov.	Dec.	Year
							Night						
Prevailing wind direction	SE	S	SSE	SE	SSE	SE	SSE	SE	SSE	SE	SE	SE	SSE
Average wind speed ($m\ s^{-1}$)	4.5	2.5	4.6	3.2	3.6	3.6	4.6	5.1	3.5	4.6	4.4	5.2	4.3
Maximum wind speed* ($m\ s^{-1}$)	14	5	13	10	10	9	13	14	15	13	11	13	15
Direction of max. wind* (deg)	130	180	157	156	163	143	156	126	117	151	161	137	117
Average station pressure (hPa)	679.4	679.7	678.9	679.1	680.4	680.9	680.5	681.2	680.1	680.5	680.2	678.7	680.0
Maximum pressure* (hPa)	683	683	682	682	683	684	683	684	683	683	683	682	684
Minimum pressure* (hPa)	675	677	676	676	678	678	678	678	678	675	678	673	673
Average air temperature (°C)	3.9	2.6	3.1	2.4	5.7	7.3	7.3	7.3	6.3	6.6	5.0	3.3	5.1
Maximum temperature* (°C)	10	9	8	11	12	14	14	12	12	11	10	8	14
Minimum temperature* (°C)	0	-2	-2	-3	2	3	3	3	0	2	0	-2	-3
Average dewpoint temperature (°C)	-13.5	-11.7	-13.7	-13.4	-11.6	-13.4	-17.3	-10.9	-15.2	-13.3	-14.4	-6.2	-12.9
Maximum dewpoint	5	6	6	3	5	5	6	8	6	5	4	5	8
Minimum dewpoint temperature (°C)	-32	-27	-27	-30	-26	-30	-31	-30	-28	-26	-32	-25	-32
Precipitation (mm)	6	3	1	1	0	0	0	0	0	0	0	23	35
							Day						
Prevailing wind direction	SE	NE	SE	NNW	NE	NE	SE	SE	NW	NE	NE	SE	NE
Average wind speed ($m\ s^{-1}$)	4.6	1.8	3.7	3.1	3.4	3.6	3.9	4.7	3.3	3.9	4.0	5.2	3.9
Maximum wind speed* ($m\ s^{-1}$)	18	5	11	8	10	10	12	15	13	13	12	14	18
Direction of max. wind* (deg)	145	201	147	161	156	32	136	122	115	148	152	152	145
Average station pressure (hPa)	679.3	679.7	679.0	279.2	680.5	680.9	680.7	681.2	680.1	680.4	680.1	678.6	680.0
Maximum pressure* (hPa)	683	683	682	682	683	684	684	685	683	683	682	682	685
Minimum pressure* (hPa)	675	676	677	677	678	678	679	678	678	676	677	673	673
Average air temperature (°C)	7.3	6.3	7.2	6.4	10.0	12.1	11.9	11.8	10.1	10.7	8.9	6.8	9.2
Maximum temperature* (°C)	16	13	12	14	15	17	18	18	17	18	14	14	18
Minimum temperature* (°C)	-1	-2	-2	-2	3	4	5	4	2	3	2	-2	-2
Average dewpoint temperature (°C)	-8.6	-6.7	-7.5	-6.5	-6.3	-7.5	-8.3	-4.5	-4.5	-6.1	-9.2	-5.3	-6.7
Maximum dewpoint temperature (°C)	6	9	10	5	6	8	8	12	8	8	5	7	12
Minimum dewpoint temperature (°C)	-29	-28	-26	-28	-24	-30	-27	-29	-29	-25	-26	-25	-30
Precipitation (mm)	2	23	1	9	11	2	1	0	0	5	0	16	71

Instrument heights: wind, 10.2 m; pressure, 3398.4 m (MSL); air temperature, 2.0 m; dewpoint temperature, 2.0 m. Wind and temperature instruments are on a tower 15 m southwest of the main building.

*Maximum and minimum values are hourly averages.

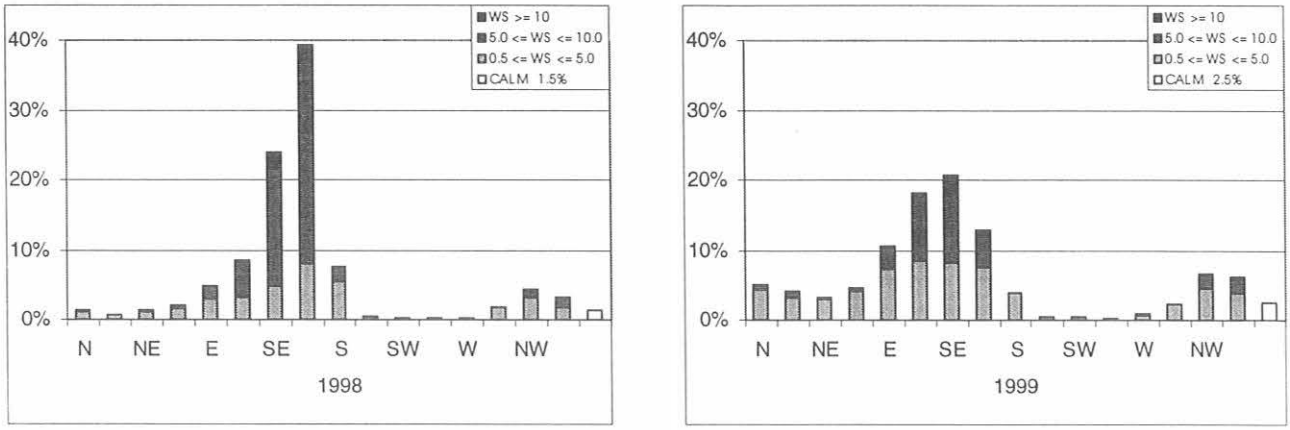

Fig. 1.6. Histograms of surface winds for SMO for 1998 (left) and 1999 (right). Percent frequency of winds is shown for each of 16 direction classes and 3 wind speed (WS) classes. Percent frequency of calm winds (WS <0.5 ms^{-1}) is indicated in the legends and is shown as an open bar on each histogram.

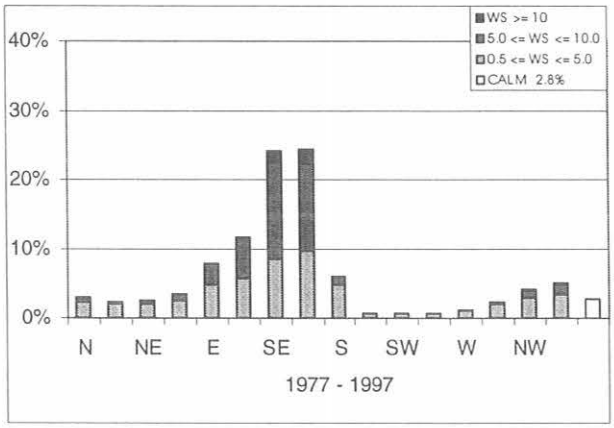

Fig. 1.7. Histogram of surface winds for SMO 1977 through 1997. Percent frequency of winds is shown for each of 16 direction classes and 3 wind speed (WS) classes. Percent frequency of calm winds (WS <0.5 ms^{-1}) is indicated in the legend and is shown as an open bar on the histogram.

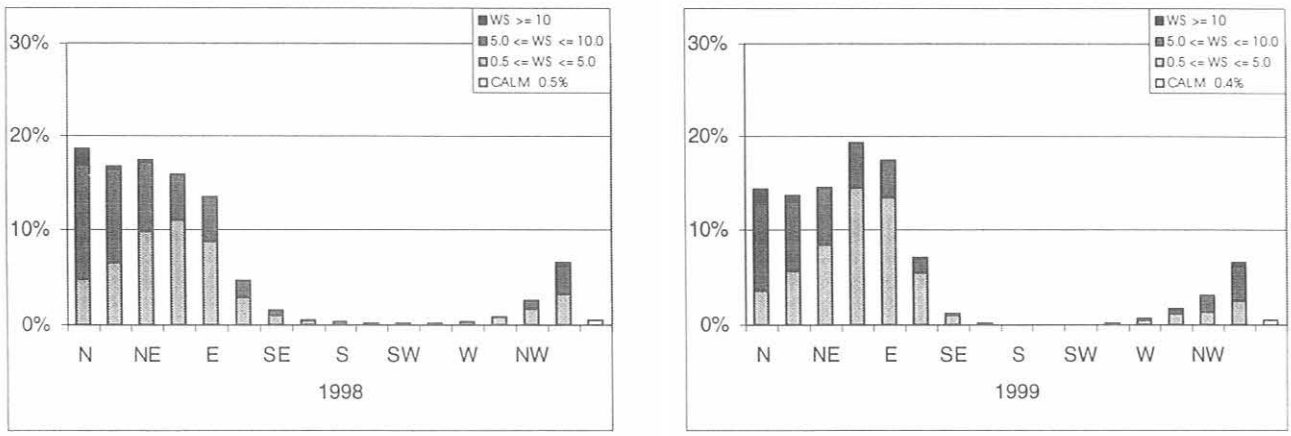

Fig. 1.8. Histograms of surface winds for SPO for 1998 (left) and 1999 (right). Percent frequency of winds is shown for each of 16 direction classes and 3 wind speed (WS) classes. Percent frequency of calm winds (WS <0.5 ms^{-1}) is indicated in the legends and is shown as an open bar on each histogram.

TABLE 1.11. SMO 1998 and 1999 Monthly Climate Summary

	Jan.	Feb.	March	April	May	June	July	Aug.	Sept.	Oct.	Nov.	Dec.	Year
							1998						
Prevailing wind direction	NW	SSE	SSE	SSE	SSE	SE	SSE	SSE	SSE	SE	SE	NNW	SSE
Average wind speed (m s^{-1})	5.6	4.1	4.4	5.9	6.1	8.1	6.5	7.5	8.0	5.9	3.8	5.2	5.9
Maximum wind speed* (m s^{-1})	13	11	12	10	11	13	11	12	13	10	10	13	13
Direction of max. wind* (deg)	135	155	132	132	165	141	138	146	157	127	95	344	141
Average station pressure (hPa)	998.4	999.8	1000.1	1003.0	1003.7	1003.7	1004.6	1004.2	1004.1	1002.6	1000.8	999.4	1002.1
Maximum pressure* (hPa)	1002	1006	1004	1006	1007	1007	1009	1009	1009	1008	1004	1004	1009
Minimum pressure* (hPa)	992	995	996	999	1000	999	1000	1000	1000	999	998	995	992
Average air temperature (°C)	27.2	27.0	27.0	26.5	25.8	25.6	24.4	25.1	25.7	26.4	27.2	27.2	26.2
Maximum temperature* (°C)	29	30	30	29	27	27	26	27	27	29	29	30	30
Minimum temperature* (°C)	25	25	24	23	24	23	21	23	23	24	24	23	21
Average dewpoint temperature (°C)	25.0	23.8	23.5	22.9	22.0	22.4	20.0	22.2	22.7	23.0	23.6	23.5	22.8
Maximum dewpoint temperature (°C)	26	26	26	26	25	24	24	25	25	25	25	26	26
Minimum dewpoint Temperature (°C)	23	22	20	19	18	18	14	19	19	18	21	20	14
Precipitation (mm)	150	42	347	18	27	56	22	10	63	101	36	300	1172
							1999						
Prevailing wind Direction	SE	NNW	SE	ESE	SSE	SE	ESE	ESE	SE	ESE	SE	N	SE
Average wind Speed (m s^{-1})	3.9	3.7	4.0	3.5	4.2	4.1	4.8	5.5	6.7	5.9	4.2	3.7	4.5
Maximum wind Speed* (m s^{-1})	11	10	9	10	14	12	9	13	19	13	10	9	19
Direction of max. Wind* (deg)	348	330	109	115	155	101	139	151	126	131	312	271	126
Average station Pressure (hPa)	1000.5	1000.2	1000.8	1001.5	1002.0	1002.9	1003.0	1004.0	1003.3	1002.6	1001.4	1000.3	1001.8
Maximum pressure* (hPa)	1004	1004	1004	1005	1005	1006	1006	1008	1007	1007	1005	1004	1008
Minimum pressure* (hPa)	997	995	997	998	999	1000	1000	1001	999	999	998	997	995
Average air Temperature (°C)	26.2	26.8	27.5	27.8	26.3	26.7	26.6	26.4	26.2	26.1	26.5	27.3	26.7
Maximum temperature* (°C)	29	29	30	30	30	29	28	28	28	28	28	29	30
Minimum temperature* (°C)	23	23	24	24	22	24	23	22	23	21	22	24	21
Average dewpoint temperature (°C)	24.3	24.7	25.0	25.4	24.4	24.5	23.9	22.7	22.4	22.7	22.9	22.9	23.8
Maximum dewpoint temperature (°C)	26	26	27	27	26	26	26	25	24	24	25	25	27
Minimum dewpoint temperature (°C)	21	22	22	23	21	22	22	19	18	20	20	18	18
Precipitation (mm)	228	160	87	38	360	97	33	75	282	147	195	155	1858

Instrument heights: wind, 13.7 m; pressure, 78.5 m (MSL); air temperature, 18.9 m; dewpoint temperature, 18.9 m. Wind and temperature instruments are on Lauagae Ridge, 110 m northeast of the main building.

*Maximum and minimum values are hourly averages.

TABLE 1.12. SPO 1998 and 1999 Monthly Climate Summary

	Jan.	Feb.	March	April	May	June	July	Aug.	Sept.	Oct.	Nov.	Dec.	Year
							1998						
Prevailing wind direction	N	NE	NE	ENE	ESE	E	NNE	NE	ENE	NE	N	NNE	N
Average wind speed (m s^{-1})	4.5	4.4	5.2	4.9	6.1	5.0	6.2	5.5	5.1	5.2	6.6	3.6	5.2
Maximum wind speed* (m s^{-1})	9	9	9	11	14	10	14	12	11	10	14	9	14
Direction of max. wind* (deg)	359	3	13	3	351	346	9	353	28	26	3	18	351
Average station pressure (hPa)	686.1	683.8	678.2	668.0	675.3	680.1	673.2	672.6	675.9	675.6	678.5	682.9	677.4
Maximum pressure* (hPa)	698	694	687	681	685	689	684	683	687	696	693	692	698
Minimum pressure* (hPa)	680	675	664	658	653	666	659	660	664	662	667	670	653
Average air temperature (°C)	-27.5	-38.4	-53.0	-62.2	-58.0	-54.6	-59.1	-63.0	-62.2	-53.8	-36.4	-28.6	-50.0
Maximum temperature* (°C)	-20	-26	-42	-46	-35	-37	-44	-47	-46	-39	-23	-21	-20
Minimum temperature* (°C)	-38	-52	-62	-73	-75	-69	-74	-73	-75	-66	-48	-34	-75
Average dewpoint temperature (°C)	-30.4	-41.7	-56.3	-64.6	-61.0	-57.8	-61.8	-65.8	-65.4	-56.8	-39.2	-31.5	-52.9
Maximum dewpoint temperature (°C)	-23	-29	-45	-49	-37	-40	-46	-49	-49	-41	-26	-24	-23
Minimum dewpoint Temperature (°C)	-42	-55	-66	-76	-78	-73	-76	-76	-79	-69	-50	-37	-79
Precipitation (mm)	0	0	0	0	0	0	0	0	0	0	0	0	0
							1999						
Prevailing wind Direction	NNW	E	ENE	NE	N	ENE	E	NE	E	N	NNE	E	ENE
Average wind Speed (m s^{-1})	4.7	4.6	4.6	5.7	6.1	5.3	5.3	6.0	5.1	5.4	4.0	3.6	5.0
Maximum wind Speed* (m s^{-1})	12	12	10	12	12	11	12	14	12	12	9	8	14
Direction of max. Wind* (deg)	341	9	336	358	10	25	348	32	6	357	17	296	32
Average station Pressure (hPa)	690.5	685.1	681.0	671.5	674.5	688.8	675.0	674.8	679.4	671.9	679.9	679.1	679.3
Maximum pressure* (hPa)	703	695	692	686	692	711	690	691	699	688	698	693	711
Minimum pressure* (hPa)	680	674	673	660	658	673	660	657	665	659	662	669	657
Average air Temperature (°C)	-26.0	-41.0	-54.0	-60.6	-56.8	-58.2	-62.7	-56.4	-62.0	-51.1	-39.4	-31.5	-49.9
Maximum temperature* (°C)	-19	-22	-39	-53	-36	-42	-46	-38	-44	-33	-32	-24	-19
Minimum temperature* (°C)	-34	-49	-69	-72	-73	-71	-74	-69	-72	-69	-51	-41	-74
Average dewpoint temperature (°C)	-28.5	-44.5	-57.6	-64.3	-60.4	-61.6	-66.3	-60.3	-65.8	-54.1	-43.2	-34.9	-53.2
Maximum dewpoint temperature (°C)	-19	-24	-42	-56	-38	-45	-50	-41	-47	-35	-34	-27	-19
Minimum dewpoint temperature (°C)	-37	-53	-73	-76	-77	-75	-78	-74	-75	-72	-55	-45	-78
Precipitation (mm)	0	0	0	0	0	0	0	0	0	0	0	0	0

Instrument heights: wind, 10.0 m; pressure, 2841 m (MSL); air temperature, 2.0 m; dewpoint temperature, 2.0 m. Wind and temperature instruments are on a tower 91.4-m grid north-northwest of the Atmospheric Research Observatory.

*Maximum and minimum values are hourly averages.

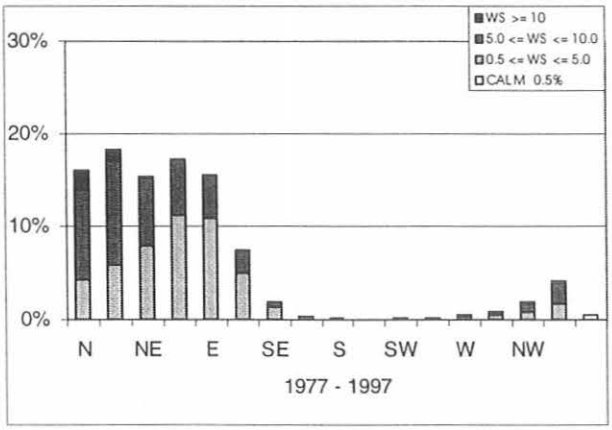

Fig. 1.9. Histogram of surface winds for SPO 1977 through 1997. Percent frequency of winds is shown for each of 16 direction classes and 3 wind speed (WS) classes. Percent frequency of calm winds (WS <0.5 ms^{-1}) is indicated in the legend and is shown as an open bar on the histogram.

Acknowledgment. The Observatory Operations group wishes to thank Brad Halter who was responsible for maintaining meteorological sensor hardware and electronics maintenance in addition to his many other contributions to CMDL.

1.6. REFERENCES

Arctic Research Consortium of the U.S. (ARCUS), *The Future of an Arctic Resource: Recommendations from the Barrow Area Research Support Workshop*, 104 pp., ARCUS, Fairbanks, AK, 1999.

Hofmann, D.J., J.T. Peterson, and R.M. Rosson (Eds.), *Climate Monitoring and Diagnostics Laboratory Summary Report No. 24 1996-1997*, 166 pp., NOAA Environmental Research Laboratories, Boulder, CO, 1998.

Peterson, J.T., and R.M. Rosson (Eds.), *Climate Monitoring and Diagnostics Laboratory No. 22 Summary Report 1993*, 152 pp., NOAA Environmental Research Laboratories, Boulder, CO, 1994.

World Meteorological Organization (WMO), *Guide to Meteorological Instrumentation and Observing Practices, No. 8, Tech Paper 3*, 347 pp., World Meteorological Organization, Geneva, 1969.

2. Carbon Cycle

P.P. TANS (EDITOR), P.S. BAKWIN, L. BRUHWILER, T.J. CONWAY, E.J. DLUGOKENCKY, D.W. GUENTHER, D.R. KITZIS, P.M. LANG, K.A. MASARIE, J.B. MILLER, P.C. NOVELLI, K.W. THONING, M. TRUDEAU, B.H. VAUGHN*, J.W.C. WHITE*, AND C. ZHAO

2.1. OVERVIEW

It is the goal of the CMDL Carbon Cycle Greenhouse Gases (CCGG) group to improve the understanding of the factors that determine the atmospheric burdens of major trace gases influencing the earth's climate, in particular CO_2, CH_4, and CO. The anthropogenic impact on each of these species is large, but natural cycles are involved as well. The international climate change negotiations during December 1997 in Kyoto, Japan, highlighted the fact that the world has tentatively started to take steps to try to control the steadily increasing climate forcing by anthropogenic greenhouse gases. One of the factors required for effective policies is a quantitative understanding of what controls the atmospheric concentrations.

Our main tool for studying the global budgets of the trace gases is the measurement of atmospheric spatial concentration patterns and their changes over time. Two experimental methods have been employed from the start of the Geophysical Monitoring for Climatic Change program, the forerunner of CMDL: continuous measurements in remote clean air locations, namely the four CMDL observatories, and weekly pairs of discrete flask samples, also at remote clean air locations. Initially the samples were analyzed only for CO_2, but gradually more species have been added (Table 2.1). The isotopic ratio measurements are being carried out at the Institute for Arctic and Alpine Research (INSTAAR) of the University of Colorado in close cooperation with the CCGG group. Anomalous ^{17}O enrichments are measured in a small subset of the flasks by a group at the University of California, San Diego. The global air samples provide a unique resource for narrowing uncertainties of greenhouse gas budgets as well as other atmospheric problems. The feasibility of adding additional measurements continues to be investigated.

Information on sources and sinks of the trace gases is obtained from their rates of change and from their spatial distributions. Numerical models of atmospheric transport, operating in both two and three dimensions, provide the quantitative link. Since this is working "backwards" from observed concentrations to the sources causing them, this problem is in the class of so-called inverse problems. The greatest limitation is sparseness of data, especially in regions close to important sources and sinks. Therefore, the spatial coverage of the global cooperative air sampling network has gradually expanded. Isotopic analyses were added because different sources/sinks may be characterized by different isotopic "signatures."

To overcome the limitation of having only measurements from the remote marine boundary layer, two new approaches were initiated. One is to continuously measure a number of chemical species and atmospheric physical parameters at different heights on very tall towers. Mixing ratios (also called mole fractions) in the continental boundary layer are highly variable, making them more difficult to interpret and require much more auxiliary data than the traditional marine air samples. The second new approach is to obtain discrete air samples from low-cost airplanes in automated fashion from the boundary layer up to about 8-km altitude. These samples are then sent back to the laboratory in Boulder for analysis. In order to provide significant regional-scale constraints on the budgets of the gases measured, it is hoped that this method will be greatly expanded, especially over North America.

TABLE 2.1. Species Analyzed in Samples of the Global Air Sampling Network

Species	Start Date	Method	Precision (One Sigma)	Collaborators
CO_2	1976	NDIR	0.05 ppm (0.02%)	
CH_4	1983	GC/FID	<1 ppb (0.07%)	
CO	1988	GC/HgO	0.5 ppb (0.5-1%)	
H_2	1988	GC/HgO	2 ppb (0.4%)	
$CO_2{}^{13}C$	1990	IRMS	0.01‰	CU/INSTAAR
$CO_2{}^{18}O$	1990	IRMS	0.03‰	CU/INSTAAR
N_2O	1996	GC/ECD	0.2 ppb (0.07%)	HATS Group
SF_6	1996	GC/ECD	0.03 ppb (1%)	HATS Group
$CO_2{}^{17}O$	1997	IRMS	0.03‰	UC San Diego
$CH_4{}^{13}C$	1998	GC/IRMS	0.06‰	CU/INSTAAR

CU, University of Colorado
INSTAAR, Institute for Arctic and Alpine Research, University of Colorado, Boulder
UC, University of California

Since the global coverage of the sampling network is unmatched, CMDL plays an active role in bringing together the measurements from many different laboratories around the world. Toward this end, measurements of standard reference gases, as well as actual field samples, are being intercompared. The CMDL link with the Commonwealth Scientific and Industrial Research Organization (CSIRO, Australia) is particularly strong in this regard. For CO_2 and CO, CMDL provides calibrated reference gas mixtures under the auspices of the World Meteorological Organization (WMO).

A common global database for CO_2, named Globalview-CO_2, is continually assembled, updated, and is currently based on the measurements from laboratories in 14 countries, hopefully without significant calibration or methodological discrepancies. Its intended use is for three-dimensional (inverse) modeling. The first data base release was in 1996 and has been updated once a year since then (http://www.cmdl.noaa.gov/ccgg/globalview/co2/default.html). Plans are to maintain and enlarge this database, as well as assemble similar ones for isotopic ratios, CH_4, CO, etc.

Full individual data records and monthly means can be obtained for each species for each sampling site from the CMDL World Wide Web page (http://www.cmdl.noaa.gov), the ftp file server's "pub" directory (ftp.cmdl.noaa.gov), from the WMO World Data Center for Greenhouse Gases in Tokyo and from the Carbon Dioxide Information Analysis Center in Oak Ridge, Tennessee.

*Institute for Arctic and Alpine Research, University of Colorado

2.2. CARBON DIOXIDE

2.2.1. IN SITU CARBON DIOXIDE MEASUREMENTS

The mixing ratio of atmospheric CO_2 was measured with a continuously operating non-dispersive infrared analyzer (NDIR) at each of the four CMDL observatories during 1998 and 1999, as in previous years. Monthly and annual mean CO_2 concentrations are given in Table 2.2. These values are provisional, pending final calibrations of station standards. Preliminary monthly average CO_2 mixing ratios, selected for background conditions for the entire record through 1999, are plotted versus time for the four observatories (Figure 2.1.)

A new data acquisition system was installed at the Samoa Observatory, American Samoa (SMO) in July of 1998. This system uses an Intel CPU-based Unix workstation for controlling the CO_2 NDIR measurements. This system replaced the Control and Monitoring System (CAMS) data acquisition unit that experienced frequent failures.

At the Mauna Loa Observatory, Hawaii (MLO) in November 1998, the continuous CO_2, CH_4, and CO systems were moved into the Network for the Detection of Stratospheric Change (NDSC) building. The computer used for controlling the data acquisition was upgraded to an Intel CPU-based Unix workstation. The CO_2 analytical system was upgraded using a new design (Figure 2.2). These design upgrades were installed at the South Pole Observatory, Antarctica (SPO) in December of 1998, and the same changes are planned for the Barrow Observatory, Alaska (BRW) and SMO in 2000.

This design involved new modular hardware to ensure each module in the CO_2 system can be replaced easily in case of failure. Three new rack-mountable boxes were installed and are shown in Figure 2.2 as dashed lines. The first contains the hardware for controlling the ambient air sample flow rates and pressure from the intake lines and pumps. This box is shared with the CH_4 and CO analysis systems. The second box controls the flow rate and elects the sample or standard gas that flows to the CO_2 analyzer. The third box is used for filling flasks from the ambient air sample lines.

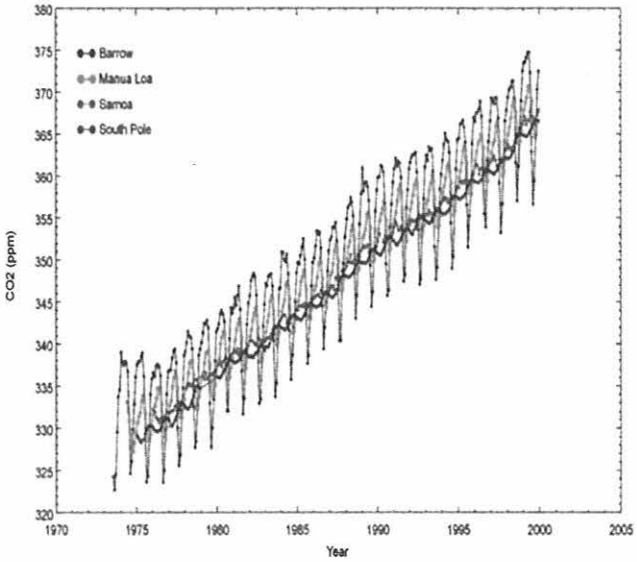

Fig. 2.1. Preliminary selected monthly mean CO_2 mole fractions in dry air expressed in ppm (μmol/mol) at the four CMDL observatories.

TABLE 2.2. Provisional 1998 and 1999 Monthly and Annual Mean CO_2 Mole Fractions From Continuous Analyzer Data (μmol mol^{-1}, Relative to Dry Air WMO Mole Fraction Scale)

Month	BRW	MLO	SMO	SPO
		1998		
Jan.	369.32	364.99	363.72	361.98
Feb.	370.29	365.80	363.25	362.10
March	370.59	366.95	363.44	362.26
April	371.27	368.44	363.04	362.58
May	371.33	369.32	–	362.90
June	369.18	368.79	–	363.39
July	361.53	367.59	364.83	363.92
Aug.	357.04	365.63	364.89	364.56
Sept.	361.14	363.84	364.98	364.86
Oct.	365.65	364.19	365.14	364.91
Nov.	368.96	365.36	365.72	364.93
Dec.	372.56	367.01	366.15	364.88
Year	367.40	366.49	364.52	363.61
		1999		
Jan.	373.52	367.93	366.55	364.86
Feb.	373.62	368.80	367.05	364.78
March	374.10	369.38	366.11	364.69
April	374.63	370.77	366.68	364.86
May	374.81	370.59	366.52	365.06
June	372.28	370.12	367.70	365.38
July	362.85	369.07	367.03	365.70
Aug.	356.71	366.65	367.08	366.09
Sept.	359.40	364.70	366.54	366.35
Oct.	364.86	365.17	366.80	366.48
Nov.	370.34	66.50	367.33	366.60
Dec.	372.50	367.89	367.69	366.52
Year	369.14	368.13	366.92	365.61

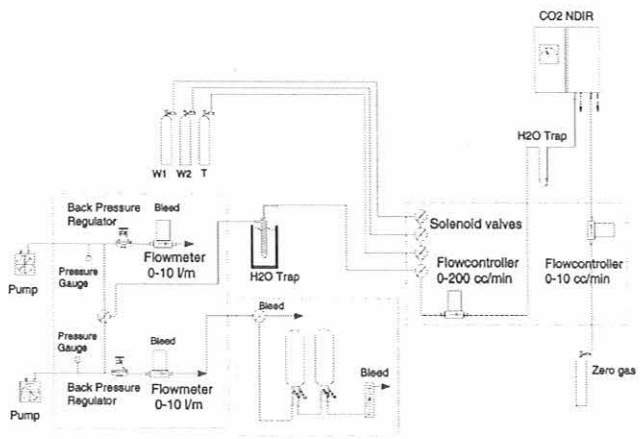

Fig. 2.2. System schematic for continuous measurement of CO_2.

Several changes occurred in the way the CO_2 system operated after the upgrade. The four CO_2 station standards were removed. These gases were used to calibrate the two working tanks at weekly intervals in order to check for any drift in mixing ratio for the working tanks. Results of calibrations over many years show that the aluminum cylinders used for containing the CO_2 standard gases were stable. Results from these calibrations did not yield enough information to justify the extra effort to prepare, maintain, and analyze the results for the station standards. In place of the weekly calibrations using the station standards, a daily 1-hr long "Target" calibration was introduced using a separate Target standard gas. These daily calibrations can be used to track any changes in working gas mixing ratios and possibly any changes in the behavior of the CO_2 analyzer.

The tubing used for carrying the gases within the system was changed to 1.6 mm (1/16 in.) OD stainless steel. This tubing is much easier to handle than the previous 3.2 mm (1/8 in.) OD stainless steel and is the same type of tubing used for the CH_4 and CO chromatographic systems. Mass flow controllers are now used for controlling the flow rate, instead of a mechanical pressure controller previously used. This provides much more stable flow rates to the analyzer and increased precision since the CO_2 analyzer is sensitive to flow rate changes.

2.2.2. Flask Sample Carbon Dioxide Measurements

Because the sources and sinks of carbon cycle gases (CO_2, CH_4, and CO) are highly variable over space and time, the CMDL global cooperative air sampling network (Figure 2.3) provides greater geographic coverage to complement the high-frequency in situ measurements at the four observatories. Air samples are collected approximately weekly at 48 land-based sites and aboard commercial ships. The samples are measured at CMDL for CO_2, CH_4, CO, H_2, N_2O, and SF_6, and at INSTAAR for ^{13}C and ^{18}O of CO_2. In 1998, 7800 samples were analyzed, and in 1999, 7500 samples were analyzed. Samples from seven sites are measured for ^{13}C of CH_4 at INSTAAR (section 2.3.3), and samples from three sites are measured for $^{17}O/^{16}O$ of CO_2 at the University of California, San Diego. The isotopic and mixing ratio measurements are used to calculate sources and sinks by numerical inverse techniques or to constrain source/sink estimates obtained from process models.

After several years of intermittent sampling because of logistical problems, weekly sampling resumed at Christmas Island (CHR) with a new sample collector in November 1998. Sampling on the island of Kaashidhoo, Republic of Maldives,

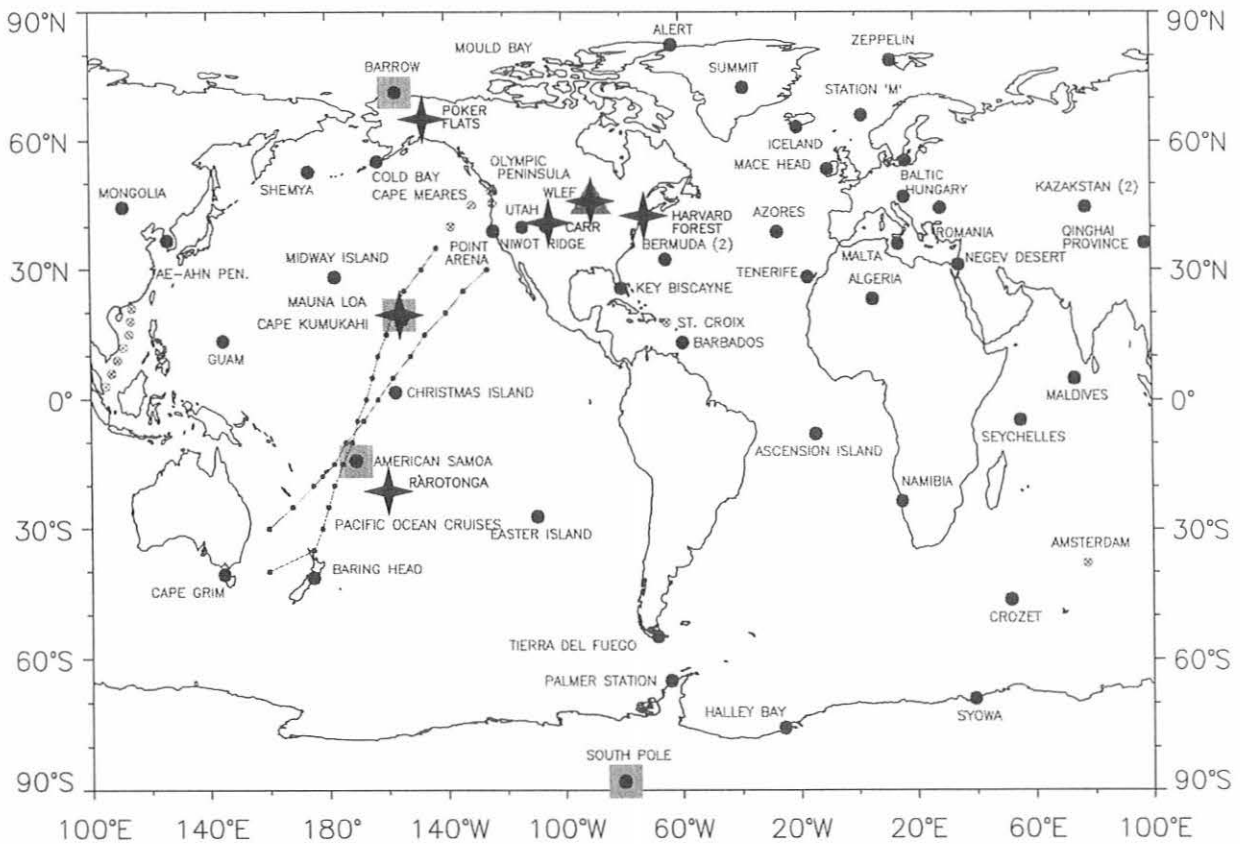

Fig. 2.3. Locations of the Carbon Cycle Greenhouse Gases Group measurement programs including the baseline observatories (squares), cooperative global air sampling network (circles), discontinued sites of same (open circles with cross), aircraft vertical profiles (stars), and the very tall tower site (triangle).

began in March 1998. Samples are collected at the Kaashidhoo Climate Observatory (KCO) in cooperation with the Maldivian Ministry of Home and Environmental Affairs and the Scripps Institution of Oceanography (SIO). The Kaashidhoo Climate Observatory was established as part of the Indian Ocean Experiment (INDOEX) project. It is hoped that sampling will continue at KCO, although no samples have been received since July 1999. Sampling at Point Arena, California, began in January 1999, thanks to the cooperation of the lighthouse keeper. This site replaces Cape Meares, Oregon, that was discontinued in March 1998. Since October 1999 monthly samples are collected at Baring Head, New Zealand. The samples are part of an intercomparison project with the National Institute for Water and Atmospheric Research (NIWA) (New Zealand). One member of each flask pair is analyzed at both NIWA and CMDL to evaluate the agreement of the two laboratories' analytical methods. Flask sampling at the tall tower site in Grifton, North Carolina (ITN) ended in June 1999 when the tower measurement program was terminated. In October 1998 the sampling program in the South China Sea (SCS) was interrupted when the M/V *Frontier Express* came off the Singapore-Hong Kong route. Sampling will resume if a suitable replacement ship can be found. The three-letter codes for two sites were changed to make them consistent with WMO conventions. The code for Mace Head, Ireland, is now MHD (formerly MHT) and the code for the site in Qinghai Province, China (formerly QPC) is now WLG (Waliguan Observatory).

The 1998 and 1999 annual mean CO_2 mixing ratios calculated from smooth curves fit to the data for 48 sites active during 1998-1999 are given in Table 2.3. Annual means for the shipboard data are given in Tables 2.4 and 2.5.

The globally averaged CO_2 mixing ratios and the long-term trend [*Thoning et al.*, 1989] calculated from the global air sampling network data for 1979 through 1999 are plotted as smooth curves in Figure 2.4a. The global CO_2 growth rate as a function of time is calculated by taking the derivative of the trend curve (Figure 2.4b). The average CO_2 growth rate for 1979-1999 is 1.5 ppm yr^{-1}. The CO_2 growth rate varied from 0.5 ppm yr^{-1} in 1982 and 1992 to 3.5 ppm yr^{-1} in 1998, and there is no significant overall trend in the growth rate over this period. The CO_2 growth rate as a function of latitude and time is shown in Figure 2.5. In this figure it is apparent that much of the interannual variability of the growth rate arises from coherent variations on hemispheric to global scales. In some cases the growth rate variations originate in the equatorial region and then propagate toward higher latitudes in both hemispheres. Also, the highs and lows tend to be more extreme at mid- and high-northern latitudes. The growth rate anomaly that began in 1997 and peaked at record high values in early 1998 is unusual in that it appears nearly simultaneously and nearly as intensely throughout both hemispheres.

The CO_2 and $\delta^{13}C$ data were combined with a two-dimensional atmospheric transport model [*Tans et al.*, 1989] to calculate the CO_2 sources and sinks underlying the growth rate variations. The model results for 1990-1999 are summarized in Table 2.6. The 1990-1997 average sources and sinks are shown with one sigma standard deviations to indicate the interannual variability during that period of time. In 1998 the net global CO_2 sink was only 0.5 Gt C compared with an average of 3.4 Gt C during the previous 8 years. Marked decreases in both the net oceanic and net terrestrial biospheric sinks contributed to this change that resulted in an atmospheric increase of 6.2 Gt C. In 1999 the oceanic sink was still only a third of the decadal average while the terrestrial sink rebounded strongly, leading to a near-average atmospheric increase. The two-dimensional model results also indicate that the 1998 growth rate anomaly was driven predominantly by variations in the tropical zone, defined from 17°S to 17°N in our model, including a large increase in the terrestrial source during late 1997.

TABLE 2.3. 1998-1999 Annual Mean CO_2 Mole Fractions From Network Sites

Code	Station	1998	1999
ALT	Alert, N.W.T., Canada	367.2	368.9
ASC	Ascension Island	365.0	366.3
ASK	Assekrem, Algeria	366.6	368.2
AZR	Terceira Island, Azores	365.6	368.8
BAL	Baltic Sea	369.8	371.0
BME	Bermuda (east coast)	366.9	368.7
BMW	Bermuda (west coast)	366.3	368.5
BRW	Barrow, Alaska	367.4	369.8
BSC	Black Sea, Constanta, Romania	372.2	376.4
CBA	Cold Bay, Alaska	369.3	371.2
CGO	Cape Grim, Tasmania	363.7	365.5
CHR	Christmas Island, Kiribati	[ ]	368.3
CRZ	Crozet Island	363.6	[ ]
EIC	Easter Island, Chile	363.3	365.0
GMI	Guam, Mariana Islands	366.7	367.9
GOZ	Gozo Island, Malta	[ ]	[ ]
HBA	Halley Bay, Antarctica	363.4	365.5
HUN	Hegyhatsal, Hungary	369.3	370.8
ICE	Vestmanaeyjar, Iceland	366.9	368.5
ITN	WITN, Grifton, North Carolina	370.3	[ ]
IZO	Izana Observatory, Tenerife	367.1	368.5
KCO	Kaashidhoo, Maldives	366.1	[ ]
KEY	Key Biscayne, Florida	367.7	369.3
KUM	Cape Kumukahi, Hawaii	366.9	368.3
KZD	Plateau Assy, Kazakstan	369.4	371.0
KZM	Sary Taukum, Kazakstan	365.6	368.0
LEF	WLEF, Park Falls, Wisconsin	367.9	370.1
MHD	Mace Head, Ireland	366.3	368.4
MID	Midway Island	366.6	368.2
MLO	Mauna Loa, Hawaii	366.6	368.3
NMB	Bobabeb, Namibia	[ ]	366.5
NWR	Niwot Ridge, Colorado	366.5	368.4
PSA	Palmer Station, Antarctica	363.7	365.7
PTA	Point Arena, California	[ ]	370.8
RPB	Ragged Point, Barbados	366.3	367.6
SEY	Mahe Island, Seychelles	365.4	366.7
SHM	Shemya Island, Alaska	367.1	368.8
SMO	American Samoa	364.6	366.9
SPO	South Pole, Antarctica	363.8	365.6
STM	Ocean Station M	366.7	368.7
SYO	Syowa Station, Antarctica	364.5	365.7
TAP	Tae-ahn Peninsula, South Korea	370.6	373.1
TDF	Tierra del Fuego, Argentina	363.6	365.6
UTA	Wendover, Utah	366.9	369.1
UUM	Ulaan Uul, Mongolia	367.5	368.7
WIS	Sede Boker, Negev Desert, Israel	367.9	369.3
WLG	Mt. Waliguan, China	365.7	368.1
ZEP	Ny-Alesund, Svalbard	367.2	370.1

The square brackets indicate insufficient data to calculate the annual mean.

The 1999 annual means are provisional.

TABLE 2.4. 1998-1999 Annual Mean CO_2 Mixing Ratios From Pacific Ocean Cruises

	CO_2 (ppm)	
Latitude	1998	1999
30°N	366.7	370.0
25°N	367.5	370.1
20°N	367.0	369.3
15°N	367.3	368.6
10°N	366.9	369.5
5°N	367.0	368.7
Equator	366.8	368.7
5°S	365.9	368.1
10°S	365.1	367.6
15°S	364.5	367.3
20°S	364.5	366.6
25°S	364.1	366.3
30°S	364.0	365.9
35°S	364.2	366.2

TABLE 2.5. 1998 Annual Mean CO_2 Mole Fractions From South China Sea

	CO_2 (ppm)
Latitude	1998
21°N	369.2
18°N	368.0
15°N	367.6
12°N	367.4
9°N	367.0
6°N	367.5
3°N	367.9

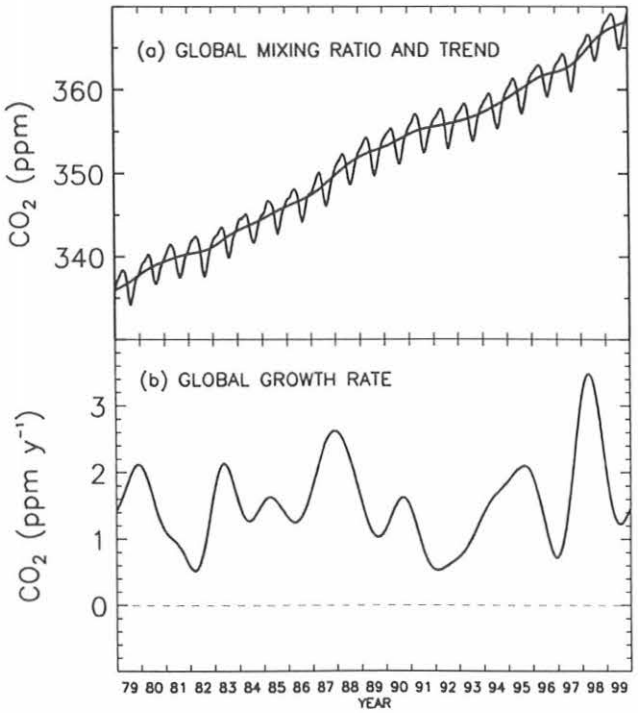

Fig. 2.4. (a) Globally averaged CO_2 mixing ratio and long term trend for 1979 through 1999 based on measurements from remote marine boundary layer sites in the global air sampling network. (b) The time variation of the global CO_2 growth rate calculated as the derivative of the trend curve in (a).

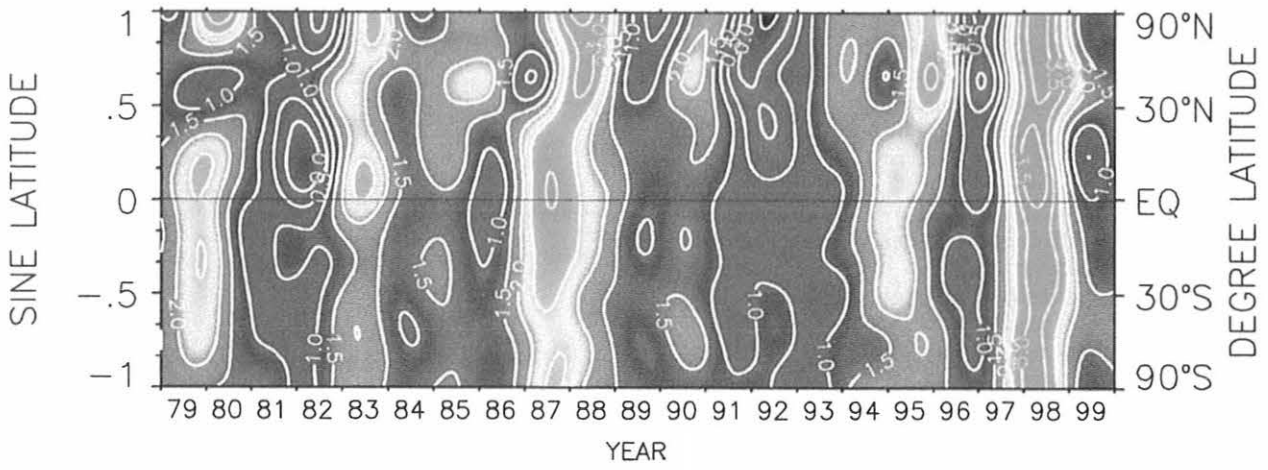

Fig. 2.5. CO_2 growth rate as a function of latitude and time based on marine boundary layer sites. Yellow, orange, and red indicate high growth rates (red is >3.5 ppm yr^{-1}). Purple and black (black is <0.0 ppm yr^{-1}) represent low growth rates. The transition between blue and green is the average CO_2 growth rate of ~1.5 ppm yr^{-1}.

TABLE 2.6. Annual CO_2 Source and Sink Strength From a Two-Dimensional Atmospheric Transport Model

	Gt C = 10^{15} g		
	1990-1997	1998	1999
Fossil fuels	6.3 (0.2)	6.7	6.8
Atmospheric increase	2.9 (0.9)	6.2	3.1
Oceanic uptake	-2.0 (0.7)	-0.6	-0.7
Terrestrial biospheric uptake	-1.4 (0.9)	0.1	-3.1

Numbers in parentheses denote interannual variations (1 σ).

2.2.3. Carbon Dioxide Standards and Reference Gas Calibrations

The 15 primary WMO standards, ranging in CO_2 mixing ratio from approximately 250 to 520 μmol mol^{-1}, were calibrated at regular yearly intervals by the CMDL manometric system [*Zhao et al.*, 1997]. From September 1996 through December 1999 there were a total of 172 individual manometric determinations of the CO_2 mole fractions (Table 2.7). For comparison the CO_2 mole fractions were measured by SIO infrared absorption relative to the WMO X93 mole fraction scale (Table 2.7). The mean precision of the manometric measurement (standard deviation) is 0.13 μmol mol^{-1}. The concentrations analyzed by SIO and CMDL in the atmospheric CO_2 concentration range of 300 to 400 μmol mol^{-1} are in good agreement; therefore, the switch from SIO to CMDL for the maintenance of the WMO Mole Fraction Scale does not result in a large shift of the scale. The function of the primary standards is to provide continuity to the WMO scale as well as a quality-control check on the performance of the manometric system. The assigned values of the primaries are ultimately determined through the manometric analyses repeated at yearly intervals. The column in Table 2.7 labeled "Old scale" contains the concentration assignments of the WMO primary cylinders until the fall of 1999. They are based on both CMDL manometric measurements and on the SIO infrared determinations but biased toward the larger number of SIO data. After the last round of CMDL manometric measurements that finished in January 2000, the values of the WMO primaries were reassigned and are now completely based on the CMDL manometric measurements. The average shift of the WMO Mole Fraction scale in the range of 350-400 ppm is +0.06 ppm (last column of Table 2.7, not using cylinder no.103).

Because we want to maximize the useful life span of the primaries, the primary calibration scale is transferred by way of NDIR measurements approximately twice a year to a set of secondary standards (not using no. 103). The secondaries, which typically have a useful lifespan of 3-4 years, are in turn used to calibrate all other cylinders in which each cylinder is always compared to a set of four bracketing secondaries. Therefore, the user will see a gradual shift of the calibration scale over a 3-yr period of about +0.06 ppm. During 1998 about 432 cylinders were assigned a value on the WMO Mole Fraction Scale in this way. The reproducibility, in the range between 250 and 520 μmol mol^{-1}, has generally been better than 0.1 μmol mol^{-1}. In the range of 325-425 ppm the reproducibility (one sigma) has been 0.014 ppm [*Kitzis and Zhao*, 1999].

On request, calibrations can be performed with the manometric system well outside of the range of atmospheric CO_2 values. Because there is some demand for calibrations well above 520 μmol mol^{-1}, new primary CO_2 standards were created at the high end of the range at approximately 600, 700, 1000, 1500, 2000, 2500, and 3000 μmol mol^{-1}. This will allow CMDL to perform CO_2 calibrations using the comparative infrared absorption technique rather than the time consuming manometric determinations.

Cylinders prepared by CMDL with a specified CO_2 concentration undergo the following procedures at the clean air pumping station at high elevation (3475 m) on Niwot Ridge, Colorado (NWR), 30 km east of Boulder, Colorado.

New or Recently Hydrotested Cylinders: (1) Cylinder is vented and then pressurized twice with dry natural air to about 20 atm (300 psi) and vented again. (2) Cylinder is filled to about

TABLE 2.7. Summary of Manometric Measurements of the WMO Primary CO_2 Standards Expressed as μ mol mol^{-1} in Dry Air (ppm)

Cylinder Serial Number	N*	CMDL (ppm)	CMDL (±)	SIO (ppm)	SIO (±)	Old Scale (ppm)	Difference (mano-old) (ppm)
110	9	246.66	0.11	246.65	0.25	246.64	0.02
102	13	304.40	0.11	304.38	0.09	304.38	0.02
111	14	324.01	0.13	324.01	0.08	324.00	0.01
130	9	337.27	0.11	337.26	0.08	337.27	0.00
121	11	349.39	0.11	349.34	0.11	349.34	0.05
103	15	353.37	0.08	353.17	0.11	353.22	0.15
139	11	360.91	0.06	360.81	0.15	360.83	0.08
105	10	369.40	0.12	369.33	0.17	369.33	0.07
136	7	381.32	0.15	381.25	0.18	381.27	0.05
146	11	389.52	0.15	389.51	0.20	389.51	0.01
101	13	396.35	0.17	396.24	0.20	396.24	0.11
106	9	412.08	0.15	411.96	0.24	411.96	0.08
123	11	423.09	0.18	422.91	0.30	423.03	0.06
107	16	453.18	0.18	452.79	0.43	452.92	0.26
132	13	521.35	0.17	521.00	0.83	521.08	0.27

*Number of CMDL manometric calibrations for each cylinder

34 atm (510 psi) with dry natural air and stored for several weeks. (3) Before the final fill the cylinder is first vented and then spiked with either 10% or zero CO_2 in air, depending on the desired final mixing ratio. (4) Final cylinder is filled with ambient and dried natural air to 135 atm (2000 psi) during which the ambient CO_2 mixing ratio is monitored. (5) When water vapor content of the filled cylinder is measured, it must be less than 5 ppm, and it is usually less than 1 ppm. Drying is accomplished with magnesium perchlorate, $Mg(ClO_4)_2$. The pump is a Rix oil-less diving compressor.

Previously Used Cylinders: Steps 1 and 2 are replaced by venting and one fill with dry natural air to a pressure of 20 atm. Other trace gases, such as CH_4 and CO, can be targeted to specified values in the same cylinders.

2.2.4. Measurements of Stable Isotopes of Atmospheric CO_2

Since 1989 the Stable Isotope Laboratory at INSTAAR has measured the stable isotopic composition of CO_2 from weekly flask samples of air obtained from the CMDL network of sites. A selection of only six sites and two ships in 1990 began the measurement effort that has grown to include approximately 45 stationary sites in the CMDL program as well as all of the shipboard samples. During 1999 over 11,000 isotopic analyses of $\delta^{13}C$ and $\delta^{18}O$ were made at INSTAAR that included 7500 flasks and 3200 tank air standards used for calibration. Combined with the CO_2 mole fraction measurements made by CMDL, the isotopic measurements offer a unique tool to investigate the sources and sinks of global carbon inferred from the spatial distribution of CO_2. The tracking of large scale sources and sinks is an important part of the basis for our understanding of the carbon cycle and is one of the key tools necessary for making credible predictions about the future CO_2 loading of the atmosphere.

The degree to which isotopic measurements made on atmospheric samples are useful is limited by the precision of the mass spectrometer used. For example a change of just 0.02‰ in $\delta^{13}C$ globally translates into a shift of 1.0×10^9 metric tons of carbon between an oceanic or terrestrial source to the atmosphere. Hence the measurements need to be of the highest precision attainable. In 1990 the program began making measurements with a VG SIRA Series 2 mass spectrometer. This instrument and extraction system produced an overall reproducibility of 0.03‰ for $\delta^{13}C$ and 0.05‰ for $\delta^{18}O$ (1σ of nine replicates). A Micromass Optima mass spectrometer was purchased and tested in 1996, fitted with a custom manifold and extraction system, and has been used since late 1996 exclusively for making flask measurements. The overall reproducibility for the Optima system is (1σ for replicate analyses) ±0.012‰ $\delta^{13}C$ and ±0.031‰ for $\delta^{18}O$. The Optima system incorporates an automated 40-port custom manifold and a sample extraction system using all stainless steel parts and is based on the methods that were proven on the SIRA instrument.

The increased capacity attained with the 40-port manifold allowed us to make over 45,360 separate analyses on flasks and reference gases since the instrument was brought on-line in 1996. Instrument down time experienced during 1999 is calculated to be 2%. The combined effect of improved precision, increased capacity, and decreased down time, has resulted in more high-quality isotopic measurements that help characterize the present day carbon cycle.

Addition of Aircraft Samples

Very few changes or improvements were necessary to the mass spectrometer, sample preparation system, or protocols used in analysis during the last year. However, a few small hardware and software modifications were made to allow aircraft sampling kits to be analyzed for $\delta^{13}C$ and $\delta^{18}O$ of CO_2. Protocols identical to normal flask measurements are used with the exception that longer pump times are added to evacuate the longer manifold connections to the aircraft suitcases. Tank air from the Niwot Ridge site was used to fill and test the aircraft kits, and results indicated a reproducibility slightly less than that of normal flasks. However, on repeated analyses of the same 20 aircraft flasks of tank air, the mean $\delta^{13}C$ values remained stable (-0.05‰ change) while the mean $\delta^{18}O$ values drifted (-0.38‰ change), showing what appear to be signs of moisture in the flasks from previous samples. These effects increase until the water in the flask has equilibrated with the CO_2. These preliminary tests indicate that care should be taken to keep the aircraft sample flasks dry initially and to use some type of air drying system, particularly when sampling at lower altitudes. Thus far, over 400 aircraft flasks have been analyzed, and plans continue to allow for increased capacity to analyze these types of samples.

Data Quality Checks

The measurement protocol that began in late 1996 calls for three aliquots of air from a standard cylinder in the middle of every 40-flask run on the mass spectrometer. This additional cylinder, called the "quality control tank," provided an independent check on the performance of the entire system, all the way from the manifold, through the extraction system, to the ionization in the source of the mass spectrometer, and the final data reduction and corrections for N_2O and ^{17}O made in software. In this manner, the day-to-day quality of data produced can be monitored before each run and steps to correct problems can be taken immediately. Figure 2.6 shows the standard deviation (1σ) for the $\delta^{13}C$ value measured on three aliquots of air from a quality control tank measured at midpoint during each analysis run plotted as a 10-point running mean. The average standard deviation during the entire period (November 1998 to May 2000) is 0.010‰ and is usually less than 0.015‰. The unusually high values (>0.02‰) around run number 470 may be because of contamination from a reference gas regulator and a change in capillaries. The dramatic improvement (mean = 0.0061‰) after run number 720 resulted from a cleaning and rebuilding of the mass spectrometer source. The more transient fluctuations in between these periods are likely the result of water contamination in the manifold originating from flasks that contain moist air.

The same information is shown in Figure 2.7 for $\delta^{18}O$ in the quality control tank. The average standard deviation is 0.044‰. The standard deviation of $\delta^{18}O$ displays a similar but lagged response to the source rebuild relative to the $\delta^{13}C$ record. This may be due to the extra time required to remove contaminants (including water) from the system following the rebuild.

Two other key tools in data quality checks have been the circulation of the so-called "Classic" standards with three other laboratories and the flask InterComparison Program (ICP). INSTAAR has and will continue to participate in these programs. The Classic standards are five tanks of air with a wide range of greenhouse gas constituents, including isotopic compositions of CO_2 that range over several permil. Regulators

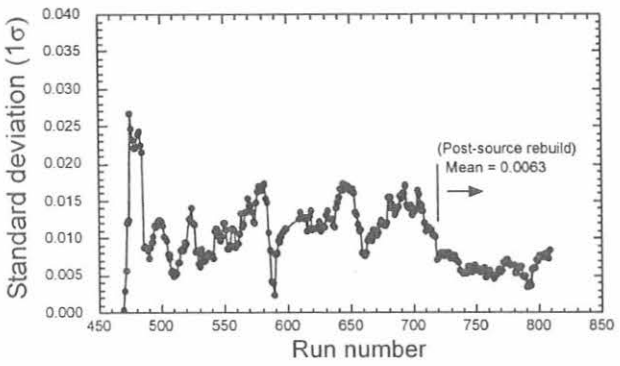

Fig. 2.6. Ten-point running mean of the standard deviation of the quality control tank $\delta^{13}C$ as a function of run number. The data cover the period from November 1998 to May 2000.

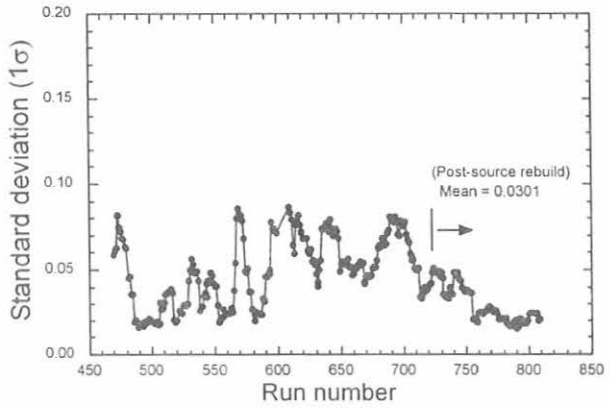

Fig 2.7. Ten-point running mean of the standard deviation of the quality control tank $\delta^{18}O$ as a function of run number. The data cover the period from November 1998 to May 2000.

each flask. The problem with wet air can be seen in the percentage of flask pairs that are considered similar enough to be retained in the data set. In order for a value to be retained, flask pair difference must be less than 0.09‰ for $\delta^{13}C$ analyses and 0.15‰ for $\delta^{18}O$ analyses. The average percentage of flask pairs that have been retained at 45 (fixed) stations is 93.4% for $\delta^{13}C$ and only 69.7% for $\delta^{18}O$ analyses. The reason for the lower success rate in $\delta^{18}O$ pair agreement is closely tied to the moisture problem as seen in the low pair agreements at sites with high humidity (for example, see Figure 2.8).

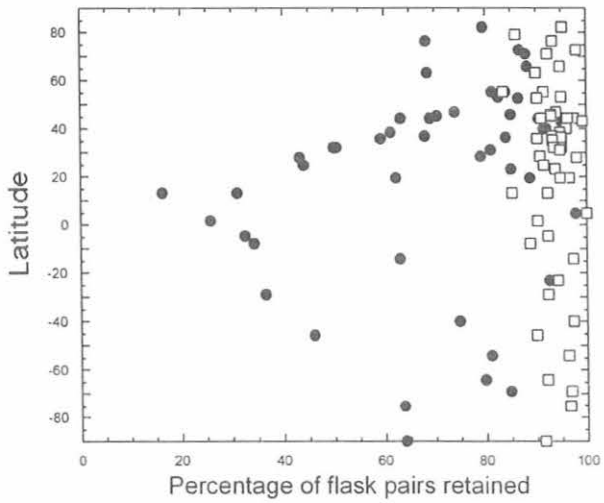

Fig. 2.8. $\delta^{18}O$ (filled circle) and $\delta^{13}C$ (open square) pair agreement in flask samples from the CMDL flask sampling network, plotted by latitude.

are shipped with the tanks to ensure similar circumstances for measurement by the four different laboratories. This program is an important intercomparison tool, but one circuit among four laboratories takes many months to complete. The ICP protocol, where two or more laboratories sample the same air in flasks that go to both laboratories for analysis, provides a method for ongoing frequent comparison that has a higher chance of illuminating discrepancies between laboratories. However, the ICP measurements cannot be repeated, and thus the results carry larger error bars. Such programs are essential to the success of global integration of isotopic data.

Sampling Humid Air

In samples collected at humid, tropical locations without drying, the $^{18}O/^{16}O$ measurements are highly variable and consistently more depleted in ^{18}O because of the exchange of oxygen atoms between CO_2 and H_2O molecules on the walls of the flasks. Systematic tests at INSTAAR [*Gemery et al.*, 1996] showed that the exchange takes place during storage in the flasks when the relative humidity of the air sample is above 50%. There is also some dependence on the physical characteristics of

Field testing of a new prototype air sampling apparatus began at SMO in September 1994 and at Cape Kumukahi, Hawaii (KUM) in May 1995. The new Air Kitzis sampler (AIRKIT) differs from the older Martin and Kitzis Sampler (MAKS) in two important ways: (1) it has a thermoelectrically cooled condenser to remove water vapor from the air stream, and (2) it has a microprocessor to control the sampling process so that collecting the sample is more automated and less subject to operator error. The effect of drying the air sample is most dramatic for the measurement of $^{18}O/^{16}O$ in CO_2 (Figure 2.9). While large improvements in the reproducibility were gained when shifting analyses from the SIRA to the OPTIMA mass spectrometer, future improvements are expected for both $\delta^{13}C$ and $\delta^{18}O$ as more flask samples in the network are dried and wet air issues are overcome.

Seasonality and Temporal Trends in Isotopes of CO_2

A sample of the isotope data is given in Figure 2.10, which shows time series of the CO_2 mole fraction, $\delta^{13}C$, and $\delta^{18}O$ at Barrow, Alaska, from 1990 through 2000. The striking anticorrelation between the seasonal cycles of mixing ratio and

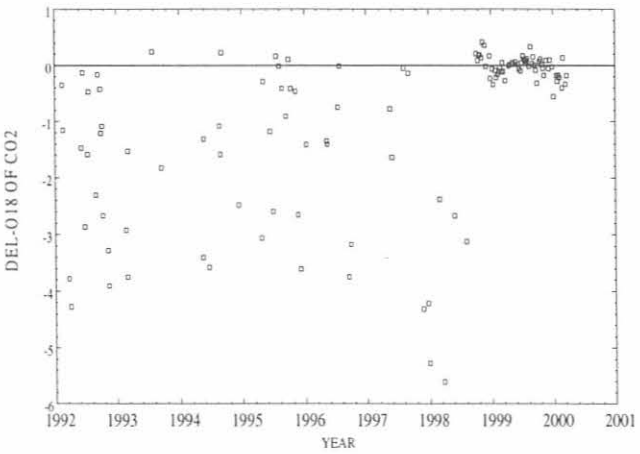

Fig. 2.9. $\delta^{18}O$ values of atmospheric CO_2 from Seychelles (Mahe Island, 4°40'S, 55°10'E). Note the switch to collecting dried air in September 1998.

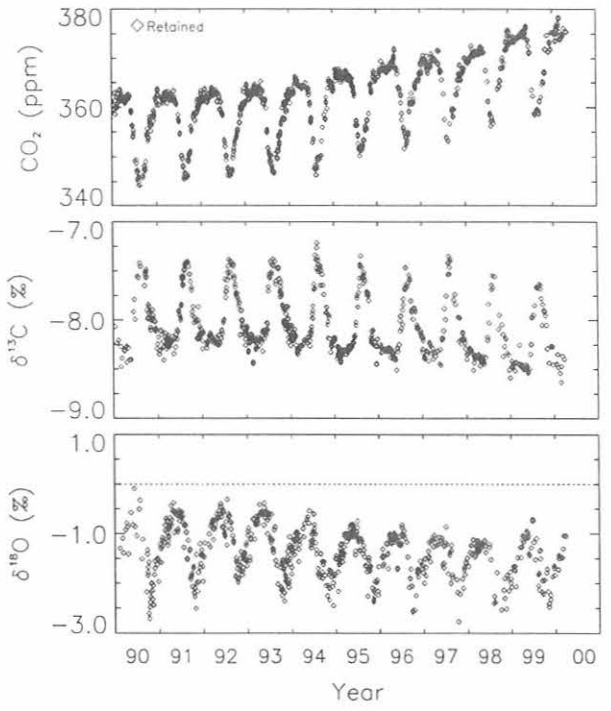

Fig. 2.10. Isotopic and concentration data for carbon dioxide at Point Barrow, Alaska.

$\delta^{13}C$, reflects the strong influence of the annual cycle of photosynthesis and respiration imposed on the atmosphere by the terrestrial biosphere in the northern hemisphere. Whereas the mixing ratio shows an increasing long-term trend because of the use of fossil fuels, the trend of $\delta^{13}C$ is to lighter values reflecting the depletion in $\delta^{13}C$ of fossil fuel relative to the atmosphere.

The seasonal cycle of $\delta^{18}O$ lags behind CO_2 and $\delta^{13}C$, and while its interannual variability shows no steady trend, the $^{18}O/^{16}O$ ratio appears somewhat unstable from year to year, most likely because of the large isotopic exchanges of oxygen between CO_2 and different reservoirs of water in plant leaves and in soils.

2.3. Methane

2.3.1. In Situ Methane Measurements

Quasi-continuous measurements of atmospheric methane continued at MLO and BRW at a frequency of four ambient measurements each hour. The relative precision is 0.07%. Details of the measurement techniques and analysis of the in situ data through early 1994 were published in 1995 [*Dlugokencky et al.*, 1995]. Daily averaged methane mole fractions (in 10^{-9} mol mol^{-1}, nmol mol^{-1}) are plotted in Figure 2.11 for BRW (a) and MLO (b). The data were edited for instrument malfunction using a rule-based expert system [*Masarie et al.*, 1991], and they were selected for meteorological conditions. Briefly, the BRW data are constrained to the clean air sector that includes wind direction of 020-110° and wind speed greater than 1 m s^{-1}. MLO data are constrained to periods typically with downslope winds that correspond to 0000-0659 local time.

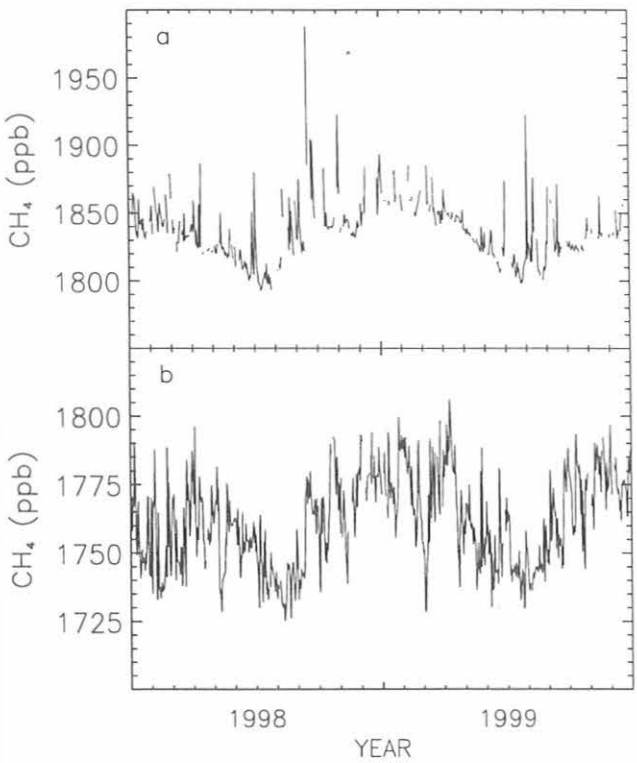

Fig. 2.11. Daily mean CH_4 mixing ratios for (a) Barrow and (b) Mauna Loa for 1998 and 1999. The data are constrained for wind regime, and they have undergone a quality control step to ensure that the analytical instrument was working optimally when they were obtained [*Masarie et al.*, 1991].

2.3.2. Measurements of Methane in Discrete Samples

During 1998-1999 the determination of the global distribution of atmospheric methane continued from 48 sampling sites of the global cooperative air sampling network. Provisional annual mean values for 1998-1999 are given in Table 2.8. Some sites that began prior to 1998 and now have longer, more complete records have been added to Table 2.8. These sites are Assekrem, Algeria (ASK); Christmas Island, Kiribati (CHR); Bobabeb, Namibia (NMB); Plateau Assy, Kazakstan (KZD); and Sary Taukum, Kazakstan (KZM).

During 1998 an interesting anomaly was observed in the CH_4 growth rate, particularly at mid- to high-latitudes in the northern hemisphere. In Figure 2.12 preliminary CH_4 mole fractions for the high northern hemisphere (HNH) are plotted for 1984-1999 in panel a, and the instantaneous deseasonalized and smoothed growth rate is plotted in panel b. Though the increased growth rate in 1998 is unmistakable in Figure 2.12b, a better appreciation of the magnitude of the anomaly may be achieved from Figure 2.12c. In that panel, residuals from a function fitted to the zonal means are plotted as a function of time. The function consists of a second-order polynomial and four harmonic terms. It is reasonable to think of this function as a model of methane's average behavior in the atmosphere where the polynomial represents the long-term average trend and the harmonics represent the average seasonal cycle. This "model" is consistent with the previous suggestion that atmospheric CH_4 is approaching steady state [*Dlugokencky et al.*, 1998]. The residuals plotted in Figure 2.12c represent deviations from this model, and they are the result of perturbations to the "average" balance of CH_4 sources and sinks.

Evident in the residuals is noise with three cycles yr^{-1} and an amplitude varying from 4 to 15 ppb. During 1984-1992 the residuals trended upwards, but in 1992 there was a dramatic drop in the residuals followed by a decreasing trend through 1997. *Dlugokencky et al.* [1995] suggested that the decreased growth rate in 1992 could not be explained entirely by decreased emissions from natural wetlands and that perhaps decreased emissions from the fossil fuel sector in the former Soviet Union (FSU), coincident with the collapse of that economy, resulted in the observed change in growth rate. Although the following is quite speculative, one might expect that if decreased emissions from wetlands was the only cause of the observed anomaly in growth rate in 1992, the upward trend in the residuals should have resumed after the wetland emissions recovered. The fact that it did not may suggest that emissions from the fossil sector in the FSU did contribute to the observed anomaly, and that continuing efforts to halt leaks in the natural gas pipelines of the FSU may have prevented a return to emission levels prior to 1992 for this latitude zone. Evidence for this scenario comes from two recent studies of CH_4 emissions from Russia. *Reshetnikov et al.* [2000] estimated 24-40 Tg yr^{-1} CH_4 emissions from the Russian gas industry during the late-1980s and early-1990s. *Dedikov et al.* [1999], using measurements from an extensive program in 1996 and 1997 to determine losses from Russian gas production and transmission facilities, estimated that 3.6 Tg yr^{-1} CH_4 were emitted during that time. The dramatic decrease in emissions suggested by these studies is not supported by our measurements, but decreased production and improved efforts to prevent leaks likely did lead to lower emissions.

TABLE 2.8. Provisional 1998 and 1999 Annual Mean CH_4 Mixing Ratios From the Air Sampling Network

Site Code	Location	1998 CH_4 (ppb)	1999 CH_4 (ppb)
ALT	Alert, N.W.T., Canada	1825.3	1831.7
ASC	Ascension Island	1707.7	1714.8
ASK	Assekrem, Algeria	1770.4	1779.7
AZR	Terceira Island, Azores	1796.8	1805.2
BAL	Baltic Sea	1850.7	1858.8
BME	Bermuda (east coast)	1799.3	1799.4
BMW	Bermuda (west coast)	1789.1	1795.8
BRW	Barrow, Alaska	1836.7	1841.0
BSC	Black Sea, Constanta, Romania	1919.4	1936.9
CBA	Cold Bay, Alaska	1823.5	1826.5
CGO	Cape Grim, Tasmania	1695.3	1705.7
CHR	Christmas Island, Kiribati	[ ]	1736.0
CRZ	Crozet Island	1694.6	[ ]
EIC	Easter Island, Chile	1695.8	1705.7
GMI	Guam, Mariana Islands	1754.1	1753.9
GOZ	Gozo Island, Malta	[ ]	[ ]
HBA	Halley Bay, Antarctica	1694.7	1704.8
HUN	Hegyhatsal, Hungary	1887.5	1893.2
ICE	Vestmanaeyjar, Iceland	1826.9	1827.2
ITN	WITN, Grifton, North Carolina	1853.8	[ ]
IZO	Izana Obs., Tenerife	1778.8	1782.1
KCO	Kaashidhoo, Maldives	1743.0	[ ]
KEY	Key Biscayne, Florida	1788.8	1796.8
KUM	Cape Kumukahi, Hawaii	1777.5	1778.8
KZD	Plateau Assy, Kazakstan	1844.0	1845.6
KZM	Sary Taukum, Kazakstan	1808.4	1812.2
LEF	WLEF, Park Falls, Wisconsin	1841.4	1859.6
MHD	Mace Head, Ireland	1811.7	1822.4
MID	Midway Island	1786.7	1784.2
MLO	Mauna Loa, Hawaii	1755.9	1764.2
NMB	Bobabeb, Namibia	[ ]	1715.3
NWR	Niwot Ridge, Colorado	1787.2	1793.7
PSA	Palmer Station, Antarctica	1694.9	1705.5
PTA	Point Arena, California	[ ]	1822.1
RPB	Ragged Point, Barbados	1758.3	1767.7
SEY	Mahe Island, Seychelles	1717.5	1724.4
SHM	Shemya Island, Alaska	1822.8	1825.3
SMO	American Samoa	1697.8	1713.7
SPO	South Pole, Antarctica	1694.1	1704.7
STM	Ocean Station M	1823.6	1828.2
SYO	Syowa Station, Antarctica	1694.3	1704.7
TAP	Tae-ahn Peninsula, South Korea	1851.8	1859.5
TDF	Tierra Del Fuego, Argentina	1694.7	1706.2
UTA	Wendover, Utah	1799.9	1808.4
UUM	Ulaan Uul, Mongolia	1821.6	1825.8
WIS	Sede Boker, Negev Desert, Israel	1825.6	1828.9
WLG	Mt. Waliguan, China	1790.1	1802.4
ZEP	Ny-Alesund, Svalbard	1830.3	1832.7

Note: square brackets indicate insufficient data to calculate the annual mean.

In 1998 there was a large positive anomaly in the residuals that shows signs of recovering at the end of 1999. Since natural wetlands are an important source of CH_4 in this latitude zone, changes in their emissions are always a possibility when an anomalous CH_4 growth rate is observed. The two most sensitive parameters for CH_4 emissions from wetlands are soil temperature and soil moisture. In Figure 2.13 air temperature (T) and precipitation anomalies are plotted for inundated wetland regions

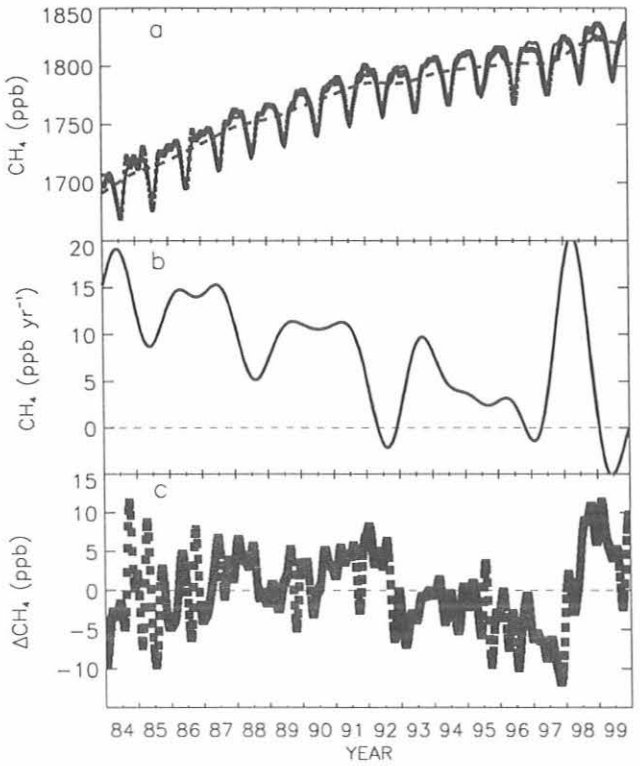

Fig. 2.12. (a) Methane mole fractions for the high northern latitudes (30-90°N; HNH). The solid line is a function (2nd-order polynomial + 4 harmonics) fitted to the zonal means. The dashed line is a deseasonalized trend fitted to the zonal means. (b) Instantaneous CH_4 growth rate for HNH. It is calculated as the derivative of the dashed curve in 2.12a; (c) Residuals from function (solid line in 2.12a) fitted to HNH zonal averages.

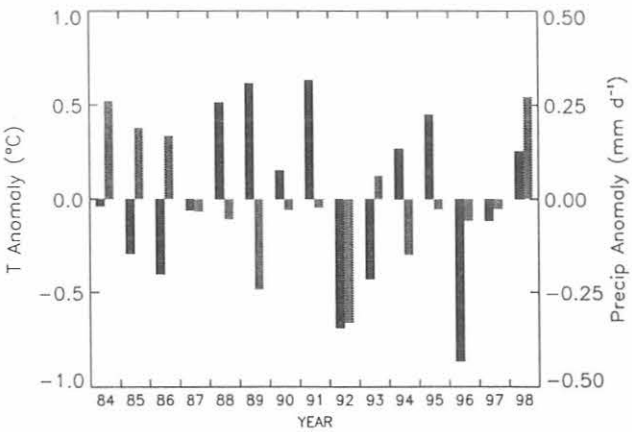

Fig. 2.13. Temperature (black) and precipitation (gray) anomalies for northern wetland regions during 1984-1998.

only; these are used as a proxy for the soil parameters. There are clear positive T and precipitation anomalies in 1998. Noteworthy are the negative T and precipitation anomalies in 1992. Using a process-model, large (10 Tg) anomalies were calculated in wetland CH_4 emissions for these 2 years, negative in 1992 and positive in 1998 (B. Walter, Columbia University, private communication, 2000). Although uncertainties on these estimates are large, they implicate wetlands as a contributor to both anomalies observed in CH_4 growth rates. Additionally, there were large boreal forest fires in North America and Siberia during 1998 that potentially contributed to the CH_4 growth rate anomaly (E. Kasischke, University of Maryland, private communication, 2000). Estimates of emissions from these fires are ongoing (see section 2.4.1).

2.3.3. Measurement of $^{13}C/^{12}C$ of Methane by Mass Spectrometry

Partitioning atmospheric methane into its bacterial, thermal, and biomass burning sources is possible through global measurements of its stable carbon isotopic ratio $^{13}C/^{12}C$. Ratios are expressed in permil (a one part per thousand relative deviation from a standard isotopic ratio). Biological sources, such as wetlands, have a characteristic isotopic composition (typically -60‰) that is more depleted in the heavy isotope, ^{13}C, than thermal sources like natural gas (-40‰), which, in turn, are more depleted than the biomass burning source (-25‰). The measured isotopic ratio of atmospheric methane (-47‰) is a composite of these sources, but it is also influenced by the enrichment in ^{13}C content (+5‰) that results from the destruction of methane by the hydroxyl radical, which is slightly more rapid for $^{12}CH_4$ than for $^{13}CH_4$.

An automated system was designed for the analysis of ^{13}C in atmospheric methane. Starting in January 1998 the system has analyzed pairs of flasks, on a weekly basis, from six sites (SPO, Cape Grim Tasmania (CGO), SMO, MLO, NWR, and BRW) of the global cooperative air sampling network. From a sampling flask, 200 mL of air is used to achieve a precision of better than 0.06‰ in less than 15 minutes. The measured precision is comparable to that of systems where at least 100 times as much air is used and where the analysis takes more than 1 hour. Starting in June 1998 an automated flask manifold was introduced that allows for a greater throughput of samples than would otherwise be possible. The CMDL standard scale is now linked to a scale maintained by the University of California, Irvine (UCI). In the summer of 2000 a program that includes both CMDL and the UCI laboratories will measure $^{13}CH_4$ in small cylinders collected at NWR.

Measurements indicate an annual average latitudinal difference of approximately -0.5‰ (BRW-SPO) (Figure 2.14). The sign of this gradient is explained by the predominance of methane sources, which are generally depleted relative to the atmospheric average, in the northern hemisphere, whereas the dominant methane sink, OH, is more evenly distributed. The magnitude of the gradient and how it changes seasonally are a result of changing OH and source emission patterns.

Distinct seasonal variations are also evident at each of the six sites. At the northern hemisphere sites of BRW and NWR seasonal variations appear to be driven by seasonality in source emissions, but the variations at the southern hemisphere sites, CGO and SPO, appear to be driven by OH seasonality (Figure 2.15). At MLO and SMO seasonal variations are less distinct.

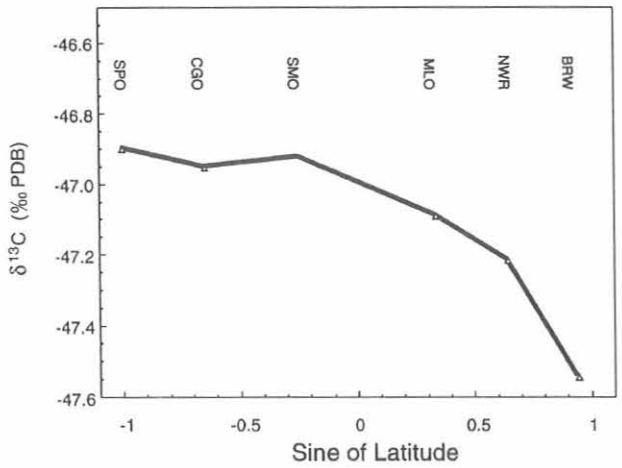

Fig. 2.14. Annual mean latitude gradient of $\delta^{13}C$ of CH_4.

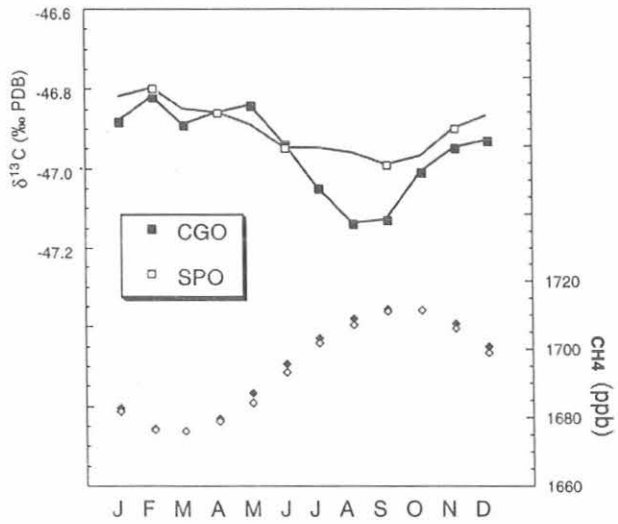

Fig. 2.15. Average seasonal cycle of CH_4 and its $^{13}C/^{12}C$ ratio at Cape Grim (CGO) and at the south pole (SPO).

Curiously the amplitude of the seasonal cycle of $\delta^{13}C$ at CGO (0.3‰) cannot be explained solely by destruction by OH, while the seasonal cycle amplitude of $\delta^{13}C$ at SPO can be. This is especially intriguing in light of the strong similarity in the amplitude of the mole fraction seasonal cycles at the two sites. The analysis of intra-annual variations in $^{13}C/^{12}C$ at individual sites as well as inter-annual variations at all the sites are likely to contribute to a better understanding of methane budgets on continental and global scales.

2.3.4. $^{13}C/^{12}C$ and D/H Isotopic Ratio Analysis of Methane by Infrared Spectroscopy

The goal of this methane isotopic measurement program is to develop a robust infrared absorption spectrometer to measure both $^{13}C/^{12}C$ and D/H isotopic ratios in atmospheric methane samples with sufficient sensitivity to resolve spatial and temporal trends. The instrument is being developed in cooperation with the Optical Frequency Measurements Group at the U.S. National Institute of Standards and Technology (NIST), and samples will be obtained from the CCGG global cooperative air sampling network to provide a good spatial distribution of sampling sites from which to obtain global methane variability data. To date, measurements of atmospheric methane $^{13}C/^{12}C$ and D/H values have been largely regional and performed almost exclusively by isotope ratio mass spectrometry (section 2.3.3) [*Tyler et al.*, 1999; *Wahlen et al.*, 1990].

Since $^{13}CH_4$ and $^{12}CH_3D$ have the same isotopic mass, their separate measurement requires extensive procedures to convert the CH_4 to CO_2 and H_2. Infrared absorption spectroscopy offers a simple, nondestructive way to measure the stable isotopic composition of atmospheric methane samples. A mid-infrared absorption spectrometer was constructed for stable isotope ratio measurements of atmospheric methane. The spectrometer employs periodically poled lithium niobate (PPLN) to generate difference frequency radiation from two near-infrared diode lasers (one at 811 nm and the other at 1066 nm). This technique yields about 10 microwatts of single mode, tunable radiation that probes the v3 rotational-vibrational absorption band at 3.4 microns. The radiation is passed through a multipass absorption cell with a path length of 36 m and a volume of 0.3 L. Second harmonic wavelength modulation is used to reduce spectrometer noise. The current 3σ detection limit is 2 ppb of methane in 50 torr of air for a noise-equivalent bandwidth of 1 Hz.

Since the tropospheric mixing ratio of $^{12}CH_3D$ is close to 1 ppb and is comparable to the instrument detection limit, a procedure to concentrate methane samples is required before isotopic analysis. Methane is extracted from 25 L of air using a cryogenic chromatographic column and is injected into the multipass cell with a final total pressure of ~70 torr. This procedure enriches the methane samples by ~1000 times. The abundance of the rare isotopic species ($^{13}CH_4$ and $^{12}CH_3D$) are measured relative to $^{12}CH_4$ by comparing the absorbance of an intrinsically strong spectral line of a rare species with a weak line of $^{12}CH_4$. Thus far a precision of 1.7% for the isotope ratios has been attained. The precision is limited by long-term spectral baseline instabilities arising from optical interference fringes in the multipass cell. With spectral baseline subtraction and the addition of a reference absorption cell, the precision is expected to improve by an order of magnitude.

2.4. Carbon Monoxide

2.4.1. Measurements of Carbon Monoxide

During 1998-1999 the study of the global distribution of CO in the lower troposphere continued using both air samples collected through the CMDL global cooperative air sampling network and in situ measurements at BRW and at MLO. In the air sampling network conversion of all sites from glass flasks with greased stopcocks to those acceptable for CO analysis (those fitted with Teflon O-ring stopcocks) was completed by 1998, and CO was measured at all active sites in the network. In situ measurements at BRW continued uninterrupted, while at MLO a rebuilt Reduction Gas Analyzer was reinstalled in late 1998. The 1998 and 1999 provisional annual mean mixing ratios from the in situ measurements at BRW (155.9 and 128.2 ppb,

respectively) were equivalent to the flask results from BRW (154.7 and 129.5 ppb, respectively). At MLO interrupted measurements provide no annual mean for 1998, but the 1999 in situ results (annual mean = 86.5 ppb) agree well with the flask measurements (88.0 ppb). These provisional flask and in situ values are believed to be somewhat low and are likely to be revised upward (section 2.4.2).

The residuals from a function approximating the annual oscillations and trend (the annual cycle as represented by four harmonics, the long-term trend by a polynomial [*Thoning et al.*, 1989]) were used to examine key features in global and hemispheric CO. A high degree of interannual variation was seen during 1991-1999 (Figure 2.16). The sharp decline in global CO during 1992 (Figure 2.16a) has been attributed to the effects of the June 1991 eruption of Mt. Pinatubo [*Bekki et al.*, 1994; *Granier et al.*, 1996]. The sharp drawdown is particularly evident in the detrended residuals from the southern hemisphere (Figure 2.16b). As the effects of the eruption diminished in 1993, CO returned to previous levels [*Novelli et al.*, 1998a; *Granier et al.*, 1996]. Other variations in the time series (1994-1996) may be related, in part, to variations in large scale biomass burning.

CO mixing ratios in the southern hemisphere showed strong enhancement in late 1997. The anomaly was largely confined to the low latitudes during late 1997. Following this well-defined increase, CO remained somewhat high during early 1998 before returning to previous levels (Figure 2.16b). Strong fires in Indonesia, which burned agricultural areas, forests, and peat swamps from mid-1997 through early 1998, produced substantial amounts of CO (>77 Tg CO; *Levine et al.* [1999]). The 1997 fires provided at least 35% more CO to the troposphere than biomass burning in a typical year. As the seasonal cycle of CO in the southern hemisphere is largely driven by emissions from biomass burning [*Granier et al.*, 2000], the fires likely contributed substantially to the high CO observed during late 1997 and early 1998. In the northern hemisphere, a weak summer minimum in 1998 was followed by a strong fall maximum (Figure 2.16c). This period of high CO is also evident in the residuals calculated from in situ measurements at BRW (Figure 2.17). For the first time since CMDL measurements began at BRW in 1988, autumn mixing ratios in the high latitudes of the northern hemisphere surpassed the typical seasonal maximum in March/April. The enhancement at Barrow was nearly twice that seen in the zonally averaged northern hemisphere time series, suggesting the boreal nature of the source. Estimates of the extent of burning in Canada, northern United States, and Russia during 1998 are twice as high as any previous year in the 1990s [*Kasischke et al.*, 1999]. Variations in the depth of the northern hemispheric seasonal CO minimum (defined as the July/August average mixing ratio) are highly correlated with the annual land area burned in the temperate and boreal forests (G. Wotawa et al., Boreal forest fires and their contribution to northern hemispheric summertime CO background concentrations during the 1990s, submitted to *Nature*, 2000). The effect of boreal forest fires on the Arctic troposphere was also shown in a comparison between CMDL CO surface measurements at BRW and total column spectroscopic measurements made at Poker Flats, Alaska. In winter and late spring 1995 surface measurements of CO were greater than the equivalent column average. However, during May and through September (the primary burning season in Canada and Russia) the column measurements were enhanced relative to the surface. Emissions from forest fires were suspected of providing CO to the free troposphere over Alaska [*Yurganov et al.*, 1998].

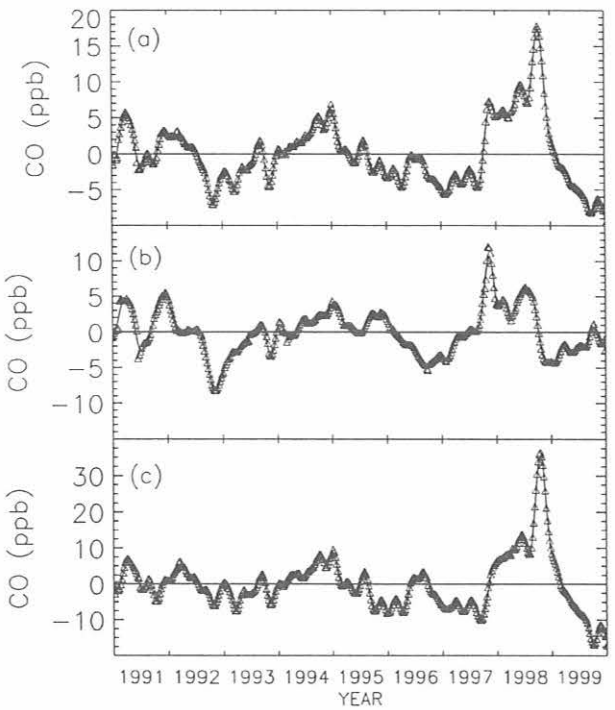

Fig. 2.16. Residuals from zonal average time series, after the average seasonal cycle and a third-order polynomial fit to the trend have been subtracted, and a smooth curve fit to those residuals (solid line): (a) global, (b) southern hemisphere, and (c) northern hemisphere.

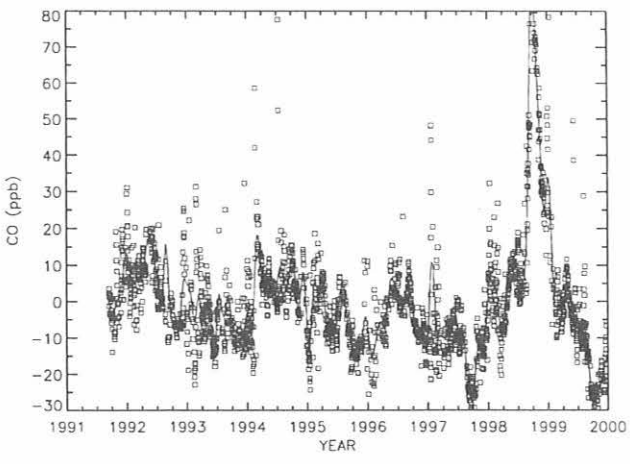

Fig. 2.17. Residuals, determined as in Figure 2.16, from the in situ measurements at Point Barrow, Alaska. The solid line is the smooth fit to the residuals.

2.4.2. CO Reference Gases

A set of eight CO standards was prepared using gravimetric methods by the CMDL Halocarbons and other Atmospheric Trace Species (HATS) group in late 1999 and early 2000. Mixing ratios assigned to CMDL working standards referenced against the new gravimetrics were significantly greater than those previously assigned based upon the original scale. The CMDL reference scale used in our measurements of atmospheric CO is based upon 17 standards prepared during 1989-1990 by gravimetric methods [*Novelli et al.*, 1991]. The scale was transferred to a set of ten natural air secondary standards with mixing ratios between 32 and 201 ppb CO. The standard scale was found to be in good agreement with our gravimetric dilutions of a NIST 9.7 ppm CO Standard Research Material (SRM), and dynamic dilutions of a NIST 10 ppm SRM made at the U.S. National Aeronautics and Space Administration (NASA) Langley Research Center and at the Fraunhofer Institute in Garmisch-Partenkirchen, Germany.

Over time the original gravimetric standards, made in high-pressure cylinders of a smaller size, were found to drift at rates of up to several ppb yr^{-1}, and the scale was maintained through the secondary and working standards. Drift in these standards was evaluated in two ways: (1) frequent intercomparison of the suite of standards maintained at CMDL, and (2) periodic preparation of new gravimetric standards. In 1991 the instrument with a linear response was changed to a new one that exhibited nonlinearity below ~125 ppb. Therefore, a multipoint calibration procedure was necessary to define the instrument response. In addition to exhibiting nonlinearity, response characteristics changed over time requiring frequent calibration of the instrument. This procedure used six to eight standards (mixing ratios between 50 and 200 ppb) plus a blank (zero air passed through Schutze reagent) and daily calibration curves. A straight line, second-, and third-order polynomial were used to define instrument response [*Novelli et al.*, 1998a]; the first two curve fits were used for diagnostics, and the reported mixing ratios were based upon the third-order fit.

In 1992 three gravimetric standards were prepared, and their assigned mixing ratios, based on the gravimetric method, agreed well with the CO mixing ratios assigned to the secondary standards [*Novelli et al.*, 1994]. The long-term calibration histories of the CMDL standards showed no evidence of drift. Figure 2.18 shows the calibration history of one 50 ppb working standard (ID CC114712). A significant drift was not detected through the first half of 1998 (Fig. 2.18a), however, higher mixing ratios determined in 1999 suggest an increase of 0.2 ppb yr^{-1} (Figure 2.18b).

In 1996 a new set of five standards was prepared using gravimetric methods. The mixing ratios assigned to the secondary and working standards when referenced against the 1996 gravimetrics were somewhat higher than those previously assigned. In 1999 and 2000 eight gravimetric standards with mixing ratios ranging from 53 to 205 ppb were prepared at CMDL. The mixing ratios assigned to the secondary and working standards referenced to the new gravimetric standards were greater than the 1996 results and definitely greater than the original values (Table 2.9). Calibration of the new gravimetrics using dynamic dilution of a NIST 9.7 ppm SRM confirmed their values based on the gravimetric preparation. This surprising result lead to a re-evaluation of the CO scale extending back to the original standards prepared in 1989 and 1990. Confidence in both the original scale and the 1999 gravimetric standards

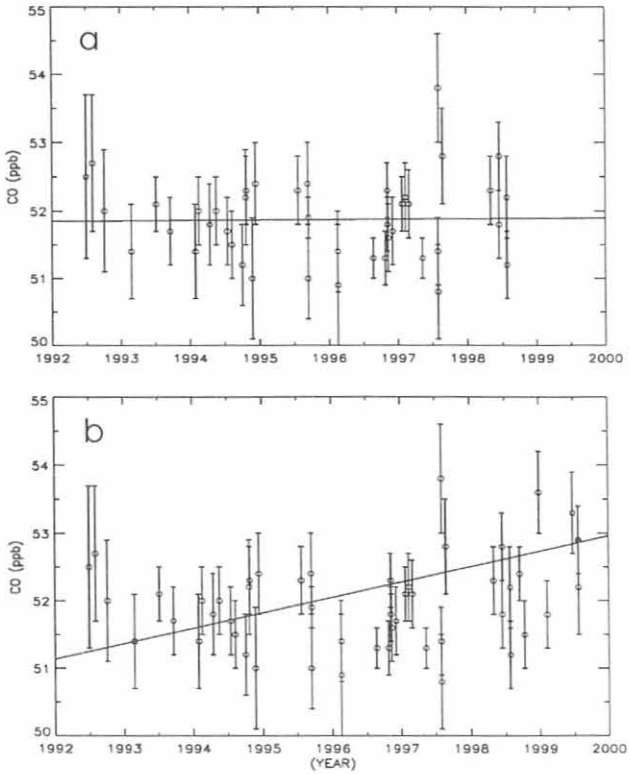

Fig. 2.18. The calibration history of CMDL working standard CC114712 (assigned a mixing ratio = 51.9 ppb in 1992). Each point represents a calibration based upon ten or more analyses. Error bars represent one standard deviation. (a) History through the first half of 1998, Y = 51.9 (±0.37) + 5.3 × 10^{-3} (±0.086)(X −1992); (b) History through 1999; Y = 51.2 (±0.31) + 0.22 (±0.55)(X-1992).

suggests drift in both the secondary and working standards over time. Calculations of linear drift at rates of 0.8 ± 0.3 ppb yr^{-1} between 1992 and 1999 are consistent with the 1996 gravimetric standards and with intercomparisons involving several other laboratories [*Novelli et al.*, 1998b] (K. Masarie et al., The NOAA/CSIRO Flask Air Intercomparison Experiment: A strategy for directly assessing consistency among atmospheric measurements made by independent laboratories, submitted to *Journal of Geophysical Research*, 2000). However, drift rates of about 1 ppb yr^{-1} are not evident in the calibration histories of the working standards because the working standards and the CMDL secondary standards were both drifting at comparable rates.

To examine whether drift in a sample could be masked by drift in the standards, a sensitivity study examined the effects of drifting standards on the calibration of simulated samples. Artificial area responses of eight standards comprising a calibration curve were allowed to change while the assigned mixing ratios were kept constant. When upward standard drift was not accounted for, the calculated sample mixing ratios were lower than the actual value. Combinations of drift in the simulated standards, on the order of the apparent rates seen in the CMDL standards, and drift in samples at various rates between 0 and 3 ppb yr^{-1}, resulted in a range of results. In general if samples were drifting at rates similar to those of the standards, the appearance of drift was largely hidden within the precision of the measurements.

TABLE 2.9. Mixing Ratios Assigned to the CMDL Secondary Standards*

Tank ID	1989/1990, 1992		1996		1999		NIST Dilution, 1999	
121999	51.7	(1.1)	56.2	(0.7)	60.4	(0.5)	61.5	(1.2)
105460	100.5	(1.2)	107.5	(0.9)	110.9	(1.1)	111.3	(1.1)
68734	159.7	(1.1)	164.4	(1.0)	167.7	(1.3)	167.0	(1.7)
73110	200.8	(1.7)	202.9	(0.9)	205.3	(0.5)	207.3	(1.5)

*Mixing ratios assigned to secondary standards by comparison to gravimetric standards prepared in 1989/1990 and 1992; 1996, 1999, and by comparison to dynamic dilution of a NIST 9.7 ppm SRM. Uncertainties (1σ) are in parentheses. All mixing ratios are in ppb by mole fraction (gravimetric calibrations) or ppb by volume (NIST dilutions).

Beginning late 1999 a number of standards were assigned mixing ratios referenced to both the CMDL working standards and the new gravimetric standards. The relationship defined by these calibrations (Figure 2.19) relates mixing ratios assigned during mid-1999 to mid-2000 by the original (but drifting) scale to mixing ratios defined by the new gravimetric standards. Correcting the time series data is more difficult, but several options are available. Most promising is a linear adjustment between 1992 and 1999. Results from this approach are consistent with both the 1996 and 1999 gravimetric standards.

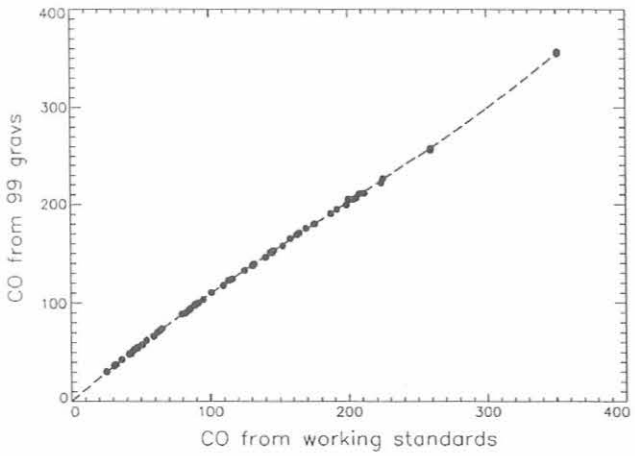

Fig. 2.19. Scatter plot of CO mixing ratios assigned to various natural air mixtures based upon the 1999 gravimetric standards versus the original CMDL CO scale. The dashed line shows a third order fit to the data and is defined by $Y = 0.320 + 1.217\ X - 0.00163\ X^2 + 2.972 \times 10^{-6}\ X^3$. The solid line represents the one-to-one relationship between the 1999 gravimetric standards and the CMDL CO working standards.

2.5. Nitrous Oxide and Sulfur Hexafluoride

Measurements of N_2O and SF_6 from all sites in the global cooperative air sampling network continued during 1998 and 1999. A significant analysis problem was found at the end of 1999. Measurements of N_2O and SF_6 appeared too high in network samples, but the problem was hardly noticeable in the record of daily test flasks. After a detailed investigation into the problem, the screens installed between the Valco sample valve body and the end of the 1.6 mm (1/16") OD tubing connected to the valve were found to be the cause of the problem. These screens are used to prevent particles from entering the valve and destroying the rotor. Over time, it appears that particles from the rotor clogged the screen affecting relaxation of the sample-loop pressure to ambient. Sample-loop pressure for samples was greater than for standards; therefore, measured mole fractions were too large. Once the screens were blown out with 2000 psig pressure, the system began working properly. All samples with analysis dates between November 1, 1999, and March 23, 2000, were flagged with "A..", indicating a problem during analysis. The end date was easy to assign; it is the date the screens were blown out and the system reassembled and tested. The exact start date of the problem is unknown. November 1 is somewhat conservative and arbitrary, but all data affected by this subtle problem were flagged. Since the magnitude of the error was a function of the pressure in the flask at the time it was analyzed, and this pressure is not measured, it was not possible to apply a correction to the data.

The N_2O and SF_6 latitude gradients are presented as the mean difference in annual means between each site and south pole for 1998 (Figures 2.20 and 2.21). Annual means were determined from a smoothed curve fitted to all data available through mid-May 2000 after outliers had been flagged. The gradients for both species are similar; higher values are observed in the northern hemisphere than the southern hemisphere, and considerable

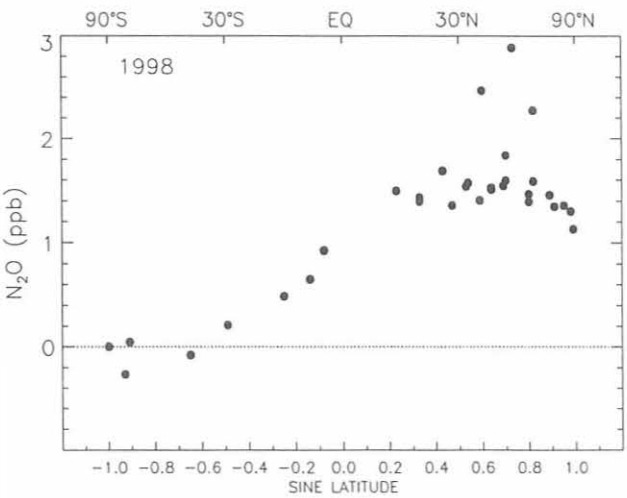

Fig. 2.20. Mean difference in annual mean nitrous oxide mole fractions (in ppb, nmol mol^{-1}) between each site and south pole for 1998, plotted versus sine of latitude. The annual means were calculated from curves fitted to the data.

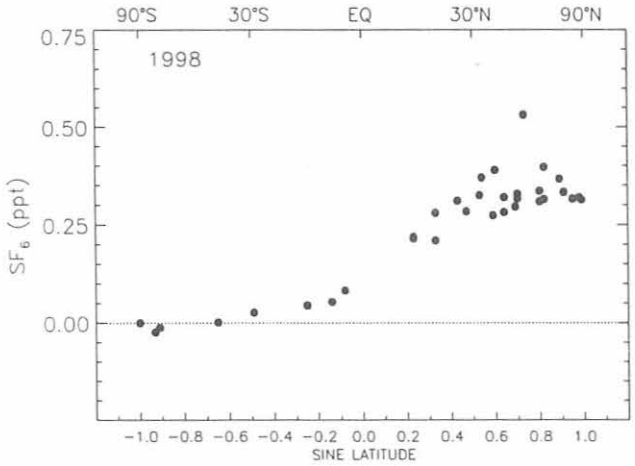

Fig. 2.21. Mean difference in annual mean SF_6 (in ppt, pmol mol^{-1}) between each site and south pole for 1998, plotted versus sine of latitude. The annual means were calculated from curves fitted to the data.

differences are observed at Hungary (HUN) and other relatively polluted continental sites. These gradients are consistent with about two-thirds of total N_2O emissions, and all SF_6 emissions, occurring in the northern hemisphere.

2.6. Measurements on Tall Towers

Measurements of mixing ratios of CO_2 and other trace species were made on a 610-m tall TV transmitter tower in North Carolina (NC, site code ITN) from June 1992 until June 1999. These measurements were discontinued because the TV company required the space occupied by our equipment on the tower and in the transmitter building in order to install HDTV as mandated by Congress. Measurements began on a 447-m tall tower in Wisconsin (WI, station code LEF) in October 1994 and are ongoing.

The CO_2 mixing ratio data through 1997 were presented in *Bakwin et al.* [1998]. Figure 2.22 provides an update of the data through 1999. *Bakwin et al.* [1998] discuss a method to account for excess fossil fuel CO_2 at the towers relative to the "background" marine boundary layer (MBL). The difference between the CO daily means at the towers and a MBL reference for CO is divided by an estimated CO/CO_2 molar emission ratio for fossil fuel combustion of 0.023 [*Bakwin et al.*, 1994]. This value is subtracted from the CO_2 mixing ratios at the towers. The results provide a means to compare more directly CO_2 mixing ratios over the continent with those in the MBL. Table 2.10 updates these data through 1999. The annual mean CO_2 mixing ratios at the towers are generally higher than in the MBL at the same latitude [*Bakwin et al.*, 1998]. However, it is estimated that excess fossil fuel CO_2 typically accounts for

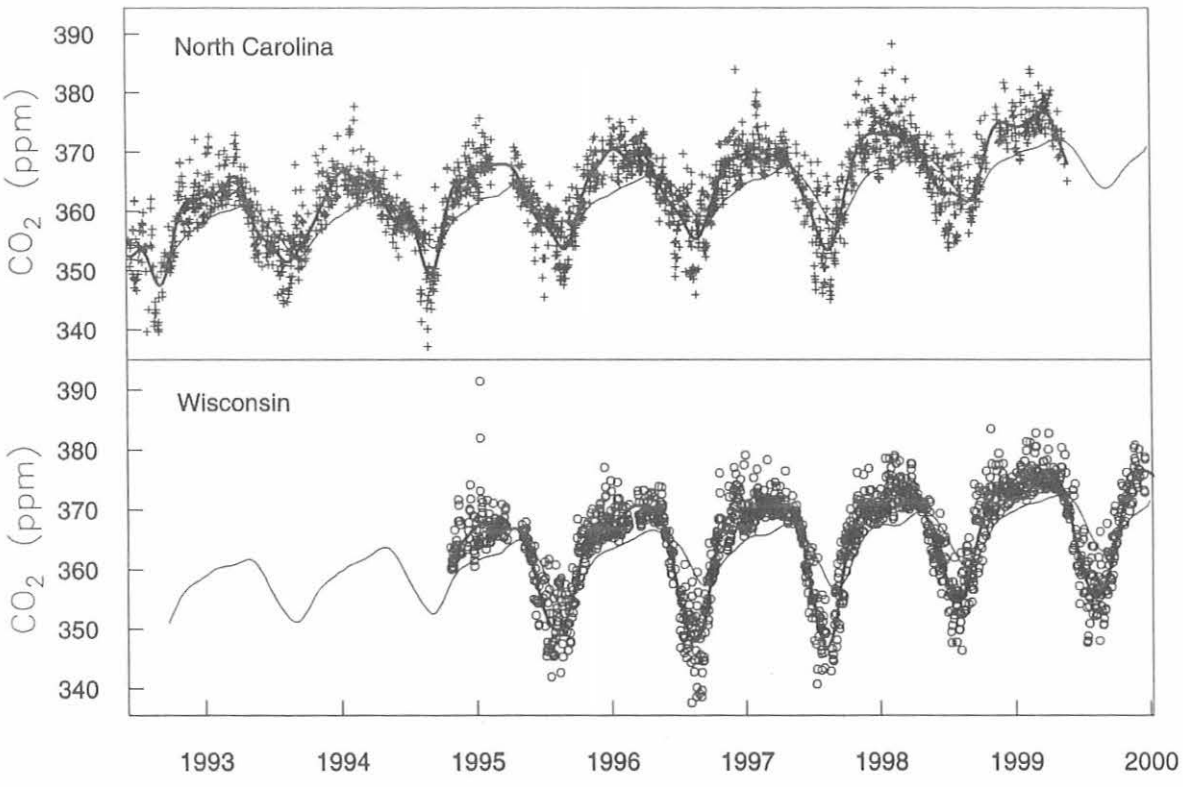

Fig. 2.22. Daily mean CO_2 mixing ratios at 496 m above the ground on the North Carolina tower and 396 m on the Wisconsin tower (points). The data are fit with smooth curves (heavy) as described by *Thoning et al.* [1989]. The thin lines show the MBL reference curves [*Globalview-CO_2*, 2000] for the latitudes of the towers.

TABLE 2.10. Carbon Dioxide Mixing Ratios (ppm) at Two Tall Towers With and Without the Estimated Fossil Fuel Contribution Subtracted as Described in the Text*

Year	NC	NC-FF	MBL at NC	WI	WI-FF	MBL at WI
1995	363.1	360.7	360.9	361.9	na	360.7
1996	364.7	362.4	363.0	363.8	362.4	363.1
1997	365.7	363.5	364.0	364.4	363.6	363.9
1998	368.9	366.8	366.7	367.6	366.6	366.5
1999	na	na	368.8	369.4	368.5	369.0

*Uncertainty of the annual mean CO_2 mixing ratios at the towers is roughly 0.2 ppm.
NC = North Carolina; FF = fossil fuel; MBL = marine boundary layer; WI = Wisconsin

2.1-2.4 ppm CO_2 at the NC tower and 0.8-1.5 ppm CO_2 at the WI tower. Subtracting these values gives annual mean values for CO_2 at the towers that are a few tenths of a ppm lower than in the MBL, suggestive of a biogenic sink for CO_2 on the continent. It is interesting that both towers show a smaller than average difference from the MBL in 1998, a year when the global atmospheric CO_2 growth rate was exceptionally large. This implies that the biogenic sink for CO_2 in North America in 1998 may have been smaller than in other years. An alternative explanation could be that interannual changes in atmospheric circulation affect the annual means. However, the contribution of recent fossil fuel-derived CO_2 did not change much at either tower.

A large program has evolved around the WI tower to study processes that regulate the carbon balance of the surrounding temperate/boreal mixed forest and to understand how the signal of CO_2 exchange at the terrestrial surface propagates to the regional and global atmosphere. The program, known as the Chequamegon Ecosystem/Atmosphere Study (ChEAS), includes scientists from several universities and government research laboratories and is funded mainly by NOAA, U.S. Department of Energy (DOE), National Science Foundation (NSF), NASA and U.S. Department of Agriculture (USDA). The backbone of the project is the CCGG measurements of the exchange of CO_2 between the atmosphere and the forest using eddy covariance and atmospheric budget methods. Information about the studies involved in ChEAS can be found at [http://cheas.umn.edu]. The first publications utilizing the CMDL measurements are *Yi et al.* [2000] and *Berger et al.* [2000].

During 1998-1999 significant progress was made towards quantifying the forest carbon balance and understanding the biophysical processes that drive interannual changes in net ecosystem exchange of carbon (NEE). Figure 2.23 shows cumulative NEE for 1997 and 1998. During the wintertime modest net release of CO_2 by the forest, due to respiration, was observed. Since the soils are mostly frozen, the rate of respiration is fairly small; the average for January 1997 is 0.3 $\mu mol\ m^{-2}\ s^{-1}$, compared to nighttime respiration of 5.0 $\mu mol\ m^{-2}\ s^{-1}$ in July. The timing of leaf-out is well predicted by degree-days, the integral of temperatures greater than 0°C starting from April 1. The spring of 1998 was unusually warm, and leaf-out occurred about 1 month earlier than in 1997. During the summer rapid photosynthesis by the vegetation leads to net uptake by the forest. The rate of uptake in midsummer was similar in 1997 and 1998. A severe drought occurred in the region during mid-to-late summer of 1998, and the moisture content of the surface soil dropped to about 25% of that in 1997. The drought suppressed both photosynthesis and respiration by the forest, and the daily

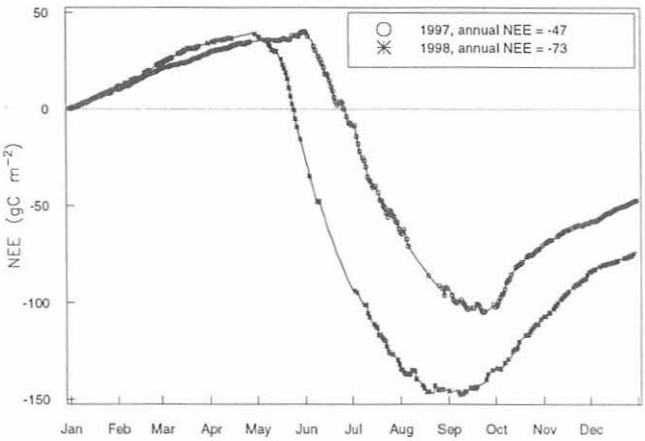

Fig. 2.23. Cumulative net ecosystem exchange of CO_2 measured at the Wisconsin tower during 1997 and 1998. Points are measured data and lines are cumulative sums of curve fits to the measured daily net ecosystem exchange (NEE).

NEE became approximately zero about 1 month earlier than in 1997. The drought reduced annual NEE by about 15 g C m^{-2} compared to the well-watered year. However, because of the early spring, the forest still took up about 50% more carbon in 1998 than in 1997. The conclusion is that weather conditions during the transition seasons of spring and fall are particularly important in setting the annual rate of carbon sequestration by the forest. The forest was a net sink for carbon during both 1997 and 1998.

The finding that the forest surrounding the WI tower was a significantly larger net sink for CO_2 in 1998 than in 1997 is especially interesting in light of the results discussed previously that terrestrial systems in North America, as a whole, may have been a smaller net sink in 1998. The NEE data (Figure 2.23) are representative of a fairly small area, roughly a few km^2. The CO_2 mixing ratio data obtained at 400-500 m above the ground on these towers is representative of a much larger area of the order of 1×10^6 km^2 (M. Gloor et al., What's the footprint of a tall tower?, *Journal of Geophysical Research*, in review, 2000).

Linking the local-to-regional NEE to the larger scale mixing ratios is a topic of current investigation using the WI tower data. That is, CCGG is working to understand how the signal of surface exchange propagates into the regional and global atmosphere. This requires a detailed understanding of the dynamics of the planetary boundary layer (PBL) and the mechanisms by which the PBL exchanges air with the overlying

free troposphere. Using data from the tall tower and from a PBL sounding radar system, there is a detailed study of seasonal changes in PBL mixing (C. Yi et al., Long-term observations of the dynamics of the continental planetary boundary layer, *Journal of Atmospheric Science*, in review, 2000). It was found that the PBL height is maximum in spring when driven by high surface sensible heat fluxes. Later in summer the surface energy partition is dominated by turbulent fluxes of latent heat because of transpiration by the forest, and sensible heat fluxes are reduced. In future work the seasonal covariance between surface fluxes of CO_2 and the depth and venting (exchange with the free troposphere) of the PBL, which is critical information for efforts to diagnose the global carbon cycle by inverse methods, will be determined.

2.7. Aircraft Program

Flights over Carr, Colorado (40.9°N, 104.8°W), to collect atmospheric samples as vertical profiles continued on a weekly basis as they have for the past few years. The Carr flights have also served as a testing facility for the initial flights of new sampling instruments after their construction at CMDL. The Carr vertical profiles were also integrated into the NASA Earth Observing System (EOS) validation experiments of the CCGG where the in situ data from those flights are used to validate the remote sensing data retrievals.

With funding from the NASA Earth Science Enterprise Experiment, CO and CH_4 in the lower and middle troposphere were measured. In collaboration with the Measurement Of Pollution In The Troposphere (MOPITT) science team, four locations were chosen for study. These sites, their three-letter site codes and locations are: Poker Flats, Alaska (PFA, 65.1°N 147.5°W), Harvard Forest, Massachusetts (HFM, 42.5°N 71.2°W), and Molokai, Hawaii (HAA, 21.4°N 157.2°W). Using portable automated sampling equipment, measurements from chartered, turboprop aircraft began at these sites during 1999. Original plans called for flights above SMO, but problems with the charter service required that the program be moved to Rarotonga in the Cook Islands (RTA, 21.2°S 159.8°W), and the first flights were made in April 2000. Sampling typically extends to an altitude of about 8 km (25,000 ft), except for RTA (7 km).

The equipment consists of two suitcases, one with 17-20 sampling flasks and a controller, and one with batteries and compressors. Only a clean air inlet and a place to stow the suitcases on the aircraft are needed. Usually a sampling inlet is created on a modified storm window. These samplers are then shipped back to NOAA for automated analysis through the flask analysis system, in which not only CO and CH_4, but also CO_2, H_2, N_2O, and SF_6 are being measured. Recently isotopic analysis of CO_2 in these samples was started through mass spectrometry by INSTAAR. A second analytical system is being readied at NOAA to absorb the increase in aircraft profile analysis.

In addition to these sites CMDL has flown the automated sampler at several experimental sites such as the WLEF tower in Wisconsin and onboard a Citation aircraft as part of the CO_2 Budget and Rectification Airborne (COBRA) campaign. Aircraft sites were also prepared at two locations in Brazil for the Large Scale Biosphere Atmosphere (LBA) experiment; one site is in the Amazon Basin and one is off of the East Brazilian coast. Intensive flights will also occur in Southern Africa in 2000 during the NASA EOS validation flights as part of the Southern African Fire-Atmosphere Research Initiative (SAFARI) 2000 campaign. In addition, NCAR test flights recently used the NOAA sampler onboard the DOE Citation aircraft.

The first attempts at shipping the sampling equipment between Boulder and the sites led to considerable damage to the units. Over the past 2 years, significant effort has been devoted to improving the design for greater ruggedness and a corresponding increase in successful analysis. An example of mixing ratios determined from these aircraft programs is shown in Figure 2.24.

2.8. Air-Sea Gas Exchange

There are several strong incentives to improve the understanding of the process of air-sea gas exchange. The strongest oceanic data constraint on the uptake of CO_2 by the oceans is a decadal one, namely the rate of increase of the ocean inventories as measured by World Ocean Circulation Experiment/Joint Global Ocean Flux Study (WOCE/JGOFS), Geochemical Ocean Sections (GEOSECS), etc. [e.g., *Gruber et al.*, 1996]. An independent estimate is obtained from measurements of ΔpCO_2 (the difference in partial pressure of CO_2 between the water and the air) at the surface of the oceans, as compiled by *Takahashi et al.* [1997]. In order to convert that information into a flux, the map of ΔpCO_2 needs to be multiplied by the space- and time-dependent air-sea transfer coefficient, which has traditionally been modeled as a function of wind speed. The currently most-often used relationship is that proposed by *Wanninkhof* [1992], in which the transfer velocity increases quadratically with wind speed. There is a large amount of scatter in the measurements that suggest there are factors other than wind speed influencing gas transfer.

Because there is not a satisfactory physical explanation of the gas exchange velocity, we cannot be very sure of fluxes derived with this relationship from observed ΔpCO_2 values. The global flux estimate is sensitive to the relative rates of gas exchange at high and low wind speeds. Low wind speeds are more prevalent at low latitudes that tend to have positive ΔpCO_2 (outgassing), whereas high wind speeds occur more often at high latitudes that tend to take up CO_2 because of negative ΔpCO_2 values. The net global uptake is the balance between these two opposing tendencies at low and high latitudes.

The first combined use of the large scale north-south gradient of atmospheric CO_2 with oceanic ΔpCO_2 data led to the hypothesis of a large terrestrial sink of CO_2 at northern midlatitudes [*Tans et al.*, 1990]. The north-south gradient determines, with the use of an atmospheric transport model, the balance of all sources and sinks of CO_2 as a function of latitude. The partitioning between land and ocean at each latitude zone depends on ΔpCO_2 data and the air-sea gas exchange velocity. The recent paper by *Fan et al.* [1998] also had to employ independent estimates of net air-sea exchange to arrive at its conclusion of unexpectedly large CO_2 uptake in North America. The lesson is that atmospheric inverse models, used to derive sources and sinks from atmospheric gradients, would gain significantly in value and power as our understanding of air-sea gas exchange is improved. Not only would terrestrial estimates be improved, but regional oceanic uptake or loss would be much better quantified based on atmospheric gradients. This is especially true over the southern oceans where the atmospheric constraint would attain serious weight.

Furthermore the $^{13}C/^{12}C$ ratio of CO_2 provides us with a tool to distinguish between terrestrial and oceanic influences on

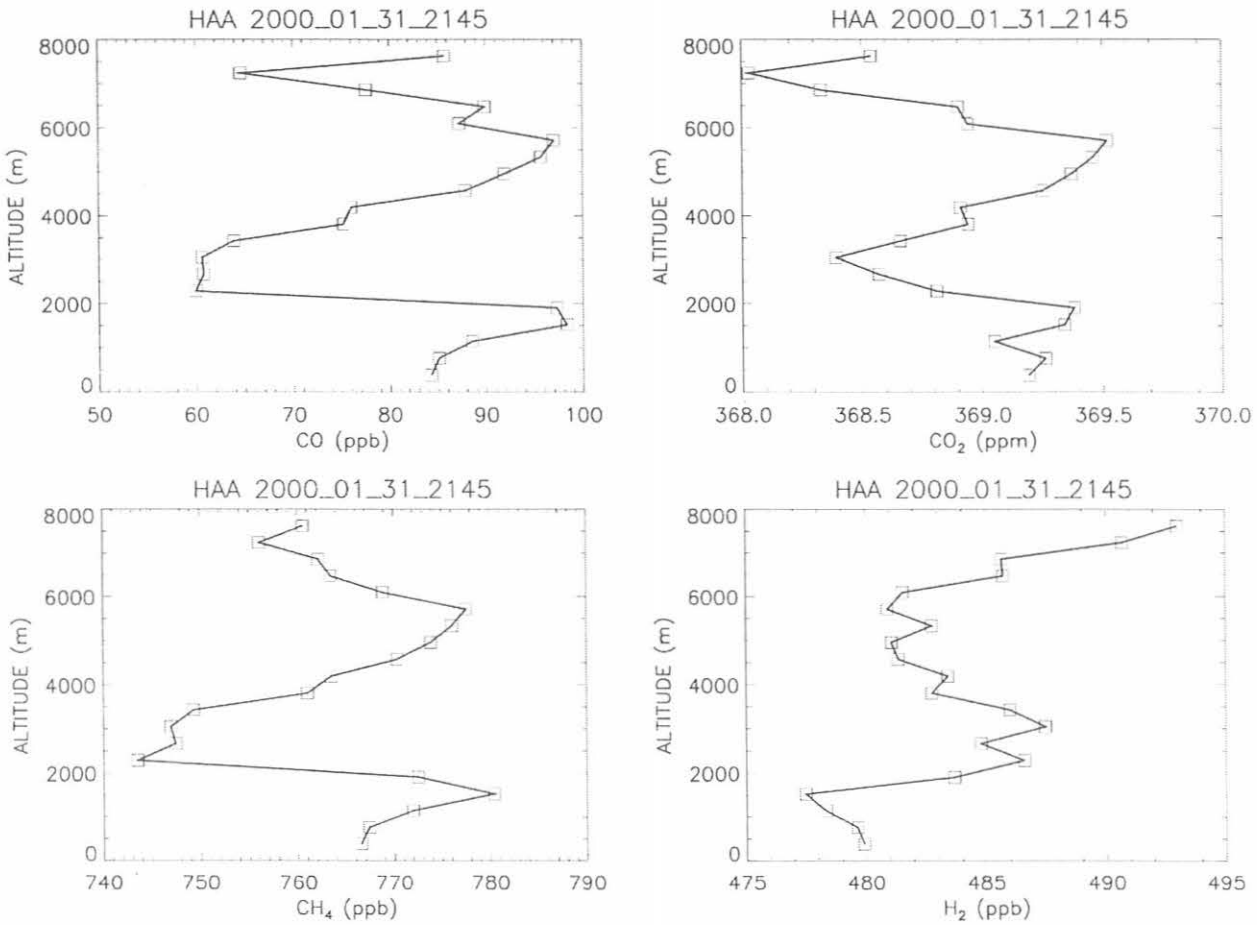

Fig. 2.24. Example of vertical profile results collected as part of the MOPITT calibration program at Molokai, Hawaii, on January 31, 2000. CO has been corrected to the 1999 gravimetric scale (section 2.4.2).

atmospheric CO_2. Unfortunately the largest term in the ^{13}C atmospheric budget, fossil fuel emissions, is followed *not* by the net uptake of CO_2 by terrestrial ecosystems, but by two-way "gross" isotopic exchange between the atmosphere and the oceans unrelated to net uptake. Also the global effect here is a balance between high latitudes that tend to decrease atmospheric $\delta^{13}C$ and low latitudes that tend to increase $\delta^{13}C$. The functional form of the gas exchange parameterization has a major effect on the use of $^{13}C/^{12}C$ to apportion carbon between the oceans and the continents.

The atmosphere, with its rapid mixing, gives us the best tool to keep track of seasonal and interannual variations of the carbon cycle on large spatial scales. The relatively large interannual variations that are being measured [e.g., *Conway et al.*, 1994] give us an opportunity to validate process models. Once such variations are mostly understood, it will be much easier to discern underlying trends in the atmospheric CO_2 burden. At present there appears to be a conflict between deductions purely from atmospheric data [*Francey et al.*, 1995] about the variability of ocean uptake, and an oceanographic approach using pCO_2 data combined with observed wind speed and temperature [*Lee et al.*, 1998]. The latter approach depends on the gas exchange velocity.

CCGG participated in a measurement campaign aboard the NOAA ship *Ronald H. Brown* from the late spring to the early summer of 1998 to specifically study gas exchange (GASEX98). Three different methods were employed to measure the CO_2 flux: on leg 2 in a cold core eddy with large negative ΔpCO_2 values north of the Azores, the small vertical CO_2 gradient created above the water by the flux was measured, and on leg 3 during the return to Miami, the flux was measured by the eddy covariance and eddy accumulation methods. An important zero bias of the eddy covariance method that affects, to a greater or lesser degree, all other such measurements that have been made to date with a rotating optical chopper wheel in the CO_2 analyzer was discovered. The motion of the ship produces a torque on the chopper that affects the analyzer response. This false signal component of the analyzer is multiplied with the ship-motion corrected vertical wind that still has a residual error. The residual error is coherent with the false analyzer signal, and multiplication leads, therefore, to an apparent CO_2 flux.

On leg 2 vertical concentration differences above the water that were significantly different from zero were measured. Several tests for potential systematic biases gave zero results. The observed concentration differences had to be converted into fluxes with the help of meteorological data and similarity theory.

When the derived gas exchange velocities are plotted as a function of wind speed, two features stand out. There is a finite gas exchange velocity at low wind speeds ($U < 6$ m s^{-1}) that appears to be independent of wind speed. It is likely that the gas exchange in this regime is controlled by thermally driven overturning of the thin skin layer of the water. At intermediate wind speeds (6 m s^{-1} < U < 11 m s^{-1}) the gas exchange velocity seems to increase linearly with wind speed. In this range CMDL results appear to agree well with the often used relationship between gas exchange velocity and the square of the wind speed [*Wanninkhof*, 1992], but our results are significantly higher at the lower wind speeds. CMDL data do not extend into the higher wind speed range.

2.9. Data Integration (Globalview)

Systematic observations of atmospheric CO_2 continue to play an essential role in advancing our understanding of the global carbon cycle. Atmospheric transport models run in the "inverse" mode and are used to estimate the magnitude and distribution of the sources of CO_2 by requiring that the modeled spatial and temporal patterns are consistent with the observations. Results from recent inverse modeling studies debate both the magnitude and distribution of the midnorthern latitude terrestrial sink. The studies agree that the most important limitation to this approach is the sparseness of observations. The growing need for greater temporal and spatial coverage requires the integration of existing observations made by different laboratories into larger merged data sets. A major challenge is ensuring that the spatial and temporal patterns observed among independent measurement records are due to emissions as affected by atmospheric mixing and transport and not because of differences in calibration scales or experimental methods.

In 1995 CCGG established the Cooperative Atmospheric Data Integration Project for carbon dioxide. Participants from 18 laboratories in 12 countries contribute their up-to-date high-precision CO_2 records from land-surface, aircraft, ship, and tower sites (Figure 2.25). These data are used to construct *Globalview-CO_2* [2000], a globally consistent data product for use with carbon cycle modeling studies (http://www.cmdl.noaa.gov/ccgg/globalview/default.html). Globalview-CO_2 consists of statistical summaries of atmospheric variability, average diurnal and seasonal patterns, and smoothed representations of the observations. The product, which is updated annually, contains no actual data. Since Globalview-CO_2 was first introduced in 1996, more than 1200 electronic requests (≈26 per month) have been made from more than 35 countries.

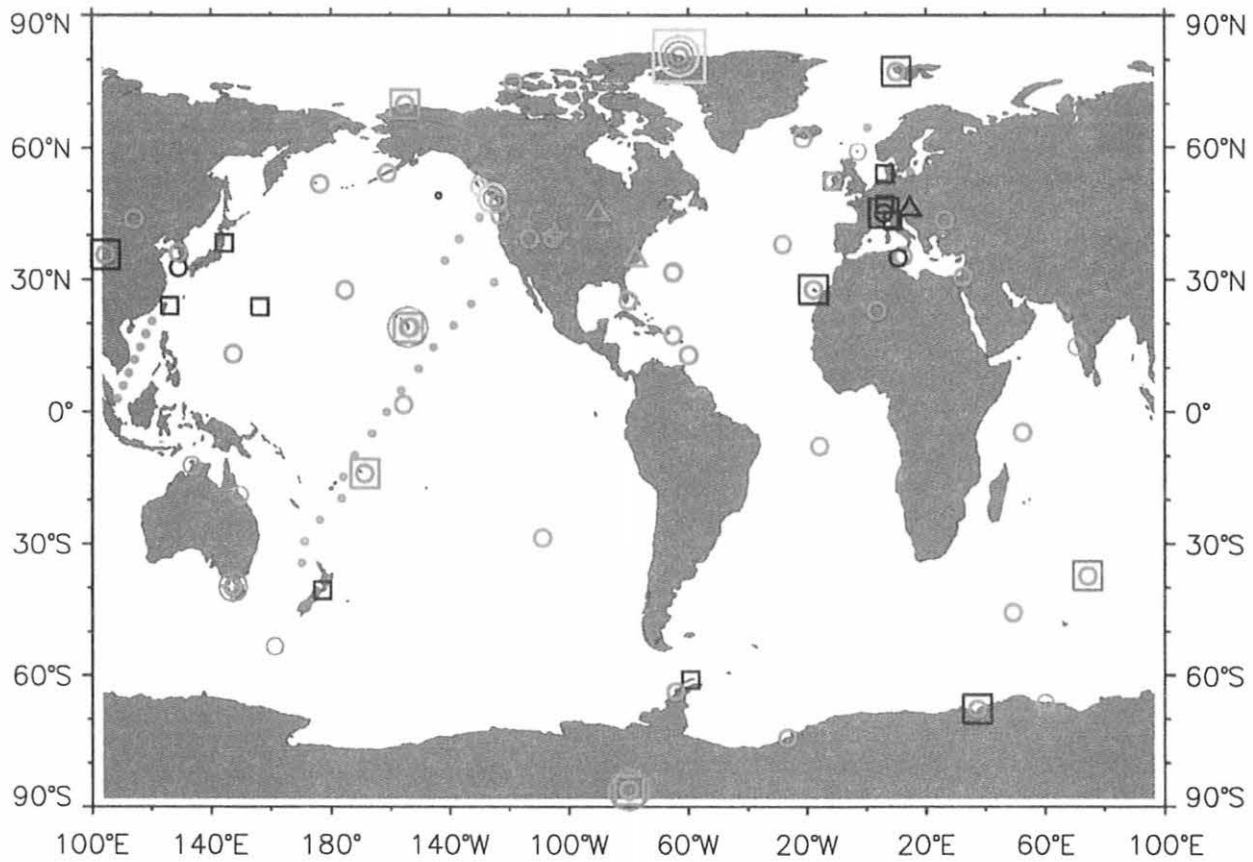

Fig. 2.25. The Cooperative Atmospheric Data Integration Project for CO_2 includes observations from land-surface discrete (○) and continuous sites (□), ships (o), aircraft (✧), and towers (Δ). Laboratories contributing four or more measurement records are identified by color. Active participants include CMDL (red); CSIRO, Australia (blue); LSCE, France (green); AES, Canada (orange); IOS, Canada; CAMS, China; UBA/IUP-HD, Germany; HMS, Hungary; CESI, IMS, and ENEA, Italy; JMA and NIPR, Japan; METRI/SNU, Republic of Korea; NIWA, New Zealand; INM, Spain; MISU, Sweden. Co-located independent sampling programs are critical for assessing comparability among atmospheric records.

A major focus of the integration project is to assess the level of comparability among observations produced by different laboratories. Nearly 2 decades ago, the CO_2 community stated that interpreting spatial and temporal gradients of CO_2 would require a level of agreement among laboratories to within 0.1 ppm [*World Meteorological Organization (WMO)*, 1981]. To assess consistency among independent measurement programs, CMDL conducted periodic intercomparison experiments (round robins) whereby more than 20 laboratories measured air from a set of traveling high-pressure cylinders. Results from the 1995-1996 intercomparison experiment show that all laboratories contributing to Globalview-CO_2 are consistent to within 0.2 ppm [*Peterson et al.*, 1999]. These experiments are critical for assessing each laboratory's ability to make high-precision CO_2 measurements and maintain a calibration scale. However, they are not designed to compare different sample collection, storage, and extraction methods that are potential sources of uncertainty when making atmospheric measurements. Thus agreement among laboratories based on comparisons of high-pressure cylinders does not necessarily imply comparability among their atmospheric CO_2 records. To complement the round-robin experiments, ongoing InterComParison (ICP) experiments were established whereby participating laboratories compare more directly the atmospheric measurements themselves. CCGG has ongoing ICP programs with the Commonwealth Scientific and Industrial Research Organization (CSIRO), Australia; Atmospheric Environment Service (AES), Canada; National Institute for Water and Atmospheric Research (NIWA), New Zealand; and HATS (U.S.). For the moment, only the ICP program with CSIRO is providing enough detail to properly assess comparability.

The effectiveness of an ICP program depends on several essential features. First, participants must view ICP activity as an additional level of quality control whereby measurements are routinely scrutinized. Potential problems identified by the collaborating laboratory should not be viewed as an embarrassment but as proof that the ICP is working effectively. Second, the ICP activity is an ongoing long-term program of routine (at least weekly) comparisons of atmospheric samples. Third, the ICP program must include supporting measurements (e.g., control samples) that can be used to narrow possible causes when differences are observed. Fourth, the ICP program should have minimal impact on daily operations. This is accomplished only if participating laboratories have advanced data management tools in place. Analysis of ICP samples and processing and data exchange between laboratories must be automatic and routine. ICP results must be summarized automatically and made readily available to participants. Timely feedback improves the likelihood that potential problems are detected early.

The CSIRO and NOAA flask air ICP program began in 1992 and has served as a model for subsequent ICP programs [*Hofmann et al.*, 1996]. The program includes the essential features described previously and demonstrates the difficulties in establishing and maintaining measurement comparability between independent laboratories. Figure 2.26 shows the level of agreement between NOAA and CSIRO measurements of the same air in a glass flask for CO_2, $\delta^{13}C$ (CO_2), CH_4, and CO. The observed variability in the differences demonstrates the need for ongoing and frequent intercomparisons. The level of agreement among CO_2 measurements combined with supporting evidence (e.g., round-robin results and pair agreement) suggests that

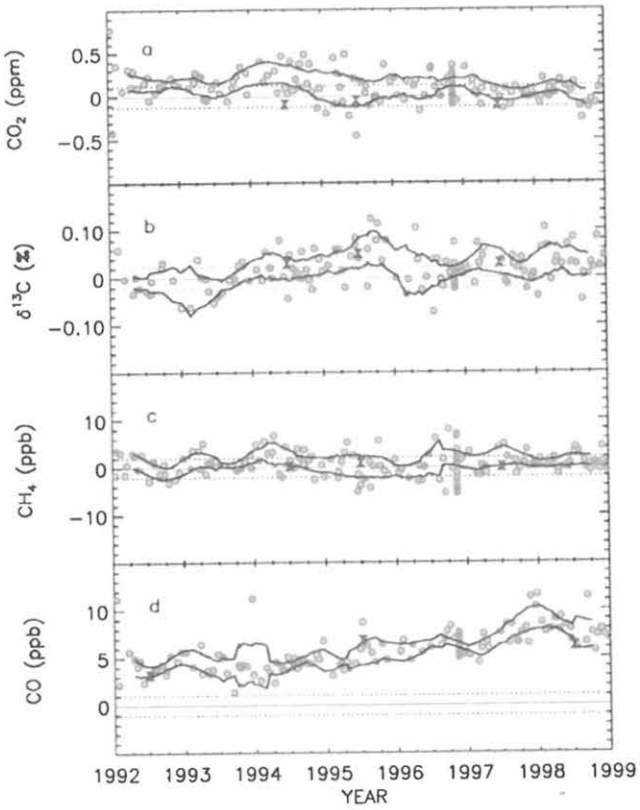

Fig. 2.26. (a-d) Differences (CSIRO minus NOAA) between independent measurements of the same air in ICP flasks for the period 1992-1999 (open circles). The mean differences (CSIRO minus NOAA) determined from multiple intercalibrations of air in high-pressure cylinders are shown as solid green hourglass symbols and plotted at the middle of the year in which the analyses took place. The dotted lines about the zero difference line represent the 67% confidence limits about the mean NOAA flask pair difference (excluding ICP flasks and mates) at Cape Grim. The band defined by solid lines represents 2 standard errors (95% confidence limit) from the mean of the residuals determined from a smooth curve fitted to the distribution. A 6-month window centered at each difference value is used to compute the standard error for that value.

NOAA and CSIRO network measurements of CO_2 are comparable to within 0.2 ppm (0.06%). Differences in the independent measurements of $\delta^{13}C$ show significant variability with time and are not yet fully understood. Methane measurements from NOAA and CSIRO network samples are comparable to within 1 ppb (0.04%) and have been integrated with observations from other laboratories to produce *Globalview-CH_4* [1999]. Differences in the independent measurements of CO show a systematic offset of about 5 ppb from 1992 to 1994. The difference increases at a rate of about 1 ppb yr^{-1} from 1995 to 1998 and appears to stabilize again in 1999. Results from high pressure cylinder intercomparison experiments are consistent with the ICP results suggesting that the problem is likely related to the maintenance of the internal CO calibration scale in one or both laboratories. Both NOAA and CSIRO are working to understand the causes of these differences.

2.10. INVERSE MODELING

Efforts to quantify the possible responses of the climate system to anthropogenic emissions of radiatively active trace species such as CO_2 and CH_4 are complicated by the significant contributions of terrestrial biospheric and oceanic sources to the budgets of these gases. Future attempts to manage carbon reservoirs depend critically on the ability to understand and quantify the distributions of carbon sources in the atmosphere and oceans. Inverse modeling techniques, which have long been applied to geophysical problems such as seismology, satellite data retrieval, and acoustic tomography, have over the past decade been applied to the problem of determining the source and sink distributions of atmospheric trace species, especially CO_2. Early attempts were aimed at obtaining the interhemispheric gradient of the CO_2 sources and sinks [*Tans et al.*, 1990; *Enting and Mansbridge*, 1991; *Ciais et al.*, 1995a,b; *Bousquet et al.*, 1996; *Law and Simmonds*, 1996]. However, with the expansion of the CO_2 observational network, attempts have been made over recent years to obtain source and sink distributions over continental scales.

Currently it seems that the observational network is too sparse to allow accurate estimates of trace gas budgets on continental scales, though it is likely that reasonable estimates over large latitude zones may be made. A further complication is that the current network is designed to sample mostly marine boundary layer air so that information from the terrestrial biosphere at regional scales is lost by mixing over large distances. In addition it is clear that even if more observations over continental regions were obtained, the current generation of models would likely not represent atmospheric boundary processes adequately, leading to significant uncertainty [e.g., *Denning et al.*, 1995]. Despite these daunting difficulties, efforts to estimate the carbon budget at continental scales with reduced uncertainty are underway. It is hoped that the observational network will be expanded and that models will improve significantly in the near future.

Ongoing work by the CCGG group is focused on development of an operational inverse calculation at continental scales. The mass balance and assimilation technique employed has been described in detail by *Bruhwiler et al.* [2000]. The global transport model to be used for operational source calculations is the NCAR MATCH model with the National Center for Environmental Predictions (NCEP) winds. Since this model requires large amounts of computational resources, development and evaluation of the inverse technique has taken place using a much simpler and faster low resolution version of TM2/TM3 [*Heimann*, 1995] with 1 year of European Center for Medium-Range Weather Forecasts (ECMWF) winds that are repeated for multi-year calculations (although multiple year wind fields and 1 year of TM2 vertical diffusion may be used with TM3 for a rough idea of the effects of interannual variability). The inversion uses the Globalview-CO_2 data set and 14 basis functions for continental and oceanic regions.

The sensitivity of source regions to a variety of conditions has been tested. Examples of these conditions include use of radon (Rn) to filter out simulated CO_2 values of recent continental origin and applying a smoothing procedure to calculated time series rather than using instantaneous values. Estimates of the long-term average (1979-1998) CO_2 sources range from about -1 to +1 Gt C yr^{-1} for the terrestrial biosphere and from 0.0 to -2.75 Gt C yr^{-1} for the oceans. In each case, the estimate is for nonrepeating meteorology. Although the estimates seem to be rather insensitive to smoothing and Rn filtering, use of nonrepeating meteorology appears to have a large impact, at least in the present configuration of TM3.

Current estimates of the North American carbon sink are -1 to -1.75 Gt C yr^{-1}, while Eurasia appears to be a carbon source on the average (about 1 Gt C yr^{-1}). The high-latitude northern hemispheric oceans are estimated to take up carbon at the rate of about 1.5 Gt C yr^{-1}(larger than suggested by ΔpCO_2 data), while the equatorial oceans, especially the equatorial Pacific, release carbon at approximately the same rate. Time series of monthly estimates of carbon sources are rather noisy, and time series of annual averages exhibit significant variability, which is due to both uncertainty in the inversion and real variability in sources and sinks. During El Niño years, for example, the emissions from the equatorial Pacific are estimated to decrease, and the total terrestrial sink appears to decrease, possibly to the point at which the terrestrial biosphere becomes a net source of CO_2.

Recent developments were aimed at reducing noise and uncertainty in the inverse calculation. The ability to retain basis function (the CO_2 pattern resulting from a well-defined source) transport information for an arbitrary length of time previous to the time of the inverse calculation was added. Tests suggest that basis functions may need to be carried for periods of half year or longer. In addition the inverse technique was modified to allow simultaneous inversion of multiple trace species. This allows the possibility that constraints relating the budgets of two or more trace species may be used to reduce noise and uncertainty. Test calculations suggest that uncertainty could be significantly reduced if the uncertainty in the constraints employed is not too large.

2.11. REFERENCES

Bakwin, P.S., P.P. Tans, and P.C. Novelli, Carbon monoxide budget in the Northern Hemisphere, *Geophys. Res. Lett., 21*, 433-436, 1994.

Bakwin, P.S., P.P. Tans, D.F. Hurst, and C. Zhao, Measurements of carbon dioxide on very tall towers: Results of the NOAA/CMDL program, *Tellus, 50B*, 401-415, 1998.

Bekki, S., K.S. Law, and J.A. Pyle, Effect of ozone depletion on CH_4 and CO concentrations, *Nature, 371*, 595-597, 1994.

Berger, B.W., K.J. Davis, P.S. Bakwin, C. Yi, and C. Zhao, Long-term carbon dioxide fluxes from a very tall tower in a northern forest: Flux measurement methodology, *J. Oceanic and Atmos. Technol.*, in press, 2000.

Bousquet, P., P. Ciais, P. Monfray, Y. Balkanski, M. Ramonet, and P.P. Tans, Influence of two different atmospheric transport models on inferring sources and sinks of atmospheric CO_2, *Tellus, 48B*, 568-582, 1996.

Bruhwiler, L., P. Tans, and M. Ramonet, A time-dependent assimilation and source retrieval technique for atmospheric tracers, in *Inverse Methods in Global Biogeochemical Cycles, Geophysical Monograph 1114*, AGU, Washington D.C., 265-277, 2000.

Ciais, P., P.P. Tans, M. Trolier, J.W.C. White, and R.J. Francey, A large northern hemisphere terrestrial CO_2 sink indicated by the $^{13}C/^{12}C$ ratio of atmospheric CO_2, *Science, 269*, 1098-1102, 1995a.

Ciais, P., P.P. Tans, J.W.C. White, M. Trolier, R.J. Francey, J.A. Berry, D.R. Randall, P.J. Sellers, J.G. Collatz, and D.S. Schimel, Partitioning of ocean and land uptake of CO_2 as inferred by $\delta^{13}C$ measurements from the NOAA CMDL global air sampling network, *J. Geophys. Res., 100*, 5051-5070, 1995b.

Conway, T.J., P.P. Tans, L.S. Waterman, K.W. Thoning, D.R. Kitzis, K.A. Masarie, and N. Zhang, Evidence for interannual variability of the carbon cycle from the NOAA/CMDL global air sampling network, *J. Geophys. Res., 99*, 22,831-22,855, 1994.

Dedikov, J.V., G.S. Akopova, N.G., Gladkaja, A.S. Piotrovskij, V.A. Markellov, S.S. Salichov, H. Kaesler, A. Ramm, A. Muller von Blumencron, and J. Lelieveld, Estimating methane releases from natural gas production and transmission in Russia, *Atmos. Environ., 33*, 3291-3299, 1999.

Denning, A.S., I.Y. Fung, and D.A. Randall, Latitudinal gradient of atmospheric CO_2 due to seasonal exchange with land biota, *Nature, 376*, 240-243, 1995.

Dlugokencky, E.J., L.P. Steele, P.M. Lang, and K.A. Masarie, Atmospheric methane at Mauna Loa and Barrow observatories: Presentation and analysis of in situ measurements, *J. Geophys. Res., 100*, 23,103-23,113, 1995.

Dlugokencky, E.J., K.A. Masarie, P.M. Lang, and P.P. Tans, Continuing decline in the growth rate of atmospheric methane, *Nature, 393*, 447-450, 1998.

Enting, I.G., and J.V. Mansbridge, Latitudinal distribution of sources and sinks of CO_2: Results of an inversion study, *Tellus, 43B*, 156-170, 1991.

Fan, S., M. Gloor, J. Mahlman, S. Pacala, J. Sarmiento, T. Takahashi, and P. Tans, A large terrestrial carbon sink in North America implied by atmospheric and oceanic carbon dioxide data and models, *Science 282*, 442-446, 1998.

Francey, R.J., P.P. Tans, C.E. Allison, I.G. Enting, J.W.C. White, and M. Trolier, Changes in oceanic and terrestrial carbon uptake since 1982, *Nature, 373*, 326-330, 1995.

Gemery, P.A., M. Trolier, and J.W.C. White, Oxygen isotope exchange between carbon dioxide and water following atmospheric sampling using glass flasks, *J. Geophys. Res., 101*, 14,415-14,420, 1996.

Globalview-CH_4: Cooperative Atmospheric Data Integration Project - Methane. CD-ROM, NOAA CMDL, Boulder, Colorado (Also available on Internet via anonymous FTP to ftp.cmdl.noaa.gov, Path: ccg/ch4/GLOBALVIEW), 1999.

Globalview-CO_2: Cooperative Atmospheric Data Integration Project - Carbon Dioxide. CD-ROM, NOAA CMDL, Boulder, Colorado (Also available on Internet via anonymous FTP to ftp.cmdl.noaa.gov, Path: ccg/co2/GLOBALVIEW), 2000.

Granier, C., J.-F. Muller, S. Madronich, and G. Brasseur, Possible causes of the 1990-1993 decrease in the global; tropospheric carbon monoxide abundance: A three dimensional sensitivity study, *Atmos. Environ., 30*, 1673-1692, 1996.

Granier, C., G. Petron, J.-P. Muller, and G. Brasseur, The impact of natural and anthropogenic hydrocarbons on the tropospheric budget of carbon monoxide, *Atmos. Environ., 34*, 5255-5271, 2000.

Gruber, N., J.L. Sarmiento, and T.F. Stocker, An improved method for detecting anthropogenic CO_2 in the oceans, *Global Biogeochem. Cycles, 10*, 809-837, 1996.

Heimann, M., The global atmospheric tracer model TM2, *Tech. Rep. 10*, 53 pp., Max Planck Institut fur Meteorologie, Germany, 1995.

Hofmann, D.J., J.T. Peterson, and R.M. Rosson (Eds.), *Climate Monitoring and Diagnostics Laboratory, No. 23, Summary Report 1994-1995*, NOAA Environ. Res. Labs., Boulder, CO, 161 pp., 1996.

Kasischke, E.S., K. Bergen, R. Fenimore, F. Sotelo, G. Stephens, A. Janetos, and H. H. Shugart, Satellite imagery gives clear picture of Russia's boreal forest fires, *Eos, Trans. Am. Geophys. Union, 80(13)*, 141-152, 1999.

Kitzis, D., and C. Zhao, CMDL/Carbon Cycle Gases Group Standards Preparation and Stability, *NOAA TM ERL CMDL-14*, 14 pp., NOAA Environ. Res. Labs., Boulder, CO, 1999.

Law, R.M., and I. Simmonds, The sensitivity of deduced CO_2 sources and sinks to variations in transport and imposed surface concentrations, *Tellus, 48B*, 613, 1996.

Lee, K., R. Wanninkhof, T. Takahashi, S.C. Doney, and R.A. Feely, Low interannual variability in recent oceanic uptake of atmospheric carbon dioxide, *Nature, 396*, 155-159, 1998.

Levine, J.S., T. Bobbe, N. Ray, A. Singh, and R.G. Witt, Wildland fires and the environment: A global synthesis, *UNEP/DEIAEW/TR.99-1*, UNEP (WMO), Geneva, 1999.

Masarie, K.A., Steele, L.P., and P.M. Lang, A rule-based expert system for evaluating the quality of long-term, in situ gas chromatographic measurements of atmospheric methane, *NOAA TM ERL CMDL-3*, 37 pp., Boulder, CO, 1991.

Novelli, P.C., J.W. Elkins, and L.P. Steele, The development and evaluation of a gravimetric reference scale for measurements of atmospheric carbon monoxide, *J. Geophys. Res., 96*, 20,731-20,750, 1991.

Novelli, P.C., J.E. Collins, R.C. Myers, G.W. Sachse, and H.E. Scheel, Reevaluation of the NOAA/CMDL carbon monoxide reference scale and comparisons with reference scales at NASA-Langley and at the Fraunhofer Institute, *J. Geophys. Res., 99*, 12,833-12,839, 1994.

Novelli, P.C., K.A. Masarie, and P.M. Lang, Distributions and recent changes of carbon monoxide in the lower troposphere, *J. Geophys. Res., 103*, 19,015-19,033, 1998a.

Novelli, P.C., V.S. Connors, H.G. Reichle, Jr., B.E. Anderson, C.A.M. Brenninkmeijer, E.G. Brunke, B.G. Doddridge, V.W.J.H. Kirchhoff, K.S. Lam, K.A. Masarie, T. Matsuo, D.D. Parrish, H.E. Scheel, and L.P. Steele, An internally consistent set of globally distributed atmospheric mixing ratios developed using results from an intercomparison of measurements, *J. Geophys. Res., 103*, 19,285-19,293, 1998b.

Peterson, J., P. Tans, and D. Kitzis, CO_2 Round-Robin Reference Gas Intercomparison, in *Report of the Ninth WMO Meeting of Experts on Carbon Dioxide Concentration and Related Tracer Measurement Techniques, Aspendale, Victoria, Australia, September 1-4, 1997*, edited by R. Francey, pp. 30-33, WMO, Geneva, 1999.

Reshetnikov, A.I., N.N. Paramonova, and A.A. Shashkov, An evaluation of historical methane emissions from the Soviet gas industry, *J. Geophys. Res., 105*, 3517-3529, 2000.

Takahashi, T., R.A. Feely, R.F. Weiss, R.H. Wanninkhof, D.W. Chipman, S.C. Sutherland, and T.T. Takahashi, Global air-sea flux of CO_2: An estimate based on measurements of sea-air pCO_2 difference, *Proc., Nat. Acad. Sci. USA 94*, 8292-8299, 1997.

Tans, P.P., T.J. Conway, and T. Kakazawa, Latitudinal distribution of the sources and sinks of atmospheric carbon dioxide derived from surface observations and an atmospheric transport model, *J. Geophys. Res., 94*, 5151-5172, 1989.

Tans, P.P., I.Y. Fung, and T. Takahashi, Observational constraints on the global atmospheric CO_2 budget, *Science, 247*, 1431-1438, 1990.

Thoning, K.W., P.P. Tans, and W.D. Komhyr, Atmospheric carbon dioxide at Mauna Loa Observatory, 2, Analysis of the NOAA GMCC data, 1974-1985, *J. Geophys. Res., 94*, 8549-8565, 1989.

Tyler, S., H. Ajie, M. Gupta, R. Cicerone, D.R. Blake, and E.J. Dlugokencky, Stable carbon isotopic composition of atmospheric methane: A comparison of surface level and free tropospheric air, *J. Geophys. Res., 104*, 13,895-13,910, 1999.

Wahlen, M., B. Deck, R. Henry, N. Tanaka, and A. Shemesh, Profiles of $\delta^{13}C$ and δD of CH_4 from the lower stratosphere, *Eos, Trans. Am. Geophys. Union, 70* (43), 1017, 1990.

Wanninkhof, R., Relationship between wind speed and gas exchange over the ocean, *J. Geophys. Res., 97*, 7373-7382, 1992.

World Meteorological Organization (WMO), Scientific Requirements, in *Report of the WMO/UNEP/ICSU meeting on instruments, standardization and measurement techniques for atmospheric CO_2, Geneva, Switzerland, September 8-11, 1981*, 27 pp., WMO, 1981.

Yi, C., K.J. Davis, P.S. Bakwin, B.W. Berger, and L.C. Marr, The influence of advection on measurements of the net ecosystem-atmosphere exchange of CO_2 from a very tall tower, *J. Geophys. Res., 105*, 9991-9999, 2000.

Yurganov, L.N., D.A. Jaffe, E. Pullman, and P.C. Novelli, Total column and surface densities of atmospheric carbon monoxide in Alaska, 1995, *J. Geophys. Res., 103*, 19,337-19,345, 1998.

Zhao, C., P. Tans, and K. Thoning, A manometric system for absolute calibrations of CO_2 in dry air, *J. Geophys. Res., 102*, 5885-5894, 1997.

3. Aerosols and Radiation

3.1. Aerosol Monitoring

D. Delene (Editor), E. Andrews, D. Jackson, A. Jefferson, J. Ogren, P. Sheridan, and J. Wendell

3.1.1. Scientific Background

Aerosol particles affect the radiative balance of Earth both directly, by scattering and absorbing solar and terrestrial radiation, and indirectly, through their action as cloud condensation nuclei (CCN) with subsequent effects on the microphysical and optical properties of clouds. Evaluation of the climate forcing by aerosols, defined here as the perturbation of the Earth's radiation budget induced by the presence of airborne particles, requires knowledge of the spatial distribution of the particles, their optical and cloud-nucleating properties, and suitable models of radiative transfer and cloud physics. Obtaining a predictive relationship between the aerosol forcing and the physical and chemical sources of the particles additionally requires knowledge of regional and global-scale chemical processes, physical transformation, and transport models for calculating the spatial distributions of the major chemical species that control the optical and cloud-nucleating properties of the particles. Developing and validating these various models require a diverse suite of in situ and remote observations of the aerosol particles on a wide range of spatial and temporal scales.

Aerosol measurements began at the CMDL baseline observatories in the mid-1970s as part of the Geophysical Monitoring for Climatic Change (GMCC) program. The objective of these "baseline" measurements was to detect a response, or lack of response, of atmospheric aerosols to changing conditions on a global scale. Since the inception of the program, scientific understanding of the behavior of atmospheric aerosols has improved considerably. One of the lessons learned is that residence times of tropospheric aerosols are generally less than 1 week, and another is that human activities primarily influence aerosols on regional and continental scales rather than global scales. In response to this increased understanding, and to more recent findings that anthropogenic aerosols create a significant perturbation in the Earth's radiative balance on regional scales [*Charlson et al.*, 1992; *National Research Council*, 1996], CMDL expanded its aerosol research program to include regional aerosol monitoring stations. The goals of this regional-scale monitoring program are: (1) to characterize means, variabilities, and trends of climate-forcing properties of different types of aerosols and (2) to understand the factors that control these properties.

A primary hypothesis to be tested by NOAA's aerosol research program is that the climate forcing by anthropogenic sulfate will change in response to future changes in sulfur emissions. The forcing is expected to decrease in and downwind of the United States as a result of emission controls mandated by the Clean Air Act, while continued economic development in China and other developing countries is expected to lead to an increased forcing in and downwind of those areas. Testing this hypothesis will require a coordinated research program involving modeling, monitoring, process, and closure studies. This report describes the observations that CMDL is conducting towards this goal.

No single approach to observing the atmospheric aerosol can provide the necessary data for monitoring all the relevant dimensions and spatial/temporal scales necessary to evaluate climate forcing by anthropogenic aerosols. In situ observations from surface sites, ships, balloons, and aircraft can provide very detailed characterizations of the atmospheric aerosol but on limited spatial scales. Remote sensing methods from satellites, aircraft, or the surface can determine a limited set of aerosol properties from local to global spatial scales, but they cannot provide the chemical information needed for linkage with global chemical models. Fixed ground stations are suitable for continuous observations over extended time periods but lack vertical resolution. Aircraft and balloons can provide the vertical dimension but not continuously. Only when systematically combined can these various types of observations produce a data set where point measurements can be extrapolated with models to large geographical scales, where satellite measurements can be compared to the results of large-scale models, and where process studies have a context for drawing general conclusions from experiments conducted under specific conditions.

Measurements of atmospheric aerosols are used in three fundamentally different ways for aerosol/climate research: algorithm development for models and remote-sensing retrievals, parameter characterization, and model validation. Laboratory and field process studies guide the development of parameterization schemes and the choice of parameter values for chemical transport models that describe the relationship between emissions and concentration fields of aerosol species. Systematic surveys and monitoring programs provide characteristic values of aerosol properties that are used in radiative transfer models for calculating the radiative effects of the aerosols and for retrieving aerosol properties from satellites and other remote sensing platforms. And finally, monitoring programs provide spatial and temporal distributions of aerosol properties that are compared to model results to validate the models. Each of these three modes of interaction between applications and measurements requires different types of data and entail different measurement strategies. *Ogren* [1995] applied the thermodynamic concept of "intensive" and "extensive" properties of a system to emphasize the relationship between measurement approach and applications of aerosol observations.

Intensive properties do not depend on the amount of aerosol present and are used as parameters in chemical transport and radiative transfer models (e.g., atmospheric residence time, single-scattering albedo). Extensive properties vary strongly in response to mixing and removal processes and are most commonly used for model validation (e.g., mass concentration, optical depth). Intensive properties are more difficult and expensive to measure than extensive properties because they generally are defined as the ratio of two extensive properties. As a result, different measurement strategies are needed for meeting the data needs of the various applications. Measurements of a few carefully chosen extensive properties, of which aerosol optical depth and species mass concentrations are prime candidates, are needed in many locations to test the ability of the models to predict spatial and temporal variations on regional to global scales and to detect changes in aerosol concentrations resulting from changes in aerosol sources. The higher cost of determining intensive properties suggests a strategy of using a limited number of highly instrumented sites to characterize means and variabilities of intensive properties for different regions or aerosol types, supplemented with surveys by aircraft

and ships to characterize the spatial variability of these parameters. CMDL's regional aerosol monitoring program is primarily focused on characterizing intensive properties.

CMDL's measurements provide ground truth for satellite measurements and global models, as well as key aerosol parameters for global-scale models (e.g., scattering efficiency of sulfate particles and hemispheric backscattering fraction). An important aspect of this strategy is that the chemical measurements are linked to the physical measurements through simultaneous, size-selective sampling that allows the observed aerosol properties to be connected to the atmospheric cycles of specific chemical species.

3.1.2. Experimental Methods

Extensive aerosol properties monitored by CMDL include condensation nuclei (CN) concentration, aerosol optical depth (δ), and components of the aerosol extinction coefficient at one or more wavelengths (total scattering σ_{sp}, backwards hemispheric scattering σ_{bsp}, and absorption σ_{ap}). At the regional sites, size-resolved impactor and filter samples (submicrometer and supermicrometer size fractions) are obtained for gravimetric and chemical (ion chromatograph) analyses. All size-selective sampling, as well as the measurements of the components of the aerosol extinction coefficient at the regional stations, is performed at a low, controlled relative humidity (<40%) to eliminate confounding effects because of changes in ambient relative humidity. Data from the continuous sensors are screened to eliminate contamination from local pollution sources. At the regional stations, the screening algorithms use measured wind speed, direction, and total particle number concentration in real-time to prevent contamination of the chemical samples. Algorithms for the baseline stations use measured wind speed and direction to exclude data that are likely to have been locally contaminated.

Prior to 1995, data from the baseline stations were manually edited to remove spikes from local contamination. Since 1995 an automatic editing algorithm has been applied to the baseline data in addition to manual editing of local contamination spikes. For the baseline stations (Barrow, Alaska (BRW); Mauna Loa, Hawaii (MLO); American Samoa (SMO); and South Pole, Antarctica (SPO), as well as Sable Island (WSA)), data are automatically removed when the wind direction is from local sources of pollution (such as generators and buildings) as well as when the wind speed is less than a threshold value (0.5-1 m s^{-1}). In addition, at MLO, data for upslope conditions (1800-1000 UTC) are excluded since the air masses do not represent "background" free tropospheric air for this case. A summary of the data-editing criteria is given in Table 3.1.

Integrating nephelometers are used to determine the light scattering coefficient of the aerosol. These instruments operate by illuminating a fixed sample volume from the side and observing the amount of light that is scattered by particles and gas molecules in the direction of a photomultiplier tube. The instrument integrates over scattering angles of 7-170°. Depending on the station, measurements are performed at three or four wavelengths in the visible and near infrared. Newer instruments allow determination of the hemispheric backscattering coefficient by using a shutter to prevent illumination of the portion of the instrument that yields scattering angles less than 90°. A particle filter is inserted periodically into the sample stream to measure the light scattered by gas molecules. This is then subtracted from the total scattered signal to determine the contribution from the particles alone. The instruments are calibrated by filling the sample volume with CO_2 gas that has a known scattering coefficient.

TABLE 3.1. Data Editing Summary for NOAA Baseline and Regional Stations

Station	Editing	Clean Sector
South Pole	a,b,c	0° < WD < 110°, 330°<WD <360°
Samoa	a,b,c	0° < WD < 165°, 285°<WD < 360°
Mauna Loa	a,b,c,d	90° < WD < 270°
Barrow	a,b,c	0° < WD < 130°
Sable Island	a,b,c	0° < WD < 35°, 85° < WD < 360°
Southern Great Plains	a	
Bondville	a	

a: Manual removal of local contamination spikes
b: Automatic removal of data not in clean sector
c: Automatic removal of data for low wind speeds
d: Removal of data for upslope wind conditions
WD: Wind direction

The aerosol light absorption coefficient is determined with a continuous light absorption photometer. This instrument continuously measures the amount of light transmitted through a quartz filter while particles are being deposited on the filter. The rate of decrease of transmissivity, divided by the sample flow rate, is directly proportional to the light absorption coefficient of the particles. Newer instruments were calibrated in terms of the difference of light extinction and scattering in a long-path extinction cell for laboratory test aerosols. Instruments at the baseline stations (aethalometers, Magee Scientific, Berkeley, California) were calibrated by the manufacturer in terms of the equivalent amount of black carbon (BC) from which the light absorption coefficient is calculated, assuming a mass absorption efficiency of the calibration aerosols of 10 m^2 g^{-1}.

Particle number concentration is determined with a CN counter that exposes the particles to a high supersaturation of butanol vapor. This causes the particles to grow to a size where they can be optically detected and counted. The instruments in use have lower particle-size detection limits of 10-20 nm diameter.

Summaries of the extensive measurements obtained at each site are given in Tables 3.2 and 3.3. Table 3.4 lists the intensive aerosol properties that can be determined from the directly measured extensive properties. These properties are used in chemical transport models to determine the radiative effects of the aerosol concentrations calculated by the models. Inversely, these properties are used by algorithms for interpreting satellite remote-sensing data to determine aerosol amounts based on measurements of the radiative effects of the aerosol.

3.1.3. Annual Cycles

The annual cycles of aerosol optical properties for the four baseline and three regional stations are illustrated in Figures 3.1 and 3.2. The data are presented in the form of box and whisker plots that summarize the distribution of values. Each box ranges from the lower to upper quartiles with a central bar at the median value, while the whiskers extend to the 5th and 95th percentiles. The statistics are based on hourly averages of each parameter for each month of the year, also shown are the annual statistics for the entire period of record. A horizontal line is given that intersects the annual median so measurements above and below the median can be easily discerned.

TABLE 3.2. CMDL Baseline Aerosol Monitoring Stations (Status as of December 1999)

Category	Baseline Arctic	Baseline Free Troposphere	Baseline Marine	Baseline Antarctic
Location	Point Barrow	Mauna Loa	American Samoa	South Pole
Designator	BRW	MLO	SMO	SPO
Latitude	71.323°N	19.539°N	14.232°S	89.997°S
Longitude	156.609°W	155.578°W	170.563°W	102.0°E
Elevation (m)	8	3397	77	2838
Responsible institute	CMDL	CMDL	CMDL	CMDL
Status	Operational, 1976 Major upgrade, 1997	Operational, 1974	Operational, 1977	Operational, 1974
Sample RH	RH <40%	Uncontrolled	Uncontrolled	Uncontrolled
Sample size fractions	D<1 μm D<10 μm	Uncontrolled	Uncontrolled	Uncontrolled
Optical measurements	$\sigma_{sp}(3\lambda)$, $\sigma_{bsp}(3\lambda)$, $\sigma_{ap}(1\lambda)$	$\sigma_{sp}(3\lambda)$, $\sigma_{ap}(1\lambda)$, $\delta(6\lambda)$	none	$\sigma_{sp}(4\lambda)$
Microphysical measurements	CN concentration	CN concentration	CN concentration	CN concentration
Chemical measurements	Major ions, mass	None	None	None

TABLE 3.3. CMDL Regional Aerosol Monitoring Sites (Status as of December 1999)

Category	Perturbed Marine	Perturbed Continental	Perturbed Continental
Location	Sable Island, Nova Scotia, Canada	Bondville, Illinois	Lamont, Oklahoma
Designator	WSA	BND	SGP
Latitude	43.933°N	40.053°N	36.605°N
Longitude	60.007°W	88.372°W	97.489°W
Elevation (m)	5	230	315
Responsible institute	CMDL	CMDL	CMDL
Collaborating institute	AES Canada, NOAA/PMEL	Univ. of Illinois, IL State Water Survey	DOE/ARM
Status	Operational, August 1992	Operational, July 1994	Operational, July 1996
Sample RH	RH <40%	RH <40%	RH <40%
Sample size fractions	D<1 μm, D<10 μm	D<1 μm, D<10 μm	D<1 μm, D<10 μm
Optical measurements	$\sigma_{sp}(3\lambda)$, $\sigma_{bsp}(3\lambda)$, $\sigma_{ap}(1\lambda)$	$\sigma_{sp}(3\lambda)$, $\sigma_{bsp}(3\lambda)$, $\sigma_{ap}(1\lambda)$	$\sigma_{sp}(3\lambda)$, $\sigma_{bsp}(3\lambda)$, $\sigma_{ap}(1\lambda)$, $\delta(7\lambda)$
Microphysical measurements	CN concentration	CN concentration	CN, n(D) concentration
Chemical measurements	Major ions, mass	Major ions, mass	None

TABLE 3.4. Intensive Aerosol Properties Derived From CMDL Network

Properties	Description
å	The Ångström exponent, defined by the power-law $\sigma_{sp} \propto \lambda^{-\text{å}}$, describes the wavelength-dependence of scattered light. In the figures below, *å* is calculated from measurements at 550 and 700 nm wavelength. Situations where the scattering is dominated by submicrometer particles typically have values around 2, while values close to 0 occur when the scattering is dominated by particles larger than a few microns in diameter.
ω_0	The aerosol single-scattering albedo, defined as $\sigma_{sp}/(\sigma_{ap} + \sigma_{sp})$, describes the relative contributions of scattering and absorption to the total light extinction. Purely scattering aerosols (e.g., sulfuric acid) have values of 1, while very strong absorbers (e.g., elemental carbon) have values around 0.3.
g, *b*	Radiative transfer models commonly require one of two integral properties of the angular distribution of scattered light (phase function): the asymmetry factor *g* or the hemispheric backscatter fraction *b*. The asymmetry factor is the cosine-weighted average of the phase function, ranging from a value of -1 for entirely backscattered light to +1 for entirely forward-scattered light. The hemispheric backscatter fraction *b* is defined as σ_{bsp}/σ_{sp}.
α_i	The mass scattering efficiency for species *i*, defined as the slope of the linear regression line relating σ_{sp} and the mass concentration of the chemical species, is used in chemical transport models to evaluate the radiative effects of each chemical species modeled. This parameter has typical units of $m^2\ g^{-1}$.

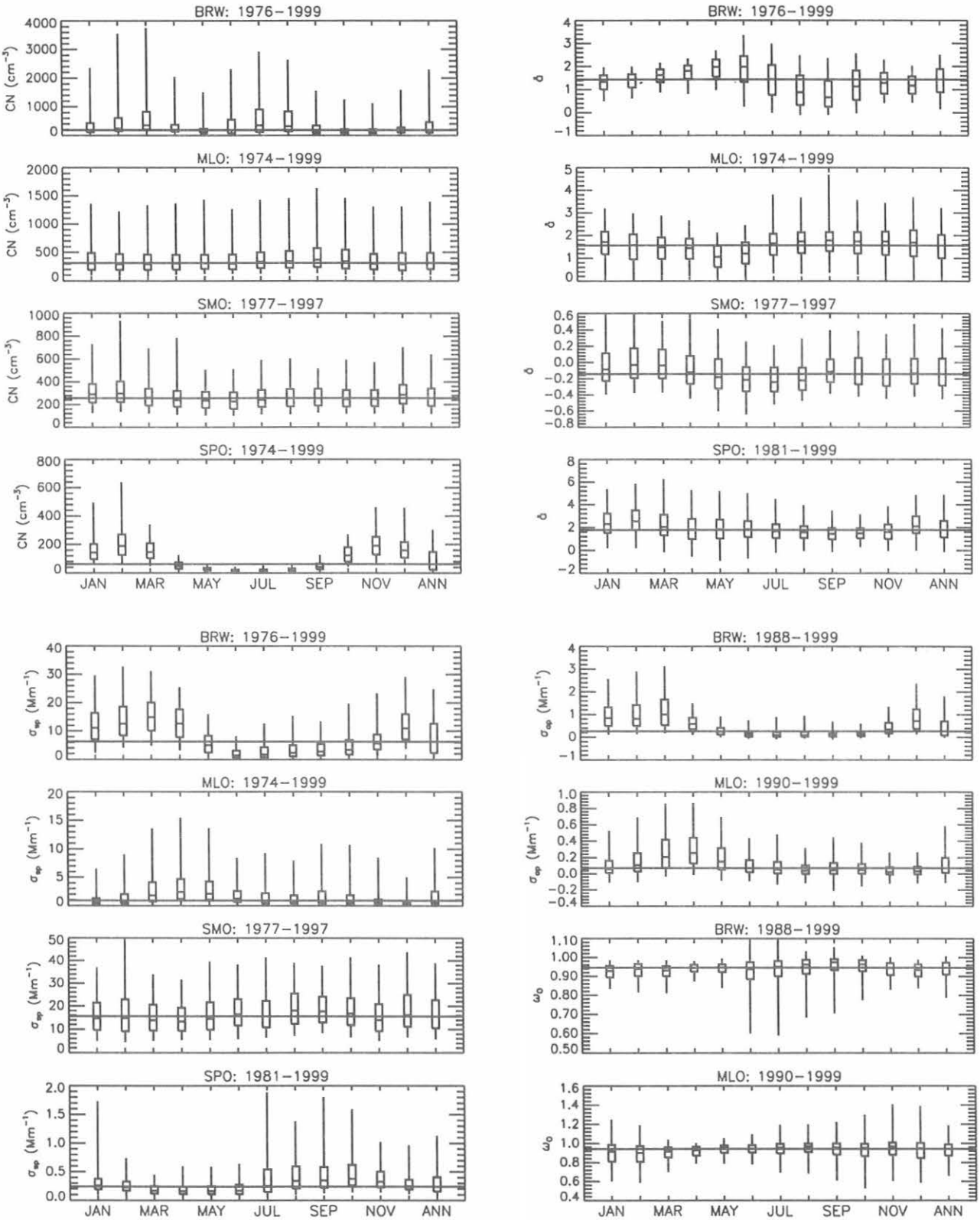

Fig. 3.1. Annual cycles for baseline stations at BRW, MLO, SMO, and SPO showing statistics for condensation nuclei (CN) concentration, total scattering coefficient (σ_{sp}), Ångström exponent (å), absorption coefficient (σ_{ap}) and single-scattering albedo (ω_0). Statistics representing the entire period are given in the last column (ANN), with the horizontal line intersecting the median value.

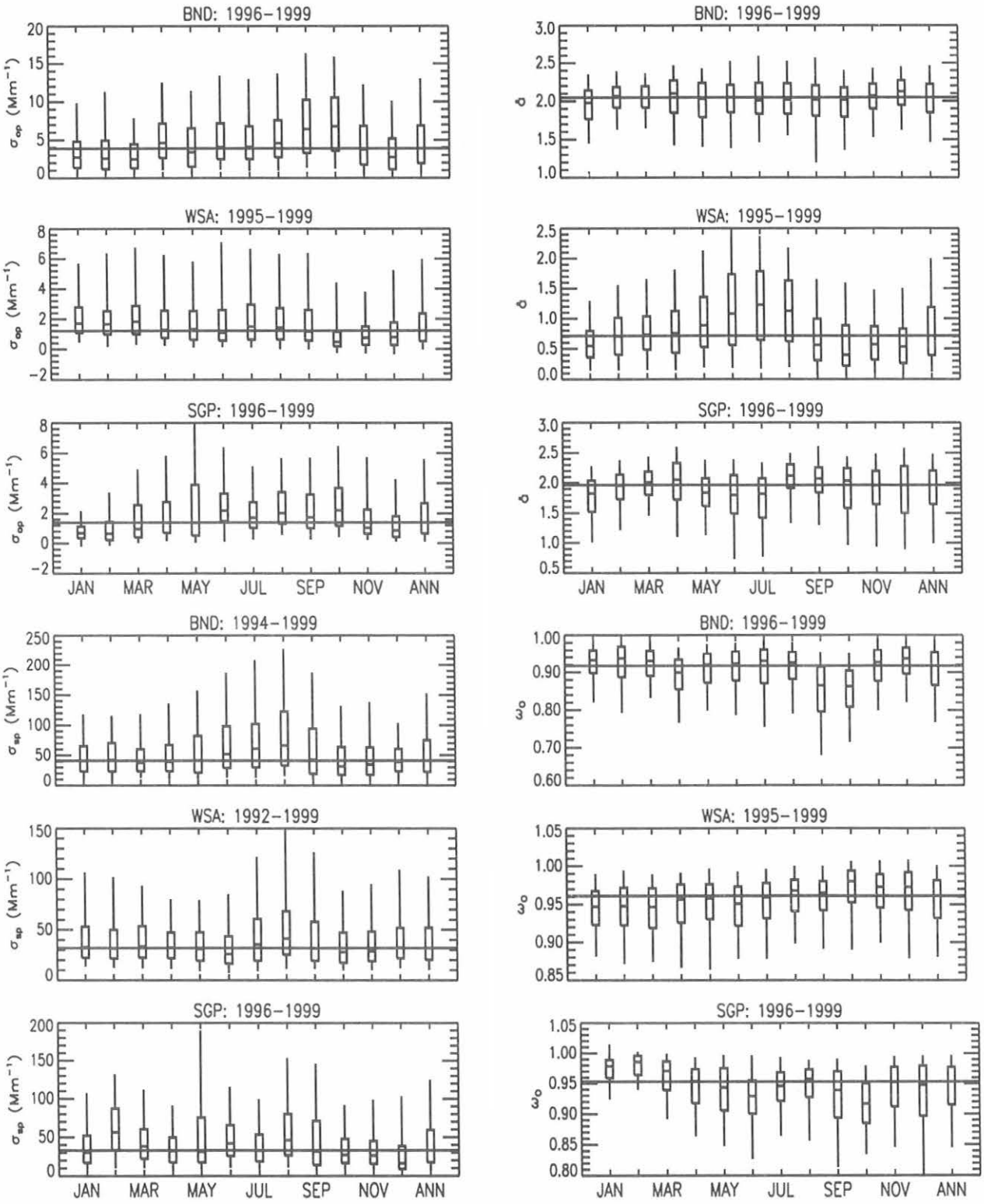

Fig. 3.2. Annual cycles for regional stations at Bondville, Illinois (BND), Sable Island, Nova Scotia (WSA), and Lamont, Oklahoma (SGP) showing statistics of absorption coefficient (σ_{ap}), total scattering coefficient (σ_{sp}), Ångström exponent (å), and single-scattering albedo (ω_o). Statistics representing the entire period are given in the last column (ANN), with the horizontal line intersecting the median value.

In general, changes in long-range transport patterns dominate the annual cycles of the baseline stations. For BRW, the highest values of CN, σ_{sp}, and σ_{ap} are observed during the spring Arctic haze period when anticyclonic activity transports pollution from the lower latitudes of Central Europe and Russia. A more stable polar front characterizes the summertime meteorology. High cloud coverage and precipitation scavenging of accumulation mode (0.1-1.0 μm diameter) aerosols account for the annual minima in σ_{sp} and σ_{ap} from June to September. In contrast, CN values have a secondary maximum in the late summer that is thought to be the result of sulfate aerosol production from gas to particle conversion of DMS oxidation products from local oceanic emissions [*Radke et al.*, 1990]. The aerosol single-scattering albedo displays little annual variability, which is indicative of highly scattering sulfate and seasalt aerosol. A September minimum is observed in å when σ_{sp} and accumulation mode aerosols are also low but when primary production of coarse mode seasalt aerosols from open water is high.

For MLO, the highest σ_{sp} and σ_{ap} values occur in the spring-time and result from the long-range transport of pollution and mineral dust from Asia. However, little seasonality is seen in CN concentrations at MLO, indicating that the smallest particles (<0.1 μm diameter), which usually dominate CN concentration, are not enriched during these long-range transport events. Both the aerosol σ_{sp} and Ångström exponent display seasonal cycles at SPO, with a σ_{sp} maximum and an å minimum in winter associated with the transport of coarse mode seasalt from the Antarctic coast to the interior of the continent. The summertime peaks in CN and å are associated with fine mode sulfate aerosol and correlate with a seasonal sulfate peak found in the ice core, presumably from coastal biogenic sources [*Bergin et al.*, 1998]. The aerosol extensive properties at SMO display no distinct seasonal variation. Instrument noise at low aerosol concentration is responsible for albedo values at BRW and MLO above 1. These high albedo values are not present in daily averaged data. Furthermore, these high albedo values are removed if you exclude data where σ_{sp} is below 1 Mm^{-1}. Hence, the high albedo values result from an instrument detection limitation problem.

Based on only 4-7 years of measurements, the annual cycles for the regional stations are less certain than those of the baseline stations. The proximity of the regional sites to North American pollution sources is apparent in the results, with a monthly median value of σ_{sp} at the Bondville site (BND) that is nearly two orders of magnitude higher than the σ_{sp} at SPO. BND is situated in a rural agricultural region and displays an autumn high in σ_{ap} and low in ω_o that coincides with the autumn harvest. As evident in the lower σ_{sp} and σ_{ap} values, the Southern Great Plains site (SGP) is more remote than BND. SGP has a similar, but less pronounced, annual cycle with late summer highs in σ_{sp} and σ_{ap} and a corresponding minimum in ω_o. Little seasonal variability is observed in aerosol properties at WSA. Values of å tend to be higher in the summer and likely result from transport of fine mode sulfate aerosol from the continent and lower coarse-mode production of particles with lower summer wind speeds.

3.1.4. Long-Term Trends

Long-term trends in CN concentration, σ_{sp}, σ_{ap}, ω_o, and å are plotted in Figures 3.3 and 3.4 for the baseline observatories. The monthly means are plotted along with a linear trend line fitted to the data. The aerosol properties at BRW exhibit an annual decrease in σ_{sp} of about 2% per year since 1980. This reduction in aerosol scattering has been attributed to decreased anthropogenic emissions from Europe and Russia [*Bodhaine*, 1989] and is most apparent during March when the Arctic haze effect is largest. The corresponding decrease in the Ångström exponent over the same time period points to a shift in the aerosol size distribution to a larger fraction of coarse mode seasalt aerosol. *Stone* [1997] noted a long-term increase in surface temperatures and cloud coverage at BRW from 1965-1995 that derives from changing circulation patterns and may account for the reduction in σ_{sp} by enhanced scavenging of accumulation mode aerosols.

Long-term trends in CN concentrations are difficult to determine at this time since the data record contains measurements from two different instruments, a GE water-based CN counter and a TSI butanol-based CN counter. New TSI butanol-based CN counters were installed in January 1989 at SPO, January 1993 at SMO, January 1991 at MLO, and January 1991 at BRW. The TSI butanol-based CN counter concentrations are 1.5-2 times higher than the old GE water-based CN counter. The reason for this difference is not known. Before any long-term trend analysis can be conducted, this difference needs to be resolved, and the data sets need to be put on the same scale.

Previous reports describing the aerosol data sets include: BRW: *Bodhaine* [1989, 1995]; *Quakenbush and Bodhaine* [1986]; *Bodhaine and Dutton* [1993]; *Barrie* [1996]; MLO: *Bodhaine* [1995]; SMO: *Bodhaine and DeLuisi* [1985]; SPO: *Bodhaine et al.* [1986, 1987, 1992]; *Bergin et al.* [1998]; WSA: *McInnes et al.* [1998].

3.1.5. Special Studies

Comparison of Aerosol Light Scattering and Absorption Measurements

CMDL has measured both aerosol light scattering (since 1976) and aerosol light absorption (since 1988) at BRW. To obtain data representative of clean baseline conditions, measurements from the polluted sector, defined by wind speed and direction, are automatically removed from the data set. Table 3.5 lists the instruments and their period of operation at Barrow. Initially, light scattering was measured using a 4-wavelength nephelometer, and light absorption was measured using an aethalometer. This original sampling system did not include size or relative humidity control of the aerosol sample. New light scattering and absorption instruments were installed at BRW (within 2 meters of the old instruments) in October 1997. The new instruments are designated for North Slope, Alaska (NSA) to distinguish them from the co-located BRW instruments. The new system obtains measurements at two size cuts by using a valve to switch between a 10 μm and 1 μm impactor. Relative humidity is maintained at or below 40% by heating the air sample. The BRW and NSA systems were operated simultaneously for approximately 1 year (fall 1997–fall 1998). One year of simultaneous light scattering measurements and 2 years of light absorption measurements from the co-located instruments were compared. It is important to understand how measurements from these instruments compare in order to maintain data consistency for the entire measurement period.

The comparison procedure was:

- Select data for the overlap period October 1997 to October 1998 for σ_{sp}, and October 1997 to October 1999 for σ_{ap}
- Estimate the absorption coefficient for the aethalometer using: $\sigma_{ap} = 10\ m^2/g * [BC]$

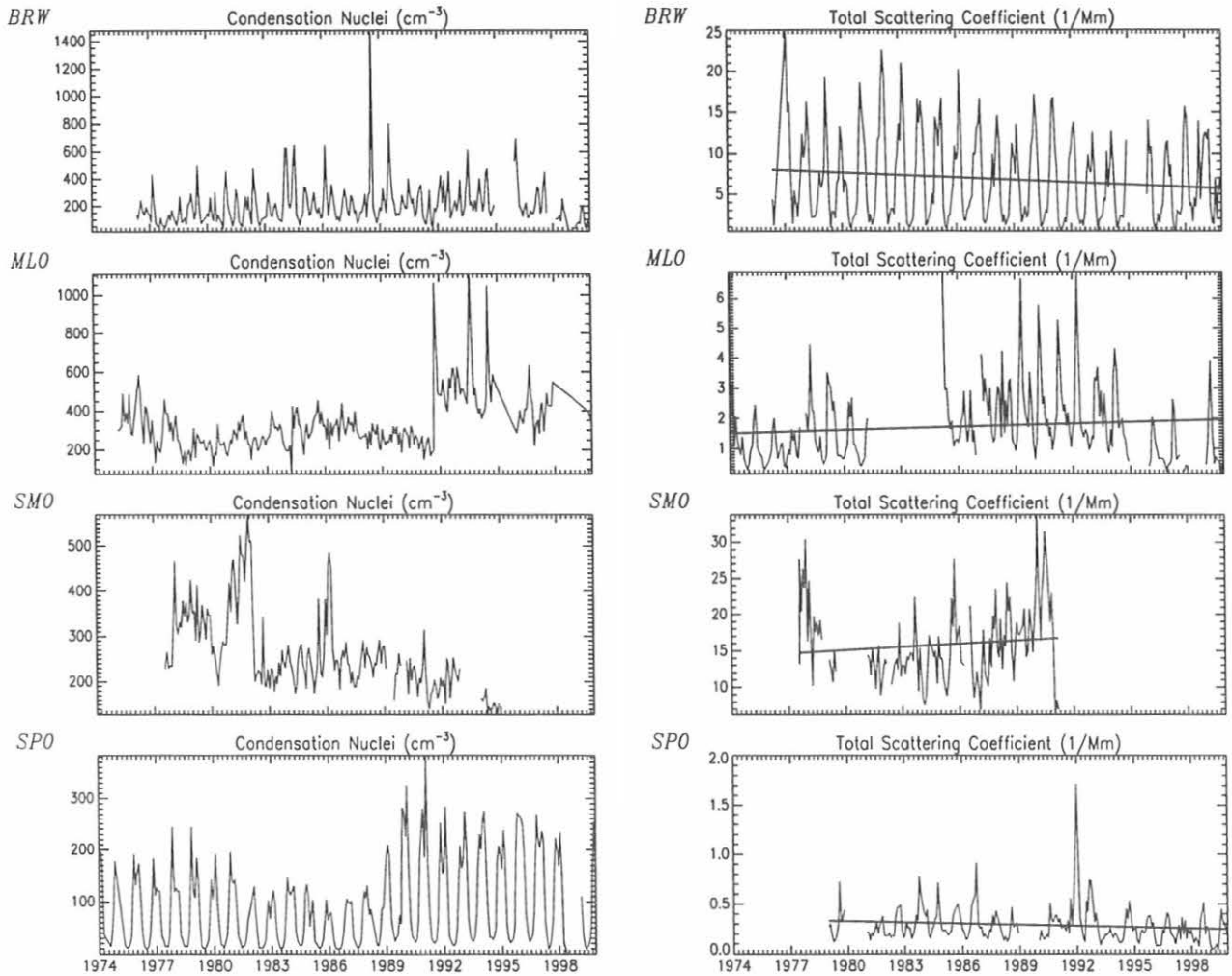

Fig. 3.3. Long-term trends for baseline stations of monthly averaged condensation nuclei concentration and total scattering coefficient at 550 nm. A simple linear fit is given for the scattering coefficient but is omitted for the condensation nuclei concentration since instrument changes make a trend line inappropriate.

- Apply quality control edit corrections to data sets (e.g., remove spikes and contaminated data)
- For the NSA data set, use only 10 μm size cut data
- Correct the NSA particle soot absorption photometer (PSAP) data for: (a) scattering by particles within the filter and (b) spot size. Also, remove low transmittance data (e.g., transmittance <0.5 as per *Bond et al.* [1999])
- Calculate hourly averages of scattering and absorption coefficients
- Calculate daily averages of absorption for the aethalometer and PSAP
- Remove obvious outliers (four points for the σ_{ap} data)
- Determine the least squares linear fit and correlation coefficient for the data sets. Perform the regression for both a calculated and forced-to-zero y-intercept

Figure 3.5 shows that, for the 2 years, there is a relatively low correlation between the hourly averaged PSAP and aethalometer measurements ($R^2 = 0.70$), although the instruments agree fairly well (the slope is 0.94). Looking at the data on a year-by-year basis, the two instruments demonstrated better agreement with each other for the second-year period than for the first year (slope = 0. 99, $R^2 = 0.77$ and slope = 0.92, $R^2 = 0.66$, respectively). This difference is statistically significant, but it is unclear what caused this difference.

For daily averaged data (Figure 3.6) there is a stronger relationship between the two instruments' measurements than for hourly averaged data and, again, good agreement for the two measurements of absorption coefficient. Because particle concentrations and hence, light absorption, are low at the site, often near the detection limits of the two instruments, there is considerable noise in the measurements. The improvement in fit for the daily averaged values with respect to the hourly averaged values is most likely a result of averaging noise in the data over a longer time period.

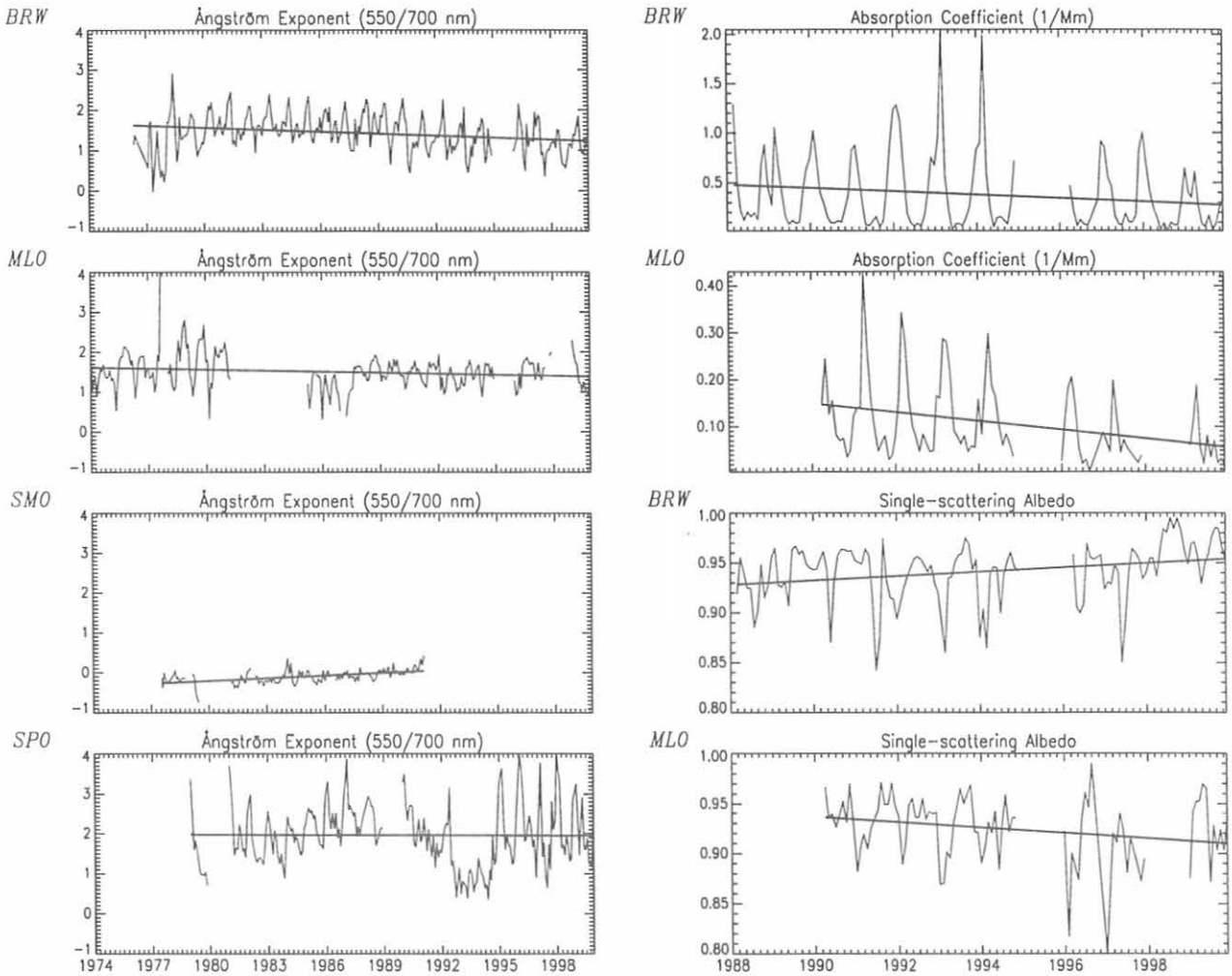

Fig. 3.4. Long-term trends for baseline stations of monthly averaged Ångström exponent (550/700 nm), absorption coefficient, and single-scattering albedo. A simple linear fit to the data is shown.

TABLE 3.5. Description of Instrumentation at Barrow, Alaska

Instrument	Period of Operation	Station	Comments
MRI nephelometer	1976-fall 1998	BRW	4 wavelength, no size cut
Magee Scientific aethalometer	1988-present	BRW	Broadband, no size cut Specific absorption of 10 m^2/g used to convert [BC] to σ_{ap}
TSI nephelometer (model no. 3563)	Fall 1997-present	NSA	3 wavelength, 1 and 10 μm size cut
Radiance Research particle soot absorption photometer (PSAP)	Fall 1997-present	NSA	565 nm wavelength, 1 and 10 μm size cut

Figure 3.7 shows the hourly variability in the ratio of the two instrument measurements as a function of absorption coefficient. The relationship between the two instruments appears less variable at higher absorption coefficients ($\sigma_{ap} > 1$ Mm^{-1}) but only about 10% of the data are in this range. At low absorption values ($\sigma_{ap} <$ 1 Mm^{-1}) there is considerable variability due to instrument noise. Interestingly, while the aethalometer data are lower than PSAP data for high absorption coefficients (consistent with the linear fit results), the aethalometer measurements tend to be lower than the PSAP's at low σ_{ap}.

Table 3.6 summarizes the fit parameters for the absorption coefficient. Overall, the linear fits suggest that the BRW measurements were consistently lower than the NSA measurements. There are other questions that need to be addressed in the future with respect to measurements of σ_{ap} at Barrow. These include: How much do the differences in

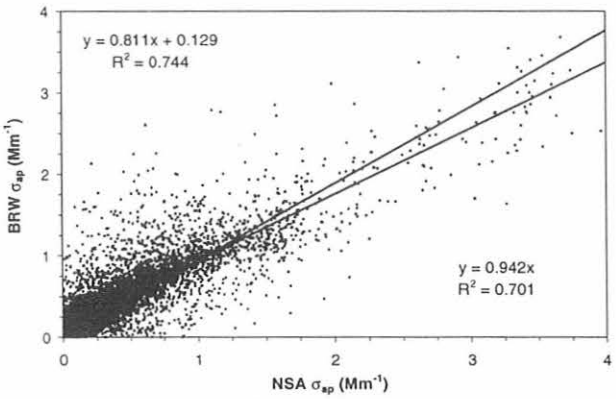

Fig. 3.5. Comparison of hourly averaged absorption data from NSA and BRW, October 1997-October 1999.

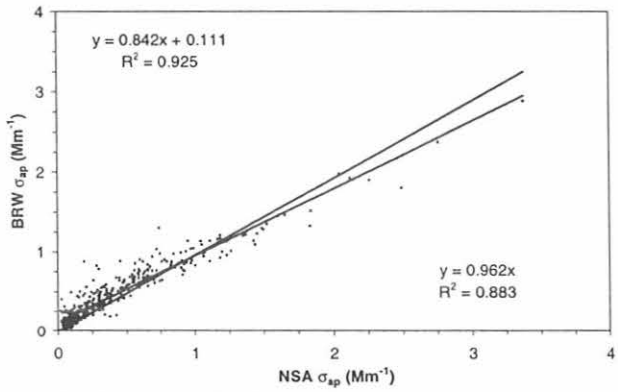

Fig. 3.6. Comparison of daily averaged absorption data from NSA and BRW, October 1997-October 1999.

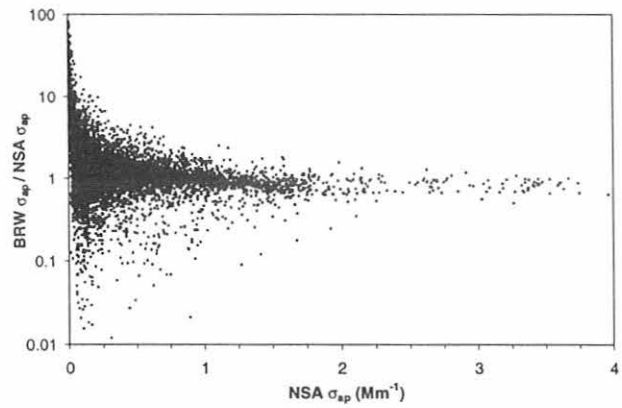

Fig. 3.7. Variation in the ratio of absorption measured at BRW to that measured at NSA as a function of hourly averaged absorption coefficient.

wavelength of the two instruments influence σ_{ap}? Are there corrections that should be applied to the aethalometer: for example some sort of spot size correction? How appropriate is the arbitrarily chosen 10 m^2/g used to convert from mass concentrations measured by the aethalometer into scattering coefficients?

TABLE 3.6. Results From Linear Fits of Data to Equation: BRW = m*NSA for Absorption Coefficient

Parameter	Slope (m)	R^2	Number of Points
σ_{ap} (hourly) year 1	0.92 ± 0.01	0.66 ± 0.01	3456
σ_{ap} (hourly) year 2	0.99 ± 0.01	0.77 ± 0.01	3562
σ_{ap} (hourly) both years	0.94 ± 0.01	0.70 ± 0.01	7018
σ_{ap} (daily) year 1	0.94 ± 0.03	0.88 ± 0.02	223
σ_{ap} (daily) year 2	1.03 ± 0.03	0.87 ± 0.02	226
σ_{ap} (daily) both years	0.96 ± 0.02	0.89 ± 0.01	449

In addition to comparing absorption coefficient measurements, comparisons of scattering coefficient as a function of wavelength for the BRW and NSA nephelometers were also made for 1 year starting October 1997 (Table 3.7). For the two nephelometers there is high correlation despite low particle concentrations and hence low scattering measurements. The blue scattering coefficients (σ_{spB}) have the weakest agreement (slope = 0.92). This may be because of problems with the blue photomultiplier in the BRW nephelometer. The blue scattering measurement at BRW was often similar to or even lower than the green scattering measurement, while at NSA the $\sigma_{spB}/\sigma_{spG}$ ratio was typically greater than 1 as expected.

Differences between the two instruments may be attributable to several factors. Optically, the two nephelometers are (almost) identical, so it was assumed that correcting for the truncation angle would not improve the comparison. Thus for this comparison no corrections for truncation were applied to either instrument. Changes in filter bandpass and calibration error may also play a role.

Optical Property of Indian Ocean Aerosols

During February and March 1999 the CMDL aerosol group participated in the Indian Ocean Experiment (INDOEX), a multi-platform field campaign that took place over the Indian Ocean. A central focus of the campaign was to assess the role of aerosols from the Indian subcontinent on direct and indirect radiative forcing, as well as the role of convective cirrus in aerosol transport and photochemical processing.

This region of the world has a fast growing population that is becoming more industrialized with emissions of CO_2, aerosols, and sulfates expected soon to surpass those of North America and Europe. Because of these potentially high future emissions, an understanding of climate forcing and transport of trace gases and aerosols in this region is critical to being able to predict global climate forcing.

TABLE 3.7. Results From Linear Fits of Data to Equation: BRW = m*NSA for Scattering Coefficient

Parameter	Slope (m)	R^2	Number of Points
σ_{spB}	0.92 ± 0.00	0.95 ± 0.01	3456
σ_{spG}	1.00 ± 0.00	0.94 ± 0.01	3456
σ_{spR}	0.97 ± 0.00	0.94 ± 0.01	3456

The INDOEX campaign was based at the Maldive Islands, about 700 km southwest of India. As part of the campaign, CMDL performed in situ measurements of aerosol optical properties on two separate platforms: the Scripps Institution of Oceanography (SIO) climate observatory on the island of Kaashidhoo (KCO) and onboard the NCAR C-130 aircraft. These measurements included the aerosol total and hemispheric backscattering coefficients, the aerosol hygroscopic growth factor (f(RH)), and the aerosol absorption coefficient. Here the aerosol hygroscopic growth factor is defined to be the ratio of the aerosol scattering coefficient at 85% relative humidity to the aerosol scattering coefficient at 40% relative humidity.

During the northeast monsoon season (January-April) the Intertropical Convergence Zone is south of the island and air circulation is from the Indian subcontinent. Thus aerosols measured at KCO during this time represent polluted continental air masses. Figure 3.8 shows a time series of the measured aerosol optical properties at KCO.

Back trajectory calculations show a change in the air mass origin on March 7 (Day 66) from the east Bay of Bengal region to the west Arabian Sea. Evidence of this change is apparent in a decreased aerosol loading and accompanied by lower σ_{sp} and σ_{ap} values. Despite this difference in aerosol loading, the aerosol intensive properties of single-scattering albedo, backscatter fraction, and hygroscopic growth are similar between the two regions. The lower aerosol loading in the Arabian Sea air masses likely resulted in a larger contribution to the total scattering from supermicron seasalt particles as evident in the smaller fractions of submicron aerosol scattering and absorption from the Arabian Sea.

In addition to surface-based measurements at KCO, aerosol optical properties were measured in situ from the NCAR C-130 research aircraft using an aircraft version of the ground-based CMDL aerosol measurement system. Aircraft measurements were necessary for information on spatial (i.e., horizontal and vertical) and temporal variability of aerosol optical properties. Vertical profiles and horizontal legs at altitude were conducted to characterize aerosol variability in the region with coverage of much of the Indian Ocean Basin between 8°S and 17°N.

The measured aerosol light scattering coefficients over the northern Indian Ocean were typically several times those observed at perturbed continental sites in the United States. The highest aerosol concentrations were observed in the northern Indian Ocean (north of the Maldives). The aerosol was substantially darker than U.S. sites with an average single-scattering albedo for all flights near 0.85. The optical depths in the region, calculated using aircraft aerosol optical property data, were in the 0.15-0.35 range for most days. Elevated aerosol layers, decoupled from the surface, were observed in over one-third of the vertical profiles. Figure 3.9 shows two vertical profiles, with one profile showing an elevated aerosol layer.

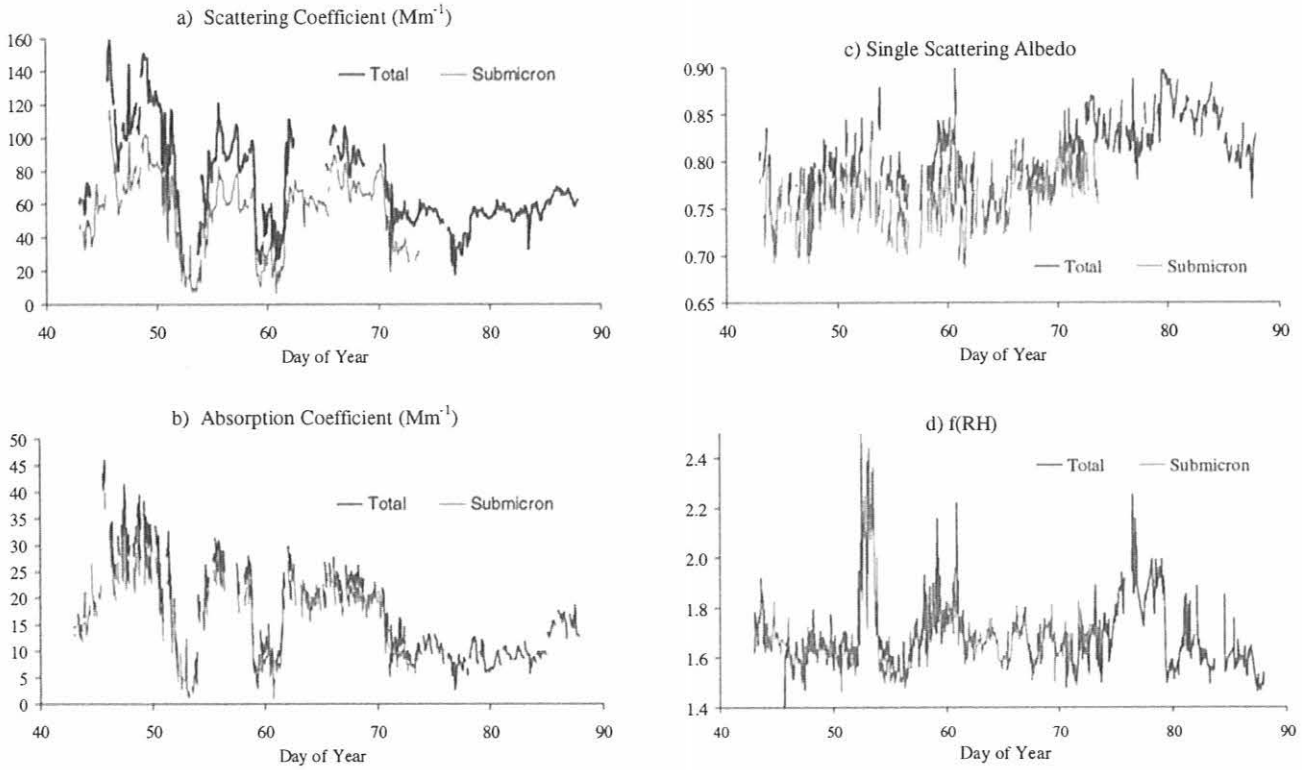

Fig. 3.8. Time series of measurements from KCO in 1999: (a) aerosol total and submicron scattering coefficient, (b) aerosol total and submicron absorption coefficient, (c) aerosol total and submicron single scattering albedo, (d) aerosol total and submicron hygroscopic growth. All values are reported for 550 nm wavelengths.

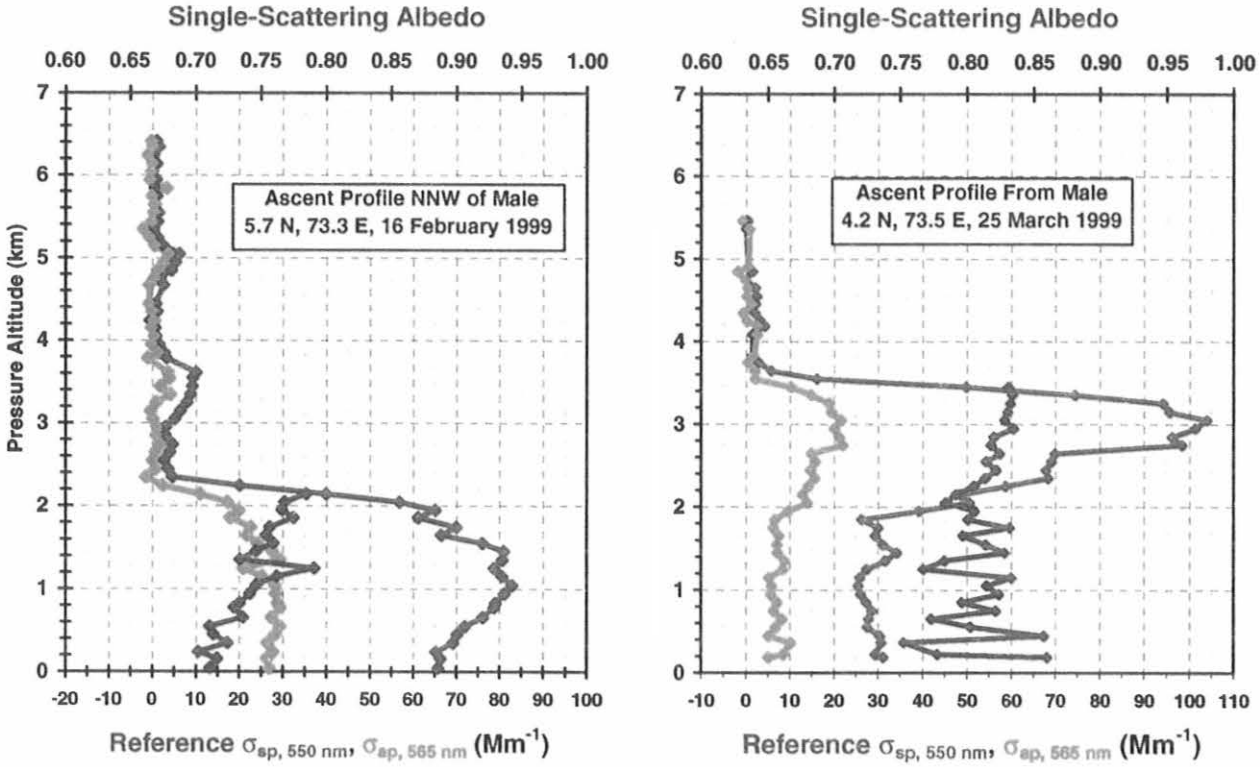

Fig. 3.9. Two vertical profiles of total scattering coefficient (σ_{sp}, red), absorption coefficient (σ_{ap}, blue), and single-scattering albedo (green) obtained by CMDL instruments onboard the NCAR C-130 aircraft. The profile on the left shows a thick aerosol layer from the surface to ~2 km. The profile on the right shows an elevated aerosol layer with a peak at ~3 km altitude.

Table 3.8 lists the mean values of the measured parameters and compares them to those from other CMDL surface sites. In comparison to aerosol properties measured at Bondville (a U.S. continental site) and Sable Island (a Canadian marine site) the aerosol from the Indian subcontinent has a far greater absorption coefficient. Unlike aerosols from U.S. continental sites, the single scattering albedo at KCO declines with an increase in aerosol loading (Figure 3.10). Apparently under highly polluted conditions the aerosol soot fraction relative to sulfate is higher than that from U.S. sites. This difference could reflect the regional sources of sulfate and carbon as well as rates of in-cloud sulfate oxidation. Although the Indian subcontinent aerosol has a large absorbing fraction, its mean hygroscopic growth is similar to that from regions with less absorbing aerosol. This difference points to either a significantly different composition or morphology for the absorbing components of aerosols from the Indian subcontinent with respect to North America.

TABLE 3.8. Means and Variabilities of Pollution Aerosols

Aerosol Property	Bay of Bengal	Arabian Sea	Sable Island	Bondville
σ_{sp}	95 ± 20	54 ± 9	42 ± 35	60 ± 49
σ_{ap}	25 ± 7	10 ± 3	2 ± 2	5 ± 4
$F\sigma_{sp}$	0.70 ± 0.06	0.62 ± 0.05	0.26 ± 0.10	0.86 ± 0.07
$F\sigma_{ap}$	0.85 ± 0.04	0.80 ± 0.07	0.81 ± 0.10	0.82 ± 0.10
f(RH)	1.65 ± 0.10	1.67 ± 0.14	1.7 ± 2.7*	1.5 ± 0.4†

*McInnes et al. [1998]

†S. Koloutsou-Vakakis, et al., Aerosol properties at a midlatitude northern hemisphere continental site, submitted to *J. Geophys. Res.*, 1999

Scattering coefficients, σ_{sp}, are measured at □ = 550 nm. Absorption coefficients are measured at □ = 565 nm. $F\sigma_{sp}$ and $F\sigma_{ap}$ are the submicron fractions of aerosol scattering and absorption, respectively. f(RH) is given for a relative humidity of 85% relative to 40%. Variabilities are reported as ±1 standard deviation. Sable Island, Nova Scotia, and Bondville, Illinois, are anthropogenically perturbed marine and continental sites, respectively. The range of f(RH) at Sable Island is between polluted and clean air masses observed over a ~10-day period. Time periods of 4 hours before and after rain events were excluded from the KCO data.

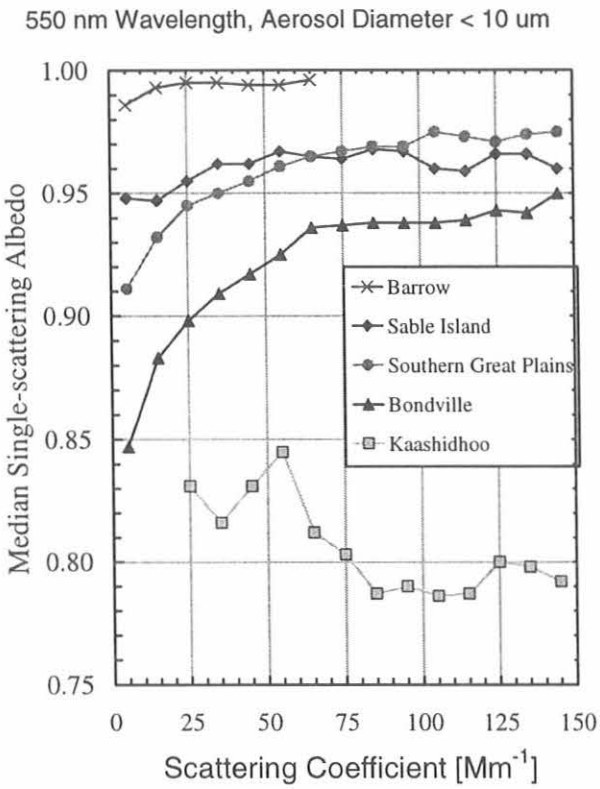

Fig. 3.10. Aerosol single-scattering albedo plotted against scattering coefficient (hourly average data). Data are from the four CMDL North American monitoring stations (entire period of record) and the Kaashidhoo Island station in the Indian Ocean (February and March 1999).

3.2. Solar and Thermal Atmospheric Radiation

B. Bodhaine (Editor), G. Anderson, G. Carbaugh, E. Dutton, B. Halter, D. Jackson, D. Longenecker, D. Nelson, R. Stone, R. Tatusko, and N. Wood

3.2.1. Radiation Measurements

Introduction

The CMDL Solar and Thermal Atmospheric Radiation (STAR) group provides supporting radiation information for baseline climate monitoring activities and investigates trends and variations in the observed surface radiation budget. Energy derived from the earth's radiation budget is responsible for not only maintaining the temperature of the planet but for atmospheric and oceanic motions. Predicted anthropogenic trends in surface radiation quantities at globally remote sites are near or below the level of detectability, on the decadal time scale, for the currently available instrumentation. However, fundamental climatological variability in the global surface radiation budget is not adequately understood. Therefore, STAR measurements contribute to this basic knowledge. These contributions include the definition of diurnal and annual cycles, effects of cloudiness, variations on daily to decadal time scales, effects of major volcanic eruptions, unexpectedly high concentrations of anthropogenic pollution in the arctic, effects of constituent variations on narrowband irradiance (e.g., ozone and UV changes), and possible anthropogenic modification to cloudiness. The STAR group also makes remote sensing measurements of various atmospheric constituents that are potentially responsible for variations in surface radiative quantities. In addition to the research conducted by CMDL, STAR measurements contribute to several international databases. International databases are needed to evaluate the radiation and energy budget necessary to diagnose the climatic time scale general circulation of the atmosphere. These observations also contribute to satellite-based projects by helping verify spot estimates and to allow features of the intervening atmosphere to be deduced. Still, a major goal of the monitoring program is to obtain as long and as complete a record as possible of surface radiation parameters that will permit examination of the record for all scales of natural and modified variability. Of particular interest is the determination of the magnitude, representativeness, and possible consequences of any observed changes. To this end, the STAR group maintains complete and continuous surface radiation budget observations at several globally diverse sites with various ancillary observations. The following describes those projects and recent changes.

Baseline Monitoring

Surface radiation measurements have been made at the four principal CMDL baseline observatories (BRW, MLO, SMO, and SPO) since the mid-1970s. The different environments and conditions at the various sites resulted in somewhat different programs evolving at each site. The basic measurements made at all sites include the downward components of solar radiation: global, diffuse, and direct. Broadband thermal infrared irradiance measurements were added over the past 15 years. Upward solar and thermal infrared irradiances are measured at sites where the surrounding terrain is representative of a larger regional area, as at SPO and BRW, for at least part of the year. The records acquired at these sites constitute some of the longest known in the U.S. for solar radiation research. The raw data are routinely transmitted over telephone lines or the Internet to the central data processing facility in Boulder, where data editing, final calibrations, graphical inspection, and archiving, are performed, as discussed in section 3.2.11.

Other Measurement Sites

Boulder Atmospheric Observatory (BAO tower). Observations of upwelling and downwelling solar and thermal irradiances began in 1985 at the top of a 300-m tower, known as the Boulder Atmospheric Observatory (BAO) located near Erie, Colorado. Nearly continuous observations of all quantities have been made with hourly resolution until 1992, 3-min resolution until 1998, and 1-min resolution thereafter. The upwelling radiation data provide a unique view of surrounding agricultural land making the data more representative than typical surface based solar radiation budget observations. The data from the site are being used by the National Aeronautics and Space Administration/Clouds and Earth's Radiant Energy System (NASA/CERES) and NOAA Geophysical Fluid Dynamics Laboratory (GFDL)/General Circulation Model (GCM) programs and have been used by *Nemesure et al.* [1994], *Cess et al.* [1995], *Dutton and Cox* [1995], *Garrett and Prata* [1996], and several earlier papers. Since 1990 observations of direct solar and downwelling solar irradiances have also been made

near the base of the tower. This site has contributed data to the World Climate Research Program (WCRP) Baseline Surface Radiation Network (BSRN).

Kwajalein. Observations of direct solar and downwelling solar and thermal IR irradiance began at Kwajalein in 1989. Kwajalein is a small, <4 km^2, island in the tropical west Pacific. Data obtained at this location are virtually free of any effects of the island and therefore are often taken as representative of the open ocean in that region. Data from Kwajalein have been used as oceanic representative by *Dutton* [1993], *Whitlock et al.* [1995], and *Bishop et al.* [1997], and are currently being used by CERES and the European Center for Medium-Range Weather Forecasts (ECMWF) GCMs. Substantial upgrades to the Kwajalein radiation measurements were carried out in recent years, including the addition of spectral total and diffuse, broadband diffuse, UV-B, and PAR instruments, as well as improved solar tracking capability, including a shade disk pyrgeometer. Data from Kwajalein have been submitted to the BSRN data archive.

Bermuda. Observations of downwelling solar and thermal IR began at the NASA Bermuda Tracking Station at the eastern end of Bermuda in 1990. The rather small size and low relief of the island in the lower midlatitude westerlies has minimal influence on the irradiance measurements, although some clouds of orographic origin are known to exist there in the summer months under certain synoptic meteorological conditions. Data from Bermuda have been submitted to the BSRN data archive and have been used by *Whitlock et al.* [1995], *Bishop et al.* [1997], and currently by the CERES program in satellite comparison and validation studies and by ECMWF and GFDL in their GCM testing. On December 8, 1998, the monitoring site was moved from the NASA tracking station (32.2670°N, 64.6670°W) near the east end of the island to the top of Prospect Hill near the center of the island (32.3009°N, 64.7659°W). This move was necessitated by the imminent closing of the tracking station and by the desirability of operating further from the influence of occasional island-induced clouds that are generated at, and dynamically attached to, the east end of the island. The new site is ably tended by the Bermuda Biological Station for Research.

Basic Measurements

Broadband irradiance. The basic measurements currently conducted at each of the four baseline observatories for the past 24 years include normal direct and downward broadband solar irradiance, downward solar irradiance in the 0.695-2.8 μm band, and wideband spectral direct solar irradiance. Downward broadband thermal irradiance measurements were added at all sites in more recent years, as well as upwelling irradiance measurements at SPO and BRW. The wideband spectral direct observations are obtained manually with a filter wheel pyrheliometer under clear-sky conditions while the others are sampled at 1 Hz with 1-min averages recorded on computer media. Preliminary data from all CMDL radiation sites are generally available graphically within a couple of days of acquisition in the radiation section of the CMDL Web home page and subsequently as described in Section 3.2.11. Figure 3.11 shows different summaries of the 24-yr record of total solar irradiance collected at Samoa using the single pyranometer technique.

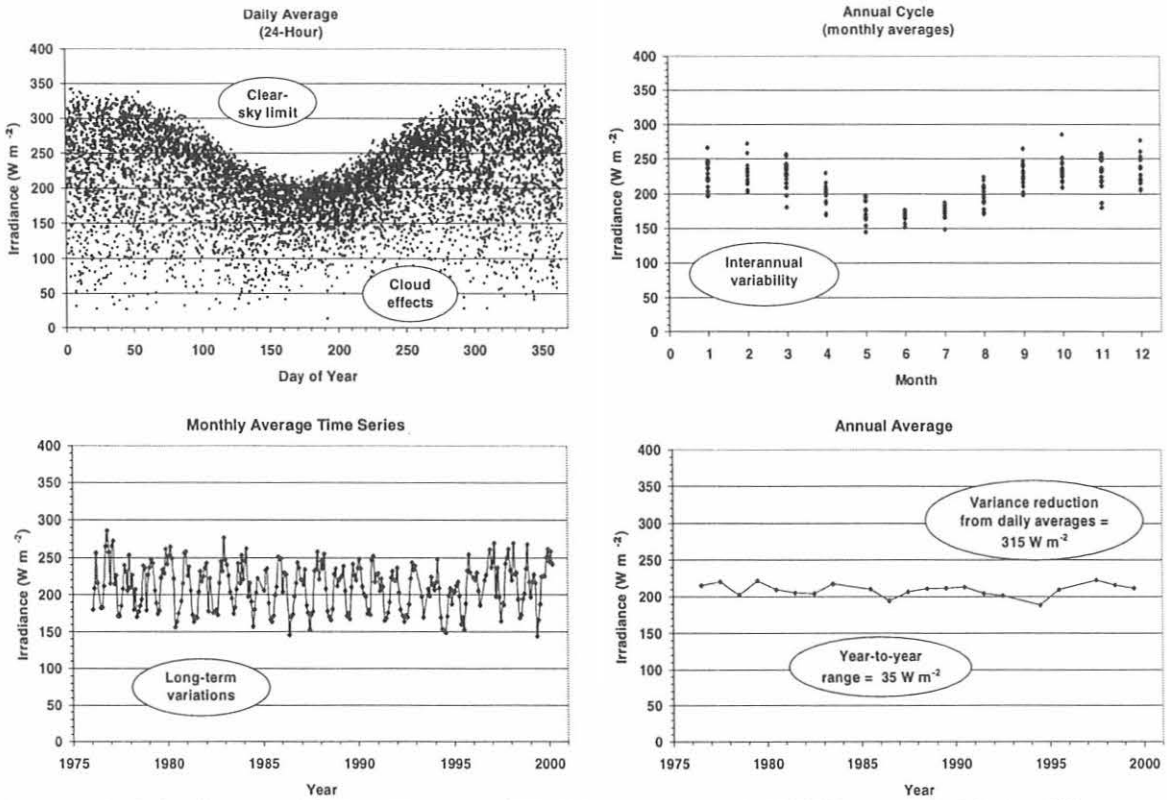

Fig. 3.11. Total solar irradiance record for American Samoa obtained from a pyranometer (1975-2000), summarized for four different presentation methods. The comments in the ovals in each figure section point out some of the highlights of that particular presentation.

Filter wheel NIP. The wideband spectral direct solar irradiance measurements are made with a filter wheel normal incidence pyrheliometer (FWNIP). The data from these observations are compared to a higher spectral resolution radiative transfer model [*Bird and Riordan,* 1986]. The model is based on Beer's law and is intended for use at the surface only. The aerosol optical depth and precipitable water are adjusted within the model to obtain a best match with the FWNIP observations. This provides a low precision but relatively stable estimate of mean visible aerosol optical depth and water vapor at the four baseline observatories. The accuracy of the method of obtaining aerosol optical depth and water vapor is limited by the dependence on the absolute values of the extraterrestrial solar spectrum and instrument calibration, unlike typical applications in sunphotometry. The data record from this observation is shown in Figure 3.12 through 1999. The accuracy of the data is no better than 0.03 optical depth units and should only be used accordingly when sunphotometer-derived data are not available.

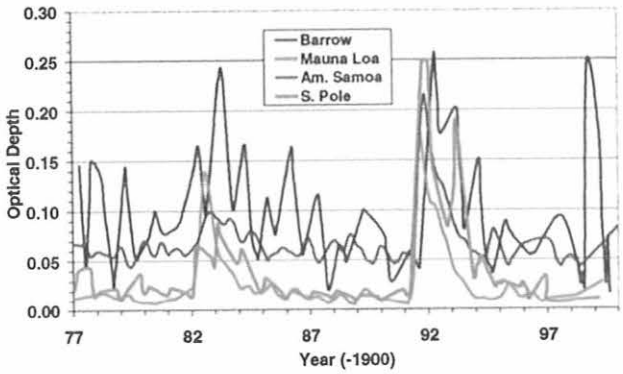

Fig. 3.12. Aerosol optical depth (monthly averages from wideband estimates) at the four CMDL baseline observatories. The values are derived from filter-wheel pyrheliometers that produce lower accuracy and precision measurements than sunphotometers but have proven to be more stable and viable than sunphotometers in the CMDL monitoring program. Seasonal, volcanic, and inter-site variations are seen in the figure. The recent spike at Barrow is believed to be caused by smoke events originating in Russia.

MLO apparent transmission. The transmission for direct broadband solar irradiance through the atmosphere above MLO is monitored using a quantity known as the apparent transmission. The quantity is computed by taking the average of three ratios of direct solar irradiance where each ratio is the quotient of the irradiance at an integer airmass divided by the irradiance at the next smaller integer air mass as first defined by *Ellis and Pueschel* [1971]. The apparent transmission measurement is inherently stable over time because it is independent of a radiometer calibration value and also, therefore, quite sensitive to small changes in transmission that can be due to aerosols, ozone, or water vapor. Previous studies [*Bodhaine et al.,* 1981; *Dutton et al.,* 1985] have shown that aerosols tend to dominate observed changes in the monthly averages of apparent transmission such that the major observed excursions in the record, given in Figure 3.13, are because of aerosols. The major observable features in Figure 3.13 are the effects of several volcanoes, particularly Agung in 1963, El Chichón in 1982, and

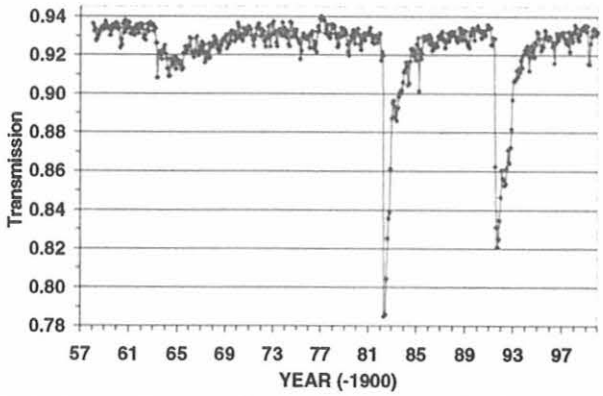

Fig. 3.13. Monthly means of apparent solar transmission for clear skies at Mauna Loa. Data are updated through the end of 1999 and show continued recovery towards the baseline conditions last established in the late 1950s. Another few years of data will be required to determine if the earlier baseline level will once again be attained or if a different background level exists.

Pinatubo in 1991 and an annual oscillation caused primarily by the springtime transport of Asian aerosol over the site [*Bodhaine et al.,* 1981]. Figure 3.13 is complete through 1999 and most recently shows that recovery from the eruption of Mt. Pinatubo required several years. The fact that the Mauna Loa apparent transmission record took several years to recover from Pinatubo is evidence of the sensitivity of the measurement since it is known from other measurements by CMDL and others that the optical depth of Pinatubo in 1995 was already very low, on the order of 0.005 at 500 nm.

Optimal Total Solar Irradiance Measurements

Total downwelling solar irradiance is the primary input component of the earth's energy budget. Instruments for measuring this quantity at the earth's surface first appeared in the 19th century with current single-instrument technology for routine observations maturing in the 1950s and 1960s. Many of the current commercially available instruments meet the highest standards of the World Meteorological Organization (WMO) for such measurements, but only specimen instruments are typically well characterized. The uncertainties in the measurements using these instruments are often given for extended averaging, days to months, which reduces the uncertainties inherent in instantaneous measurements. In recent years there has been increased interest in near-instantaneous solar irradiance observations for various research applications. These applications include comparisons to values derived from satellite overpasses and radiative transfer model calculations using a nearly instantaneous quantification of the atmospheric state. For these comparisons the full extent of the uncertainty of the irradiance measurement is important and needs to be low enough to be useful in improving the satellite algorithms and radiative transfer models, particularly when there are significant parameterizations used. While different individuals had ideas about improving surface solar irradiance observations, the first internationally organized effort to make improved irradiance measurements (solar and thermal IR) a primary goal was the BSRN (http://bsrn.ethz.ch/) project of the WCRP (http://www.wmo.ch/web/wcrp/wcrp-home.html).

The first step in the improvement of the instantaneous surface-based solar irradiance measurements was the recommendation for the use of the combination of separately measured direct and diffuse irradiance, which incorporates the highly accurate direct beam measurement capabilities developed over the past 4 decades with the greatly reduced cosine response error inherent in the single-instrument flat-plate receiver of the pyranometer. This method of measuring total solar irradiance led to improvements discussed by *Ohmura et al.* [1998], *Michalsky et al.* [1999], and *Bush et al.* [1999]. As a result this measurement method has made a large amount of direct and diffuse solar irradiance data available to the research community, which was useful because the most sophisticated and physically complete radiative transfer models also separately calculate these quantities. The easiest to calculate and also easiest to measure is the direct component, and most significant problems in measurements and models have been solved so that the agreements between the two are very good, typically less than 3 W m^{-2}, if there are no blatant errors in either. Such is not the case for the diffuse component. For the diffuse, there are difficulties in specifying correct modeling procedures, specifying correct model input values, and knowing the measurement truth since no standards exist. From the instrument perspective, not only can signal strengths be low, but also there are no reference standards that exist to which the measurement can be compared to absolutely determine measurement error. This has resulted in some recent modifications in the way in which STAR is making diffuse irradiance measurements, both in the type of instruments used and the adjustments for thermal offsets induced in the certain diffuse pyranometers. The specifics of the new measurements and adjustments to older data are given by *Dutton et al.* [2000]. With these changes it is estimated that diffuse irradiance is currently measured to within about 5 W m^{-2}. This results in accuracies to within about 8 W m^{-2} for total solar irradiance when determined from the combined diffuse and direct measurements.

Improved Thermal IR Irradiance Measurements

Although there has been a substantial reduction in the uncertainty of thermal infrared irradiance measurements in the last 10 years, from nearly 30 W m^{-2} in the late 1980s to about 5 W m^{-2} now, there still appears to be room for further improvements and the potential for the establishment of a measurement reference standard for these measurements. Over the past 2 years, STAR has become involved in the efforts of BSRN and the World Radiation Center (WRC) in Davos, Switzerland, to work towards these potential improvements. This work is conducted through the recent establishment of new radiance measurement capabilities that rely on absolute, self-calibrating, sky-scanning instruments. CMDL, working with BSRN, organized and participated in the first International Pyrgeometer and All-sky Scanning Radiometer Comparison (IPASRC-I) in September 1998 where this process to establish such capabilities and reference standards was begun [*Philipona et al.*, 1998].

3.2.2. Solar Radiation Calibration Facility

Solar Radiation Monitoring Support

CMDL baseline observatories. Support for monitoring surface radiation budget components at the four CMDL baseline observatories (BRW, MLO, SMO and SPO) was maintained during 1998 and 1999. Routine instrument exchanges and recalibrations were completed as required, and modifications and enhancements were incorporated as necessary.

CMDL BSRN monitoring sites. At the three CMDL BSRN sites located at Bermuda, BAO, and Kwajalein, measurements continued and operational additions and improvements were completed. The Bermuda site was relocated during 1998, and a new instrument platform was designed, purchased, and deployed. Additional measurements were also added to the relocated Bermuda BSRN site with the installation of meteorological sensors. Wind speed, direction, pressure, temperature, and relative humidity are now being monitored at all three sites. The Bermuda meteorology sensors were installed in late 1998, and Kwajalein meteorology sensors were installed in late 1999.

Collaborative activities. Post mission performance checks of sensors used during the Study of the Heat Budget in the Arctic (SHEBA) project were completed and provided to the institutions involved (NOAA Air Resources Laboratory, National Center for Atmospheric Research (NCAR), United States Navy/Post Graduate School, and University of Washington). Other checks were performed on sensors used by the NOAA Environmental Technology Laboratory, Indian Ocean Experiment (INDOEX), NOAA aircraft facility, University of Utah, and NCAR.

SRF Reference Radiometers

All CMDL solar radiation measurements are referenced to the World Radiometric Reference (WRR) as defined using the absolute scale. Comparison of the Boulder, Colorado, Solar Radiation Facility (SRF) reference radiometers to peer radiometers is the accepted method of ensuring long-term stability of their performance. The SRF has been comparing its reference radiometers annually with radiometers at the National Renewable Energy Laboratory (NREL) located in Golden, Colorado. At these comparisons, NPCs (NREL pyrheliometer comparisons), a WRR is constructed by forming an average irradiance with a group of radiometers that participated in the latest International Pyrheliometer Comparisons (IPC) in Davos. Typically this group consists of at least five radiometers.

Additionally, the SRF reference radiometers are compared every 5 years with the World Standard Group of radiometers maintained at the World Radiation Center in Davos. These comparisons are referred to as IPC. Regular checks of reference radiometer performance are also performed using groups of SRF sensors and checking their performance against each other.

Table 3.9 illustrates the results of comparisons of SRF references and their variability with respect to the WRR over time periods on the order of years.

TABLE 3.9. Comparisons of SRF References

Pyrheliometer Comparison	AHF 28553 WRR Factor	TMI 67502 WRR Factor
IPC VIII (1995)	0.99756	0.99869
NPC 1998	0.99783	
NPC 1999	0.99741	

SRF Windowed Reference Radiometer Development

The reference radiometers used by the SRF have cavity-type receivers that are open to the environment, which makes them

unsuitable for continuous deployment at a monitoring site in an unmanned mode since dust, dirt, rain, insects, and other debris can enter the cavity receiver. Typically, reference cavity radiometer measurements are limited to fair weather, clear days, and manned operation. Testing of unmanned, all-weather cavity radiometers equipped with windows was begun by the SRF during 1998. Initial results using a cavity equipped with a quartz window material were compromised by the sprectral limitations of the quartz window. The longwave cutoff of the quartz window material blocked solar radiation in the region above 4 microns. During atmospheric conditions when water vapor concentration is low, there is solar energy present beyond 4 microns. These conditions can occur in Colorado. Calcium fluoride window material with a longwave cutoff beyond 4 microns was selected as a possible replacement for the quartz. Comparisons between windowed and unwindowed cavity radiometers were conducted during 1999 using quartz and calcium fluoride windows as presented in Figure 3.14.

The data in Figure 3.14 illustrate the differences that are potentially present between windowed and unwindowed cavity radiometers under various atmospheric conditions. One cannot assign a unique window transmission factor, because each day generates a different factor depending upon the transmission of the atmosphere with the apparent dominant factor being the water vapor concentration. This presence of the water vapor effect is also suggested by results obtained using conventional pyrheliometers. Special calcium fluoride windows were fabricated to replace the usual quartz windows on SRF pyrheliometers. The pyrheliometers were calibrated with an unwindowed reference cavity and then operated side by side at the SRF, and the data show an apparent water vapor effect when pyrheliometers with calcium fluoride windows were compared with pyrheliometers with quartz windows. Some results of these comparisons are presented in Figure 3.15.

Cavity radiometers and conventional pyrheliometers equipped with calcium fluoride windows were deployed at the SRF roof facility in early 1999, and the long-term feasibility of using calcium fluoride windows is being investigated. Deployment of the first all-weather cavity radiometer will be to the BAO BSRN site in late 2000. Results of the SRF all-weather windowed cavity work were presented at the 1998 BSRN meeting, the CMDL annual meeting in 1999, and the American Meteorological Society Tenth Conference on Radiation in June 1999.

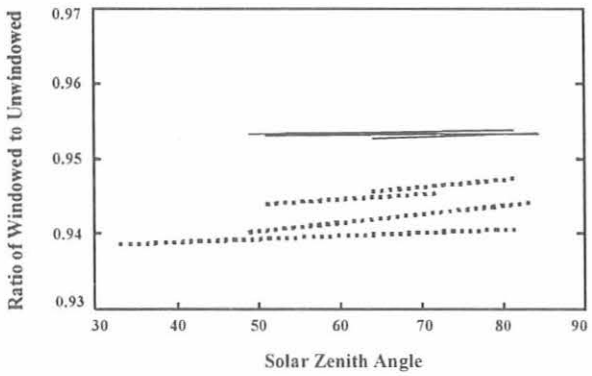

Fig. 3.14. Examples of clear-sky window transmissions for windowed cavity radiometers used for measurements at the CMDL facility in Boulder, Colorado. The calcium fluoride (solid line) window results in less day-to-day variability compared with the Suprasil 300 (dotted line) that is a type of quartz.

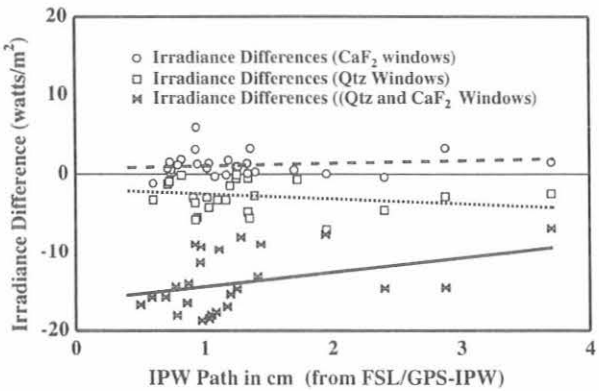

Fig. 3.15. Examples of measured irradiance differences between two pyrheliometers equipped with quartz windows, two pyrheliometers equipped with CAF_2 winds, or two pyrheliometers equipped with the quartz and CAF_2 windows. Measurements were made on clear sky days at the DSRC in Boulder.

SRF Relocation

During March 1999 the SRF was relocated to the new David Skaggs Research Center (DSRC) on the National Institute of Standard Technology (NIST) campus at 325 South Broadway in Boulder from its prior site at 3100 Marine Street site where it operated for for 24 years. Measurements were begun at the new location during April 1999, and the facility was fully operational by mid-summer 1999.

SRF International Activities

Global Atmosphere Watch (GAW). Visitors from GAW baseline stations at Ushuaia, Tierra del Fuego, Argentina; West Sumatra, Indonesia; Tamanrasset, Indonesia; and the Chinese station at Waliguan sent personnel to Boulder for training and site upgrade activity in 1998 and 1999. Contacts were also maintained with the Brazil GAW station at Arembepe. Collaboration with NREL personnel regarding data archiving procedures was begun, with NREL also hosting personnel from GAW stations and conducting site visits to Arembepe and Ushuaia for the purpose of installing data processing software and training site personnel in data editing, analysis, and archiving procedures.

Baseline Surface Radiation Network (BSRN) activities. The SRF coordinated the process of upgrading the Algerian GAW site to BSRN status. This involved purchase of a dual tracking disk shading system, pyrgeometer, pyranometer, new data logger, and desktop computer as well as training of the Algerian site personnel in the installation and use of the new items.

3.2.3. Aerosol Optical Depth Remote Sensing

Aerosol optical depth measurements with the FWNIP continued at the CMDL baseline stations at BRW, MLO, SMO,

and SPO. The Physikalish-Meteorologisches Observatorium Davos (PMOD) tracking sunphotometer continues to collect data in the Mauna Loa dome, as it has for the past 17 years. In addition a new precision filter radiometer (PFR) was installed in the MLO tracking dome at the end of 1999. This PFR has four channels (367.6, 412.0, 501.2, and 862.4 nm) and is the next generation tracking sunphotometer from PMOD in Switzerland. A small group of handheld instruments is still used for special projects, and instrument calibrations have been maintained at MLO. These handheld instruments were used in the Aerosol Characterization Experiment (ACE-I) and ACE-II field programs, as well as in the arctic and antarctic.

A group of multifilter rotating shadowband radiometers (MFRSR) were deployed at BAO, Boulder, Bermuda, and Kwajalein. These MFRSRs were installed at Bermuda (February 1996), Kwajalein (April 1996), Boulder Atmospheric Observatory (November 1996), and Boulder (July 1999) in conjunction with the BSRN program. The main goal of this program is to obtain a spectral optical-depth time series and to maintain calibrations using Langley analysis. Data are currently downloaded from the sites automatically and archived on the STAR computer.

A four-channel (368, 412, 500, and 865 nm) tracking sunphotometer (SPO1-A) manufactured by Carter-Scott Design was purchased for operation at BRW during the northern summer and at SPO during the austral summer. This instrument travels from pole to pole every year and is installed temporarily in the MLO tracking dome after every move for comparison with the MLO optical depth instruments, particularly the PFR because of the similar wavelengths.

3.2.4. MLO AND BOULDER UV SPECTRORADIOMETERS

Introduction

UV spectroradiometers were installed at MLO in July 1995 and at the Boulder DSRC in June 1998. The first instrument (UVL) operated at MLO until June 1997. The next instrument (UV3) was installed at MLO in November 1997 and is still in operation. After removal from MLO, the UVL instrument was installed in Boulder and then replaced by a new instrument (UV4) in September 1999. UV data from MLO were described by *Bodhaine et al.* [1996, 1997], and briefly in *CMDL Summary Reports No. 23 and 24* [*Hofmann et al.*, 1996, 1998]. The UV irradiances measured at MLO are much larger than at low-altitude midlatitude locations, primarily because of less Rayleigh scattering, but also because of lower column ozone in the subtropics. The complete data set selected for clear mornings at MLO and clear mornings and afternoons at Boulder is presented in this report. Clear mornings occur at MLO approximately 60% of the time providing an excellent site for solar radiation measurements. All processed spectral data are available from the solar radiation division of the CMDL program.

Instrumentation

The UVL spectroradiometer was described by *McKenzie et al.* [1992] and *Bodhaine et al.* [1997]. Briefly, a diffuser designed to minimize cosine error and machined from Teflon is mounted as a horizontal incidence receptor to view the whole sky. For UVL, stepper-motor driven gratings cover the spectral range of 290-450 nm in a single scan with a bandpass of about 1 nm. The newer instruments (UV3 and UV4) cover the range 285-450 nm with a bandpass of about 0.8 nm and use fiber optic cables to transmit the light from the sensor to the spectrometer. A complete forward scan for UVL requires about 3 minutes. The UV3 and UV4 instruments do a backward scan and then a forward scan centered at the desired solar zenith angle (SZA) and, therefore, require about 6 minutes for a complete measurement. All instruments are programmed to perform scans every 5 degrees of SZA during daytime hours.

Absolute calibrations of the spectroradiometers are performed at approximately 6-mo intervals using 1000-W FEL lamps traceable to NIST standards. Weekly stability calibrations are performed using mercury lamps and 45-W standard lamps as long-term stability checks. The expected long-term accuracy of the spectroradiometer systems is expected to be better than ±5%.

Data Analysis

For the following analyses, UV spectroradiometer data for 45° SZA were chosen for clear mornings at MLO during the July 1995-December 1999 time period. This gives approximately 4.5 years data and includes ozone values in the range of 212-330 Dobson units (DU). For Boulder data, 70° SZA and the period July 1998-December 1999 were used, covering an ozone range of 230-390 DU. Clear mornings at MLO and Boulder were determined in the same manner as in previous studies; that is, a day was accepted as a clear day at MLO if the sky was cloudless from dawn through the time of the desired scan and if Dobson ozone data were available for that morning. At Boulder, generally speaking, the sky had to be clear at the time of the scan. Figure 3.16 shows MLO ozone and UV erythema data for July 1995-December 1999. Figure 3.17 shows similar data for Boulder for July 1998-December 1999. Erythemal radiation data were obtained from the spectroradiometer data for both sites by applying the erythemal weighting function of *McKinlay and Diffey* [1987] and integrating over wavelength for each scan, as discussed by *Bodhaine et al.* [1997]. Figures 3.16 and 3.17 also show the time series of ozone at the two sites. The inverse relationship of UV erythema and ozone is apparent.

Figures 3.18 and 3.19 show the relationships between UV erythema and ozone at MLO and Boulder, respectively, for the time period July 1998-December 1999. The radiative amplification factor (RAF), defined as the percent change of UV (erythemal) irradiance divided by the percent change of total

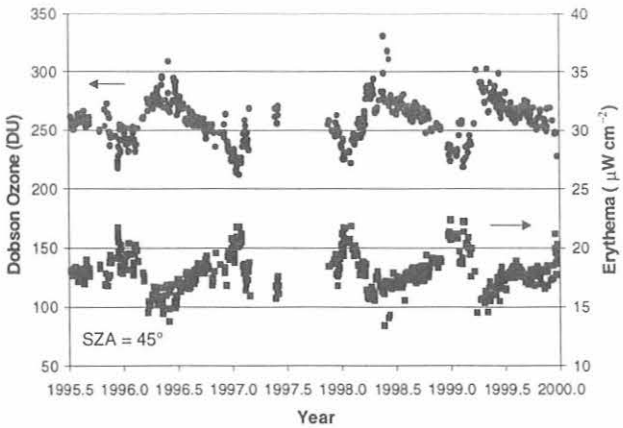

Fig. 3.16. Erythemal irradiance at SZA 45° (bottom, squares) and total ozone (top, circles) for clear-sky mornings at MLO from July 1995-December 1999.

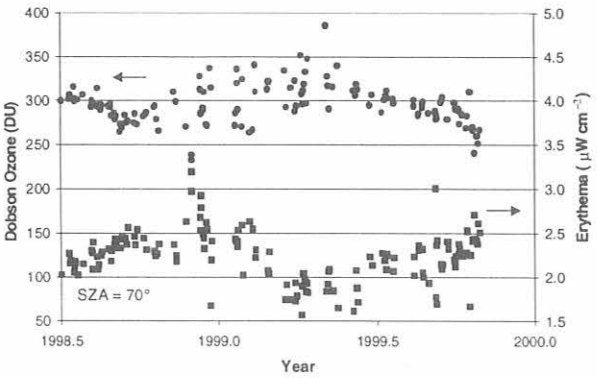

Fig. 3.17. Erythemal irradiance at SZA 70° (bottom, squares) and total ozone (top, circles) for clear-sky mornings and afternoons at Boulder from July 1998-December 1999.

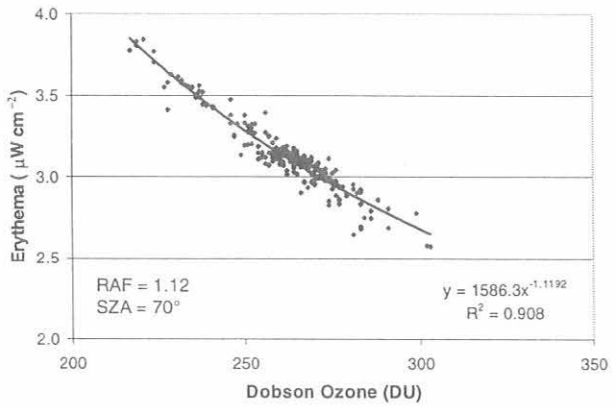

Fig. 3.18. Power law regression between erythemal irradiance at SZA 70° and Dobson total ozone at MLO from July 1998-December 1999. The graph is plotted on a linear scale to facilitate reading the units. The coefficient of the power law function (1.12) gives the RAF.

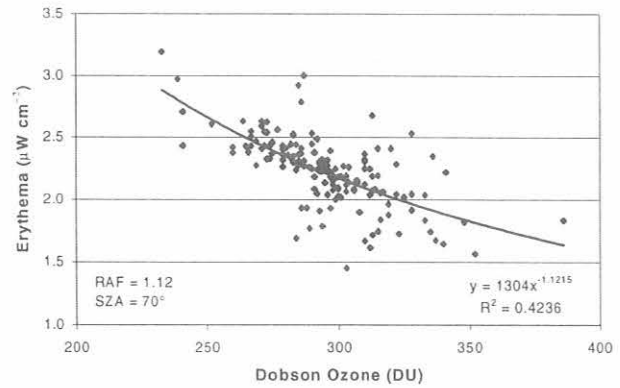

Fig. 3.19. Power law regression between erythemal irradiance at SZA 70° and Dobson total ozone at Boulder from July 1998-December 1999. The graph is plotted on a linear scale to facilitate reading the units. The coefficient of the power law function (1.12) gives the RAF.

ozone, was calculated for both sites for 70° SZA using the power-law formulation of *Madronich* [1993]: RAF = $-\Delta\ln(I)/\Delta\ln(O_3)$, where I is UV irradiance. The RAF is simply the slope of a straight-line fit on a log-log plot. The data for Boulder are subject to more scatter because of less pristine clear sky conditions than for MLO.

Conclusions

1. Erythema irradiance calculated from UV spectra at MLO and Boulder is inversely correlated with Dobson total ozone.
2. The erythema RAF measured at MLO and Boulder for the 1.5-yr period is about 1.12 for both sites, in reasonable agreement with current modeling efforts.
3. No significant trend in UV irradiance may be inferred because of the limited time period.

3.2.5. Broadband UV

Introduction

Broadband UV instruments (Yankee UVB-1) were operational at MLO, BRW, BAO, Bermuda, Kwajalein, and Boulder as part of the various programs being operated by the STAR group. These instruments were all compared at various times with the MLO instrument and with the MLO UV spectroradiometer installed at MLO in July 1995 [*Bodhaine et al.,* 1998]. Because the erythemal response defined for human skin is significantly different than that of the broadband instrument, the calibration of the broadband instrument reporting in erythemal units is strongly dependent on total ozone [*Bodhaine et al.,* 1998]. When a broadband instrument is placed in the field, it is necessary to know the calibration as a function of ozone to determine accurate erythemal irradiance. However, the manufacturers of broadband instruments do not generally provide information on the ozone dependence of the calibration.

Instrumentation

The UVB-1 instrument uses a UV-sensitive phosphor that absorbs radiation in the UV-B region and re-emits in the green region. A photodiode that has its peak response in the green part of the spectrum is used to measure the green light emitted by the phosphor. The UVB-1 is temperature stabilized at 45°C. The manufacturer provides conversion factors for estimating various portions or weighted integrals of the UV spectrum, such as total UV-B (280-315 nm or 280-320 nm), Diffey Action Spectrum, Parrish Action Spectrum, or the DNA-weighted spectrum. However, these estimates can be significantly in error because of the fact that the actual spectral response of the instrument can be significantly different than the portion of the spectrum being estimated, which in turn causes strong ozone dependence of the measurements. Because of these uncertainties the broadband measurement program is currently being reviewed.

3.2.6. Baseline Surface Radiation Network

The STAR group has the leadership role in the BSRN having fulfilled the duties of International Project Manager for the past 5 years. The BSRN is intended to not only supply the international climate research community with the highest-quality surface irradiance data from a globally and climatologically diverse long-term network, but also to keep advancing the state of the art in improving those measurements so that research uses of the data can continue to be challenged. Support of the U.S. BSRN

program comes from several agencies (NOAA National Weather Service, NOAA Oceanic and Atmospheric Research, NASA, and the Department of Energy) and is funded internationally by the participating countries that operate surface BSRN stations and contribute technical experts. The BSRN data are being utilized in major satellite and GCM research programs mentioned previously. The program was conceived in 1988, began operations in 1992, and is intended to operate indefinitely until there are no further extensive research needs for such data. Current activities of the BSRN are further summarized by *Ohmura et al.* [1998].

3.2.7. Barrow Snow Melt Date

Snow Melt Analysis

An important process that occurs every spring over continental regions of the arctic is the melting of the snow pack. Variability in the date when the tundra becomes snow free is expected to affect the annual net energy budget of the region. As the global mean temperature continues to increase, the arctic is predicted to experience enhanced warming because of a positive radiative feedback caused by decreasing surface albedo in response to accelerated melting of ice and snow. Albedo is derived from the ratio of reflected to downwelling, shortwave, broadband irradiances. Of particular interest to CMDL has been the timing of the spring snowmelt at BRW that has historically been designated as the day when albedo drops below 0.30 [*Dutton and Endres,* 1991]. Fresh snow has an albedo exceeding 0.85, whereas dry tundra has a value of about 0.17 [*Stone et al.,* 1996]. Once the daily average albedo drops below 0.3, it seldom increases again until snow accumulates the following autumn. This fact makes monitoring the melt relatively straightforward and provides an important record for evaluating regional climate change. Figure 3.20 shows daily average albedos spanning the period of melting for 1998 and 1999. Although the final melt typically occurs in a matter of a few days as shown in the figure, the actual timing of this event is highly variable from year to year at any particular location, depending on many factors. Temperature is usually presumed to be a primary factor; however, changes in cloud cover that affect solar intensity or thermal emissions, the stability of the atmosphere, and boundary layer turbulence (winds) are also factors. Another important variable is the amount of snow that accumulates during the preceding months. Any long-term variation in these or other factors may affect the spatial or temporal distribution of snow and lead to a perturbation in the regional energy balance. It is essential that these processes be understood and be parameterized correctly in models to improve climate simulations.

Foster [1989] found that the disappearance of snow in spring at Barrow has occurred progressively earlier since the 1950s and has speculated that this was a manifestation of global warming. His analysis was based on observations of snow cover made at the Barrow NWS station. *Dutton and Endres* [1991] argued that the apparent trend was attributable to local urbanization effects, basing their analysis on the more objective, radiometric determination of melt made at BRW (e.g., Figure 3.20). Because BRW is located on open tundra several kilometers upwind of town, it has not been affected by such development. *Foster et al.* [1992] expanded on these earlier studies using satellite data to show that the earlier melt was regional in scale. In this report, the record from BRW is updated in an attempt to explain the trend and variability of the annual melt there.

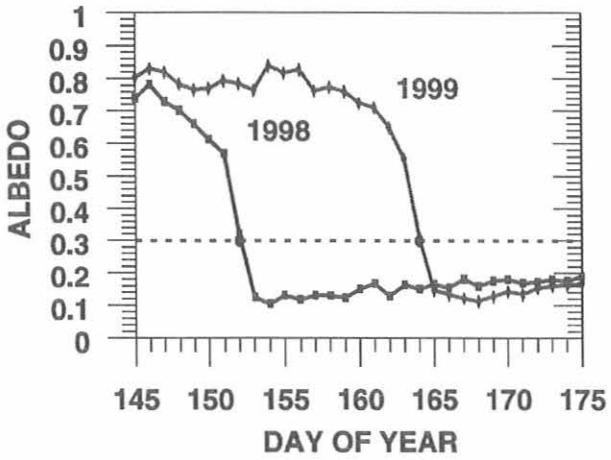

Fig. 3.20. Time series of daily average surface albedo for 1998 and 1999 at BRW. The snowmelt date is determined radiometrically as the date when the surface albedo drops below 0.30 (30%).

Updated time series for NWS and BRW indicate a further divergence as shown in Figure 3.21. It is now known for certain that the NWS record was contaminated because of new construction and a dramatic increase in traffic directly upwind of that site. The development began in the late 1960s in anticipation of developing the North Slope oil reserves. Thus the NWS data subsequent to this time are progressively more suspect. To construct a valid, long-term time series of melt dates for Barrow, the BRW radiometric record was appended onto the early NWS record, bridging the gap of 1966-1985 using proxy

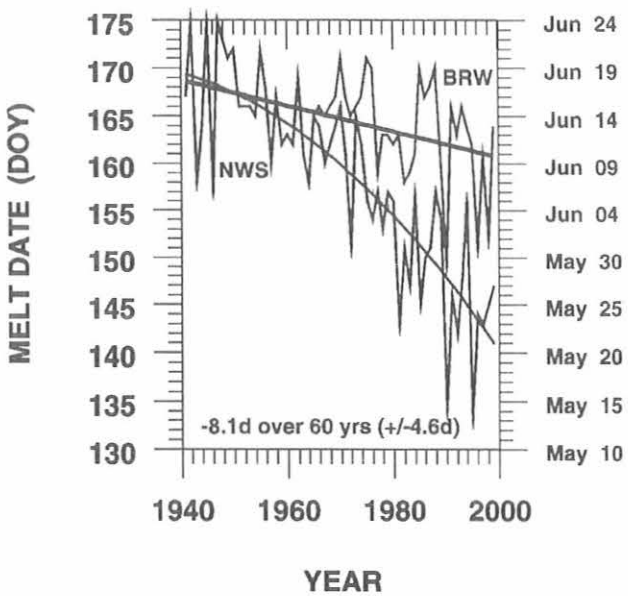

Fig. 3.21. The date of snowmelt in the vicinity of Barrow shows a trend. At the NWS site in town the disappearance of snow is occurring much earlier than at BRW because of local urbanization effects. The linear trend for BRW is given in the legend and is based on a 95% confidence level.

data. The proxy data were derived from careful examinations of temperature records that show a distinct seasonal signature related to the melting process. This repeatable feature appears as a period of about 8 days running of near-freezing air temperatures, followed by an abrupt and sustained warming caused when solar radiation is absorbed by the exposed tundra that then releases heat to warm the overlying air.

Regression analyses were used to evaluate the time series shown in Figure 3.21. The downturn (quadratic) indicated for the NWS record is now attributed to contamination of that site by nearby development, but the composite BRW time series shows a trend that is statistically significant (−8.1 ±4.6 days over 60 years at the 95% confidence level). It is hypothesized that the earlier melting of the snow pack in the vicinity of Barrow results from less than normal accumulation of snow throughout the winter and/or warmer spring temperatures possibly associated with enhanced thermal emissions from clouds as described by *Stone* [1997]. To explore these possibilities, meteorological records were analyzed dating from the mid-1960s, the period showing the most pronounced trend. Integrated water equivalent precipitation (WEPC) from October through February is used to quantify seasonal snow accumulation because this measure is less prone to error than actual snow depth data. In addition, the temperature (T) and total sky cover (SC) averages for March and April were examined. Although the final phase of melting is obviously dependent on concurrent weather conditions, the analysis suggests that the factors mentioned previously probably condition or "ripen" the snow pack prior to the onset of melt by establishing its maximum depth and its microphysical characteristics. Figure 3.22 displays time series for each of these factors compared with the record of melt. Each time series was analyzed for a trend and was cross-correlated with melt date. The coefficients correlating melt with WEPC, T, and SC are, respectively, +0.39, –0.47, and –0.30. As expected, melt date is positively correlated with snowfall (represented by WEPC) and anti-correlated with temperature, but no one factor explains a significant portion of the variance. However, an empirical model based on a multiple regression using a nonlinear combination of these factors was found to explain >70% of the variance [R. Stone, unpublished results, 2000]. It is concluded that decreasing snowfall during winter, combined with warmer, cloudier spring conditions are primary factors that have led to an earlier melt at BRW.

Overall the melt has advanced by more than a week since the mid-60s but is characterized by significant interannual variability. The most pronounced change occurred during the last decade, with the melt dates of 1990, 1996, and 1998 being particularly early. Figure 3.22 shows that during each of these years little snow accumulated through the winter (minimal WEPC) and the following March and April periods were relatively warm. In contrast, the 1999 melt occurred late because WEPC was much higher and spring temperatures were much colder. Because the melt occurs during the peak of the annual solar cycle [*Stone et al.,* 1996], there is a dramatic increase in net surface radiation when the tundra becomes snow free. It is estimated that the trend indicated in Figure 3.21 represents an increase in the annual net radiation balance at BRW of about 10%. Analyses of melt dates for other North Slope sites (not presented here) show a similar tendency toward an earlier melt suggesting that the region as a whole has experienced an increase in net radiation in recent years. If the area affected covers a large enough region of the artic and this trend is sustained, then the implications of these findings will have even greater significance in the context of global climate change. It is important to understand what processes underlie these observations.

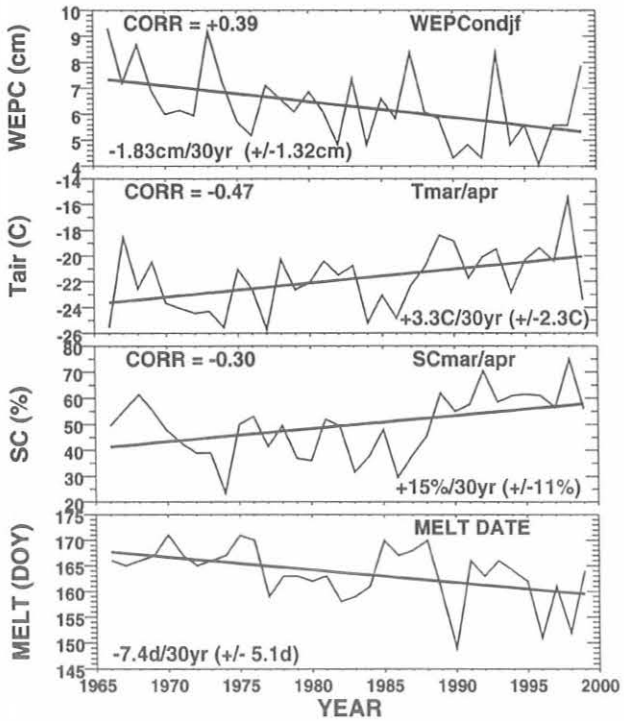

Fig. 3.22. Time series of factors that are believed to affect spring snowmelt at BRW compared with dates of melt. As labeled, top to bottom: integrated water equivalent precipitation for October through February, average March/April 2-meter air temperature, average total sky cover for March/April, and melt date determined from proxy (temperature) data and albedo measurements as described in the text. Each time series has a linear fit to determine trends based on the 95% confidence level given in the lower legends. Also, cross-correlation coefficients relating melt date with each variable are given (upper, left).

Trajectory Analysis

A previous study showed that shifts in circulation patterns influence northern Alaska climate [*Stone,* 1997]. It is very likely that similar changes underlie the variations in the annual melt at BRW through perturbations in the precipitation and temperature patterns of the region. To a large extent the climate of northern Alaska is influenced by the relative positions and intensities of two dominant pressure systems, the Aleutian Low and the Beaufort Sea anticyclone. This is revealed through analyses of back-trajectories similar to those of *Harris and Kahl* [1994] made in conjunction with an examination of geopotential height fields that highlight these synoptic patterns. Enhanced precipitation during winter was found to occur often when warm moist air reaches northern Alaska from the North Pacific as a result of circulation around the Aleutian Low. Drier conditions prevail there when upper-level winds are generated over the Beaufort Sea and effectively block the southerly flow. Year-to-year

variability of these features appears to be associated with natural shifts in planetary wave patterns rather than a response to a general warming of the arctic. It is speculated that these variations are correlated with the phase of the arctic oscillation [e.g., *Thompson and Wallace,* 1998]. This possible connection is a focus of continuing research. Eventually it is hoped to determine to what extent the annual cycle of snow cover over northern Alaska is affected by natural versus anthropogenic factors.

3.2.8. ARCTIC UV MONITORING

Introduction

In June 1998, with continued support from the NOAA Arctic Research Initiative (ARI), CMDL deployed two additional Biospherical Instruments, Inc. (BSI), five-channel UV filter-based radiometers at the NWS facilities at Nome (64°N, 165°W) and St. Paul Island (57°N, 170°W). The three Alaska UV monitoring sites are identified in Figure 3.23. The instruments at Nome and St. Paul are identical to the one deployed at BRW in September 1997 except that the 340-nm channel was replaced by a wide-band channel that measures across the 400-700 nm part of the spectrum (known as photosynthetically active radiation or PAR). Thus these instruments have three channels in the UV-B region (305 nm, 313 nm, and 320 nm) and one channel in the UV-A region (380 nm). All three UV instruments produced excellent data in 1998 and 1999, other than a temporary malfunction in the 380-nm channel at St. Paul in 1999. All three instruments continue to operate within normal parameters with the exception of 1 week of downtime at Nome in July 2000 because of a brownout requiring the return of the data acquisition computer for repair.

The three instruments continue to undergo regular annual calibration by the manufacturer during the winter period (November–January). The calibration of the BSI instrument is tied to a spectroradiometer used in the National Science Foundation's Polar UV Monitoring Network. This high resolution scanning spectroradiometer (the BSI model SUV-100) has a well-documented calibration history. In addition to the SUV-100, BSI has a series of multi-channel reference instruments (RGUVs) installed at their San Diego facility, similar to those installed at the three CMDL sites. These RGUVs have been operated next to the spectroradiometer since 1995, allowing for intercomparison on a continuous basis. Thus far solar calibrations of the RGUVs relative to the SUV have indicated the stability of the RGUVs to be about ±3% across all channels. These RGUV instruments are then used as the basis for calibration of other BSI multi-channel UV instruments. The process generates a calibration scale factor for each optical channel that is used to determine any changes in instrument sensitivity. Analysis of the calibrations for all three instruments has shown changes in sensitivity of 2-11%.

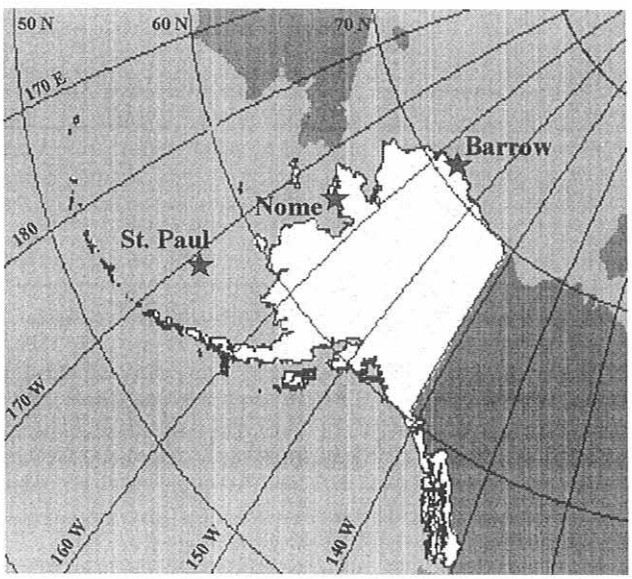

Fig. 3.23. CMDL arctic UV Network.

Data Analysis

One year of data (1998) was analyzed for all three sites. For Barrow, the observation period was May 18-October 26; for Nome, June 12-October 22; and for St. Paul, June 8-October 23. Figure 3.24 shows the daily total energy for each site at the individual UV wavelengths for the period during which the instruments were taking observations in 1998. The 400-700 nm measurements from the Nome and St. Paul instruments are not presented here, although they show the same variability as the other four channels. The 305-nm channel is multiplied by ten so that it can be more easily seen on the charts. Because of missing data during the integration process (integrated for the entire 24-hr day), Barrow is missing 2 days; Nome is missing 7 days; and St. Paul is missing 4 days. Nonetheless, the figure shows large day-to-day variations for all three sites and a decrease in UV at all wavelengths over the observation periods.

A regression analysis was conducted to investigate the correlation of ozone with each of the UV wavelengths at the three sites. This was done by first removing the variability in UV because of SZA by filtering the daily 1-min values between 69.5° and 70.5°. This yielded two reduced sets of data for each day (AM and PM values), which were then combined into one dataset, effectively yielding two data points for each day. Unfortunately this also resulted in a loss of about 1 month's data for Barrow (because of a rapidly setting sun) but captured nearly all of the observational period at Nome and St. Paul. In addition, because of limited clear-sky data at all three sites, ratios were taken to reduce the effects of clouds at the shorter wavelengths of 305 nm, 313 nm, and 320 nm. At Nome and St. Paul there are no 340-nm channels, so the ratios used the 380-nm wavelengths. Total column ozone values were obtained from the Dobson spectrophotometer at the Barrow Observatory and from the NASA Total Ozone Mapping Spectrometer (TOMS) at all three sites for the same periods as the UV observations. During the observation period in Barrow there were 62 days without Dobson observations. Only 5 days of TOMS ozone data were missing for Barrow. Therefore, a combined Dobson/TOMS ozone dataset was used for the regression. Three Dobson observation sets are usually obtained for each day: in the morning, near local noon, and in the afternoon. Where available, the Dobson value most closely matching the UV measurement time was used. When this was not possible, the single daily representative value from TOMS was used. At the other two sites, only the TOMS ozone data are available, and there were 26 days missing for

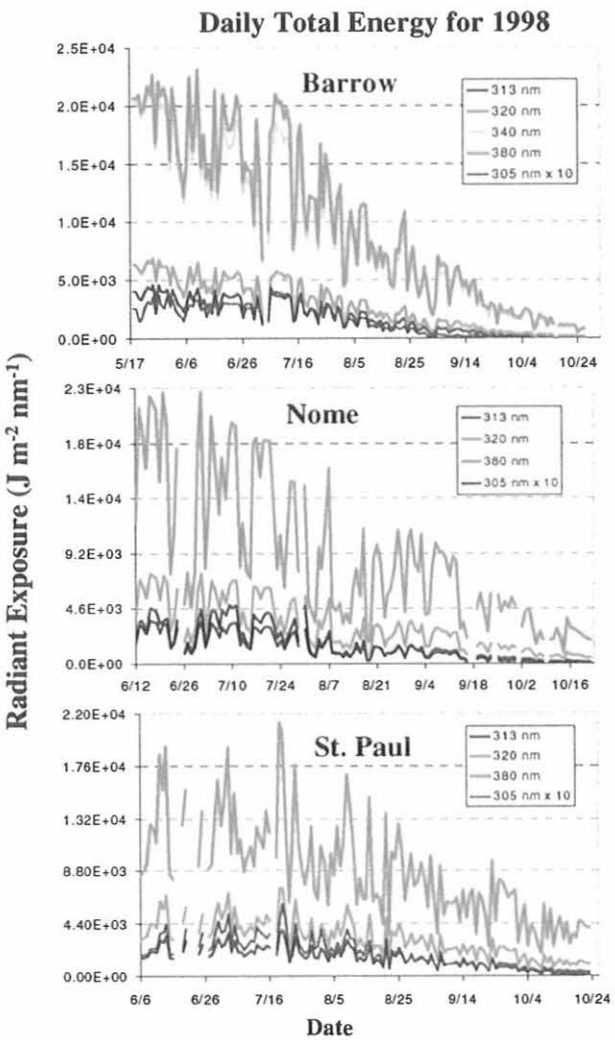

Fig. 3.24. The 1998 daily total energy for Barrow, Nome, and St. Paul, Alaska.

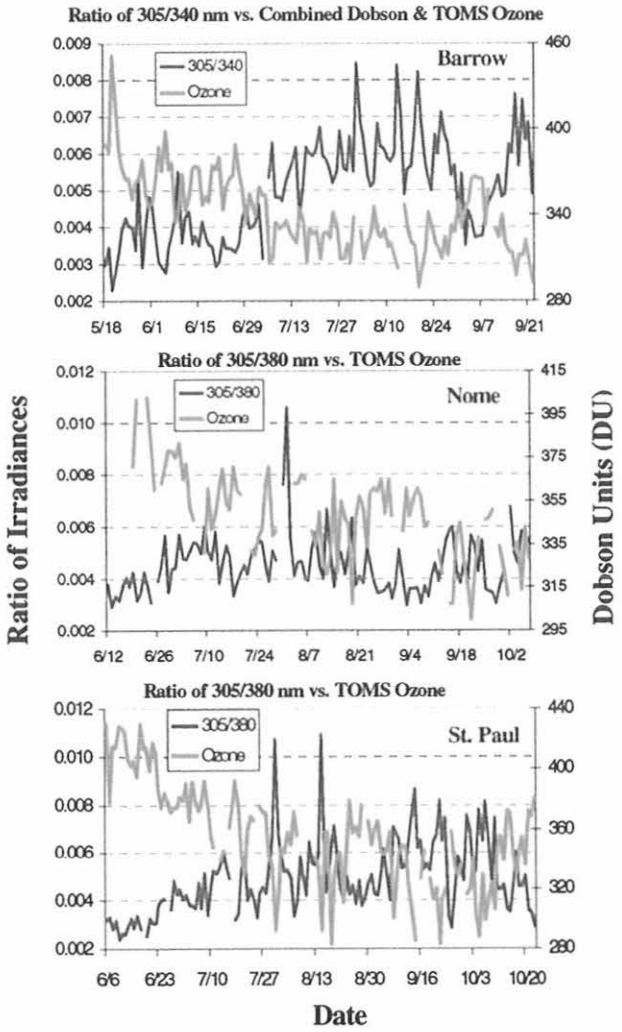

Fig. 3.25. The 1998 time series of ozone and UV for Barrow, Nome, and St. Paul, Alaska.

Nome and 11 days missing for St. Paul. However, this allowed a sufficient sample size to obtain significant correlations. Figure 3.25 shows the time series of the ratio of irradiances and ozone at the three sites using the shortest wavelength of 305 nm, to illustrate the direct correspondence between these two variables. Figure 3.26 shows three regressions demonstrating the correlation between ozone and the 305-nm/380-nm wavelengths (305-nm/340-nm for BRW). As expected there is a strong negative correlation between ozone and UV at the 305 nm wavelength at both Barrow and St. Paul. However, there is only a weak negative correlation at Nome. It is not clear why Nome would have such a significant difference from the other two sites. It is possible that the Nome UV instrument is being affected by pollutants emitted from aircraft, since the installation is on the roof of the NWS office right next to the airport. This will necessitate further investigation.

A multiple linear regression analysis was conducted using UV (the ratio of the irradiances for the 305-, 313-, and 320-nm wavelengths, but individually for 340 and 380 nm, and PAR), ozone, and cloud cover. Cloud cover data were obtained from the NOAA National Climatic Data Center. The cloud cover is a fraction of the total celestial dome in tenths. In order to ensure equality across all three variables, the cloud cover value most closely matching the period of time for the AM and PM values of UV observations was used. The relative strengths of the individual predictors (ozone and clouds) with the five wavelengths are shown in Table 3.10 for Nome and St. Paul and in Table 3.11 for Barrow. As expected the bivariate correlations between ozone and the shorter wavelengths (305, 313, and 320 nm) are negative at all three sites with the strongest relationship seen for Barrow and St. Paul. There is no relationship between ozone and UV at the 380-nm and PAR (400-700 nm) wavelengths, as expected. On the basis of the correlation analyses with ozone and clouds, ozone alone contributed most of the variance in UV at 305, 313, and 320 nm. The cloud cover fraction offers little additional predictive power in the regression model summary, although the correlations (Tables 3.10 and 3.11) at the longer wavelengths at St. Paul and Barrow (380 nm) and at all five wavelengths at Nome are significant. For St. Paul and Barrow this would be expected, given that the 380-nm

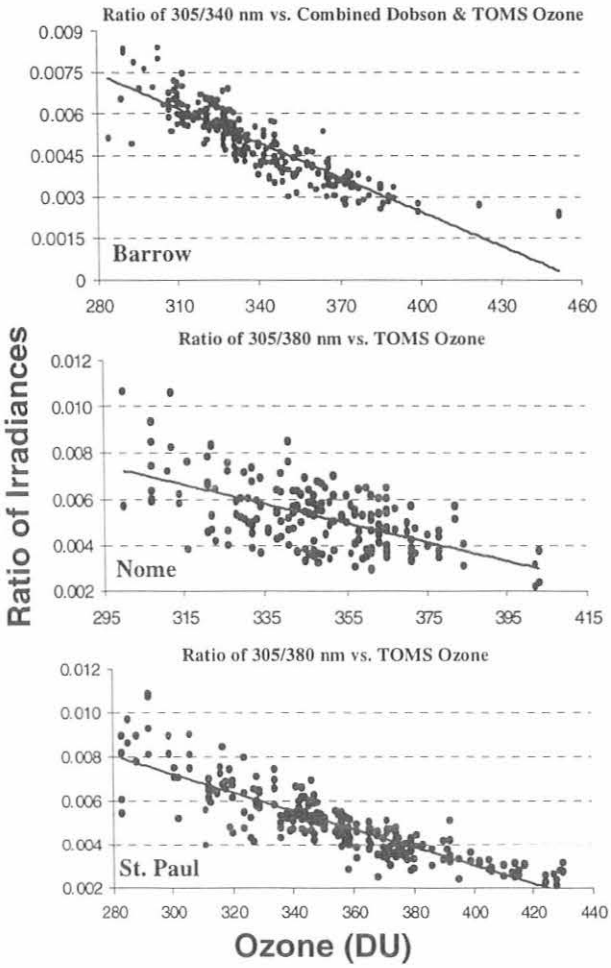

Fig. 3.26. The 1998 linear regressions of UV and ozone at Barrow, Nome, and St. Paul, Alaska. For all three sites, the regression equation is $y = (-4 \times 10^{-5}) \times +0.02$. The Pearson product-moment correlation coefficient (r) for Barrow, Nome, and St. Paul was 0.88 (n = 248), 0.58 (n = 178), and 0.87 (n = 254), respectively.

wavelength and PAR are more influenced by clouds instead of ozone. It is not entirely clear why there are significant correlations between clouds and all five wavelengths at Nome.

TABLE 3.10. The 1998 Nome and St. Paul Pearson Correlations (r) Between Each Predictor (Ozone and Clouds) and UV

	Nome (64°N, 165°W)		St Paul (57°N, 170°W)	
Wavelength	TOMS (n = 178)	Clouds (n = 225)	TOMS (n = 254)	Clouds (n = 261)
305 nm/380 nm	-0.58*	0.26*	-0.87*	-0.01
313 nm/380 nm	-0.43*	-0.26*	-0.79*	0.03
320 nm/380 nm	-0.27*	0.27*	-0.59*	0.09
380 nm	0.10	-0.28*	0.01	-0.29*
400-700 nm (PAR)	0.06	-0.27*	-0.01	-0.30*

*Correlation is significant at the 0.01 level (2 tailed).

TABLE 3.11. The 1998 Barrow Pearson Correlations (r) Between Each Predictor (Ozone and Clouds) and UV

Wavelength	Dobson (n = 115)	TOMS (n = 246)	Combined (n = 248)	Clouds
305 nm/340 nm	-0.90*	-0.91*	-0.88*	-0.06
313 nm/340 nm	-0.83*	-0.87*	-0.83*	-0.03
320 nm/340 nm	-0.62*	-0.70*	-0.65*	0.01
340 nm	0.39*	0.41*	0.49*	-0.12
380 nm	0.34*	0.36*	0.34*	-0.15†

*Correlation is significant at the 0.01 level.
†Correlation is significant at the 0.05 level.

Conclusions

The existence of these three new sites in Alaska greatly enhances the capability of monitoring UV in the arctic. The data are currently being archived at CMDL and are available to any user upon request. As shown in this preliminary analysis, the data can be used to investigate the relationship between changes in ozone and changes in UV. With a continued decrease in ozone in the arctic (as demonstrated by the SAGE III Ozone Loss and Validation Experiment), these three sites provide an excellent opportunity to establish baseline values of UV in the Alaskan arctic. The data can be used to determine column ozone amounts (for comparison with the Dobson spectrophotometer at Barrow), UV doses, and cloud effects. The data can be used to test and validate algorithms aimed at determining surface UV exposure in the arctic from satellite data. Finally, the data can be used by ecologists who are interested in studying the potential effects of increasing UV on arctic marine and terrestrial ecosystems, as well as on human health.

3.2.9. Pyrgeometer Comparison

Introduction

The broadband hemispheric downwelling longwave irradiance at the earth's surface ($F_{IR}\downarrow$) is a significant component of the surface energy budget. It is a function of both the thermal structure and the optical structure of the atmosphere and, therefore, includes radiation because of the greenhouse properties of atmospheric constituents. Measurements of $F_{IR}\downarrow$ typically made by pyrgeometers, have uncertainties thought to be of the same magnitude or larger than the potential change in $F_{IR}\downarrow$ because of anthropogenic greenhouse forcing. Several factors contribute to the uncertainties in these measurements: lack of an adequate traceable, absolute calibration standard; variations in calibration techniques; and uncertainties in the thermal balance within the instruments.

A recent intercomparison conducted with a suite of pyrgeometers, a new scanning absolute IR radiometer (sky-scanner) (R. Philipona, personal communication, 1999), and radiative transfer model calculations suggests that significant reductions in the uncertainty of pyrgeometer measurements may be achieved. A comparison of averaged nighttime measurements shows excellent agreement between pyrgeometer and sky-scanner measurements (within -0.1 ± 0.2 W m^{-2} out of 280 W m^{-2}) (R. Philipona, personal communication, 1999) when all pyrgeometers are calibrated using a common technique. The development of the sky-scanner, which utilizes a cavity detector

referenced in near-real time to a blackbody calibration target, suggests that a stable reference standard radiometric scale for IR (similar to the World Radiometric Reference scale for shortwave) is achievable and transferable to pyrgeometers for field use. The modeled irradiances (calculated using MODTRAN4 [*Anderson et al.,* 1999] with radiosonde data as input) exhibit a positive mean bias of 1.0 W m^{-2} versus the measurements. The radiative impacts of other model components unspecified by the sonde data (CFCs and aerosols, for example) are being evaluated.

Instrumentation and Models

The first International Pyrgeometer and Absolute Scanning Radiometer Comparison (IPASRC-I) was held at the Department of Energy Atmospheric Radiation Measurement (ARM) program's Southern Great Plains Cloud and Radiation Testbed (CART) site at Lamont, Oklahoma, during September 20-October 1, 1999. A suite of 15 pyrgeometers and the sky-scanner were deployed at the site's Radiometer Calibration Facility (RCF). The pyrgeometers measure the spectrally integrated (e.g., approximately 3.5-50 μm for Eppley model PIR pyrgeometers), horizontally incident longwave irradiance. All pyrgeometers had user-supplied calibrations. In addition, all pyrgeometers were calibrated by CMDL and seven pyrgeometers were calibrated by Physikalish-Meteorologisches Observatorium Davos (PMOD) prior to the field experiment. The CMDL calibrations were performed using a method similar to that described by *Albrecht and Cox* [1977]. The PMOD calibration technique is described by *Philipona et al.* [1995].

The sky-scanner is a directional instrument that measures the normal, unfiltered, spectrally integrated atmospheric longwave irradiance. This irradiance is measured at multiple directions, and then the measurements are cosine-weighted and integrated over the solid angle to produce the horizontally incident irradiance. The sky-scanner periodically measures a temperature-controlled blackbody target, which allows for absolute calibration. ARM performs periodic radiosonde launches from a site located near the RCF. These nearly co-located sonde data can be applied in radiative transfer models to simulate the downwelling irradiances observed by the instruments and help account for instrumental differences in spectral range and implementation. MODTRAN4, an Air Force radiative transfer algorithm with flexible simulation capabilities, was chosen for this use.

Data Analysis

Measurements were taken at 1-s intervals for half-hour periods during the day and night over the course of 5 clear days. Pyrgeometer measurements were converted to irradiance using first the user-supplied calibrations, then the CMDL calibrations, and finally (for seven of the pyrgeometers) the PMOD calibrations. The measurements were averaged over each half hour for each instrument, and then the pyrgeometers were further averaged by calibration grouping. Sonde data (temperature, pressure, relative humidity) were obtained for the launch nearest in time to the observations. The vertical resolution of the sonde data was reduced to levels appropriate to MODTRAN4; these reduced-resolution data were validated by running several test cases with a version of MODTRAN4 specially modified at CMDL to accept the full 2000+ layers of sonde data. Model calculations were performed to match the spectral range of the sky-scanner. Because the calculations were not completely defined by the sonde data, other input parameters (specifically CFCs and aerosols) were set at realistic default values.

Under the four nighttime comparisons, the agreement between the averaged user-calibrated pyrgeometers and the sky-scanner is within 1.6 ± 0.4 W m^{-2} out of 280 W m^{-2}, while for PMOD-calibrated pyrgeometers the agreement is within -0.7 ± 0.4 W m^{-2} (Figure 3.27). If the CMDL calibrations are employed, the agreement is exceptional, within -0.1 ± 0.2 W m^{-2}. However, significant differences exist among the 15 pyrgeometers. The spread, averaged over all nighttime measurements, is 8.4 W m^{-2} with CMDL calibrations, 3.4 W m^{-2} with PMOD calibrations, and 11.9 W m^{-2} with user calibrations. These results are consistent with prior estimates of the uncertainty associated with single measurements (±10 W m^{-2} [*Philipona et al.,* 1995] or about ±5% [*Dutton,* 1993]). Future intercomparisons are being planned that will incorporate other absolute scanning radiometer instruments, as available, and additional sites.

The MODTRAN4-modeled irradiances exhibit a somewhat consistent positive mean bias of 1.0 W m^{-2} relative to the sky-scanner measurements. Potential sources of the bias include the use of default values for CFCs and aerosols, as mentioned previously, and the treatment of the water vapor continuum within the model. An investigation into the magnitude of the influence of CFCs and aerosols on $F_{IR}\downarrow$ suggests that the effect of aerosols is significant compared to the size of the bias (Figure 3.28), while that of CFCs is not. Further work is being done to evaluate the influence of the water vapor continuum treatment.

3.2.10. Rayleigh Optical Depth Calculations

Introduction

A variety of different techniques are used for the calculation of Rayleigh optical depth in the atmosphere. In some cases, differences among these techniques can be important, especially in the UV region of the spectrum and under clean atmospheric conditions. It is recommended that Rayleigh optical depth be calculated from first principles of Rayleigh scattering theory rather than the variety of curve fitting techniques currently in use. This approach requires the accurate calculation of the refractive index of air based on the latest published measurements. Small inaccuracies in Rayleigh optical depth

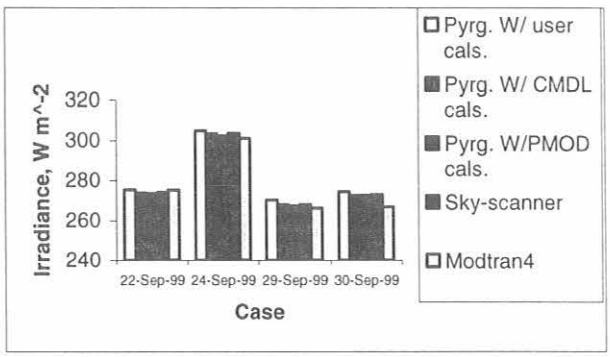

Fig. 3.27. IR irradiances from user-calibrated pyrgeometers, CMDL-calibrated pyrgeometers, PMOD-calibrated pyrgeometers, the sky-scanner instrument and MODTRAN4 model results for four nighttime comparisons.

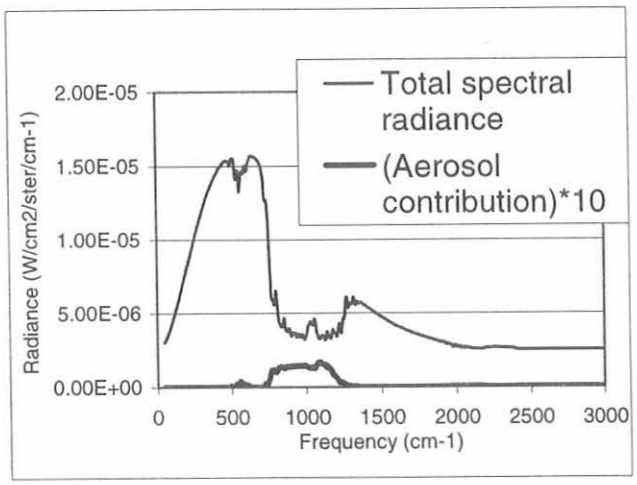

Fig. 3.28. Downwelling spectral irradiance (offset by $+2.5 \times 10^{-6}$) and the contribution by aerosols (scaled up by a factor of 10). The aerosol spectrum accounts for 2 W m^{-2}.

calculations can equal or even exceed other quantities being estimated, such as aerosol optical depth, particularly in the UV region of the spectrum. The procedure described here was presented by *Bodhaine et al.* [1999].

Rayleigh scattering calculations for air have traditionally been made using the method of *Penndorf* [1957] where the refractive index was calculated for "standard" air (760 mm Hg, 15° C) using the equation of *Edlén* [1953], and the scattering cross section per molecule was calculated using the classical equation presented in many textbooks [e.g., *van de Hulst,* 1957; *McCartney,* 1976]. This calculation includes the depolarization term, or the King factor, which describes the effect of molecular anisotropy and is the least well known for these purposes. Results of such calculations were presented by *Penndorf* [1957]. It is this table of values that has been used by many workers in the field to estimate Rayleigh optical depths, usually by some curve fitting routine over a particular wavelength range of interest.

Possible errors in the depolarization term were considered by *Hoyt* [1977], *Fröhlich and Shaw* [1980], and *Young* [1980, 1981]. The correction proposed by *Young* [1981] had been accepted for modern Rayleigh scattering calculations in atmospheric applications. However, *Bates* [1984] and *Bucholtz* [1995] discussed the depolarization in detail as a function of the individual constituents, and as a function of wavelength, and presented new values.

Optical Depth

A quantity of fundamental importance in atmospheric studies is the optical depth (or optical thickness). This quantity has been discussed by numerous authors [e.g., *Dutton et al.,* 1994; *Stephens,* 1994] and is derived from the exponential law of attenuation variously known as Bouguer's law, Lambert's law, or Beer's law. For purposes of illustration only, Bouguer's law may be simply written as:

$$I(\lambda) = I_0(\lambda)\exp(-\tau(\lambda)/\cos\theta) \qquad (1)$$

where $I_0(\lambda)$ is the extraterrestrial flux at wavelength λ, $I(\lambda)$ is the flux reaching the ground, θ is the solar zenith angle, and $\tau(\lambda)$ is the optical depth. Clear-sky measurements of $I(\lambda)$ as a function of θ, and plotted as $\ln I(\lambda)$ against $\sec\theta$, should yield a straight line with slope $-\tau(\lambda)$ and intercept I_0 (extrapolated back to $\sec\theta = 0$). An important point is that $\tau(\lambda)$, may be composed of several components given by:

$$\tau(\lambda) = \tau_R(\lambda) + \tau_a(\lambda) + \tau_g(\lambda) \qquad (2)$$

where $\tau_R(\lambda)$ is the Rayleigh optical depth, $\tau_a(\lambda)$ is aerosol optical depth, and $\tau_g(\lambda)$ is the optical depth due to absorption by gases such as O_3, NO_2, and H_2O. In principle it is possible to measure $\tau(\lambda)$ and then derive aerosol optical depth by subtracting estimates of $\tau_R(\lambda)$ and $\tau_g(\lambda)$. In practice, however, arriving at reasonable estimates of these quantities can be difficult, particularly during fairly clean atmospheric conditions such as those found at Mauna Loa, Hawaii. To isolate the individual components of optical depth it is necessary to provide accurate estimates of Rayleigh optical depth.

Rayleigh optical depth is relatively easy to calculate once the scattering cross section per molecule has been determined for a given wavelength and composition because it depends only on the atmospheric pressure at the site. That is, it is only necessary to calculate the total number of molecules per unit area in the column above the site, and this depends only on the pressure, as shown in the formula:

$$\tau_R(\lambda) = \sigma\frac{PA}{m_a g} \qquad (3)$$

where σ is scattering cross section per molecule, P is the pressure, A is Avogadro's number, m_a is the mean molecular weight of the air, and g is the acceleration due to gravity. Note that m_a depends on the composition of the air, whereas A is a constant of nature. Although g may be considered a constant of nature, it does vary significantly with height and location on the earth's surface and may be calculated according to the formulas of *List* [1968].

Rayleigh Optical Depth of Air

Bodhaine et al. [1999] outlined a method for the calculation of Rayleigh optical depth that goes back to first principles as suggested by *Penndorf* [1957] rather than using curve fitting techniques, although the refractive index of air is still derived from a curve fit to experimental data. All of the latest values of the physical constants of nature were used, and the effects of CO_2 on the refractive index and the mean molecular weight of air were included, even though these effects are in the range of 0.1-0.01%. It should be noted that aerosol optical depths are often as low as 0.01 at Mauna Loa. Since Rayleigh optical depth is of the order of 1 at 300 nm, it is seen that a 0.1% error in Rayleigh optical depth translates into a 10% error in aerosol optical depth.

The effects of high concentrations of water vapor on the refractive index of air may be of the same order as for CO_2 [*Edlén,* 1953, 1966]. However, for practical atmospheric situations the total water vapor in the vertical column is small and does not significantly affect the calculations. Furthermore, the water vapor in the atmosphere is usually confined to a thin layer near the surface, which significantly complicates the

calculation, whereas CO_2 is generally well mixed throughout the atmosphere.

It is recommended that *Peck and Reeder's* [1972] formula for the refractive index of dry air with 300 ppm CO_2 be used after corrections have been applied for the actual CO_2 concentration of the air. Next the scattering cross section per molecule of air should be calculated from the classical equation using the same temperature and pressure as were used for refractive index (1013.25 mb and 288.15 K). Note that the scattering cross section per molecule is independent of pressure and temperature. The depolarization should be calculated taking into account the CO_2 concentration. Finally the Rayleigh optical depth can be calculated using Equation (3), taking into account the effect of CO_2 concentration on the average density of air, the surface pressure, and the effective value of gravitational acceleration using the correct latitude and the correct mass-weighted mean altitude of the column of air above sea level. By following these guidelines it is possible to calculate the Rayleigh optical depth as a function of wavelength for any point at ground level or in the atmosphere at any location on the earth.

Some Example Calculations

Using the previous equations *Bodhaine et al.* [1999] presented a table of values of Rayleigh scattering cross section, and of Rayleigh optical depth for dry air containing 360 ppm CO_2 at sea level, 1013.25 mb, and at latitude 45°; and at MLO (altitude 3400 m, pressure 680 mb, and latitude 19.533°). For those readers who wish to use curve-fitting techniques, *Bodhaine et al.* [1999] investigated several different equations similar to those currently in use by other authors. They found that the accuracies of those equations were not sufficient and therefore looked for a better approach. They found that the equation

$$y = \frac{a + b\lambda^{-2} + c\lambda^{2}}{1 + d\lambda^{-2} + e\lambda^{2}} \qquad (4)$$

gives excellent accuracy. This five-parameter equation falls in the class of "ratio of polynomials" commonly used in curve-fitting applications. It gives an excellent fit in this case because the general form of the data being fit by the equation is also a ratio of polynomials. For the scattering cross section data the best fit equation is:

$$\sigma\left(\times 10^{-28}\,\mathrm{cm}^2\right) = \frac{1.0455996 - 341.29061\lambda^{-2} - 0.90230850\lambda^{2}}{1 + 0.0027059889\lambda^{-2} - 85.968563\lambda^{2}} \qquad (5)$$

Equation (5) is accurate to better than 0.01% over the 250-850 nm range, and still better than 0.05% out to 1000 nm. In fact, this equation is accurate to better than 0.002% over the range 250-550 nm. Best fits for sea level at 45°N, and for MLO are:

τ_R (sea level, 45°N) =

$$0.0021520 \bullet \frac{1.0455996 - 341.29061\lambda^{-2} - 0.90230850\lambda^{2}}{1 + 0.0027059889\lambda^{-2} - 85.968563\lambda^{2}} \qquad (6)$$

and:

τ_R (MLO, 3.4 km, 680 mb) =

$$0.0014484 \bullet \frac{1.0455996 - 341.29061\lambda^{-2} - 0.90230850\lambda^{2}}{1 + 0.0027059889\lambda^{-2} - 85.968563\lambda^{2}} \qquad (7)$$

It should be noted that the leading coefficients in Equations (6) and (7) are the only difference from Equation (5). These numerical values represent the columnar density for the two cases.

Conclusion

For the most accurate calculation of Rayleigh optical depth it is recommended that users employ first principles and that *Peck and Reeder's* [1972] formula be used to estimate the refractive index of standard air. Next, *Penndorf's* [1957] method should be used to calculate the scattering cross section per molecule of air, taking into account the concentration of CO_2. In most cases the effects of water vapor may be neglected. The recommendations of *Bates* [1984] were used for the depolarization of air as a function of wavelength. Finally the Rayleigh optical depth should be calculated using the atmospheric pressure at the site of interest. Note the importance of taking into account variations of g. Curve fitting techniques are not necessarily recommended for estimating Rayleigh optical depth because the inaccuracies that arise can equal or even exceed other quantities being estimated, such as aerosol optical depth. However, for those who wish to use a simple equation and are satisfied with less accuracy, the techniques used to produce Equations (5)-(7) may be of interest.

In some calculations of optical depth it may be desired to take into account the vertical distribution of the composition of air, particularly CO_2 and H_2O. In this case a layer-by-layer calculation may be done using the estimated composition for each layer, and then the total optical depth may be estimated by summing the optical depths for all of the layers.

3.2.11. Data Processing

Shortwave and longwave radiation are monitored at the four CMDL baseline stations (BRW, SPO, MLO, SMO) and three other stations (Bermuda, Kwajalein, and BAO). Data are collected using Campbell Scientific data loggers. Meteorology data from the last three stations are also collected. Standard telephone lines are used to download the data from all stations except SPO, where the Internet is used. The telephone download intervals vary from station to station, but are typically 4 hours. The Internet transfer of data takes place once a day.

The Mauna Loa Automated Solar Dome data are collected on a PC by a custom program. These data are downloaded once a day to Boulder via the Internet. Multifilter, rotating shadowband radiometers (MFRSR) are operated at four sites: Bermuda, Kwajalein, BAO, and Boulder. Data from these stations are downloaded locally to a PC system and transferred over the Internet once a day to the Boulder server. UV radiation is monitored at three sites in Alaska: Nome, St. Paul, and Barrow. BSI instruments are used to gather data, and the data are stored on an on-site PC. These data are transferred to Boulder once a day over the Internet. In addition, a Norwegian Institute for Air Research instrument is also used to monitor UV at Barrow. Data from this instrument are stored locally on a PC and transferred to Boulder over the Internet. It should be noted that this transfer has to be initiated manually.

All data mentioned are permanently archived on a server in Boulder. Each morning plots of the previous day's data are

created and made available on local-access-only Web pages. Data listings are also available. With this information, scientists in the Boulder laboratory can review the data collection performance and make changes if problems occur.

The radiation data are edited using qualitative and quantitative methods developed in the laboratory. These data are available to researchers through the CMDL web pages. CMDL is a contributing member to the BSRN. Monthly files are made from Barrow, South Pole, Bermuda, Kwajalein and BAO data and sent to the BSRN archive in Zurich, Switzerland.

All-sky photographs are collected at three sites: Barrow, BAO, and Boulder. Images are taken at 1-min intervals and analyzed on a dedicated PC. Once every 15 minutes an image and a calculated cloud-cover image are transferred to one of the laboratory servers and made available on the Web.

3.3. REFERENCES

Albrecht, B., and S.K. Cox, Procedures for improving pyrgeometer performance, *J. Appl. Meteorol., 16,* 188-197, 1977.

Anderson, G.P., A. Berk, L.S. Bernstein, J.H. Chetwynd, P.K. Acharya, H. Dothe, M.W. Matthew, S.M. Adler-Golden, R.J. Ratkowski, G.W. Felde, J.A. Gardner, M.L. Hoke, S.C. Richtsmeier, B. Pukall, J. Mello, and L.S. Jeong, MODTRAN4: Radiative transfer modeling for remote sensing and atmospheric correction, *Proc., EUROPTO Remote Sensing Congress*, Florence, Italy, 1999.

Barrie, L.A., Occurrence and trends of pollution in the Arctic troposphere, in *Chemical Exchange Between the Atmosphere and Snow*, edited by E. W. Wolff and R. C. Bales, Springer-Verlag, Berlin, 1996.

Bates, D.R., Rayleigh scattering by air, *Planet. Space Sci., 32,* 785-790, 1984.

Bergin, M.H., E. Meyerson, J.E. Dibb, and P. Mayewski, Comparison of continuous aerosol measurements and ice core chemistry over a 10 year period at the South Pole, *Geophys. Res. Lett., 25,* 1189-1192, 1998.

Bird, R.E., and C. Riordan, Simple solar spectral model for direct and diffuse irradiance on horizontal and tilted planes at the earth's surface for cloudless atmospheres, *J. Appl. Meteorol., 25,* 87-97, 1986.

Bishop, J.K.B., W.B. Rossow, and E.G. Dutton, Surface solar irradiance from the International Satellite Cloud Climatology Project 1983-1991, *J. Geophys. Res., 102,* 6883-6910, 1997.

Bodhaine, B.A., Barrow surface aerosol: 1976-1987, *Atmos. Environ., 23,* 2357-2369, 1989.

Bodhaine, B.A., Aerosol absorption measurements at Barrow, Mauna Loa and South Pole, *J. Geophys. Res., 100,* 8967-8975, 1995.

Bodhaine, B.A., and J.J. DeLuisi, An aerosol climatology of Samoa, *J. Atmos. Chem., 3,* 107-122, 1985.

Bodhaine, B. A., and E. G. Dutton, A long-term decrease in Arctic Haze at Barrow, Alaska, *Geophys. Res. Lett., 20,* 947-950, 1993.

Bodhaine, B.A., B.G. Mendonca, J.M. Harris, and J.M. Miller, Seasonal variation in aerosols and atmospheric transmission at Mauna Loa Observatory, *J. Geophys. Res., 88,* 6769-6772, 1981.

Bodhaine, B.A., J.J. DeLuisi, J.M. Harris, P. Houmere, and S. Bauman, Aerosol measurements at the South Pole, *Tellus, 38B,* 223-235, 1986.

Bodhaine, B.A., J.J. De Luisi, J.M. Harris, P. Houmere, and S. Bauman, PIXE analysis of south pole aerosol, *Nucl. Instrum. Methods Phys. Res., B22,* 241-247, Elsevier, Holland, 1987.

Bodhaine, B.A., Harris, J.M., and J.A. Ogren, Aerosol optical properties at Mauna Loa Observatory: Long-range transport from Kuwait?, *Geophys. Res. Lett., 19,* 581-584, 1992.

Bodhaine, B.A., R.L. McKenzie, P.V. Johnston, D.J. Hofmann, E.G. Dutton, R.C. Schnell, J.E. Barnes, S.C. Ryan, and M. Kotkamp, New ultraviolet spectroradiometer measurements at Mauna Loa Observatory, *Geophys. Res. Lett., 23,* 2121-2124, 1996.

Bodhaine, B.A., E.G. Dutton, D.J. Hofmann, R.L. McKenzie, and P.V. Johnston, UV measurements at Mauna Loa: July 1995 to July 1996, *J. Geophys. Res., 102,* 19,265-19,273, 1997.

Bodhaine, B.A., E.G. Dutton, R.L. McKenzie, and P.V. Johnston, Calibrating broadband UV instruments: Ozone and solar zenith angle dependence, *J. Atmos. Oceanic Technol., 15,* 916-926, 1998.

Bodhaine, B.A., N.B. Wood, E.G. Dutton, and J.R. Slusser, On Rayleigh optical depth calculations, *J. Atmos. Oceanic Technol., 16,* 1854-1861, 1999.

Bond, T.C., T.L. Anderson, and D. Campbell, Calibration and intercomparison of filter-based measurements of visible light absorption by aerosols, *Aerosol Sci. Technol., 30,* 582-600, 1999.

Bucholtz, A., Rayleigh-scattering calculations for the terrestrial atmosphere, *Appl. Opt., 34,* 2765-2773, 1995.

Bush, B.C., F.P.J. Valero, A.S. Simpson, and L. Bignone, Characterization of thermal effects in pyranometers: A data correction algorithm for improved measurement of surface insolation, *J. Atmos. Oceanic Technol., 17,* 165-175, 1999.

Cess, R.D., et al., Absorption of solar radiation by clouds: Observations versus models, *Science, 267,* 496-499, 1995.

Charlson, R.J., S.E. Schwartz, J.M. Hales, R.D. Cess, J.A. Coakley, Jr., J.E. Hansen, and D.J. Hofmann, Climate forcing by anthropogenic aerosols, *Science, 255,* 423-430, 1992.

Dutton, E.G., An extended comparison between LOWTRAN7-computed and observed broadband thermal irradiances: Global extreme and intermediate surface conditions, *J. Atmos. Oceanic Technol., 10,* 326-336, 1993.

Dutton, E.G., and S.K. Cox, Tropospheric radiative forcing from El Chichón and Mt. Pinatubo: Theory and observations, Atmos. Science Paper No. 586, Colorado State University, Fort Collins, CO, 209 pp., 1995.

Dutton, E.G., and D.J. Endres, Date of snow melt at Barrow, Alaska, USA, *Arc. Alp. Res., 23,* 115-119, 1991.

Dutton, E.G., J.J. DeLuisi, and A.P. Austring, Interpretation of Mauna Loa atmospheric transmission relative to aerosols, using photometric precipitable water amounts, *J. Atmos. Chem., 3,* 53-68, 1985.

Dutton, E.G., P. Reddy, S. Ryan, and J.J. DeLuisi, Features and effects of aerosol optical depth observed at Mauna Loa, Hawaii: 1982-1992, *J. Geophys. Res., 99,* 8295-8306, 1994.

Dutton, E.G., J.J. Michalsky, T. Stoffel, B.W. Forgan, J. Hickey, D.W. Nelson, T.L. Alberta, and I. Reda, Measurement of broadband diffuse solar irradiance using current commercial instrumentation with a correction for thermal offset errors, *J. Ocean. Atmos. Technol.*, in press, 2000.

Edlén, B., The dispersion of standard air, *J. Opt. Soc. Amer., 43,* 339-344, 1953.

Edlén, B., The refractive index of air, *Metrologia, 2,* 71-80, 1966.

Ellis, H.T., and R.F. Pueschel, Solar radiation: Absence of air pollution trends at Mauna Loa, *Science, 172,* 845-846, 1971.

Foster, J.L., The significance of the date of snow disappearance on the arctic tundra as a possible indicator of climatic change, *Arc. Alp. Res., 21,* 60-70, 1989.

Foster, J.L., J.W. Winchester, and E.G. Dutton, The date of snow disappearance on the arctic tundra as determined from satellite, meteorological station and radiometric in situ observations, *IEEE Trans. Geosci. Remote Sens., 30,* 793-798, 1992.

Fröhlich, C., and G.E. Shaw, New determination of Rayleigh scattering in the terrestrial atmosphere, *Appl. Opt., 19,* 1773-1775, 1980.

Garrett, J.R., and A.J. Prata, Downwelling longwave fluxes at continental surfaces: A comparison of observations with GCM simulations and implications for the global land-surface radiation budget, *J. Clim., 9,* 646-655, 1996.

Harris, J.M., and J.D.W. Kahl, Analysis of 10-day isentropic flow patterns for Barrow, Alaska: 1985-1992, *J. Geophys. Res., 99,* 25,845-25,855, 1994.

Hofmann, D.J., J.T. Peterson, and R.M. Rosson (Eds.), *Climate Monitoring and Diagnostics Laboratory No. 23 Summary Report 1994-1995,* NOAA Environmental Research Laboratories, Boulder, CO, 161 pp., 1996.

Hofmann, D.J., J.T. Peterson, and R.M. Rosson (Eds.), *Climate Monitoring and Diagnostics Laboratory No. 24 Summary Report 1996-1997*, NOAA Environmental Research Laboratories, Boulder, CO, 166 pp., 1998.

Hoyt, D.V., A redetermination of the Rayleigh optical depth and its application to selected solar radiation problems, *J. Appl. Meteorol., 16*, 432-436, 1977.

List, R.J., *Smithsonian Meteorological Tables*, Smithsonian, Washington, D.C., 527 pp., 1968.

Madronich, S., The atmosphere and UV-B radiation at ground level, in *Environmental UV Photobiology*, edited by A. R. Young et al., Plenum Press, New York, 1-39, 1993.

McCartney, E.J., *Optics of the Atmosphere*, Wiley, New York, 408 pp., 1976.

McInnes, L.M., M.H. Bergin, J.A. Ogren, and S.E. Schwartz, Differences in hygroscopic growth between marine and anthropogenic aerosols, *Geophys. Res. Lett., 25*, 513-516, 1998.

McKenzie, R.L., P.V. Johnston, M. Kotkamp, A. Bittar, and J.D. Hamlin, Solar ultraviolet spectroradiometry in New Zealand: Instrumentation and sample results from 1990, *Appl. Opt., 31*, 6501-6509, 1992.

McKinlay, A.F., and B.L. Diffey, A reference action spectrum for ultraviolet induced erythema in human skin, *J. Int. Comm. Illum., 6*, 17-22, 1987.

Michalsky, J., E. Dutton, D. Nelson, M. Rubes, T. Stoffel, M. Wesley, M. Splitt, and J. DeLuisi, Optimal measurement of surface shortwave irradiance using current instrumentation, *J. Atmos. Oceanic Technol., 16*, 55-69, 1999.

National Research Council (NRC), *Aerosol Radiative Forcing and Climatic Change*, National Academy Press, Washington, D.C., 161 pp., 1996.

Nemesure, S., R.D. Cess, E.G. Dutton, J.J. DeLuisi, Z. Li, and H.G. Leighton, Impact of the shortwave radiation budget of the surface-atmosphere system for snow-covered surfaces, *J. Clim., 7*, 579-585, 1994.

Ogren, J.A., A systematic approach to in situ observations of aerosol properties, In *Aerosol Forcing of Climate*, edited by R.J. Charlson and J. Heintzenberg, 215-226, John Wiley, 1995.

Ohmura, A., et al., Baseline Surface Radiation Network (BSRN/WCRP): New precision radiometry for climate research, *Bull. Amer. Meteorol. Soc., 79*, 2115-2136, 1998.

Peck, E.R., and K. Reeder, Dispersion of air, *J. Opt. Soc. Amer., 62*, 958-962, 1972.

Penndorf, R., Tables of the refractive index for standard air and the Rayleigh scattering coefficient for the spectral region between 0.2 and 20.0 μ and their application to atmospheric optics, *J. Opt. Soc. Amer., 47*, 176-182, 1957.

Philipona, R., C. Fröhlich, and C. Betz, Characterization of pyrgeometers and the accuracy of atmospheric long-wave radiation measurements, *Appl. Opt., 34*, 1598-1605, 1995.

Philipona, R.,C., et al., The BSRN pyrgeometer round-robin calibration experiment, *J. Atmos. Oceanic Technol. 15*, 687-696, 1998.

Quakenbush, T.K., and B.A. Bodhaine, Surface aerosols at the Barrow GMCC observatory: Data from 1976 through 1985, *NOAA Data Rep. ERL ARL-10*, 230 pp., NOAA Air Resources Laboratory, Silver Spring, MD, 1986.

Radke, L., C.A. Brock, R.J. Ferek, and D.J. Coffman, Summertime Arctic hazes, abstract, presented at the American Geophysical Union Fall Annual Meeting, San Francisco, December 3-7, *Eos. Trans. AGU 71(43), Fall Meet. Suppl., 1264*, 1990.

Stephens, G.L., *Remote sensing of the lower atmosphere*, Oxford, New York, 523 pp., 1994.

Stone, R.S., Variations in western arctic temperatures in response to cloud-radiative and synoptic-scale influences, *J. Geophys. Res., 102*, 21,769-21,776, 1997.

Stone, R., T. Mefford, E. Dutton, D. Longenecker, B. Halter, and D. Endres, Surface radiation and meteorological measurements: January 1992 to December 1994, *NOAA Data Rep. ERL-CMDL-11*, Environ. Res. Lab., Boulder, CO, 81 pp., 1996.

Thompson, D.W.J., and J.M. Wallace, The arctic oscillation signature in the wintertime geopotential height and temperature fields, *Geophys. Res. Lett., 25*, 1297-1300, 1998.

van de Hulst, H.C., *Light Scattering by Small Particles*, Wiley, New York, 470 pp., 1957.

Whitlock, C.H., et al., First global WCRP shortwave surface radiation budget dataset, *Bull. Amer. Meteorol. Soc., 76*, 905-922, 1995.

Young, A.T., Revised depolarization corrections for atmospheric extinction, *Appl. Opt., 19*, 427-428, 1980.

Young, A.T., On the Rayleigh-scattering optical depth of the atmosphere, *J. Appl. Meteorol., 20*, 328-330, 1981.

4. Ozone and Water Vapor

S. OLTMANS, J. BARNES, M. CLARK, R. EVANS, J. HARRIS (EDITOR), B. JOHNSON, G. CARBAUGH, M. O'NEILL, D. QUINCY, D. SHERMAN, H. VÖMEL, AND E. RICE

4.1. CONTINUING PROGRAMS

4.1.1. TOTAL OZONE OBSERVATIONS

Total ozone observations continued throughout 1998 and 1999 at 15 of the 16 stations that comprise the U.S. Dobson spectrophotometer network (Table 4.1). Of the 16 stations, CMDL personnel operated 5, NOAA National Weather Service (NWS) operated 5, 2 are university stations, and 4 are foreign cooperative stations. All stations are either fully or semi-automated. In addition, a Brewer spectrophotometer was operated on a nearly continuous basis at Boulder.

The Peruvian station became operational in the middle of 1999 when the instrument was installed at the new Global Atmospheric Watch station at Marcapomacocha (11.401°S, 76.324°W, 4513 m above sea level). The site does not have reliable power, and few observations were made. The instrument was sent to Buenos Aires in December 1999 for a calibration check against the Dobson secondary standard D065. The shelter for the Dobson instrument at the CMDL Samoa Observatory, American Samoa (SMO) was replaced in December 1998. Observations at Tallahassee are continuing at Florida State University until the new NWS office is completed in January 2002. The station in Haute Provence, France, was struck by lightning in October 1999 and was not operational by the end of the year.

Provisional daily total ozone amounts applicable to local apparent noon for the stations listed in Table 4.1 were archived at the World Ozone and Ultraviolet Data Center (WOUDC), 4905 Dufferin Street, Ontario M3H 5T4, Canada, in Ozone Data for the World. Table 4.2 lists the monthly mean total ozone amounts measured at the various stations for 1998 and 1999.

4.1.2. UMKEHR OBSERVATIONS

Umkehr observations made with the Automated Dobson Network instruments continued in 1998 and 1999 at Boulder, Colorado; Haute Provence, France; Lauder, New Zealand; CMDL Mauna Loa Observatory, Hawaii (MLO); Perth, Western Australia; and at the Geophysical Institute, University of Alaska. Data processing has been completed for all stations through December 1998, and the vertical profiles are available from WOUDC. Processing has also been completed through November 1999 for Boulder, Lauder, Perth, and the Geophysical Institute. Problems at MLO and Haute Provence have yet to be resolved.

Preliminary results from a number of Umkehr "intercomparisons" were presented at the Meteorological Service of Canada (MSC)-WOUDC Umkehr Meeting, November 17-18, 1999, in Toronto, Canada. The results showed that, in general, instruments well calibrated in total ozone mode agreed to within 3-5% of the standard in Umkehr layers 4, 5, and 6 and to within 10% in layers 3, 7, 8, and 9. However, there appeared to be systematic differences between some of the instruments. Further investigation will to be done in an attempt to determine the possible causes of these differences.

4.1.3. CALIBRATION OF DOBSON SPECTROPHOTOMETERS

Seven Dobson ozone spectrophotometers in the CMDL network, as well as 20 others (Table 4.3), were calibrated during 1998 and 1999. Table 4.3 lists the calibration difference expressed as a percent ozone difference. This percent difference

TABLE 4.1. U.S. Dobson Ozone Spectrophotometer Station Network for 1998-1999

Station	Period of Record	Instrument No.	Agency
Bismarck, North Dakota	Jan. 1, 1963-present	33	NOAA
Caribou, Maine	Jan. 1, 1963-present	34	NOAA
Wallops Is., Virginia	July 1, 1967-present	38	NOAA; NASA
SMO	Dec. 19, 1975-present	42	NOAA
Tallahassee, Florida	May 2, 1964-Nov. 30, 1989; Nov. 1, 1992-present	58	NOAA; Florida State University
Boulder, Colorado	Sept. 1, 1966-present	61	NOAA
Fairbanks, Alaska	March 6, 1984-present	63	NOAA; University of Alaska
Lauder, New Zealand	Jan. 29, 1987-present	72	NOAA; NIWA
MLO	Jan. 2, 1964-present	76	NOAA
Nashville, Tennessee	Jan. 2, 1963-present	79	NOAA
Perth, Australia	July 30, 1984-present	81	NOAA; Australian Bureau Meteorology
SPO	Nov. 17, 1961-present	82	NOAA
Haute Provence, France	Sept. 2, 1983-present	85	NOAA; CNRS
Huancayo, Peru	Feb. 14, 1964-Dec. 31, 1992	87	NOAA; IGP
BRW	June 6, 1986-present	91	NOAA
Fresno, California	June 22, 1983-March 13, 1995	94	NOAA
Hanford, California	March 15, 1995-present	94	NOAA

TABLE 4.2. Provisional 1998 and 1999 Monthly Mean Total Ozone Amounts (DU)

Station	Jan.	Feb.	March	April	May	June	July	Aug.	Sept.	Oct.	Nov.	Dec.
					1998							
Bismarck, North Dakota	340	355	343	363	347	334	300	288	297	283	276	328
Caribou, Maine	361	360	[390]	408	[374]	[362]	339	329	318	-	310	334
Wallops Is., Virginia	313	318	359	357	361	332	314	309	295	300	270	291
SMO	233	234	235	246	247	247	256	258	262	267	262	[268]
Tallahassee, Florida	[283]	[263]	312	311	290	-	-	-	-	[261]	270	[255]
Boulder, Colorado	326	346	349	372	328	321	302	294	279	280	264	286
Fairbanks, Alaska	-	[423]	421	430	[387]	363	339	[324]	-	-	-	-
Lauder, New Zealand	275	263	268	267	283	312	341	342	351	367	320	290
MLO	229	245	265	276	282	281	271	263	266	255	246	236
Nashville, Tennessee	317	314	336	340	337	308	303	301	284	268	263	271
Perth, Australia	265	263	266	271	263	289	292	296	320	321	302	284
SPO	267	264	-	-	[266]	[260]	[262]	[243]	-	122	162	252
Haute Provence, France	321	314	[338]	393	363	335	320	316	311	298	292	293
Huancayo, Peru	Not in operation											
BRW	-	-	446	444	409	357	325	321	323	[316]	-	-
Hanford, California	303	332	327	355	356	333	322	-	-	286	268	280
					1999							
Bismarck, North Dakota	340	355	343	363	347	334	300	288	297	283	276	328
Caribou, Maine	[344]	341	376	386	354	342	-	[360]	[284]	-	[271]	[331]
Wallops Is., Virginia	299	306	330	341	351	324	312	311	[278]	285	286	299
SMO	257	254	244	240	245	242	248	249	[257]	261	257	244
Tallahassee, Florida	[264]	[264]	[298]	[271]	-	[306]	[288]	287	-	-	-	-
Boulder, Colorado	291	313	313	332	335	317	301	296	296	281	266	309
Fairbanks, Alaska	-	-	-	[433]	376	[337]	317	293	316	[326]	[336]	-
Lauder, New Zealand	264	253	257	274	266	292	312	332	325	340	327	295
MLO	235	232	261	287	278	272	267	264	265	258	257	250
Nashville, Tennessee	292	307	312	306	-	322	305	301	296	279	264	290
Perth, Australia	263	263	263	262	265	276	273	290	318	319	311	283
SPO	257	253	-	[278]	[261]	[246]	[248]	[221]	-	122	164	258
Haute Provence, France	276	327	360	371	340	332	325	302	294	[294]	-	-
Huancayo, Peru	Not in operation											
BRW	-	-	[451]	420	365	319	311	277	292	-	-	-
Hanford, California	273	291	327	355	322	317	297	297	291	273	259	295

Monthly mean ozone values in square brackets are derived from observations made on fewer than 10 days per month.

is between ozone calculated from the test and the standard instrument measurements with the most common observation type averaged from μ (optical path length through the atmosphere calculated from solar zenith angle) values of 1, 2, and 3, and a total ozone value of 300 Dobson Units (DU), before any repair or calibration adjustment is made. The table also lists the place of the calibration and the standard instrument used.

CMDL participated in international Dobson spectrophotometer calibrations at the WMO Region VI (Europe) Regional Dobson Calibration Center at Hohenpeissenberg, Germany, and the Swiss Meteorological Institute (SMI) Lichklimatisches Observatorium (LKO) at Arosa, Switzerland, in July-August 1999, and the Argentine Servicio Meteorológico Nacional (SMN) Buenos Aires Observatory in November-December 1999 as part of its role as the World Center for Dobson Calibrations. Instruments for Lerwick, Scotland, Buenos Aires, Argentina, and the Japanese regional standard Dobson instrument were calibrated in Boulder during this period.

4.1.4. Surface Ozone

Observations of surface ozone continued at each of the four baseline observatories, as well as Niwot Ridge, Colorado; Westman Islands, Iceland; and Arrival Heights, Antarctica. In November 1999 a TEI Model 49C ozone analyzer was added at the CMDL South Pole Observatory, Antarctica (SPO), and it will operate alongside the Dasibi 1003AH analyzer. In mid-1999 the Dasibi 1003AH analyzer at SMO malfunctioned and could not be repaired. It ran alongside the TEI Model 49 for nearly 2 years. The operation of the Dasibi was discontinued temporarily but will be resumed when the instrument is repaired. Data from the CMDL Barrow, Alaska, Observatory (BRW), MLO, and SPO have been processed through 1999. The monthly mean data for the three sites are given for 1998 and 1999 (Table 4.4). For MLO the average is based on downslope (10-18 Universal Time Coordinated (UTC)) data. The data system at SMO experienced a number of outages after the measurements were restarted in 1997 following about a 1-yr gap. Although the data were recorded on a backup chart recorder, resources have not been available to process these data and bring the record up to date.

At Arrival Heights, Antarctica (near McMurdo Station), a surface ozone analyzer was installed near the end of 1996. This instrument is operated in cooperation with the National Institute for Water and Atmospheric Research, New Zealand (NIWA). The data for 1996-1999 for this site are included in Table 4.4. In Figure 4.1 the seasonal behavior for 1997-1999 is compared to

TABLE 4.3. Dobson Ozone Spectrophotometers Calibrated in 1998-1999

Station	Instrument Number	Previous Calibration Date	Calibration Correction (%)	Standard Number	Place
		1998			
Tallahassee, Florida	58	Sept. 23, 1994	+1.2	65	Boulder, Colorado
Fairbanks, Alaska	63	May 29, 1992	+0.4	65	Boulder, Colorado
Hanford, California	94	Sept. 15, 1994	+0.6	65	Boulder, Colorado
Buenos Aires, Argentina	97	June 1994	N/A*	83	Boulder, Colorado
Tsukuba, Japan	116	July 1995	-2.0	65	Boulder, Colorado
		1999			
Wallops Island, Virginia	38	April 27, 1995	0.0	83	Boulder, Colorado
Barrow, Alaska	91	Sept. 15, 1994	+0.5	83	Boulder, Colorado
Armenia (Proposed)	44	N/A	N/A	65	Hohenpeissenberg, Germany
Camborne, United Kingdom	41	July 30, 1995	+0.6	65	LKO Arosa
Sestola, Italy	48	July 25, 1995	-0.5	65	LKO Arosa
Bordeaux, France	49	July 30, 1995	+0.2	65	LKO Arosa
Oslo, Norway	56	June 22, 1994	-0.9	65	LKO Arosa
Arosa, Switzerland	62	1995	+0.9	65	LKO Arosa
Hohenpeissenberg, Germany	64	July 22, 1997	+0.4	65	LKO Arosa
Aswan, Egypt	69	May 25, 1993	+2.5	65	LKO Arosa
Hradec Kralove, Czech Republic	74	July 22, 1997	-0.3	65	LKO Arosa
L'OHP, France	85	July 10, 1992	+1.5	65	LKO Arosa
Arosa, Switzerland	101	1995	+1.3	65	LKO Arosa
Moscow, Russia	107	July 30, 1995	-0.3	65	LKO Arosa
El Arenosillo, Spain	120	June 22, 1994	+1.6	65	LKO Arosa
Marcapomacocha, Peru	87	June 22, 1994	+0.7	65	Buenos Aires, Argentina
Buenos Aires, Argentina	97	June 7, 1998	0.0	65	Buenos Aires, Argentina
Marambio, Antarctica (Argentina)	99	Aug. 31, 1992	+2.5	65	Buenos Aires, Argentina
Cachoeira Paulista, Brazil	114	Nov. 24, 1980 referenced to 1995	+0.1	65	Buenos Aires, Argentina
Ushuaia, Argentina	131	June 22, 1994	+0.2	65	Buenos Aires, Argentina
Comodoro Rivadavia, Argentina	133	April 12, 1995	-0.5	65	Buenos Aires, Argentina
Salto, Uruguay	134	April 12, 1995	-0.8	65	Buenos Aires, Argentina

*Instrument damaged

TABLE 4.4. Monthly Mean Surface Ozone Mixing Ratios (ppbv)

Year	Jan.	Feb.	March	April	May	June	July	Aug.	Sept.	Oct.	Nov.	Dec.
						BRW						
1998	33.3	28.9	22.7	25.3	21.6	19.2	21.6	18.8	21.2	25.1	27.5	24.8
1999	23.4	21.9	9.3	6.3								
						MLO (nighttime only)						
1998	49.0	47.5	55.4	57.7	57.0	45.3	46.4	39.7	46.7	37.1	35.9	43.2
1999												
						SPO						
1998	23.5	23.7	22.2	25.5	28.7	32.4	33.3	33.6	33.0	31.4	32.6	29.5
1999	26.9	20.1	21.1	25.1	29.3	32.9	36.3	37.0	35.2	31.3	32.3	29.6
						Arrival Heights, Antarctica						
1996												15.5
1997	13.7	17.1	21.9	26.4	30.3	33.0	34.4	32.6	30.4	28.0	23.5	14.5
1998	9.2	14.5	17.9	22.2	26.0	29.1	30.5	31.2	29.1	25.6	18.0	17.4
1999	15.9	16.5	19.3	24.7	27.7	32.5	33.6	32.6	30.0	27.6	20.9	15.7

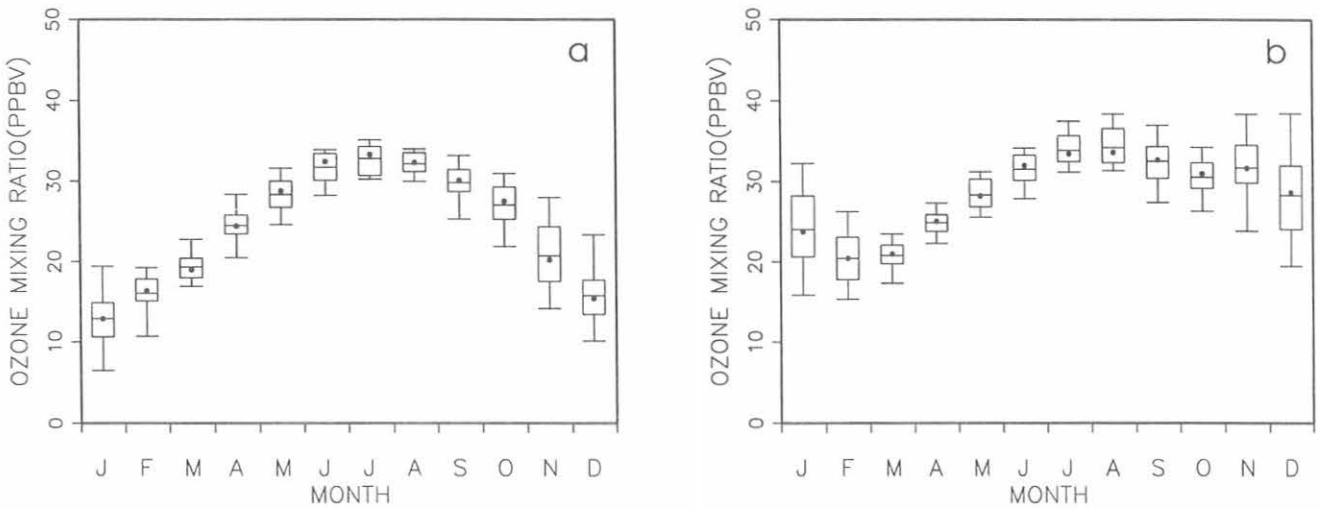

Fig. 4.1. Seasonal variation of surface ozone mixing ratio at (a) Arrival Heights, Antarctica, and (b) SPO. The solid dot is the mean; the horizontal bar is the median; the box is the inner 50th percentile; and the "whiskers" are the inner 90th percentile of the data. The data are for the period 1997-1999.

that for SPO. The winter maximum in ozone at each site is almost identical in magnitude, but the summer minimum at Arrival Heights is much deeper. At Arrival Heights the minimum is reached in January, while at SPO it is in February. The depth and timing of the minimum at these antarctic sites likely reflects the photochemical loss mechanism in the southern hemisphere in which ozone is lost in the formation of the hydroxyl radical where nitrogen oxide (NO_x) concentrations are low.

4.1.5. OZONESONDES

Table 4.5 summarizes the 1998-1999 CMDL ozonesonde projects. Nine sites, supplied by CMDL, launched one ozonesonde per week. The longest continuous ozonesonde records (>12 years data) are from Boulder, Colorado; MLO; and SPO. One United States site at Trinidad Head, California (August 1997), and the newest site at the University of Alabama-Huntsville (April 1999) are part of the NOAA "Health of the Atmosphere" Air Quality Research Program. These two sites and the Boulder site, represent a broad longitudinal transect across the United States that can be helpful in identifying the impact of anthropogenic emissions on tropospheric ozone levels during the general west-to-east flow across the continental United States.

SMO began launching weekly ozonesondes again in August 1995 as part of the Pacific Exploratory Mission in the Tropics

TABLE 4.5. Summary of 1998-1999 Ozonesonde Projects

	1998		1999		
Ozonesonde Sites	Totals	Dates	Totals	Dates	Project
			Station (weekly)		
Boulder, Colorado	60	Full year	51	Full year	NOAA long term
MLO	44	Full year	47	Full year	NOAA long term
SPO	65	Full year	78	Full year	NOAA long term
Tahiti	33	Jan. 15-Nov. 24	54	Full year	PEM Tropics/SHADOZ
Fiji	42	Full year	53	Full year	PEM Tropics/SHADOZ
SMO	43	Full year	53	Full year	PEM Tropics/SHADOZ
Trinidad Head, California	47	Full year	44	Full year	NOAA "Health of the Atmosphere"
Huntsville, Alabama	0		30	April 20-Dec. 31	NOAA "Health of the Atmosphere"
Galapagos	19	March 25-Dec. 31	58	Full year	SOWER/SHADOZ
			Intensives (~daily)		
Old Hickory, Tennessee	0		30	June 14-July 15	Southern Oxidant Study
Kaashidhoo, Maldives	0		57	Jan. 27-March 28	CMDL/NASA/SCRIPPS
			Ship Cruise		
Atlantic Ocean	0		35	Jan. 15-May 10	SHADOZ NOAA ship *Ronald H. Brown*

PEM Tropics - Pacific Exploratory Mission in the Tropics (a global tropospheric experiment)
SHADOZ - Southern Hemisphere Additional Ozonesondes
SOWER - Soundings of Ozone and Water in the Equatorial Region

(PEM Tropics). The PEM Tropics sites also included Papeete, Tahiti (July 1995) and Suva, Fiji (February 1997). The PEM Tropics A and B missions were designed to collect baseline data from aircraft platforms and ozonesondes in the South Pacific Basin to aid in the determination of the controlling factors related to the oxidizing power of the troposphere. The PEM Tropics missions ended in late 1999. However, Fiji and SMO continued operation under the Southern Hemisphere Additional Ozonesondes (SHADOZ) campaign. This project uses ozonesonde profile data to validate tropospheric ozone derived from satellite measurements in the tropics and subtropics [*Hudson and Thompson*, 1998]. Additional SHADOZ ozonesondes were launched at San Cristóbal, Galapagos, an island in the eastern equatorial Pacific (0.9°N, 110.0°W), for Special Observations of Ozone and Water in the Equatorial Region (SOWER), and on the NOAA ship *Ronald H. Brown*. The ship cruise went from Norfolk, Virgina, to Capetown, South Africa, and finally to Mauritius (east of Madagascar).

The third intensive field campaign for the Southern Oxidants Study (SOS) was conducted in the Nashville, Tennessee, area from June 15 to July 15, 1999. Daily ozonesondes were launched from Old Hickory, Tennessee. The SOS project included several research groups studying the formation of ozone in the troposphere and evaluating strategies to reduce pollution precursors leading to the high ozone levels often observed in the southern United States in the spring and summer months.

Daily ozonesonde measurements were flown at Kaashidhoo Observatory in the Maldives during early 1999 in a joint project with CMDL, National Aeronautics and Space Administration (NASA) Goddard, and the Center for Clouds, Chemistry and Climate, Scripps Institution of Oceanography (SIO) as part of the Indian Ocean Experiment (INDOEX). And finally, daily ozonesondes were flown in Boulder for 5 days in June of 1998 to provide ozone profiles for the International Photolysis Frequency Measurement and Modeling Intercomparison.

SPO is a key CMDL ozonesonde site. The continuous data set, beginning in 1986, characterizes the typical development of the yearly ozone hole over Antarctica. First signs of the ozone hole recovery will be observed by comparing future ozonesonde data to the long-term south pole record [*Hofmann et. al.*, 1997]. Figure 4.2 shows the severe depletion that occurred in both 1998 and 1999, especially in the 14 to 21-km layer. Total ozone dropped by 64%, reaching 95 DU in 1998 and 90 DU in 1999. Table 4.6 lists the minimum total ozone values and the date on which they occurred since 1986.

4.1.6. Atmospheric Water Vapor

Water vapor measurements using balloonborne, frostpoint hygrometers continued in Boulder, Colorado. In addition, water vapor soundings were done from Kiruna, Sweden, during November 1999 as part of the NASA Stratospheric Aerosol and

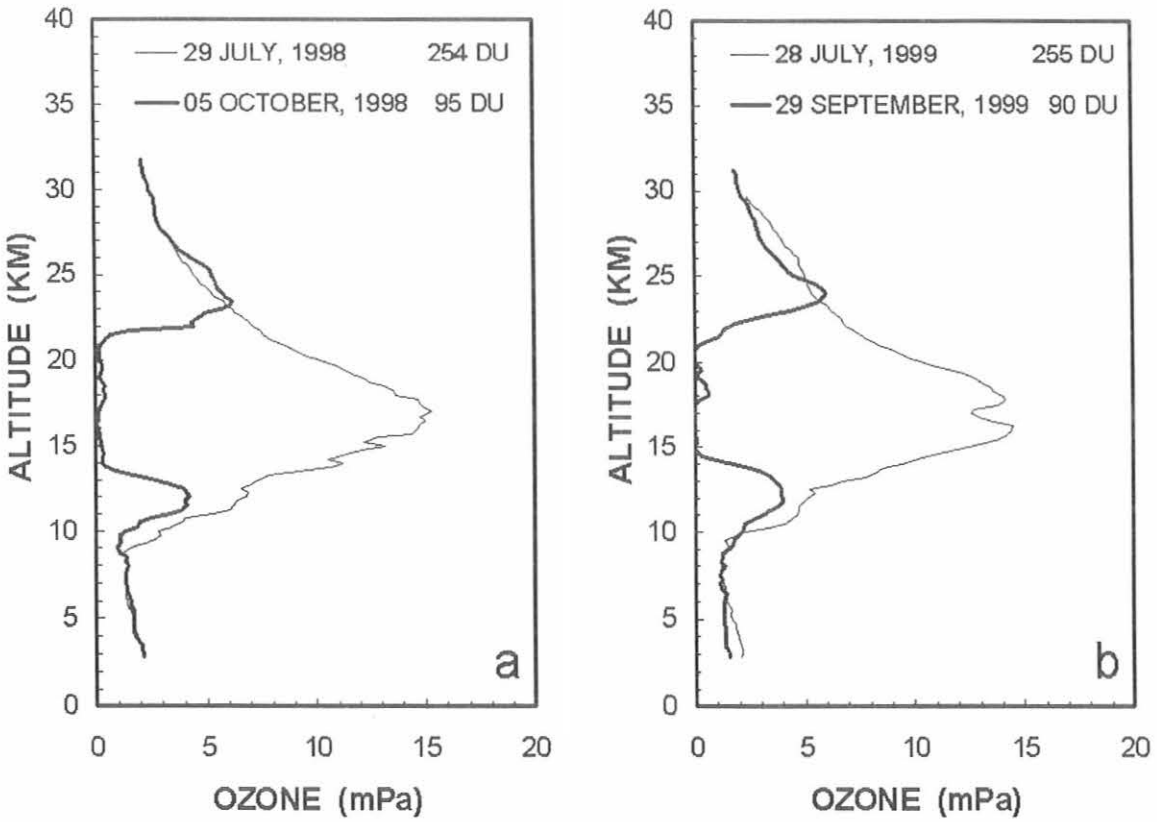

Fig. 4.2. Vertical profiles of ozone partial pressure in millipascals (mPa) at the South Pole Observatory during (a) 1998 and (b) 1999. The thin line represents the pre-depletion profile. The thick line is the profile observed during the minimum in total ozone.

TABLE 4.6. Summary of the Minimum Total Ozone Measured at SPO* and the Date of the Ozonesonde Flight

Year	Date	Total Ozone	Year	Date	Total Ozone
1986	Oct. 7	140	1993	Oct. 6	89
1987	Oct. 9	115	1994	Oct. 5	102
1988	Oct. 10	185	1995	Oct. 5	93
1989	Oct. 9	131	1996	Oct. 6	114
1990	Oct. 7	130	1997	Oct. 8	117
1991	Oct. 7	128	1998	Oct. 5	95
1992	Oct. 11	100	1999	Sept. 29	90

*The uncertainty is ±5 Dobson Units.

Gas Experiment (SAGE) III Ozone Loss and Validation Experiment (SOLVE) campaign. The long-term record of stratospheric water vapor measurements at Boulder continues to show an increase of about 1% yr^{-1} as illustrated in the time series for the 20 to 22-km layer (Figure 4.3). This layer is typical of the increase seen at all altitudes above about 16 km over Boulder. An earlier set of water vapor soundings made in Washington, D.C., from 1964-1977 (Figure 4.4) also shows an increase of about the same magnitude as seen at Boulder, suggesting that the increase in stratospheric water vapor has been occurring for several decades.

4.1.7. Atmospheric Transport

The CMDL isentropic trajectory model continues to be a valuable tool for diagnosis of the origins of air parcels measured at the CMDL observatories, as well as those measured on ships, aircraft, and at miscellaneous experimental sites. The atmospheric transport project in CMDL is designed for a high volume of output. Improvements made over 1998 and 1999 enhanced this capability. The standard gridded meteorological data used as input to the CMDL trajectory model come from the European Centre for Medium Range Weather Forecasts (ECMWF) through the U.S. National Center for Atmospheric Research (NCAR). These data have become available in a more timely fashion, reducing the lag time of the data to about 1 month. Another factor that has greatly improved the speed at which trajectories can be produced is accessing the input data in direct access mode on disk rather than accessing these data sequentially from magnetic tape. Fifteen years of meteorological data (1985-1999) are now readily available on disk, eliminating the need for magnetic tapes. The trajectory program is automated so that obtaining large volumes of trajectories (e.g., for a site climatology) is straightforward.

The trajectory input data are fairly coarse because of storage and processing constraints. The data have a horizontal resolution of 2.5 degrees latitude × 2.5 degrees longitude, a vertical resolution of 14 levels (from surface to 10 hPa) and a temporal

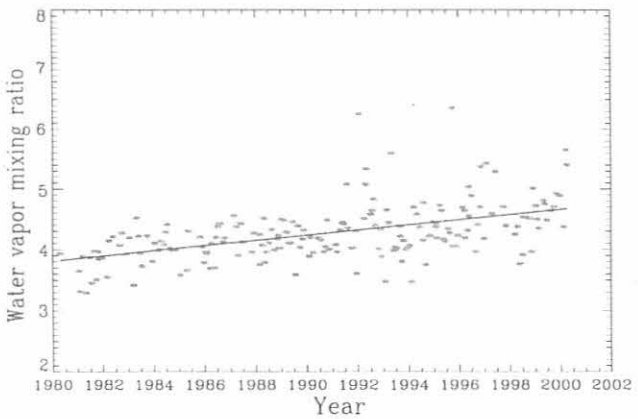

Fig. 4.3. Water vapor mixing ratios (ppmv) for the 20-22 km layer over Boulder, Colorado. The solid line is a linear fit to the individual sounding layer average mixing ratios. The trend value is 1.0 ± 0.2% yr^{-1}, and the error is for the 95% significance level.

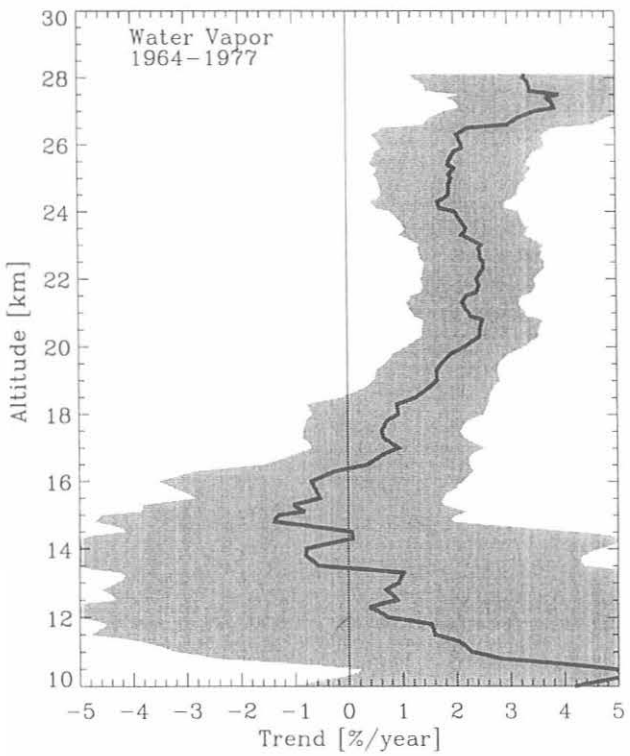

Fig. 4.4. The linear trend in percent per year as a function of altitude for the water vapor mixing ratio over Washington, D.C., during 1964-1977. The shaded area represents the 95% significance level (i.e., if the shaded area intersects the zero line, the trend is not significantly different from zero).

resolution of 12 hours. Trajectories produced with these data are not suitable for diagnosis of mesoscale transport, but rather they track large-scale regional air flow. The gridded winds are interpolated kinematically to isentropic surfaces with the specification of arrival height, arrival pressure, or potential temperature. The method of wind interpolation to the isentropic surface is detailed in section 3.13.4 of Summary Report No. 11 [*Harris and Bodhaine*, 1983]

Aside from the standard ECMWF trajectories, trajectories are provided in real-time on the trajectory web site (http://www.cmdl.noaa.gov/ozwv/traj). These trajectories are made with meteorological data downloaded twice daily from the National Centers for Environmental Prediction (NCEP). The differences between the ECMWF and NCEP data sets are usually slight, but to avoid confusion, it is recommended that the real-time trajectories be used only as a first look. Trajectories for publication should be based on the ECMWF data.

Trajectories have been used to investigate the relationships of trace gas and aerosol measurements to their sources and sinks. Published transport studies for each of the four CMDL observatories are cited in section 4.1.7 of CMDL Summary Report No. 24 [*Hofmann et al.*, 1998]. A special project, in section 4.2.3 of this report, presents some highlights of a new transport study for BRW that was recently completed. Section 4.2.4 presents an analysis of O_3 and CO at Cape Point Observatory that also uses trajectories.

4.1.8. Stratospheric Aerosols

At MLO in early 1998, both the ruby and Nd:YAG (neodymium doped yttrium aluminum garnet type laser) lidars were moved into the new Network for the Detection of Stratospheric Change (NDSC) building. The NDSC has three rooms devoted to the CMDL lidar program that are used as a control room, a laser room, and a telescope room. The entire optical structure was redesigned to house the lasers and the telescopes more compactly. The optical rails extend through the wall to rigidly tie the telescopes and lasers together. Separating the telescopes from the lasers reduced the signal-induced noise on some of the detectors. The new facilities are far better for maintaining the equipment and developing new measurements. The move was accomplished in about 2 weeks because the hatches were installed previously. The Nd:YAG laser required a service call to get the power back to specification.

The ruby lidar signal strength was severely reduced in the new configuration. After exchanging several of the components, the signal was still too weak for reasonable data. Since the backscatter at 694 nm can be interpolated from the Nd:YAG backscatter measured at 532 nm and 1064 nm more accurately then the actual ruby lidar measurement, it was decided to end the ruby lidar measurement. Over 1 year (44 measurements) of overlapping data showed the interpolated and measured 694 nm backscatter agreed to a few percent, well within the 20% error of the ruby lidar data.

A grant from the NOAA National Environmental Satellite, Data, and Information Service (NESDIS) was received for the rescue of the ruby lidar database. Although the integrated aerosol data were available, the individual profiles (over 700 measurements) were in various formats and could not be analyzed consistently. The database will be standardized and errors will be estimated. The data can then be submitted to the NDSC archive for use by other researchers. Interactive Data Language (IDL) software was acquired under the grant to use for the lidar temperature analysis. A temperature analysis by the Jet Propulsion Laboratory (JPL) lidar group, written in IDL and well researched, will be used for the reanalysis of the temperature record.

The background conditions in the stratospheric aerosol [*Barnes and Hofmann*, 1997] that began in 1996 at MLO continued through 1999. Figure 4.5 shows (a) the quasi-biennial oscillation (QBO) winds, (b) the backscatter from the upper part of the stratospheric aerosol layer (25-33 km), and (c) the backscatter from the total stratospheric layer (15.8-33 km). The total layer is dominated by the 16 to 22-km region.

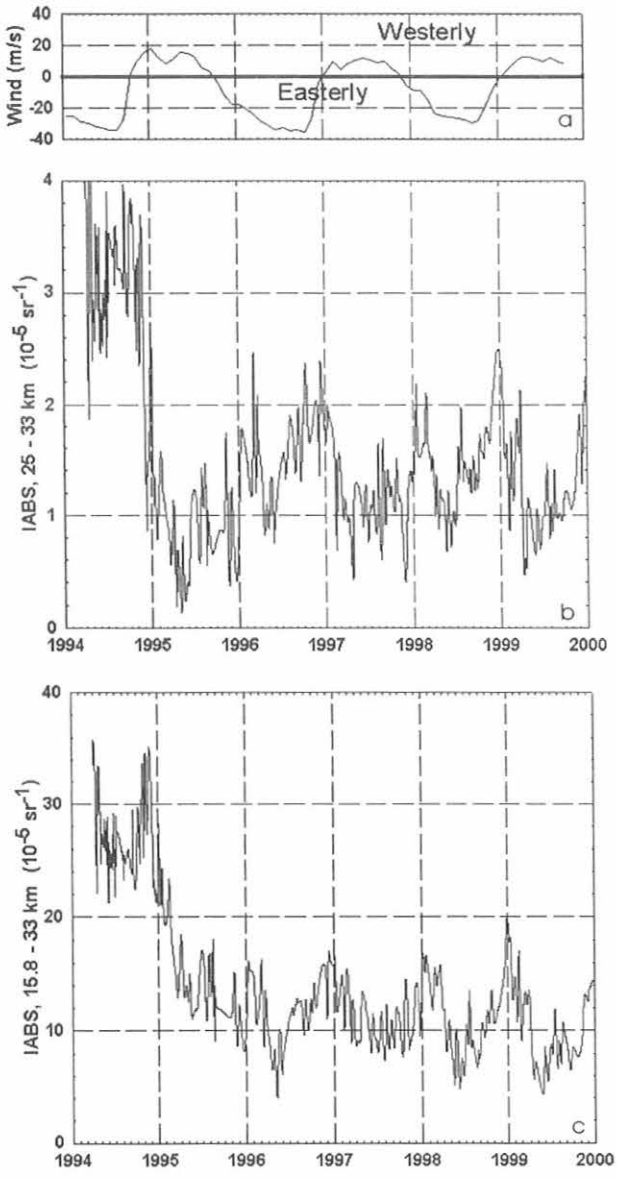

Fig. 4.5. (a) Quasi-biennial oscillation (QBO) winds (30 hPa at Singapore), and Integrated Aerosol Backscatter (IABS) from (b) the upper part of the stratospheric aerosol layer (25 to 33 km), and from (c) the total stratospheric layer (15.8 to 33 km) observed over MLO.

The 4 years (1996-1999) show a clear annual cycle in the total layer, peaking in the winter. The winter peak coincides with the doubling of the vertical transport of air through the tropical tropopause [*Rosenlof and Holton*, 1993] during the winter compared to the summer months. It is not clear if the winter peak in the aerosols is consistent with the stronger vertical transport. Although this would mean that more sulfur-rich air would enter the stratosphere during the winter, the residence time necessary for aerosol formation would be shorter.

There is no clear QBO effect in the total aerosol layer. Both the easterly and westerly phases have about the same yearly averages, 1.1×10^{-4} per steridian (sr^{-1}). However, a QBO effect is discernable in the upper part of the layer. During the westerly phase, the aerosol loading is a factor of two less than during the easterly phase. This is consistent with the lofting of the aerosol layer during the easterly phase when the tropical stratospheric reservoir is sequestered from mixing with midlatitude air.

In Boulder a new stratospheric aerosol lidar was built and installed in one of CMDL's rooftop domes in August 1999. The lidar uses a single, electronically gated photomultiplier tube and a 61 cm telescope (152 cm focal length), similar to the ones at MLO. A much smaller Nd:YAG, frequency doubled laser (Big Sky Lasers) is used for the 532 nm source. A multi-channel scaler data acquisition board is used, and the MLO software was modified for the Boulder configuration. The lower tropopause at Boulder increases the dynamic range needed to profile the entire stratospheric layer on one channel. Preliminary measurements at Boulder show that there is often no clear lower boundary of the layer in contrast to the case at MLO. This makes the interpretation of the data more difficult.

4.2. Special Projects

4.2.1. Evidence for the Influence of Biomass Burning on Tropospheric Ozone in Both the Eastern and Western Tropical Pacific

Beginning in August 1995, as part of the Pacific Exploratory Mission (PEM) Tropics A, ozone vertical profile measurements were started at the airport in Pago Pago, American Samoa (14.5°S, 170.5°W) and Papeete, Tahiti (14.5°S, 150.5°W). Profile measurements were continued at Tahiti and Samoa through PEM Tropics B with the program at Tahiti completed in December 1999. At Samoa weekly soundings continue as part of the SHADOZ project. During most of the measurement period, soundings were done weekly. During two aircraft field campaigns in September-October 1996 (PEM Tropics A) and March-April 1999 (PEM Tropics B), soundings were done twice a week. In January 1997 weekly soundings were begun at Suva, Fiji (18.0°S, 170.0°W). As part of the SOWER project, ozone profile measurements were started on a campaign basis in March 1998 at San Cristóbal, Galapagos, and were upgraded to biweekly soundings in September 1998, and to weekly soundings as part of SHADOZ early in 1999. The ozone vertical profiles were obtained using the electrochemical concentration cell (ECC) ozonesonde [*Komhyr et al.*, 1995]. This has become a standard technique for obtaining ozone profiles with high vertical resolution in both the troposphere and stratosphere to altitudes of approximately 35 km. For the purpose of characterizing the tropospheric airflow patterns influencing transport to the tropical sites, isentropic trajectories were calculated. The trajectories are computed from the ECMWF analysis using the model described in *Harris and Kahl* [1994].

Variations on the order of several days and the seasonal cycle are the two largest sources of the variability seen in tropospheric ozone at the Pacific tropical sites studied here. These variations were studied from surface observations at Samoa [*Harris and Oltmans*, 1998] and were found to result from changes in airflow to the site that tapped different sources and sinks. In the middle troposphere (2-10 km) both the shorter term and seasonal variability are primarily associated with the appearance of layers with enhanced (>70 ppbv) ozone mixing ratios (Figures 4.6 and 4.7). These peaks occur primarily during the August-October time period. This leads to a seasonal maximum in this layer during the austral spring at both the western and eastern Pacific sites. At the western Pacific sites there is prominent westerly flow during all times of the year, but it is more frequent and more vigorous during the austral spring. At the Galapagos, on the other hand, easterly flow dominates in the midtroposphere

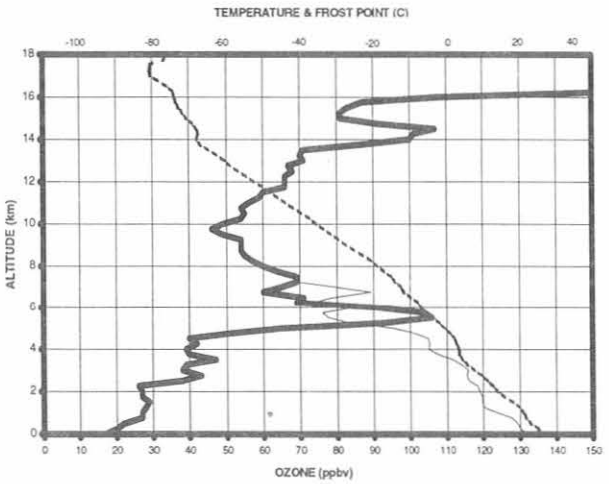

Fig. 4.6. Ozone mixing ratio (thick line), temperature (dashed line), and frost-point temperature (thin line) profiles at Pago Pago, American Samoa, for October 30, 1998.

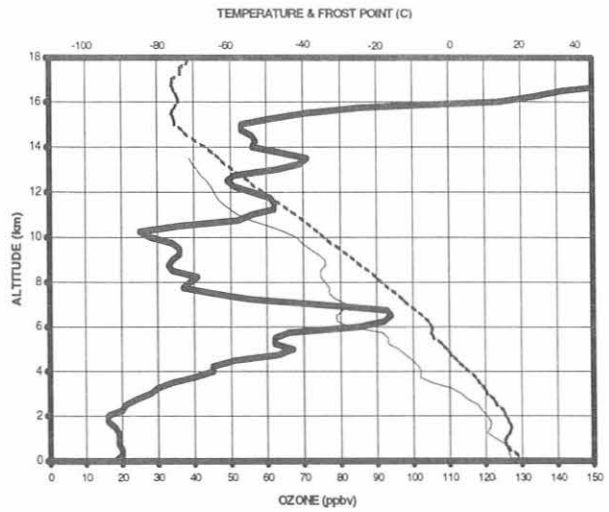

Fig. 4.7. Ozone mixing ratio (thick line), temperature (dashed line), and frost-point temperature (thin line) profiles at San Cristóbal, Galapagos, for October 9, 1999.

and is particularly pronounced in the austral spring. An important difference between the western and eastern Pacific is the very low ozone amounts throughout the troposphere during the summer and early autumn (December-April) in the western Pacific. Although this is also the time of the seasonal minimum in the troposphere at the Galapagos, mixing ratios do not get nearly as low above the boundary layer as in the western Pacific. This reflects the greater influence of convection in the west in mixing boundary layer ozone throughout the troposphere.

The tropics are known to be a significant area of biomass burning (see TRACE A and SAFARI, Special Issue of the *Journal of Geophysical Research, 101*, 1996). An ozone profile with an enhanced midtropospheric layer, often seen during the September and October period, is shown in Figure 4.6 for a sounding done at SMO. The peak ozone mixing ratio of 105 ppbv at ~6 km for the October 30, 1998, profile at SMO has a trajectory that reaches back to southern Africa 10 days prior to the sounding. Biomass burning heavily influences ozone in this region [*Fishman et al.*, 1996]. Trajectories identified with peaks greater than about 70 ppbv do not always reach back to Africa in 10 days, but they always have paths that have a strong westerly component that goes to the west of Australia into the Indian Ocean. On many occasions the trajectories pass over Australia but usually through the middle or southern part of the continent.

In the Galapagos the profiles also show a similar midtropospheric peak, e.g., October 9, 1999 (Figure 4.7). The trajectory for this event crosses Brazil in less than 10 days over a region that is also heavily impacted by biomass burning [*Fishman et al.*, 1996]. Investigation of each profile with an enhanced ozone layer in the midtroposphere during this time of the year showed a trajectory that passed over Brazil.

In 1997 extensive burning took place in Indonesia associated with drought conditions that were a consequence of the strong El Niño. Several studies have shown high ozone amounts in Indonesia and Malaysia in connection with the burning in the region [e.g., *Fujiwara et al.*, 1999]. At the western Pacific sites, the incidences of elevated midtropsopheric ozone begin to decline in most years by mid-November. On November 19 and 20 at Fiji and Samoa, some of the highest tropospheric ozone amounts were seen for any event recorded at these sites, and they extended from above the boundary layer to the tropopause. These enhancements increased the total tropospheric column by about 20 DU or more than 70% over average values for the month. The trajectories show that at both sites the air was coming from Indonesia. Although these profiles were the only ones measured during the event, the trajectories show that the flow persisted for about 5 days around the time that the profiles were obtained.

4.2.2. Water Vapor and Ozone Observations at San Cristóbal, Galapagos

In March 1998 profile measurements of ozone and water vapor were started at San Cristóbal. This project is conducted in cooperation with the University of Ibaraki, Japan, the University of Hokkaido, Japan, and the SHADOZ project. Water vapor profiles were measured in four campaigns during the spring and fall seasons of 1998 and 1999 and are scheduled to continue in the fall of 2000. The main instrument is a balloonborne frost-point hygrometer, and in three cases a new commercial frost-point hygrometer was tested that could extend the altitude range of upper tropospheric humidity measurements for smaller radiosonde-type soundings. Regular ozone soundings have been launched biweekly since September 1998 and weekly since March 1999. The excellent location and the outstanding data quality received from this site will hopefully allow continued soundings. Despite the political and economic problems of Ecuador, which continue to impact the operation of this project, it was undertaken successfully.

San Cristóbal is strongly influenced by El Niño/La Niña events and is, therefore, a natural laboratory for atmospheric processes controlled by the upwelling and the downwelling part of the Walker circulation. It is one of the few tropical regions that has significant periods of clear sky and is highly suitable for remote sensing studies and radiometry as well. It is currently the only tropical site where water vapor near the tropopause is measured and is the only site adding to the database for water vapor entering the stratosphere through the tropical tropopause. Its remoteness from industrial pollution sources allows for the study of long-range transport of pollutants across the tropical Pacific region.

Water Vapor Crossing the Tropical Tropopause

Since the discovery of the stratospheric dryness [*Brewer,* 1949], it is generally accepted that air enters the stratosphere predominantly in the tropics because only the tropical tropopause is cold enough to explain the low water vapor content of the stratosphere. Early investigations based on radiosonde and in situ measurements [*Newell and Gould-Stewart*, 1981; *Kley et al.*, 1982] indicated that there is a regional and temporal preference for air entering the stratosphere. A strong focus of the early investigations has been deep convective systems and their cirrus anvils [*Danielsen*, 1982, 1993]. These systems can achieve water vapor mixing ratios at the tropopause well below the mean stratospheric water vapor concentration [*Vömel et al.*, 1995]. *Yulaeva et al.* [1994] have shown that the mean tropical tropopause temperature is mostly controlled by the seasonal cycle of the mean residual vertical velocity in the stratosphere, which implies that tropical tropopause regions not influenced by tropical deep convection might still become sufficiently cold to dry slow rising air. Several studies [*Dessler,* 1998; *Sherwood*, 2000; *Gettelman et al.*, 2000] indicate that a regional preference for air crossing the tropical tropopause may not be necessary to explain the stratospheric dryness.

Our first campaign took place in March 1998 at the end of the very strong El Niño event of 1997/1998. During this campaign the average minimum temperature near the tropopause was around -83°C with a saturation mixing ratio of about 3.6 ppmv (Figure 4.8a). While the atmosphere was convectively more active during this campaign because of the El Niño event, there is no indication that the deep convection reached the local tropopause. Therefore, the tropopause temperature did not appear to be directly controlled by the deep convection. This is in strong contrast to our results from the Central Equatorial Pacific Experiment (CEPEX) in 1993, where deep convection reached the tropopause and directly caused extremely low tropopause temperatures and water vapor mixing ratios. Nevertheless, the first frost-point sounding at San Cristóbal showed a saturated layer between 13 km and the tropopause at 17 km above a very dry layer between 6 and 12 km with humidity values between 10 and 20%. The later soundings of this campaign showed a warmer tropopause and only up to 90%

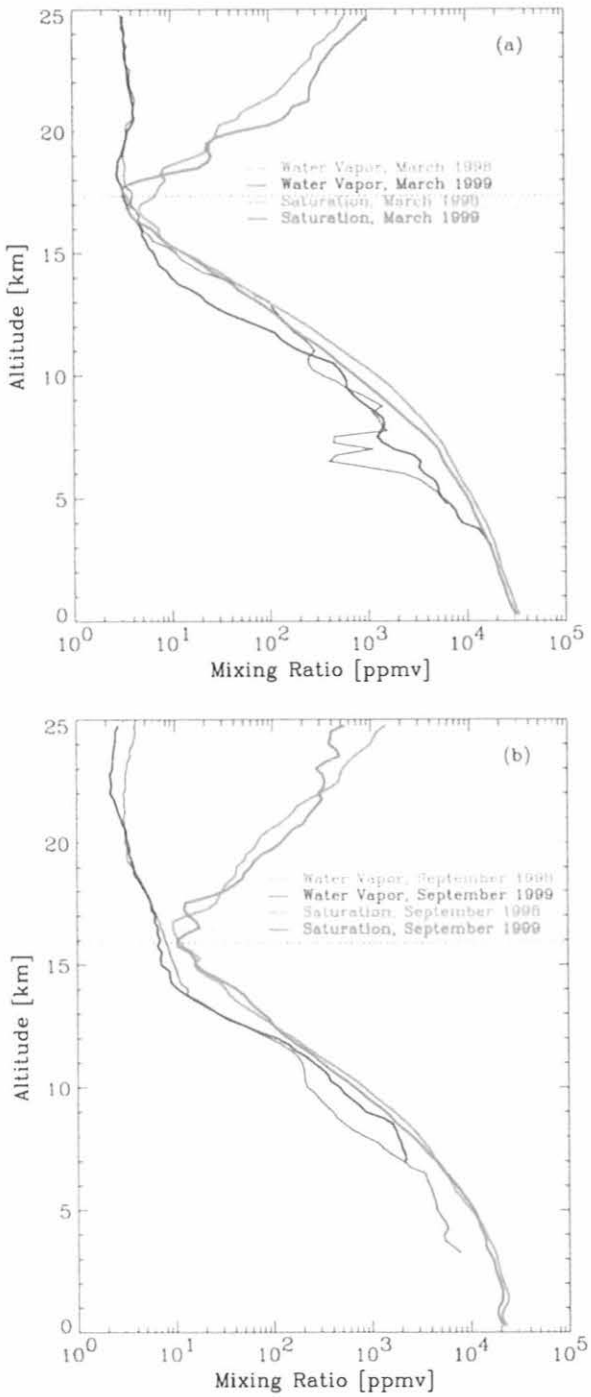

Fig. 4.8. San Cristóbal, Galapagos, average water vapor (blue) and saturation (red) mixing ratios for (a) March 1998 and March 1999, (b) September 1998 and September 1999. The dotted line shows the height of the tropopause in 1998 (light blue) and 1999 (dark blue).

saturation of water vapor over ice with a more moist middle troposphere. These soundings indicate local drying at the tropopause may occur but is not necessarily related to deep convection. The campaign in March 1999 confirmed this result clearly without the influence of deep convection. The soundings typically showed a dry layer between 11 km and 16 km and a considerable increase in ozone above 11 km. This indicates downward transport in the upper troposphere corresponding to the descending part of the Walker circulation.

In both fall campaigns (Figure 4.8b) the tropopause was significantly warmer, around –78°C, with a saturation mixing ratio between 5 and 12 ppmv. The water vapor soundings showed a dry layer below and up to the tropopause except for the actual temperature minimum, which in some cases could reach up to 90% relative humidity (ice). The measured water vapor mixing ratio at the temperature minimum of the tropopause ranged between 5.5 and 7.5 ppmv. Local drying at the tropopause level was not observed; however, relatively higher water vapor mixing ratios at the tropopause indicate air may enter the tropical lower stratosphere without being dried locally at the temperature minimum.

CMDL observations at San Cristóbal indicate there is a region below the local tropopause that is not directly influenced by deep convection. This region constitutes a barrier to vertical mixing below the local tropopause. This result has been found for other tropical sites [*Folkins et al.*, 1999] and is indicated here in terms of ozone and water vapor.

The results during CEPEX in the western Pacific showed that deep convection can reach the local tropopause causing extremely low temperatures and drying air to extremely low water vapor mixing ratios. In contrast to these observations, our results at San Cristóbal indicate that in the eastern Pacific region deep convection does not reach as high, and that cold tropopause temperatures are achieved by stratospheric processes rather than by tropospheric deep convection. Local drying does occur during the northern spring seasons, but not during the northern fall seasons. Furthermore, air that is unsaturated at the local temperature minimum near the tropopause may enter the tropical lower stratosphere during these months.

Tropospheric Ozone Observations

Extremely low ozone values observed in the middle and upper troposphere in the western Pacific [*Vömel et al.*, 1995] have not been observed in the eastern Pacific (Figure 4.9). This indicates that deep convection, which can transport ozone-poor air rapidly from the boundary layer to the upper troposphere, is not as vigorous in the eastern Pacific as it can be in the western Pacific. However, there is a significant difference in the upper tropospheric ozone observed during the March 1998 campaign compared to the March 1999 campaign (Figure 4.9a). The first campaign in March 1998 was still under the influence of the El Niño of 1997/1998 that moved the typical upwelling region of the Walker circulation towards the central and eastern Pacific. The upper tropospheric ozone during this campaign shows lower values compared to the campaign of the following year, indicating that the El Niño event caused increased transport of boundary layer ozone into the upper troposphere. In the fall campaigns (Figure 4.9b) ozone concentrations in the upper troposphere are significantly higher than for March 1999. In both years the average ozone profiles during the fall campaigns do not show the difference that was seen in the two March profiles, possibly because both campaigns were under similar La Niña conditions.

San Cristóbal is considered a remote marine site, far from industrial sources of pollution. However, it is often influenced by long-range transport from biomass burning regions and other pollution sources of South America. Figure 4.10 shows a time/height cross section of the ozone mixing ratio for 1999 over

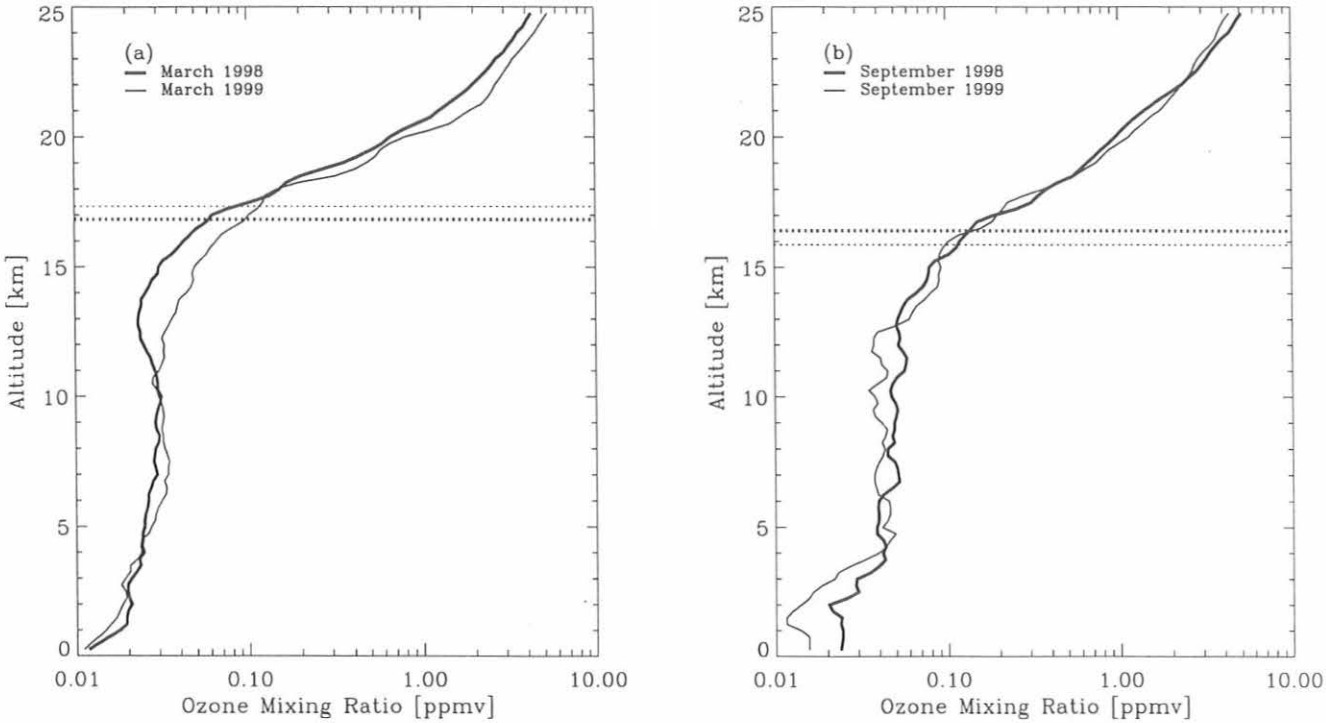

Fig. 4.9. San Cristóbal, Galapagos, average ozone mixing ratios for (a) March 1998 and March 1999, (b) September 1998 and September 1999. The height of the tropopause is shown for 1998 (dark dashed line) and 1999 (light dashed line).

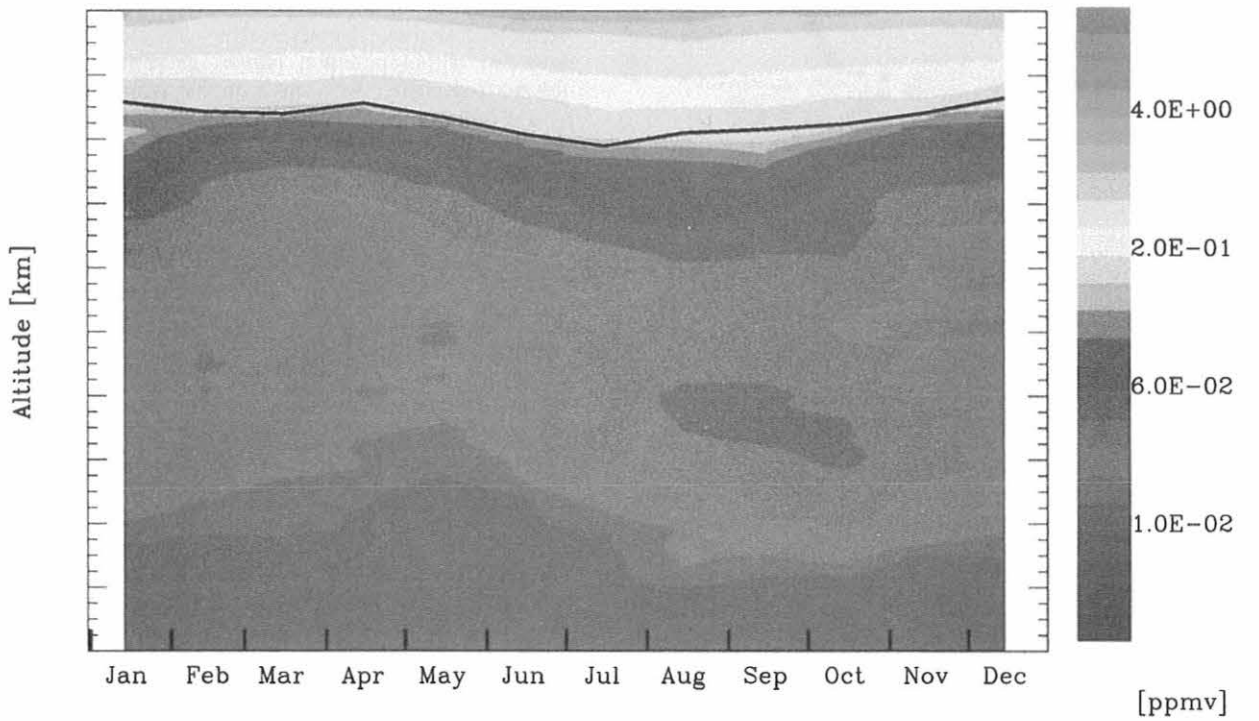

Fig. 4.10. Time/height climatology of monthly averages of ozone mixing ratio over San Cristóbal, Galapagos, in 1999. The solid line indicates the average tropopause height.

San Cristóbal. The middle troposphere shows a seasonal cycle with higher ozone values typically found between August and October and lower values between January and May. Trajectory analyses show that during most time periods the air comes predominantly from equatorial South America. During June through August, for example, more than 90% of all trajectories arriving at 6 km over San Cristóbal originate over equatorial South America, in particular from the biomass burning regions of the Amazon basin and northeastern Brazil.

The sounding on May 18, 2000, shows some direct evidence for long-range transport from the South American continent (Figure 4.11). At 5 km altitude this sounding displays a shallow layer apparently devoid of ozone. While ozone is most likely undisturbed within this layer, its signal is masked by an artifact of the instrument caused by high concentrations of SO_2. The likely source for this layer is an eruption plume of Tungurahua volcano (78.44°W, 1.74°S) on May 13 transported to Galapagos within 5 days.

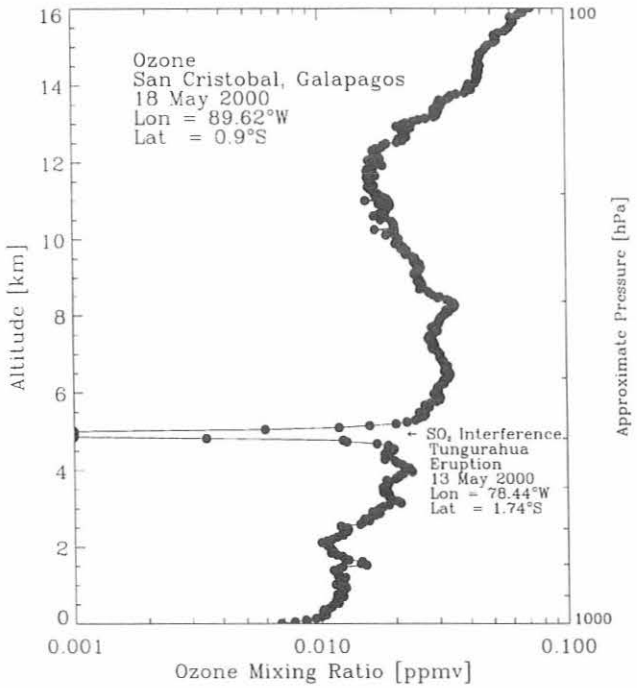

Fig. 4.11. SO_2 interference layer caused by long range transport of volcanic gases emitted by Tungurahua volcano May 13, 2000, and observed May 18, 2000, at San Cristóbal, Galapagos.

Outlook

The location of this site is very unique and continued observations are planned in the near future. These observations will be included in satellite validation studies. A new surface ozone monitor at this site will give 24-hr observations of boundary layer concentrations of ozone that will allow for the study of some interesting aspects of the chemistry of the lower troposphere.

4.2.3. Evidence of O_3 Titration During BRW Winter Dark Periods

Trace gas measurements from BRW during the winter dark periods of 1986-1997 were examined. After ensuring that local pollution from the Barrow town site was not present in the data set, a smooth curve consisting of a function and filtered residuals was removed from each data record. The smooth curve was designed so that its removal leaves residuals containing only the highest frequency variations on the order of synoptic scale changes [*Thoning et al.*, 1989]. Variability caused by changes in transport can be examined with these residuals.

Figure 4.12 shows a negative correlation between O_3 and CO_2 residuals for Siberian transport. CO_2, CO, and CH_4 residuals were positively correlated with one another (e.g., Figure 4.13). On the basis of trajectory analysis, it is speculated that the positive correlations among CO_2, CO, and CH_4 indicate industrial sources either in Siberia or further upwind (e.g., the Ural region). By limiting the data to transport from this direction, the slope of the fitted line did not change much in comparison to that derived from all transport types, and the correlation of the fit improved slightly. This may reflect the fact that winter transport conditions result in the Siberian pollution signature becoming regionally widespread throughout the Alaskan Arctic. The other transport pathways to Barrow yield few or no man-made sources within 10 days.

The negative correlations between O_3 and the other species may be caused by chemical removal of O_3 by NO_X (titration) that occurs when NO_X is plentiful in the absence of sunlight. Based on the chemical reactions that likely take place, the range of 1.5-2 O_3 molecules destroyed per NO molecule emitted was used. There is negligible NO_X in the remote Arctic near Barrow. However, it is surmised that O_3 is being destroyed within pollution plumes generated in Siberia or upwind from there. As a check on this assumption, the molar ratio of NO_X to CO_2 was calculated. The delta (Δ) symbol is

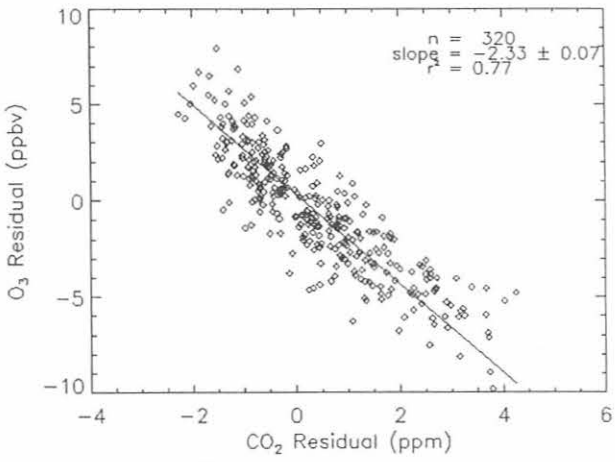

Fig. 4.12. O_3 versus CO_2 residuals for the winter dark periods, 1986-1997, at BRW. Only data corresponding to transport from the direction of Siberia are included.

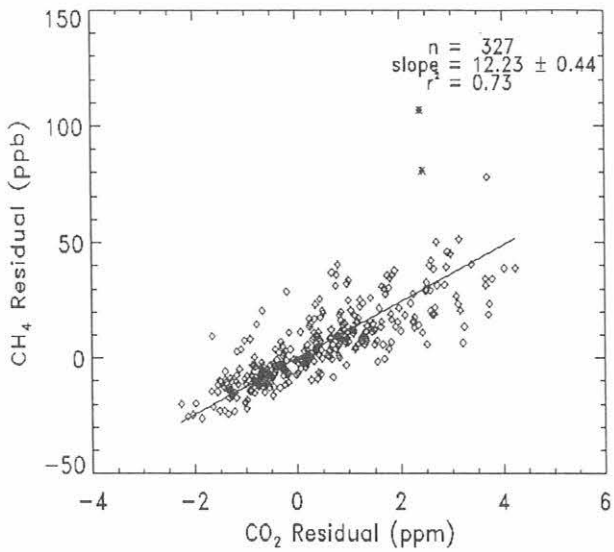

Fig. 4.13. CH_4 versus CO_2 residuals for the winter dark periods, 1986-1997, at BRW. Only data corresponding to transport from the direction of Siberia are included.

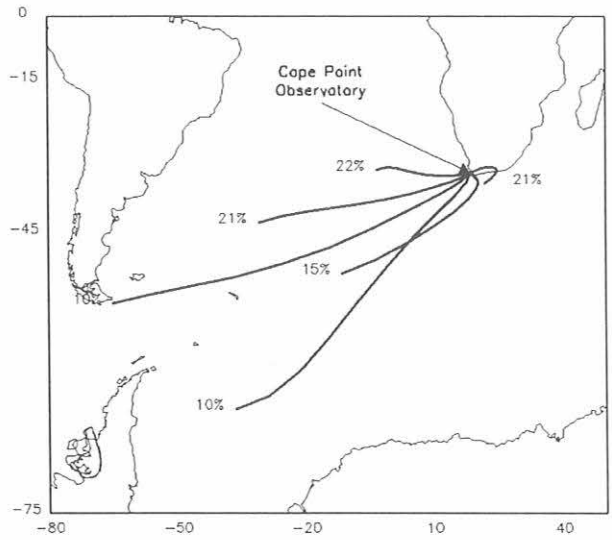

Fig. 4.14. Average transport pathways to CPT with their frequency of occurrence, based on 1994-1998 5-day back isentropic trajectories arriving at 500 m.

used to denote a change in concentration over time or an emission rate: $\Delta NO_X/\Delta CO_2 = \Delta NO_X/\Delta O_3 \times \Delta O_3/\Delta CO_2$. Inverting the titration factor and with the empirical slope of $\Delta O_3/\Delta CO_2$ determined from the Barrow data (-2.33×10^{-3}), $\Delta NO_X/\Delta CO_2 = (1.2\text{-}1.6) \times 10^{-3}$ is obtained. This is close to, or within, the lower end of the range expected from coal-fired industrial processes $(1.39\text{-}3.49) \times 10^{-3}$ (W. Barbour, Environmental Protection Agency, personal communication, 1999). It is possible that the natural gas burned in this region causes the $\Delta NO_X/\Delta CO_2$ ratio to be lower than that for pure coal burning. Likewise, with the empirically derived slope for $\Delta O_3/\Delta CO$ (-3.45×10^{-1}), $\Delta NO_X/\Delta CO = 0.17\text{-}0.23$ is obtained and is consistent with the ratio determined for eastern North America of 0.19 [*Saeger et al.*, 1989]. The empirical ratios indicate air measured at Barrow during the winter has a pollution component and that the negative O_3 correlations could be caused by titration that occurs days upwind of Barrow.

4.2.4. Analysis of CO and O_3 Data from Cape Point Observatory (1994-1998)

Cape Point Observatory (CPT) is located at the southern tip of Africa (34°S) on a peninsula (Figure 4.14). This figure shows the average transport pathways to CPT and their frequency of occurrence. The 5-day fetch is often in the remote South Atlantic. Cape Point is one of a few sites measuring trace gases transported from the southern oceans. However, Cape Point is also located 60 km from Cape Town, a city of more than two million people; therefore, pollution from car exhaust and industry does at times reach the observatory. In collaboration with the two sponsors of the observatory, the Fraunhofer Institute in Germany and the South African Weather Bureau, 5 years (1994-1998) of hourly CO and O_3 measurements were obtained to develop an automated selection technique that removes Cape Town pollution and then analyzes the remaining baseline data.

Figure 4.15 shows the results of the selection procedure. The red plus signs are rejected data; the blue dots are selected data. Most of the discarded data points occur during austral winter when local meteorology makes pollution episodes at CPT more likely to occur. The selection procedure is an iterative technique that first fits a smooth curve to the hourly data and then removes the smooth curve to obtain residuals. The residuals are filtered and points above the +1 standard deviation (S.D.) limit are discarded. The process continues until no points are discarded. The O_3 measurements were selected by pairing them with the selected CO data set. To further reduce the data set, 3-hr averages were formed about 0000 and 1200 GMT corresponding to arrival times for the trajectories. These twice-daily averages are shown in Figure 4.15.

Figure 4.16 shows how the distribution of CO is changed by selection. For each color/fit, the upper line represents a fit to all of the data while the lower line represents a fit to the selected data. The blue line is a polynomial representing the long-term trend. Although the unedited data appear to have a downward trend, the selected data show no linear trend, merely a slow oscillation. The red curve is the polynomial combined with four harmonics representing the average seasonal cycle. The selection shifts the CO average seasonal maximum from July to October and the minimum from the end of January to the end of February. Finally, the green curve is the red curve combined with residuals filtered in the frequency domain. The residuals have variations with periods of about 2 months or more.

CO and O_3 variations on the synoptic time scale attributed to changes in transport were not large. Strong southerly flow resulted in average CO values up to 1 ppb lower and O_3 values 1 ppbv higher than average values in air transported from the latitude of the observatory. These results are consistent with the latitudinal gradients of these species.

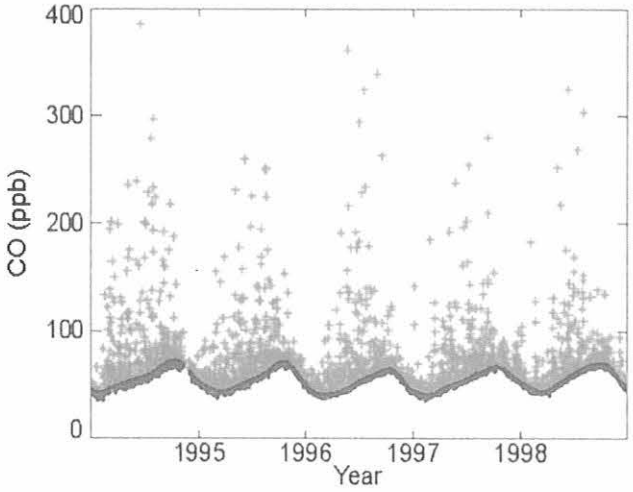

Fig. 4.15. Results of the +1 S.D. selection process. Red plus signs mark rejected data; blue dots are the final selected points for CPT CO data.

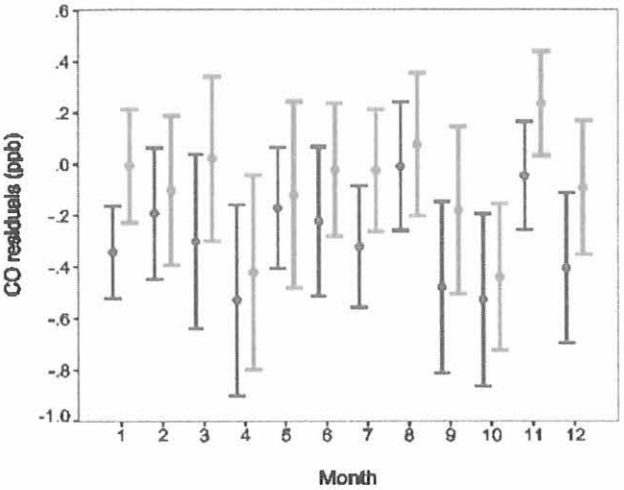

Fig. 4.17. CPT selected CO data set with nighttime values (blue) and daytime values (red). The dots are the monthly average value, and the bars show the 95% confidence interval for 1994-1998.

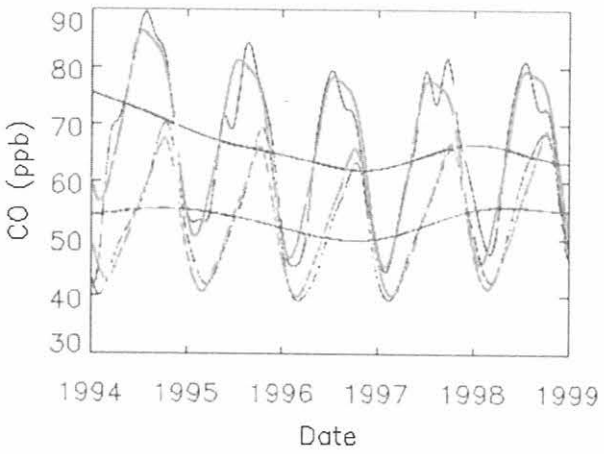

Fig. 4.16. The change to the CPT CO distribution made by selection: for each color, the upper curve is fitted to all the data, and the lower curve is fitted to the selected data. (See text for description of curves.)

Diurnal CO variations in the unedited data set can be up to 80 ppb. The most extreme pollution events occur during winter when local meteorological factors allow more stagnant conditions and recirculation of polluted air. Inversion characteristics and mesoscale winds (land/sea breezes) may contribute to pollution at Cape Point. Figure 4.17 shows the selected CO data set with nighttime values (blue) and daytime values (red). A small diurnal cycle persists in the selected CO data set of 0.2-0.4 ppb (depending on the grouping of the data). This diurnal cycle is statistically significant if all selected data are considered. The selected O_3 data also show small (up to 1 ppbv) diurnal cycles that vary with season. The sources of these remaining diurnal cycles will be investigated in the future.

4.2.5. Laboratory Testing of ECC Ozonesondes

It is important to conduct regular testing to evaluate the precision and accuracy of ECC ozonesondes, as the tests provide assurance that the best possible data are obtained from ozonesondes used in the wide variety of projects. The testing conducted in 1998 and 1999 always included ECC sondes from Science Pump Corporation and ENSCI Corporation, the two manufacturers and suppliers of ECC ozonesondes. Comparisons were also done using two different cathode sensing solution recipes, 1% KI buffered and 2% KI unbuffered. The ingredients for these solutions are listed in Table 4.7. CMDL switched from the 1% KI buffered to the 2% KI unbuffered solution after tests confirmed that the buffers were producing a side reaction that resulted in high ozone measurements [*Hofmann et al.*, 1998]. The dates for the switch to 2% KI unbuffered solutions are given in Table 4.8. CMDL testing in 1998 and 1999 included surface ozone comparisons in Boulder and triple ozonesonde flights at SPO.

Eleven surface ozone comparisons were done with ozonesondes and a TEI model 49C UV ozone analyzer in July and August 1999. The sondes were run for 4 to 7 hours. Both 6A and 2Z models were used in the tests. Figure 4.18 shows a typical comparison between the ozonesondes and the TEI ozone

TABLE 4.7. Cathode Solution Recipes Used by CMDL ECC Ozonesondes*

Ingredients:	1% KI Buffered	2% KI Unbuffered
KI (potassium iodide)	10 g	20 g
KBr (potassium bromide)	25 g	0 g
Sodium phosphate buffers:		
$NaH_2PO_4 \cdot H_2O$	1.25 g	0 g
$Na_2HPO_4 \cdot 12H_2O$	5.00 g	0 g

*1 L of solution made with distilled, deionized water

TABLE 4.8. Dates when 2% KI Unbuffered Solution Replaced 1% KI Buffered Solution

Location	Date	Flight Number
Boulder, Colorado	Aug. 21, 1997	BL413
MLO	April 15, 1998	HI321
SPO	March 4, 1998	AS557
Tahiti	May 6, 1998	TA119
Fiji	April 30, 1998	FJ045
SMO	April 17, 1998	SA138
Trinidad Head, California	Aug. 21, 1997	TH001 (TH002 and TH003 used 1% buffered)

All field campaigns and new sites used 2% KI unbuffered solutions after January 1, 1998.

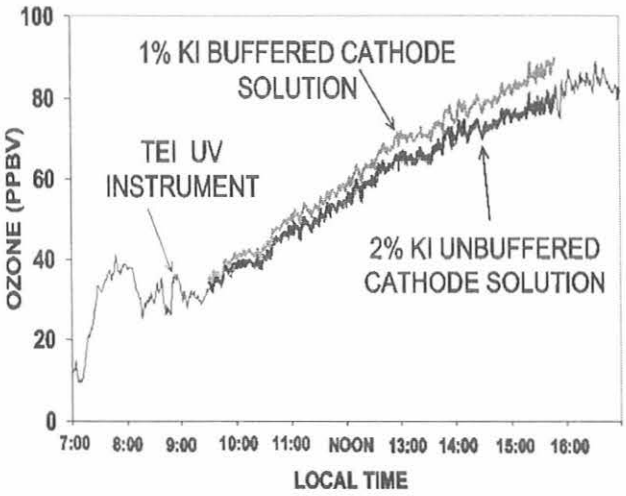

Fig. 4.18. Surface ozone measurements at Boulder, Colorado, using ozonesondes (with 1% KI buffered and 2% KI unbuffered solutions) and a TEI 49C UV ozone instrument.

analyzer. The ozonesonde using a 2% KI unbuffered cathode solution was consistently about 1% to 2% higher than the TEI. The sonde containing the 1% KI buffered cathode solution was 7 to 10% higher than the TEI. These results confirmed previous laboratory tests showing the better agreement of the 2% KI unbuffered solution with UV instruments at surface pressures.

4.2.6. South Pole: Triple Ozonesonde Flights

Special SPO ozonesonde flights were part of the Teachers Experiencing Antarctica project sponsored by the National Science Foundation. A teacher from the United Nations International School in New York was assigned to work with CMDL at SPO to participate in the preparation of ozonesondes, distribute the ozone profile data to students, including examples of ozone hole measurements from ozonesondes, and later to present numerous lectures to students on experiences with ozone science at the south pole.

Three different models of ECC ozonesondes were flown on four triple-ozonesonde flights at the south pole in January 1999. The objective of the experiment was to observe any differences between the Science pump 4A, 6A, and ENSCI 2Z ECC ozonesondes. The 4A model was used in the 1980s. Because the 4A's used in this test had been stored for more than 8 years, they were sent to the manufacturer to be reconditioned. The 6A and 2Z sondes are the current models manufactured by the two different suppliers. The 2Z model uses a molded plastic sensor instead of Teflon. The 2Z also has its own interface board that transmits data every second. The 4A and 6A sondes use a TMAX board that sends data every 7 seconds. The 4A sonde pump runs on a 6-V motor versus 12-V for the 6A and 2Z models. A secondary objective was to observe the differences in the ozone sensor response using 1% KI buffered cathode solutions and 2% KI unbuffered. The first ozonesonde package was a dual sonde using 6A sondes, each with a different cathode solution. Different solutions were not used in individual sondes on the triple flights since the main objective was model comparison. However, the four triple-ozonesonde packages were flown in pairs (one triple in the morning and one in the afternoon) with 2% KI or 1% KI buffered for each pair of triple ozonesondes. Table 4.9 summarizes the results and gives the total ozone measured by each ozonesonde and the Dobson

TABLE 4.9. SPO Dual and Triple Ozonesonde Flights: January 1999

Flight No.	TypeE	GMT: Day/Time	Sonde No.	Board	Cathode Solution	Total Sonde (DU)	Ozone Dobson (DU)
AS617-a	Dual	Jan. 11	6A6367	TMAX	1% KI buff.	305	266
AS617-b		00:22	6A6368		2%KI unbuf	269	"
AS618-a	Triple	Jan. 14	6A6255	TMAX	1% KI buff	296	264
AS618-b		23:18	4A1043-r		"	278	"
AS619			2Z1039	V2C	"	299	"
AS620-a	Triple	Jan. 15	6A6247	TMAX	2%KI unbuf	267	265
AS620-b		04:36	4A1039-r		"	255	"
AS621			2Z1032	V2C	"	276	"
AS622-a	Triple	Jan. 17	6A6292		2%KI unbuf	255	263
AS622-b		22:04	4A1012-r	TMAX	"	253	"
AS623			2Z1091	V2C	"	266	"
AS624-a	Triple	Jan. 18	6A6325	TMAX	1%KI buff	281	260
AS624-b		03:35	4A1031-r		"	272	"
AS625			2Z1100	V2C	"	291	"

spectrophotometer measured values. The residual ozone for the ozonesonde total above balloon burst altitude was computed by the constant mixing ratio method at 7 hPa or lower if the balloon did not make it to 7 hPa.

The different ECC models agree very well in the troposphere. Even at low concentrations, all of the ozone measurements nearly always fall within about ±10%. In the stratosphere the ENSCI 2Z tends to give 1-5% higher ozone than the Science Pump 6A model. The reconditioned 4A sondes were generally about 1 to 5% lower in ozone that the 6A models. The ozonesondes using the 1% KI buffered solutions gave about 10% more ozone than the Dobson spectrophotometer. The 2% KI solution profiles compare much better at 2-3% greater total ozone than the Dobson.

Acknowledgments. The work at San Cristóbal was conducted in cooperation with the Instituto Nacionál de Meteorología y Hidrología (INAMHI), Ecuador. We are very grateful for the work done by Mario Agama, Francisco Paredes, and Jaime Cornejo at the radiosonde station in San Cristóbal.

4.3. REFERENCES

Barnes, J.E., and D.J. Hofmann, Lidar measurements of stratospheric aerosol over Mauna Loa Observatory, *Geophys. Res. Lett.*, *24*, 1923-1926, 1997.

Brewer, A.W., Evidence for a world circulation provided by measurements of helium and water vapor distribution in the stratosphere, *Q. J. R. Meteorol. Soc.*, *75*, 351-363, 1949.

Danielsen, E.F., A dehydration mechanism for the stratosphere, *Geophys. Res. Lett.*, *9*, 605-608, 1982.

Danielsen, E.F., In situ evidence of rapid, vertical, irreversible transport of lower tropospheric air into the lower tropical stratosphere by convective cloud turrets and by larger-scale upwelling in tropical cyclones, *J. Geophys. Res.*, *98*, 8665-8681, 1993.

Dessler, A.E., A reexamination of the "stratospheric fountain" hypothesis, *Geophys. Res. Lett.*, *25*, 4165-4168, 1998.

Fishman, J., J.M. Hoell Jr., R.D. Bendura, R.J. McNeal, V.W.J.H. Kirchhoff, NASA GTE TRACE A Experiment (September-October 1992): Overview, *J. Geophys. Res.*, *101*, 23,865-23,879, 1996.

Folkins, I., M. Loewenstein, J. Podolske, S.J. Oltmans, and M. Proffitt, A barrier to vertical mixing at 14 km in the tropics: Evidence from ozonesondes and aircraft measurements, *J. Geophys. Res.*, *104*, 22,095-22,102, 1999.

Fujiwara, M., K. Kita, S. Kawakami, T. Ogawa, N. Komala, S. Saraspriya, and A. Suripto, Tropospheric ozone enhancements during the Indonesian forest fire events in 1994 and 1997 as revealed by ground-based observations, *Geophys. Res. Lett.*, *26*, 2417-2420, 1999.

Gettelman, A., J. R. Holton, and A. R. Douglass, Simulations of water vapor in the lower stratosphere and upper troposphere, *J. Geophys. Res.*, *105*, 9003-9023, 2000.

Harris, J.M., and B.A. Bodhaine (Eds.), *Geophysical Monitoring for Climatic Change, No. 11, Summary Report 1982*, NOAA Environ. Res. Labs., Boulder, CO, 160 pp., 1983.

Harris, J.M., and J.D. Kahl, Analysis of 10-day isentropic flow patterns for Barrow, Alaska: 1985-1992, *J. Geophys. Res.*, *99*, 25,845-25,855, 1994.

Harris, J.M., and S.J. Oltmans, Variations in tropospheric ozone related to transport at American Samoa, *J. Geophys. Res.*, *102*, 8781-8791, 1998.

Hofmann, D.J., S.J. Oltmans, J.M. Harris, B.J. Johnson, and J.A. Lathrop, Ten years of ozonesonde measurements at the south pole: Implications for recovery of springtime Antarctic ozone, *J. Geophys. Res.*, *102*, 8931-8943, 1997.

Hofmann, D.J., J.T. Peterson, and R.M. Rosson (Eds.), *Climate Monitoring and Diagnostics Laboratory, No. 24, Summary Report 1996-1997*, NOAA Environ. Res. Labs., Boulder, CO, 166 pp., 1998.

Hudson, R.D., and A.M. Thompson, Tropical tropospheric ozone from total ozone mapping spectrometer by a modified residual method, *J. Geophys. Res.*, *103*, 22,129-22,145, 1998.

Kley, D., A.L. Schmeltekopf, K.K. Kelly, R.H. Winkler, T.L. Thompson, and M. McFarland, Transport of water vapor through the tropical tropopause, *Geophys. Res. Lett.*, *9*, 617-620, 1982.

Komhyr, W.D., R.A. Barnes, G.B. Brothers, J.A. Lathrop, and D.P. Opperman, Electrochemical concentration cell ozonesonde performance evaluation during STOIC 1989, *J. Geophys. Res.*, *100*, 9231-9244, 1995.

Newell, R.E., and S. Gould-Stewart, A stratospheric fountain?, *J. Atmos. Sci.*, *38*, 2789-2796, 1981.

Rosenlof, K.H., and J.R. Holton, Estimates of the stratospheric residual circulation using the downward control principle, *J. Geophys. Res.*, *98*, 10,465-10,479, 1993.

Saeger, M., J. Langstaff, R. Walters, L. Modica, and D. Zimmerman, NAPAP emissions inventory (Version 2): Development of the annual data and modelers' tapes, *Rep. EPA-600/7-89-012A*, U.S. Environ. Protect. Agency, Washington, D.C., 693 pp., 1989.

Sherwood, S.C., A "stratospheric drain" over the maritime continent, *Geophys. Res. Lett.*, *27*, 677-680, 2000.

Thoning, K.W., P.P. Tans, and W.D. Komhyr, Atmospheric carbon dioxide at Mauna Loa Observatory: 2, Analysis of the NOAA/GMCC data, 1974-1985, *J. Geophys. Res.*, *94*, 8549-8565, 1989.

Vömel, H., S.J. Oltmans, D. Kley, and P.J. Crutzen, New evidence for the stratospheric dehydration mechanism in the equatorial Pacific, *Geophys. Res. Lett.*, *22*, 3235-3238, 1995.

Yulaeva, E., J.R. Holton, and J.M. Wallace, On the cause of the annual cycle in tropical lower stratospheric temperatures, *J. Atmos. Sci.*, *52*, 169-174, 1994.

5. Halocarbons and Other Atmospheric Trace Species

B.D. HALL (EDITOR), J.W. ELKINS, J.H. BUTLER, S.A. MONTZKA, T.M. THOMPSON, L. DEL NEGRO, G.S. DUTTON, D.F. HURST, D.B. KING, E.S. KLINE, L. LOCK, D. MACTAGGART, D. MONDEEL, F.L. MOORE, J.D. NANCE, E.A. RAY, AND P.A. ROMASHKIN

5.1. CONTINUING PROGRAMS

5.1.1. INTRODUCTION

The mission of the Halocarbons and other Atmospheric Trace Species (HATS) group, formerly known as the Nitrous Oxide and Halocarbons (NOAH) group, is to study trace atmospheric species that cause chemical and radiative change in the atmosphere. The goal of the HATS group is to measure and interpret the distributions and trends of many halocarbons, nitrous oxide (N_2O), sulfur hexafluoride (SF_6), fluorocarbons, perfluorocarbons (PFCs), organic nitrates (e.g., peroxyacetyl nitrate (PAN)), organic sulfur gases (e.g., OCS), and hydrocarbons (HCs) in the troposphere, stratosphere, and oceans with the best analytical tools available. The halocarbons include the chlorofluorocarbons (CFCs), chlorocarbons (CCs like CCl_4, CH_3CCl_3, $CHCl_3$, CH_2Cl_2, C_2Cl_4, etc.), hydrochlorofluorocarbons (HCFCs), hydrofluorocarbons (HFCs), methyl halides (CH_3Br, CH_3Cl, CH_3I), bromocarbons (CH_2Br_2, $CHBr_3$), and halons.

These trace gases affect the quality of the Earth's atmosphere. All of these trace gases, except the HCs and organic nitrates, produce direct climate forcing on the Earth's atmosphere. Many of these chemicals, including the halocarbons and N_2O, are involved in stratospheric ozone depletion. The production of some of these compounds is currently restricted for the developed countries by the Montreal Protocol and its amendments [*UNEP*, 1987]. The hydrocarbons, some sulfur gases, organic nitrates, and CCs play a major role in tropospheric air quality. Recent changes to the U.S. Clean Air Act now restrict the emissions of some CCs and HCs by certain industries and manufacturing processes.

Activities conducted by HATS in 1998 and 1999 included: (1) weekly flask sampling and analysis of air from remote and semi-remote sites, (2) operation of instrumentation for hourly, in situ measurements of trace gases at the four CMDL baseline observatories and four non-baseline sites, (3) preparation and maintenance of trace gas standards, (4) participation on airborne campaigns using in situ gas chromatographs (GCs) on aircraft and balloon payloads, and (5) investigation of oceanic processes influencing trace gas composition of the atmosphere.

Continuing programs within the group are based upon in situ and flask measurements of the atmosphere from the four CMDL baseline observatories and ten cooperative stations (Figure 5.1). Table 5.1 lists the geographic locations and other useful information on all of the sites. There are currently 13 flask sites and 10 in situ sampling sites in the HATS Atmospheric Sampling Network. Flask samples and in situ trace gas measurements obtained in cooperation with the CMDL Carbon Cycle Greenhouse Gases (CCGG) group were ceased at the WITN, Grifton, North Carolina (ITN) tower on June 12, 1999, because the laboratory layout was changed to accommodate only digital television equipment. A high tower site in Texas is being studied as its replacement. A new in situ GC was prepared for installation and operation sometime in early 2001 at Ushuaia, Argentina, with funds from the World Meteorological Organization (WMO).

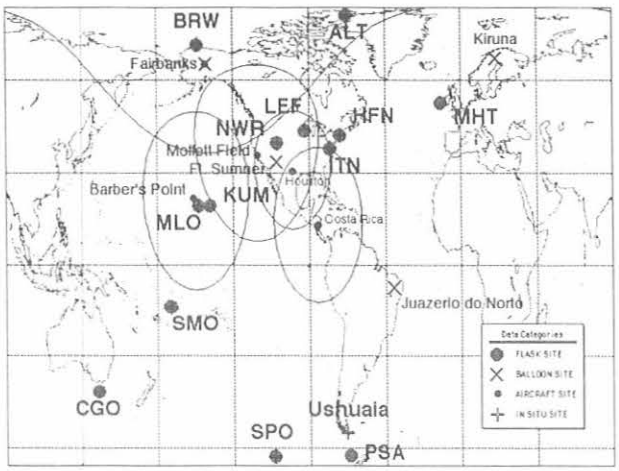

Fig. 5.1. Geographic locations of old and new stations in the HATS flask (gray circles) and in situ (crosses) networks. The sites for balloon launches are noted by "X"s. The location (small black filled circles) and the range of the aircraft operations (arcs and ovals) also are indicated.

One of the highlights of this report is that the total Effective Equivalent Chlorine (EECl) continues to decrease at about 1% yr^{-1} as a result of the Montreal Protocol. The main reason for this decline is that methyl chloroform (CH_3CCl_3) concentrations continued to decline to less than half of the peak levels present in 1992. However, atmospheric concentrations of the halons and CFC-12 are still increasing because of allowed production in the developing countries and the large bank of chemicals present in the developed countries. After CH_3CCl_3 concentrations drop to near zero, continued production and release of the halons may introduce a significant change in the trend of EECl. Other significant results include the observed global increases in atmospheric N_2O and SF_6 (identified through both flask and in situ monitoring), the continued growth of the CFC replacements (HCFCs and HFCs), and the decline in the northern hemispheric concentrations of $CHCl_3$, CH_2Cl_2, and C_2Cl_4 as a result of the U.S. Clean Air Act.

Airborne measurements were conducted in the upper troposphere and lower stratosphere in tropical, midlatitude, and polar regions during 1998 and 1999 (Figure 5.1). The exchange of air between the lower stratosphere and the troposphere and midlatitude upper stratosphere was quantified. The development and deployment of the next generation airborne gas chromatograph with electron capture and mass selective detection was funded by the National Aeronautic and Space Administration's (NASA) Instrument Incubation Program to measure trace gases, including acetone and PAN that influence atmospheric chemistry in the upper troposphere.

TABLE 5.1. Geographic and Network Information on HATS Network Sites

Code	Station	Latitude	Longitude	Elevation (m)	LST-GMT (hr)	Type
ALT	Alert, Northwest Territories, Canada (AES)*	82.45°N	62.52°W	210	-4	F, I
BRW	Point Barrow, Alaska	71.32°N	136.60°W	11	-9	F, I
MHT	Mace Head, Ireland (University College)	53.33°N	9.90°W	42	0	F
LEF	WLEF tower, Wisconsin (CMDL-CCGG)	45.95°N	90.28°W	470	-6	F, I
HFM	Harvard Forest, Massachusetts (Harvard University)	42.54°N	72.18°W	340	-5	F, I
NWR	Niwot Ridge, Colorado (University of Colorado)	40.04°N	105.54°W	3013	-7	F, I
ITN†	WITN tower, North Carolina (CMDL-CCGG)	35.37°N	77.39°W	9	-5	F, I
MLO	Mauna Loa, Hawaii	19.54°N	155.58°W	3397	-10	F, I
KUM	Cape Kumukahi, Hawaii	19.52°N	154.82°W	3	-10	F
SMO	Tuluila, American Samoa	14.23°S	170.56°W	77	-11	F, I
CGO	Cape Grim, Tasmania, Australia‡	40.41°S	144.64°E	94	+10	F
TDF	Ushuaia, Tierra Del Fuego, Argentina (WMO GAW station)§	54.82°S	68.32°W	10	-3	I
PSA	Palmer Station, Antarctica**	64.92°S	64.00°W	10	+12	F
SPO	South Pole, Antarctica	89.98°S	102.00°E	2841	+12	F, I

Cooperative sites (F = flasks, I = in situ) with:
*In situ GC: Only N_2O and SF_6; flask sampling for all gases, however.
†ITN site's flask and in situ GC were discontinued on June 12, 1999 (see text).
‡Commonwealth Scientific and Industrial Research Organization (CSIRO) and Bureau of Meteorology, Australia
§Starts collecting data in March 2001.
**Only glass flasks used.

Oceanic measurements of CH_3Br and other gases were obtained on two research cruises during 1998-1999. Measurements in marine air and surface seawater showed that the oceans are still a significant sink for atmospheric CH_3Br, but the magnitude of the sink is slightly smaller than previously determined.

5.1.2. Flask Samples

Overview

No new sampling stations were added in 1998-1999, although Mace Head, Ireland (MHS) and Palmer, Antarctica (PSA) were added at the end of 1997 (Figure 5.1). Sampling at PSA continued throughout 1998-1999, but sampling from MHS was discontinued temporarily because of a high rate of loss of flasks during transit. Efforts were made during the past 2 years to improve the sampling frequency and precision at all sites with considerable success. Progress, however, was delayed somewhat by the CMDL move to the NOAA Broadway site in 1999. One of the analytical instruments (Low Electron Attachment Potential Species (LEAPS) gas chromatograph with electron capture detection (GC-ECD)) experienced considerable difficulties following the move and required the replacement of two electron capture detectors.

Flasks brought into the laboratory were analyzed on two to four instruments depending on the species being examined and the size of the individual sampling flask (Table 5.2). Although all 300-mL flasks were retired from the system, there are still some 850-mL flasks that contain a marginal amount of air for all of the low-level analyses. Most flask analyses were of samples from the network, although many were from research cruises, firn air sampling, and other special projects.

An intercomparison of SF_6 and N_2O analyses was started with the CCGG group, but it is still in its early stages. Although HATS records extend back into the 1970s for N_2O and the 1980s for SF_6 (including archived samples), the CCGG network has the advantage of sampling from many more sites per week, thus allowing a better spatial picture of the distributions of these compounds to be obtained.

TABLE 5.2. Instrumentation for HATS Flask Analysis

Instrument	Type	Gases	Frequency of Network Data
OTTO	GC-ECD, 3-channel, isothermal	N_2O, CFCs (3), CCs (2), SF_6	Weekly
LEAPS	GC-ECD, 1-channel, temperature programmed	halons (2), CH_3Cl, CH_3Br, $CHCl_3$	Semi-monthly to monthly
HCFC-MS	GC-MS, 1-channel, temperature programmed	HCFCs (3), HFCs (1), CFCs (3), halons (1), CCs (6), BrCs (3)	Semi monthly
HFC-MS	GC-MS, 1-channel, temperature programmed	HCFCs (5), HFCs (2), CFCs (2), halons (2), CCs (6), BrCs (3), ClBrCs (3)	Semi-monthly to monthly

Sampling and Analysis

In 1996, 269 flasks from the network were filled and delivered to the Boulder laboratory for analysis. This number has increased each year reaching a total of 399 in 1999 (Figure 5.2). This increase is the result of added sites (1996-1997) and a more efficient turnover of flasks between Boulder and the field sites. This was accomplished through improved record keeping of flasks coming to Boulder and by adding additional flasks to the network in 1996-1997 to accommodate additional sites. Sampling success

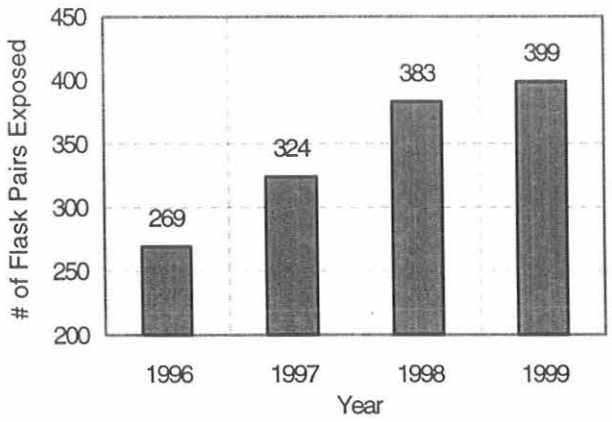

Fig. 5.2. Number of flask pairs filled and returned to Boulder each year from the HATS station network.

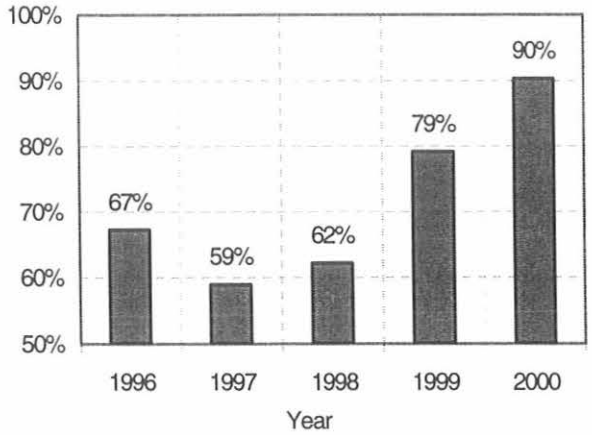

Fig. 5.3. The percentage of flask pairs agreeing within 1 psi in total pressure upon arrival in Boulder.

was improved substantially from that for 1996 at nearly all of our sites (Table 5.3). This was mainly the result of repairing small leaks and replacing valves where necessary on flasks following analysis in Boulder. These repairs greatly improved the agreement in flask pressure within simultaneously sampled pairs (Figure 5.3).

While most of the time the GC-ECD instruments were utilized to process flasks from the station network, 10-20% of the time was devoted to calibrating gas standards, and about 5% of the instruments' operation was dedicated to other quality-control experiments. Special projects involving flask measurements over the past few years included primarily firn air analyses and analysis of flask samples from research cruises.

Results

Results for most of the major ozone-depleting gases are also discussed in the subsection "Overall Trends in Ozone-Depleting Gases." Many of these gases are analyzed by both GC-ECD and gas chromatography with mass selective (GC-MS) detection. CFC-12 continues to increase in the atmosphere while mixing ratios of CFC-11 continue to drop slowly at about 1% yr^{-1} (Figure 5.4). CFC-113 and CCl_4 are also decreasing at about 1% yr^{-1}, and CH_3CCl_3, which has driven the overall decline in atmospheric chlorine, continues to drop about 18% yr^{-1} (subsection on "Overall Trends"). Gases analyzed only by GC-ECD are N_2O, SF_6, and $CBrF_3$ (H-1301). Nitrous oxide has been monitored by the in situ instruments for the past 12 years. The record from flask samples goes back to the mid-1970s (Figure 5.5). The global growth rate of N_2O from 1978 to 2000 was 0.74 ± 0.01 (95% confidence level, C.L.) nmol mol^{-1} yr^{-1} (parts-per-billion, or ppb, yr^{-1}), which amounts to a mean of about 0.25% yr^{-1}. From 1996 to 2000, the global growth rate was 0.85 ± 0.06 ppb yr^{-1}, which differs significantly at the 95% C.L. from the 20-year

TABLE 5.3. Flask Sampling Success at CMDL Observatories and Cooperative Sampling Sites

Sampling Station	1996	1997	1998	1999
Barrow, Alaska	69%	94%	88%	87%
Mauna Loa, Hawaii	69%	83%	90%	96%
American Samoa	54%	67%	73%	87%
South Pole	77%	69%	77%	88%
Alert, Canada	52%	46%	67%	67%
Niwot Ridge, Colorado	63%	92%	87%	77%
Cape Grim, Australia	60%	69%	85%	85%
WLEF tower, Wisconsin	12%	35%	69%	92%
Harvard Forest, Massachusetts	46%	62%	69%	69%
Kumukahi, Hawaii	50%	54%	67%	69%
Palmer, Antarctica	--	8%	65%	81%
Mace Head, Ireland	--	--	8%	15%
WITN tower, North Carolina	65%	62%	62%	38%

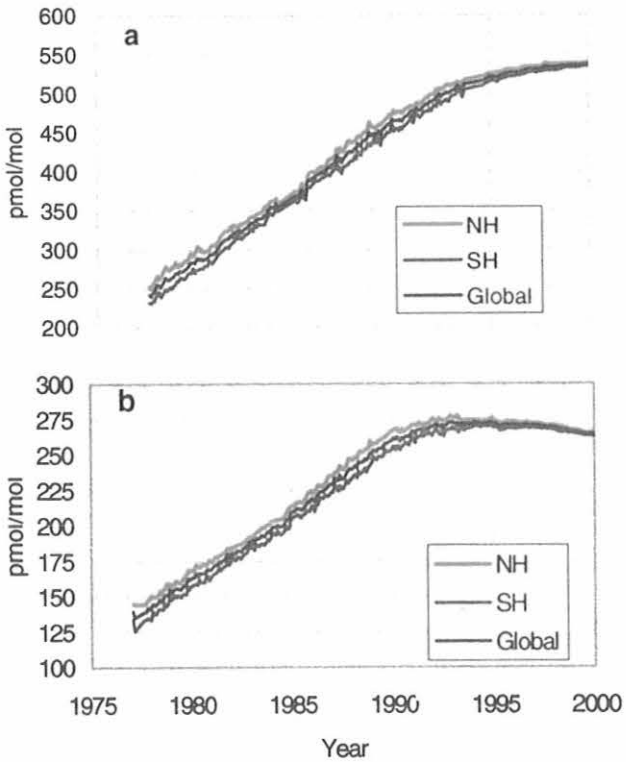

Fig. 5.4. CFC-12 (a) and CFC-11 (b) from flask samples. Data are monthly averages.

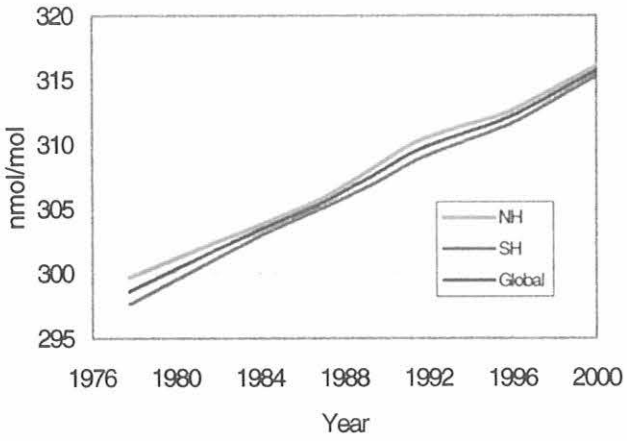

Fig. 5.5. Atmospheric history of N_2O derived from CMDL flask measurements. Data are smoothed with a lowess fit.

average. This suggests that N_2O concentrations were increasing more rapidly in the atmosphere near the end of the 20th century. Whether this was a temporary or long-term feature will be borne out in future data.

Sulfur hexafluoride still appears to be increasing linearly in the atmosphere with a growth rate of about 0.24 ± 0.01 (95% C.L.) pmol mol^{-1} (parts per-trillion, or ppt, yr^{-1}) since 1996 (Figure 5.6). CMDL measurements of polar firn air confirmed the early history of this gas as derived from emission inventories [*Butler et al.*, 1999], indicating natural sources are absent or insignificant in the global SF_6 budget.

CMDL measurements show that halons are still increasing slowly in the atmosphere in spite of a ban on their production as of 1994. The global growth rate of H-1301 in 1998-1999, at 0.09 ± 0.04 ppt yr^{-1}, does not differ significantly at the 95% C.L. from the 1995 to 2000 average of 0.06 ± 0.01 ppt yr^{-1}, nor from the 1995-1996 average of 0.044 ± 0.011 ppt yr^{-1} reported in *Butler et al.* [1998a] (Figure 5.7). However, at the 90% confidence level, a 30-40% increase in H-1301 emissions is suggested during the past few years. H-1211 is still increasing at a rate of 0.1-0.2 ppt yr^{-1}, which means that there has been no curtailment of its global emissions since the 1994 ban on its production in developed countries.

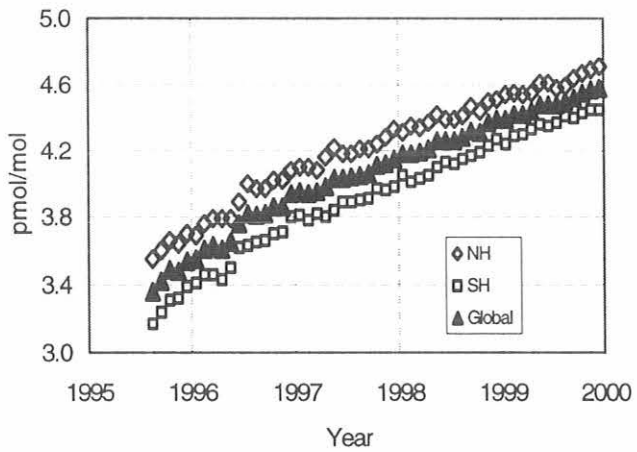

Fig. 5.6. Recent history of atmospheric SF_6 from CMDL flask measurements. Data are monthly averages.

Chlorofluorocarbon Alternatives Measurement Program

Measurements of chlorofluorocarbon alternatives from flask air samples continued during 1998-1999. On average nearly three flask pairs per month were sampled and analyzed from nine remote sampling stations across the globe. Slightly fewer than two pairs per month were sampled from the WLEF tower in Wisconsin (LEF), ITN, and Harvard Forest, Massachusetts (HFM). The main change during this period involved building a new inlet isolation box for the instrument and moving the instrument and laboratory to the new building site in Boulder, Colorado, in early 1999. These improvements allow for more precise and reproducible measurements of gases that are present at high levels in laboratory air such as HFC-134a, HCFC-142b, and CH_2Cl_2. Moving the instruments does not seem to have caused any unexpected shifts in the results from the GC-MS flask program.

Mixing ratios of HCFCs measured in the flask program (HCFC-22, HCFC-141b, HCFC-142b) continued to increase in the troposphere (Figure 5.8, Table 5.4). Concentrations reported

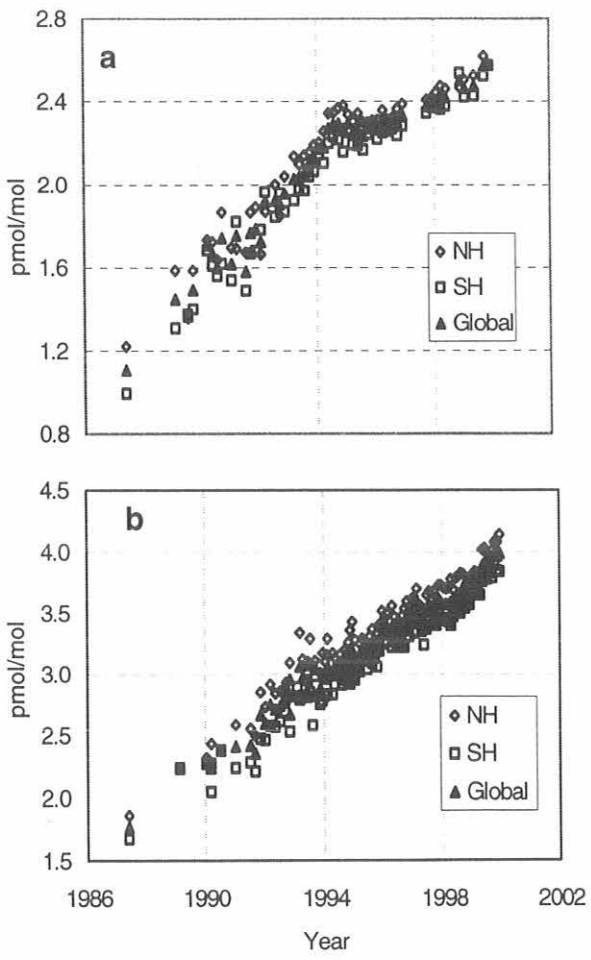

Fig. 5.7. Halons H-1301 (a) and H-1211 (b) from CMDL flask measurements. Data are monthly averages.

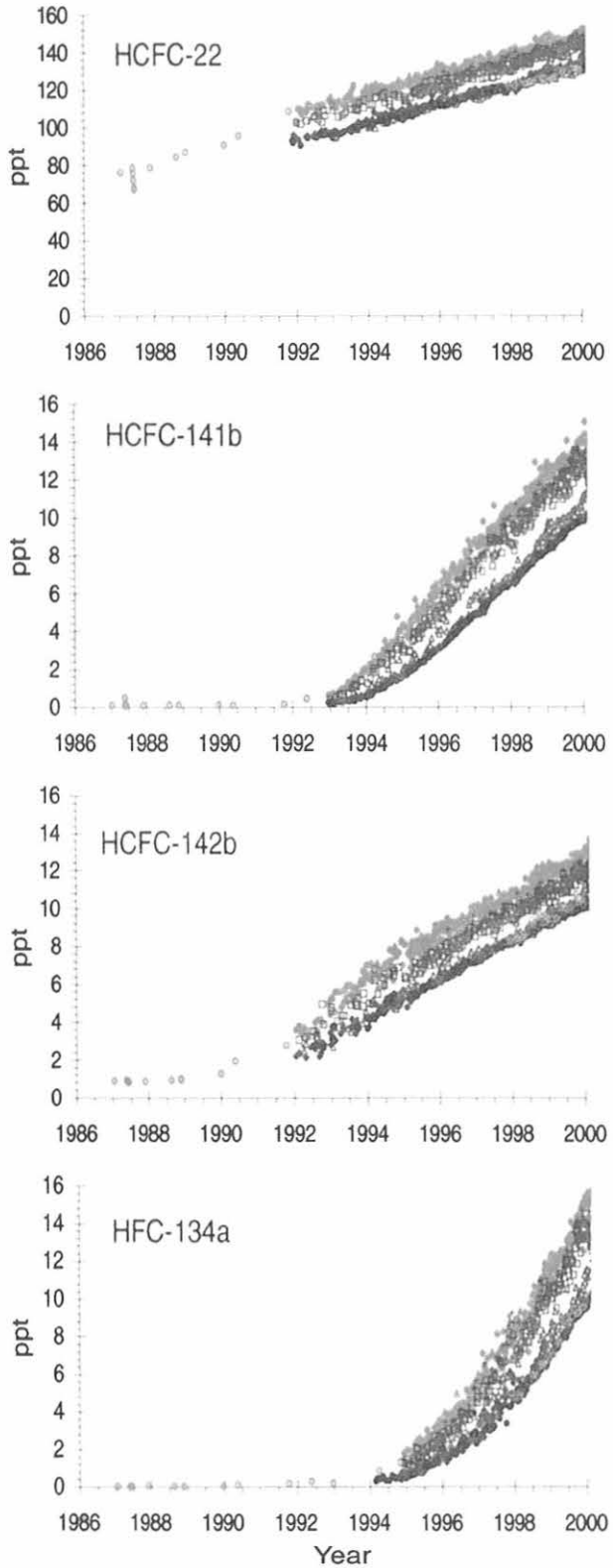

Fig. 5.8. Atmospheric dry mole fractions (ppt) of selected HCFCs and HFC-134a measured by GC-MS in the CMDL flask program. Each point represents the mean of two flasks from one of eight or nine stations: ALT, BRW, NWR, red; KUM and MLO, green; SMO, CGO, PSA, and SPO, blue. Also plotted are results from analysis of archived air samples (open red circles) filled at NWR or on cruises in both hemispheres.

TABLE 5.4. Global Burden and Rate of Change for HCFCs and HFC-134a

Compound	Mean 1998 Mixing Ratio (ppt)	Mean 1999 Mixing Ratio (ppt)	Growth Rate (ppt yr^{-1})
HCFC-22	131.4	136.9	5.1 (1992-1999)
HCFC-141b	9.1	10.9	1.8 (1996-1999)
HCFC-142b	9.7	10.8	1.0 (1996-1999)
HCFC-134a	7.6	10.6	3.1 (1998-1999)

Quantities estimated from latitudinally-weighted measurements at seven remote stations: SPO, CGO, SMO, MLO, NWR, BRW, and ALT.

for these gases in past publications have been referenced to a constant set of gravimetric standards (section 5.1.4) [*Montzka et al.*, 1993, 1994, 1996b, 1999a, 2000]. Fairly linear rates of increase were measured for these three HCFCs since the beginning of 1996. In mid-1999 these HCFCs accounted for about 6%, or 170 ppt, of the atmospheric burden of chlorine contained in long-lived anthropogenic halocarbons. When combined with an estimate of atmospheric lifetimes, measurements of anthropogenic halocarbons can be used to infer emission rates. Such an analysis suggests that since 1998, total molar emissions of HCFCs surpassed the aggregate moles emitted of other ozone-depleting substances (CFCs + CCl_4 + halons + CH_3CCl_3).

Continued increases were observed for HFC-134a during 1998-1999 (Figure 5.8, Table 5.4). The observed concentrations are in reasonable agreement with the amounts expected based upon the available industrial production and emission data and an atmospheric lifetime of ~15 years [*Montzka et al.*, 2000].

Continued declines in the concentration of CH_3CCl_3 were observed from flask measurements during 1998-1999 (Figure 5.9). These data are reasonably consistent with the results from the in situ Radiatively Important Trace Species (RITS) GC-ECD instruments. Accurately describing the atmospheric decline of CH_3CCl_3 can provide unique information regarding the

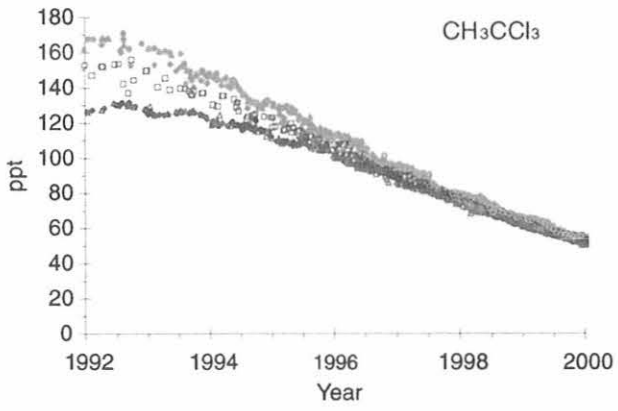

Fig. 5.9. Atmospheric dry mole fractions (ppt) of CH_3CCl_3 measured by GC-MS in the CMDL flask program. Each point represents the mean of two simultaneously filled flasks from one of eight or nine stations (symbols the same as in Figure 5.8).

atmospheric abundance and distribution of the hydroxyl radical, an important atmospheric oxidant [*Ravishankara and Albritton*, 1995; *Montzka et al.*, 2000; *Spivakovsky et al.*, 2000].

Flask Measurements of CH_3CCl_3 and Their Implications for Atmospheric Hydroxyl

The analysis of CH_3CCl_3 in flask air by GC-MS provides some unique advantages over other techniques, such as linear response (Figure 5.10), good chromatographic resolution (Figure 5.11), and the ability to monitor more than one ion. During 1998-1999 repeat injection precision for GC-MS analysis of flasks was typically 0.4% (the median standard deviation from repeat injections on 1028 flasks during that period); for 95% of all analyses the repeat injection precision was <1.3%. A disadvantage of flask sampling for measurements of CH_3CCl_3 is that degradation of CH_3CCl_3 during the interim between sampling and analysis can be observed in flasks filled with extremely dry air. This problem is apparent in results from the South Pole, Antarctica, CMDL Observatory (SPO), where poor flask pair agreement and anomalously low mixing ratios are observed from some flask samples. Because the rate of this loss is flask-dependent, its occurrence is readily identifiable by poor agreement between simultaneously filled flasks. Samples in which degradation is suspected are not considered in further data analysis.

In recent years many unique features have appeared in the atmospheric data for CH_3CCl_3 that confirm a dramatic decline in

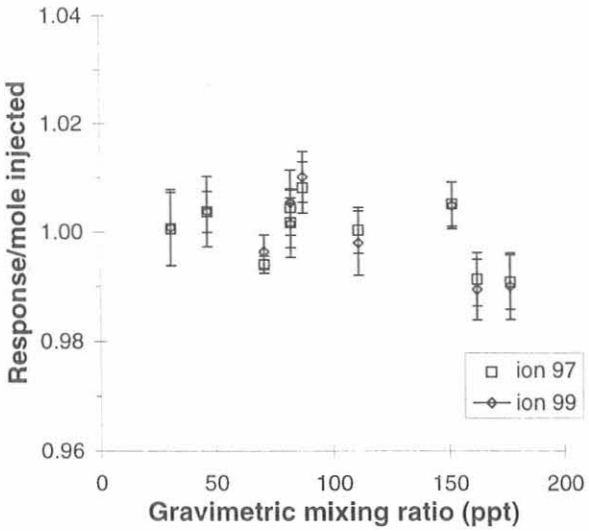

Fig. 5.10. Consistency of gravimetrically prepared standards containing CH_3CCl_3 as analyzed on the GC-MS during 1997-1999. For well-made standards analyzed on an instrument with a linear response, the response factor should be independent of mixing ratio. Response factors (measured response divided by the gravimetrically determined mixing ratio) for two different ions are plotted for individual gravimetric standards and are normalized to the mean response factor for all standards. The error bars are one standard deviation of the measured response factor for each tank (from seven to nine measurements of each standard during 1997-1999). The results for one standard at 195.7 ppt (ALM-64596) do not appear in this figure because its response factor was much different from the other standards (0.90 in late 1999), and was changing over time, presumably from slow degradation of CH_3CCl_3 in that tank.

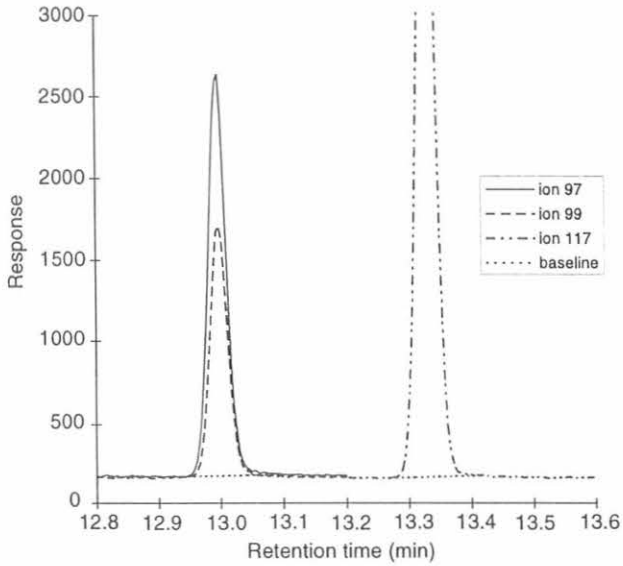

Fig. 5.11. A portion of a chromatogram from the GC-MS flask instrument showing the signals observed for CH_3CCl_3 (ions 97 and 99) and CCl_4 (ion 117; peak maximum not shown) in ambient air collected at Samoa. Concentrations were determined to be 47 ppt CH_3CCl_3 and 100 ppt CCl_4. The peak height relative to the standard deviation of the baseline was 800 and 600 for CH_3CCl_3 at m/z = 97 and m/z = 99 and ~2000 for CCl_4 at m/z = 117 in this air sample. Also shown are baselines drawn from our custom automatic integration routine (short-dashed line).

emissions. Not only has the mixing ratio decreased exponentially recently (Figure 5.9), but the difference observed between the hemispheres (Figure 5.12) has declined substantially as the emissions, which emanated predominantly from the northern hemisphere, have declined. Furthermore, the gradient observed within each hemisphere is now very similar, suggesting that the atmospheric distribution of CH_3CCl_3 in 1998-1999 was controlled by the distribution of loss processes rather than the distribution of sources during this period (Figure 5.13).

The measured rate of decay during 1998-1999 at nine remote stations and LEF allows us to estimate an upper limit to the global lifetime of CH_3CCl_3 of 5.5 (±0.1) years [*Montzka et al.*, 2000]. Because the decay observed for CH_3CCl_3 arises predominantly from OH oxidation (Table 5.5), this lifetime limit allows estimation of upper limits to the lifetime of other chemically reduced gases that degrade predominantly by OH oxidation in the atmosphere (Table 5.5). This lifetime limit is completely independent of calibration standard accuracy and emission estimates, but depends upon a consistent calibration reference over time. An uncertainty of ±0.1 year is estimated on the measured e-fold time from potential drift of 0.3% yr^{-1} based on comparisons between a reference air sample and ten gravimetric standards (Figure 5.14).

When the magnitude of emissions of CH_3CCl_3 during 1998-1999 are considered (A. McCulloch, personal communication, 2000), the rate of decay measured implies that the true global lifetime of CH_3CCl_3 is 5.2 (+0.2, -0.3) years [*Montzka et al.*, 2000]. Unlike previous estimates of global lifetime, this estimate is insensitive to calibration standard accuracy and includes a factor of two uncertainty in the magnitude of emissions.

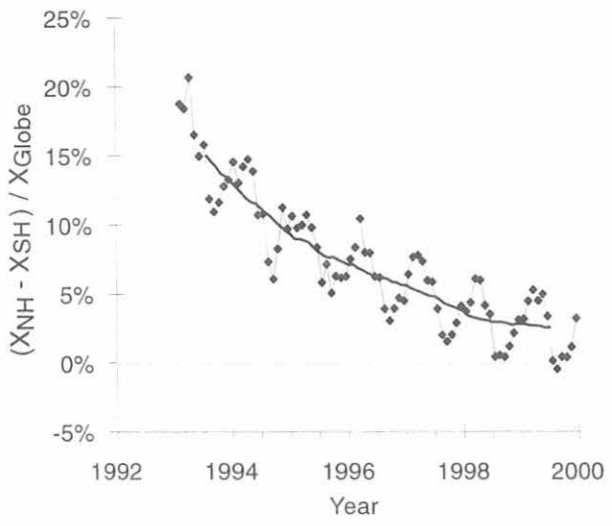

Fig. 5.12. The hemispheric mixing ratio difference for CH_3CCl_3 in recent years. The difference was inferred from weighted, monthly mean mixing ratios at three to six sampling stations in each hemisphere. Monthly differences (solid diamonds) are connected with a thin line; the heavy line represents a 12-month running mean difference. The results suggest that northern hemisphere emissions have declined substantially in recent years [*Montzka et al.*, 2000].

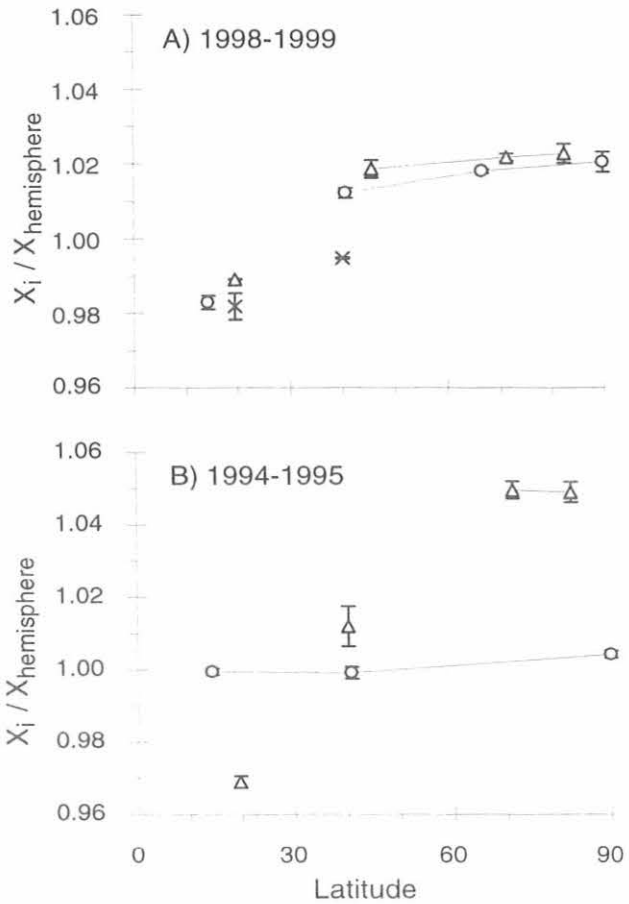

Fig. 5.13. Measured intrahemispheric gradients in annual mean mixing ratios of CH_3CCl_3 [*Montzka et al.*, 2000]. (A) Annual means for individual sites (X_i) are shown normalized to respective hemispheric annual means for the 2 years 1998-1999. Northern hemispheric data from low altitude sites (<1000m) (triangles) are connected with lines to allow for appropriate comparisons to similar sites in the southern hemisphere (circles). High altitude sites (MLO and NWR) are shown (crosses) but are not connected with lines because there is a clear difference in the intrahemispheric gradient between low and high altitude sites during this period. (B) Same as (A) but for the 2 years 1994-1995 when northern hemispheric emissions were substantial. Because of a lack of measurements from all sites in this earlier period, data from both low and high altitude locations are shown with similar symbols in this panel. Error bars in both panels represent one standard deviation of the annual mean ratios estimated for the 2 years.

The recent measurements also provide a unique opportunity to discern hemispheric loss rates for CH_3CCl_3. The rate of change observed in the southern hemisphere is determined by emissions within the southern hemisphere, chemical loss in the southern hemisphere, and the CH_3CCl_3 delivered from the northern hemisphere through net hemispheric exchange. Because emissions in the southern hemisphere have always been <10% of the total emissions, this term is insignificant compared to the others. From the observed difference in the hemispheric concentration of CH_3CCl_3, the net exchange of this gas between the hemispheres can be estimated. By also including the observed decline of CH_3CCl_3 in the southern hemisphere, the lifetime of CH_3CCl_3 in the southern hemisphere is estimated to be 4.9 (+0.2, -0.3) years [*Montzka et al.*, 2000]. This estimate is also insensitive to calibration standard accuracy and emission estimate figures.

These results suggest that the mean hemispheric loss frequency for CH_3CCl_3 and the mean hemispheric concentration of OH are slightly larger (by 15 ± 10%) in the southern hemisphere than in the northern hemisphere despite the higher levels of precursors for OH such as NO_x and O_3 found in the northern hemisphere. This conclusion hinges on emission figures for 1998-1999 being reasonably accurate; higher mean concentrations of OH in the northern hemisphere could be reconciled with the observations only if emissions were substantially underestimated in 1998-1999 (by about a factor of 3 or more). Higher mean concentrations of OH in the southern hemisphere may result because certain OH sinks, such as CO, are greater in the northern hemisphere, and because the southern hemisphere contains more of the OH-rich tropics compared to the northern hemisphere (given that the intertropical convergence zone (ITCZ) is on average a few degrees north of the equator).

Overall Trends in Ozone-Depleting Gases

Emissions of most ozone-depleting gases decreased during the 1990s. The atmospheric response to reduced emissions was most pronounced for the industrial gas CH_3CCl_3 (Figure 5.9). The global concentration of this gas decreased at an exponential rate of ~18% yr^{-1} during 1998-1999. Such a rapid decline is observed for this gas because it has a fairly short atmospheric lifetime, and its past use as a solvent caused changes in emissions to be closely linked to changes in production. This link is not as strong for CFCs and other gases because their emissions can be sustained from devices and foams for years after production has ceased. For example, although similar declines in emissions are inferred for CFC-11 and CFC-12 in the

TABLE 5.5. Lifetimes of Chemically Reduced Gases (in Years) for 1998-1999

	Partial lifetime with respect to:			
	OH Loss*	Stratospheric Loss	Total Lifetime†	Total Lifetime‡ Upper Limit
CH_4	10.5 (+0.5, –0.6)	110	9.0 (+0.4, –0.6)	9.5 (±0.2)
HCFC-22	13.6 (+ 0.6, –0.8)	306	13.0 (+0.6, –0.8)	13.8 (±0.3)
HCFC-141b	11.5 (+0.5, –0.7)	81	10.1 (+0.4, –0.6)	10.6 (±0.2)
HCFC-142b	21.8 (+1.0, –1.3)	372	20.6 (+0.9, –1.3)	21.8 (±0.4)
HFC-134a	15.7 (+0.7, –1.0)	377	15.1 (+0.7, –0.9)	16.0 (±0.3)
CH_3CCl_3	6.3 (+0.3, –0.4)	45	5.2 (+0.2, –0.3)	5.5 (±0.1)

*Partial lifetimes with respect to oxidation by OH are derived from the estimate of the total lifetime for CH_3CCl_3 of 5.2 (+0.2, –0.3) years, a partial lifetime with respect to oceanic loss of 94 years, and with respect to stratospheric loss of 45 years, and from rate constant ratios evaluated at 272 K [*Spivakovsky et al.*, 2000; *Prather and Spivakovsky*, 1990]. Quoted uncertainties in these lifetime limits do not include uncertainties in rate constants.

†Total lifetimes were calculated as the inverse of summed rate constants. The lifetime quoted for CH_4 also includes a partial lifetime with respect to soil loss of about 145 years.

‡Upper limits to trace gas lifetimes were derived in the same way as the best estimates, except that the upper limit for the total atmospheric lifetime of CH_3CCl_3 of 5.5 ± 0.1 years is considered. Note that these limits are entirely independent of calibration accuracy and emissions figures.

1990s compared to the 1980s on a relative basis, the atmospheric concentration of CFC-11 is now decreasing but CFC-12 continues to increase. This difference arises because the lifetime of CFC-12 is approximately 100 years or about twice that of CFC-11.

While the tropospheric concentration of some ozone-depleting gases decreased and some increased during 1998-1999, the overall ozone-depleting capacity of the atmosphere has decreased since 1993-1994. Estimates of Effective Equivalent Chlorine (EECl) and Equivalent Chlorine (ECl) [*Daniel et al.*, 1995; *Montzka et al.*, 1996a] from tropospheric measurements provide a very rough estimate of ozone-depleting halogen concentrations in the future stratosphere (once a 3-5 year time lag associated with mixing processes is considered). The EECl and ECl burdens of the troposphere have decreased since 1993-1994 primarily because of the rapid decline in the trace gas methyl chloroform. By the end of 1999, tropospheric EECl was ~5% below its peak and was decreasing at ~1% yr^{-1} (Figure 5.15).

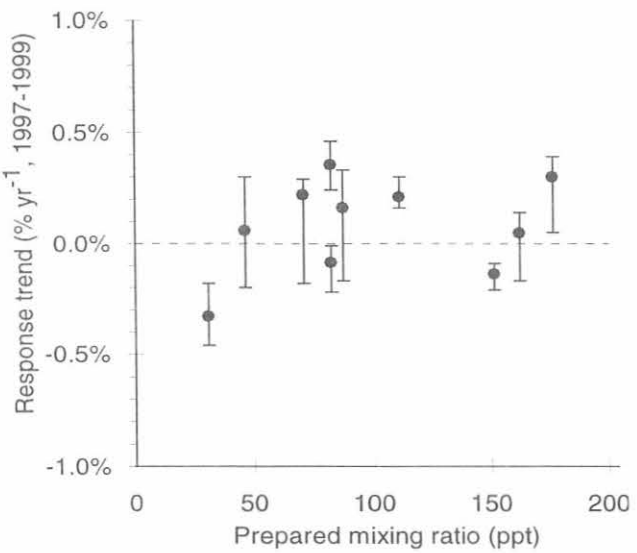

Fig. 5.14. The stability of calibration for CH_3CCl_3 during 1997-1999. From multiple (7-9) comparisons of 10 gravimetric standards to a single high-pressure sample of ambient air during 1997-1999, trends in the response ratio (ratio of the response for CH_3CCl_3 in the standard to that observed in the high-pressure real-air sample) were calculated and are expressed as linear regression slopes. Error bars represent the range in linear regression slopes calculated when any single response ratio determination was removed from the slope calculation. Drift in the response ratio for ALM-64596 was so large that it does not appear on this figure (the standard at 195.7 ppt drifted at -3.2 (±0.1)% yr^{-1}).

As the influence of methyl chloroform on EECl and ECl diminishes, continued declines in EECl and ECl will be realized only if emissions of CFCs and related ozone-depleting gases become smaller than estimated for 1997 [*Montzka et al.*, 1999a]. An update of the *Montzka et al.* [1999a] analysis suggests that overall emissions of ozone-depleting gases have decreased only slightly since 1997 (Figure 5.15).

Emissions of halon-1211 have not decreased significantly during the 1990s despite stringent restrictions on production in developed countries since 1994 [*Butler et al.*, 1998a; *Fraser et al.*, 1999; *Montzka et al.*, 1999a]. The lack of a decline in emissions of this gas likely stems from the large reservoir of this chemical that currently exists in portable fire extinguishers in developed countries. Furthermore, production of halon-1211 in developing nations continued to increase in the 1990s each year through 1998 (the latest year for which production data are available). Production in developing countries is slated for reduction during 2002-2010. Continued emissions from the large amount of halon in existing fire extinguishers, and from new production, have resulted in a steady increase in the atmospheric concentration of halon-1211 through the end of 1999 (Figure 5.7b). This increase continues to retard the decline in EECl and ECl more than other gases. Unless further efforts are made to restrict continued production and emission of this halon, its concentration will likely increase for a number of years into the future because of the substantial reservoir of halon produced but not yet released to the atmosphere.

Emissions of the CFC-substitutes, known as the HCFCs and HFCs, also increased through the 1990s as use of CFCs and related ozone-depleting substances declined. These gases contribute less to reactive halogen in the stratosphere because a

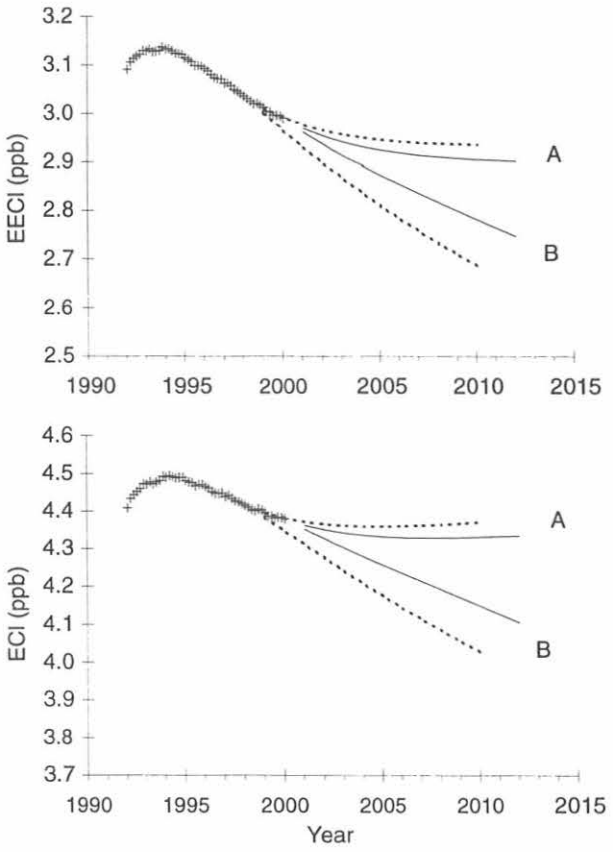

Fig. 5.15. The measured and potential future burden of ozone-depleting halogen in the lower atmosphere. Ozone-depleting halogen is estimated from tropospheric measurements of halocarbons by appropriate weighting factors to calculate Effective Equivalent Chlorine (EECl) for midlatitudes and Equivalent Chlorine (ECl) as an upper limit for polar latitudes [*Daniel et al.*, 1995; *Montzka et al.*, 1996a, 1999a]. Projections into the future are based on two scenarios: (A) emissions of all long-lived halogenated gases (CFCs, HCFCs, CH_3CCl_3, CCl_4, and halons) remain constant at 1999 levels, (B) scenario A with the exceptions that emissions of CFCs, CH_3CCl_3, and CCl_4 continue decreasing at ~10% yr^{-1}. Future scenarios indicated with dashed lines were formulated with ambient air measurements through 1997 [*Montzka et al.*, 1999a]; scenarios indicated with solid lines incorporated CMDL halocarbon measurements through the end of 1999.

large percentage of these gases is removed from the atmosphere in the troposphere, and certain HCFCs (HCFC-22 and HCFC-142b) degrade slowly in the stratosphere.

Measurements of Shorter-Lived Halogenated Gases

Measurements from flasks of shorter-lived gases continued during 1998-1999 (Figure 5.16). Both CH_3Cl and CH_3Br contribute significantly to the halogen burden of the stratosphere. Significant interannual variability was measured for both gases during 1995-1999 [*Montzka et al.*, 1999b]. For CH_2Cl_2 and C_2Cl_4 a trend towards lower mixing ratios is evident, particularly in the northern hemisphere. These decreases may result from efforts to reduce emissions of toxic organic compounds in some nations. Although such gases (CH_2Cl_2, C_2Cl_4, $CHCl_3$) contribute some to the halogen burden of the stratosphere, global measurements of them also provide an improved understanding

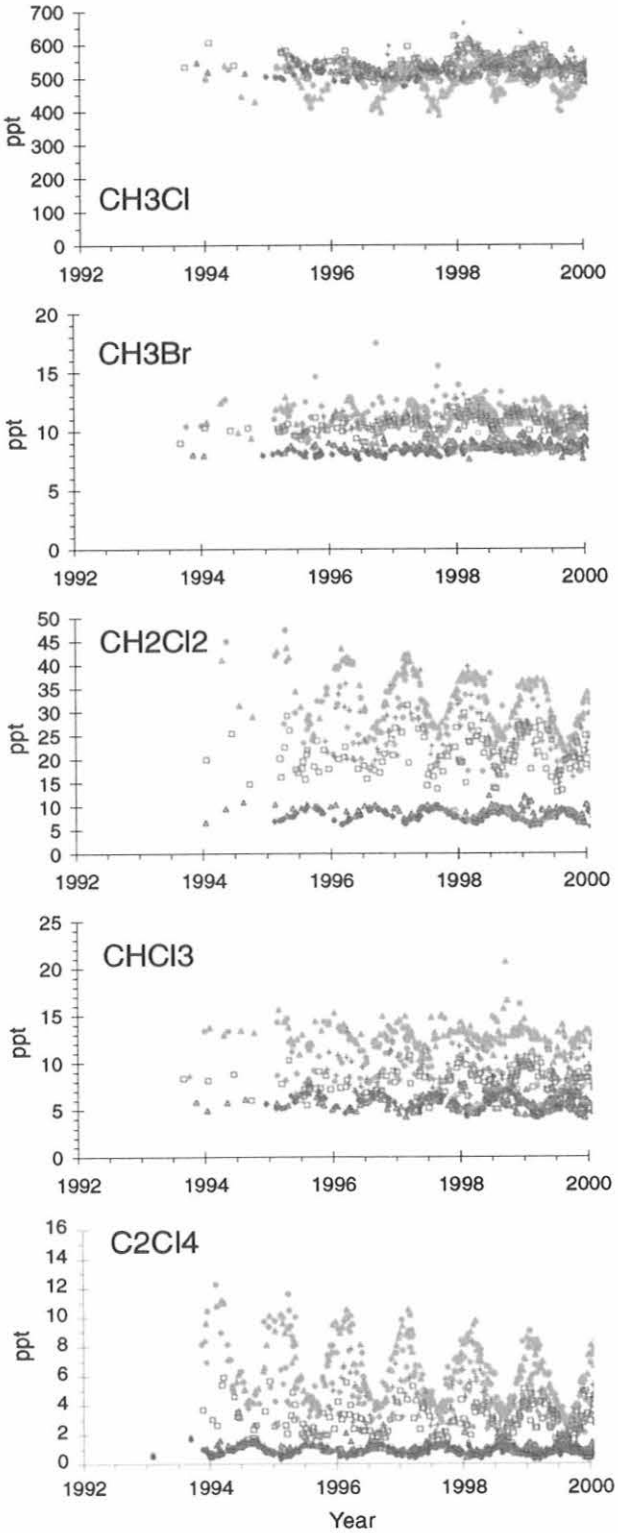

Fig. 5.16. Atmospheric dry-air mole fractions (ppt) determined for selected chlorinated trace gases and CH_3Br by GC-MS in the CMDL flask program. Each point represents the mean of two simultaneously filled flasks from one of eight or nine stations (symbols the same as in Figure 5.8). Results shown for all compounds except C_2Cl_4 are from 2.4-L flasks only.

of atmospheric processes such as trace-gas oxidation by OH and Cl atoms and atmospheric transport rates.

CMDL results for CH_2Cl_2 and C_2Cl_4 from GC-MS flask measurements were compared to mixing ratios calculated in a three-dimensional model [*Spivakovsky et al.*, 2000]. The comparison revealed that industrial emissions of CH_2Cl_2 are sufficient to account for the amount observed in the atmosphere; the addition of a relatively small oceanic source would cause the model to over-predict the observations in both hemispheres. The data also suggest that the actual loss rate of C_2Cl_4 is somewhat greater than can be accounted for by reaction with OH. This additional loss suggests either the bimolecular rate constant for the reaction OH + C_2Cl_4 is underestimated by ~30%, or additional atmospheric loss arises from significant Cl atom oxidation. The results for CH_2Cl_2 also provide unique constraints to the distribution of OH on hemispheric scales provided that air transport rates are well known. Concentrations of shorter-lived gases such as CH_2Cl_2 and C_2Cl_4 are more sensitive to rates of interhemispheric mixing than longer-lived gases such as CFCs and ^{85}Kr [*Spivakovsky et al.*, 2000]. Further improvement in our understanding of OH and Cl concentrations on smaller spatial scales from measurements of these gases will require a better understanding of air exchange rates. Measurements of long-lived gases that are increasing rapidly (such as HCFCs and HFCs) may provide this additional constraint.

5.1.3. In Situ Gas Chromatograph Measurements

Operations Update

Four-channel GC-ECD instruments, developed to replace the aging RITS instruments and add new measurement capabilities, were installed at the CMDL field sites (Barrow Observatory, Alaska (BRW); Mauna Loa Observatory, Hawaii (MLO); Samoa Observatory, American Samoa (SMO); and SPO). This new instrument is called Chromatograph for Atmospheric Trace Species (CATS). Three of the channels have packed gas chromatographic columns and the fourth contains a capillary column. The three packed-column channels are similar to those used in the RITS in situ GCs. They are used to measure three chlorofluorocarbons (CFC-11, CFC-12, and CFC-113), chlorinated solvents (CH_3CCl_3, $CHCl_3$, and CCl_4), N_2O, SF_6, and halon-1211. The capillary column is used to measure three new compounds for the HATS in situ program: HCFC-22 ($CHClF_2$) and two methyl halides (CH_3Cl and CH_3Br). The CATS GCs analyze an air sample once every hour.

New techniques were developed by the HATS group to measure HCFC-22 and the methyl halides with an ECD. An ECD is less sensitive to methyl halides than to the CFCs. To enhance the methyl halide response a larger air sample is required. An 80 cm^3 air sample is pre-concentrated on a cold trap held at about –60°C. The trap is subsequently heated to release and inject the sample onto the capillary column for separation. More detailed information on the chromatography of this channel can be found on a Web page at http://stndstealth.cmdl.noaa.gov/channel4.html.

The CATS GCs are controlled by a PC-based data acquisition system using the QNX operating system (QNX Software Systems Ltd., Kanata, Ontario). QNX is a multi-tasking UNIX operating system for PC that allows for simultaneous control of the GC, preliminary data processing, data backup and storage, and World Wide Web access. Each CATS GC is accessible via the Internet. System status and preliminary data can be accessed on-line.

The first CATS instrument was installed at SPO in late January 1998. A CATS instrument was installed at BRW in mid-June 1998. After 8 months the data comparison was deemed sufficient, and the RITS instrument was shut off (February 17, 1999). The MLO equipment was deployed in late September 1998, and the SMO instrument was deployed in December 1998. Comparisons of RITS and CATS instruments continue at SMO, SPO, and MLO. It is expected that these RITS instruments will soon be shut down.

Data Analysis – RITS

Trace gas mixing ratios measured by ground-based in situ instruments have shown marked changes over the 10-13 year record (Figure 5.17). These trends reflect changes in chemical usage, atmospheric lifetimes, and mandated world-wide termination of production and consumption of some chemicals. The RITS data sets, which include individual measurements, daily, monthly, hemispheric and global averages, are available on the Internet at ftp.cmdl.noaa.gov/hats.

Mixing ratios of CFC-11 leveled off in late 1993 indicating a temporary balance between source and sink strengths. The average global rate of decrease for the past few years is 1.6 ppt yr^{-1}. With an estimated atmospheric lifetime of 45 years, a global mean mixing ratio of 267 ppt at the beginning of 1999, and assuming negligible sources, the expected decrease in 1999 should have been 5.9 ppt yr^{-1}. Thus CFC-11 continues to be emitted to the atmosphere, albeit at rates that are less than those of the previous decade.

The average global concentration of CFC-12 reached 537 ppt at the end of 1999 and continues to grow in the troposphere at a reduced rate of 2 ppt yr^{-1}. From the average rate of decrease in the growth rate since 1995, it is projected that CFC-12 will peak in the atmosphere in the next 3-4 years (Figure 5.18).

Methyl chloroform emissions have decreased dramatically since early 1993. The effects of reduced emissions can be seen as a decrease in atmospheric mixing ratio (Figure 5.17). The global rate of decrease reached a maximum of 13.5 ppt yr^{-1} in 1996-1997. The interhemispheric difference is now very small (Figure 5.12), indicative of similar emissions in both hemispheres (near zero in this case). As emissions become negligibly small, the atmospheric lifetime can be estimated solely from the trend in atmospheric mixing ratio (Figure 5.19) [*Montzka et al.*, 2000]. Based on in situ measurements from 1998-1999, the globally averaged lifetime is estimated to be 5.6 years. This result is consistent with that obtained from flask-air measurements over the same time period (section 5.1.2). It is encouraging that the flask and in situ programs, employing different sampling methods, different detection methods, and slightly different calibration methods, can provide the same result over this period.

Mixing ratios of carbon tetrachloride have been decreasing globally since 1990 at an average rate near –0.8 ppt yr^{-1}. The interhemispheric difference indicates that sources are located primarily in the northern hemisphere. Because CCl_4 is used mainly as feedstock for the production of CFCs, which were banned in the industrialized nations, developing nations may be responsible for current emissions of CCl_4.

The tropospheric mixing ratio of N_2O continues to grow at a steady rate near 0.7 ppb yr^{-1} and has reached a global mean of 315.5 ppb at the end of 1999. A north-to-south gradient of 1.2 ppb persists over the period of record because of differences in the balance of sources and sinks in the northern and southern hemispheres.

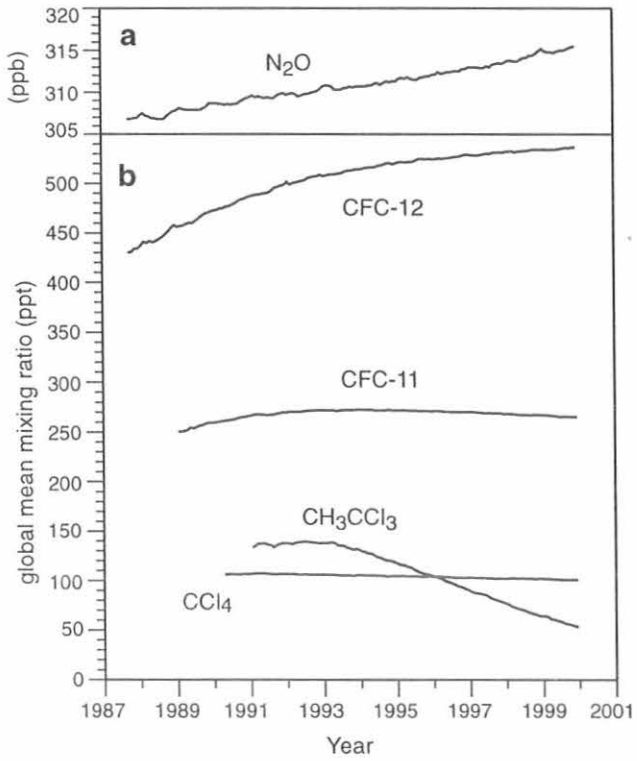

Fig. 5.17. Global monthly mean mixing ratios for (a) N_2O and (b) CFC-12, CFC-11, CH_3CCl_3, and CCl_4 from the in situ gas chromatographs.

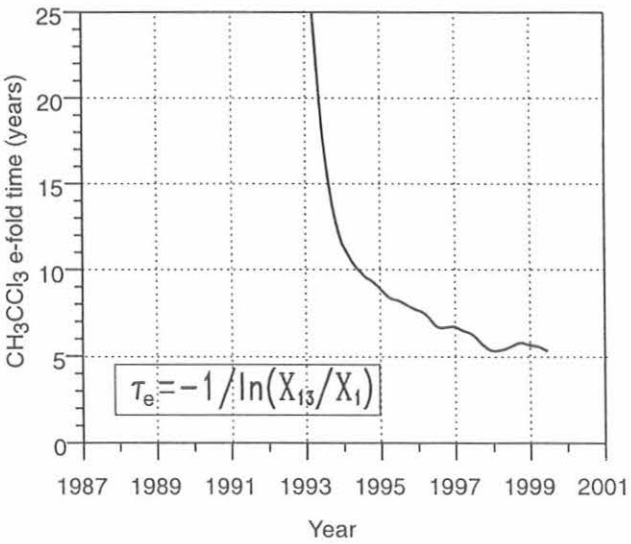

Fig. 5.19. Using a single box model for the atmosphere with emissions assumed to be negligible, the e-fold time (τ_e) is estimated using measured global mean methyl chloroform mixing ratios one year apart. X_1 is the monthly mean global mixing ratio for the first month and X_{13} is the mixing ratio 1 year later (13^{th} month). Calculated values approach a limit as the emissions truly become negligible.

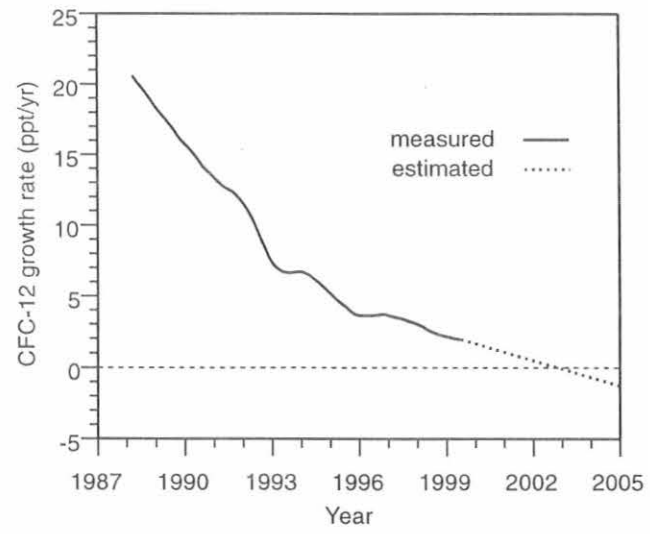

Fig. 5.18. Growth rate of CFC-12 as determined from in situ measurements. The growth rate is projected to reach zero in the next 3-4 years based on the average rate of decrease since 1995.

Data Analysis - CATS

Over the pasts 5 years the HATS instruments have monitored the decrease of several important ozone-depleting gases [*Elkins et al.*, 1993; *Montzka et al.*, 1996a, 1999a]. The new CATS GCs provide insight into additional ozone-depleting gases while still monitoring the trends of the CFCs and chlorinated solvents. HCFC-22 is a refrigerant compound that is replacing some of the phased-out CFCs. The CATS in situ measurements, in corroboration with the HATS flask program, have monitored the global atmospheric increase of HCFC-22 (Figure 5.20a). Emissions of HCFC-22 are solely anthropogenic, dominated by the industrial northern hemisphere. This can be seen as a mixing ratio gradient from north to south.

In situ measurements obtained by the HATS group have traditionally focused on long-lived compounds that have predominately anthropogenic sources. Recent measurements of the methyl halides have added important natural halocarbons to the suite of ozone-depleting gases measured by the HATS group. As the CFCs and other chlorinated compounds are phased out, the natural sources of methyl halides will become more important sources of atmospheric chlorine and bromine. Moreover, the sources of these compounds are not well understood [*Butler*, 2000]. Monthly mean trends of the CATS in situ data for CH_3Cl and CH_3Br show strong seasonal cycles in the northern hemisphere (Figures 5.20b and 5.20c). The seasonal cycle is at its minimum during the summer in both hemispheres when the dominant sink, hydroxyl radical (OH), is at its maximum.

With the addition of the CATS in situ methyl halide measurements at the CMDL observatories, there is the ability to not only monitor these compounds, but also help locate and quantify their sources. A recent study points to coastal vegetation as a source of CH_3Cl [*Yokouchi et al.*, 2000].

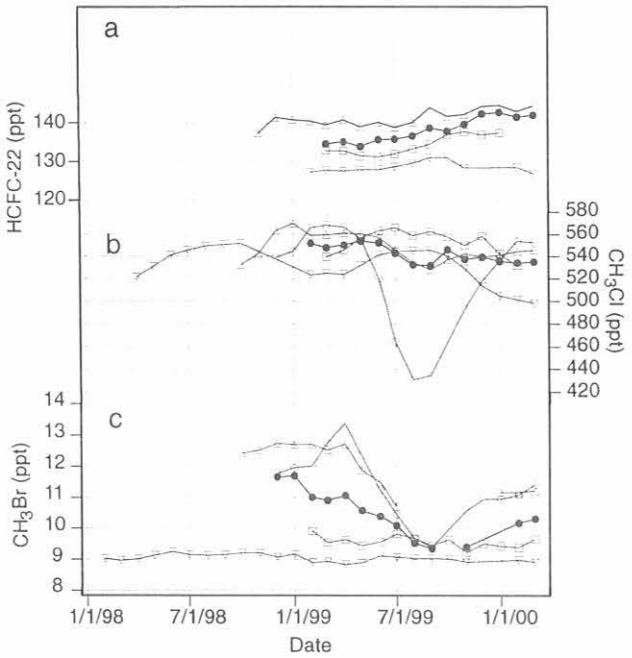

Fig. 5.20. Monthly mean mixing ratios of (a) HCFC-22, (b) methyl chloride, and (c) methyl bromide measured by the CATS in situ gas chromatographs deployed at the CMDL observatories (BRW, triangle; MLO, open circle; SMO, square; SPO, inverted triangle). The solid circles are global averages of the four sites calculated by cosine latitudinal weighting.

Measurements of CH_3Cl at our two tropical coastal sites, MLO and SMO, also point to a coastal terrestrial source. Figure 5.21 shows rapid changes in the CH_3Cl mixing ratio at Mauna Loa (Figure 5.21a) and corresponding changes in wind direction (Figure 5.21b). High concentrations of CH_3Cl are associated with periods of northerly winds (daytime up-slope conditions) that bring CH_3Cl-rich air from the vegetated northern section of the island of Hawaii up to MLO.

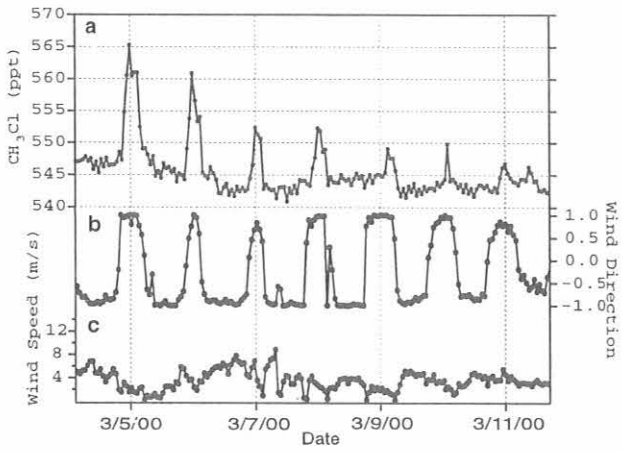

Fig. 5.21. Hourly measurements of CH_3Cl in air at MLO (a) show rapid variability in the CH_3Cl mixing ratio, indicating local sources. The cosine of the wind direction (values near 1 correspond to northerly winds, values near –1 correspond to southerly winds) (b) and wind speed (c) are plotted for comparison.

5.1.4. Gravimetric Standards

Calibration of Working Standards

In May 1999 the three-channel gas chromatograph system used to calibrate standards for the in situ monitoring program was replaced by a four-channel, custom-built GC. The four-channel GC is similar to the four-channel CATS instruments used for in situ monitoring at the observatories. The GC is operated under slightly different conditions compared to those at the observatories in order to optimize chromatography for cylinder calibration (Table 5.6).

The new four-channel instrument was compared to the old GC to ensure that the new GC would provide similar calibration results. For calibrations of ambient-level working standards, the new GC agreed to within 0.1% for N_2O, 0.4% for CFC-113, 0.5% for CH_3CCl_3, and 1% for CFC-11 and CCl_4. Initial tests revealed a 2-3% discrepancy for CFC-12. This experiment was repeated several months later, and the discrepancy could not be reproduced. Testing in December 1999 showed that the GCs agreed to within 0.2% for CFC-12. Following this CFC-12 experiment, the old three-channel GC instrument was retired. The four-channel GC is now used to calibrate working standards. Each standard is typically analyzed for 2 full days over a 2-3 week period (8-12 injections each day) (Table 5.7).

Preparation of Working Standards

Working standards for use with laboratory and in situ GCs continue to be filled at the C-1 site at Niwot Ridge, Colorado (40.04°N, 105.54°W, elevation 3013 m). Cylinders are filled using a three-stage, SA-6B compressor from Rix Industries (Oakland, California). Cylinders have occasionally been contaminated with trace amounts of unknown compounds that elute near CFC-11 and CFC-113 on the columns used in the CMDL in situ program. Contaminated standards have traditionally been associated with warm temperatures, while clean standards have been obtained during winter when ambient air temperatures are often below 5°C. The contaminants are thought to result from outgassing of material from the piston rings of one or more of the compressor stages (Ray Weiss, personal communication, 1999). Outgassing may be more severe at higher operating temperatures. To reduce the operating temperature of the first stage of the compressor, the compressor was modified in order to allow a small amount of distilled, de-gassed water to be injected into the air stream just upstream of

TABLE 5.6. Configuration of the Four-Channel GC for Calibration of Working Standards

Channel	Column	Detector	Compounds Resolved
1	Porapak Q	Valco ECD	N_2O, SF_6
2	Unibeads 1s	Shimadzu ECD	CFC-12, CFC-11, halon-1211
3	OV-101	Valco ECD	CFC-12, CFC-11, halon-1211, CFC-113, $CHCl_3$, CH_3CCl_3, CCl_4
4	Poraplot Q	Shimadzu ECD	HCFC-22, CH_3Cl, CH_3Br

TABLE 5.7. Analytical Precision Typically Obtained for a Complete Calibration of a Working Standard on the Four-Channel GC-ECD

Compound*	Precsion (%)
N_2O	0.05
CFC-12	0.08
CFC-11	0.10
CFC-113	0.15
halon-1211†	0.2
$CHCl_3$	1.0
CH_3CCl_3	0.2
CCl_4	0.1
SF_6	0.8

*Calibration of HCFC-22, CH_3Cl and CH_3Br is only performed on the flask GC-MS instrument at this time.

†The calibration scale for halon-1211 is determined on the flask GC-ECD instrument. Halon-1211 calibration on the four-channel instrument is complicated by a co-eluting peak occurring on both channels 2 and 3.

the first stage. Injection of water in this manner reduces the operating temperature of the first stage cylinder head from >100°C to ~50°C. Contamination is substantially reduced by injecting water at a rate of 10-20 mL min^{-1} (Figure 5.22).

Standards Preparation

A total of 66 natural-air standards were filled at Niwot Ridge during the 1998-1999 period. Fifty-eight of these were used by CMDL or related projects; eight standards were prepared for outside laboratories. A total of 10 gravimetric standards were prepared. Four were prepared for CMDL use, while 6 were prepared for outside laboratories.

Calibration Scales

A summary of the calibration scales used in conjunction with measurements performed by the HATS group is reported here. Table 5.8 lists the year that each calibration scale was established. Table 5.9 lists the gravimetric standards and mixing ratios used to define each calibration scale. Factors that influence the number of gravimetric standards used to define a particular scale include the time-history of the measurements, the range of concentrations investigated, and the linearity of response (e.g., CFC-12 measurements were made over more extensive spatial and temporal scales than CH_3Br, thus a large number of CFC-12 standards were prepared over the years). All of the standards listed in Table 5.9 were prepared in 5.9-L or 29.5-L Aculife-treated aluminum cylinders (Scott Specialty Gases, Plumsteadville, Pennsylvania).

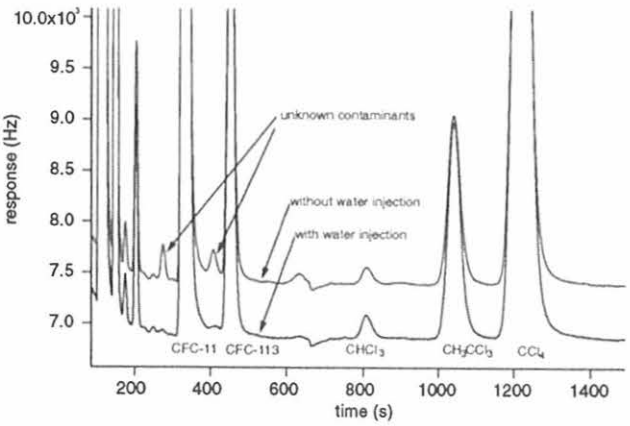

Fig. 5.22. Chromatograms of air samples from tanks pumped at Niwot Ridge, Colorado, with and without water injection (see text). The chromatogram (top) without water injection shows more contamination peaks.

TABLE 5.8. Reference Dates for HATS Calibration Scales

Compound	Year*	Reference‡
N_2O	1993	*Swanson et al.* [1993]
CFC-12	1997	*Butler et al.* [1998b]
CFC-11	1992	*Elkins et al.* [1993]
CFC-113	1993	*Swanson et al.* [1993]
CH_3CCl_3	1996	*Butler et al.* [998b]
CCl_4	1996	*Butler et al.* [1998b]
HCFC-22	1992	*Montzka et al.* [1993]
HCFC-141b	1994	*Montzka et al.* [1994]
HCFC-142b	1994	*Montzka et al.* [1994]
HCFC-134a	1995	*Montzka et al.* [1996b]
CH_3Cl	1996	*Butler et al.* [1998b]
CH_3Br	1996	*Butler et al.* [1998b]
CH_2Cl_2†	1992	*Spivakovsky et al.* [2000]
C_2Cl_4†	1992	*Hurst et al.* [1997]
$CHCl_3$†	1992	*Hurst et al.* [1997]
halon-2402†	1992	*Butler et al.* [1998b]
halon-1211	1996	*Butler et al.* [1998a]
halon-1301	1990	*Butler et al.* [1998a]
SF_6	1994	*Geller et al.* [1997]
H_2	1995	*Novelli et al.* [1999]
CO	1991	*Novelli et al.* [1991]

*Calibration scales are defined by a particular set of gravimetric standards (see Table 5.9). In some cases only a single standard is used. The year shown for each species refers to either the year during which the standards were prepared or the year in which a significant change in calibration scale occurred. Thus data reported prior to the year listed are associated with a different calibration scale than those reported in subsequent years.

†These species are measured by CMDL, but their calibration is defined only by an incomplete set of standards.

‡The reference listed for each species refers to a publication that describes a calibration change or a publication that includes recent results.

Examples of calibration response curves determined on the CATS GC instrument are shown in Figure 5.23. The uncertainty associated with the calibration curves (expressed as the standard error of the residuals) is typically 0.2-0.5%.

The number of gravimetric standards used to define scales for N_2O and SF_6 will be expanded in the near future. A number of standards with N_2O and SF_6 mixing ratios near ambient levels will be prepared. The addition of numerous standards at near-ambient concentrations will enable high-precision maintenance of the scales over time.

5.2. AIRBORNE PROJECTS

5.2.1. AIRBORNE CHROMATOGRAPH FOR ATMOSPHERIC TRACE SPECIES (ACATS-IV)

Overview

Airborne Chromatograph for Atmospheric Trace Species (ACATS-IV) is a four-channel gas chromatograph designed to

TABLE 5.9. Gravimetric Standards Used to Define Calibration Scales for the HATS Group

Compound	Cylinder Number	Prepared Gravimetric Concentration	Compound	Cylinder Number	Prepared Gravimetric Concentration
N_2O	*ALM-38408	96.2 ppb	SF_6	*CLM-7506	3.1 ppt
	*ALM-26738	172.0 ppb		*CLM-7519	23.2 ppt
	*ALM-26743	331.0 ppb		*CLM-7494	60.6 ppt
	*ALM-26737	359.9 ppb		*CLM-7503	107.6 ppt
	*CLM-30135	801.1 ppb	CH_3Br	†CLM-7490	5.3 ppt
CFC-11	*ALM-38408	25.5 ppt		†ALM-62626	5.3 ppt
	*CLM-2431	49.5 ppt		†ALM-39771	25.6 ppt
	*ALM-38417	80.9 ppt	CH_3Cl	†ALM-39971	1024 ppt
	*CLM-2482	69.2 ppt	HCFC-22	†ALM-26738	105 ppt
	*ALM-26735	75.16 ppt		†ALM-26743	145 ppt
	*CLM-2413	136.3 ppt		†ALM-26735	105 ppt
	*ALM-26743	288.2 ppt		†ALM-38417	111.6 ppt
	*ALM-26737	313.6 ppt		†ALM-26737	158 ppt
CFC-12	*CLM-2426	77.8 ppt	HCFC-141b	†ALM-39758	5.0 ppt
	*CLM-2431	163.5 ppt		†ALM-39744	25.5 ppt
	*CLM-9015	189.2 ppt		†ALM-39749	51.3 ppt
	*CLM-2482	228.8 ppt	HCFC-142b	†ALM-39758	5.0 ppt
	*CLM-9041	274.4 ppt		†ALM-39744	25.4 ppt
	*CLM-9018	370.3 ppt		†ALM-39749	51.1 ppt
	*CLM-2413	450.7 ppt	HCFC-134a	†CLM-8952	5.44 ppt
	*CLM-9038	646.9 ppt		†CLM-9036	10.22 ppt
CFC-113	*CLM-2482	19.1 ppt	halon-1211	*†CLM-9039	3.02 ppt
	*CLM-2413	37.5 ppt		*†CLM-9024	5.41 ppt
	*†ALM-26735	48.0 ppt	halon-1301	*†CLM-2416	95.4 ppt
	†ALM-26738	48.0 ppt		*†FF-30071	6.08 ppb
	*†ALM-26743	82.8 ppt	halon-2402	†ALM-26748	47.5 ppt
	*†ALM-26737	90.0 ppt	CH_2Cl_2	†ALM-26748	122.0 ppt
CH_3CCl_3	*†ALM-52792	30.9 ppt	C_2Cl_4	†ALM-26748	157.0 ppt
	*†ALM-52788	70.8 ppt	$CHCl_3$	†ALM-26748	141.0 ppt
	*†ALM-59967	111.0 ppt			
	*†ALM-52811	151.4 ppt			
CCl_4	*†ALM-52792	22.1 ppt			
	*†ALM-52788	50.6 ppt			
	*†ALM-59967	79.4 ppt			
	*†ALM-52811	108.3 ppt			

*These standards are used to define the calibration scales associated with GC-ECD instruments.
†These standards are used to define the calibration scales associated with GC-MS instruments.

measure atmospheric trace gases in the upper troposphere and lower stratosphere onboard the NASA high-altitude ER-2 aircraft [*Elkins et al.*, 1996]. ACATS-IV measures six chlorinated trace gases (CFC-12, CFC-11, CFC-113, $CHCl_3$, CH_3CCl_3, CCl_4) in addition to halon-1211, N_2O, CH_4, H_2, and SF_6. ACATS-IV has been part of the ER-2 payload for studies of stratospheric transport and ozone depletion since 1994, and in 1997 participated in the Photochemistry of Ozone Loss in the Arctic Region in Summer (POLARIS) study. The principal objective of POLARIS was to determine the roles of photochemistry and transport in summertime decreases of stratospheric ozone over the arctic. Nineteen instruments onboard the NASA high-altitude ER-2 aircraft made in situ measurements of trace gases, radicals, aerosols, radiation, and meteorology in the upper troposphere and lower stratosphere of the northern hemisphere during spring, early summer, and late summer. The edge of the arctic polar vortex was penetrated during one flight in late April, and fragments of the eroding vortex were sampled during several other flights in May and June. The observed 35% decrease of the ozone column above Fairbanks, Alaska, was largely attributed to photochemistry, predominantly catalytic reactions between O_3 and NO in air parcels continuously exposed to sunlight for up to 10 days. ACATS-IV data from POLARIS were incorporated in several publications that appeared during 1999 [e.g., *Hurst et al.*, 1999; *Romashkin et al.*, 1999; *Sen et al.*, 1999; *Toon et al.*, 1999].

Hydrogen Budget

The total hydrogen budget of the northern hemisphere lower stratosphere was recently evaluated for closure from in situ measurements of H_2O, CH_4, and H_2 onboard the NASA ER-2 aircraft during POLARIS and the 1995-1996 Stratospheric Tracers of Atmospheric Transport (STRAT) mission [*Hurst et al.*, 1999]. Budget closure requires that measured abundance relationships between these principal hydrogen reservoirs corroborate theoretical hydrogen partitioning predicted by reactions that oxidize CH_4 to H_2O and H_2, and oxidize H_2 to H_2O. A simple evaluation of these reactions predicts that H_2O production (ΔH_2O) should equal two times CH_4 loss ($-2 \cdot \Delta CH_4$) plus the net change in H_2 (ΔH_2). ACATS-IV measurements revealed that H_2 mixing ratios are relatively constant in the lower stratosphere (Figure 5.24). From the measured $\Delta H_2/\Delta CH_4 = -0.027 \pm 0.003$ (Figure 5.24), the ratio of H_2O production to CH_4 destruction ($\Delta H_2O/\Delta CH_4$) was predicted to be -1.973 ± 0.003 [*Hurst et al.*, 1999].

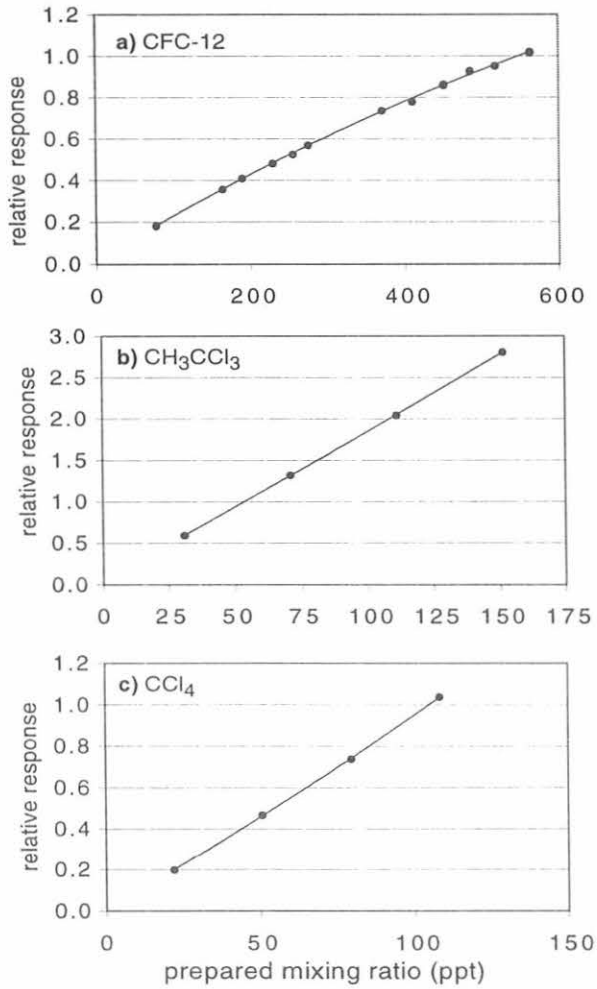

Fig. 5.23. Sample calibration curves for CFC-12 (a), CH_3CCl_3 (b), and CCl_4 (c). Each filled circle represents the response of a gravimetric standard relative to a working standard. Solid lines are second-order polynomial fits to response data.

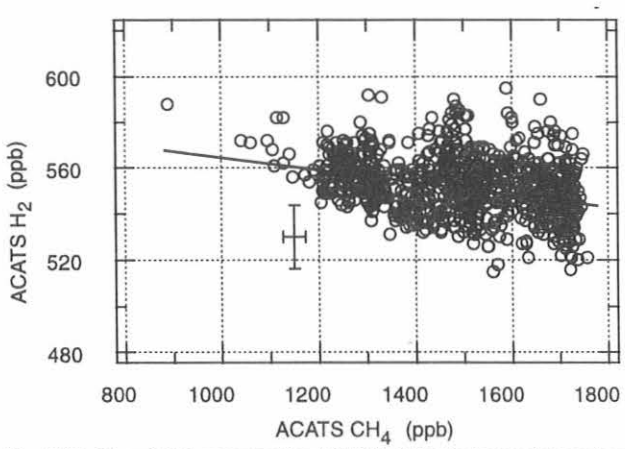

Fig. 5.24. H_2 and CH_4 measured by ACATS-IV in the lower stratosphere between 3°S and 60°N latitude during STRAT (1995-1996). The solid line is an ODR fit to the data with a slope of -0.027 ± 0.003, indicating that H_2 production slightly exceeds H_2 destruction in the strtosphere. The crossed error bars represent the average random errors (1σ) of the measurements.

This predicted relationship was compared to the slope of the anticorrelation between H_2O and CH_4 mixing ratios measured in the lower stratosphere during STRAT and POLARIS. H_2O was measured during both campaigns by the Harvard University Lyman-α hygrometer [*Hintsa et al.*, 1999] and also by the Jet Propulsion Laboratory (JPL) tunable diode laser (TDL) hygrometer during POLARIS. CH_4 was measured by ACATS-IV and a JPL TDL spectrometer. The anticorrelation between H_2O and CH_4 in the lower stratosphere was found to be tight and linear for air masses with mean ages greater than 3.8 years (Figure 5.25). In younger air masses large variations in H_2O mixing ratios degrade the compactness of the anticorrelation. These variations result from the seasonal cycle of temperature near the tropical tropopause, the entry point for most stratospheric air masses. Air masses passing through the tropical tropopause are regularly imprinted with an H_2O mixing ratio dictated by the lowest temperature they encounter [e.g., *Mote et al.*, 1996]. As young air masses age in the stratosphere, they gradually lose their H_2O imprint as they mix with air masses of different H_2O content.

Data from each unique combination of H_2O and CH_4 instruments were fit with an orthogonal distance regression (ODR). Data for air masses with mean ages <3.8 year (or alternately CH_4 >1450 ppb) were excluded from the fits. For all instrument combinations the mean slope ($\Delta H_2O/\Delta CH_4$) was -2.15 ± 0.18 (1σ). The mean slope using only ACATS-IV CH_4 data, -2.02 ± 0.17, is in excellent agreement with the predicted $\Delta H_2O/\Delta CH_4 = -1.973$. The annual mean mixing ratio of H_2O in air masses entering the stratosphere was estimated from the slope and intercept values from each ODR and a CH_4 mixing ratio of 1.7 ppm (the annual mean CH_4 mixing ratio entering the stratosphere). The result, 4.0 ± 0.4 ppm H_2O, agrees well with the 3.8 ± 0.3 ppm H_2O deduced from a recent re-evaluation of radiosonde temperature data near the tropical tropopause [*Dessler*, 1998].

Tracer Correlations

Measurements of CH_3CCl_3 and CFC-11 in the lower stratosphere during POLARIS revealed significant differences in the CH_3CCl_3-CFC-11 correlation between spring and summer, 1997 [*Romashkin et al.*, 1999]. These differences were associated with the rapid decrease of tropospheric CH_3CCl_3 that began in 1992 (see sections 5.1.2, 5.1.3) and the fact that the mean ages of the air masses observed during spring and summer differed by up to 1 year.

Before the CH_3CCl_3-CFC-11 correlations could be used to gain insight into stratospheric transport, the influences of the large tropospheric CH_3CCl_3 trend on the lower stratospheric CH_3CCl_3 distribution had to be minimized. Initially, the CH_3CCl_3 mixing ratio in each air mass sampled by ACATS-IV was normalized to the CH_3CCl_3 mixing ratio in air masses that entered the stratosphere on January 1, 1997. The normalization was based on the well-documented trend of tropospheric CH_3CCl_3 (Figure

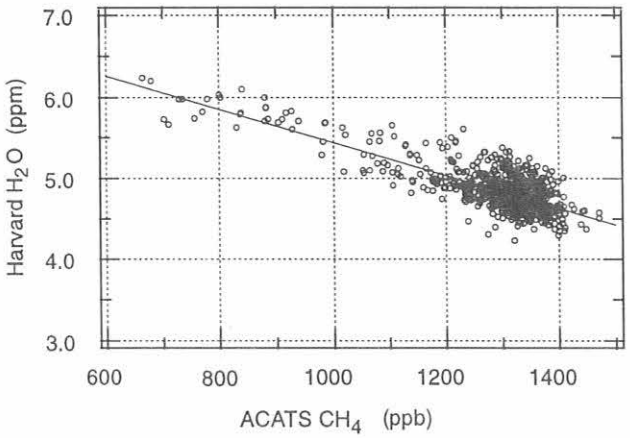

Fig. 5.25. A tight, linear anticorrelation between Harvard H_2O and ACATS-IV CH_4 was observed in the lower stratosphere during STRAT (1995-1996) and POLARIS (1997). The solid line is an ODR fit to the data with a slope of -2.01 ± 0.16. Data for air masses with mean ages <3.8 years were omitted from this analysis.

5.9) and the mean ages of stratospheric air masses calculated from ACATS-IV measurements of SF_6.

This normalization procedure, based solely on mean age, is inexact because an air mass is better characterized by a spectrum of ages [*Hall and Plumb*, 1994]. Two methods were used to quantify the effect of age spectra width on the initial normalization. In the first method, the stratospheric entry mixing ratio of CH_3CCl_3 was expressed as the mean tropospheric mixing ratio of CH_3CCl_3 over ±1.25-year intervals, the estimated width of the age spectrum [*Volk et al.*, 1997]. For the second method, a 10-year-wide age spectrum (Green's) function based on a one-dimensional diffusive model (equation 21 of *Hall and Plumb* [1994] with diffusion coefficient $K = 1.5\ m^2\ s^{-1}$) was used to weight the CH_3CCl_3 tropospheric trend. The model-derived, weighted trend was used in combination with mean ages from ACATS-IV because the model underpredicts mean ages by a factor of two or more. The two normalization methods were similar in their influences on lower stratospheric CH_3CCl_3 mixing ratios.

Correlations between normalized CH_3CCl_3 and CFC-11 mixing ratios (Figure 5.26c) exhibit greater curvature than the raw correlations (Figure 5.26b). The induced curvature reveals straight lines of data between different parts of the correlation, evidence that air has mixed between the polar vortex and the midlatitudes (lines α and β on Figure 5.26c). These mixing lines were not visible in the linear, un-normalized correlations (Figure 5.26b). The study confirms that stratospheric correlations between trace gases can be significantly altered by a strong tropospheric trend in one of the gases.

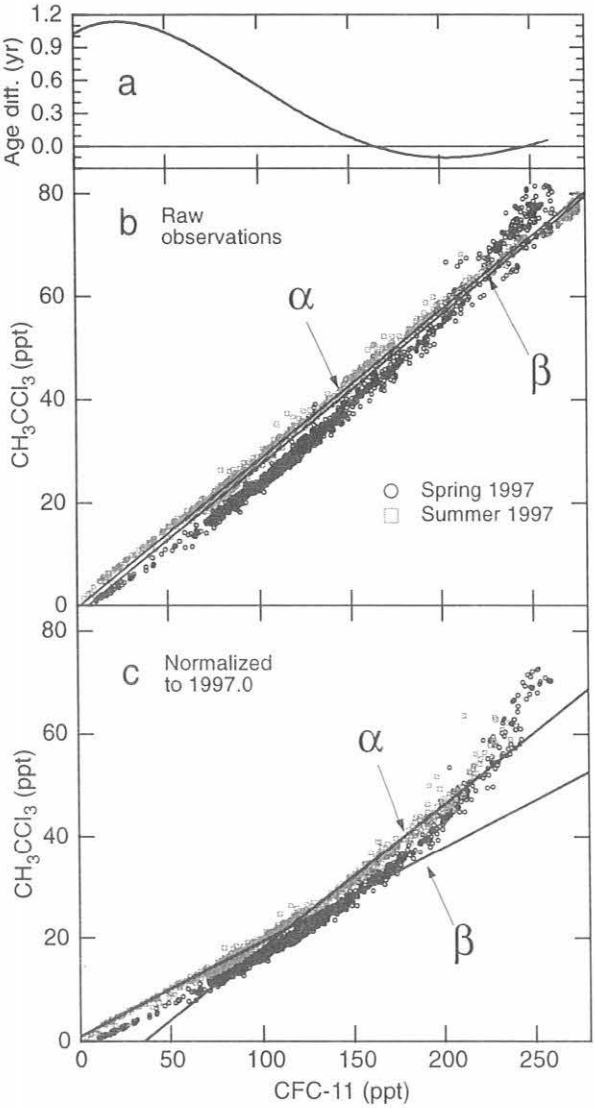

Fig. 5.26. Results from CH_3CCl_3 and CFC-11 measurements made during the POLARIS campaign (1997): (a) differences between the SF_6-based mean ages of air masses sampled by ACATS-IV (summer-spring), (b) correlations between CH_3CCl_3 and CFC-11 during spring and summer, and (c) same correlations as (b) with the effects of the tropospheric CH_3CCl_3 trend removed using 10-year-wide age spectrum, normalized to January 1, 1997. Solid lines in (b) and (c) are least squares fits to the following data subsets: α, 100 ppt<CFC-11<225 ppt measured on June 26, 1997; β, 0 ppt<CFC-11<125 ppt measured on June 29, 1997.

Total Inorganic Chlorine

Sen et al. [1999] compared two methods of determining the total inorganic chlorine content (Cl_y) of air masses sampled in the arctic stratosphere during POLARIS. In the first method, Cl_y was calculated as the difference between the total chlorine content (Cl_{tot}) of an air mass when it entered the stratosphere and the total organic chlorine content (CCl_y) of the same air mass at the time it was sampled by the ER-2. CCl_y was determined from ACATS-IV in situ measurements of chlorinated source gases near 20 km altitude (lower stratosphere) during the ER-2 flight of April 26, 1997. Cl_{tot} values for the sampled air masses were compiled from time series of source gas mixing ratios measured at the Earth's surface in flasks and at NOAA observatories [*Woodbridge et al.*, 1995; *Montzka et al.*, 1996a]. The date of stratospheric entry of each sampled air mass was determined from its mean age calculated from ACATS-IV SF_6 data. Cl_y was also calculated as the sum of remotely sensed solar occultation Fourier transform infrared (FTIR) measurements

of HCl, $ClONO_2$, and HOCl by the JPL MkIV interferometer and estimates of ClO from a photochemical model. The MkIV observations were made during a balloon flight on May 8, 1997. These two methods of estimating Cl_y agree to within 10% (Figure 5.27), adding confidence to both the in situ and remotely sensed data and suggesting that the photochemical model estimates of ClO are realistic for the sunlit lower stratosphere.

Intercomparison of Trace Gas Measurements

ACATS-IV measurements of CFC-11, CFC-12, CFC-113, CCl_4, and SF_6 during POLARIS were compared to remotely sensed solar occultation FTIR measurements by the JPL MkIV interferometer on a balloon floating at 38 km altitude [*Toon et al.*, 1999]. Both sets of tracer data were correlated with N_2O to account for the different dynamical histories of air masses sampled several days apart by the two instruments. Differences were less than 2% for both CFC-11 and CFC-12, well within the experimental uncertainties of the MkIV measurements. CFC-113 and CCl_4 data agreed to within experimental uncertainties (11-15%) between 13 and 21 km altitude, but the MkIV mixing ratios of both gases increased anomalously below 13 km. The anomalous increases were not observed for other long-lived tracers and were attributed to interfering absorption lines in the spectral regions used to quantify these gases. ACATS-IV SF_6 mixing ratios were on average 0.5 ppt (14%) lower than the MkIV values. This bias is surprising given that there was no discernable bias between SF_6 data from ACATS-IV and the Atmospheric Trace Molecule Spectroscopy (ATMOS) FTIR instrument aboard the space shuttle during 1993 and 1994 [*Chang et al.*, 1996; *Michelson et al.*, 1999]. The reason for this discrepancy has not yet been determined.

Instrument Modifications for TIES and SOLVE

ACATS-IV was modified twice during the second half of 1999 in preparation for the 2000 Stratospheric Aerosol and Gas Experiment-III (SAGE) Ozone Loss and Validation Experiment (SOLVE) in Kiruna, Sweden. The first modifications were made for the 1999 Tracer Intercomparison Experiment for SOLVE (TIES) mission, a side-by-side intercomparison of coincident measurements by the three in situ N_2O and CH_4 instruments selected for the SOLVE ER-2 payload. TIES was conducted at NASA Dryden, Edwards Air Force Base, California, during September-October 1999. The mission was a critical evaluation of N_2O and CH_4 measurements by the JPL TDL spectrometer and a new, lightweight, compact TDL spectrometer that will replace a heavy, large TDL spectrometer that provided high quality N_2O data aboard the ER-2 for many years. ACATS-IV was modified to include a new, rapid chromatography channel to measure N_2O and SF_6 every 70 seconds. The new channel was operated in parallel with the "old" 250-s N_2O and SF_6 channel during TIES, and the coincident data were in excellent agreement. ACATS-IV measurements of N_2O and CH_4 were used to assess the reliability of higher-frequency measurements by the TDL instruments. The assessment demonstrated that the quality of TDL N_2O data was, at times, inadequate for the upcoming SOLVE mission, and that further refinements of the spectrometers and their retrieval algorithms were necessary.

ACATS-IV was again modified after the TIES mission by replacing the "old" N_2O and SF_6 channel with a new, rapid chromatographic channel to measure CFC-12 and halon-1211 every 70 seconds. This channel was thoroughly tested in the laboratory for artifacts, flown during SOLVE test flights in December 1999 and then adopted as part of the final instrument configuration for SOLVE. The two modifications to ACATS-IV enabled 70-s measurements of N_2O, SF_6, CFC-12, and halon-1211, 140-s measurements of CFC-11, CFC-113, $CHCl_3$, CH_3CCl_3, CCl_4, CH_4, and H_2, and improved the precision of SF_6 and halon-1211 measurements to about ±1% during SOLVE.

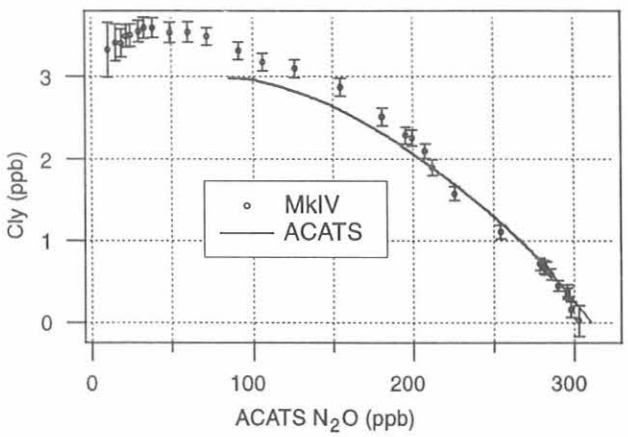

Fig. 5.27. Two independent methods were used to determine the total inorganic chlorine content (Cl_y) of stratospheric air masses during POLARIS (1997). One method (solid line) utilized CMDL surface measurements of chlorinated source gases and ACATS-IV (1997) measurements of organic chlorine compounds in the lower stratosphere. The other method (open circles) combined MkIV measurements of HCl, $ClONO_2$, and HOCl and modeled estimates of ClO. The two methods agree to within 10%.

5.2.2. LIGHTWEIGHT AIRBORNE CHROMATOGRAPH EXPERIMENT (LACE)

LACE is a three-channel gas chromatograph that operates on the NASA-sponsored Observations in the Middle Stratosphere (OMS) gondola and the NASA WB-57F aircraft. The OMS platform represents a collaboration with scientists from CMDL, Cooperative Institute for Research in Environmental Sciences (CIRES), NOAA Aeronomy Laboratory (AL), JPL, NASA Ames Research Center, Harvard University, and Penn State University. The WB-57F platform represents collaboration with scientists from CMDL, CIRES, AL, National Center for Atmospheric Research (NCAR), University of Denver, JPL, NASA, and California Institute of Technology.

OMS deployments at Fairbanks, Alaska, and Brazil were reported in *Ray et al.* [1999]. On May 18, 1998, CMDL participated in a midlatitude OMS balloon flight out of Fort Sumner, New Mexico, as a follow-up to the STRAT and POLARIS campaigns. After finalizing the data from this flight, the LACE instrument was modified for the Atmospheric Chemistry and Combustion Effects Near the Tropopause (ACCENT) campaign designed to investigate the effects of rocket and aircraft combustion in the upper troposphere and lower stratosphere and the SOLVE campaign designed to examine the processes controlling ozone levels at mid- to high latitudes.

A new chromatography channel was developed that proved advantageous for both campaigns. This channel measures molecular hydrogen, methane, and carbon monoxide once every

140 seconds. Carbon monoxide was included on the ACCENT mission to help identify rapid convection in the troposphere. Molecular hydrogen and carbon monoxide were included on the SOLVE campaign because of their strong mesospheric sources, and methane was included to help close the hydrogen budget [*Hurst et al.*, 1999].

The ACCENT campaign in Houston, Texas, (September 1999) utilized an unpressurized chamber in a WB-57F aircraft. Substantial thermodynamic, mechanical, and electrical modifications of the LACE instrument were required in order to participate in the ACCENT mission. LACE operated successfully on all eight ACCENT science flights, including a tropical flight, a flight over the eye of hurricane Floyd, a flight within the commercial airline flight corridor, and a rocket plume intercept. The ACCENT data were finalized and submitted to the NASA archive. Following the ACCENT campaign, LACE was reconfigured to fly on the balloon platform as part of the OMS SOLVE campaign in Kiruna, Sweden.

The SOLVE campaign began with a balloon flight well inside the northern vortex just days after the vortex had formed (November 19, 1999). Preliminary analysis of these data revealed many interesting features of atmospheric transport such as the rate of descent of air within the vortex, the degree of entrainment of midlatitude air into the vortex, and mixing characteristics within the vortex.

Tracers such as CO, H_2, and SF_6 that have large vertical gradients in the mesosphere can also provide an estimate of the distribution of altitudes from which air originated before descending into the vortex. Estimates of the mesospheric sources and sinks for these molecules can also be made. After quantifying the mesospheric losses of SF_6 and CO_2, limits on the corrections to the age profiles calculated from these molecules can be quantified. In addition to providing information on vortex air descent, these measurements contributed to ongoing studies of transport in the lowermost stratosphere [*Ray et al.*, 1999].

5.2.3. PAN AND OTHER TRACE HYDROHALOCOMPOUNDS EXPERIMENT (PANTHER)

The next step in evolution for the HATS airborne gas chromatographs is the development of the PANTHER instrument. ACATS-IV and LACE instruments use packed columns and electron capture detectors. In addition to these technologies, PANTHER will incorporate cryogenic trapping to collect larger samples, capillary columns to increase separation and signal-to-noise, and a Hewlett Packard (HP, now Agilent Technologies) model 5973 quadrupole mass selective detector (MSD). These added technologies will enable PANTHER to make in situ measurements of the CFC replacement molecules, methyl halides, peroxyacetyl nitrate (PAN, $CH_3C(O)OONO_2$), and one of PAN's precursors, acetone.

Initial activities focused on proof of concept studies. Three basic concepts (chromatography, calibration, and data acquisition) had to be addressed before design and construction of the flight instrument could begin.

The first objective was to show that adequate chromatography could be achieved. Reliable chromatography of the CFC replacements and the methyl halides has already been demonstrated within the HATS group by the flask, ocean, and in situ projects. Chromatography for PAN and acetone are new concepts for the HATS group. This year, in collaboration with NOAA Aeronomy Laboratory, PAN was successfully separated from the air peak using a 5-m, 0.53-mm inside diameter, megabore column with a 1-µm thick RTX 200 coating, cooled to 15°C. Output from this column was directed into the HP-G1533A anode-purged ECD and the MSD. A detection limit of better than 3 ppt was demonstrated for the ECD, and an impressive detection limit of better than 0.8 ppt was demonstrated for the MSD using the chemical ionization source, with a flow of 1 sccm CH_4. Peroxypropionyl nitrate (PPN, $CH_3CH_2C(O)\text{-}OONO_2$) was also detected.

A modest sensitivity to acetone was detected on the MSD; the ECD has no sensitivity to acetone. However, large (100 cm^3), cryo-focused samples are needed. A 30-m, 0.25-mm inside diameter HP-5MS capillary column was used with a 0.25-µm thick 5% PH ME siloxane film to separate acetone and many of the HCFCs from the air peak. Using an electron ionization source and running the quadrupole in single ion mode, tuned to mass/charge (m/z) ratios of 58 and 43, a detection limit of 1 ppt was obtained for acetone. A detection limit of 0.3 ppt for HCFC-141b at m/z of 81 was verified. No chromatographic interference was found when 50 ppm of O_3 was dynamically mixed with the inlet stream. For ease, this work was done with a liquid N_2 cryogen. Thermal electric coolers will be employed in the flight instrument.

Calibration of ACATS-IV and LACE systems was achieved by in situ analysis of gas mixtures stored in Aculife-treated aluminum cylinders. This method will not work for PAN because it cannot be reliably stored as a gas mixture. An in-flight PAN source will be required for calibration. The generation of PAN from a calibrated NO source dynamically diluted to the ppt level was studied. PAN was produced by photolyzing acetone at 285 nm in the presence of NO. Carbon monoxide was added to quench competing reactions.

The third proof of concept area was to resolve incompatibilities between the HP MSD instrument control, data acquisition involving Chemstation on a Windows NT operating system utilizing an HPIB bus, and the airborne HATS approach using DOS with a metrobite bus. The most recent GCs built within the HATS group are the CATS GCs with QNX. Substantial development of reliable GC control and data acquisition was invested in this operating system. QNX requires a relatively small memory overhead compared to the NT operating system and is less prone to system crashes prevalent with the Windows NT environment. Both HP-IB (IEEE) and RS-485 drivers for the QNX operating system exist. Using these drivers the HP MSD runs entirely from QNX. The new smart electrometers, gas-sample valves, and the stream-selection valve were moved off of the stack built by Tommy Thompson and onto RS-232 and RS-485 serial communication lines, reducing wiring and power requirements. This should result in an instrument that is lighter, easier to work with, and more dependable.

With these three issues resolved, the design and construction phase of the project will proceed in 2000. Validation flights onboard the ER-2, WB-57F, or both will take place in 2001.

5.3. OCEAN PROJECTS

Observations

The oceans play an important role in the atmospheric budgets of halogenated, organic gases, both as sources and sinks. Natural halocarbons contribute a substantial amount of chlorine and bromine to the troposphere and, in some cases, the stratosphere. Methyl bromide (CH_3Br) and methyl chloride (CH_3Cl) together contribute about one quarter of the total equivalent chlorine to the atmosphere [*Butler*, 2000]. As the production and use of the anthropogenic, halogenated gases are phased out, methyl halides, which are primarily natural in origin, will play an increasingly important role in regulating stratospheric ozone.

Other halogenated compounds, such as dibromomethane (CH_2Br_2) and bromoform ($CHBr_3$), could be important sources of bromine to the stratosphere. While these compounds are generally present at low concentrations in the atmosphere and have short lifetimes, rapid vertical transport, particularly in the tropics, could provide a mechanism by which they could participate in stratospheric ozone depletion. An understanding of the sources and sinks of these compounds is needed to predict recovery of stratospheric ozone in the event of climate change.

The HATS group participated in two research cruises during 1998-1999 with the goal of quantifying the fluxes that constitute the oceanic cycle of CH_3Br. On both cruises, conducted aboard the NOAA ship *Ronald H. Brown*, the group made saturation measurements in conjunction with CH_3Br production and degradation measurements made by other groups. The first cruise, RB-98-02, Gas Exchange Experiment (GasEx 98), focused on the North Atlantic and coastal northeastern Pacific Oceans during May-July 1998 [*King et al.*, 2000]. The cruise departed from Miami, Florida, and ended in Newport, Oregon, with port stops in Lisbon, Portugal, Ponta Delgada, Azores, and Miami, Florida (Figure 5.28). The focal point of this cruise was a month-long air-sea exchange experiment in a cold-core eddy northeast of the Azores. The second cruise, RB-99-06, Bromine Air-Sea Cruise Pacific (BACPAC 99), was conducted in the North Pacific during September-October 1999, departing from Kwajalein, Marshall Islands, and ending in Seattle, Washington, with port stops in Oahu, Hawaii, and Dutch Harbor, Alaska (Figure 5.28).

During GasEx 98 CH_3Br was supersaturated in temperate waters and undersaturated in tropical and subtropical waters (Table 5.10). Supersaturation implies a net flux from the ocean to the atmosphere, while undersaturation implies the reverse. These trends were particularly evident during the third leg of the cruise from the Azores to Miami, as the saturation anomaly became more pronounced with decreasing latitude (Figure 5.29). The CH_3Br supersaturations in the temperate northeastern Atlantic Ocean during GasEx 98 differed from previous observations [*Lobert et al.*, 1996; *Groszko and Moore*, 1998]. Direct comparison of springtime supersaturations (23 ± 8%, standard error of the mean, s.e., *King et al.* [2000]) and fall undersaturations (-15 ± 4%, s.e., *Lobert et al.* [1996]) in the same region of the North Atlantic (37-45°N, 17-26°W) suggests that there may be a seasonal cycle in temperate North Atlantic waters. When seasonal cycling in temperate waters is incorporated into global flux calculations, estimates of the net, global, air-sea flux of CH_3Br range from -11 to -20 Gg yr^{-1} [*King et al.*, 2000]. This net CH_3Br sink is not as strong as previously reported [*Lobert et al.*, 1997], but the oceans are still estimated to provide an overall net sink for atmospheric methyl bromide.

Methyl bromide was undersaturated throughout most of the BACPAC 99 cruise with supersaturations observed primarily in coastal regions (Table 5.10, Figure 5.29c). In general CH_3Br was more undersaturated in the subtropics and closer to equilibrium in the temperate waters. The undersaturations in the temperate North Pacific during fall are consistent with the existence of a seasonal cycle in temperate waters as suggested by observations in the temperate North Atlantic. The data from BACPAC 99 showed less variability than that from GasEx 98. While the precision during BACPAC 99 was significantly better than during GasEx 98 (2.6% versus 5.8%, 1σ), this difference cannot completely explain the increased variability in the GasEx 98 data. It is likely that the remaining variability was a result of natural processes in the North Atlantic at that time of year.

Mean saturation anomalies for CH_3Cl, methyl iodide (CH_3I), CH_2Br_2, and $CHBr_3$ are provided from both GasEx 98 and BACPAC 99 on a regional basis (Table 5.10). In contrast to CH_3Br, these trace gases were generally more supersaturated in the subtropics and tropics than in the temperate waters. Higher supersaturations of these compounds in the tropics are particularly important as tropical deep convection could transport these short-lived compounds to the upper troposphere and lower stratosphere, where they could participate in stratospheric ozone depletion.

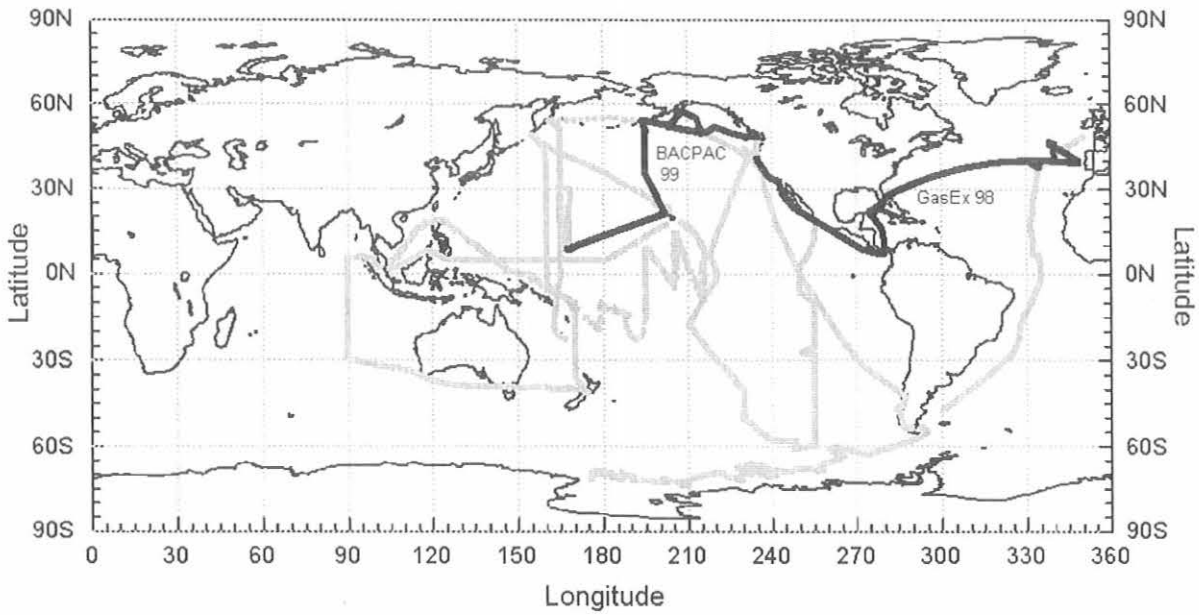

Fig. 5.28. Cruise tracks from RB-98-02 (GasEx 98) and RB-99-06 (BACPAC 99) and previous cruises (light gray) by the HATS group between 1987 and 1996.

TABLE 5.10. Average Measured Saturation Anomalies and Associated Standard Errors for Two Oceanic Regions From CMDL Cruises in 1998 (GasEx 98) and 1999 (BACPAC 99)

	Saturation Anomaly (%) Spring/Summer 1998		Saturation Anomaly (%) Fall 1999	
Compound	Subtropics/Tropics*	Temperate*	Subtropics/Tropics*	Temperate*
CH_3Br	-12 ± 2	37 ± 3	-35 ± 1	-19 ± 1
CH_3Cl	122 ± 3	37 ± 1	71 ± 3	2 ± 1
CH_3I	5067 ± 110	3351 ± 65	2603 ± 78	1113 ± 37
CH_2Br_2	334 ± 75	76 ± 3	33 ± 3	37 ± 2
$CHBr_3$	173 ± 11	69 ± 3	230 ± 17	69 ± 6

*Subtropics and tropics are defined as the region between 0° and 30°N, and temperate regions are defined to be between 30° and 60°N.

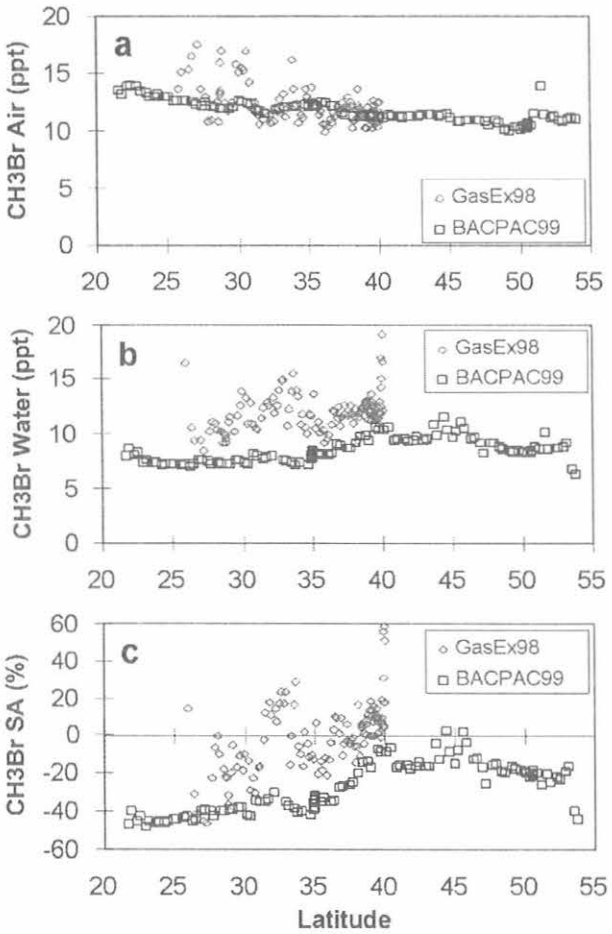

Fig. 5.29. Methyl bromide measurements in air (a) and air equilibrated with surface seawater (b). Saturation anomaly (c) is the percent difference between the partial pressure in water and air. Data from GasEx 98 are only shown from the third leg, between the Azores and Miami, Florida. Data from BACPAC 99 are only shown from the second leg, between Hawaii and Dutch Harbor, Alaska.

Temperature Dependence

Groszko and Moore [1998] suggested that there is a relationship between methyl bromide concentrations in the surface water and sea surface temperature. CH_3Br saturation anomalies were used from five CMDL research cruises to test this relationship for a wider range of waters (Figure 5.30a). The correlation observed from the CMDL data is similar to that reported by *Groszko and Moore* [1998] with CH_3Br supersaturated in ocean waters between 11° and 21°C. Based on this relationship, sea surface temperature can account for 40-70% of the variability in CH_3Br saturation anomaly on a global basis. However, only a small fraction of the observed seasonal cycle in temperate waters can be accounted for by the change in sea surface temperature [*King et al.*, 2000].

A global oceanic net flux of methyl bromide of –14 Gg yr^{-1} can be calculated with the temperature relationship shown in Figure 5.30a and a global map of sea surface temperature, wind speed, solubility from *De Bruyn and Saltzman* [1997], and a gas exchange coefficient based on the equation from *Wanninkhof* [1992]. This estimate falls within the range predicted by other methods [*Lobert et al.*, 1997; *King et al.*, 2000]. However, it does not accurately describe the temporal and spatial distribution of dissolved CH_3Br, especially in temperate waters, where widespread supersaturations are predicted year-round. Predicted supersaturations in temperate waters are not supported by data obtained from several field campaigns [*Lobert et al.*, 1995, 1996; *Groszko and Moore*, 1998], which indicates temperature is not the only variable controlling the concentration of CH_3Br in surface waters.

Methyl chloride and methyl iodide have a different relationship to sea surface temperature than that of methyl bromide (Figures 5.30b and 5.30c). For both of these compounds, this relationship is best described with a linear regression. About three-quarters of the variability in the saturation anomaly of CH_3Cl can be explained by the variability in sea surface temperature. For CH_3I, only about one-half of the variability in the saturation anomaly can be explained by the variability in sea surface temperature. Global maps of both CH_3Cl and CH_3I will be created in the near future to estimate global air-sea fluxes for these compounds.

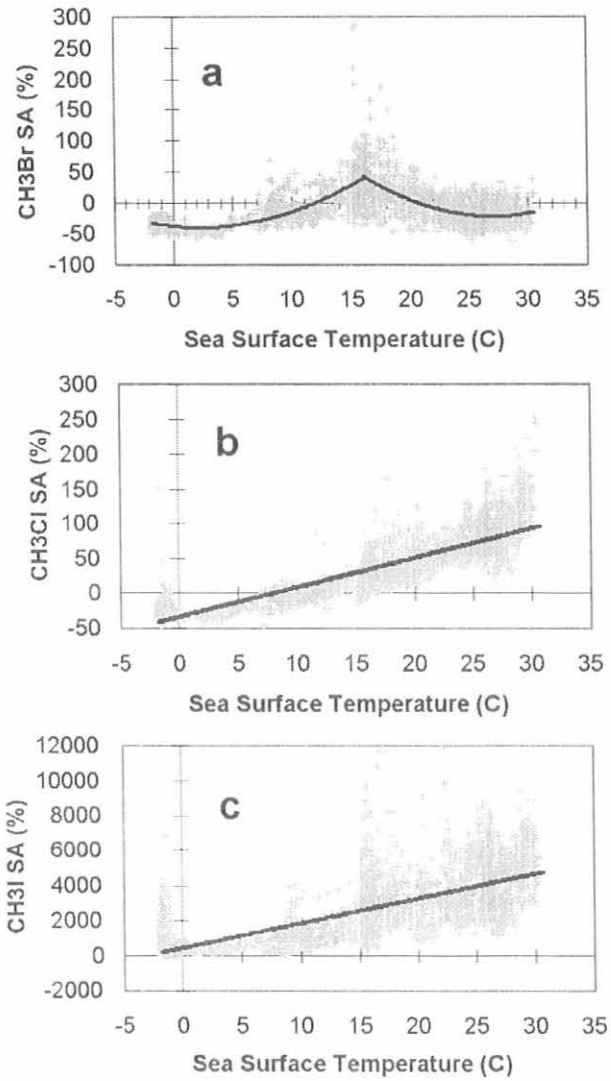

Fig. 5.30. Correlations between the saturation anomalies of the methyl halides (methyl bromide (a), methyl chloride (b), and methyl iodide (c)) and sea surface temperature based on data from five CMDL research cruises between 1994 and 1999.

5.4. REFERENCES

Butler, J.H., Better budgets for methyl halides?, *Nature, 403*, 260, 2000.

Butler, J.H., S.A. Montzka, A.D. Clarke, J.M. Lobert, and J.W. Elkins, Growth and distribution of halons in the atmosphere, *J. Geophys. Res., 103*, 1503-1511, 1998a.

Butler, J.H., et al., 5. Nitrous Oxide and Halocompounds, in *Climate Monitoring and Diagnostics Laboratory Summary Report No. 24, 1996-1997*, D.J. Hofmann, J.T. Petersen, and R.M. Rosson (eds.), 91-121, NOAA Environ. Res. Labs., Boulder, CO, 1998b.

Butler, J.H., M. Battle, M. Bender, S.A. Montzka, A.D. Clarke, E.S. Saltzman, C. Sucher, J. Severinghaus, and J.W. Elkins, A twentieth century record of atmospheric halocarbons in polar firn air, *Nature, 399*, 749-765, 1999.

Chang, A.Y., et al., A comparison of measurements from ATMOS and instruments aboard the ER-2 aircraft: Halogenated gases, *Geophys. Res. Lett., 23*, 2393-2396, 1996.

Daniel, J.S., S. Solomon, and D.L. Albritton, On the evaluation of halocarbon radiative forcing and global warming potentials, *J. Geophys. Res., 100*, 1271-1285, 1995.

De Bruyn, W.J., and E.S. Saltzman, The solubility of methyl bromide in pure water, 35‰ sodium chloride and seawater, *Mar. Chem., 56*, 51-57, 1997.

Dessler, A.E., A reexamination of the "stratospheric fountain" hypothesis, *Geophys. Res. Lett., 25*, 4165-4168, 1998.

Elkins, J.W., T.M. Thompson, T.H. Swanson, J.H. Butler, B.D. Hall, S.O. Cummings, D.A. Fisher, and A.G. Raffo, Decrease in the growth rates of atmospheric chlorofluorocarbons 11 and 12, *Nature, 364*, 780-783, 1993.

Elkins, J.W., D.W. Fahey, J.M. Gilligan, G.S. Dutton, T.J. Baring, C.M. Volk, R.E. Dunn, R.C. Myers, S.A. Montzka, P.R. Wamsley, A.H. Hayden, J.H. Butler, T.M. Thompson, T.H. Swanson, E.J. Dlugokencky, P.C. Novelli, D.F. Hurst, J.M. Lobert, S.J. Ciciora, R.J. McLaughlin, T.L. Thompson, R.H. Winkler, P.J. Fraser, L.P. Steele, and M.P. Lucarelli, Airborne gas chromatograph for in situ measurements of long-lived species in the upper troposphere and lower stratosphere, *Geophys. Res. Lett., 23* , 347-350, 1996.

Fraser, P.J., D.E. Oram, C.E. Reeves, S.A. Penkett, and A. McCulloch, Southern hemispheric halon trends (1978-1998) and global halon emissions, *J. Geophys. Res., 104*, 15,985-15,999, 1999.

Geller, L.S., J.W. Elkins, J.M. Lobert, A.D. Clarke, D.F. Hurst, J.H. Butler, and R.C. Meyers, Tropospheric SF_6: Observed latitudinal distribution and trends, derived emissions, and interhemispheric exchange time, *Geophys. Res. Lett., 24*, 675-678, 1997.

Groszko, W., and R.M. Moore, Ocean-atmosphere exchange of methyl bromide: NW Atlantic and Pacific Ocean studies, *J. Geophys. Res., 103*, 16,737-16,741, 1998.

Hall, T.M., and R.A. Plumb, Age as a diagnostic of stratospheric transport, *J. Geophys. Res., 99*, 1059-1070, 1994.

Hintsa, E.J., E.M. Weinstock, J.G. Anderson, R.D. May, and D.F. Hurst, On the accuracy of in situ water vapor measurements in the troposphere and lower stratosphere with the Harvard Lyman-α hygrometer, *J. Geophys. Res., 104*, 8183-8189, 1999.

Hurst, D.F., P.S. Bakwin, R.C. Meyers, and J.W. Elkins, Behavior of trace gas mixing ratios on a very tall tower in North Carolina, *J. Geophys. Res., 102*, 8825-8835, 1997.

Hurst, D.F., G.S. Dutton, P.A. Romashkin, P.R. Wamsley, F.L. Moore, J. W. Elkins, E. J. Hintsa, E. M. Weinstock, C.R. Webster, R.D. May, R.L. Herman, E.J. Moyer, and D.C. Scott, Closure of the total hydrogen budget of the northern extratropical lower stratosphere, *J. Geophys. Res., 104*, 8191-8200, 1999.

King, D.B., J.H. Butler, S.A. Montzka, S.A. Yvon-Lewis, and J.W. Elkins, Implications of methyl bromide supersaturations in the temperate North Atlantic Ocean, *J. Geophys. Res., 105*, 19,763-19,769, 2000.

Lobert, J.M., J.H. Butler, S.A. Montzka, L.S. Geller, R.C. Myers, and J.W. Elkins, A net sink for atmospheric CH_3Br in the East Pacific Ocean, *Science, 267*, 1002-1005, 1995.

Lobert, J.M., J.H. Butler, L.S. Geller, S.A. Yvon, S.A. Montzka, R.C. Myers, A.D. Clarke, and J.W. Elkins, BLAST94: Bromine Latitudinal Air/Sea Transect 1994: Report on oceanic measurements of methyl bromide and other compounds, *NOAA Tech. Memo. ERL CMDL-10*, 39 pp., Environmental Research Labs., Boulder, CO, 1996.

Lobert, J.M., S.A. Yvon-Lewis, J.H. Butler, S.A. Montzka, and R.C. Myers, Undersaturation of CH_3Br in the Southern Ocean, *Geophys. Res. Lett., 24*, 171-172, 1997.

Michelson, H.A., *et al.*, Intercomparison of ATMOS, SAGE II, and ER-2 observations in arctic vortex and extravortex air masses during spring 1993, *Geophys. Res. Lett., 26*, 291-294, 1999.

Montzka, S.A., R.C. Myers, J.H. Butler, J.W. Elkins, and S.O. Cummings, Global tropospheric distribution and calibration scale of HCFC-22, *Geophys Res. Lett., 20*, 703-706, 1993.

Montzka, S.A., R.C. Myers, J.H. Butler, and J.W. Elkins, Early trends in the global tropospheric abundance of hydrochlorofluorocarbon-141b and -142b, *Geophys. Res. Lett., 21*, 2483-2486, 1994.

Montzka, S.A., J.H. Butler, R.C. Myers, T.M. Thompson, T.H. Swanson, A.D. Clarke, L.T. Lock, and J.W. Elkins, Decline in the tropospheric abundance of halogen from halocarbons: Implications for stratospheric ozone depletion, *Science, 272*, 1318-1322, 1996a.

Montzka, S.A., R.C. Meyers, J.H. Butler, J.W. Elkins, L.T. Lock, A.D. Clarke, and A.H. Goldstein, Observations of HCFC-134a in the remote troposphere, *Geophys. Res. Lett.*, *23*, 169-172, 1996b.

Montzka, S.A., J.H. Butler, J.W. Elkins, T.M. Thompson, A.D. Clarke, and L.T. Lock, Present and future trends in the atmospheric burden of ozone-depleting halogens, *Nature*, *398*, 690-694, 1999a.

Montzka, S.A., J.H. Butler, J.W. Elkins, L. Lock, and D. Mondeel, Seasonal and inter-annual variability of methyl bromide and methyl chloride from a global flask sampling network, *Eos Trans. AGU*, *80(46)*, F149, 1999b.

Montzka, S.A., C. M. Spivakovsky, J. H. Butler, J.W. Elkins, L.T. Lock, and D.J. Mondeel, New observational constraints for atmospheric hydroxyl on global and hemispheric scales, *Science*, *288*, 500-503, 2000.

Mote, P.W., K.H. Rosenlof, M.E. McIntyre, E.S. Carr, J.C. Gille, J.R. Holton, J.S. Kinnersley, H.C. Pumphrey, J.M. Russell III, and J.W. Waters, An atmospheric tape recorder: The imprint of tropical tropopause temperatures on stratospheric water vapor, *J. Geophys. Res.*, *101*, 3989-4006, 1996.

Novelli, P.C., J.W. Elkins, and L.P. Steele, The development and evaluation of a gravimetric reference scale for measurements of atmospheric carbon monoxide, *J. Geophys. Res.*, *96*, 13,109-13,121, 1991.

Novelli, P.C., P.M. Lang, K.A. Masarie, D.F. Hurst, R. Meyers, and J.W. Elkins, Molecular hydrogen in the troposphere: Global distribution and budget, *J. Geophys. Res.*, *104*, 30,427-30,444, 1999.

Prather, M.J., and C.M. Spivakovsky, Tropospheric OH and the lifetimes of hydrochlorofluorocarbons, *J. Geophys. Res.*, *95*, 18,723-18,729, 1990.

Ravishankara, A.R., and D.L. Albritton, Methyl chloroform and the atmosphere, *Science*, *269*, 183-184, 1995.

Ray, E.A., F.L. Moore, J.W. Elkins, G.S. Dutton, D.W. Fahey, H. Vömel, S.J. Oltmans, and K.H. Rosenlof, Transport into the northern hemisphere lowermost stratosphere revealed by in situ tracer measurements, *J. Geophys. Res.*, *104*, 26,565-26,580, 1999.

Romashkin, P.A., D.F. Hurst, J.W. Elkins, G.S. Dutton, and P.R. Wamsley, Effect of the tropospheric trend on the stratospheric tracer-tracer correlations: Methyl chloroform, *J. Geophys. Res.*, *104*, 26,643-26,652, 1999.

Sen, B., G.B. Osterman, R.J. Salawitch, G.C. Toon, J.J. Margitan, J.-F. Blavier, A.Y. Chang, R.D. May, C.R. Webster, R.M. Stimpfle, G.P. Bonne, P.B. Voss, K.K. Perkins, J.G. Anderson, R.C. Cohen, J.W. Elkins, G.S. Dutton, D.F. Hurst, P.A. Romashkin, E.L. Atlas, S.M. Schauffler, and M. Loewenstein, The budget and partitioning of stratospheric chlorine during the 1997 Arctic summer, *J. Geophys. Res.*, *104*, 26,653-26,665, 1999.

Spivakovsky, C.M., J.A. Logan, S.A. Montzka, Y.J. Balkanski, M. Foreman-Fowler, D.B.A. Jones, L.W. Horowitz, A.C. Fusco, C.A.M. Brenninkmeijer, M.J. Prather, S.C. Wofsy, and M.B. McElroy, Three-dimensional climatological distribution of tropospheric OH: Update and evaluation, *J. Geophys. Res.*, *105*, 8931-8980, 2000.

Swanson, T. H. *et al.*, 5. Nitrous Oxide and Halocarbons Division, in *Climate Monitoring and Diagnostics Laboratory Summary Report No. 21, 1992*, J.T. Petersen and R.M. Rosson (eds.), 59-75, NOAA Environ. Res. Labs., Boulder, CO, 1993.

Toon, G.C., J.-F. Blavier, B. Sen, J.J. Margitan, C.R. Webster, R.D. May, D. Fahey, R. Gao, L. Del Negro, M. Proffitt, J. Elkins, P.A. Romashkin, D.F. Hurst, S. Oltmans, E. Atlas, S. Schauffler, F. Flocke, T.P. Bui, R.M. Stimpfle, G.P. Bonne, P.B. Voss, and R.C. Cohen, Comparison of MkIV balloon and ER-2 aircraft measurements of atmospheric trace gases, *J. Geophys. Res.*, *104*, 26,779-26,790, 1999.

United Nations Environmental Programme (UNEP), *Montreal Protocol to Reduce Substances that Deplete the Ozone Layer Report*, 15 pp., UN, New York, 1987.

Volk, C.M., J.W. Elkins, D.W. Fahey, G.S. Dutton, J.M. Gilligan, M. Loewenstein, J.R. Podolske, K.R. Chan, and M.R. Gunson, Evaluation of source gas lifetimes from stratospheric observations, *J. Geophys. Res.*, *102*, 25,543-25,564, 1997.

Wanninkhof, R., Relationship between wind speed and gas exchange over the ocean, *J. Geophys. Res.*, *97*, 7373-7382, 1992.

Woodbridge, E.L., J.W. Elkins, D.W. Fahey, L.E. Heidt, S. Solomon, T.J. Baring, T.M. Gilpin, W.H. Pollock, S.M. Schauffler, E.L. Atlas, M. Loewenstein, J.R. Podolske, C.R. Webster, R.D. May, J.M. Gilligan, S.A. Montzka, K.A. Boering, and R.J. Salawitch, Estimates of total organic and inorganic chlorine in the lower stratosphere from in situ and flask measurements during AASE II, *J. Geophys. Res.*, *100*, 3057-3064, 1995.

Yokouchi, Y., Y. Noijiri, L.A. Barrie, D. Toom-Sauntry, T. Machida, Y. Inuzuka, H.-J. Akimoto, Y. Fujinuma, and S. Aoki, A strong source of methyl chloride to the atmosphere from tropical coastal land, *Nature*, *403*, 295-298, 2000.

6. Cooperative Programs

UV Spectroradiometer Monitoring Program: Influence of Total Ozone, Cloud Cover and Surface Albedo on UV Doses in Barrow, Alaska

G. BERNHARD, C.R. BOOTH, J.C. EHRAMJIAN, S.A. LYNCH, AND V.V. QUANG
Biospherical Instruments Inc., San Diego, California 92110-2621

INTRODUCTION

The United States National Science Foundation's (NSF) Ultraviolet Spectroradiometer Monitoring Network for Polar Regions was established in 1988 to collect data on the consequences of ozone depletion. The network currently consists of several automated, high-resolution spectroradiometers (Table 1). Three network stations are located in Antarctica, including the CMDL site at the South Pole Station (SPO). Another instrument is deployed close to the CMDL facility in Barrow, Alaska (BRW). Additional instruments are located in Ushuaia, Argentina, and San Diego, California; the latter serves as a training and testing facility. Finally, a portable system is available for instrument intercomparisons. Now in its thirteenth year of operation, the network continues to make measurements of ultraviolet (UV) spectral irradiance and provides a variety of data products to quantify biologically relevant UV exposures. Biospherical Instruments Inc. is responsible for operating and maintaining the network and distributing data to the scientific community.

The network is equipped with Biospherical Instruments Inc. Model SUV-100 spectroradiometers. Each instrument contains a double monochromator with holographic gratings and a photomultiplier tube detector. A vacuum-formed Teflon diffuser serves as an all-weather irradiance cosine collector. All systems are temperature stabilized for optimum radiometric stability. Spectra are sampled automatically every 15 minutes between 280 and 600 nm with a spectral bandwidth of 1.0 nm full width at half maximum. Tungsten-halogen and mercury vapor calibration lamps are used for daily automatic internal calibrations of both responsivity and wavelength registration. All instrument functions, calibration activities, and solar data acquisition are computer controlled. Further details on the spectroradiometers are described by *Booth et al.* [1994, 2000].

UV RADIATION CLIMATE AT THE SPO AND BRW NETWORK INSTALLATIONS

This report focuses on data from the CMDL facilities at the SPO and BRW network installations. The SPO site is characterized by very high surface albedo throughout the year. Clouds are usually thin and clear sky days are relatively frequent. Because of the stable weather conditions, the high air purity, and high latitude, SPO is an ideal place to study the influence of variations in total column ozone on UV irradiance [*Booth and Madronich*, 1994].

The conditions at BRW are quite different from SPO. Cloud cover is highly variable, and significant changes in surface albedo occur because of both the springtime snowmelt [*Dutton and Endres*, 1991] and changes in sea ice coverage. Also, Barrow experiences significant changes in incident irradiance because of Arctic storms.

Figure 1 contrasts the radiation pattern of both sites. Time-series of integrated spectral irradiance at local solar noon are depicted for two wavelength bands covering 1991-1999. One spectral band (Figure 1a) represents DNA-weighted irradiance calculated from measured solar spectra and the action spectrum for DNA damage suggested by *Setlow* [1974]. DNA-weighted irradiance has a high contribution from wavelengths in the UV-B and is, therefore, very sensitive to changes in atmospheric ozone concentrations. The other band (Figure 1b) is spectral irradiance in the visible part of the spectrum, integrated between 400 and 600 nm. From Figure 1b it is evident that visible radiation at SPO shows little variation from year to year. Moreover, irradiances in this wavelength band are usually close to the envelope formed by the clear-sky level, confirming that cloud influence at SPO is small. In contrast, irradiances in the 400-600 nm band at BRW show a high variability because of day-to-day changes in cloud cover. The cloud influence is clearly more pronounced in the second part of the year. Because of the difference in latitude, radiation levels in the visible part of the spectrum are usually lower at SPO than at BRW.

TABLE 1. Installation Sites

Site	Latitude	Longitude	Established	Location
South Pole	90°00'S	-	February 1988	ARO*
McMurdo Station	77°51'S	166°40'E	March 1988	Arrival Heights
Palmer Station	64°46'S	64°03'W	May 1988	T-5 Building
Ushuaia, Argentina	54°49'S	68°19'W	November 1988	CADIC†
Barrow, Alaska	71°18'N	156°47'W	December 1990	UIC-NARL‡
San Diego, California	32°45'N	117°11'W	October 1992	Biospherical Instruments Inc.

*ARO: Atmospheric Research Observatory, system relocated to this new, joint NSF/CMDL facility in January 1997.
†CADIC: Centro Austral de Investigaciones Cientificas, Argentina.
‡ UIC-NARL: Ukpeagvik Inupiat Corporation-Naval Arctic Research Laboratory.

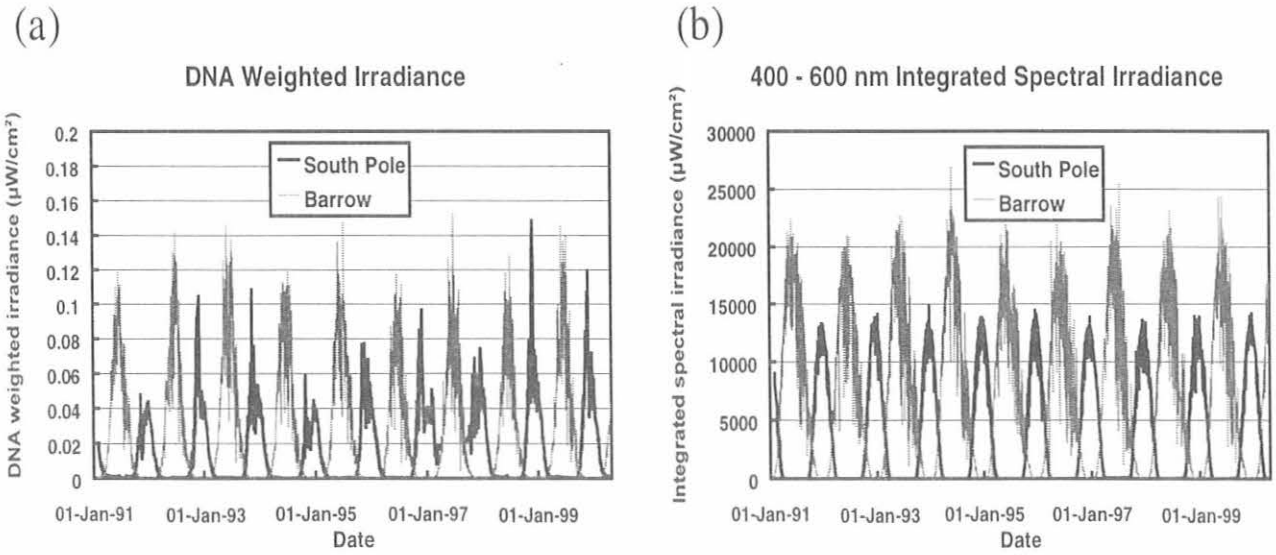

Fig. 1. Local solar noontime integrated spectral irradiance at South Pole and Barrow for 1991-1999: (a) DNA-weighted irradiance and (b) visible irradiance (400-600 nm integral). Note that 1999 data are preliminary and subject to revision.

In contrast to visible radiation, DNA-weighted irradiance at SPO (Figure 1a) shows high day-to-day fluctuations because of the ozone influence. For example, the peak in DNA-weighted irradiance observed at SPO in late November 1998 is due to extraordinarily low total column ozone values and the comparatively high solar elevations prevailing during this part of the year.

Influence of Ozone, Cloud Cover, and Albedo on Radiation Doses in Barrow

Figure 2 shows daily doses calculated from both DNA-weighted irradiance data and irradiance measurements in the 400-600 nm band. In order to remove year-to-year variability, both doses were averaged over 1991-1997.

The average daily DNA-weighted dose is quite symmetrical with respect to the solstice (June 21) (Figure 2). The average daily dose in the visible band, however, appears to be shifted by approximately 14 days towards spring. Figure 3 shows this asymmetry more clearly. Here, both doses of Figure 2 were mirrored at the solstice, and the ratio of spring-to-fall values was calculated. The resulting ratios depicted in Figure 3 are, therefore, independent from solar zenith-angle dependence and normalized to 1 at the solstice. Average doses in the 400-600 nm band appear to be a factor of 2 higher in spring than in fall. DNA-weighted doses, on the other hand, do not show a clear spring-fall asymmetry.

The spring-fall ratio for the DNA-weighted dose derived from the measurements was compared with analogous ratios that were computed from the expected influence of ozone, cloud cover, and surface albedo on the DNA-weighted dose (Figure 4). Line 1 in Figure 4 is identical to the measured DNA ratio in Figure 3. Line 2 reflects the spring-fall DNA ratio that would be expected if the seasonal cycle in total column ozone was the only parameter affecting the DNA dose. This curve was calculated with Total Ozone

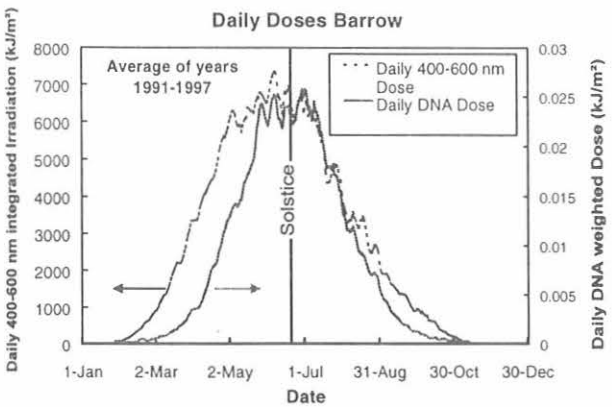

Fig. 2. Daily doses at BRW averaged from 1991-1997. The dashed line (left axis) is the average daily dose in the 400-600 nm band; the solid line (right axis) is average daily DNA-weighted dose.

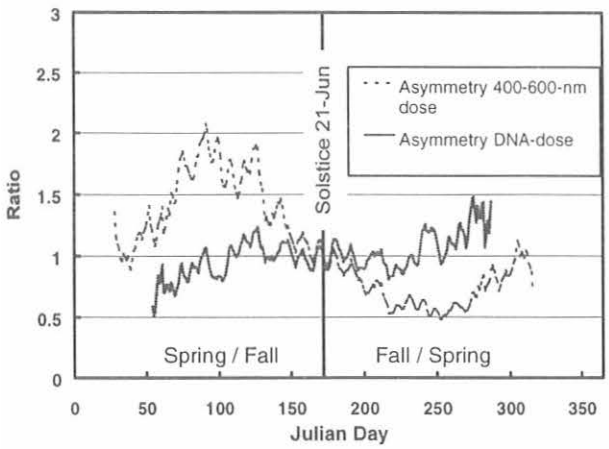

Fig. 3. Spring-fall asymmetry of the radiation doses in BRW. The dashed line is the spring-fall ratio for the 400-600 nm dose; the solid line is the analogous ratio for DNA-weighted dose.

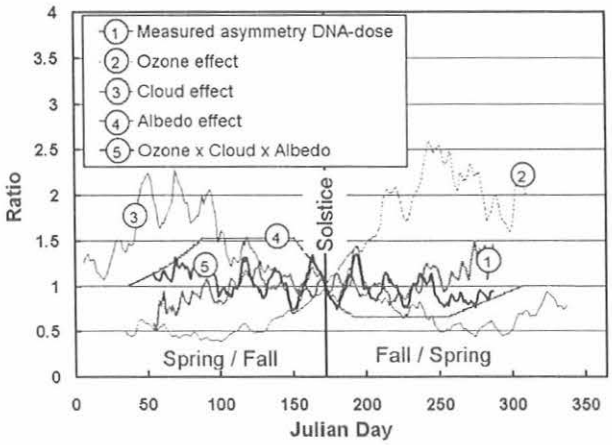

Fig. 4. Explanation of spring-fall differences in the average daily DNA-dose at BRW. Line 1: Measured spring-fall ratio of the DNA-dose. Line 2: Expected spring-fall ratio from the annual cycle in total column ozone. Line 3: Expected ratio from the seasonal cycle in cloud cover. Line 4: Expected ratio from the seasonal differences in albedo. Line 5: Product of ozone, cloud, and albedo influences. Line 5 is similar to line 1, indicating that the measurements can be well explained by the influence of the three factors.

Mapping Spectrometer (TOMS) total ozone data and a parameterization of the anti-correlation of ozone and UV suggested by *Booth and Madronich* [1994] with a radiation amplification factor of 2.2. With the presumption that all atmospheric parameters, except ozone, were constant throughout the year, line 2 indicates the DNA-weighted dose is a factor of 2.5 higher in fall than in spring. This large difference can be explained by the fact that total column ozone at Barrow is about 150 DU lower in fall than in spring.

Line 3 in Figure 4 shows the spring-fall DNA ratio that would be expected from the annual cycle in cloud cover if clouds were the only parameter affecting UV. Cloud cover data provided by the National Climatic Data Center shows the relationship between cloud cover and attenuation of DNA-weighted irradiance, and was parameterized according to *Thiel et al.* [1997], assuming stratocumulus clouds are prevailing. Line 3 indicates that DNA doses can be expected to be higher in spring by about a factor of 2 because of fewer clouds in the first part of the year. Thus the annual cycle in cloud cover partly cancels out the influence of the ozone cycle.

Variability in surface albedo is another important parameter affecting DNA irradiance at BRW. Albedo measurements from BRW indicate that the ground is completely covered by snow between the beginning of November and the end of May [*Dutton and Endres*, 1991]. According to data from the National Ice Center the adjoining ocean is covered by sea ice during approximately the same period, thus causing high albedo beyond the immediate vicinity of the measurement site. Comparisons of SUV-100 spectral measurements to radiative transfer model calculations show that the effective UV albedo is 0.85 during this period. This causes an increase of DNA-weighted irradiance of about 52% compared to snow-free conditions that prevail in Barrow between the beginning of July and mid-September. Finally, line 4 in Figure 4 indicates the spring-fall ratio of the DNA dose that can be expected from the albedo variability.

By multiplying the spring-fall ratios that were calculated previously for the effects of ozone, clouds, and albedo on the DNA dose, the combined influence of all three parameters was determined. The resulting product is line 5 in Figure 4. The curve is very similar to the measured spring-fall asymmetry in the DNA dose (line 1), indicating that the measurement can be well explained by the seasonal cycles of the three factors. Remaining deviations are partly due to the simple parameterizations applied. For example, nonlinear interference of albedo and cloud reflections were not taken into account. In addition not all time-series were complete for the 1991-1997 period; for example, no TOMS data exist for 1995.

Summary

High spectral resolution scanning UV spectroradiometers have been established at six sites, including SPO and BRW, and are successfully providing multi-year data sets. The database is now sufficiently large to investigate the UV climatology at all sites beyond year-to-year variability. This has been demonstrated for Barrow, where data from 1991-1997 were used to analyze the impact of ozone, cloud, and albedo variations on biologically relevant levels of DNA-weighted daily doses.

Data from the network are distributed by Biospherical Instruments Inc. via CD-ROMs and the Internet to interested researchers. Investigations based on this dataset were published or referenced by scientists from around the world in more than 100 peer-reviewed publications. The Data and Network Operation Report ordering, more detailed information on the deployed instrumentation, and an extensive list of references are available on the website (http://www.biospherical.com).

Acknowledgments. This research and monitoring activity was established under the guidance of P. Wilkniss, former Director of the NSF Office of Polar Programs. The network is operated and maintained under the contract OPP-89-22832 of NSF-OPP (Contracting Officer P. Penhale) with subcontracts to Antarctic Support Associates (ASA) and Raytheon Polar Services. Cordial thanks to the current Barrow operators D. Endres and M. Gaylord (CMDL). The Ukpeagvik Inupiat Corporation of Barrow provided assistance in the original installation. Operators at Palmer, South Pole and McMurdo were provided by ASA. Albedo data from Barrow were provided by E. Dutton and D. Longenecker (CMDL).

References

Booth, C.R., and S. Madronich, Radiation amplification factors: Improved formulation accounts for large increases in ultraviolet radiation associated with Antarctic ozone depletion, edited by C.S. Weiler and P.A. Penhale, *Antarct. Res. Ser., 62*, 39-42, 1994.

Booth, C.R., T.B. Lucas, J.H. Morrow, C.S. Weiler, and P.A. Penhale, The United States National Science Foundation's polar network for monitoring ultraviolet radiation, edited by C.S. Weiler and P.A. Penhale, *Antarct. Res. Ser., 62*, 17-37, 1994.

Booth, C.R., G. Bernhard, J.C. Ehramjian, L.W. Cabasug, V.V. Quang, and S.A. Lynch, *NSF Polar Programs UV Spectroradiometer Network 1997-1998 Operations Report*, 233 pp., Biospherical Instruments Inc., San Diego, 2000.

Dutton, E.G., and D.J. Endres, Date of snowmelt at Barrow, Alaska, U.S.A., *Arctic Alpine Res., 23(1)*, 115-119, 1991.

Setlow, R.B., The wavelength in sunlight effective in producing skin cancer: A theoretical analysis, *Proc. Natl. Acad. Sci., 71(9)*, 3363-3366, 1974.

Thiel, S., K. Steiner, and H.K. Seidlitz, Modification of global erythemal effective irradiance by clouds, *Photochem. Photobiol., 65(6)*, 969-973, 1997.

Whole Air Sampling at Barrow, Alaska

DONALD R. BLAKE AND F. SHERWOOD ROWLAND
University of California, Irvine 92697-2025

The University of California-Irvine (UCI) has been collecting whole air samples at the NOAA Climate Monitoring and Diagnostics Laboratory (CMDL) station at Barrow, Alaska, since April 1983. The Barrow measurements are the northernmost sampling site of the UCI global CH_4 monitoring network that extends from 71°N to 47°S. The UCI and CMDL CH_4 networks have a second co-located sampling site in Samoa.

In the UCI sampling strategy, approximately 60-80 whole air samples are collected over a 3-wk period in 40-45 locations four times a year (usually March, June, September, and December). Of these samples, four or five are collected in Barrow, usually over a 2-3 day period. The air samples are collected in conditioned, evacuated 2-L stainless steel canisters equipped with a single stainless steel bellows valve. During sampling, the canister is filled to ambient pressure over a period of about 1 minute. At the end of the collection period the sampling canisters are returned to the UCI laboratory for analysis.

The CH_4 mixing ratio within an air sample is determined by gas chromatography (HP-5890A) with flame ionization detection. The CH_4 mixing ratios are reported for dry air relative to primary standards purchased in 1977 and a National Institute of Standards and Technology (NIST) (formerly known as the National Bureau of Standards (NBS)) standard purchased in August 1982. The uncertainty in the NIST standard is ±1%. The analytical precision is determined from intersample comparisons that are obtained by alternating measurements of secondary standards with aliquots from an individual air sample. The UCI analytical precision was 3 ppbv in the 1980s and is currently better than 2 ppbv. Data points are individually inspected, and points that do not represent remote values are removed from further analysis.

The UCI global CH_4 monitoring program complements the fixed station network of the CMDL program. The UCI sampling strategy emphasizes intense latitudinal sampling over a short (3-wk) period while sacrificing the knowledge and statistical confidence gained from multiple or continual measurements at individual sites. The UCI sampling locations are not fixed, and sampling personnel scout out the best location and time for a remote air sample according to the prevailing physical and meteorological conditions. As a result, the method has the flexibility to easily switch sampling sites if local contamination is suspected.

Individual CH_4 mixing ratios measured at Barrow by UCI over the 2-yr period from March 1998 to December 1999 are shown in Figure 1. Unlike the other sites in the UCI monitoring network, the Barrow and Samoa sampling locations are fixed at the CMDL stations. As a result, the CH_4 mixing ratios measured at these sites are sometimes elevated as a result of local contamination. At Barrow local contamination can occur when the prevailing wind is from the direction of town rather than from the ocean or tundra. During 1998-1999 the measurements collected in September 1998 and March 1999 were elevated as a result of local contamination and have not been included in Figure 1. Indeed, the CH_4 mixing ratio exceeded 2 ppmv in two of the UCI samples collected in September 1998. The CMDL measurements were similarly elevated at this time, confirming that the enhancements were real and not a result of measurement error.

The remaining six sets of seasonal data generally show very low variability within a given season (Figure 1). The measurement precision (2 ppbv) is roughly the same size as the data points that have been plotted, and the difference among the data points within a given season represents real variability, rather than measurement error. The mixing ratios over the 2-yr period show a characteristic seasonal pattern with a summertime minimum and a winter maximum (Figure 1).

The CMDL and UCI networks are two of just three global monitoring networks for tropospheric CH_4. The overlapping sampling at Barrow provides a valuable opportunity for measurement intercomparison. Over the years we have found that the UCI CH_4 mixing ratios typically exceed those of the CMDL network by ~20 ppbv. The difference is caused by an offset in the calibration scales used by the two groups. A scaling factor of 0.989 would make the UCI measurements agree with the CMDL values. Many other groups require similar scaling factors, again as a result of different calibration scales that are used (e.g., Atmospheric Environment Service (AES) Canada, Institute of Atmospheric Chemistry (IAC) China, Ente per le Nuove Tecnologie, l'Energia e l'Ambiente (ENEA) Italy, National Institute for Water and Atmospheric Research (NIWA) New Zealand; see http://www.cmdl.noaa.gov/ccgg/globalview/ch4/methods.html).

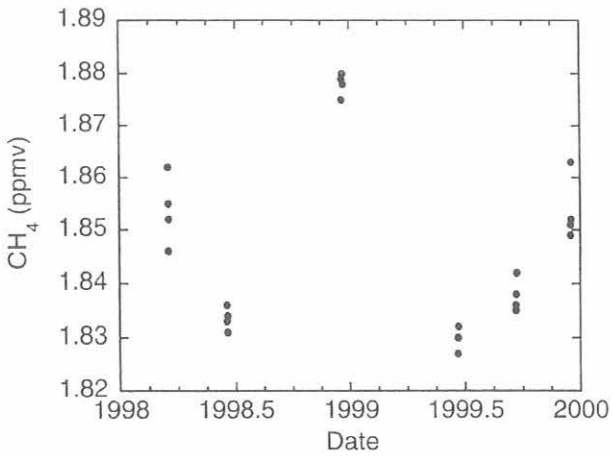

Fig. 1. Methane mixing ratios (ppmv) measured by the University of California-Irvine (UCI) at the NOAA CMDL station in Barrow, Alaska, between March 1998 and December 1999. Mixing ratios measured in September 1998 and March 1999 were enhanced by local contamination and have not been included in the graph.

Correlation Between Anthropogenic Aerosols and Gases at MLO

THOMAS A. CAHILL, STEVEN S. CLIFF, THOMAS M. CAHILL
DELTA Group, University of California, Davis 95616-8569

KEVIN D. PERRY
Department of Meteorology, San Jose State University, California 95192

The recent availability of size- and time-resolved aerosol data at the CMDL Mauna Loa Observatory (MLO) [*Perry et al.*, 1999] allows for comparison with gas and aerosol measurements made routinely at MLO. The three-drum DELTA IMPACTOR instrument is the prototype of the unit being proposed for many Pacific sites for the Aerosol Characterization Experiment (ACE)-Asia study in spring 2001. Fine mass was established both gravimetrically and as a sum of all measured species, and was highly correlated with aerosol scattering coefficients (σ_{sp}). Using NOAA trajectory analysis and trace element analysis, the period of May 8-22, 1996, was divided into five classifications: (1) oceanic, in which the trajectory remains over the ocean for at least 12 days, (2) North Asia, including Japan, (3) Central Asia 1 (north of the Yangtze River), (4) Central Asia 2 (south of the Yangtze River), and (5) Central America. All data, gas, and aerosol were averaged in these categories, and a ratio to the values in oceanic periods was calculated (Figure 1). The CO_2 excess value was the CO_2 data with the average annual rate of rise over 10 years removed, leaving the strong annual cycle. The CO and methane data have a constant value removed to emphasize the variability over the 2-wk period. With the availability of high time resolution data, we can now attempt to combine the aerosol data, trajectory analysis, optical parameters for scattering (σ_{sp}) and absorption (σ_{ap}), gases such as CO_2, methane, and CO, and tracers such as Radon 222 into a single statistical package.

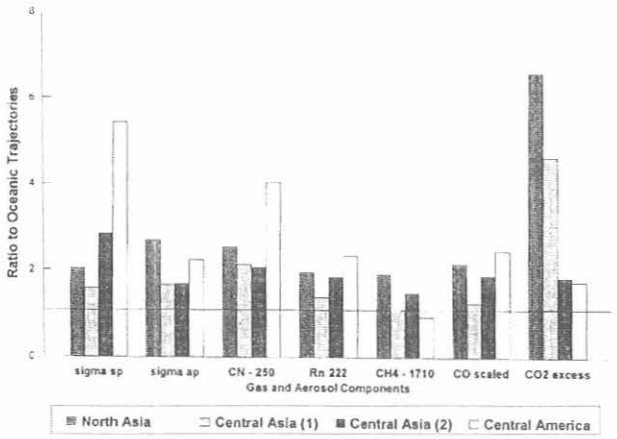

Fig. 1. Air mass trajectory analysis combined with aerosol and gaseous data. Ratio of gas and aerosol components to oceanic periods at MLO, May 1996 (nighttime winds only).

Trajectory analysis shows increased values for all parameters when compared to oceanic periods, with particularly large ratios for CO_2 from North and North-Central Asia and optical scattering from Central America. Central American transport coincided with large peaks of sulfates and biomass smoke. The satellite imagery of the May 1996 dust event is convincing proof of the impact of these major dust events on the Earth's albedo. Additional data are required, however, to ascertain if the lower free tropospheric sulfates, organics, and soot particles have an impact.

An absolute principal components analysis (PCA) was performed on the data. Two trajectories both anchored in the "Oceanic" conditions summarize the entire 2-wk period. Surprisingly, the midlatitude transport from middle and southern China has almost the same statistical signature as that from Central America. In general, trace element analysis will aid in source identification as trace elements are highly indicative of particular sources. Thus it appears that MLO is heavily influenced by anthropogenic sources around the Pacific Rim, making MLO a unique and valuable diagnostic site for future changes in Asian and American air pollutants.

REFERENCE

Perry, K.D., T.A. Cahill, R.C. Schnell, and J.M. Harris, Long-range transport of anthropogenic aerosols to the NOAA Baseline Station at Mauna Loa Observatory, Hawaii, *J. Geophys. Res., 104*, 18,521-18,533, 1999.

NIWA Lauder NDSC UV/Visible Measurements at the Mauna Loa Observatory

PAUL JOHNSTON
National Institute for Water and Atmospheric Research (NIWA), Lauder, New Zealand 9182

The National Institute of Water and Atmospheric Research (NIWA) started Network for the Detection of Stratospheric Change (NDSC) certified ultraviolet (UV)/visible spectroscopic measurements of stratospheric nitrogen dioxide (NO_2) in July 1996 at the NOAA Mauna Loa Observatory (MLO). These measurements continued with the same instrument through 1999. Some degradation of data quality occurred between February and October because of the failure of a mechanical coupling in the wavelength drive rotator mechanism. This was rectified in October when a NIWA scientist visited MLO to help diagnose radio interference in the NIWA UV spectroradiometer operating there. On subsequent examination of the coupling at Lauder, it was determined that the failure was caused by volcanic dust that had penetrated the spectrometer box. Although the presence of a problem was diagnosed in March using standard quality-control procedures, it was not possible to implement repairs earlier than October. Fortunately the failure did not significantly compromise the value of the NO_2 measurements over this period with the measurement random errors increasing by less than a factor of 2 over those normally expected.

In December 1999 a new UV/visible spectrometer was installed to measure stratospheric bromine monoxide, an important species in current attempts to model future nonpolar ozone trends. In addition to this new instrument, a second NO_2 measuring spectrometer was also installed in the NDSC building. It is planned to operate both NO_2 spectrometers for several months to provide a good overlap for intercalibration. The two new spectrometers are monitored and controlled over the Internet from Lauder, minimizing the work of MLO staff. The only routine task required is the cleaning of the two viewing windows.

Archiving of UV/visible data measured at MLO in the NDSC database has continued as required.

No publications have used just the MLO UV/visible data to date. However, global ground-based and satellite-derived NO_2 climatological studies are using the NDSC archive data sets.

Operation of Brewer Instruments at Mauna Loa Observatory

J.B. KERR

Meteorological Service of Canada, Environment Canada, Downsview, Ontario, Canada M3H 5T4

Two Brewer instruments continue to make measurements at the Mauna Loa Observatory (MLO) in support of the Brewer Instrument World Calibration Centre at the Meteorological Service of Canada (MSC) site in Downsview, Ontario [*Kerr et al.*, 2000]. A single monochromator (instrument no. 9) and a double monochromator (instrument no. 119) have been measuring direct solar, zenith sky and global ultraviolet radiation on most days during 1998 and 1999. The instruments are programmed and controlled from Downsview, where the data are sent automatically on a daily basis, and routine maintenance and calibrations are carried out by staff on site. One of the Brewer reference triad instruments (instrument no. 8) was brought to MLO for calibration in March-April 1999, and comparison with the onsite instruments simplified the calibration process.

The instruments routinely measure total ozone, ozone profile (Umkehr measurements), sulfur dioxide, aerosol optical depth, the extraterrestrial solar spectrum (via daily airmass extrapolations of direct solar spectra) and global UV irradiance spectra. In addition, a new scanning technique was developed to determine the temperature of atmospheric ozone. Some preliminary results of these measurements were reported at the Quadrennial Ozone Symposium in Sapporo [*Kerr*, 2000].

Brewer instrument no. 9 includes an all-sky camera that records and stores images of the sky every 10 minutes. These images are displayed on the MLO Web site and are useful for obtaining real time information regarding the sky conditions at MLO. They are also valuable for reviewing sky conditions at times when unusual events are noticed in the data set. For example, large values of sulfur dioxide have been observed (particularly between January and March) on several occasions, and the sky images assist in determining the cause of these events.

REFERENCES

Kerr, J.B., Measurement of total ozone and ozone temperature from spectral direct sun measurements, *Proc., Quad. Ozone Symp.*, Sapporo, Japan, 473-474, 2000.

Kerr, J.B., C.T. McElroy, D.I. Wardle, and T.S. Grajnar, The Brewer instrument calibration centre 1984-2000, *Proc., Quad. Ozone Symp.*, Sapporo, Japan, 177-178, 2000.

Isotopic Studies of Carbon Monoxide at Mauna Loa

John E. Mak

Marine Sciences Research Center, State University of New York, Stony Brook, New York 11794-5000

As part of an ongoing program to characterize the chemistry, sources, and seasonality of carbon monoxide in the tropics the Marine Sciences Research Center, State University of New York (SUNY), has been analyzing air samples for CO concentration, $\delta^{13}C$, $\delta^{18}O$, and ^{14}CO from the Mauna Loa Observatory since October 1998. During the first year CO concentrations (Figure 1a) at Mauna Loa ranged from a minimum of 50 ppb on August 11, 1999, to a maximum of 198 ppb on March 17, 1999, with a yearly averaged concentration of 86 ppb. CO concentration data reveal an asymmetric seasonal cycle with maximum concentrations in the spring and minimum concentrations in the summer. The seasonality of $\delta^{13}C$ of CO (Figure 1b) generally follows that of CO concentration. Values of $\delta^{13}C$ peaked during the spring followed by an abrupt decrease in the early summer. Through the late summer, fall and winter, $\delta^{13}C$ increased gradually. Comparisons of $\delta^{18}O$ (Figure 1c) and CO concentrations show a close correlation during all times of the year. Again, $\delta^{18}O$ values increase during the spring and decrease abruptly in the early summer.

The stable isotope data were used along with the isotopic signatures of the major sources to constrain the relative source strengths over time. The model results combined with back trajectories show the predominant sources are from fossil fuel combustion and biomass burning during the spring maximum, which is in agreement with other studies.

^{14}CO is used separately as a tracer of OH abundance. This is based on the fact that the dominant loss rate of ^{14}CO is via reaction with OH, and its primary source is cosmogenic. Mauna Loa is only the second tropical site for routine ^{14}CO measurements in the northern hemisphere.

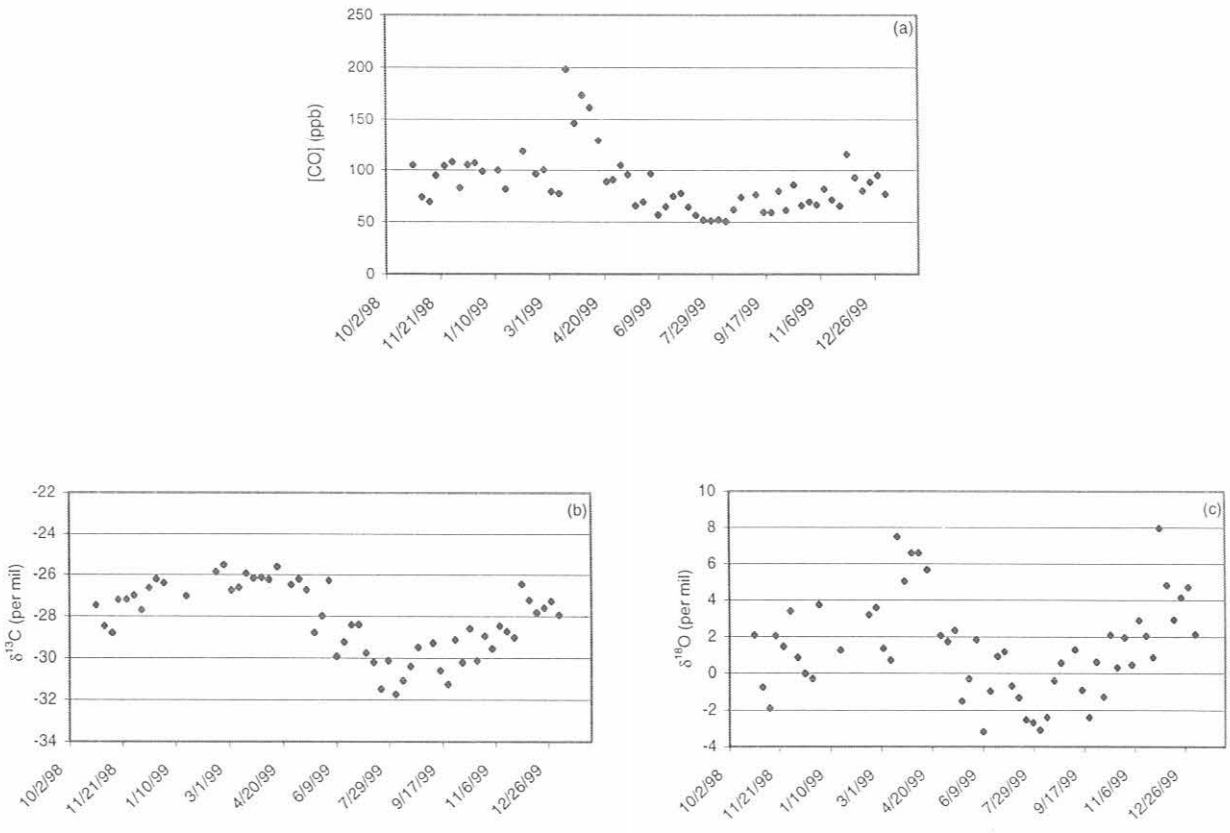

Fig. 1. Time series of (a) CO, (b) $\delta^{13}C$, and (c) $\delta^{18}O$ at Mauna Loa, Hawaii, from October 1998 through December 1999.

Interpreting Seasonal Cycles of Atmospheric Oxygen and Carbon Dioxide Concentrations at American Samoa Observatory

ANDREW C. MANNING, RALPH F. KEELING, AND LAURA E. KATZ
Scripps Institution of Oceanography, University of California, San Diego, La Jolla, California 92093-0244

INTRODUCTION AND METHODOLOGY

Precise atmospheric oxygen (O_2) measurements can be used as a tool for studying the global carbon cycle. *Keeling and Shertz* [1992] calculated global land and ocean carbon sinks from O_2 and CO_2 concentrations measured from flask samples collected at three different locations. From an analysis of the seasonal cycles of O_2 and CO_2 they were also able to provide an estimate of net biological productivity in the oceans. Their work has been updated with more recent data and findings by *Bender et al.* [1996], *Keeling et al.* [1996], and *Battle et al.* [2000]. Atmospheric O_2 measurements can also be used in a variety of other biogeochemical applications such as measuring air-sea gas exchange rates [*Keeling et al.*, 1998a], assessing the performance of ocean carbon cycle models [*Stephens et al.*, 1998], and interpreting and validating satellite ocean color data [*Balkanski et al.*, 1999].

From June 1993 to the present, CMDL staff have collected flask samples from Cape Matatula, American Samoa (SMO) as part of the Scripps global atmospheric oxygen sampling network. These data up to June 2000 are presented in this report. Flask sampling protocols are described in detail in *Keeling et al.* [1998b]. Briefly, ambient air samples are collected approximately biweekly, in triplicate, in 5-L glass flasks equipped with two stopcocks that are sealed with Viton o-rings. Air is drawn through a Dekoron intake line mounted up a tower or mast. A small compressor pump maintains an air flow of approximately 5 STP L min^{-1}, flushing ambient air through each flask. Flushing continues until a minimum of 15 flask volumes has passed through each flask, and then the sample is sealed off at a pressure of about 1 bar. A cryogenic cold trap at about -70°C pre-dries the air to remove water vapor. Flask samples are shipped back to the laboratory in La Jolla, California, for measurements of both O_2 and CO_2 concentrations.

Flask samples are collected by station personnel during what are considered to be "clean, background air" conditions; sample air that has not been contaminated by local or regional anthropogenic or terrestrial processes is required. In this manner seasonal and interannual temporal patterns in O_2 and CO_2 concentrations can be observed. The general criteria used to determine when these conditions are met are a pre-established wind direction and speed and relatively steady, non-fluctuating, in situ atmospheric CO_2 concentrations. At Samoa the criteria used are a wind direction between 330° and 160°, a wind speed greater than 2 ms^{-1}, and 2 consecutive hours of CO_2 concentration agreeing to within 0.25 ppm [*Waterman et al.*, 1989].

In the Scripps laboratory, flask samples are analyzed simultaneously for CO_2 concentration on a Siemens nondispersive infrared analyzer (NDIR) and for O_2/N_2 ratio on our interferometric analyzer [*Keeling*, 1988]. Samples are analyzed relative to a working gas, which in turn is calibrated each day against a pair of secondary reference gases of predetermined O_2/N_2 ratios and CO_2 concentrations. A suite of 12 primary reference gases are analyzed roughly every 6 months as a check on the long-term stability of the secondary reference gases. (See *Keeling et al.* [1998b] for a detailed discussion of reference gases and calibration procedures.)

Measurements of O_2/N_2 ratios are used to report changes in O_2 concentration, relying on the assumption that N_2 concentrations are constant. Based on the results of other studies [*Manning*, 2000], the possibility of O_2 fractionation relative to N_2 in our samples collected at Samoa became a concern. It was discovered that under certain flow, pressure, and temperature conditions, O_2 will fractionate relative to N_2 at "tee" junctions where an incoming air stream divides into two. Room temperature variability and the ratio of the flow rates at the tee junction appear to be the two most crucial parameters [*Manning*, 2000]. At Samoa a tee existed in the intake line because this line is shared with the continuous CO_2 analyzer operated by CMDL personnel. Therefore in May 1999 the intake setup was modified by installing a dedicated line with no tee junctions. At the same time the physical location of the intake line was shifted from the top of a mast at 42 m above sea level to the top of a newly constructed communications tower located approximately 100 m further inland and at a height of 93 m. To assess any potential changes in the O_2/N_2 ratios or CO_2 concentrations of the sampled air created by the removal of the tee or shift in physical location of the inlet, the old setup was left in place, and a schedule was begun alternating the biweekly flask collection between the two intakes. This schedule was started in May 1999 and plans are to continue it for a 2-yr period. There are now 13 months of data from this overlapping collection period, and a preliminary comparison shows no discernible difference between the two intakes. However, further data are needed to validate this conclusion.

LONG-TERM AND SEASONAL TRENDS IN O_2/N_2 RATIOS AND CO_2 CONCENTRATIONS

In Figure 1 the raw O_2/N_2 ratio and CO_2 concentration data collected at Samoa are shown. The differences are expressed in O_2/N_2 ratios in "per meg" units, where

$$\delta(O_2/N_2)\ (\text{per meg}) = \frac{(O_2/N_2)_{sam} - (O_2/N_2)_{ref}}{(O_2/N_2)_{ref}} \times 10^6 , \quad (1)$$

where $(O_2/N_2)_{sam}$ is the ratio of the sample gas and $(O_2/N_2)_{ref}$ is the ratio in an arbitrary reference gas cylinder. One per meg is equivalent to 0.001 per mil, the unit typically used in stable isotope work. By making the assumption that atmospheric N_2 concentrations are constant, this ratio essentially reports variations in atmospheric O_2 concentrations. In these units, 4.8 per meg are essentially equivalent to 1 ppm (i.e., 1 μmole O_2 per mole of dry air). CO_2 concentrations are expressed in ppm. In this figure the y axes have been scaled in such a way that changes in O_2 and CO_2 are comparable visually on a mole-to-mole basis. The curve fits are computed as a least squares fit to the sum of a four harmonic annual seasonal cycle and a stiff Reinsch spline [*Reinsch*, 1967] to account for the interannual trend and other nonseasonal variability.

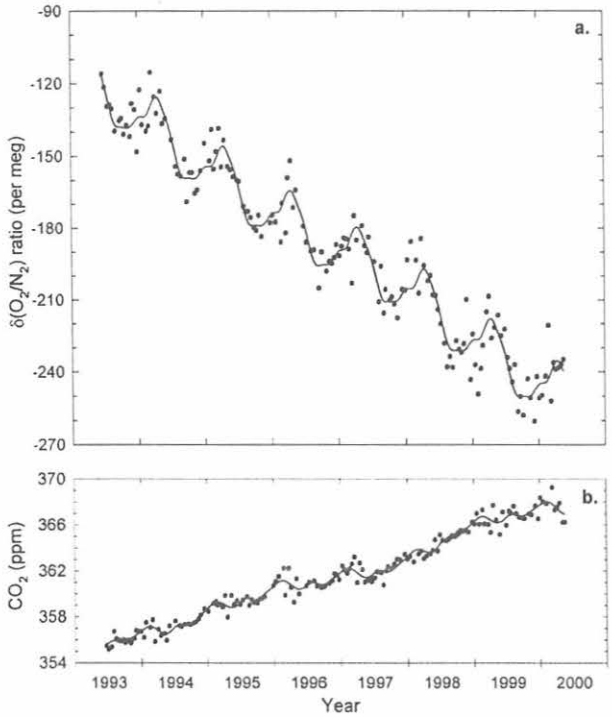

Fig. 1. O_2/N_2 ratios (a) and CO_2 concentrations (b) measured from flask samples collected at Cape Matatula, American Samoa (14°S, 171°W). Plots (a) and (b) were scaled so that changes in O_2 and CO_2 can be compared visually on a mole-to-mole basis. Curve fits are least squares fit to the sum of a four harmonic annual seasonal cycle and a stiff spline. The O_2/N_2 decreasing trend and CO_2 increasing trend are primarily because of fossil fuel combustion.

The figure shows the well-known increasing trend in CO_2 concentrations owing to fossil fuel combustion and also a corresponding decreasing trend in O_2/N_2 ratios. For the 7-yr period from June 1993 to June 2000 an average increase in CO_2 concentration of 1.9 ppm yr^{-1} and an average decrease in O_2/N_2 ratio of 18.8 per meg yr^{-1} were observed, or in comparable units, CO_2 increased by 3.3×10^{14} mol yr^{-1} and O_2 decreased by 7.0×10^{14} mol yr^{-1}. By contrast, over the same time period, fossil fuel combustion released an average of 5.4×10^{14} mol yr^{-1} of CO_2 into the atmosphere and consumed 7.6×10^{14} mol yr^{-1} of O_2. The O_2 consumption by fossil fuel combustion was offset by net growth in the land biosphere, producing atmospheric O_2 and consuming a portion of atmospheric CO_2. The overall decrease in atmospheric O_2 is greater than the increase in CO_2 because a further portion of the CO_2 emitted by fossil fuels is taken up by the oceans. There is no corresponding flux out of the oceans offsetting the O_2/N_2 decrease because O_2 (and N_2) is much less soluble in seawater than CO_2.

Figure 1 also shows a small seasonal cycle in CO_2 and a much larger-amplitude cycle in O_2/N_2. Seasonal variability in CO_2 is generally attributed to seasonality in photosynthesis and respiration processes on land. Because there is relatively little land cover in the temperate and high latitudes of the southern hemisphere apart from the sterile antarctic continent, and because there is little seasonality in the tropics, only a small seasonal cycle in atmospheric CO_2 at Samoa would be expected. This is what was observed, but in fact the contributions to the seasonal cycle at Samoa are also influenced by long-range atmospheric transport as discussed in more detail in the following section. Seasonality in atmospheric O_2/N_2 is generally caused by seasonality in photosynthesis and respiration of both land and marine biota. There is no corresponding marine biotic seasonal component in the atmospheric CO_2 signal. Biologically induced seasonal variability in pCO_2 in seawater is significantly buffered because of both the inverse correlation with seasonal solubility changes driven by temperature and the geochemical reactions of CO_2 with water to form carbonic acid and carbonate and bicarbonate ions [*Keeling et al.*, 1993]. Oxygen, on the other hand, is chemically neutral in the oceans, and biologically induced changes are in phase with temperature-induced solubility changes and are, therefore, reinforced in the atmospheric O_2/N_2 seasonal imprint.

Unique Features Observed in Atmospheric Data Collected at Samoa

When compared to other stations in our flask sampling network, data from Samoa are unusual, exhibiting higher short-term variability and seasonal cycles not in phase with other stations. The unusual seasonality is illustrated in Figure 2, which

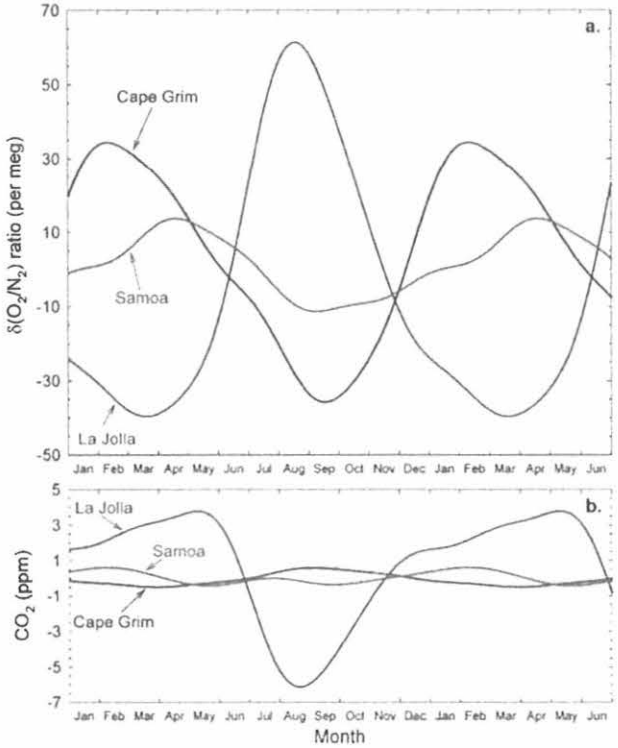

Fig. 2. Four-harmonic seasonal components of the curve fits in Figure 1 showing O_2/N_2 ratios (a) and CO_2 concentrations (b). Also shown for comparison are similar seasonal curve fits calculated from our flask sampling programs at Cape Grim, Tasmania (41°S, 145°E), and La Jolla, California (33°N, 117°W), representing the midlatitudes of the southern and northern hemisphere respectively. To show the seasonal characteristics more clearly, the first 6 months of each cycle are repeated. Southern hemisphere and northern hemisphere cycles are roughly 6 months out of phase with each other, whereas Samoa shows a more complicated signal. Plots (a) and (b) have been scaled so that changes in O_2 and CO_2 can be compared visually on a mole-to-mole basis.

shows the four-harmonic seasonal component of the O_2/N_2 and CO_2 curve fits in Figure 1. The curves shown are the average seasonal cycles calculated from all data over the 7-yr record. Also shown are similar curve fits calculated from data collected at our sampling stations at Cape Grim, Tasmania, Australia (CGO) (41°S, 145°E), and La Jolla, California (LJO) (33°N, 117°W), that are assumed to be broadly representative of midlatitudes in the southern and northern hemispheres, respectively. To illustrate the characteristics of the seasonal variability more clearly, the first 6 months of data are repeated in order to generate an 18-month-long record.

As shown in Figure 2a the maximum O_2/N_2 ratio at Samoa occurs in April, approximately 2 months later than the peak at Cape Grim occurring in February. The minimum O_2/N_2 ratio at Samoa occurs in late August or early September, a few weeks earlier than Cape Grim. There is some evidence of a weak second maximum in late December at Samoa. CO_2 data in Figure 2b show an even larger contrast to typical southern hemisphere patterns. Maximum CO_2 at Samoa occurs in February in contrast to September for Cape Grim, whereas the minimum occurs in May at Samoa and April at Cape Grim. CO_2 also exhibits a clearer second maxima and minima at Samoa as seen in the figure. The La Jolla curves show that Samoa O_2/N_2 ratios and CO_2 concentrations are also not in phase with northern hemisphere trends. In addition at each of the sampling stations at La Jolla and Cape Grim, O_2/N_2 and CO_2 changes are to a good approximation anticorrelated with each other, whereas at Samoa this is clearly not the case.

The unique climatological conditions at Samoa and their impact on concentrations of atmospheric constituents have been noted before. *Halter et al.* [1988] presented 3 years of CO_2 data from 1979-1981. They discussed the seasonal dependence of the variability observed in their CO_2 data and related this to air masses arriving at Samoa from different source regions. Following the wind climatology at Samoa presented by *Bortniak* [1981] and from an analysis of air mass backward trajectories, *Halter et al.* [1988] were able to show that the air arriving at Samoa came from one of three broadly-defined source regions centered on anticyclones named A_{NP}, A_{SP}, and A_{ANZ} representing the north Pacific tropical anticyclone, the southeast Pacific tropical anticyclone, and the Australia-New Zealand anticyclone, respectively.

Halter et al. [1988] further demonstrated that the observed Samoa CO_2 seasonal cycle was a superposition of three distinct seasonal cycles originating from each of these three air mass source regions. Because the seasonal cycles of CO_2 in the northern and southern hemispheres are out of phase, these cancel out partially, but not completely, at Samoa resulting in the complex seasonal pattern that was also observed as shown in Figure 2b. *Halter et al.* [1988] then showed that the seasonal dependence of the CO_2 variability observed at Samoa is a function of the seasonally varying interhemispheric gradient in CO_2 concentration and also of the seasonally varying frequency of occurrence that air arriving at Samoa originated from the northern hemispheric A_{NP} anticyclone. This frequency of occurrence varies because of seasonal variations in the position and strength of the Intertropical Convergence Zone (ITCZ) and the South Pacific Convergence Zone (SPCZ). These two effects result in greater CO_2 variability during austral summer and autumn.

Prinn et al. [1992] and *Hartley and Black* [1995] found relatively high short-term variability in methyl chloroform concentrations measured at Samoa during austral summers but only in non-El Niño years. *Hartley and Black* [1995] showed that these observations could be explained by changes in large-scale atmospheric circulation patterns at Samoa similar to the seasonal changes described by *Halter et al.* [1988] and *Bortniak* [1981]. It was demonstrated that the frequency of occurrence of air originating from the A_{NP} anticyclone during El Niño years was significantly reduced, explaining the lack of methyl chloroform variability in these years. The CO_2 data in Figure 1b support this conclusion where it can be seen that during the strong 1997-1998 El Niño, CO_2 variability during the austral summer is significantly reduced compared to other years.

Harris and Oltmans [1997] observed variability in tropospheric ozone concentrations at Samoa approximately 6 months out of phase with the variability in CO_2 described by *Halter et al.* [1988]. They also attributed these observations to summer-winter changes in atmospheric transport, in this case explaining the high austral winter variability not by variations in the latitudinal origin of the air masses arriving at Samoa, but by variations in the altitudinal origin that impacts the relative strengths of ozone sources and sinks, thus influencing the concentration of arriving air masses.

Land and Ocean Partitioning of Air Mass Influences at Samoa

With the O_2/N_2 ratio measurements, to a good approximation, Scripps is able to distinguish between land and ocean processes affecting the air masses arriving at Samoa. This is done by defining a tracer, Atmospheric Potential Oxygen (APO), that is conservative with respect to O_2 and CO_2 exchanges in land biota. APO is defined as

$$\mathrm{APO\ (per\ meg)} = \delta(O_2/N_2) + \frac{R_{O_2:C}}{X_{O_2}}\delta X_{CO_2}, \qquad (2)$$

where R_{O_2}:C represents the $-O_2$:C exchange ratio for land biotic photosynthesis and respiration, X_{O_2} is the standard mole fraction of O_2 in dry air, and δX_{CO_2} is the difference in the CO_2 mole fraction of the sample from an arbitrary reference gas, in ppm. This definition is a simplified version of the formula presented in *Stephens et al.* [1998] where minor influences from CH_4 and CO oxidation have been neglected. R_{O_2}:C = 1.1 based on measurements of *Severinghaus* [1995] and X_{O_2} = 0.20946 from *Machta and Hughes* [1970] were used.

To a good approximation APO is not influenced by land biotic exchanges, and variations in APO can only be caused by air-sea exchanges of O_2, N_2, and CO_2 and by combustion of fossil fuels since the $-O_2$:C exchange ratio for fossil fuels is approximately 1.4 higher than the value of 1.1 for land biotic exchanges [*Keeling et al.*, 1998a; *Stephens et al.*, 1998]. In contrast to APO, variations in CO_2 on seasonal and shorter time-scales are mainly caused by land biotic exchanges because of the buffering of CO_2 changes in the ocean as mentioned previously.

Figure 3 shows plots of APO and CO_2 concentrations representing oceanic and land influences, respectively. The symbols on each plot show all flask samples collected at Samoa from June 1993 to June 2000 where all samples have been collapsed into 1 calendar year. The curves shown are the four-harmonic seasonal component of the curve fits to data from Cape Grim and Cape Kumukahi, Hawaii (KUM) (20°N, 155°W), representing the nearest sampling stations from which there are data in the southern and northern hemispheres, respectively.

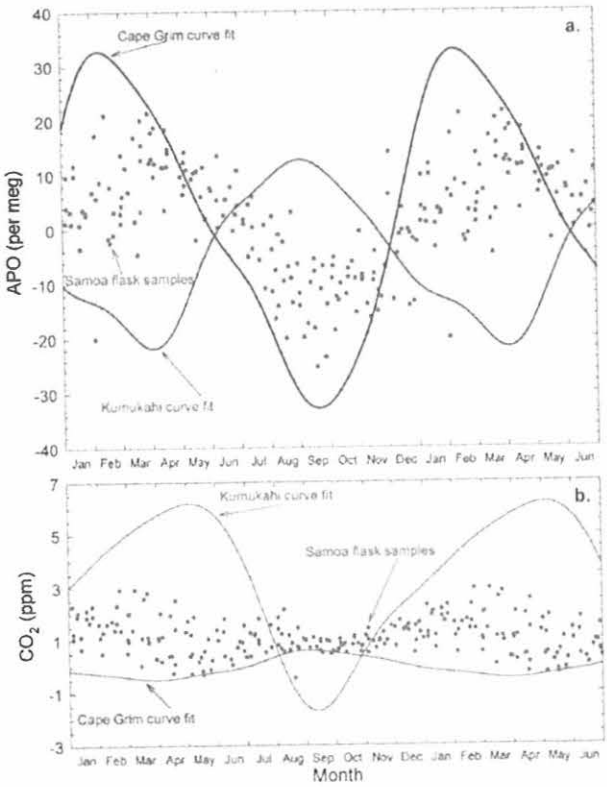

Fig. 3. Oceanic (a) and land biotic (b) influences on the air masses arriving at Samoa are shown. Atmospheric Potential Oxygen (APO), defined in the text, is essentially not influenced by land biotic processes and, therefore, represents oceanic influences. The seasonal component of the Samoa flask samples are shown as well as seasonal curve fits from Cape Grim, Tasmania, and Cape Kumukahi, Hawaii, representing the nearest stations from which we have data in the southern and northern hemisphere, respectively. Data were normalized as described in the text. As for the previous figure, the first 6 months of each cycle are repeated, and the plots were scaled to be able to visually compare mole-to-mole changes in APO and CO_2 concentrations.

Typically, data that have been interannually detrended are centered on zero and have no absolute frame of reference. Here, in order to compare detrended data across different stations, all data have been normalized to the Cape Grim interannual trend. In other words, the Samoa flask data shown are the raw data points of Figure 1 with the interannual spline component of the Cape Grim curve fit subtracted. Because of slight variability from year to year in the interannual trends, the Kumukahi four-harmonic curve fit is not shown in the same manner. Instead, the average offset between the Kumukahi and Cape Grim spline components was calculated from 1993 to 2000 ($\Delta O_2/N_2$ = -3.6 per meg; ΔCO_2 = 2.8 ppm), and this offset was added to the Kumukahi four-harmonic curve fit resulting in the Kumukahi curves shown in Figures 3a and 3b. The Cape Grim curves shown are simply the Cape Grim four-harmonic components of the Cape Grim curve fits. As with Figure 2, the first 6 months are repeated to generate 18 months of data, and APO and CO_2 changes are comparable visually on a mole-to-mole basis.

There are several prominent features apparent in Figure 3. Samoa CO_2 data in Figure 3b agree very well with the earlier data presented by *Halter et al.* [1988], showing greater variability in the austral summer and autumn. However, based on additional information from our APO data, a slightly different hypothesis of source air mass origins is suggested to explain this variability. For periods of May, June, and December in the APO signal, and from August to October in the CO_2 signal, Samoa data exhibit persistently higher concentrations than seen in air masses either to the north or to the south. It is believed that these data represent recirculated air, perhaps as a component of the Pacific Walker cell circulation. In other words, this is air not recently originating from the north or the south, but from the tropics at some point in the past.

To further support this hypothesis Figure 4 presents the statistical variability in the data. The residuals of all flask samples shown in Figure 1 were calculated from the curve fits also shown in Figure 1. The standard deviation of these residuals for each month was then calculated where, for example, all January samples from 1993 to 2000 were binned together. These standard deviations for each month are shown in the top plots of Figures 4a and 4b for APO and CO_2, respectively. Thus these plots give a statistical measure of the variability in APO and CO_2 at monthly time intervals. To provide a comparison, Cape Grim data are calculated in the same manner. As for Figures 2 and 3, the first 6 months are repeated. Figure 4b shows what was readily apparent in Figure 3b, a clear seasonal pattern to the variability in the CO_2 signal, and a good correlation of this variability with the north-south interhemispheric gradient, shown in the bottom plot of Figure 4b. In contrast, Figure 4b shows that Cape Grim does not exhibit such seasonal variability, and that during the austral winter and spring, Samoa variability is similar to that at Cape Grim. Figure 4a shows that there may also be a seasonal component to the APO variability. However, such seasonality is much less readily apparent than the CO_2 seasonality, is not of the same phasing as CO_2, and is almost equally apparent in Cape Grim APO as it is in Samoa APO.

Relatively low monthly standard deviations are observed for all of the months described previously in Figure 3 exhibiting APO or CO_2 concentrations higher than present in the northern or southern hemisphere for that month with the exception of APO in December (Figure 4). This lower variability also suggests that this air has had more time to mix and become homogenized and has not been influenced to the same extent by air masses from the north or the south, supporting the hypothesis of recirculated tropical air.

Figures 3 and 4 both show a clear difference in the pattern of variability in the APO signal compared with the CO_2 signal. APO does not show as clear a seasonal distinction in variability as CO_2 and does not show significant differences from Cape Grim variability (Figure 4). The top plots of Figure 4 have been scaled to enable direct comparison of the magnitude of variability of APO with CO_2. Thus it is clear that APO exhibits about twice the magnitude of variability of CO_2. These differences between APO and CO_2 cannot be directly explained either by the seasonally varying interhemispheric gradient or by the seasonally varying frequency of occurrence of the different air masses arriving at Samoa, both of which can be expected to affect APO in a similar manner as CO_2. There is, however, a difference in the southern hemisphere with respect to APO and CO_2. Regional sources and sinks for CO_2 are relatively small, whereas sources and sinks for APO are comparable to those in the northern hemisphere.

Therefore, from July to November CO_2 variability is lowest both because of a smaller interhemispheric gradient (Figure 4b, bottom plot) and because of a lower frequency of occurrence of

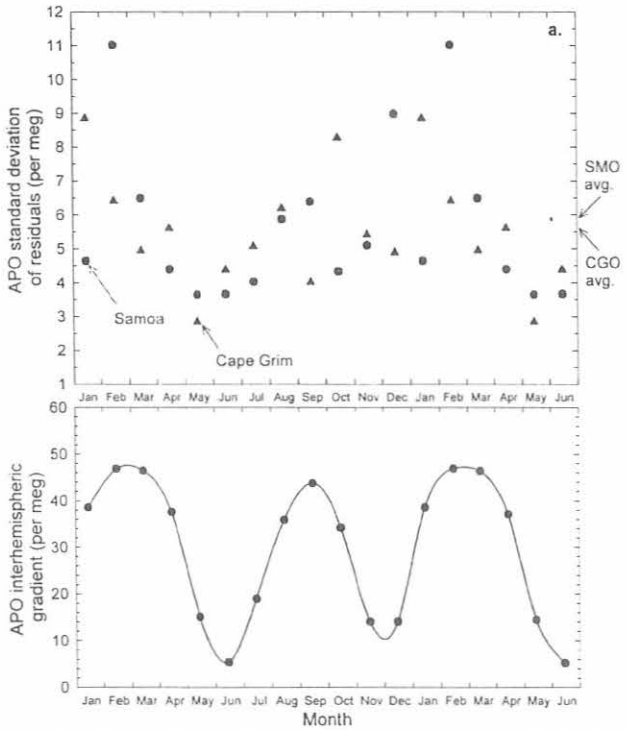

Fig. 4a. (Top) APO monthly standard deviations of the residuals of the flask data from the curve fits. Results are shown for both Samoa and Cape Grim, and the first 6 months are repeated. The annual average residual at each station is indicated on the right. There is little to distinguish Samoa and Cape Grim, and there is only weak evidence of a seasonal trend in the residuals at both stations. (Bottom) The absolute magnitude of the north-south interhemispheric gradient, calculated each month, and using Cape Grim and Cape Kumukahi data as representative of the southern and northern hemisphere, respectively.

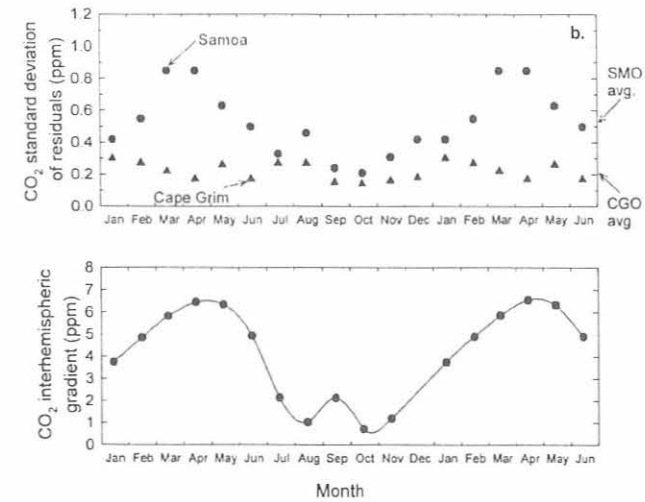

Fig. 4b. Top and bottom plots as for Figure 4a. As for Figures 2 and 3, APO and CO_2 changes are visually comparable between Figures 4a and 4b. In contrast to APO, CO_2 shows a clear seasonal pattern in variability at Samoa, indicated here with higher standard deviations, whereas Cape Grim does not appear to show any seasonality. The pattern at Samoa appears to correlate well with the north-south interhemispheric gradient. Contrasting the magnitude of APO variability with CO_2, it can be seen that the APO signal is much "noisier", reflecting the presence of larger sources and sinks for O_2 in the southern hemisphere compared to CO_2.

A_{NP} air masses arriving at Samoa [*Halter et al.*, 1988]. By contrast even when air masses are entirely of southern hemispheric origin, APO variability is still high because regional sources and sinks prevent the air from becoming as well homogenized in APO. Figure 4a shows little distinction in APO variability between Samoa and Cape Grim, further supporting this conclusion. In addition, the backward wind trajectory analyses of *Harris and Oltmans* [1997] showed that air masses originating from the southern hemispheric A_{ANZ} anticyclone arriving at Samoa were more variable in their originating altitude than air masses arriving from A_{NP} or A_{SP}. Because the source and sink mechanisms for APO occur via air-sea gas exchange, this altitudinal variability in air mass origin will contribute further to the variability observed in the APO signal at Samoa. Furthermore, the frequency of occurrence of air arriving from the A_{ANZ} anticyclone was higher during austral winter and spring, coinciding with the lowest CO_2 variability.

Thus APO variability is a function of the interhemispheric gradient, the frequency of occurrence of air masses originating from A_{NP} when this gradient is large, and the frequency of occurrence of air masses originating from A_{ANZ}. These three effects, with regional sources and sinks of comparable magnitude in both hemispheres, combine to result in higher variability in the APO signal than the CO_2 signal, and very little if any seasonal pattern to this APO variability.

SUMMARY

A 7-yr record of atmospheric O_2/N_2 ratios and CO_2 concentrations measured from flask samples collected at American Samoa have been presented. These data show O_2/N_2 ratios decreasing and CO_2 concentrations increasing because of the combustion of fossil fuels. O_2/N_2 ratios are decreasing at a faster rate than the observed CO_2 increase because of the uptake of some fossil fuel-emitted CO_2 by the oceans. Uptake of CO_2 by the land biosphere also influences both the O_2/N_2 and CO_2 trends. When compared to other stations in the flask sampling network, data from Samoa are unusual, exhibiting higher short-term variability and seasonal cycles not in phase with other stations. This has been noted before from measurements of CO_2, methyl chloroform, and ozone and has been attributed to the unique geographical position of Samoa in relation to the IPCZ and SPCZ, whose positions vary seasonally, resulting in different air masses arriving at Samoa at different times of the year. The Scripps atmospheric O_2 data, expressed as APO, exhibit characteristics different from other atmospheric gases. The main differences are greater magnitude in the short-term variability, but, in contrast, almost no seasonal pattern to this variability. This is explained by significant regional sources and sinks existing for APO in both hemispheres, in contrast to CO_2, and related to this, a dependence on the altitudinal origins of air masses arriving at Samoa in addition to a dependence on the latitudinal origins.

REFERENCES

Balkanski, Y., P. Monfray, M. Battle, and M. Heimann, Ocean primary production derived from satellite data: An evaluation with atmospheric oxygen measurements, *Global Biogeochem. Cycles, 13*, 257-271, 1999.

Battle, M., M.L. Bender, P.P. Tans, J.W.C. White, J.T. Ellis, T. Conway, and R.J. Francey, Global carbon sinks and their variability inferred from atmospheric O_2 and $\delta^{13}C$, *Science, 287*, 2467-2470, 2000.

Bender, M., T. Ellis, P. Tans, R. Francey, and D. Lowe, Variability in the O_2/N_2 ratio of southern hemisphere air, 1991-1994: Implications for the carbon cycle, *Global Biogeochem. Cycles*, *10*, 9-21, 1996.

Bortniak, J.C., The wind climatology of American Samoa, NOAA Tech. Memo., *ERL ARL-98*, 67 pp., Boulder, CO, 1981.

Halter, B.C., J.M. Harris, and T.J. Conway, Component signals in the record of atmospheric carbon dioxide concentration at American Samoa, *J. Geophys. Res.*, *93*, 15,914-15,918, 1988.

Harris, J.M., and S.J. Oltmans, Variations in tropospheric ozone related to transport at American Samoa, *J. Geophys. Res.*, *102*, 8781-8791, 1997.

Hartley, D.E., and R.X. Black, Mechanistic analysis of interhemispheric transport, *Geophys. Res. Lett.*, *22*, 2945-2948, 1995.

Keeling, R.F., Measuring correlations between atmospheric oxygen and carbon dioxide mole fractions: A preliminary study in urban air, *J. Atmos. Chem.*, *7*, 153-176, 1988.

Keeling, R.F., and S.R. Shertz, Seasonal and interannual variations in atmospheric oxygen and implications for the global carbon cycle, *Nature*, *358*, 723-727, 1992.

Keeling, R.F., R.P. Najjar, M.L. Bender, and P.P. Tans, What atmospheric oxygen measurements can tell us about the global carbon cycle, *Global Biogeochem. Cycles*, *7*, 37-67, 1993.

Keeling, R.F., S.C. Piper, and M. Heimann, Global and hemispheric CO_2 sinks deduced from changes in atmospheric O_2 concentration, *Nature*, *381*, 218-221, 1996.

Keeling, R.F., B.B. Stephens, R.G. Najjar, S.C. Doney, D. Archer, and M. Heimann, Seasonal variations in the atmospheric O_2/N_2 ratio in relation to the kinetics of air-sea gas exchange, *Global Biogeochem. Cycles*, *12*, 141-163, 1998a.

Keeling, R.F., A.C. Manning, E.M. McEvoy, and S.R. Shertz, Methods for measuring changes in atmospheric O_2 concentration and their applications in southern hemisphere air, *J. Geophys. Res.*, *103*, 3381-3397, 1998b.

Machta, L., and E. Hughes, Atmospheric oxygen in 1967 to 1970, *Science*, *168*, 1582-1584, 1970.

Manning, A.C., Temporal variability of atmospheric oxygen from both continuous measurements and a flask sampling network: Tools for studying the global carbon cycle, Ph.D. thesis, University of California, San Diego, La Jolla, California, 2000.

Prinn, R., D. Cunnold, P. Simmonds, F. Alyea, R. Boldi, A. Crawford, P. Fraser, D. Gutzler, D. Hartley, R. Rosen, and R. Rasmussen, Global average concentration and trend for hydroxyl radicals deduced from ALE/GAGE trichloroethane (methyl chloroform) data for 1978-1990, *J. Geophys. Res.*, *97*, 2445-2462, 1992.

Reinsch, C.M., Smoothing by spline functions, *Num. Math.*, *10*, 177-183, 1967.

Severinghaus, J.P., Studies of the terrestrial O_2 and carbon cycles in sand dune gases and in Biosphere 2, Ph.D. thesis, Columbia University, New York, 1995.

Stephens, B.B., R.F. Keeling, M. Heimann, K.D. Six, R. Murnane, and K. Caldeira, Testing global ocean carbon cycle models using measurements of atmospheric O_2 and CO_2 concentration, *Global Biogeochem. Cycles*, *12*, 213-230, 1998.

Waterman, L.S., D.W. Nelson, W.D. Komhyr, T.B. Harris, K.W. Thoning, and P.P. Tans, Atmospheric carbon dioxide measurements at Cape Matatula, American-Samoa, 1976-1987, *J. Geophys. Res.*, *94*, 14,817-14,829, 1989.

Artificial Windshielding of Precipitation Gauges in the Arctic

RICHARD J. MCCLURE
Soil Conservation Service, Anchorage, Alaska 99508-4362

INTRODUCTION

Precipitation gauges can provide good measurements of the water equivalent of snow precipitation, provided the gauge is protected or shielded from wind effects. Unfortunately, there are no standards for collecting snow precipitation. Gauges located in exposed and windy areas may be totally unshielded, partially shielded by one or more buildings, or equipped with one of several types of artificial shields. The various shielding options in common use, therefore, produce a wide range of gauge catch efficiency. Also, the various studies of artificial shields in the United States and Canada have produced a wide range of results. This must be, in part, due to the wide range of weather conditions under which the various studies have been conducted. A lingering problem is applying the results to the local conditions of Alaska's tundra regions.

METHODS

A study of the windshield alternatives, under the unique conditions of Alaska's arctic coastal region, was set up at the CMDL Barrow facility during September 1989. Snowfall catches from four installed precipitation storage gauges were compared with that from an existing storage gauge protected by a Wyoming shield [*Hanson*, 1988]. Two of the four gauges were shielded, one with a Nipher shield [*Goodison et al.*, 1983] and the other with an Alter shield [*Alter*, 1937], and two were unshielded. One of the unshielded gauges was serviced on an event basis, the same as the three shielded gauges. The other unshielded gauge was treated as if it were a remote gauge, allowing rime to build up and dissipate naturally to see what effects rime had on the overall catch. The four gauges are each 20.3 cm in diameter × 100 cm tall, mounted with the orifice 2 m above the normal ground surface. The existing Wyoming-shielded gauge is 30.5 cm in diameter × 2 m tall and is equipped with a Leupold-Stevens water-level recorder. Because the anchors melted out in the permafrost, the 1993 wind storms blew over the Wyoming wind shield. This was an unusual wind event for that time of year. The gauge was not rebuilt.

RESULTS

Six winter seasons of total precipitation are available for comparison of the four gauges in Table 1. The results continue to confirm the catch of the Alter shield is 37 to 58% of the Nipher shield with the unshielded gauges ranging from 10 to 36% of the Nipher shielded precipitation gauge.

TABLE 1. Comparison of Total Precipitation of the Four Remaining Gauges

	Nipher	Alter	Unshielded Serviced	Unshielded Unserviced
Oct. 5, 1993-				
June 1, 1994	76.2 mm	38.1 mm	no record	23.9 mm
% of Nipher		50%		31%
Oct. 1, 1994-				
June 17, 1995	104.6 mm	54.6 mm	36.3 mm	37.3 mm
% of Nipher		52%	35%	36%
Oct. 3, 1995-				
June 3, 1996	84.1 mm	49.3 mm	28.7 mm	23.9 mm
% of Nipher		58%	34%	28%
Oct. 3, 1996-				
June 5, 1997	80.8 mm	30.0 mm	10.4 mm	7.9 mm
% of Nipher		37%	13%	10%
Oct. 1, 1997-				
June 2, 1998	89.4 mm	45.5 mm	18.3 mm	29.5 mm
% of Nipher		51%	20%	33%
Oct. 1, 1998-				
June 2, 1999	113.8 mm	59.9 mm	36.6 mm	38.9 mm
% of Nipher		53%	32%	34%

Acknowledgment. Appreciation is expressed to D. Endres, Station Chief, Barrow, Alaska, who serviced the precipitation gauges and collected the snow samples.

REFERENCES

Alter, S.C., Shield storage precipitation gauges, *Mon., Weather Rev., 65*, 262-265, 1937.

Goodison, B.E., W.R. Turner, and J.E. Metcalfe, A Nipher-type shield for recording precipitation gauges, *Proc., 5th Symposium on Meteorological Observations and Instrumentation*, Toronto, Ontario, Canada, pp. 2-126, Am. Meteorol. Soc., Boston, 1983.

Hanson, C.L., Precipitation measured by gauges protected by the Wyoming shield and the dual-gauge system, *Proc., 56th Western Snow Conference*, Kalispell, MT, pp. 174-177, Colorado State University, Fort Collins, 1988.

Investigation of the Transfer Function between Atmosphere and Snow Concentrations of Hydrogen Peroxide at South Pole

JOSEPH R. MCCONNELL
Division of Hydrologic Sciences, Desert Research Institute, Reno 89512

ROGER C. BALES
Department of Hydrology and Water Resources, University of Arizona, Tucson 85721

Oxidation by OH is the main atmospheric sink for many environmentally important gases including methane (CH_4), carbon monoxide (CO), and halogenated hydrocarbons involved in stratospheric ozone depletion. With a very short lifetime, OH is not preserved in snow and ice. Hydrogen peroxide (H_2O_2) is a sink for OH, and, because H_2O_2 is preserved in polar snow, firn, and ice, an ice core record of H_2O_2 is potentially a proxy for changes in atmospheric OH through time. In addition, recent springtime depletion of stratospheric ozone has changed the level of solar radiation in the lower troposphere over Antarctica, thereby changing tropospheric photochemistry and also the chemistry of the surface and near-surface snow. However, deposition of H_2O_2 from the atmosphere to the near-surface snow and firn is reversible; some fraction of the originally deposited mass cycles between the atmosphere and the snow as the snow ages and is buried while environmental conditions change. The result is an atmosphere-to-snow transfer relationship that is highly nonlinear with temperature, as well as accumulation rate and accumulation timing. Our research is aimed at better understanding this transfer relationship and developing physically based numerical models of the transfer processes. The eventual goal is to quantitatively invert the ice core record to an atmospheric record of H_2O_2 and provide constraints on past OH concentration.

Field and modeling studies are conducted at a number of remote locations in the arctic and antarctic. The objective is to develop information on H_2O_2 transfer and preservation in as many depositional environments as possible for use in model development and validation. Current antarctic study sites are shown in Figure 1. South pole is the key site for detailed process level studies because of a long record of high quality atmospheric and meteorological measurements, year round occupation, low mean annual temperature, and relatively high accumulation rate. Through our cooperative agreement with CMDL, surface and near-surface snow samples have been collected since November 1994. Replicate snow samples are collected by CMDL staff approximately once each week throughout the year and shipped back to our laboratories in Tucson and Reno for chemical determinations. The record of H_2O_2 concentration in surface snow at south pole (Figure 2) shows a highly repeatable annual cycle with a distinct peak in mid-November of each year, well before the summer solstice. Efforts to understand and model both surface and near-surface snow concentrations at south pole have been described previously [*McConnell*, 1997; *McConnell and Bales*, 1998; *McConnell et al.*, 1997, 1998, 1999; *Stewart and McConnell*, 1999].

Collaboration with CMDL staff at the south pole continues under NSF grants 9903744 and 9811875. Five shallow firn cores were collected in 1999 and 2000 within 15 km of the station.

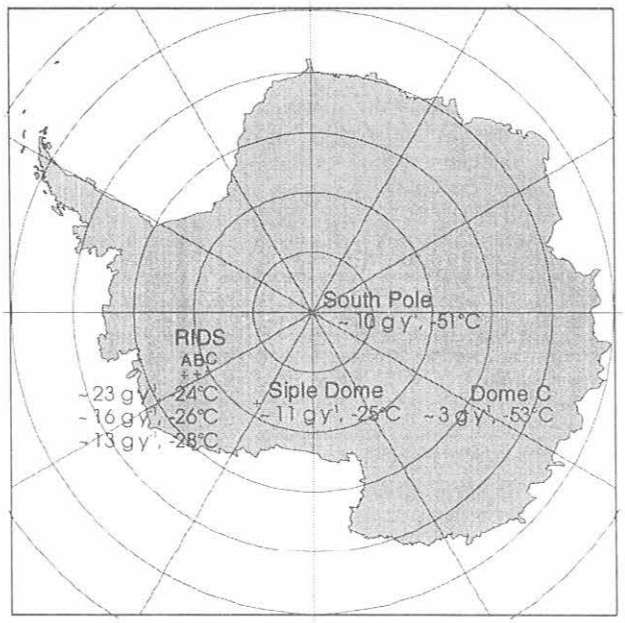

Fig. 1. Locations of study sites used by current atmosphere-snow transfer modeling. Also shown are the mean annual snow accumulation rates and air temperatures.

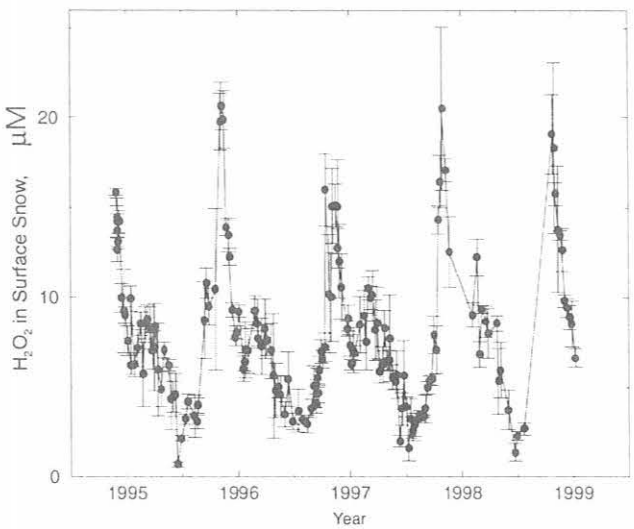

Fig 2. Hydrogen peroxide in surface snow at south pole. Error bars show one standard deviation in replicate measurements.

Three of these cores were sectioned and analyzed for H_2O_2 and formaldehyde (HCHO) on site at the Atmospheric Research Observatory (ARO). Formaldehyde, a highly volatile, photochemically linked atmospheric chemical species, is also preserved in snow and ice. Preliminary field and modeling results of HCHO transfer and preservation were reported by *Hutterli et al.* [1999]. An atmospheric H_2O_2 detector was installed in ARO and maintained for much of the 1999/2000 summer field season under the supervision of CMDL staff.

REFERENCES

Hutterli, M.A., J.R. McConnell, R.W. Stewart, R. Röthlisberger, and R.C. Bales, Modeling reversible atmosphere-to-snow transfer of HCHO in Antarctica, *Eos Trans. AGU, 80(46),* F198, 1999.

McConnell, J.R., Investigation of the atmosphere-snow transfer process for hydrogen peroxide, Ph.D. dissertation, Department of Hydrology and Water Resources, University of Arizona, 1997.

McConnell, J.R., and R.C. Bales, Investigation of the transfer function between atmosphere and snow concentrations of hydrogen peroxide at south pole, in *Climate Monitoring and Diagnostics Laboratory No. 24, Summary Report 1996-1997*, edited by D.J. Hoffman, J.T. Peterson, and R.M. Rosson, NOAA Environ. Res. Labs., Boulder, CO, 142-144, 1998.

McConnell, J.R., J. R. Winterle, R.C. Bales, A.M. Thompson, and R.W. Stewart, Physically based inversion of surface snow concentrations of hydrogen peroxide to atmospheric concentrations at south pole, *Geophys. Res. Lett., 24(4),* 441-444, 1997.

McConnell, J.R., R.C. Bales, R.W. Stewart, A.M. Thompson, M.R. Albert, and R. Ramos, Physically based modeling of atmosphere-to-snow-to-firn transfer of hydrogen peroxide at south pole, *J. Geophys. Res., 103(D9),* 10,561-10,570, 1998.

McConnell, J.R., R.W. Stewart, M. Hutterli, and R.C. Bales, Modeling reversible atmosphere-to-snow transfer and preservation of hydrogen peroxide in Antarctica, *Eos Trans. AGU, 80(46),* F192, 1999.

Stewart, R.W., and J.R. McConnell, Antarctic photochemistry: Uncertainty analysis, *Eos Trans. AGU, 80(46),* F197-198, 1999.

Stratospheric Ozone Climatology from Lidar Measurements at Mauna Loa

STUART MCDERMID, THIERRY LEBLANC, RICHARD CAGEAO, AND DANIEL WALSH
Table Mountain Facility, Jet Propulsion Laboratory, California Institute of Technology, Wrightwood, California 92397

INTRODUCTION

The Jet Propulsion Laboratory (JPL) lidar at Mauna Loa Observatory (MLO) continues to make regular measurements of ozone, temperature, and aerosol profiles for the Network for the Detection of Stratospheric Change (NDSC) program. This report describes the development of an ozone climatology from one aspect of the lidar results.

The routine measurement modes for the lidar are based upon the NDSC requirement for a long-term ozone survey. The usual measurements comprise an approximately 1.5-hour long data acquisition at the beginning of the night several times a week, weather and instrument permitting (the normal starting time is the end of astronomical twilight that ensures there is no sunlight falling on any part of the atmosphere sensed by the lidar). Additional full-night measurements have been made in the past 4 years at given periods of the year to study the tidal signature in the middle atmospheric temperature [*Leblanc et al.*, 1999]. However, to avoid any contamination by possible diurnal variations, only the profiles taken before 0930 UT were selected to build this climatology. The data set from the full-night campaigns will be used in the future for the study of the ozone diurnal variations. This temporal selection leaves more than 800 profiles between July 1, 1993, and June 30, 1999. The JPL lidars have participated in numerous intercomparison and validation exercises with nearly co-located and/or simultaneous measurements. The results of these campaigns have been extensively published and clearly indicate the quality of the lidar results [e.g., *McDermid et al.*, 1995; *Tsou et al.*, 1995; *Planet et al.*, 1995; *Baily et al.*, 1996; *Bruhl et al.*, 1996; *Froidevaux et al.*, 1996; *Grant et al.*, 1998; *McPeters et al.*, 1999].

OZONE PROFILES

In the present study the ozone concentration profiles were interpolated to a 1-km vertical interval in order to homogenize the entire data set. This operation reduces the magnitude of smaller vertical scale fluctuations, but these fluctuations are not needed for the climatological study presented. Figure 1 shows two typical profiles measured at MLO in late winter and midsummer. Unlike at more northern latitudes, such as the JPL Table Mountain Facility, there is no significant seasonal change in the altitude of the ozone peak. Also unlike northern midlatitudes, the ozone concentration in the lower stratosphere is not significantly higher in winter than in summer (5×10^{12} cm^{-3} in summer and 4-4.2 $\times$ 10^{12} cm^{-3} in winter near 24-26 km). Instead, the whole winter profile tends to have lower values than the summer profile. This is consistent with a more photochemically and/or radiatively driven tropical ozone abundance where the role of transport and mixing by the mid- and high-latitude planetary waves is much less significant. However, there remains a layer in the winter lower stratosphere where ozone is slightly more abundant than in summer. This feature, typical of the extra-tropical latitudes, is expected to disappear closer to the equator.

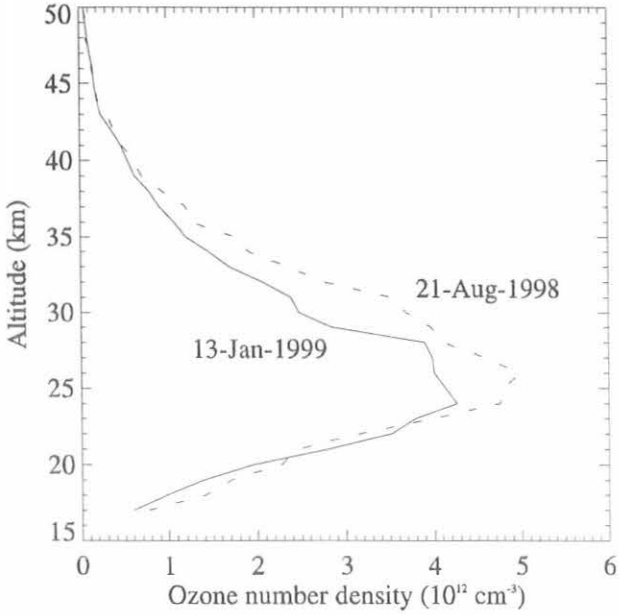

Fig. 1. Typical wintertime and summertime ozone profiles at MLO.

OZONE CLIMATOLOGY

The overall mean ozone number density was calculated as a function of altitude. The mean profile obtained is representative of an annual mean since the data distribution for each month is similar. Then, the deviations (in percent) from the quasi-annual mean were calculated for each day of measurement.

The two-dimensional contours of these filtered ozone deviations are shown in Figure 2. The color scale extends from –24% (violet) to +24% (red) with a 4% contour interval. The white solid line near 25 km represents the mean altitude of the ozone concentration peak. This altitude is nearly constant throughout the entire year. The seasonal variation of the ozone concentration at MLO is not as pronounced as for higher latitudes. Figure 2 nevertheless highlights a residual annual cycle at 30 km and above, similar to that observed at midlatitudes and related to the seasonal variation of the radiative balance of the upper stratosphere (more sunlight in summer). Figure 2 also reveals a springtime maximum near 19-20 km as the result of a residual contamination by the midlatitude planetary wave activity. No clear annual cycle is observed below 25 km. However, despite the strong variability at the bottom of the profiles (near the tropopause) persistent high ozone concentrations are observed during the summer months and persistent low concentrations are observed in December and January, indicating the dominant role of the photochemical and radiative effects over the dynamics. The annual cycles observed are in agreement within a few percent with previous climatologies such as that obtained from SAGE II data [*Shiotani and Hasebe*, 1994].

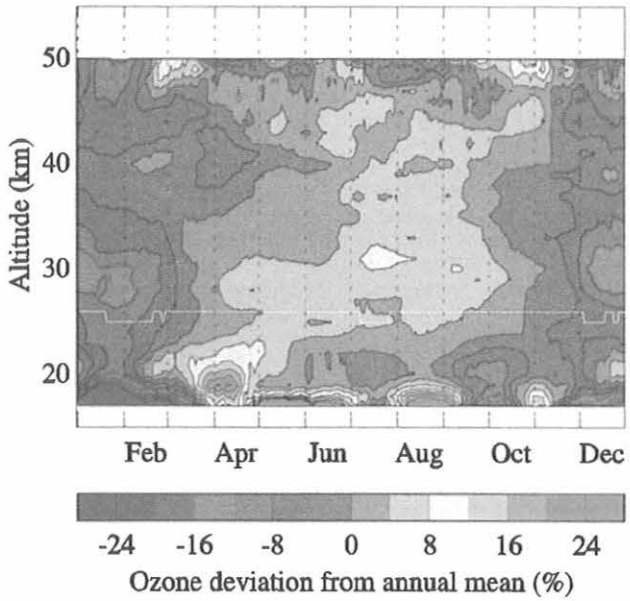

Fig. 2. Ozone number density deviation from the annual mean (%) as a function of altitude (km) and day-of-year at MLO. Contour interval is 4%.

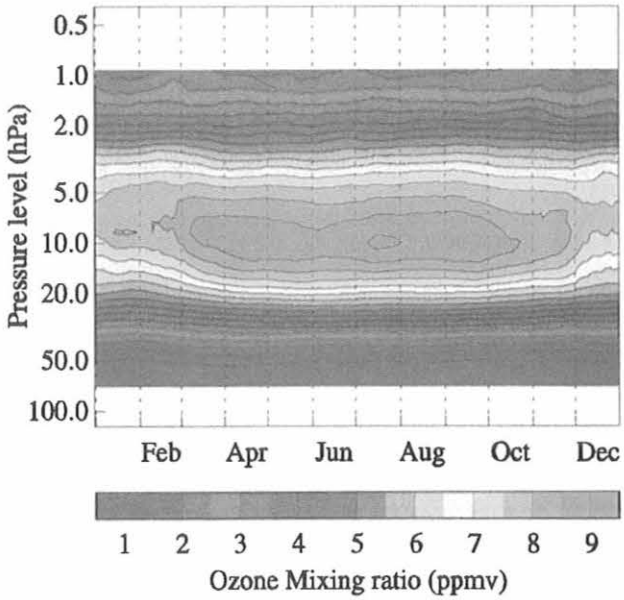

Fig. 3. Ozone mixing ratio (ppmv) at MLO, derived using the ozone results in Figure 2 and MSISE-90 density and temperature data, as a function of pressure altitude (hPa).

Derived Quantities

For a convenient comparison with model results and other observations, the ozone number densities measured by the lidar were converted into ozone mixing ratios. The Mass Spectrometer Incoherent Scatter Extended-90 (MSISE) empirically modeled air densities and temperatures [*Hedin*, 1991] were used to calculate the ozone-mixing ratio as a function of pressure. Figure 3 shows the seasonal variations of the derived ozone mixing ratios for the periods. Since the densities and temperatures (i.e., pressures) used do not come from actual simultaneous measurements, a slight vertical distortion of the contours is expected, especially during the winter months. This distortion can lead to some 10-15% differences in the regions of sharp vertical gradient like in the late spring and summer lower stratosphere.

Discussion and Conclusion

A 6-year stratospheric ozone climatology obtained by the JPL DIAL instrument located at Mauna Loa Observatory (19.5°N) has been described. The lidar provided high-resolution vertical profiles of nighttime ozone number density between ~15-50 km several nights a week since 1993. The climatology presented is typical of early night ozone values and includes a negligible fraction of Pinatubo-influenced ozone values [*Parrish et al.*, 1998]. It includes ozone values typical of a time of low solar activity since the measurement period is approximately centered on the 1996 11-year solar cycle minimum.

At MLO the ozone concentration tends to be higher during the summer months and lower during the winter months throughout the entire ozone layer. Only a weak signature of the extra-tropical latitudes is observed near 19-20 km with a secondary ozone maximum in late March-early April. As emphasized previously, the 1993-1999 measurement period at MLO is nearly centered on the 1996 11-year solar cycle minimum. Therefore, the upper stratospheric ozone values are expected to be slightly lower (~2-3%) than those obtained over a full solar cycle [*Chandra and McPeters*, 1994].

The current climatology will be complemented by ongoing detailed investigations of the day-to-day variability of the tropopause height, diurnal variations, interannual variability (Quasi-Biennial Oscillation, El Niño and the Southern Oscillation, solar cycle, etc.) and the long-term trends of ozone. The results from these investigations, combined with the present climatology, will eventually provide a comprehensive overview of the stratospheric ozone vertical distribution at MLO.

Acknowledgment. The work described in this report was carried out by the Jet Propulsion Laboratory, California Institute of Technology, under an agreement with the National Aeronautics and Space Administration.

References

Baily, P.L., D.P. Edwards, J.C. Gille, L.V. Lyjak, S.T. Massie, A.E. Roche, J.B. Kumer, J.L. Mergenthaler, B.J. Connor, M.R. Gunson, J.J. Margitan, I.S. McDermid, and T.J. McGee, Comparison of cryogenic limb array etalon spectrometer (CLAES) ozone observations with correlative measurements, *J. Geophys. Res., 101*, 9737-9756, 1996.

Bruhl, C., S.R. Drayson, J.M. Russell, P.J. Crutzen, J.M. McInerney, P.N. Purcell, H. Claude, H. Gernandt, T.J. McGee, and I.S. McDermid, Halogen Occultation Experiment ozone channel validation, *J. Geophys. Res., 101*, 10,217-10,240, 1996.

Chandra, S., and R.D. McPeters, The solar cycle variation of ozone in the stratosphere inferred from Nimbus 7 and NOAA 11 satellites, *J. Geophys. Res., 99*, 20,665-20,671, 1994.

Froidevaux, L., W.G. Read, T.A. Lungu, R.E. Cofield, E.F. Fishbein, D.A. Flower, R.F. Jarnot, B.P. Ridenoure, Z. Shippony, J.W. Waters, J.J. Margitan, I.S. McDermid, R.A. Stachnik, G.E. Peckham,

G. Braathen, T. Deshler, J. Fishman, D.J. Hofmann, and S.J. Oltmans, Validation of UARS Microwave Limb Sounder ozone measurements, *J. Geophys. Res., 101*, 10,017-10,060, 1996.

Grant, W.B., M.A. Fenn, E.V. Browell, T.J. McGee, U.N. Singh, M.R. Gross, I.S. McDermid, L. Froidevaux, and P.-H. Wang, Correlative stratospheric ozone measurements with the airborne UV DIAL system during TOTE/VOTE, *Geophys. Res. Lett., 25*, 623-626, 1998.

Hedin, A.E., Extension of the MSIS thermosphere model into the middle and lower atmosphere, *J. Geophys. Res., 96*, 1159-1172, 1991.

Leblanc, T., I.S. McDermid, and D.A. Ortland, Lidar observations of the middle atmospheric thermal tides and comparison with the High Resolution Doppler Imager and Global Scale Wave Model. 1. Methodology and winter observations at Table Mountain (34.4°N), *J. Geophys. Res., 104*, 11,917-11,929, 1999.

McDermid, I.S., S.M. Godin, T.D. Walsh, Results from the Jet Propulsion Laboratory stratospheric ozone lidar during STOIC 1989, *J Geophys. Res., 100*, 9263-9272, 1995.

McDermid, I.S., T.J. McGee, and D.P.J. Swart, NDSC lidar intercomparisons and validation: OPAL and MLO3 campaigns in 1995, in *Advances in Atmospheric Remote Sensing with Lidar*, pp. 525-528, Springer-Verlag, New York, 1996.

McPeters, R.D., D.J. Hofmann, M. Clark, L. Flynn, L. Froidevaux, M. Gross, B. Johnson, G. Koenig, X. Liu, I.S. McDermid, T. McGee, F. Murcray, S. Oltmans, A. Parrish, R. Schnell, U. Singh, J.J. Tsou., T.D. Walsh, and J.M. Zawodny, Results from the 1995 stratospheric ozone profile intercomparison at Mauna Loa (MLO3), *J. Geophys. Res., 104*, 30,505-30,514, 1999.

Parrish, A., B.J. Connor, J.J. Tsou, G. Beyerle, I.S. McDermid, and S.M. Hollandsworth, Microwave ozone and lidar aerosol profile observations at Table Mountain, California, following the Pinatubo eruption, *J. Geophys. Res., 103*, 22,201-22,208, 1998.

Planet, W.G., A.J. Miller, J.J. DeLuisi, D.J. Hofmann, S.J. Oltmans, J.D. Wild, I.S. McDermid, R.D. McPeters, and B.J. Connor, Comparison of NOAA-11 SBUV/2 ozone vertical profiles with correlative measurements, *Geophys. Res. Lett., 23*, 293-296, 1995.

Shiotani, M., and F. Hasebe, Stratospheric ozone variations in the equatorial region as seen in stratospheric aerosol and gas experiment data, *J. Geophys. Res., 99*, 14,564-14,584, 1994.

Tsou, J.J., B.J. Connor, A. Parrish, I.S. McDermid, and W.P. Chu, Ground-based microwave monitoring of middle atmosphere ozone-comparison to lidar and stratospheric and gas experiment-II satellite-observations, *J. Geophys. Res., 100*, 3005-3016, 1995.

Microwave Measurements of Middle Atmospheric Water Vapor From Mauna Loa, 1996-2000

GERALD E. NEDOLUHA, RICHARD M. BEVILACQUA, R. MICHAEL GOMEZ, AND BRIAN C. HICKS
Naval Research Laboratory, Code 7227, Washington, D.C. 20375-5320

INTRODUCTION

Measurements have been taken of middle atmospheric water vapor at Mauna Loa, Hawaii (19.5°N, 204.4°E) since March 1996. These measurements are taken at 22 GHz using the Naval Research Laboratory Water Vapor Millimeter-wave Spectrometer (WVMS). Because of the relatively small seasonal variations, combined with the small tropospheric water vapor signal, Mauna Loa is an ideal site for the monitoring of long term changes in middle atmospheric water vapor.

Measurements of water vapor provide important information on several processes in the middle atmosphere. Water vapor is an ideal transport tracer and has been used in numerous studies of atmospheric transport in the middle atmosphere [e.g., *Bevilacqua et al.,* 1990; *Nedoluha et al.,* 1996; *Summers et al.,* 1997]. Water vapor is also the reservoir of odd hydrogen in the middle atmosphere, and is, therefore, important to ozone chemistry. Variations in humidity in the middle atmosphere, therefore, have implications for variations in ozone [*Siskind and Summers,* 1998]. Changes in middle atmospheric water vapor may also impact stratospheric temperatures and thus indirectly affect ozone depletion [*Kirk-Davidoff et al.,* 1999].

WVMS MEASUREMENTS

The WVMS instrument deployed at Mauna Loa is the third such instrument to be deployed. It is essentially identical to the WVMS2 instrument that operated at the Network for the Detection of Stratospheric Change (NDSC) site at Table Mountain, California (34.4°N, 242.3°E) from August 1993 to November 1997. These instruments are both very similar to the WVMS1 instrument that is taking measurements at the NDSC site at Lauder, New Zealand (45.0°S, 169.7°E).

The retrieval of a vertical water vapor profile with ground-based microwave measurements relies upon the change in pressure as a function of altitude. The line width of the spectrum monotonically decreases with altitude because of the dependence on pressure broadening. Thus the resultant signal, which is the sum of the emission from all altitudes, can be deconvolved to retrieve a vertical profile. Details of the measurement technique and instrumentation are given by *Nedoluha et al.* [1995, 1996].

Nedoluha et al. [1999] compared the WVMS3 instrument at Mauna Loa with Halogen Occultation Experiment (HALOE). Once differences in resolution are taken into account, the average difference is <10% at almost all altitudes between 40 and 80 km. The only exception is a small range near 60 km where the average HALOE measurements show an unexpected local minimum in mixing ratio. The differences between the measurements taken at Mauna Loa and Table Mountain in 1996 and 1997 were generally consistent with the latitudinal difference in water vapor measured by HALOE. In particular, the shape of the difference profile between the two WVMS sites was very similar to the shape of the difference profile for the HALOE measurements at these latitudes between 40 and 70 km.

In Figure 1 the mixing ratios retrieved from 40 to 80 km using 500 scan (~1 week) integrations are shown. There is a summer peak in the upper mesospheric mixing ratio consistent with the upward motion of the atmosphere in the Mountain or Lauder [cf. *Nedoluha et al.,* 1997]. There is no sign of the positive trend in water vapor that was observed by the WVMS instruments and by HALOE in the early 1990s [*Nedoluha et al.,* 1998]. There is a suggestion of a very slight negative trend since 1996, a result that is qualitatively consistent with the global variation in stratospheric water vapor observed during this period by HALOE [*Randel et al.,* 1999].

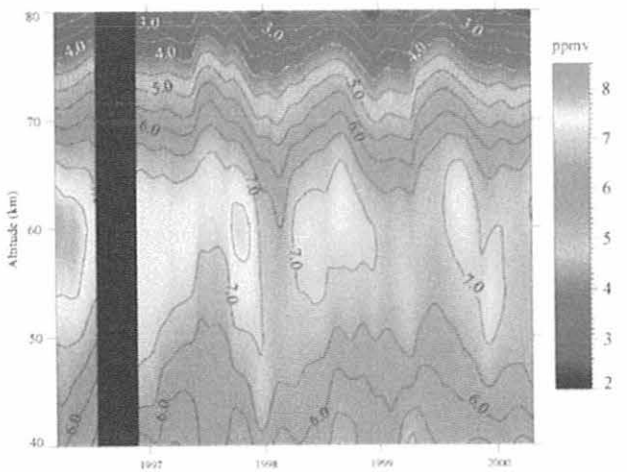

Fig. 1. Weekly integrated spectra of water vapor mixing ratios retrieved from WVMS3 measurements at Mauna Loa. The data are smoothed using a Gaussian filter with a (1/e) width of 25 days.

Acknowledgments. We wish to thank S. McDermid, Rich Cageao, and D. Walsh for their technical assistance with the Mauna Loa radiometer. This project is funded by NASA under the Upper Atmospheric Research Program.

REFERENCES

Bevilacqua, R.M., D.F. Strobel, M.E. Summers, J.J. Olivero, and M. Allen, The seasonal variation of water vapor and ozone in the upper mesosphere: Implications for vertical transport and ozone photochemistry, *J. Geophys. Res., 95,* 883-893, 1990.

Kirk-Davidoff, D.B., E.J. Hintsa, J.G. Anderson, and D.W. Keith, The effect of climate change on ozone depletion through changes in stratospheric water vapour, *Nature, 402*, 399-401, 1999.

Nedoluha, G.E., et al., Ground-based measurements of water vapor in the middle atmosphere, *J. Geophys. Res., 100,* 2927-2939, 1995.

Nedoluha, G.E., et al., Measurements of water vapor in the middle atmosphere and implications for mesospheric transport, *J. Geophys. Res., 101,* 21,183-21,193, 1996.

Nedoluha, G.E., et al., A comparative study of mesospheric water vapor measurements from the ground-based Water Vapor Millimeter-wave Spectrometer and space-based instruments, *J. Geophys. Res., 102*, 16,647-16,661, 1997.

Nedoluha, G.E., et al., Increases in middle atmospheric water vapor as observed by the Halogen Occultation Experiment and the ground-based Water Vapor Millimeter-wave Spectrometer from 1991 to 1997, *J. Geophys. Res., 103,* 3531-3543. 1998.

Nedoluha, G.E., et al., Measurements of middle atmospheric water vapor from low latitudes and midlatitudes in the Northern Hemisphere, 1995-1998, *J. Geophys. Res., 106,* 19,257-19,266, 1999.

Randel, W.J., et al., Space-time patterns of trends in stratospheric constituents derived from UARS measurements, *J. Geophys. Res., 104,* 3711-3727, 1999.

Siskind, D.E., and M.E. Summers, Implications of enhanced mesospheric water vapor observed by HALOE, *Geophys. Res. Let., 25,* 2133-2136, 1998.

Summers, M.E., D.E. Siskind, J.T. Bacmeister, R.R. Conway, S.E. Zasadil, and D.F. Strobel, Seasonal variations of middle atmospheric CH_4 and H_2O with a new chemical-dynamical model, *J. Geophys. Res., 102,* 3503-3526, 1997.

Carbon Flux Using Eddy Covariance Methodology in Arctic Coastal Wet Sedge Tundra

WALTER C. OECHEL, ROMMEL ZULUETA, AND HYOJUNG KWON
Global Change Research Group, San Diego State University, California 92182

INTRODUCTION

Tower-based eddy covariance measurements provided a near continuous temporal record of mass and energy over hectare spatial-scales. However, in a regional context, these measurements still represent a "point" measurement [*Baldocchi et al.*, 1996; *Vourlitis and Oechel*, 1997, 1999]. Aircraft-based measurements provide a relatively detailed measure of the large-scale (e.g., km^2) spatial variance in mass and energy exchange, but because of safety reasons, are temporally restricted to daytime periods and favorable weather conditions [*Crawford et al.*, 1996; *Desjardins et al.*, 1997]. The information gained from each technique is complimentary and essential for understanding spatial and temporal patterns in fluxes [*Desjardins et al.*, 1997].

Two of the primary objectives of the National Science Foundation Arctic Transitions in the Land-Atmosphere System (ATLAS) flux program are to quantify the plot (0.5 m^2), landscape (0.5-4 ha), and regional (e.g., 3 km^2) net ecosystem exchange (NEE) over several growing seasons and to develop methods for scaling point-measurements of mass and energy flux over varying spatial and temporal scales [*Weller et al.*, 1995]. As a preliminary exercise to fulfill these objectives, it is important to quantify the interrelationships between the mass and energy fluxes measured from different sampling techniques. The data presented here provide a baseline for comparison with future aircraft flux measurements.

METHODS

Fluctuations in wind speed, temperature, CO_2, and H_2O vapor were measured at 2.5 m above ground level. Vertical wind speed and temperature fluctuations were measured at 10 Hz using a three-dimensional sonic anemometer-thermometer (SWS-211/3K, Applied Technologies Inc., Boulder, Colorado) aligned into the mean wind. Carbon dioxide and H_2O vapor fluctuations were measured at 10 Hz with a fast response open-path infrared gas analyzer. The CO_2 and H_2O vapor channels of both sensors were calibrated at a minimum of every other week with 300 and 400 ppm standard gases and a portable dewpoint generator (LI-610, LI-COR Inc., Lincoln, Nebraska), respectively. For detailed information on methodology see *Vourlitis and Oechel* [1997, 1999].

Barrow and Atqasuk are the northern and southern anchor points, respectively, for the aircraft transect. The Barrow site (71°19'N, 156°36'W) is located in the Barrow Environmental Observatory (BEO) that covers several square kilometers dedicated to long-term arctic research and includes several different representative wet-moist coastal sedge tundra types. It is located 2 km south of the Arctic Ocean and comprised of low- and high-centered polygon ice wedges (polygon troughs) and drained lake tundra land forms [*Brown et al.*, 1980]. The Atqasuk site [70°29'N, 157°25'W] is located 100 km south of Barrow, Alaska. Soils are developed on aeolian sands of Quaternary age [*Everett*, 1980]. The site is comprised of a variety of moist-wet coastal sedge tundra and moist-tussock tundra surfaces in the more well-drained upland areas [*Batzli*, 1980]. Vegetation that dominate the area include the tussock-forming sedge, *Eriophorum vaginatum*, as well as other evergreen and deciduous forbs and shrubs [*Komarkova* and *Webber*, 1980; *Walker et al.*, 1989]. This site is also an intensive site for year-round measurements of net CO_2 flux and energy balance. Atqasuk's more continental climate and sandy substrate make a useful contrast with conditions at Barrow.

RESULTS

Net sink activity increased up to 4.0 gC m^{-2} d^{-1}, thaw depth (active layer depth) was –32 cm, and soil moisture content was 66% between mid-July and late July 1999 at the Barrow site (Figure 1). As thaw depth increased and soil moisture content decreased (to 63% in early August) sink strength of CO_2 flux decreased because of the soil respiration caused by microbial activation in the soil. After a precipitation event in mid-August, soil moisture content increased up to 71%, and there was rapid

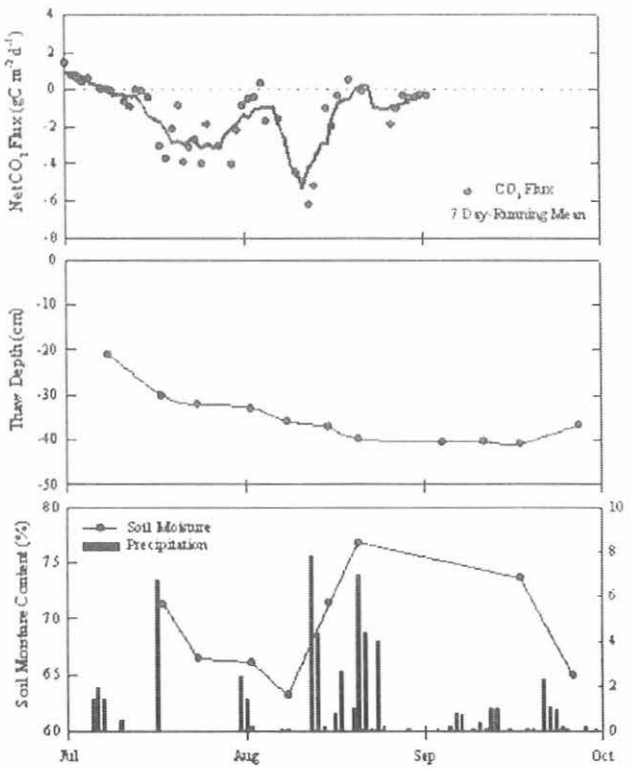

Fig. 1. Seasonal trend of daily integrated net CO_2 flux with thaw depth, soil moisture content, and precipitation at Barrow in 1999.

increase of sink activity (to 6.2 gC m^{-2} d^{-1}) even though thaw depth was -37 cm deep. It is assumed that soil moisture affected soil temperature, which in turn affected soil respiration, and there was a decrease of soil respiration resulting in a strong sink activity of net CO_2 flux. In late August net sink activity was small; thaw depth increased up to –41 cm; and soil moisture was 76%.

Acknowledgment. The authors thank Dan Endres, Station Chief at the CMDL Barrow station, for providing facilities, help in maintaining the tower, and periodic assistance with instrumentation and data acquisition computers.

REFERENCES

Baldocchi, D.D., R. Valentini, S. Running, W. Oechel, and R. Dahlman, Strategies for measuring and modeling carbon dioxide and water vapor fluxes over terrestrial ecosystems, *Global Change Biol.*, 2, 159-168, 1996.

Batzli, G.O., Patterns of vegetation and herbivory in arctic tundra: Results from the Research on Arctic Tundra Environment (RATE) program, *Arct. Alp. Res.*, *12*, 401-578, 1980.

Brown, J, P.C. Miller, L.L. Tieszen, and F.L. Bunnell, *An Arctic Ecosystem: The Coastal Tundra at Barrow, Alaska*, 571 pp., Dowden, Hutchinson, and Ross, Stroudsburg, PA, 1980.

Crawford, T.L., R.J. Dobosy, R.T. McMillen, C.A. Vogel, and B.B. Hicks, Air-surface exchange measurement in heterogeneous regions: Extending tower observations with spatial structure observed from small aircraft, *Global Change Biol.*, *2*, 275-285, 1996.

Desjardins, R.L., J.I. MacPherson, L. Mahrt, P. Schuepp, E. Pattey, H. Neumann, D. Baldocchi, S. Wofsy, D. Fitzjarrald, H. McCaughey, and D. W. Joiner, Scaling up flux measurements for the boreal forest using aircraft-tower combinations, *J. Geophys. Res.*, *102*, 29,125-29,133, 1997.

Everett, K.R., Distribution and variability of soils near Atkasook, Alaska, *Arc. Alp. Res.*, *12*, 433-446, 1980.

Komarkova, V., and P.J. Webber, Two low arctic vegetation maps near Atkasook, Alaska, *Arc. Alp. Res.*, *12*, 447-472, 1980.

Vourlitis, G.L., and W.C. Oechel, Landscape-scale CO_2, water vapor, and energy flux of moist-wet coastal tundra ecosystems over two growing seasons, *J. Ecol.*, *85*, 575-590, 1997.

Vourlitis G.L., and W.C. Oechel, Eddy covariance measurements of net CO_2 flux and energy balance of an Alaskan moist-tussock tundra ecosystem, *J. Ecol.*, *80*, 686-701, 1999.

Walker, D. A., E. Binnian, B.M. Evans, N.D. Lederer, E. Nordstrand, and P.J. Webber, Terrain, vegetation, and landscape evolution of the R4D research site, Brooks Range Foothills, Alaska, *Holarct. Ecol.*, *12*, 238-261, 1989.

Weller, G., F.S. Chapin III, K.R. Everett, J.E. Hobbie, D. Kane, W.C. Oechel, C.L. Ping, W.S. Reeburgh, D. Walker, and J. Walsh, The arctic flux study: A regional view of trace gas release, *J. Biogeogr.*, *22*, 365-374, 1995.

Preliminary Intercomparison Results from the NDSC Microwave Ozone Profiling Instrument at Mauna Loa Observatory

ALAN PARRISH
University of Massachusetts, Amherst, Massachusetts 01003

I. S. BOYD AND B. J. CONNOR
National Institute for Water and Atmospheric Research, Lauder, New Zealand

I. S. MCDERMID
Jet Propulsion Laboratory, Table Mountain Facility, Wrightwood, California 92397

S. OLTMANS
NOAA Climate Monitoring and Diagnostics Laboratory, Boulder, Colorado 80303

J. J. TSOU
Science Applications International Corporation, Hampton, Virginia 23666

J. M. ZAWODNY
National Aeronautics and Space Administration, Langley Research Center, Hampton, Virginia 23681

Since July 1995, the University of Massachusetts has operated a microwave instrument that measures vertical profiles of stratospheric ozone at the Climate Monitoring and Diagnostics Laboratory (CMDL) Mauna Loa Observatory (MLO). Results of intercomparisons with four other ozone profiling experiments using data recorded during 1995-1998 are reported here.

The microwave instrument measures a spectral line produced by a rotational transition of ozone at 110.836 GHz. Profiles covering an altitude range of 56-0.1 hPa (about 20-66 km) are retrieved from the details of the pressure-broadened line shape. The vertical resolution of the measurements is 8-10 km from about 20 to 40 km. At higher altitudes it smoothly degrades to a maximum of 17 km at about 60 km. Details regarding the instrument are given in *Parrish et al.* [1992], *Connor et al.* [1995] and *Tsou et al.* [1995].

The microwave instrument participated in the Network for Detection of Stratospheric Change (NDSC) sponsored MLO3 intercomparison campaign [*McPeters et al.*, 1999] in July 1995. During that campaign the microwave instrument, two lidars, and Stratospheric Aerosol and Gas Experiment-II (SAGE-II) agreed within 5% from 22-43 km. Agreement at that level between microwave, SAGE-II, and one set of lidar measurements continued up to about 50 km. A further assessment, including a relative trend analysis, can now be made from intercomparisons using data obtained since the end of the MLO3 campaign through 1998.

Microwave data were recorded from July-September 1995, November 1995-March 1996, and from July 1996 on. Calibrated profiles were retrieved from these data through December 1998 and are considered preliminary because we are aware of two small, correctable defects in the data. First, the 1997 data were processed on a different implementation of the calibration and retrieval software. There is a slight difference between profiles produced by this algorithm and its predecessor in the 20-25 km region. Second, a small amount of 1995 and 1996 data may be affected by an occasional intermittent electronic fault that became apparent in 1997. Affected 1997 data were deleted from this dataset. While the microwave group intends to reprocess the data to eliminate the known defects, it is believed that the errors produced by these faults are small enough to make it worthwhile to proceed with the comparison described in the following text.

The previously described microwave data were compared with those produced by lidar, ozonesonde, SAGE-II [*Cunnold et al.*, 1989], and Halogen Oscillation Experiment (HALOE) [*Bruhl et al.*, 1996] instruments. The lidar was provided and operated by the Jet Propulsion Laboratory (JPL), California Institute of Technology [*McDermid et al.*, 1990], and sondes were launched nearby at Hilo by CMDL personnel [*Oltmans et al.*, 1998, and references therein]. Profiles in number density versus altitude format were converted to mixing ratio versus pressure assuming hydrostatic equilibrium with the NOAA National Center for Environment Prediction (NCEP) temperature profiles in the calculation. There are two points to note regarding the comparison datasets: The KI solution concentration in the sondes was increased from 1% to 2% in April 1998 for reasons discussed in *Oltmans et al.* [1998]. Data from earlier flights were adjusted to be consistent with those using the new solution. Problems with the lidar data that affect the profiles below 25 km have been found, and a revised dataset is being prepared. Therefore, the microwave-lidar comparison was cut off at 24 hPa (about 25 km.).

The average difference between the microwave profiles and those from the other instruments is mostly less than 5% (Figure 1). The spread of differences in the several comparisons is largest in the lower stratosphere (~40 hPa), from -8 to +12%. The difference would be slightly positive when averaged over the SAGE, HALOE, and ozonesonde comparisons, suggesting that the microwave measurements may be biased slightly high. However, the large spread makes this result inconclusive. In the middle stratosphere (~10 hPa), the microwave values are generally a few percent smaller than the others. For both the SAGE-II and HALOE comparisons, the average differences stay below 5-6% up to 0.6 hPa, and the variability in individual difference profiles remains small. Although microwave-lidar differences grow rapidly above a few hPa, similar increases are seen between sets of measurements made with two lidar instruments during intercomparison campaigns (e.g., *McPeters et al.* [1999]). The variability in the microwave-lidar difference

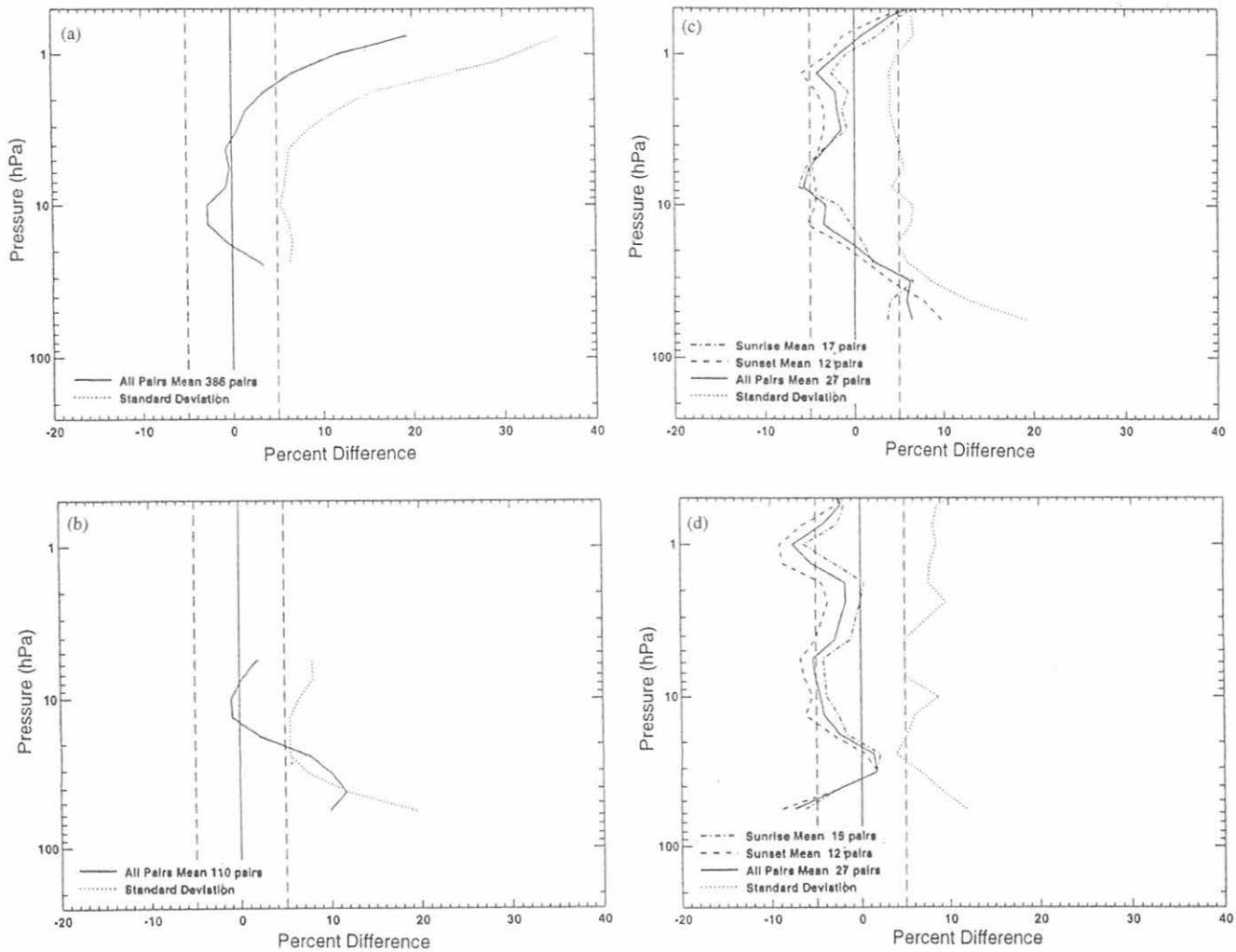

Fig. 1. Solid lines: Differences between ozone profiles recorded with the microwave instrument at Mauna Loa and those recorded with the co-located (a) JPL lidar, (b) NOAA ozonesondes, and during overpasses of the (c) HALOE (version 19) and (d) SAGE-II (version 5.96) instruments averaged from August 1995 through December 1998. Dotted lines: The root-mean-square of individual difference profiles. The percent difference is calculated by subtracting the specified instrument ozone amount from the microwave ozone amount, dividing by the sum of the ozone amount from the two instruments, and multiplying by 100.

profiles also increases rapidly above 4-5 hPa. These facts suggest that the increasing average difference between these lidar and microwave measurements with altitude above a few hPa is due to the decreasing intensities of the signals returned to the lidar. We have not extended comparisons to higher altitudes because of the difficulty in accounting for the effect of diurnal, photolysis-induced changes in ozone levels along the line of sight of the satellite-borne occultation type instruments.

Regression analyses were performed to calculate relative trends between our measurements and the others used in the preceding difference profile discussion; results are shown as functions of altitude (Figure 2). There are 110 sonde-microwave coincidences, 386 lidar-microwave coincidences, 29 HALOE coincidences, and 27 SAGE coincidences. There are statistically significant altitude-dependent relative trends of 1-2% per year between the microwave and lidar measurements around 5 hPa. The relative trends in the other comparisons are more uncertain. Because they generally have the same sign and similar magnitude in this region, there may have been some form of systematic change in the microwave measurements during the 1995-1998 period. Because the present microwave dataset is known to have small defects that occur irregularly, it seems more likely that any systematic effect in the microwave data is quasi-random in nature than a steady drift. If so, the magnitude of the relative trends would decrease with increasing record length, even in the absence of an upgraded microwave data set.

A preliminary set of microwave ozone profiles (covering about 20-66 km) measured at MLO during 1995 through 1998 was compared with ozonesonde, lidar, SAGE-II, and HALOE profiles measured nearby. The average differences depend most strongly on the instrument being compared in the lower stratosphere. Above 30 hPa (about 24 km), the differences are generally less than 5% at altitudes where the comparison instruments are expected to work well. Relative trends of 1-2%

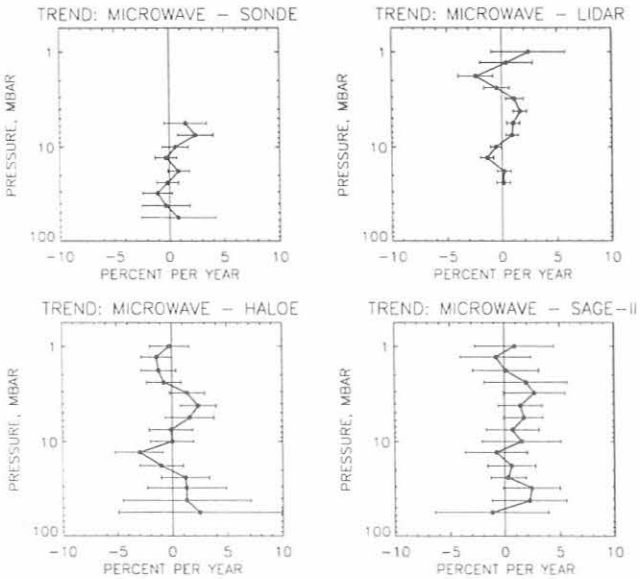

Fig. 2. Relative trends versus pressure calculated by linear regression from microwave profiles at Mauna Loa, those recorded by co-located JPL lidar, and NOAA sondes, and during overpasses of the SAGE-II and HALOE instruments. Error bars correspond to the 95% confidence interval. Trends are calculated from August 1995 through December 1998.

per year were found between time series of lidar and microwave measurements. The other three trend comparisons are less certain, but suggest that the lidar-microwave trends may be caused by flaws in the present microwave data. These trends are expected to integrate down as the record length increases. The relative trend also may be reduced when the microwave data are reviewed and uniformly reprocessed.

Acknowledgments. The microwave, lidar, SAGE-II, and HALOE experiments are supported by NASA, and the ozonesondes are supported by NOAA.

REFERENCES

Bruhl, C., S.R. Drayson, J.M. Russell, P.J. Crutzen, J.M. McInerney, P.N. Purcell, H. Claude, H. Gernandt, T.J. McGee, and I.S. McDermid, HALOE Ozone Channel Validation, *J. Geophys. Res., 101*, 10,217-10,240, 1996.

Connor, B.J., A. Parrish, J.J. Tsou, and M.P. McCormick, Error analysis for the ground-based microwave ozone measurements during STOIC, *J. Geophys. Res., 100*, 9283-9291, 1995.

Cunnold, D.M., W.P. Chu, R.A. Barnes, M.P. McCormick, and R.E. Veiga, Validation of SAGE-II ozone measurements, *J. Geophys. Res., 94*, 8447-8460, 1989.

McDermid, I.S., S.M. Godin, and L.O. Lindquist, Ground-based laser DIAL system for long-term measurements of stratospheric ozone, *App. Opt., 29*, 3603-3612, 1990.

McPeters, R.D., D.J. Hofmann, M. Clark, L. Froidevaux, M. Gross, B. Johnson, G. Koenig, I.S. McDermid, F. Murcray, S. Oltmans, A. Parrish, U. Singh, J.J. Tsou, and J. Zawodny, Results from the 1995 stratospheric ozone profile intercomparison at Mauna Loa, *J. Geophys. Res., 104*, 30,505-30,514, 1999.

Oltmans, S., M. Clark, R. Evans, E. Hackathorn, J. Harris, B. Johnson, G. Koenig, M. O'Neill, D. Quincy, and H. Vömel, Ozone and Water Vapor, in *Climate Monitoring and Diagnostics Laboratory Summary Report No. 24*, D.J. Hofmann et al. (Eds.), NOAA Environ. Res. Labs., Boulder, CO, pp. 76-90, 1998.

Parrish, A., B.J. Connor, J.J. Tsou, I.S. McDermid, and W.P. Chu, Ground-based microwave monitoring of stratospheric ozone, *J. Geophys. Res., 97*, 2541-2546, 1992.

Tsou, J.J., B.J. Connor, A. Parrish, I.S. McDermid, and W.P. Chu, Ground based microwave monitoring of middle atmosphere ozone: Comparison to lidar and Stratospheric Aerosol and Gas Experiment II satellite observations, *J. Geophys. Res., 100*, 3005-3016, 1995.

Advanced Global Atmospheric Gases Experiment (AGAGE)

R.G. PRINN
Massachusetts Institute of Technology, Cambridge, Massachusetts 02139

R.F. WEISS
Scripps Institution of Oceanography, University of California, San Diego, La Jolla, California 92093

D.M. CUNNOLD
Georgia Institute of Technology, Atlanta, Georgia 30332

P.J. FRASER
CSIRO, Division of Atmospheric Research, Victoria, Australia 3195

P.G. SIMMONDS
University of Bristol, School of Chemistry, Bristol, United Kingdom BS8 1TS

INTRODUCTION

In this global network program continuous high-frequency gas chromatographic measurements of biogenic and anthropogenic gases are carried out at globally distributed sites in order to quantitatively determine the source and sink strengths and circulation of a large number of chemically and radiatively important long-lived gases. The program that started in 1978 is conveniently divided into three parts associated with three changes in instrumentation: the Atmospheric Lifetime Experiment (ALE), the Global Atmospheric Gases Experiment (GAGE) and the Advanced Global Atmospheric Gases Experiment (AGAGE).

AGAGE began during the 1993-1996 time period. AGAGE, which continues to the present, has two instrumental components. First, a highly improved gas chromatographic system measures five biogenic/anthropogenic gases (CH_4, N_2O, $CHCl_3$, CO, and H_2) and five anthropogenic gases (CCl_3F, CCl_2F_2, CH_3CCl_3, CCl_2FCClF_2, and CCl_4) [*Prinn et al.*, 1995; *Fraser et al.*, 1996; *Cunnold et al.*, 1997; *Simmonds et al.*, 1998a]. Each species is measured 36 times per day using an electron capture detector (ECD), flame ionization detector (FID), or mercuric oxide reduction detector (MRD); the latter detector is for CO and H_2 and is currently present at only two of the stations, Mace Head, Ireland, and Cape Grim, Tasmania.

Second, a new gas chromatographic-mass spectrometric system (GC-MS) began measuring a wide range of hydrochlorofluorocarbons and hydrofluorocarbons (CH_2FCF_3 (HFC-134a), CH_3CCl_2F (HCFC-141b), CH_3CClF_2 (HCFC-142b), etc.) [*Simmonds et al.*, 1998b] that are now serving as interim or permanent alternatives to the chlorofluorocarbons and other long-lived halocarbons regulated by the Montreal Protocol [*UNEP*, 1996]. Also measured by the GC-MS system are the methyl halides (CH_3Cl, CH_3Br, CH_3I) and the halons ($CBrF_3$, $CBrClF_2$). AGAGE also included development and use of new, much more accurate absolute calibrations for most of the measured gases.

The ALE, GAGE, and AGAGE stations have been located in five globally distributed localities: (a) Ireland: first at Adrigole, 52°N, 10°W (1978-1983), then at Mace Head, 53°N, 10°W (1987-present); (b) USA West Coast: first at Cape Meares, Oregon, 45°N, 124°W (1979-1989), then at Trinidad Head, California, 41°N, 124°W (1995-present); (c) Ragged Point, Barbados, 13°N, 59°W (1978-present); (d) Cape Matatula, American Samoa, 14°S, 171°W (1978-present); (e) Cape Grim, Tasmania, 41°S, 145°E (1978-present).

The AGAGE operation at Samoa has significant added value because it enables a direct intercomparison with the similar real-time measurements (and also with the flask measurements) by CMDL. This intercomparison has already aided us in determining the net effect of calibration and instrumental differences on the measurements by each group, so that the data from both the AGAGE and CMDL networks can be utilized in combination by theoreticians to investigate chemical and meteorological phenomena.

RECENT PROGRESS

Accomplishments over the entire period from 1978 through the present have recently been published [*Prinn et al.*, 2000]. In the publication, the instrumentation and calibrations used in the ALE, GAGE and AGAGE experiments and a history of the majority of the anthropogenic ozone-depleting and climate-forcing gases in air, based on these experiments, is described in detail. Beginning in 1978 these three successive automated high frequency in situ experiments have documented the long-term behavior of the measured concentrations of these gases over the past 20 years and show both the evolution of latitudinal gradients and the high frequency variability from sources and circulation. These experiments enable estimation of the long-term trends in total chlorine contained in long-lived halocarbons involved in ozone depletion, and these measurements are summarized using inverse methods to determine trace gas lifetimes and emissions. Finally, a combined observational and modeled reconstruction of the evolution of chlorocarbons by latitude in the atmosphere over the past 60 years is provided that can be used as boundary conditions for interpreting trapped air in glaciers and oceanic measurements of chlorocarbon tracers of the deep oceanic circulation.

The ALE/GAGE/AGAGE data are available through the U.S. Department of Energy (DOE) CDIAC World Data Center (e-mail to: cpd@ornl.gov, Dataset No. DB-1001). Some specific conclusions from the data are [*Prinn et al.*, 2000]:

(1) For ozone-depleting gases, ALE/GAGE/AGAGE and other measurements show: (a) Major changes in the rates of accumulation of many ozone-depleting gases occurred in the

1990s. Mole fractions of CH_3CCl_3, CCl_4, and CCl_3F have been decreasing for several years; mole fractions of CCl_2FCClF_2 reached approximately constant levels and are now beginning to decrease very slowly; the rate of accumulation of CCl_2F_2 has slowed significantly. However, mole fractions of N_2O continue to steadily increase. The latitudinal gradients of CCl_3F, CCl_2F_2, CCl_2FCClF_2, CH_3CCl_3 and to a lesser extent, CCl_4, are essentially zero, or are rapidly approaching zero, consistent with rapid decreases in their largely northern hemispheric emissions [see also *Fraser et al.,* 1996; *Simmonds et al.*, 1998a; *Prinn et al.*, 1995]. (b) International compliance with the Montreal Protocol is so far resulting in chlorofluorocarbon and chlorocarbon mole fractions equal to or lower than target levels. (c) Levels of total chlorine contained in 10 dominant halocarbons in the global lower troposphere have apparently reached maximum values of about 3.6 ppb and are beginning to decrease slowly (to about 3.5 ppb in 1997). This decrease is driven largely by declines in CH_3CCl_3 and to a lesser extent, CCl_4 [see also *Cunnold et al.*, 1997; *Prinn et al.*, 1999; *Kurylo et al.*, 1999].

(2) Optimal estimations using global ALE/GAGE/AGAGE measurements and atmospheric chemical models show: (a) The chlorofluorocarbons have atmospheric lifetimes consistent with destruction in the stratosphere being their principal removal mechanism. (b) Estimation of the lifetime of CH_3CCl_3 continues to provide an accurate determination of the weighted-average global OH concentration, but the rapidly decreasing mole fractions of CH_3CCl_3 will ultimately limit its usefulness for this purpose. (c) Multi-annual variations in chlorofluorocarbon and chlorocarbon emissions are consistent approximately with variations estimated independently from industrial production and sales data where available (CCl_2FCClF_2 and CCl_2F_2 are exceptions).

(3) The mole fractions of the major hydrochlorofluorocarbons and hydrofluorocarbons that are replacing the regulated halocarbons are rising rapidly in the atmosphere (specifically in the 1994 to 1998 time period at rates of about 44% per year for CH_2FCF_3, 13% per year for CH_3CClF_2, and 28% per year for CH_3CCl_2F at Mace Head, Ireland). With the exception of $CHClF_2$, which was in use well before the latter three species, they are not yet at levels to significantly contribute to atmospheric chlorine loading [see also *Miller et al.*, 1998; *Simmonds et al.*, 1998b]. In the future, these replacement species could provide independent estimates of the global-weighted average OH concentration provided their industrial emissions are more accurately documented.

(4) The current rapidly changing magnitudes and geographical locations of emissions of chlorocarbons and chlorofluorocarbons may mandate a more dense measurement network than provided presently by AGAGE alone in order to obtain accurate solutions to inverse problems involving regional emissions and lifetime estimation; at a minimum, the data from all existing networks (ALE/GAGE/AGAGE, CMDL, etc.) should be carefully intercalibrated, so they can be utilized to better compute global and regional average concentrations.

(5) In the future, analysis of pollution events measured using high frequency in situ measurements of chlorofluorocarbons and their replacements may enable emission estimates at the regional level that are sufficiently accurate to be used for identifying regional noncompliance with the Montreal Protocol [see also *Derwent et al.*, 1998a, b].

Acknowledgments. In its initial years the global network (ALE) was supported by grants from the Chemical Manufacturers Association and later also by the Upper Atmospheric Research Program of the National Aeronautics and Space Administration (NASA). GAGE was subsequently supported by multiple grants from NASA. In its latest phase (AGAGE), support came (and comes) primarily from NASA (grants NAGW-732, NAG1-1805, NAG5-3974 to MIT; grants NAGW-2034, NAG5-4023 to SIO), with important contributions also from the United Kingdom Department of Environment (now Department of Environment, Transport and the Regions) (contracts PECD 7/10/154 and EPG 1/1/37 and 1/1/82 to Inscon), Commonwealth Scientific and Industrial Research Organization (Australia), Bureau of Meteorology (Australia), and the Alternative Fluorocarbons Environmental Acceptability Study (AFEAS). Support for the Barbados Station during GAGE/AGAGE has been shared approximately equally between NASA and the National Oceanic and Atmospheric Administration (NOAA). We also thank NOAA for their infrastructure support at the Samoa Station by Cooperative Agreement. The suite of six CH_4-in-air standards used for AGAGE was purchased by CSIRO Atmospheric Research from Nippon Sanso with funds secured from the Multi Function Polis (Australia) Agency.

REFERENCES

Cunnold, D.M., R.F. Weiss, R.G. Prinn, D.E. Hartley, P.G. Simmonds, P.J. Fraser, B.R. Miller, F.N. Alyea, and L. Porter, GAGE/AGAGE measurements indicating reductions in global emissions of CCl_3F and CCl_2F_2 in 1992-1994, *J. Geophys. Res.*, *102*, 1259-1269, 1997.

Derwent, R.G., P.G. Simmonds, S. Seuring, and C. Dimmer, Observation and interpretation of the seasonal cycles in the surface concentrations of ozone and carbon monoxide at Mace Head, Ireland from 1990 to 1994, *Atmos. Environ.*, *32(2)*, 145-157, 1998a.

Derwent, R.G., P.G. Simmonds, S. O'Doherty, and D.B. Ryall, The impact of the Montreal Protocol on halocarbon concentrations in northern hemisphere baseline and European air masses at Mace Head, Ireland, from 1987-1996, *Atmos. Environ*, *32(21)*, 3689-3702, 1998b.

Fraser, P.J., D.M. Cunnold, F.N. Alyea, R.F. Weiss, R.G. Prinn, P.G. Simmonds, B.R. Miller, and R.L. Langenfelds, Lifetime and emission estimates of 1,1,2-trichlorotrifluoroethane (CFC-113) from daily global background observations, June 1982 to June 1994, *J. Geophys. Res.*, *101*, 12,585-12,599, 1996.

Kurylo, M.J., et al., Short-Lived Ozone-Related Compounds, Chapter 2, in *Scientific Assessment of Ozone Depletion: 1998*, World Meteorological Organization (WMO) Global Ozone Research and Monitoring Project, Geneva, Report 44, pp. 2.1-2.56, 1999.

Miller, B.R., J. Huang, R.F. Weiss, R.G. Prinn, and P.J. Fraser, Atmospheric trend and lifetime of chlorodifluoromethane (HCFC-22) and the global tropospheric OH concentration, *J. Geophys. Res.*, *103*, 13,237-13,248, 1998.

Prinn, R.G., R.F. Weiss, B.R. Miller, J. Huang, F.N. Alyea, D.M. Cunnold, P.J. Fraser, D.E. Hartley, and P.G. Simmonds, Atmospheric trends and lifetime of CH_3CCl_3 and global OH concentrations, *Science*, *269*, 187-192, 1995.

Prinn, R.G., et al., Long-Lived Ozone-Related Compounds, Chapter 1, in *Scientific Assessment of Ozone Depletion: 1998*, World Meteorological Organization Global Ozone Research and Monitoring Project, Geneva, Report 44, WMO, pp. 1.1-1.54, 1999.

Prinn, R.G., R.F. Weiss, P.J. Fraser, P.G. Simmonds, D.M. Cunnold, F.N. Alyea, S. O'Doherty, P. Salameh, B.R. Miller, J. Huang, R.H.J. Wang, D.E. Hartley, C. Harth, L.P. Steele, G. Sturrock, P.M. Midgley, and A. McCulloch, A history of chemically and radiatively important gases in air deduced from ALE/GAGE/AGAGE, *J. Geophys. Res.*, *105(D14)*, 17,751-17,792, 2000.

Simmonds, P.G., D.M. Cunnold, R.F. Weiss, R.G. Prinn, P.J. Fraser, A. McCulloch, F.N. Alyea, and S. O'Doherty, Global trends and emission estimates of CCl_4 from in situ background observations from July 1978 to June 1996, *J. Geophys. Res.*, *103*, 16,017-16,027, 1998a.

Simmonds, P.G., S. O'Doherty, J. Huang, R.G. Prinn, R.G. Derwent, D. Ryall, G. Nickless, and D.M. Cunnold, Calculated trends and the atmospheric abundance of 1,1,1,2-tetrafluoroethane, 1,1-dichloro-1-fluoroethane, and 1-chloro-1,1-difluoroethane using automated in-situ gas chromatography-mass spectrometry measurements recorded at Mace Head, Ireland from October 1994 to March 1997, *J. Geophys. Res., 103*, 16,029-16,038, 1998b.

United Nations Environmental Programme (UNEP), *Handbook for the International Treaties for the Protection of the Ozone Layer*, 4th ed., Nairobi, Kenya, 1996.

Winter Sampling of Shallow Firn Air at the South Pole to Understand Processes Affecting Firn Atmospheric Histories and Ice Core Gas Records

JEFFREY P. SEVERINGHAUS
Scripps Institution of Oceanography, University of California, San Diego, La Jolla, CA 92093-0244

In January and July 1998 a cooperative project was carried out at the South Pole CMDL Clean Air Laboratory to sample air from the top 15 m of the snow (firn). The goal was to better understand gas fractionation processes that may affect the atmospheric gas histories obtained from the air in the deep firn column. Previous studies in summer have shown a marked isotopic anomaly in the top 10 m of the firn, driven by thermal fractionation in response to the strong temperature gradient in the top few meters. No samples had been taken in winter, however, so Scripps Institution of Oceanography (SIO) was curious to know (1) if the opposite sign of the temperature gradient produced an opposite isotope anomaly, as expected, (2) if the air in the firn convects spontaneously during winter in response to colder air overlying warmer air, which could bias the ice core record of gas isotopes, and (3) if adsorption and desorption on snow grains could explain anomalies in some halogenated species. For comparison a summer sampling was done first. Both data sets show the expected isotope fractionation because of temperature gradients. The winter data reveal a robust isotope anomaly of opposite sign, as expected, that exceeds a diffusion-only model prediction driven by Automatic Weather Station surface temperature data. No evidence for vigorous gas mixing because of convection was found, although the misfit of the data to the model may suggest slow downward motion or a sampling artifact. It appears unlikely that rectification of seasonality biases the deep firn or ice core record at this site, although this study is just a "snapshot" and may have missed episodic events. No evidence for adsorption or desorption was found.

INTRODUCTION

The porous and permeable layer of snow on top of polar ice sheets is typically 50-100 m thick and is known as the firn layer. At the base of this layer the firn is continuously transformed into impermeable ice. The air in firn mixes slowly with the atmosphere, primarily by molecular diffusion [*Schwander et al.*, 1988]. Consequently, the mean age of the air (defined as the time elapsed since the air crossed the surface) increases downward in the firn and reaches several decades at sites with thick firn [*Schwander et al.*, 1993].

A number of recent studies have exploited this fact to reconstruct atmospheric concentration histories of various gases, such as halocarbons [*Butler et al.*, 1999], O_2/N_2 ratios and N_2O [*Battle et al.*, 1996], and ^{13}C of CO_2 [*Francey et al.*, 1999]. Other recent studies have taken advantage of the fact that temperature gradients in the firn arising from rapid climate variation leave an isotope record of abrupt climate change in trapped air in ice cores [*Severinghaus et al.*, 1998; *Leuenberger et al.*, 1999; *Severinghaus and Brook*, 1999; *Lang et al.*, 1999]. At many polar sites, surface temperature varies by >30°C seasonally. This creates strong temperature gradients in the top few meters of the firn due to the fact that the firn at ~10 m depth closely maintains the mean annual temperature at all times [*Paterson*, 1969]. Theory predicts that these gradients will lead to a characteristic pattern of thermally fractionated gases in the upper ~15 m of the firn column. A model of heat and gas diffusion in the firn enables a precise numerical prediction of the magnitude and shape of this pattern, when forced with the known surface temperature history. The model has no adjustable parameters and thus serves as a stringent test of our understanding of the physical processes governing gas-isotope ratios in shallow firn:

$$\frac{\partial C}{\partial t} = \frac{\partial}{\partial z}\left(D(z,T)\left[\frac{\partial C}{\partial z} - \underbrace{\frac{\Delta m g}{RT}}_{\text{gravitational settling}} + \underbrace{\Omega \frac{dT}{dz}}_{\text{thermal diffusion}}\right]\right) \quad (1)$$

where

- C isotope delta value (e.g., $\delta^{15}N$)
- t time
- z depth
- D effective molecular diffusivity of gas in porous snow
- T temperature, K
- Δm mass difference between isotopes
- g gravitational acceleration
- R gas constant
- Ω thermal diffusion sensitivity, ‰ K^{-1}

A separate model of heat delivers temperatures to the gas model [*Alley and Koci*, 1990]. Comparison of the modeled temperature profiles with several measurements (taken from thermisters buried in the borehole) shows good agreement (Figure 1a).

SAMPLING AND ANALYSIS

Because of the difficulty of handling samples outdoors in winter, gas sampling was arranged to be done from indoors. Using a hand coring tool, on January 18, 1998, a 15-m deep borehole located 42 m due grid E of the NE corner of the Clean Air Building was drilled. Tubes with stainless steel intake screens on the ends were placed in the hole at desired depths, and

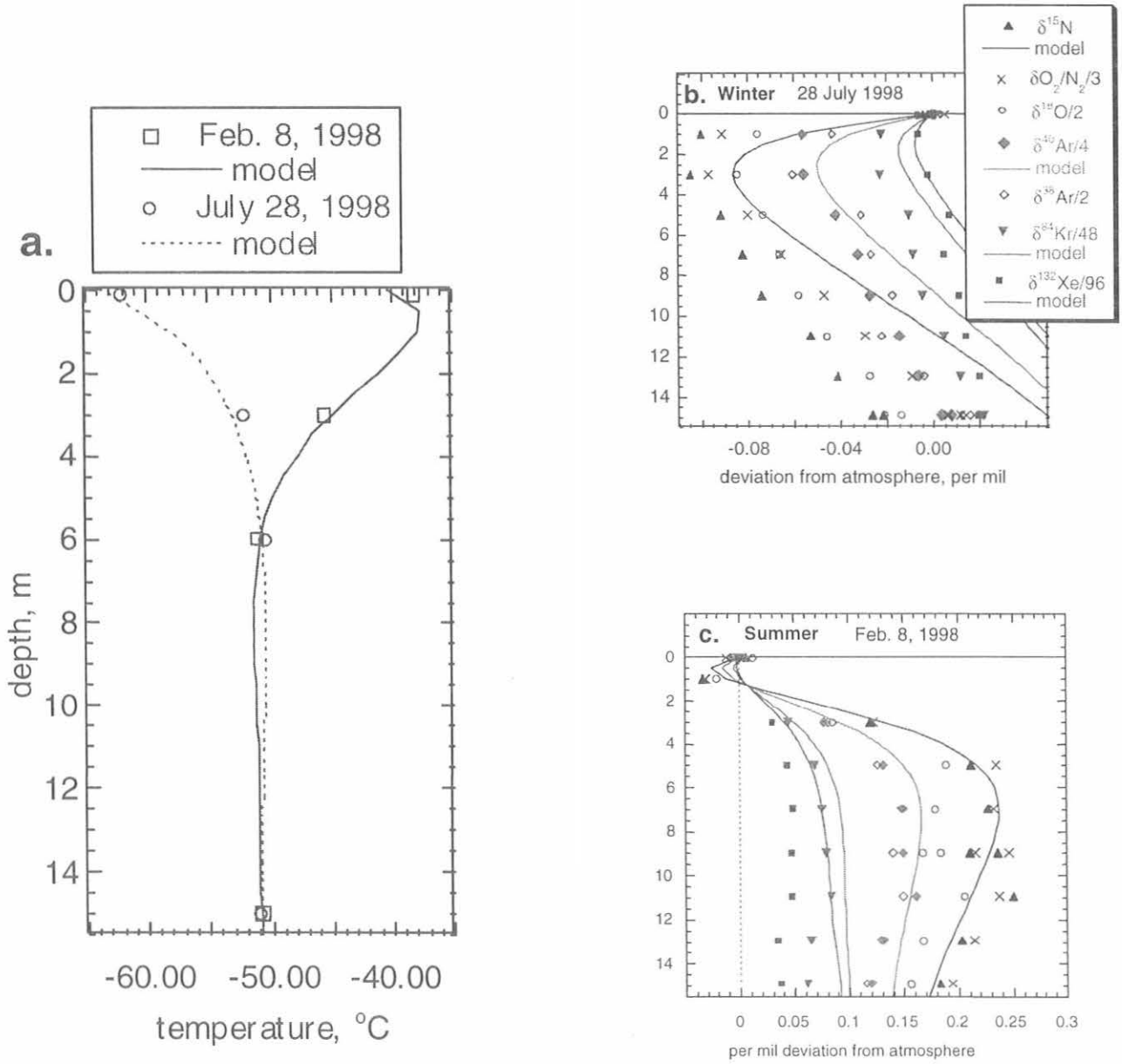

Fig. 1. Depth profiles of measured temperature (a) and gas composition in the shallow firn at the south pole. Winter sampling (b) reveals a large negative isotope excursion due to thermal isotope fractionation caused by the cold temperatures at the surface relative to the temperature at 10 m depth. Summer sampling (c) reveals the opposite pattern, as expected. Model calculations (shown as lines) are based on the measured surface temperature history for this site and the known diffusivities of these gases. Gravitational settling causes a steady linear downward increase that is independent of season and that is additive to the thermal fractionation signal. The strong winter anomaly, even stronger than predicted from the model, argues against any vigorous convective mixing that would have erased the signal by homogenizing it with the atmosphere.

the tubes were extended into the building for samples to be taken indoors. The hole was backfilled with snow and layers of slush to impede downward movement of surface air. After backfilling, the tubes were pumped on to remove as much contamination as possible. Sampling by pumping on the tubes was done on February 8 and again on July 28. This technique is similar to that used to sample air in sand dunes [*Severinghaus et al.*, 1997]. Samples were pumped at 4 L min^{-1} for 16 minutes to flush the lines and the sample flasks. The air was dried by passing it through a column packed with granular phosphorous pentoxide. The air was stored in 2-L flow-through glass flasks as described by *Battle et al.* [1996]. Flasks were analyzed mass

spectrometrically at the University of Rhode Island and SIO for $^{15}N/^{14}N$ and $^{40}Ar/^{36}Ar$ ratios and other gas ratios including $^{40}Ar/^{38}Ar$, $^{18}O/^{16}O$ of O_2, O_2/N_2, $^{84}Kr/^{36}Ar$, and $^{132}Xe/^{36}Ar$. Results of two aliquots, measured for $\delta^{15}N$, $\delta^{18}O$, and $\delta O_2/N_2$ from 3 m depth at south pole February 8, were rejected on the basis of high CO_2 concentrations (22 and 31% above normal) that suggested gross contamination with laboratory air.

Results

Gravitational settling enriches the heavier molecules at the bottom of a stagnant air column in proportion to the mass difference Δm, so gravity should affect $\delta^{40}Ar$ four times as much as $\delta^{15}N$ [*Lindemann and Aston*, 1919; *Craig et al.*, 1988; *Sowers et al.*, 1989; *Schwander*, 1989]. In other words, if gravity were the only process acting on a gas mixture, $\delta^{15}N$ would be equal to $\delta^{40}Ar/4$. To facilitate comparison all results are presented here with the δ value divided by Δm.

SIO wanted to know what the shallow firn gas profile did in winter when the temperature gradient was reversed from the more commonly studied summer profile. In winter cold dense air overlies warmer air in the firn and might become unstable and undergo Bernard convection [*Powers et al.*, 1985]. If the wintertime thermal diffusion anomaly were not expressed because of convection, the mean annual thermal fractionation signal would be nonzero even when annual mean temperature change was zero. In other words, there would be a rectifier of seasonal temperature change, and this signal would be transmitted to the deep firn and create a bias in the bubble air-based thermal diffusion paleoindicator.

The tendency to undergo Bernard convection in a porous media can be estimated from the dimensionless Rayleigh number [*Powers et al.*, 1985]. Taking the coefficient of thermal expansion of air as 0.0045 K^{-1}, the depth of the layer with strong temperature gradient as 5 m, the temperature difference across this layer as 10 K, the permeability of the firn as 4×10^{-9} m^2, the dynamic viscosity of air as 1.4×10^{-5} kg m^{-1} s^{-1}, and the thermal diffusivity as 0.22 m^2 s^{-1}, a Rayleigh number of 4 is obtained. This is sufficiently close to the critical value for the onset of convection (10-30) that natural convection in snow cannot be ruled out by this calculation. Further, this assumes a one-dimensional firn without irregularities (snow dunes or sastrugi) that might get convection started much more easily. If vigorous convective stirring during winter were important, one would expect to see a greatly attenuated thermal fractionation signal. In fact a fully developed negative isotope anomaly, with an amplitude slightly larger than that predicted by a pure diffusion model driven by observed surface air temperature (Figure 1b) was observed. The summer data are shown for comparison (Figure 1c).

The marked deviation of the winter data from the deeper part of the model is not understood. It seems possible that gradual downward flow is advecting the values obtained at shallower depths to deeper levels, as hypothesized at Siple Dome (J. Severinghaus, Thermal fractionation of air in polar firn by seasonal temperature gradients, in preparation, 2000). Alternatively, intermittent turbulent convective mixing may be weak enough that it does not homogenize and erase the isotope fractionation, yet strong enough that it acts to transport the isotope signal downward into the firn faster than would molecular diffusion alone. In other words, mixing by eddy diffusion would double or triple the effective diffusivity over the molecular diffusivity. Adding an arbitrary intermittent eddy diffusion term to our model produces this effect, demonstrating plausibility but not proof.

Conclusions

Seasonal effects penetrate no deeper than 40 m in the firn at current measurement precision. Therefore, the firn-ice transition at 114 m is effectively isolated from seasonality and records a time-averaged value of the fluctuations in the shallow firn. Trapped air in ice is, therefore, susceptible to rectification in principle. The gas isotope profile observed in the shallow firn during winter is nearly symmetrical to that observed during summer, suggesting that they should cancel in the annual mean. However, this conclusion assumes that the sampling dates were representative of average conditions and did not miss strong episodes of convection by chance. Deep firn isotopes do fit a pure gravitational model well, though, indicating that seasonal anomalies probably do cancel [*Battle et al.*, 1996]. No sign of thermally driven adsorption or desorption was seen. These conclusions should be regarded as valid for one site at one time, and generalized to other sites with caution.

Acknowledgments. I thank Ralph Keeling, Mark Battle, and Michael Bender for discussions; James Butler for inviting me to do a wintertime sampling at the south pole using CMDL resources; Lt. Nathan Hill of CMDL for taking the samples; Julie Palais of NSF-OPP for making the south pole travel possible; Michael Bender for hosting J.P.S. in his laboratory at the University of Rhode Island; Alexi Grachev for making thermal diffusion sensitivity measurements; and Charles R. Stearns at the University of Wisconsin-Madison for surface temperature data from the Automatic Weather Station Project funded by the National Science Foundation (NSF). Support came from NSF grant OPP 9725305.

References

Alley, R.B., and B.R. Koci, Recent warming in central Greenland?, *Ann. Glaciol., 14*, 6-8, 1990.

Battle, M., et al., Atmospheric gas concentrations over the past century measured in air from firn at the South Pole, *Nature, 383*, 231-235, 1996.

Butler, J.H., M. Battle, M.L. Bender, S.A. Montzka, A.D. Clarke, E.S. Saltzman, C.M. Sucher, J.P. Severinghaus, and J.W. Elkins, A record of atmospheric halocarbons during the twentieth century from polar firn air, *Nature, 399*, 749-755, 1999.

Craig, H., Y. Horibe, and T. Sowers, Gravitational separation of gases and isotopes in polar ice caps, *Science, 242*, 1675-1678, 1988.

Francey, R.J., M.R. Manning, C.E. Allison, S.A. Coram, D.M. Etheridge, R.L. Langenfelds, D.C. Lowe, and L.P. Steele, A history of delta C-13 in atmospheric CH_4 from the Cape Grim air archive and antarctic firn air, *J. Geophys. Res., 104*, 23,631-23,643, 1999.

Lang, C., M. Leuenberger, J. Schwander, and S. Johnsen, 16°C Rapid temperature variation in central Greenland 70,000 years ago, *Science, 286*, 934-937, 1999.

Leuenberger, M., J. Schwander, and C. Lang, Delta (15)N measurements as a calibration tool for the paleothermometer and gas-ice age differences: A case study for the 8200 BP event on GRIP ice, *J. Geophys. Res., 104*, 22,163-22,170, 1999.

Lindemann, F.A., and F.W. Aston, The possibility of separating isotopes, *Phil. Mag. Ser. 6, 37*, 523-534, 1919.

Paterson, W.S.B., *The Physics of Glaciers*, 250 pp., Pergamon, 1969.

Powers, D., K. O'Neill, and S.C. Colbec, Theory of natural convection in snow, *J. Geophys. Res., 90*, 10,641-10,649, 1985.

Schwander, J., The transformation of snow to ice and the occlusion of gases, in *The Environmental Record in Glaciers and Ice Sheets*, edited by H. Oeschger and C.C. Langway, Jr., pp. 53-67, John Wiley, New York, 1989.

Schwander, J., B. Stauffer, and A. Sigg, Air mixing in firn and the age of the air at pore close-off, *Ann. Glaciol., 10*, 141-145, 1988.

Schwander, J., J.-M. Barnola, C. Andrie, M. Leuenberger, A. Ludin, D. Raynaud, and B. Stauffer, The age of the air in the firn and the ice at Summit, Greenland, *J. Geophys. Res., 98*, 2831-2838, 1993.

Severinghaus, J.P., and E.J. Brook, Abrupt climate change at the end of the last glacial period inferred from trapped air in polar ice, *Science, 286*, 930-934, 1999.

Severinghaus, J.P., R.F. Keeling, B.R. Miller, R.F. Weiss, B. Deck, and W.S. Broecker, Feasibility of using sand dunes as archives of old air, *J. Geophys. Res., 102*, 16,783-16,792, 1997.

Severinghaus, J.P., T. Sowers, E.J. Brook, R.B. Alley, and M.L. Bender, Timing of abrupt climate change at the end of the Younger Dryas period from thermally fractionated gases in polar ice, *Nature, 391*, 141-146, 1998.

Sowers, T., M.L. Bender, and D. Raynaud, Elemental and isotopic composition of occluded O_2 and N_2 in polar ice, *J. Geophys. Res., 94*, 5137-5150, 1989.

Barrow Magnetic Observatory

JACK TOWNSHEND
College International Geophysical Observatory, Fairbanks, Alaska 99775-6920

The Barrow Magnetic Observatory (BMO) is the northernmost of the U.S. Geological Survey (USGS) 14 continuously recording, digital magnetic observatories. As such, it serves as a singularly important site in a global network of observing stations whose combined data help describe the Earth's magnetic field and track its secular change. Ground stations such as the Barrow Observatory serve as controls for field modeling, as reference stations for airborne and satellite surveys, and as absolute calibration locations for field surveys. Data from Barrow are forwarded electronically to the USGS Central Region Geologic Hazards Team, Geomagnetism Group in Golden, Colorado. From there the data are distributed worldwide and sent to the international INTERMAGNET organization. Final processed data from Barrow and the other 13 USGS observatories are sent to the NOAA World Data Center A for archiving.

The primary instrumentation operated are: triaxial fluxgate magnetometer, proton precision magnetometer, Observatory Magnetometer Data Collection Platform (DCP), and instruments for absolute control observations. Data output consists of 1-min values of three vector components of the Earth's magnetic field, as well as the total field.

In August 1993, the USGS and NOAA negotiated a Memorandum of Agreement (MOA) to have CMDL personnel at Barrow service the USGS BMO equipment, make instrument observations, and provide some logistic support. The weekly absolute measurements and equipment service made by NOAA personnel are essential for maintaining high standards for the observatory operation and data quality. At the time of writing this report, USGS and NOAA are renegotiating and updating the MOA.

The Barrow Magnetic Observatory receives its authorization to operate from the USGS Central Region Geologic Hazards Team.

Principal investigators for the Barrow Observatory are located at the USGS College Observatory at the UAF in Fairbanks, Alaska, and the USGS Central Region Geologic Hazards Team, Geomagnetism Group.

7. Publications by CMDL Staff, 1998-1999

Anderson, T.L., and J.A. Ogren, Determining aerosol radiative properties using the TSI 3563 integrating nephelometer, *Aerosol Sci. Technol., 29*, 57-69, 1998.

Anderson, T.L., D.S. Covert, J.D. Wheeler, J.M. Harris, K.D. Perry, B.E. Trost, D.J. Jaffe, and J.A. Ogren, Aerosol backscatter fraction and single-scattering albedo: Measured values and uncertainties at a coastal station in the Pacific Northwest, *J. Geophys. Res., 104*, 26,793-26,807, 1999.

Angevine, W.M., P.S. Bakwin, and K.J. Davis, Wind profiler and RASS measurements compared with measurements from a 450-m-tall tower, *J. Atmos. Oceanic Technol., 15*, 818-825, 1998.

Bacmeister, J.T., V. Kuell, D. Offermann, M. Riese, and J.W. Elkins, Intercomparison of satellite and aircraft observations of ozone, CFC-11, and NO_y using trajectory mapping, *J. Geophys. Res., 104(D13)*, 16,379-16,390, 1999.

Bakwin, P.S., Carbon Cycle, in *The Encyclopedia of Geochemistry*, C.P. Marshall and R.W. Fairbridge (eds.), pp. 65-67, Kluwer Academic, Boston, MA, 1999.

Bakwin, P.S., P.P. Tans, D.F. Hurst, and C. Zhao, Measurements of carbon dioxide on very tall towers: results of the NOAA/CMDL program, *Tellus, 50B*, 401-415, 1998.

Bakwin, P.S., P.P. Tans, J.W.C. White, and R.J. Andres, Determination of the isotopic ($^{13}C/^{12}C$) discrimination by terrestrial biology from a global network of observations, *Global Biogeochem. Cycles, 12(3)*, 555-562, 1998. (Corrigendum, *Global Biogeochem. Cycles, 13*, 255, 1999.)

Bell, G.D., M.S. Halpert, C.F. Ropelewski, V.E. Kousky, A.V. Douglas, R.C. Schnell, and M.E. Gelman, Climate Assessment for 1998, *Bull. Am. Meteorol. Soc., 80(5)*, S1-S48, 1999.

Bergin, M.H., E.A. Meyerson, J.E. Dibb, and P.A. Mayewski, Relationship between continuous aerosol measurements and firn core chemistry over a 10-year period at the South Pole, *Geophys. Res. Lett., 25(8)*, 1189-1192, 1998.

Bodhaine, B.A., E.G. Dutton, R.L. McKenzie, and P.V. Johnston, Calibrating broadband UV instruments: Ozone and solar zenith angle dependence, *J. Atmos. Oceanic Technol., 15*, 916-926, 1998.

Bodhaine, B.A., N.B. Wood, E.G. Dutton, and J.R. Slusser, On Rayleigh optical depth calculations, *J. Atmos. Oceanic Technol., 16*, 1854-1861, 1999.

Borys, R.D., D.H. Lowenthal, M.A. Wetzel, F. Herrera, A. Gonzalez, and J. Harris, Chemical and microphysical properties of marine stratiform clouds in the North Atlantic, *J. Geophys. Res., 103(D17)*, 22,073-22,085, 1998.

Bruhwiler, L.P., and K. Hamilton, A numerical simulation of the stratospheric ozone quasi-biennial oscillation using a comprehensive general circulation model, *J. Geophys. Res., 104(D23)*, 30,525-30,557, 1999.

Butler, J.H., S.A. Montzka, A.D. Clarke, J.M. Lobert, and J.W. Elkins, Growth and distribution of halons in the atmosphere, *J. Geophys. Res., 103(D1)*, 1503-1511, 1998.

Butler, J.H., M. Battle, M.L. Bender, S.A. Montzka, A.D. Clarke, E.S. Saltzman, C.M. Sucher, J.P. Severinghaus, and J.W. Elkins, A record of atmospheric halocarbons during the twentieth century from polar firn air, *Nature, 399*, 749-755, 1999.

Carrico, C.M., M.J. Rood, and J.A. Ogren, Aerosol light scattering properties at Cape Grim, Tasmania, during the First Aerosol Characterization Experiment (ACE 1), *J. Geophys. Res., 103*, 16,565-16,574, 1998.

Chan, L.Y., H.Y. Liu, K.S. Lam, T. Lang, S.J. Oltmans, and J.M. Harris, Analysis of the seasonal behavior of tropospheric ozone at Hong Kong, *Atmos. Environ., 32(2)*, 159-168, 1998.

Ciais, P., P. Friedlingstein, D.S. Schimel, and P.P. Tans, A global calculation of the $\delta^{13}C$ of soil respired carbon: Implications for the biospheric uptake of anthropogenic CO_2, *Global Biogeochem. Cycles, 13(2)*, 519-530, 1999.

Conway, T.J., and P.P. Tans, Development of the CO_2 latitude gradient in recent decades, *Global Biogeochem. Cycles, 13(4)*, 821-826, 1999.

Cooper, O.R., J.L. Moody, J.C. Davenport, S.J. Oltmans, B.J. Johnson, X. Chen, P.B. Shepson, and J.T. Merrill, Influence of springtime weather systems on vertical ozone distributions over three North American sites, *J. Geophys. Res., 103(D17)*, 22,001-22,013, 1998.

Curtis, J., G. Wendler, R. Stone, and E. Dutton, Precipitation decrease in the western arctic, with special emphasis on Barrow and Barter Island, Alaska, *Int. J. Clim., 18*, 1687-1707, 1998.

Deshler, T., and S.J. Oltmans, Vertical profiles of volcanic aerosol and polar stratospheric clouds above Kiruna, Sweden: Winters 1993 and 1995, *J. Atmos. Chem., 30*, 11-23, 1998.

Dlugokencky, E.J., K.A. Masarie, P.M. Lang, and P.P. Tans, Continuing decline in the growth rate of the atmospheric methane burden, *Nature, 393*, 447-450, 1998.

Elkins, J.W., Chlorofluorocarbons (CFCs), in *Encyclopedia of Environmental Science,* D.E. Alexander and R.W. Fairbridge (eds.), pp. 78-80, Kluwer Academic, Boston, MA, 1999.

Elkins, J.W., J.H. Butler, S.A. Montzka, T.M. Thompson, D.J. Mondeel, L.T. Lock, G.S. Dutton, and M.R. Pender, NOAA/CMDL measurements of trace halocompounds and nitrous oxide from flask samples and in situ instrument at Alert, in *Canadian Baseline Program Summary of Progress to 1998*, pp. 5-24-5-30, Atmos. Environ., Service, Environment Canada, Toronto, 1999.

Feely, R.A., R. Wanninkhof, T. Takahashi, and P. Tans, Influence of El Niño on the equatorial Pacific contribution to atmospheric CO_2 accumulation, *Nature, 398*, 597-601, 1999.

Frost, G.J., M. Trainer, G. Allwine, M.P. Buhr, J.G. Calvert, C.A. Cantrell, F.C. Fehsenfeld, P.D. Goldan, J. Herwehe, G. Hübler, W.C. Kuster, R. Martin, R.T. McMillen, S.A. Montzka, R. B. Norton, D.D. Parrish, B.A. Ridley, R.E. Shetter, J.G. Walega, B.A. Watkins, H.H. Westberg, and E.J. Williams, Photochemical ozone production in the rural southeastern United States during the 1990 Rural Oxidants in the Southern Environment (ROSE) program, *J. Geophys. Res. 103(D17)*, 22,491-22,508, 1998.

Gao, R.S., D.W. Fahey, L.A. Del Negro, S.G. Donnelly, E.R. Keim, J.A. Neuman, E. Teverovskaia, P.O. Wennberg, T.F. Hanisco, E.J. Lanzendorf, M.H. Proffitt, J.J. Margitan, J.C. Wilson, J.W. Elkins, R.M. Stimpfle, R.C. Cohen, C.T. McElroy, T.P. Bui, R.J. Salawitch, S.S. Brown, A.R. Ravishankara, R.W. Portmann, M.K.W. Ko, D.K. Weisenstein, and P.A. Newman, A comparison of observations and model simulations of NO_x/NO_y in the lower stratosphere, *Geophys. Res. Lett., 26(8)*, 1153-1156, 1999.

Glosík, J., G. Bánó, E.E. Ferguson, and W. Lindinger, Selected ion flow drift tube study of the formation and dissociation of $CO^+.N_2$ ions in nitrogen buffer gas: the $CO^+.N_2$ bond energy, *Int. J. Mass Spectrom., 176,* 177-188, 1998.

Grant, W.B., R.B. Pierce, S.J. Oltmans, and E.V. Browell, Seasonal evolution of total and gravity wave induced laminae in ozonesonde data in the tropics and subtropics, *Geophys. Res. Lett., 25(11)*, 1863-1866, 1998.

Halthore, R.N., S. Nemesure, S.E. Schwartz, D.G. Imre, A. Berk, E.G. Dutton, and M.H. Bergin, Models overestimate diffuse clear-sky surface irradiance: A case for excess atmospheric absorption, *Geophys. Res. Lett., 25(19)*, 3591-3594, 1998.

Hansel, A., C. Scheiring, M. Glantschnig, W. Lindinger, and E.E. Ferguson, Thermochemistry of HNC, HNC^+, and CF_3^+, *J. Chem. Phys., 109(5)*, 1748-1750, 1998.

Hansel, A., M. Glantschnig, C. Scheiring, W. Lindinger, and E.E. Ferguson, Energy dependence of the isomerization of HCN^+ to HNC^+ via ion molecule reactions, *J. Chem. Phys., 109(5)*, 1743-1747, 1998.

Harris, J.M, S.J. Oltmans, E.J. Dlugokencky, P.C. Novelli, B.J. Johnson, and T. Mefford, An investigation into the source of the springtime tropospheric ozone maximum at Mauna Loa Observatory, *Geophys. Res. Lett., 25(11)*, 1895-1989, 1998.

Herman, R.L., D.C. Scott, C.R. Webster, R.D. May, E.J. Moyer, R.J. Salawitch, Y.L. Yung, G.C. Toon, B. Sen, J.J. Margitan, K.H. Rosenlof, H.A. Michelsen, and J.W. Elkins, Tropical entrainment time scales inferred from stratospheric N_2O and CH_4 observations, *Geophys. Res. Lett., 25(15)*, 2781-2784, 1998.

Heymsfield, A.J., L.M. Miloshevich, C. Twohy, G. Sachse, and S. Oltmans, Upper-tropospheric relative humidity observations and implications for cirrus ice nucleation, *Geophys. Res. Lett., 25(9)*, 1343-1346, 1998.

Hicke, J., A. Tuck, and H. Vömel, Lower stratospheric radiative heating rates and sensitivities calculated from Antarctic balloon observations, *J. Geophys. Res., 104(D8)*, 9293-9308, 1999.

Hintsa, E.J., P.A. Newman, H.H. Jonsson, C.R. Webster, R.D. May, R.L. Herman, L.R. Lait, M.R. Schoeberl, J.W. Elkins, P.R. Wamsley, G.S. Dutton, T.P. Bui, D.W. Kohn, and J. G. Anderson, Dehydration and denitrification in the Arctic polar vortex during the 1995-1996 winter, *Geophys. Res. Lett., 25*, 501-504, 1998.

Hintsa, E.J., E. M. Weinstock, J.G. Anderson, R.D. May, and D.F. Hurst, On the accuracy of in situ water vapor measurements in the troposphere and lower stratosphere with the Harvard Lyman-α hygrometer, *J. Geophys. Res., 104(D7)*, 8183-8189, 1999.

Hochlaf, M., C. Léonard, E.E. Ferguson, P. Rosmus, E.-A. Reinsch, S. Carter, and N.C. Handy, Potential energy function and vibrational states of N_2CO^+, *J. Chem. Phys., 111(11)*, 4948-4955, 1999.

Hofmann, D.J., R.S. Stone, M.E. Wood, T. Deshler, and J.M. Harris, An analysis of 25 years of balloonborne aerosol data in search of a signature of the subsonic commercial aircraft fleet, *Geophys. Res. Lett., 25(13)*, 2433-2436, 1998.

Hofmann, D.J., J.A. Pyle, J. Austin, N. Butchart, C.H. Jackman, D.K. Kinnison, F. Lefevre, G. Pitari, D.T. Shindell, R. Toumi, and P. von der Gathen, Predicitng future ozone changes and detection of recovery, in Chapter 12, Scientific Assessments of Ozone Depletion: 1998, World Meteorol. Organ. (WMO), *Global Ozone and Res. and Monitoring Project, Report 44*, 57 pp., 1999.

Hurst, D.F., P.S. Bakwin, and J.W. Elkins, Recent trends in the variability of halogenated trace gases over the United States, *J. Geophys. Res., 103(D19)*, 25,299-25,306, 1998.

Hurst, D.F., G.S. Dutton, P.A. Romashkin, P.R. Wamsley, F.L. Moore, J.W. Elkins, E.J. Hintsa, E.M. Weinstock, R.L. Herman, E.J. Moyer, D.C. Scott, R.D. May, and C.R. Webster, Closure of the total hydrogen budget of the northern extratropical lower stratosphere, *J. Geophys. Res., 104(D7)*, 8191-8200, 1999.

Jobson, B.T., S.A. McKeen, D.D. Parrish, F.C. Fehsenfeld, D.R. Blake, A.H. Goldstein, S.M. Schauffler, and J.W. Elkins, Trace gas mixing ratio variability versus lifetime in the troposphere and stratosphere: Observations, *J. Geophys. Res., 104(D13)*, 16,091-16,113, 1999.

Kahl, J.D.W., N.A. Zaitseva, V. Khattatov, R.C. Schnell, D.M. Bacon, J. Bacon, V. Radionov, and M.C. Serreze. Radiosonde observations from the former Soviet "North Pole" series of drifting ice stations, 1954-90, *Bull. Am. Meteorol. Soc., 80(10)*, 2019-2026, 1999.

Kallenborn, R., M. Oehme, D.D. Wynn-Williams, M. Schlabach, and J. Harris, Ambient air levels and atmospheric long-range transport of persistent organochlorines to Signy Island, Antarctica, *Sci. Total Environ., 220*, 167-180, 1998.

Kato, S., T.P. Ackerman, E.G. Dutton, N. Laulainen, and N. Larson, A comparison of modeled and measured surface shortwave irradiance for a molecular atmosphere, *J. Quan. Spectrosc. Radiat. Transfer, 61(4)*, 493-502, 1999.

Kinne, S., R. Bergstrom, O.B. Toon, E. Dutton, and M. Shiobara, Clear-sky atmospheric solar transmission: An analysis based on FIRE 1991 field experiment data, *J. Geophys. Res., 103(D16)*, 19,709-19,720, 1998.

Kitzis, D., and C. Zhao, CMDL/Carbon Cycle Gases Group standards preparation and stability, *NOAA TM ERL CMDL-14*, 14 pp., Environ. Res. Labs., Boulder, CO, 1999.

Knapp, K.G., M.L. Jensen, B.B. Balsley, J.A. Bognar, S.J. Oltmans, T.W. Smith, and J.W. Birks, Vertical profiling using a complementary kite and tethered balloon platform at Ferryland Downs, Newfoundland, Canada: Observation of a dry, ozone-rich plume in the free troposphere, *J. Geophys. Res., 103(D11)*, 13,389-13,397, 1998.

Koenig, G.L., S.J. Oltmans, J.A. Lathrop, R.D. Evans, B.J. Johnson, D.M. Quincy, and M.A. Clark, Umkehr observations at three automated Dobson spectrophotometer stations from 1983 to 1995, *Proc., XVIII Quad. Ozone Symp.*, R.D. Bojkov and G. Visconti (eds.), pp. 135-138, Parco Scientifico e Technologico d'Abruzzo, Italy, 1998.

Lloyd, S., W.H. Swartz, T. Kusterer, D. Anderson, C.T. McElroy, C. Midwinter, R. Hall, K. Nassim, D. Jaffe, W. Simpson, J. Kelley, D. Nicks, D. Griffin, B. Johnson, R. Evans, D. Quincy, S. Oltmans, P. Newman, R. McPeters, G. Labow, L. Moy, C. Seftor, G. Toon, B. Sen, and J.-F. Blavier, Intercomparison of total ozone observations at Fairbanks, Alaska, during POLARIS, *J. Geophys. Res., 104(D21)*, 26,767-26,778, 1999.

Maslanik, J.A., R. Stone, J. Pinto, J. Wendell, and C. Fowler, Mobile-platform observations of surface energy budget parameters at the SHEBA site, in *Proc., Fifth Conf. Polar Meteorol. and Ocean.*, Am. Meteorol. Soc., Dallas, TX, January 10-15, 1999.

Masarie, K., and P. Tans, Guidelines for atmospheric trace gas data management, *WMO GAW TD 907*, 46 pp., World Meteorol. Organ., Geneva, Switzerland, 1998.

Mészáros, E., A. Molnár, and J. Ogren, Scattering and absorption coefficients vs. chemical composition of fine atmospheric aerosol particles under regional conditions in Hungary, *J. Aerosol Sci., 29*, 1171-1178, 1998.

McInnes, L., M. Bergin, J. Ogren, and S. Schwartz, Apportionment of light scattering and hygroscopic growth to aerosol composition, *Geophys. Res. Lett., 25(4)*, 513-516, 1998.

McPeters, R.D., D.J. Hofmann, M. Clark, L. Flynn, L. Froidevaux, M. Gross, B. Johnson, G. Koenig, X. Liu, S. McDermid, T. McGee, F. Murcray, M.J. Newchurch, S. Oltmans, A. Parrish, R. Schnell, U. Singh, J.J. Tsou, T. Walsh, and J.M. Zawodny, Results from the 1995 stratospheric ozone profile intercomparison at Mauna Loa, *J. Geophys. Res., 104(D23)*, 30,505-30,514, 1999.

Michalsky, J., E. Dutton, M. Rubes, D. Nelson, T. Stoffel, M. Wesley, M. Splitt, and J. DeLuisi, Optimal measurement of surface shortwave irradiance using current instrumentation, *J. Atmos. Oceanic Technol., 16*, 55-69, 1999.

Miller, J.B., D. Yakir, J.W.C. White, and P.P. Tans, Measurement of $^{18}O/^{16}O$ in the soil-atmosphere CO_2 flux, *Global Biogeochem. Cycles, 13(3)*, 761-774, 1999.

Montzka, S.A., J.H. Butler, J.W. Elkins, T.M. Thompson, A.D. Clarke, and L.T. Lock, Present and future trends in the atmospheric burden of ozone-depleting halogens, *Nature, 398*, 690-694, 1999.

Munger, J.W., S.-M. Fan, P.S. Bakwin, M.L. Goulden, A.H. Goldstein, A.S. Colman, and S.C. Wofsy, Regional budgets for nitrogen oxides from continental sources: Variations of rates for oxidation and deposition with season and distance from source regions, *J. Geophys. Res,. 103(D7)*, 8355-8368, 1998.

Nelson, D.W., J. Hickey, N. Wood, and E. Dutton, Broadband direct solar beam measurements utilizing absolute cavity radiometers equipped with calcium fluoride windows, Preprint, 10th Conf. on Atmos. Radiation, Madison, WI, June 28-July 2, 1999, Am. Meteorol. Soc., Boston, MA, 205-207, 1999.

Novelli, P.C., K.A. Masarie, and P.M. Lang, Distributions and recent changes of carbon monoxide in the lower troposphere, *J. Geophys. Res., 103(D15)*, 19,015-19,033, 1998.

Novelli, P.C., V.S. Connors, H.G. Reichle, Jr., B.E. Anderson, C.A.M. Brenninkmeijer, E.G. Brunke, B.G. Doddridge, V.W.J.H. Kirchhoff, K.S. Lam, K.A. Masarie, T. Matsuo, D.D. Parrish, H.E. Scheel, and L.P. Steele, An internally consistent set of globally distributed atmospheric carbon monoxide mixing ratios developed using results from an intercomparison of measurements, *J. Geophys. Res., 103(D15)*, 19,285-19,293, 1998.

Novelli, P.C., P.M. Lang K.A. Masarie, D.F. Hurst, R. Myers, and J.W. Elkins, Molecular hydrogen in the troposphere: Global distribution and budget, *J. Geophys. Res., 104(D23)*, 30,427-30,444, 1999.

Ohmura, A., E.G. Dutton, B. Forgan, C. Fröhlich, H. Gilgen, H. Hegner, A. Heimo, G. König-Langlo, B. McArthur, G. Müller, R. Philipona, R. Pinker, C.H. Whitlock, K. Dehne, and M. Wild, Baseline surface radiation network (BSRN/WCRP): New precision radiometry for climate research, *Bull. Am. Meteorol. Soc., 79(10)*, 2115-2136, 1998.

Oltmans, S.J., A.S. Lefohn, H.E. Scheel, J.M. Harris, H. Levy II, I.E. Galbally, E.-G. Brunke, C.P. Meyer, J.A. Lathrop, B.J. Johnson, D.S. Shadwick, E. Cuevas, F.J. Schmidlin, D.W. Tarasick, H. Claude, J.B. Kerr, O. Uchino, and V. Mohnen Trends of ozone in the troposphere, *Geophys. Res. Lett., 25(2)*, 139-142, 1998.

Perry, K.D., T.A. Cahill, R.C. Schnell, and J.M. Harris, Long-range transport of anthropogenic aerosols to the National Oceanic and Atmospheric Administration baseline station at Mauna Loa Observatory, Hawaii, *J. Geophys. Res., 104(D15)*, 18,521-18,533, 1999.

Peterson, M.C., R.E. Honrath, D.D. Parrish, and S.J. Oltmans, Measurements of nitrogen oxides and a simple model of NO_y fate in the remote North Atlantic marine atmosphere, *J. Geophys. Res., 103(D11)*, 13,489-13,503, 1998.

Peylin, P., P. Ciais, A.S. Denning, P.P. Tans, J.A. Berry, and J.W.C. White, A 3-dimensional study of $\delta^{18}O$ in atmospheric CO_2: Contribution of different land ecosystems, *Tellus, 51B*, 642-667, 1999.

Philipona, R., C. Frohlich, K. Dehne, J. DeLuisi, J. Augustine, E. Dutton, D. Nelson, B. Forgan, P. Novotny, J. Hickey, S.P. Love, S. Bender, B. McArthur, A. Ohmura, J.H. Seymour, J.S. Foot, M. Shiobara, F.P.J. Valero, and A. W. Strawa, The baseline surface radiation network pyrgeometer round-robin calibration experiment, *J. Atmos. Oceanic Technol., 15(3)*, 687-696, 1998.

Pinto, J.O., J.A. Curry, J.A. Maslanik, C.W. Fairall, and R.S. Stone, Horizontal variability in surface radiative fluxes surrounding SHEBA from airborne and ground-based sensors, in *Proc., Fifth Conf. on Polar Meteorol. and Ocean.*, Am. Meteorol. Soc., Dallas, TX, January 10-15, 319-320, 1999.

Pinto, J.O., J.A. Curry, J. A. Maslanik, C.W. Fairall, and R.S. Stone, Surface energy budget and atmospheric effects of a freezing lead at SHEBA, in *Proc., Fifth Conf. on Polar Meteorol. and Ocean.*, Am. Meteorol. Soc., Dallas, TX, January 10-15, 397-400, 1999.

Polissar, A.V., P.K. Hopke, J.M. Harris, B.A. Bodhaine, and E.G. Dutton, Source regions for atmospheric aerosol measured in the western Arctic, *J. Aerosol Sci., 29*, S513-S514, 1998.

Polissar, A.V., P.K. Hopke, P. Paatero, Y.J. Kaufmann, D.K. Hall, B.A. Bodhaine, E.G. Dutton, and J.M. Harris, The aerosol at Barrow, Alaska: Long-term trends and source locations, *Atmos. Environ., 33*, 2441-2458, 1999.

Quay, P., J. Stutsman, D. Wilbur, A. Snover, E. Dlugokencky, and T. Brown, The isotopic composition of atmospheric methane, *Global Biogeochem. Cycles, 13(2)*, 445-461, 1999.

Randerson, J.T., C.B. Field, I.Y Fung, and P.P. Tans, Increases in early season ecosystem uptake explain recent changes in the seasonal cycle of atmospheric CO_2 at high northern latitudes, *Geophys. Res. Lett., 26*, 2765-2768, 1999.

Ray, E.A., F.L. Moore, J.W. Elkins, G.S. Dutton, D.W. Fahey, H. Vömel, S.J. Oltmans, and K.H. Rosenlof, Transport into the northern hemisphere lowermost stratosphere revealed by in situ tracer measurements, *J. Geophys. Res., 104(D21)*, 26,565-26,580, 1999.

Ridley, B., J. Walega, G. Hübler, D. Montzka, E. Atlas, D. Hauglustaine, F. Grahek, J. Lind, T. Campos, R. Norton, J. Greenberg, S. Schauffler, S. Oltmans, and S. Whittlestone, Measurements of NO_x and PAN and estimates of O_3 production over the seasons during Mauna Loa Observatory Photochemistry Experiment 2, *J. Geophys. Res., 103(D7)*, 8323-8339, 1998.

Romashkin, P.A., D.F. Hurst, J.W. Elkins, G.S. Dutton, and P.R. Wamsley, Effect of the tropospheric trend on the stratospheric tracer-tracer correlations: Methyl chloroform, *J. Geophys. Res., 104(D21)*, 26,643-26,652, 1999.

Running, S.W., D.D. Baldocchi, D.P. Turner, S.T. Gower, P.S. Bakwin, and K.A. Hibbard, A global terrestrial monitoring network integrating tower fluxes, flask sampling, ecosystem modeling and EOS satellite data, *Remote Sens. Environ., 70*, 108-127, 1999.

Sen, B., G.B. Osterman, R.J. Salawitch, G.C. Toon, J.J. Margitan, J.-F. Blavier, A.Y. Chang, R.D. May, C.R. Webster, R.M. Stimpfle, G.P. Bonne, P.B. Voss, K.K. Perkins, J.G. Anderson, R.C. Cohen, J.W. Elkins, G.S. Dutton, D.F. Hurst, P.A. Romashkin, E.L. Atlas, S.M. Schaufler, and M. Lowenstein, The budget and partitioning of stratospheric chlorine during the 1997 Arctic summer, *J. Geophys. Res., 104(D21)*, 26,653-26,665, 1999.

Sheridan, P.J., and R.B. Norton, Determination of the passing efficiency for aerosol chemical species through a typical aircraft-mounted, diffuser-type aerosol inlet system, *J. Geophys. Res., 103(D7)*, 8215-8225, 1998.

Sheridan, P.J., and J.A. Ogren, Observations of the vertical and regional variability of aerosol optical properties over central and eastern North America, *J. Geophys. Res., 104(D14)*, 16,793-16,805, 1999.

Slusser, J., J. Gibson, D. Bigelow, D. Kolinski, W. Mou, G. Koenig, and A. Beaubien, Comparison of column ozone retrievals by use of an UV multifilter rotating shadow-band radiometer with those from Brewer and Dobson spectrophotometers, *Appl. Opt., 38(9)*, 1543-1551, 1999.

Solomon, S., R.W. Portmann, R.W. Sanders, J.S. Daniel, W. Madsen, B. Bartram, and E.G. Dutton, On the role of nitrogen dioxide in the absorption of solar radiation, *J. Geophys. Res., 104(D10)*, 12,047-12,058, 1999.

Stimpfle, R.M., R.C. Cohen, G.P Bonne, P.B. Voss, K.K. Perkins, L.C. Koch, J.G. Anderson, R.J. Salawitch, S.A. Lloyd, R.S. Gao, L.A. Del Negro, E.R. Keim, and T.P. Bui, The coupling of $ClONO_2$, ClO, and NO_2 in the lower stratosphere from in situ observations using the NASA ER-2 aircraft, *J. Geophys. Res., 104(D21)*, 26,705-26,714, 1999.

Stone, R.S., Variations in western Arctic temperatures in response to cloud radiative and synoptic-scale influences, *J. Geophys. Res., 102(D18)*, 21,769-21,776, 1998.

Strawa, A.W., K. Drdla, G.V. Ferry, S.Verma, R.F. Pueschel, M. Yasuda, R.J. Salawitch, R.S. Gao, S.D. Howard, P.T. Bui, M. Loewenstein, J.W. Elkins, K.K. Perkins, and R. Cohen, Carbonaceous aerosol (soot) measured in the lower stratosphere during POLARIS and its role in stratospheric photochemistry, *J. Geophys. Res., 104(D21)*, 26,753-26,766, 1999.

Tans, P.P., and D.W.R. Wallace, Carbon cycle research after Kyoto, *Tellus, 51B*, 562-571, 1999.

Toon, G.C., J.-F. Blavier, B. Sen, J.J. Margitan, C.R. Webster, R.D. May, D. Fahey, R. Gao, L. Del Negro, M. Proffitt, J. Elkins, P.A. Romashkin, D.F. Hurst, S. Oltmans, E. Atlas, S. Schauffler, F. Flocke, T.P. Bui, R.M. Stimpfle, G.P. Bonne, P.B. Voss, and R.C. Cohen, Comparison of MkIV balloon and ER-2 aircraft measurements of atmospheric trace gases, *J. Geophys. Res., 104(D21)*, 26,779-26,790, 1999.

Tyler, S.C., H.O. Ajie, M.L. Gupta, R.J. Cicerone, D.R. Blake, and E.J. Dlugokencky, Stable carbon isotopic composition of atmospheric methane: A comparison of surface level and free tropospheric air, *J. Geophys. Res., 104(D11)*, 13,895-13,910, 1999.

Vömel, H., and S. J. Oltmans, Comment on "A reexamination of the "stratospheric fountain" hypothesis" by A. E. Dessler, *Geophys. Res. Lett., 26,* 2737-2738, 1999.

Wamsley, P.R., J.W. Elkins, D.W. Fahey, G.S. Dutton, C.M. Volk, R.C. Myers, S.A. Montzka, J.H. Butler, A.D. Clarke, P.J. Fraser, L.P. Steele, M.P. Lucarelli, E.L. Atlas, S.M. Schauffler, D.R. Blake, F.S. Rowland, W.T. Sturges, J.M. Lee, S.A. Penkett, A. Engel, R.M. Stimpfle, K.R. Chan, D.K. Weisenstein, M.K.W. Ko, and R.J. Salawitch, Distribution of halon-1211 in the upper troposphere and lower stratosphere and the 1994 total bromine budget, *J. Geophys. Res,. 103(D1)*, 1513-1526, 1998.

Weatherhead, E.C., G.C. Reinsel, G.C. Tiao, X.-L. Meng, D. Choi, W.-K. Cheang, T. Keller, J. DeLuisi, D.J. Wuebbles, J.B. Kerr, A.J. Miller, S.J. Oltmans, and J.E. Frederick, Factors affecting the detection of trends: Statistical considerations and applications to environmental data, *J. Geophys. Res., 103(D14)*, 17,149-17,161, 1998.

Weinheimer, A.J., D.D. Montzka, T.L. Campos, J.G. Walega, B.A. Ridley, S.G. Donnelly, E.R. Keim, L.A. Del Negro, M.H. Proffitt, J.J. Margitan, K.A. Boering, A.E. Andrews, B.C. Daube, S.C. Wofsy, B.E. Anderson, J.E. Collins, G.W. Sachse, S.A. Vay, J.W. Elkins, P.R. Wamsley, E.L. Atlas, F. Flocke, S. Schauffler, C.R. Webster, R.D. May, M. Loewenstein, J.R. Podolske, T.P. Bui, K.R. Chan, S.W. Bowen, M.R. Schoeberl, L.R. Lait, and P.A. Newman, Comparison between DC-8 and ER-2 species measurements in the tropical middle troposphere: NO, NO_y, O_3, CO_2, CH_4, and N_2O, *J. Geophys. Res., 103(D17)*, 22,087-22,096, 1998.

Wong, A.M., J.R. Key, and R.S. Stone, The effect of clouds on surface temperature and implications for remote sensing at high latitudes, in *Proc., Fifth Conference on Polar Meteorology and Oceanography*, Am. Meteorol. Soc., Dallas, TX, January 10-15, 294-299, 1999.

8. Specialized Abbreviations and Acronyms

ACATS	Airborne Chromatograph for Atmospheric Trace Species
ACCENT	Atmospheric Chemistry and Combustion Effects Near the Tropopause
ACE	Aerosol Characterization Experiment
AERONET	Aerosol Robotics Network (NASA)
AES	Atmospheric Environment Service (Canada)
AIRKIT	Air Kitzis sampler
ALT	Alert, Canada
ANSTO	Australian Nuclear Science and Technology Organization
AO	Arctic Oscillation
APO	Atmospheric Potential Oxygen
ARM	Atmospheric Radiation Measurement (DOE)
ARO	Atmospheric Research Observatory (South Pole, Antarctica)
ASA	Antarctic Support Associates
ATLAS	Arctic Transmissions in the Land-Atmosphere System
ATMOS	Atmospheric Trace Molecule Spectroscopy
BACPAC	Bromine Air-sea Cruise Pacific
BAO	Boulder Atmospheric Observatory
BBC	British Broadcasting Company
BC	black carbon
BIF	Balloon Inflation Facility
BND	Bondville, Illinois
BRW	Barrow Observatory, Barrow, Alaska (CMDL)
BSI	Biospherical Instruments Inc., San Diego, California
BSRN	Baseline Surface Radiation Network
CAF	Clean Air Facility (South Pole, Antarctica)
CAMS	Control and Monitoring System
CART	Cloud and Radiation Testbed
CATS	Chromatograph for Atmospheric Trace Species
CCGG	Carbon Cycle Greenhouse Gases Group (CMDL)
CCN	cloud condensation nuclei
CEPEX	Central Equatorial Pacific Experiment
CERES	Clouds and Earth's Radiant Energy System
CFC	chlorofluorocarbon
CGO	Cape Grim Observatory, Tasmania, Australia
ChEAS	Chequamegon Ecosystem/Atmosphere Study
CIRES	Cooperative Institute for Research in Environmental Sciences (University of Colorado)
CMDL	Climate Monitoring and Diagnostics Laboratory (NOAA)
CN	condensation nuclei
CNC	condensation nuclei counter
COBRA	CO_2 Budget and Rectification Airborne
CSIRO	The Commonwealth Scientific and Industrial Research Organization (Australia)
DEW	distant early warning
DIAL	differential absorption lidar
DOC	U.S. Department of Commerce
DOE	U.S. Department of Energy
DSRC	David Skaggs Research Center (Boulder, Colorado)
DU	Dobson unit
ECl	equivalent chlorine
ECC	electrochemical cell
ECD	electron capture detector
ECMWF	European Center for Medium-Range Weather Forecasts
EECl	effective equivalent chlorine
ENEA	Ente per le Nuove Tecnologie, l'Energia e l'Ambiente (Italy)
EOS	Earth Observing System
EPA	Environmental Protection Agency
ETL	Environmental Technology Laboratory (NOAA)
FID	flame ionization detector
FSU	Former Soviet Union
FTIR	Fourier transform infrared (spectrometer)
FWHM	full width at half maximum
FWNIP	filter wheel normal incidence pyrheliometer
FWS	U.S. Fish and Wildlife Service
GASEX	Gas Exchange Experiment
GAW	Global Atmospheric Watch
GC	gas chromatograph
GC-ECD	gas chromatograph with electron capture detection

GCM	general circulation model
GC-MS	gas chromatograph with mass selective detection
GEOSECS	Geochemical Ocean Sections
GFDL	Geophysical Fluid Dynamics Laboratory (NOAA)
GMCC	Geophysical Monitoring for Climatic Change (now CMDL) (NOAA)
GPS	Global Positioning System
HALOE	HALogen Occultation Experiment
HATS	Halocarbons and other Atmospheric Trace Species Group (CMDL)
HCFC	hydrochlorofluorocarbon
HFC	hydrofluorocarbon
HMF	Harvard Forest, Massachusetts
HNH	high northern hemisphere
HOA	Health of the Atmosphere Air Quality Research Program (NOAA)
HP	Hewlett Packard
IAC	Institute of Atmospheric Chemistry (China)
ICP	InterComParison
INDOEX	Indian Ocean Experiment
INSTAAR	Institute for Arctic and Alpine Research (University of Colorado)
IPASRC-I	International Pyrgeometer and All-sky Scanning Radiometer Comparison
IPC	International Pyrheliometer Comparison
IR	infrared
ITCZ	Intertropical Convergence Zone
ITN	Grifton, North Carolina
JGOFS	Joint Global Ocean Flux Study
JPL	Jet Propulsion Laboratory
KUM	Cape Kumukahi, Hawaii
LACE	Lightweight Airborne Chromatograph Experiment
LEAPS	Low Electron Attachment Potential Species
LEF	Park Falls, Wisconsin
MAKS	Martin and Kitzis Sampler
MBL	marine boundary layer
MFRSR	multifilter rotating shadowband radiometer
MHS	Mace Head, Ireland
MLO	Mauna Loa Observatory, Hawaii (CMDL)
MODTRAN	Moderate Resolution Transmittance Model
MOPITT	Measurement Of Pollution In The Troposphere
MRI	Meteorology Research, Inc.
MSC	Meteorological Service of Canada
MSD	mass selective detector
MSISE	mass spectrometer incoherent scatter – extended (extended below mesopause from original thermospheric MSIS-86)
NARL	Naval Arctic Research Laboratory
NASA	National Aeronautics and Space Administration
NCAR	National Center for Atmospheric Research
NCDC	National Climatic Data Center
NCEP	National Centers for Environmental Prediction (NOAA)
NDIR	non-dispersive infrared analyzer
NDSC	Network for the Detection of Stratospheric Change
Nd:YAG	neodymium doped yttrium aluminum garnet (type of laser)
NEE	net ecosystem exchange
NILU	Norwegian Institute for Air Research
NIP	normal incidence pyrheliometer
NIST	National Institute of Standards and Technology (U.S. Dept. of Commerce)
NIWA	National Institute for Water and Atmospheric Research (New Zealand)
NOAA	National Oceanic and Atmospheric Administration (U.S. Dept. of Commerce)
NOAH	Nitrous Oxide and Halocompounds (CMDL)
NPC	NREL Pyrheliometer Comparison
NREL	National Renewable Energy Laboratory
NRL	Naval Research Laboratory
NSA	North Slope, Alaska
NSF	National Science Foundation
NWR	Niwot Ridge, Colorado
NWS	National Weather Service (NOAA)
OAR	Oceanic and Atmospheric Research (NOAA)
OD	outside diameter
ODR	orthogonal distance regression
OMS	Observations of the Middle Stratosphere
OTTO	automated flask GC-ECD instrument
PAN	peroxyacetyl nitrate
PANTHER	PAN and Trace Hydrohalocarbon ExpeRiment
PAR	photosynthetically active radiation

PBL	planetary boundary layer
PCB	polychlorinated biphenyl
PEM Tropics	Pacific Exploratory Mission in the Tropics (a global troposphere experiment)
PFR	Precision filter radiometer
PMOD	Physikalisch-Meteorologisches Observatorium Davos (World Radiation Center)
POLARIS	Photochemistry of Ozone Loss in the Arctic Region in Summer
PPLN	periodically poled lithium niobate
PSA	Palmer Station, Antarctica
PSAP	particle soot absorption photometer
QBO	quasi-biennial oscillation
RAF	Radiative amplification factor
RCF	Radiometer Calibration Facility
RF	radio frequency
RITS	Radiatively Important Trace Species
SA	saturation anomaly
SAFARI	Southern African Fire-Atmosphere Research Initiative
SAGE	Stratospheric Aerosol and Gas Experiment
SC	sky cover
S.D.	standard deviation
SEAREX	Sea-Air Exchange Experiment
SEASPAN	SEAREX South Pacific Aerosol Network
SGP	Southern Great Plains (Lamont, Oklahoma)
SHADOZ	Southern Hemisphere Additional Ozone Soundings
SHEBA	Study of the Heat Budget in the Arctic
SIO	Scripps Institution of Oceanography (University of California, San Diego)
SMO	Samoa Observatory, American Samoa (CMDL)
SOLVE	SAGE-III Ozone Loss and Validation Experiment
SOS	Southern Oxidant Study
SOWER	Special Observations of Ozone and Water in the Equatorial Region
SPCZ	South Pacific Convergence Zone
SPO	South Pole Observatory, Antarctica (CMDL)
SRF	solar radiation facility
SRM	Standard Research Material
STAR	Solar and Thermal Atmospheric Radiation Group (CMDL)
STRAT	Stratospheric Tracers of Atmospheric Transport
SUNY	State University of New York
SZA	solar zenith angle
TDL	tunable diode laser
TEI	thermal electron instrument
TIES	Tracer Intercomparison Experiment for SOLVE
TMF	Table Mountain Facility
TOMS	Total Ozone Mapping Spectrometer
TSI	Thermo Systems Incorporated
UCI	University of California, Irvine
UIC	Ukpeagvik Inupiat Corporation (Alaska)
UNEP	United Nations Environmental Programme
UPS	uninterruptible power supply
URAS	(a commercial CO_2 analyzer)
USDA	United States Department of Agriculture
USGS	United States Geological Survey
UTC	Universal Time Coordinated
UV	ultraviolet
UVB	ultraviolet B band
VIS	visible
WCRP	World Climate Research Program
WEPC	water equivalent precipitation
WMO	World Meteorological Organization, Geneva, Switzerland
WOCE	World Ocean Circulation Experiment
WODC	World Ozone Data Centre
WOUDC	World Ozone and Ultraviolet Data Centre (Canada)
WRC	World Radiation Center
WRR	World Radiation Reference
WSA	Sable Island, Canada
WVMS	Water Vapor Millimeter-wave Spectrometer